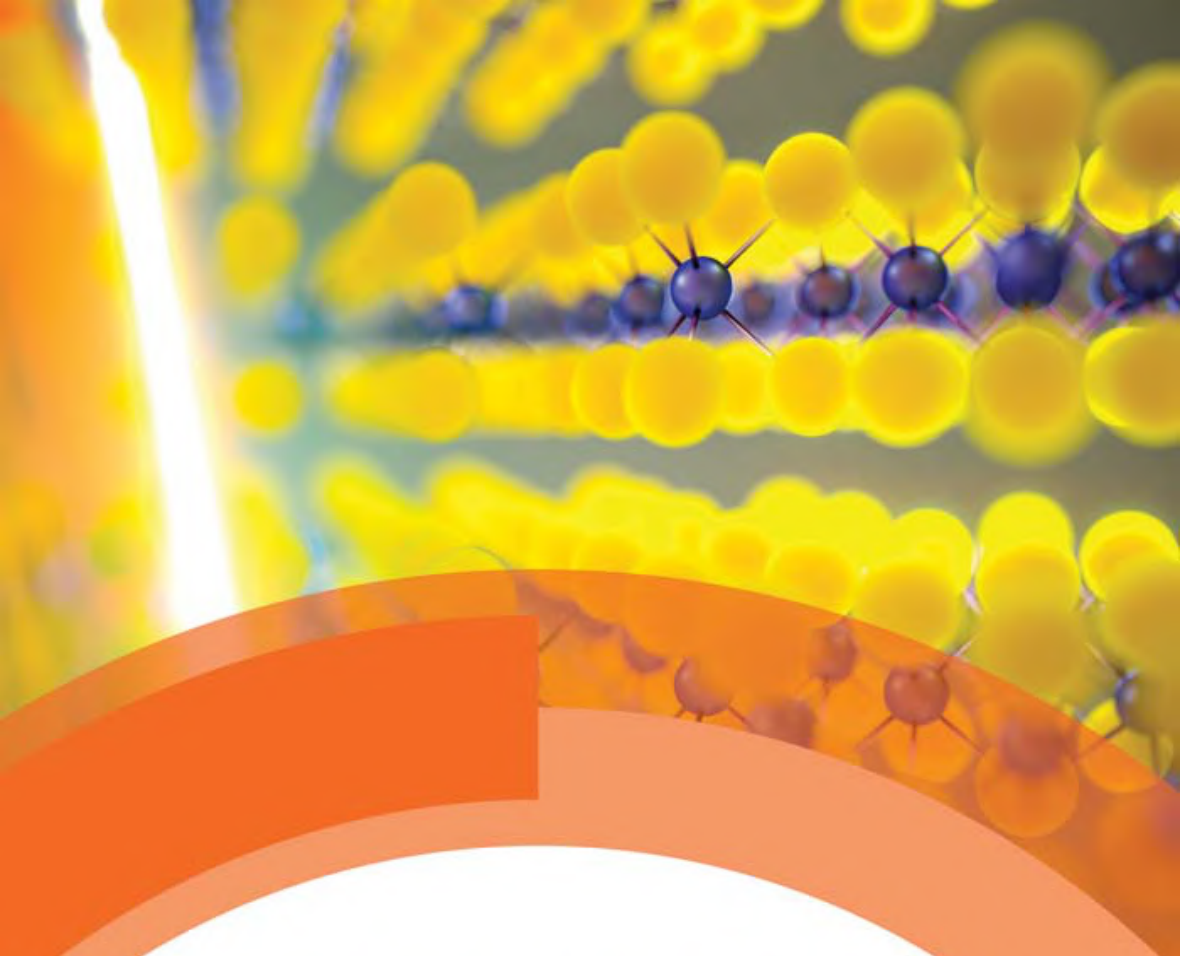

Nanoscience & Nanotechnology Series

Photothermal Nanomaterials

Edited by Enyi Ye and Zibiao Li

ROYAL SOCIETY OF CHEMISTRY

Photothermal Nanomaterials

Nanoscience & Nanotechnology Series

Editor-in-chief:
Nguyễn T. K. Thanh, *University College London, UK*

Series editors:
Gabriel Caruntu, *Central Michigan University, USA*
Shinya Maenosono, *Japan Advanced Institute of Science and Technology, Japan*
Neerish Revaprasadu, *University of Zululand, South Africa*

Titles in the series:
1: Nanotubes and Nanowires
2: Fullerenes: Principles and Applications
3: Nanocharacterisation
4: Atom Resolved Surface Reactions: Nanocatalysis
5: Biomimetic Nanoceramics in Clinical Use: From Materials to Applications
6: Nanofluidics: Nanoscience and Nanotechnology
7: Bionanodesign: Following Nature's Touch
8: Nano-Society: Pushing the Boundaries of Technology
9: Polymer-based Nanostructures: Medical Applications
10: Metallic and Molecular Interactions in Nanometer Layers, Pores and Particles: New Findings at the Yoctolitre Level
11: Nanocasting: A Versatile Strategy for Creating Nanostructured Porous Materials
12: Titanate and Titania Nanotubes: Synthesis, Properties and Applications
13: Raman Spectroscopy, Fullerenes and Nanotechnology
14: Nanotechnologies in Food
15: Unravelling Single Cell Genomics: Micro and Nanotools
16: Polymer Nanocomposites by Emulsion and Suspension
17: Phage Nanobiotechnology
18: Nanotubes and Nanowires, 2nd Edition
19: Nanostructured Catalysts: Transition Metal Oxides
20: Fullerenes: Principles and Applications, 2nd Edition
21: Biological Interactions with Surface Charge Biomaterials
22: Nanoporous Gold: From an Ancient Technology to a High-Tech Material
23: Nanoparticles in Anti-Microbial Materials: Use and Characterisation
24: Manipulation of Nanoscale Materials: An Introduction to Nanoarchitectonics
25: Towards Efficient Designing of Safe Nanomaterials: Innovative Merge of Computational Approaches and Experimental Techniques
26: Polymer–Graphene Nanocomposites
27: Carbon Nanotube-Polymer Composites
28: Nanoscience for the Conservation of Works of Art
29: Polymer Nanofibers: Building Blocks for Nanotechnology

30: Artificial Cilia
31: Nanodiamond
32: Nanofabrication and its Application in Renewable Energy
33: Semiconductor Quantum Dots: Organometallic and Inorganic Synthesis
34: Soft Nanoparticles for Biomedical Applications
35: Hierarchical Nanostructures for Energy Devices
36: Microfluidics for Medical Applications
37: Nanocharacterisation, 2nd Edition
38: Thermometry at the Nanoscale: Techniques and Selected Applications
39: Nanoceramics in Clinical Use: From Materials to Applications, 2nd Edition
40: Near-infrared Nanomaterials: Preparation, Bioimaging and Therapy Applications
41: Nanofluidics, 2nd Edition
42: Nanotechnologies in Food, 2nd Edition
43: ZnO Nanostructures: Fabrication and Applications
44: Diatom Nanotechnology: Progress and Emerging Applications
45: Nanostructured Materials for Type III Photovoltaics
46: Chemically Derived Graphene: Functionalization, Properties and Applications
47: Graphene-based Membranes for Mass Transport Applications
48: Carbon Nanostructures for Biomedical Applications
49: Surface Chemistry of Colloidal Nanocrystals
50: Reducing Agents in Colloidal Nanoparticle Synthesis
51: Carbon Nitride Nanostructures for Sustainable Energy Production and Environmental Remediation
52: Nanotubes and Nanowires, 3rd Edition
53: Bionanodesign: Old Forms for New Functions, 2nd Edition
54: Photothermal Nanomaterials

How to obtain future titles on publication:
A standing order plan is available for this series. A standing order will bring delivery of each new volume immediately on publication.

For further information please contact:
Book Sales Department, Royal Society of Chemistry, Thomas Graham House, Science Park, Milton Road, Cambridge, CB4 0WF, UK
Telephone: +44 (0)1223 420066, Fax: +44 (0)1223 420247
Email: booksales@rsc.org
Visit our website at www.rsc.org/books

Photothermal Nanomaterials

Edited by

Enyi Ye
*A*STAR, Singapore*
Email: yeey@imre.a-star.edu.sg

and

Zibiao Li
*A*STAR, Singapore*
Email: lizb@imre.a-star.edu.sg

ROYAL SOCIETY OF CHEMISTRY

Nanoscience & Nanotechnology Series No. 54

Print ISBN: 978-1-83916-238-1
PDF ISBN: 978-1-83916-517-7
EPUB ISBN: 978-1-83916-518-4
Print ISSN: 1757-7136
Electronic ISSN: 1757-7144

A catalogue record for this book is available from the British Library

The Royal Society of Chemistry is a charity, registered in England and Wales, Number 207890, and a company incorporated in England by Royal Charter (Registered No. RC000524), registered office: Burlington House, Piccadilly, London W1J 0BA, UK, Telephone: +44 (0) 20 7437 8656.

For further information see our web site at www.rsc.org

Printed in the United Kingdom by CPI Group (UK) Ltd, Croydon, CR0 4YY, UK

Preface

Nanomaterials have been researched extensively in academia because of their unique properties depending on their size, shape, and composition. They have also been optimized and used for a lot of applications. As a result, a huge amount of literature in this area has been published in many academic journals, patents, and application-specific references. However, very few of these discuss photothermal nanomaterials in detail, despite the fact that many nanomaterials exhibited photothermal properties and their applications have been extensively researched in recent years. Light–matter interaction has been of great interest for centuries, among which light-to-heat conversion has drawn much attention in previous years. The exploration of photothermal nanomaterials with high light-to-heat conversion efficiency paved the way for practical applications. In this book, the photothermal effect of different categories of light-absorbing nanomaterials is reviewed and discussed, focusing on metallic nanomaterials, 2D materials, semiconductors, carbon-based nanomaterials, polymeric nanomaterials, and their composites. Recent advancement in their preparation and photothermal applications are introduced and summarized in detail. This book provides a systematic summary of the recent advances in the fabrication and application of photothermal nanomaterials, together with the advantages, challenges and potential opportunities. Thus, we believe the publication of this book will greatly facilitate the reader in gaining a comprehensive and systematic overview of the latest developments in photothermal nanomaterials and their applications.

We gratefully acknowledge all the authors and the Royal Society of Chemistry editorial office for helping to complete this book. We would like

Nanoscience & Nanotechnology Series No. 54
Photothermal Nanomaterials
Edited by Enyi Ye and Zibiao Li

Published by the Royal Society of Chemistry, www.rsc.org

to extend gratitude to our colleagues who helped in reviewing this book. We also acknowledge the financial support provided by the Institute of Materials Research and Engineering (IMRE) under the Agency of Science, Technology and Research (A*STAR).

Enyi Ye and Zibiao Li

Contents

Nanoscience & Nanotechnology Series No. 54
Photothermal Nanomaterials
Edited by Enyi Ye and Zibiao Li

Published by the Royal Society of Chemistry, www.rsc.org

CHAPTER 1

Introduction to Photothermal Nanomaterials

SI YIN TEE,[a] KHIN YIN WIN,[a] SHERMIN S. GOH,[a] CHOON PENG TENG,[a] KAREN YUANTING TANG,[a] MICHELLE D. REGULACIO,[b] ZIBIAO LI*[a] AND ENYI YE*[a]

[a] Institute of Materials Research and Engineering, Agency for Science, Technology and Research, 2 Fusionopolis Way, Singapore 138634, Singapore; [b] Institute of Chemistry, University of the Philippines Diliman, Quezon City 1101, Philippines
*Emails: lizb@imre.a-tar.edu.sg; yeey@imre.a-star.edu.sg

1.1 Introduction

Advances in nanotechnology have resulted in a library of functional nanomaterials with well-defined size, shape, composition, and surface functionalities that enable the conversion of low-density light energy to thermal energy, known as photothermal materials. They have attracted extensive research interest among scientists for their great promise in many practical applications ranging from biomedical to environmental fields. In biomedical applications, the photothermal effect is typically stimulated by near infrared (NIR) light, which enables high penetration depth and minimal invasiveness to biological tissues. The emerging methods in the diagnosis and treatment of cancer that rely on photothermal effects show benefits of high selectivity and precision as well as low invasiveness to normal cells which reduce the significant side effects of the conventional treatment methods. Upon NIR laser irradiation, the induced photothermal effect elevates the temperature within the tumor and

Nanoscience & Nanotechnology Series No. 54
Photothermal Nanomaterials
Edited by Enyi Ye and Zibiao Li

Published by the Royal Society of Chemistry, www.rsc.org

causes irreversible destruction to cancer cell membranes, protein denaturation, and followed by cell death, while sparing the healthy cells.[1,2] Similarly, nanomaterials with NIR-responsive photothermal effects can have good capacity for fighting bacterial infections using the produced heat to inhibit the growth of bacteria as well as prevent bacterial biofilm formation.

Photothermally active materials have also emerged as a frontier area of research for their potential application in solar-driven vapor generation in aqueous systems.[3–6] In this regard, photothermal conversion is the simplest way to utilize NIR light in the solar light spectrum for practical transformation of solar energy into thermal energy. Accordingly, the NIR radiation in the range of 780–2500 nm constitutes nearly half of the solar energy. The solar-driven water evaporation (*e.g.* seawater desalination and wastewater purification) represents one of the most promising green and sustainable solutions through combining two of the most abundant resources on Earth (*i.e.* solar energy and water) for low-energy fresh water production. This technology is based on the harvesting of solar energy by a photothermal material and converting it to thermal energy for heating up liquid water to generate steam.[5,7]

Material and structural design are the most important criteria for photothermal applications. Over recent decades, a great number of NIR-responsive photothermal materials and structural engineering strategies have been developed to suit different applications. In general, photothermal materials can be categorized into four functional categories, such as plasmonic metals, semiconductors, carbon-, and polymer-based materials. The photothermally active plasmonic metals are mainly comprised of nanostructures of noble metals (*e.g.* Au, Ag, Pd) while semiconductors are composed of transition metal oxides (*e.g.* WO_3, Fe_3O_4), transition metal chalcogenides (*e.g.* CuS, Cu_2Se), and transition metal dichalcogenides (*e.g.* WS_2, MoS_2). The diversified carbon-based nanomaterials are based on 1D, 2D, and 3D architectures (*e.g.* carbon nanotubes, graphene) and polymer-based materials including conjugated polymers (*e.g.* polyaniline, polypyrrole) as well as crystalline porous organic polymers (*e.g.* covalent organic framework). In this book chapter, we will first (1) introduce the fundamentals of various photothermal conversion mechanisms and (2) review the recent development of unique nanomaterials and related nanostructures that exhibit outstanding photothermal performance, as well as their (3) potential applications in photothermal therapy (PTT), photothermal sterilization and solar-driven water evaporation. Finally, we (4) present a summary and the perspectives of photothermal materials (see Figure 1.1).

1.2 Photothermal Conversion Mechanism

Photothermal effect refers to the temperature increase of a material due to the absorption of light. The distinct photothermal effect induced by nanostructured photothermal materials can reduce the defined region of heat modulation to the nanoscale. Considering the different light–matter interactions in various materials that relate to their inherent electronic or

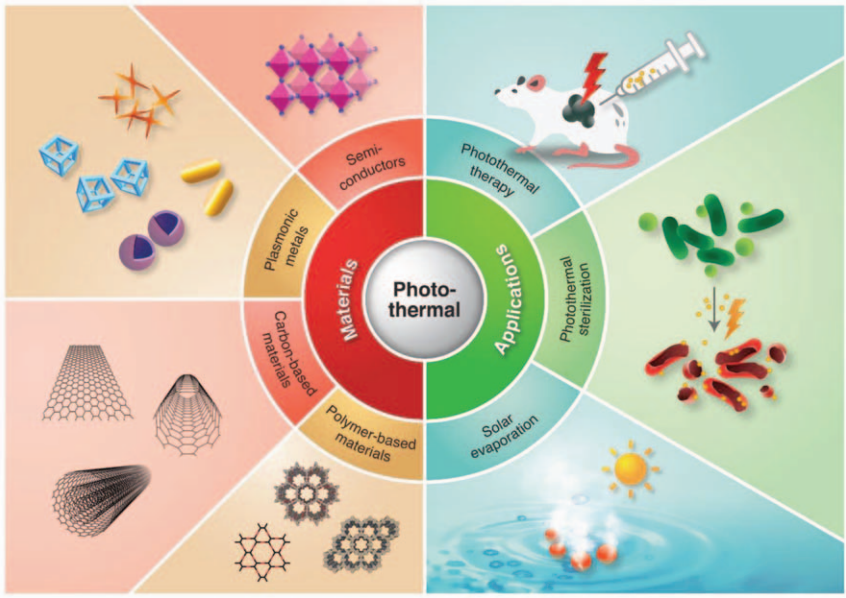

Figure 1.1 Schematic illustration of the development of photothermal materials (plasmonic metals, semiconductors, carbon-based materials, polymer-based materials) and applications (photothermal therapy, photothermal sterilization, solar evaporation).
The figure of carbon-based materials is reproduced from ref. 8, https://doi.org/10.3390/app9112174, under the terms of the CC BY 4.0 license, https://creativecommons.org/licenses/by/4.0/. The figure of polymer-based materials is reproduced from ref. 9 with permission from American Chemical Society, Copyright 2020.

bandgap structures, photothermal conversion mechanisms can be categorized into three main groups: (1) plasmonic localized heating of metals, (2) electron–hole generation and relaxation of semiconductors, and (3) HOMO–LUMO excitation and lattice vibration of molecules.

1.2.1 Plasmonic Localized Heating of Metals

Metallic nanomaterials (*e.g.* gold and silver) have gained great scientific and technological interest for their key ability to interact with light in the visible to NIR region. When interacting with light at the appropriate wavelengths, free electrons on the metallic nanoparticle surface are excited and conduction-band electrons collectively oscillate at the same frequency. This phenomenon is identified as localized surface plasmon resonance (LSPR).[10,11] The LSPR is able to decay through two competitive pathways namely the radiative and nonradiative decay processes. The radiative decay process provides the main role in the plasmonic enhancement of the electric field in the near-field regime, while the nonradiative decay process *via* intraband or interband transitions is responsible for forming energetic or hot

electrons, leading to particle heating. A typical example of the decay dynamics of photoexcited gold nanoparticles is described in three phenomena[12] (see Figure 1.2a): firstly, relaxation from a non-Fermi to Fermi electron distribution *via* 'electron–electron scattering' (<100 fs), secondly, cooling of hot-electron gas through 'electron–phonon scattering' (1–10 ps), and lastly, heat dissipation from gold nanoparticles to the surrounding environment *via* 'phonon–phonon scattering' (~100 ps).[10,13,14] The LSPR effect is strongly dependent on many factors, including the metallic particle morphology, size, composition, interparticle distance, dielectric constant or medium around a particle.[15,16] Up to now, noble metals such as gold and silver nanostructures have been the most frequently used plasmonic metals, while several other non-noble metals that show metal-like optical properties in specific wavelength ranges include transition metals (*e.g.* Al, Cu, Co, Ni),[17–20] transition metal oxides (*e.g.* WO_{3-x} and MoO_{3-x}),[21–23] and transition metal chalcogenides (*e.g.* $Cu_{2-x}E$, E = S, Se).[24,25]

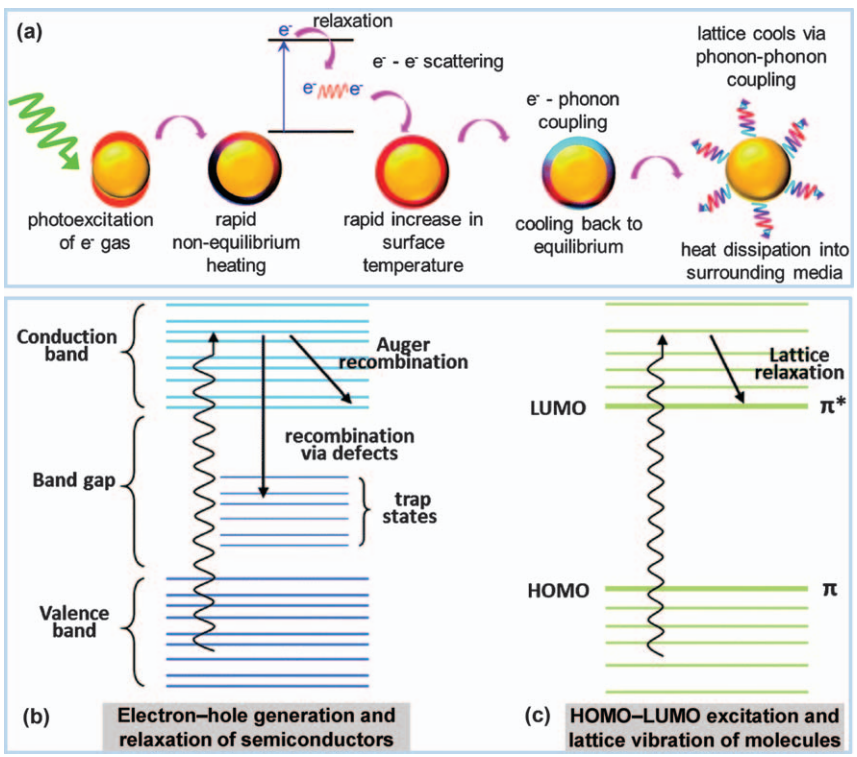

Figure 1.2 Different mechanisms of the photothermal effect. (a) Schematic illustration of light to heat conversion by plasmonic nanoparticles. Reproduced from ref. 12 with permission from the Royal Society of Chemistry. (b) Schematic illustration of electron–hole generation and relaxation of semiconductors, and (c) HOMO–LUMO excitation and lattice vibration of molecules. Reproduced from ref. 26 with permission from the Royal Society of Chemistry.

1.2.2 Electron–Hole Generation and Relaxation of Semiconductors

The generation and relaxation of electron–hole pairs usually occur in semiconductors (see Figure 1.2b).[26] When irradiated by an incident light with an energy equal to or greater than the band gap, the semiconductor absorbs photons to produce active electron–hole pairs. The act of photoexcitation generates electrons in the conduction band and leaves electronic vacancies or holes in the valence band. The subsequent relaxation from the higher excited states to the lower energy states can occur either *via* radiatively in the form of photons, or non-radiatively in the form of phonons. The latter causes a heat liberation when carriers distribute part of their energy to the crystal lattice. As a result, the thermal (vibrational) energy of the lattice rises, which is measured as an increase in its temperature. A temperature distribution is thus established, depending on the optical absorption and nonradiative bulk/surface recombination. This establishment of a temperature distribution in the material charge by carrier diffusion and recombination is referred to as the photothermal effect.[27]

1.2.3 HOMO–LUMO Excitation and Lattice Vibration of Molecules

Carbon- and polymer-based materials have been investigated as photothermal materials due to their strong light-absorbing and photon-to-heat conversion abilities through lattice vibrations (see Figure 1.2c).[26] In these materials, the less tightly held electrons in π bonds can be easily excited from the π orbital to π^* orbital with a lower energy input. Notably, the conjugation (π–π or p–π) and hyperconjugation effects (σ–π) facilitate the excitation of electrons by light irradiation ($\pi \rightarrow \pi^*$) and induce a strong absorption in the NIR region, where the excited electrons return to the ground state by releasing the absorbed energy into heat.[28–30] Accordingly, the excited electron is promoted from the ground state (highest occupied molecular orbital, HOMO) to a higher energy orbital (lowest unoccupied molecular orbital, LUMO) upon illumination with light energy that matches a possible electronic transition within the molecule. Then, the relaxation from the higher excited states to the lower energy states can occur by means of electron–phonon coupling. Therefore, the energy gained is transferred from the excited electrons to vibrational modes within the atomic lattices, resulting in an increase in the temperature of the material.[31]

1.3 Classification of Photothermal Materials

1.3.1 Plasmonic Metal Nanostructures

Plasmonic metals, like silver and gold, exhibit photothermal effects arising from their LSPR. For instance, triangular silver nanoplates have been widely

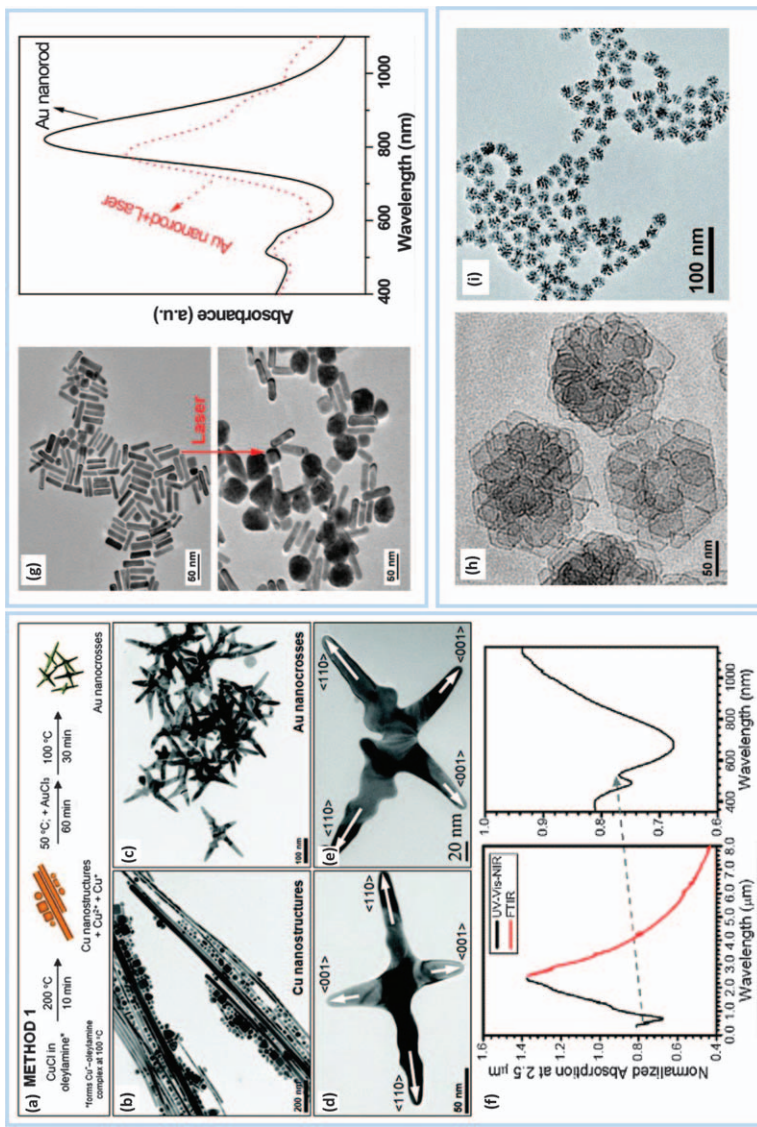
(a) METHOD 1
CuCl in oleylamine*
200 °C
10 min
*forms Cu²⁺-oleylamine complex at 100 °C
Cu nanostructures + Cu²⁺ + Cu⁺
50 °C; + AuCl₃
60 min
100 °C
30 min
Au nanocrosses
(b)
Cu nanostructures
200 nm
(c)
Au nanocrosses
100 nm
(d)
<001>
<110>
<110>
50 nm
(e)
<110>
<110>
<001>
<001>
20 nm
(f)
UV-Vis-NIR
FTIR
Normalized Absorption at 2.5 μm
Wavelength (μm)
Wavelength (nm)
(g)
Laser
50 nm
50 nm
Absorbance (a.u.)
Au nanorod+Laser
Au nanorod
Wavelength (nm)
(h)
50 nm
(i)
100 nm

explored for their photothermal effects under NIR laser irradiation.[32–35] As for gold, a typical absorption band of gold nanospheres is presented in the 500 to 550 nm region due to their LSPR.[36] When the particle size increases, there is some LSPR red shift due to electromagnetic retardation in larger particles. With continuous improvement and development in the synthetic methodologies, various gold nanomaterials including rods, shells, prisms, plates, and cages/boxes, hollow, and branched nanostructures have been synthesized successfully.[37–41] By changing their sizes or shapes, the plasmon resonance peak can be tuned to the NIR spectral region to achieve maximum thermal conversion for photothermal application.[42–44] Gold nanorods are among the most studied metal nanostructures as inorganic photothermal materials, owing to their anisotropic shape, tunable aspect ratio, and strong NIR absorption of the longitudinal plasmon band with high thermal conversion efficiency.[45–49] The absorption range of gold nanorods can be tuned through altering the aspect ratio, so the heating efficiency can be optimized by using an absorption maxima ~800 nm. Our group synthesized multiple-branched gold nanostructures that exhibited a distinct near- and mid-IR LSPR *via* a template-directed approach.[50,51] The synergistic coupling between the branches enables the multiple-branched nanocrosses to efficiently absorb IR light (see Figure 1.3a–f). As compared to gold nanospheres and gold nanorods, the absorption cross-section of gold nanocrosses of 100 nm in the longitudinal and traverse directions was calculated to be 7.5×10^{-15} m^2 by using discrete dipole approximation simulations,[52] which is higher than the gold nanospheres of 40 nm (2.93×10^{-15} m^2)[53,54] and 150 nm (5.73×10^{-15} m^2)[55] in size as well as gold nanorods of 45 nm×20 nm in dimension (1.83×10^{-15} m^2).[55] Thus, the gold nanocrosses can effectively improve the light absorption with a great extension to the longer wavelengths relative to the gold nanospheres or nanorods at shorter wavelengths.

Despite all the advantages associated with the gold nanostructures, they often suffer from poor photothermal stability and hence easy loss of shape and NIR SPR properties upon strong NIR laser irradiation (see Figure 1.3g).[56–58]

Figure 1.3 Preparation of Au nanocrosses *via* a template-directed approach. (a) Schematic illustration of gold nanocross formation based on $AuCl_3$ reduction by a Cu-based reducing agent. (b) TEM image of the preformed Cu nanostructures. (c) TEM image of the as-prepared Au nanocrosses. (d and e) TEM images of a representative Au nanocross with (d) D_{2h} symmetry and (e) C_{2v} symmetry. Reproduced from ref. 51 with permission from the Royal Society of Chemistry. (f) UV–vis–NIR absorbance of Au nanocrosses. Reproduced from ref. 50 with permission from American Chemical Society, Copyright 2011. (g) Photothermal stability of gold nanorods upon 980 nm laser irradiation (2 $W\,cm^{-2}$, 30 min). Reproduced from ref. 57 with permission from American Chemical Society, Copyright 2013. (h) TEM image of the palladium nanocollora. Reproduced from ref. 62 with permission from American Chemical Society, Copyright 2011. (i) TEM image of the porous palladium nanoparticles. Reproduced from ref. 63 with permission from the Royal Society of Chemistry.

As such, palladium nanostructures have been developed to overcome the photothermal instability drawback because of its significantly higher melting point. Huang *et al.* prepared ultrathin hexagonal palladium nanosheets that exhibited unusual optical features with tunable (826–1068 nm) and intense LSPR absorption (molar extinction coefficient of 4.1×10^9 $M^{-1}cm^{-1}$) in the NIR region, which is comparable with the most studied gold nanorods (5.5×10^9 $M^{-1}cm^{-1}$).[59,60] Most importantly, these palladium nanosheets do not undergo a shape transformation into spherical particles under high intensity NIR laser irradiation. Further study on the palladium nanosheets demonstrated a high photothermal conversion efficiency of 52.0% at 808 nm.[61] In another study, palladium nanocorolla composed of unidirectionally aligned, well-spaced, and connected ultrathin palladium nanosheets was synthesized through an etching growth strategy (see Figure 1.3h).[62] Upon 808 nm laser irradiation, the photothermal effect of palladium nanocorolla induced by the NIR SPR absorption gave rise to a temperature increase from 26.6 to 50.4 °C. Likewise, Xiao *et al.* reported palladium nanoparticles with a porous architecture (see Figure 1.3i), exhibiting high NIR absorption (6.3×10^7 $M^{-1}cm^{-1}$) nearly two times that of solid palladium nanocubes at the same mass concentration.[63]

1.3.2 Semiconductors

1.3.2.1 Transition Metal Oxides

Several narrow bandgap semiconductors, such as hydrogenated black TiO_2,[64] Ti_2O_3 nanoparticles,[65] oxygen-deficient MoO_3 nanostructures,[23] and magnetic microspheres (*e.g.* Fe_3O_4, $MnFe_2O_4$, $ZnFe_2O_4$, and $CoFe_2O_4$),[66] have been studied as photothermal materials in recent years. Zhu *et al.* constructed black TiO_2 nanocages with enhanced absorption due to the light trapping effect.[64] The black TiO_2 efficiently absorbed the solar irradiation and the well-crystallized interconnected nanograins structure accelerated the heat transfer in the system, thus achieving a light-to-thermal conversion efficiency of 70.9%. Wang *et al.* reported Ti_2O_3 nanoparticles with outstanding absorption capability across the full solar spectrum.[65] It was suggested that the small bandgap ($\approx$0.1 eV) and nano-sized features of the Ti_2O_3 nanoparticles deliver a remarkable solar-to-thermal conversion efficiency of $\sim$92%.

Unlike conventional wide-bandgap TiO_2 which only absorbs UV light, Ti_2O_3, which can be considered as oxygen-deficient phases of TiO_2, is able to absorb the full solar spectrum. Likewise, there are other oxygen-deficient metal oxides such as WO_{3-x} and MoO_{3-x}, which exhibit strong photoabsorption properties in the broad wavelength range up to the NIR region.[67,68] Among the active photothermal metal oxides, WO_{3-x} exhibits strong LSPR due to oxygen vacancies contributing free electrons. In contrast to WO_3 which is yellow in color, WO_{3-x} are generally blue in color, with many forms of oxygen-deficient stoichiometries such as $WO_{2.9}$, $WO_{2.83}$, and $WO_{2.72}$.[21,68] Apart from the intrinsic absorption of WO_3 at 480 nm (*i.e.* indirect band gap 2.6 eV), the oxygen-deficient WO_{3-x} exhibits a broad absorption peak in the 480–1800 nm

region which is ascribed to the new discrete energy bands below the conduction band, generated by the oxygen vacancies and the collective oscillations of surface-free conduction band electrons (700–1800 nm) that induce the SPR.[69] Among the transition metal oxides, iron oxide nanoparticles possess dual functionalities of NIR absorption and magnetism. In comparison with individual magnetic Fe_3O_4 nanoparticles, studies have shown that clustered Fe_3O_4 nanoparticles can induce a higher temperature increase because of their strong absorption in the NIR region.[70] Likewise, the formation of self-assembled Fe_3O_4 architectures is capable of improving the photothermal performance, exhibiting rapid temperature increments in larger Fe_3O_4 superstructures than the smaller ones due to the enhanced molar extinction coefficient in the NIR region.[71]

1.3.2.2 Transition Metal Chalcogenides

Transition metal chalcogenides are another important group of inorganic photothermal materials that are receiving intense research due to their strong absorption in the NIR region, good photostability, and other benefits such as low cytotoxicity, low cost, and abundance. Particularly, a well-known p-type semiconductor material, copper sulfide (CuS), has been found to show intrinsic NIR region absorption originating from d–d energy band transitions of Cu^{2+} ions rather than SPR. A notable example of CuS photothermal materials is the synthesis of 3D flower-like CuS superstructures which exhibited high NIR photothermal conversion efficiency.[72] The CuS superstructures can rapidly convert 980 nm laser energy into thermal energy, leading to an increase in the temperature of CuS superstructure aqueous dispersion as a function of irradiation time and concentration. It was revealed that the faceted end planes of the crystalline CuS superstructures function as the laser-cavity mirrors for the 980 nm laser, giving rise to the enhancement of reflection, absorption, and photothermal conversion. Our group has synthesized the multiply-voided $Cu_{12}Sb_4S_{13}$ tetrahedron architecture with significant absorption in the NIR region. Upon radiation from an 808 nm laser, the temperature of the aqueous dispersions of tetrahedrite nanostructures elevates with increasing concentrations, showing an increment of 18.2 °C at a concentration of 0.4 mg mL^{-1} compared to 2.4 °C in pure water (see Figure 1.4a–c).[73]

The phenomenon of intra-band transition appears to be a unique characteristic of CuS nanostructures of 1 : 1 stoichiometry, as nonstoichiometric copper chalcogenides (*e.g.* $Cu_{2-x}S/Cu_{2-x}Se$) have been found to show stable LSPR behavior similar to metals.[74,75] Upon irradiation by NIR light at 800 nm, the $Cu_{2-x}Se$ nanocrystals generate an intense NIR absorbance peak relating to the plasmon resonance. The significant photothermal heating effect resulted in a photothermal transduction efficiency of 22%.[25] Copper sulfides such as Cu_9S_5 and $Cu_{7.2}S_4$ nanocrystals (see Figure 1.4d–e) demonstrated photothermal conversion efficiencies up to 25.7% and 56.7% respectively, which are both higher than that of gold nanorods of 24.6% under 980 nm light irradiation.[76,77] The outstanding photothermal conversion efficiencies can be

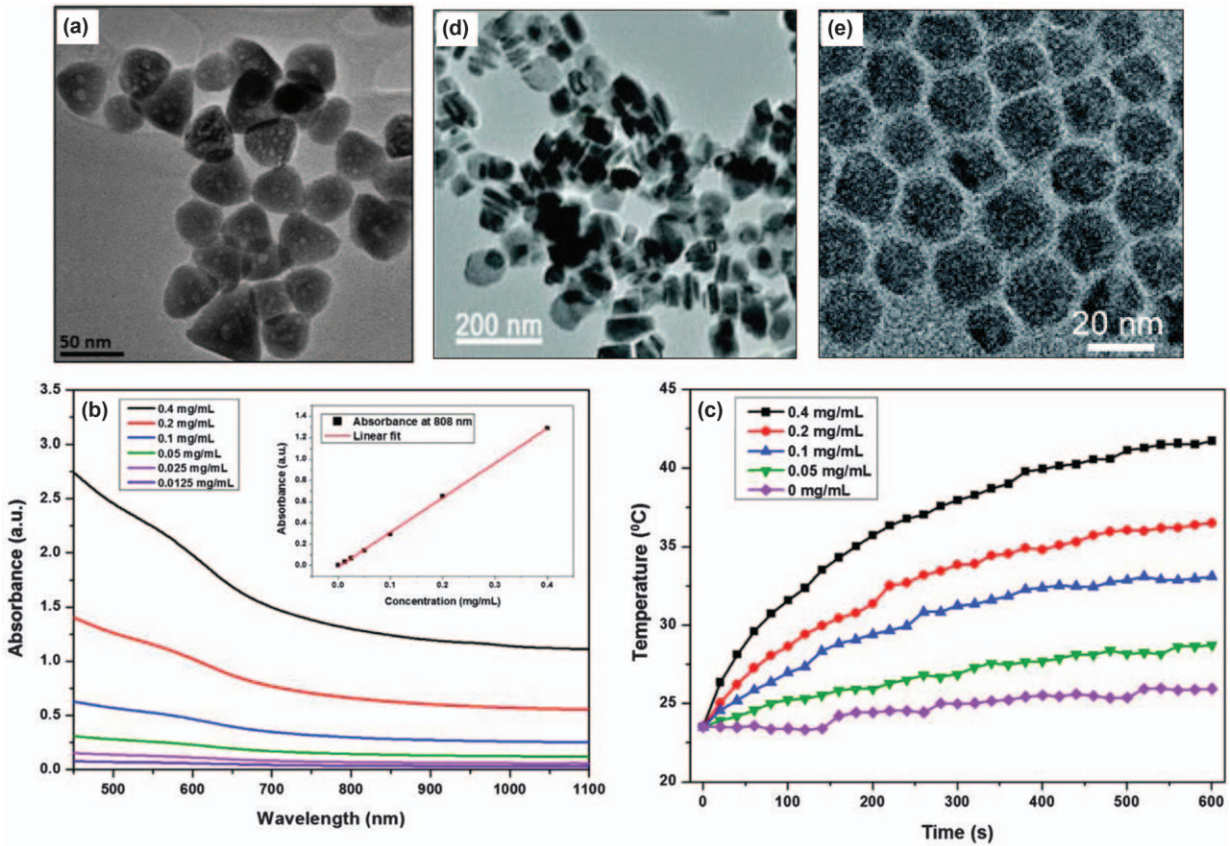

Figure 1.4 Copper chalcogenide-based nanostructures as photothermal materials. (a) TEM image of porous $Cu_{12}Sb_4S_{13}$ tetrahedron architectures. (b) The corresponding absorption spectra with different concentrations. The inset shows the Beer's law plot at 808 nm. (c) The corresponding temperature measurements with different concentrations under 808 nm laser irradiation. Reproduced from ref. 73 with permission from the Royal Society of Chemistry. (d) TEM image of Cu_9S_5 nanoplates. Reproduced from ref. 76 with permission from American Chemical Society, Copyright 2011. (e) TEM image of $Cu_{7.2}S_4$ nanocrystals. Reproduced from ref. 77 with permission from the Royal Society of Chemistry.

explained by strong absorption in the NIR region due to the LSPR arising from p-type carriers in vacancy-doped nanocrystals.[78] In the case of $Cu_{7.2}S_4$ nanocrystals, the plasmon resonance peak is centered at 968 nm which is close to the wavelength of the NIR laser of 980 nm, leading to higher NIR absorption than that of Cu_9S_5 nanocrystals. When $Cu_{1.94}S$ nanocrystals were self-assembled into ordered plant-like structures, the NIR photothermal conversion efficiency of the assembled architectures was enhanced by about 50% compared with individual $Cu_{1.94}S$ nanocrystals, upon irradiation with a 1064 nm laser.[79] In addition, 2D transition metal dichalcogenides such as MoS_2 and WS_2 also show strong absorbance in the NIR region. In particular, MoS_2 nanosheets presented a higher mass extinction coefficient at 808 nm than that of graphene.[80,81]

1.3.3 Carbon-based Materials

Several classes of carbon-based materials including carbon nanotubes (CNTs), graphene, graphene oxide/reduced graphene oxide, carbon black, graphite, and carbon composites have been nominated as potential photothermal materials owing to their excellent light absorption over a wide range of wavelengths and superior light-to-heat conversion efficiency.[82–90] Moreover, they are relatively low cost and abundant compared to metallic materials. Diversified carbon-based nanomaterials based on 1D, 2D, and 3D architectures have been designed and synthesized for photothermal applications.[7,91] Unlike conventional amorphous carbon, the conjugation and hyperconjugation in the molecular structure of CNTs and graphene permit strong absorption in the NIR region and increasing the π-conjugation gives rise to a red-shift of the absorption light spectrum.

CNTs are made of sp^2 carbons and regarded as typical 1D nanomaterials. They can be categorized into either single-walled (SWCNTs) or multi-walled (MWCNTs). The structure of SWCNTs is a rolled-up tubular shell of a graphene sheet, while MWCNTs consist of a stack of graphene sheets rolled up into concentric cylinders.[92,93] Each type has different properties and specific photothermal effects. As CNTs are potentially toxic in their bare state and hydrophobic in nature, one effective strategy is to chemically modify or functionalize the CNTs to render solubility in aqueous medium, particularly for biomedical applications. Du *et al.* introduced amino groups onto the surface of SWCNTs by HNO_3 oxidation and amidation treatment to enhance dispersibility of SWCNTs.[94] This significantly improved the solar-thermal conversion under sunlight irradiation experiments. In many other cases, CNTs are noncovalently functionalized by simple adsorption of different kinds of molecules including polymers, biomolecules such as saccharides/polysaccharides, proteins, enzymes, and DNA. Wang *et al.* modified the SWCNTs using PEG-grafted amphiphilic polymer, leading to stable dispersion in various physiological media.[95] The PEG-coated SWCNTs exhibited strong absorbance in the NIR region and were able to warm up rapidly under 808 nm NIR laser irradiation, resulting in significant photothermal effects.

Graphene is a 2D material composed primarily of sp^2 hybridized carbon. Due to the hydrophobic feature of graphene, additional hydrophilic treatments are often required. Reports have shown that functionalization of graphene through nitrogen doping[96] and hydrophilic groups (*e.g.* hydroxyl and carboxyl)[97] can enhance the photothermal performance. On the other hand, graphene oxide is a chemically modified graphene with additional reactive oxygen functional groups, such as hydroxyl, carboxyl, and epoxy groups. It is hydrophilic due to the oxygen-containing functionalities and therefore it can be easily dispersed in aqueous media. It can also be converted to reduced graphene oxide at high yields. Robinson *et al.* developed biocompatible reduced graphene oxide sheets of ~20 nm through non-covalent functionalization with amphiphilic PEGylated polymer chains and yielded a 6-fold increase in NIR absorbance than with graphene oxide.[98] Besides PEG coating, the photothermal absorbing ability of reduced graphene oxide has been studied by using different functional groups.[99] Arginine modification of reduced graphene oxide increases the stability in aqueous solutions and shows a higher absorption cross-section of 3.2 times that of graphene oxide at 808 nm.[88] When graphene sheets were assembled into a vertically aligned graphene sheet membrane, the 3D graphene-based materials exhibited outstanding light absorption in the full solar spectrum range (250–2500 nm) for excellent photothermal transduction, featuring high efficiency of 86.5% under one sun illumination.[100]

1.3.4 Polymer-based Materials

Apart from inorganic nanomaterials, organic materials particularly the polymeric ones have been reported for their outstanding light-harvesting capability and photothermal conversion efficiency with excellent biocompatibility.[101] Conjugated polymers are macromolecules characterized with π-conjugated backbones, which have emerged as new generation NIR-absorbing photothermal materials.[102–105] The successful examples of biocompatible conjugated polymer-based photothermal materials mainly include polyaniline,[106,107] poly(3,4ethylenedioxythiophene): poly(4-styrenesulfonate) (PEDOT:PSS),[108,109] polypyrrole,[110,111] polydopamine,[112,113] and donor–acceptor (D–A) structured polymer molecules.[103,114]

Covalent organic frameworks (COFs) are newly emerged crystalline porous organic polymers with extended structures, in which their backbones are constructed entirely from light elements (B, C, N, O, Si), and connected *via* covalent bonds into 2D or 3D structures.[115] The key features of COFs include low density, high surface area, high thermal and mechanical stability, highly ordered π–π stacking structure, easy functional modification, amenable topologies, and are structurally pre-designable, *etc.*[9,116,117] In general, COFs were formed by reversible condensation reactions between various organic building blocks. They were first demonstrated by Yaghi and co-workers in 2005 using condensation reactions of phenyl diboronic acid and hexahydroxytriphenylene.[118] The versatility enables COFs to be modified with many

kinds of functional groups for different applications. Accordingly, COFs were widely employed as a perfect support for integration or encapsulation of functional nanoparticles in a controllable and predictable way. Tan *et al.* developed COF–Fe_3O_4 core–shell microspheres through an amorphous-to-crystalline transformation process, whereby Fe_3O_4 nanoclusters were encapsulated by an imine-linked COF network.[119] Due to the well-organized stacking in shell, the resultant COF–Fe_3O_4 microspheres exhibited NIR absorbance and obtained a high molar extinction coefficient of 4.2×10^{10} $m^{-1}\,cm^{-1}$ at 785 nm. As such, the photothermal conversion efficiency of COF–Fe_3O_4 microspheres was determined to be 21.5%, which is 2–3 times higher than that of Fe_3O_4 nanoclusters alone. Hu *et al.* synthesized COF–CuSe nanocomposites with NIR photothermal conversion ability *via* a solution-phase synthesis approach under ambient conditions.[120] Upon 808 nm laser irradiation, the corresponding COF–CuSe nanocomposites displayed a photothermal effect with a photothermal conversion efficiency of 26.34% (see Figure 1.5).

Organic–inorganic hybrid crystalline porous materials such as metal–organic frameworks (MOFs), are similar to COFs, but instead of being composed of light elements, the structure of MOFs is composed of metal ions or clusters cross-linked by organic linkers. The photothermal effect has been demonstrated in most representative subfamilies of MOFs, including HKUST-1, UiO-66, ZIF-8, CPO-27, Fe–MIL-101–NH_2, and IRMOF-3, with significant heating of up to 167 °C (for CPO-27–Ni) achieved within 5 min of UV–vis irradiation. This effect was attributed to the d–d transitions of the metal ion centers, as observed in their broad absorption bands within the irradiation range (300–650 nm); while MOFs without absorption bands in this range showed only a small temperature increment even after irradiation for 30 min.[121] The photothermal effect in MOFs has been used for solvent removal and chemical activation, with localized heating resulting in a more rapid activation than heating with an external source, as well as chemical modification in solid-state reactions.[121,122] They have also been combined with polymers such as polyaniline for photothermal therapy.[123]

1.4 Applications of Photothermal Materials

1.4.1 Photothermal Therapy

Cancer refers to a large group of diseases characterized by the development of abnormal cells that spread uncontrollably. It is a global public health crisis due to its high incidence and mortality rates.[124] To date, there is no comprehensive approach for cancer treatment; common options are primarily focused on chemotherapy, radiotherapy, immunotherapy, and surgery, while surgery in many cases is not able to remove cancerous tissue fully. Despite these approaches offering considerable therapeutic efficacy, they are limited by their risk to normal cells and tissues as well as their potential to destroy the immune system. For this reason, it is highly

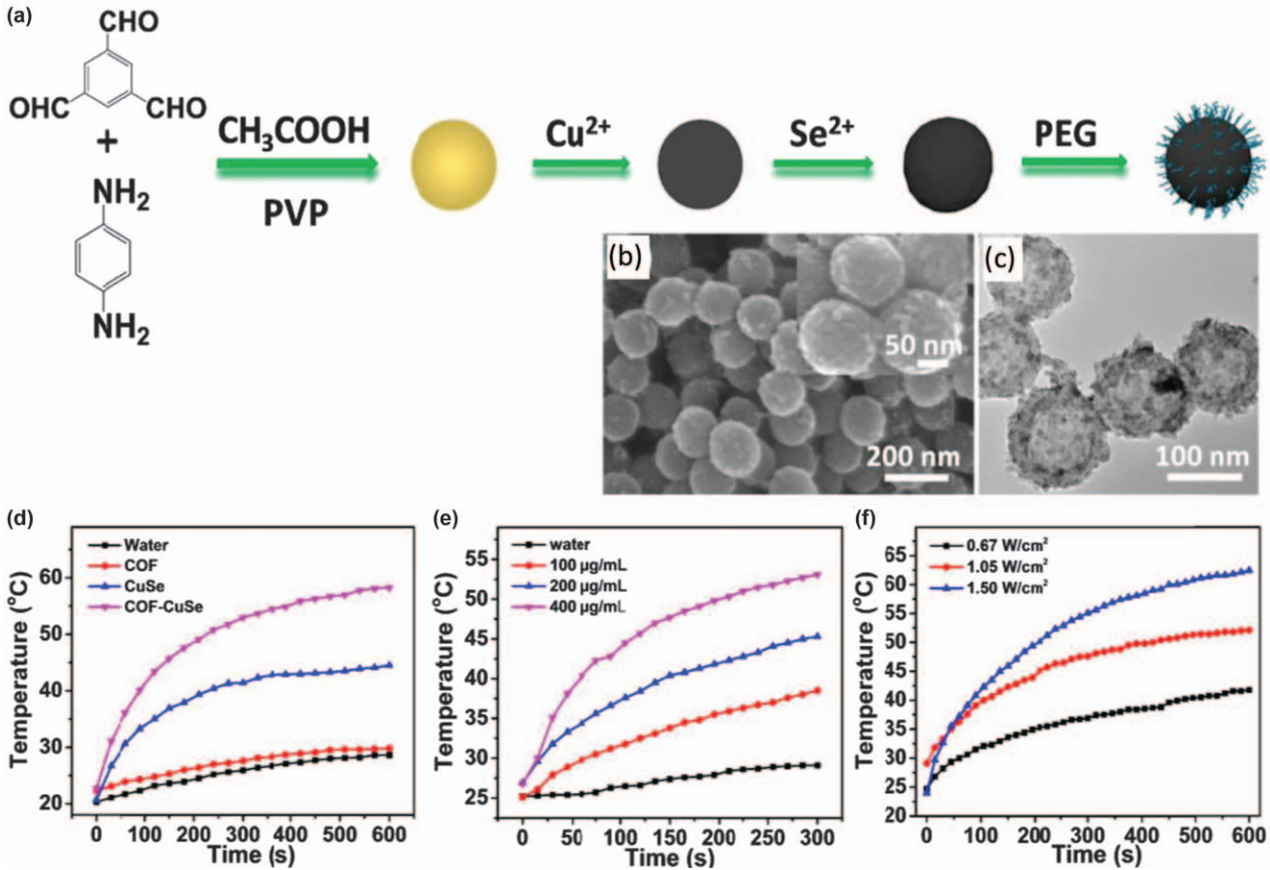

Figure 1.5 (a) Schematic formation of COF–CuSe nanoparticles. (b) SEM image and (c) TEM image of COF–CuSe. Temperature measurements of (d) water, COF, COF–CuSe, and CuSe aqueous solution. (e) COF–CuSe solution with different concentrations under 808 nm laser irradiation. (f) COF–CuSe solution irradiated by an 808 nm laser with different laser power densities. Reproduced from ref. 120 with permission from American Chemical Society, Copyright 2019.

desirable to develop an effective cancer therapy to overcome the limitations of conventional therapies, particularly focusing on minimal invasiveness and reducing undesirable side effects while enhancing efficacy. Toward this goal, photothermal therapy (PTT) is emerging as a promising alternative therapeutic approach for cancer treatment, involving the application of benign light wavelengths ($\lambda = 700$–1100 nm) in conjunction with photothermal agents that transform light energy to localized heat to ablate cancer cells. The ideal photothermal agents should possess several distinct features, including (1) biocompatibility and low toxicity, (2) strong absorption in the NIR region, (3) large extinction coefficient and high photothermal conversion efficiency, and (4) size between 30–200 nm to prolong circulation and enhance tumor accumulation.[1,125]

In the pursuit of increasing therapeutic efficiency, continuous efforts have been devoted to enhancing the intrinsic photothermal performance of photothermal agents. Accordingly, the photothermal performance is related to the nanoscale properties of materials in terms of composition, size, structure, morphology, and surface functionalities. At present, the successful examples of photothermal agents with a relatively high tissue transparency in the NIR window are mainly focused on noble metal nanostructures, tungsten-, copper-, and iron-based semiconductors, carbon-based materials, as well as polymer-based materials. Among these, gold-based nanostructures were the earliest nanomaterials used in cancer photothermal therapy research and have remained one of the most widely studied inorganic photothermal agents today.[126] Examples of gold-based structures for photothermal study include nanoparticles,[127,128] nanorods,[129–131] nanoshells,[132–134] nanocages,[135,136] nanostars,[137–139] nanoflowers,[40] and nanocrosses,[50,52] which are capable of inducing localized hyperthermia effects. Our group demonstrated that branched gold nanostructures such as nanocrosses and nanoflowers could act as efficient absorbers for NIR-assisted photothermal destruction of living cells. The percentage of cell death is dependent on the laser intensity as well as the exposure time. Upon 900 nm laser irradiation (4.2 $W\,cm^{-2}$), human lung cancer cells (A549) associated with gold nanocrosses were killed rapidly within 30 s, indicating the hyperthermia effect induced by gold nanocrosses.[50] This observation is also demonstrated in gold nanoflowers for both *in vitro* and *in vivo* photothermal therapy under 808 nm laser irradiation. *In vitro* photothermal heating of gold nanoflowers in the presence of MCF-7 cancer cells caused the destruction of the cancer cells after irradiation for 30 s. Meanwhile, the gold nanoflower-mediated photothermal ablation of MCF-7 tumors in mice led to effective ablation of the tumors using an NIR laser, suggesting an excellent *in vivo* photothermal therapeutic efficacy of gold nanoflowers (see Figure 1.6).[40] Apart from gold nanostructures, other inorganic nanostructured materials such as palladium (*e.g.* nanosheets,[61] nanocorolla,[62] and porous/hollow nanoparticles[63,140]) have shown great potential in NIR photothermal cancer therapy. Zhang and co-workers demonstrated *in vitro* photothermal heating of liver cancer cells in the presence of palladium

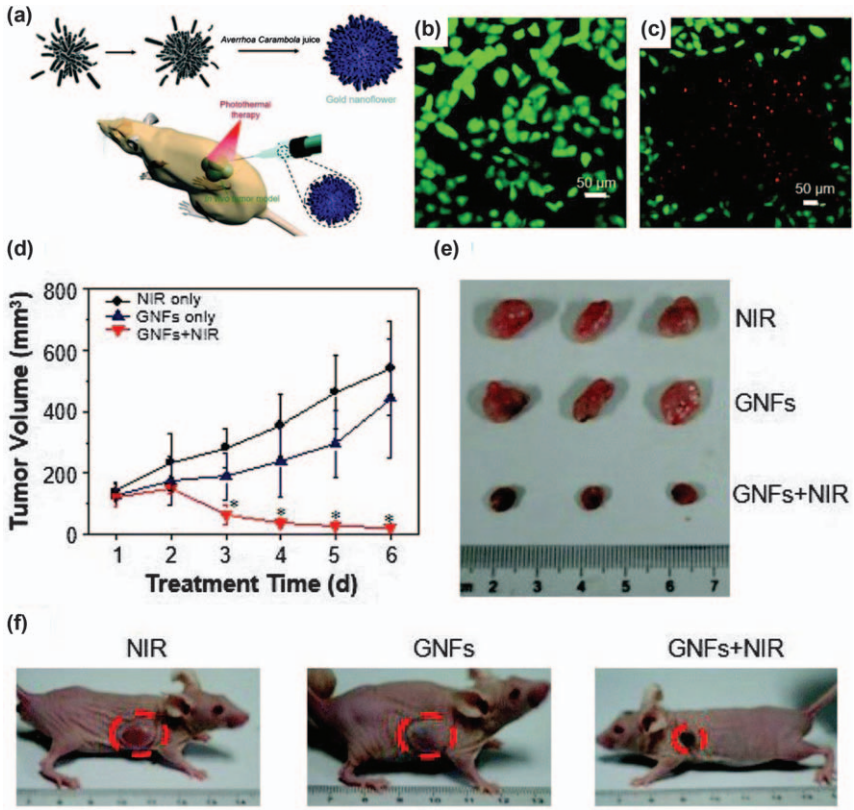

Figure 1.6 (a) Schematic illustration of the formation of gold nanoflowers using $AuCl_3$ and starfruit juice as the reducing agent. (b and c) NIR-mediated photothermal destruction of MCF-7 cancer cells using gold nanoflowers. (b) Live MCF-7 cells incubated with gold nanoflowers before laser irradiation, and their corresponding confocal image (c) of dead MCF-7 cells after laser irradiation with an 808 nm laser. (d–f) *In vivo* photothermal ablation of tumor by gold nanoflowers under NIR irradiation. (d) Time-dependent tumor growth rate. (e) Photographs of excised tumors from different groups after treatment for 6 days. (f) The corresponding photographs of mice with the different treatments after 6 days.
Reproduced from ref. 40 with permission from the Royal Society of Chemistry.

nanocorolla, causing almost 100% cell death upon 808 nm NIR irradiation ($1.4\ W\,cm^{-2}$, 2 min).[62]

Semiconductors, like transition metal oxides (WO_{3-x}, MoO_{3-x})[21–23,68] and transition metal chalcogenides ($Cu_{2-x}E$, E = S, Se)[24,25] have emerged as a new class of plasmonic materials owing to crystal lattice oxygen vacancies that contribute free electrons. With an LSPR signal at around 900 nm,[141] WO_{3-x} is an excellent candidate for biomedical applications.[142,143] Particularly, nanostructured tungsten oxides (nanoparticles,[144] nanorods,[145,146] nanowires,[147] nanosheets[22]) have been developed as photothermal agents for *in vitro* and

in vivo cancer therapy. When oxygen-deficient tungsten oxide nanosheets were subjected to 808 nm NIR irradiation (2.5 $W\,cm^{-2}$), the temperature of the tungsten oxide dispersion increased rapidly to 64.2 °C at a dose of 100 $\mu g\,mL^{-1}$.[22] This photothermal effect is responsible for >90% of MCF-7 cell death upon 2 min irradiation and an efficient tumor inhibition rate of 96.8%. Likewise, nanostructured copper sulfide (nanoparticles, nanoplates,[148] hollow structures[149,150]) are promising new materials for photothermal cancer therapy.[151–153] It has been reported that the PEGylated copper sulfide nanoparticles of pure covellite phase possess strong LSPR absorption in the NIR, yielding an outstanding photothermal heat conversion efficiency of 71.4%.[154] Li *et al.* presented a nuclear-targeted PTT strategy based on RGD and TAT peptide-modified copper sulfide nanoparticles, to effectively destroy residual cancer cells and prevent local cancer recurrence.[155] Upon 980 nm NIR laser irradiation, the copper sulfide nanoparticles rapidly elevated the temperature of the nucleus, causing DNA damage and protein denaturation, thereby leading to an exhaustive apoptosis of the cancer cells. The therapeutic effect of the designed nanoparticles was demonstrated by the cell activity experiments, which showed 84% mortality arising from targeted nanoparticles compared to that of non-targeted nanoparticles which showed 42% mortality. Moreover, *in vivo* experiments showed that the xenografted tumor was fully eliminated after 14 days with only a single treatment and no recurrence of the cancer (see Figure 1.7).

Carbon-based materials (*e.g.* CNTs,[156–161] graphene, and its derivatives[86,162–165]) have been extensively applied as photothermal agents in biomedical applications. They are often assembled with other functional molecules or nanostructures to afford hybrid functional materials in order to provide better properties than their individual counterparts. Due to their large surface area to volume ratio and distinct surface properties, graphene can act as a platform in PTT by incorporating drugs or varieties of other nanomaterials *via* covalent and non-covalent conjugation means. For instance, through integrating reduced graphene oxide and gold superparticles *via* an emulsion-based self-assembly method, Lin *et al.* were able to develop a theranostic nanoplatform for PTT of cancer based on the reduced graphene oxide coated gold superparticles.[163] This combination improves the photothermal conversion properties due to the plasmonic coupling of adjacent gold nanoparticles and the interaction of gold superparticles with reduced graphene oxide, leading to efficient photothermal ablation of U87MG tumors *in vivo* (see Figure 1.8).

All the above-described inorganic nanomaterials have shown favorable absorbance features, high photothermal conversion efficiencies, and good photo-stabilities. Unfortunately, their potential long-term safety concerns due to poor biodegradability may restrict their further application in clinical translation. On the other hand, organic photothermal agents exhibit excellent biodegradability and biocompatibility as an alternative approach for PTT in cancer treatment. Nevertheless, it must be considered that organic nanomaterials have their own limits associated with poor photostability, low absorptivity, or limited photothermal conversion efficiency. In many cases,

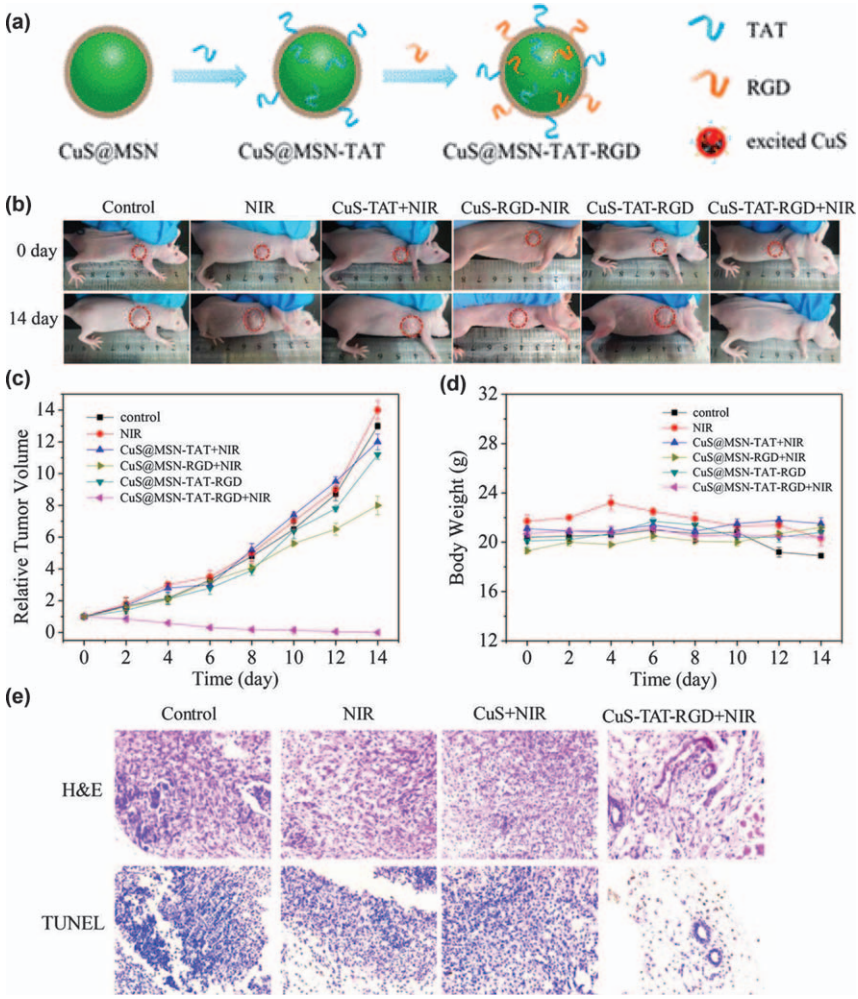

Figure 1.7 (a) Schematic illustration of TAT-RGD modified copper sulfide nanoparticle formation. *In vivo* PTT of modified copper sulfide nanoparticles in mice *via* intravenous injection. (b) Photographs of tumor-bearing mice subjected to different treatments. (c–d) Time-dependent tumor growth rate and body weight. (e) H&E staining and TUNEL staining of the HeLa tumor. Reproduced from ref. 155 with permission from American Chemical Society, Copyright 2018.

combining PTT with other therapies such as chemotherapy and immunotherapy can further improve on the suppression of tumor growth and metastasis.[166,167] For example, PEG-modified PEDOT:PSS was reported as a drug carrier to load doxorubicin and SN38 for combined photothermal- and chemotherapy, to realize a synergistic effect in cancer cell killing.[109] A study by Yu *et al.* revealed that both NIR dye and chemotherapeutic agent were covalently conjugated for combating doxorubicin resistance in breast cancer.[168]

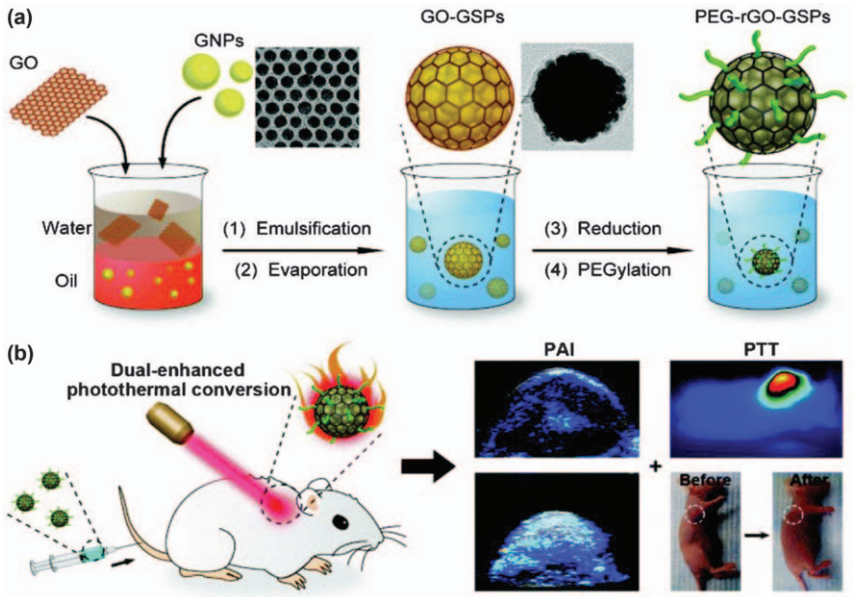

Figure 1.8 (a) Schematic illustration of the formation of PEG-functionalized reduced graphene oxide-coated gold superparticles *via* an emulsion-based self-assembly method. (b) NIR light-triggered acoustic and thermal theranostics based on PEG-functionalized reduced graphene oxide-coated gold superparticles for *in vivo* cancer therapy.
Reproduced from ref. 163 with permission from the Royal Society of Chemistry.

In this study, a hybrid micelle with a pH and NIR light dual-responsive property was developed based on enzyme-responsive doxorubicin polymeric prodrugs and cypate-linked polymers. Upon NIR laser irradiation, the hybrid micelles induced a hyperthermia effect and improved tumor penetration and cytoplasm release of doxorubicin, thus significantly improving the therapeutic efficacy for treatment of doxorubicin-resistant MCF-7/ADR breast cancer.

1.4.2 Photothermal Sterilization

The increasing development of antibiotic resistance in bacteria has become a major global health threat. In particular, the eradication of antibiotic-resistant bacteria (*i.e.* multidrug-resistant bacteria) and their biofilms is very challenging with conventional antibiotics. It is therefore important to develop a non-antibiotic strategy with high antimicrobial efficacy against multidrug-resistant bacteria. Among which, nanomaterials with photothermal effect under irradiation of NIR have a good capacity for fighting bacterial infections, making use of the produced heat to inhibit antibiotic-resistant bacterial growth as well as bacterial biofilm formation.[169]

Our group has developed multi-branched gold nanocrosses with strong NIR absorption to destroy antibiotic resistant bacteria, *P. aeruginosa* and its biofilms, with an 800 nm laser (3.0 W cm^{-2}, 5 min).[52] The NIR-assisted photothermal effect was clearly shown through the effective inhibition of the growth of *P. aeruginosa* by means of conjugated gold nanocrosses with pathogen-specific antibodies (see Figure 1.9a).

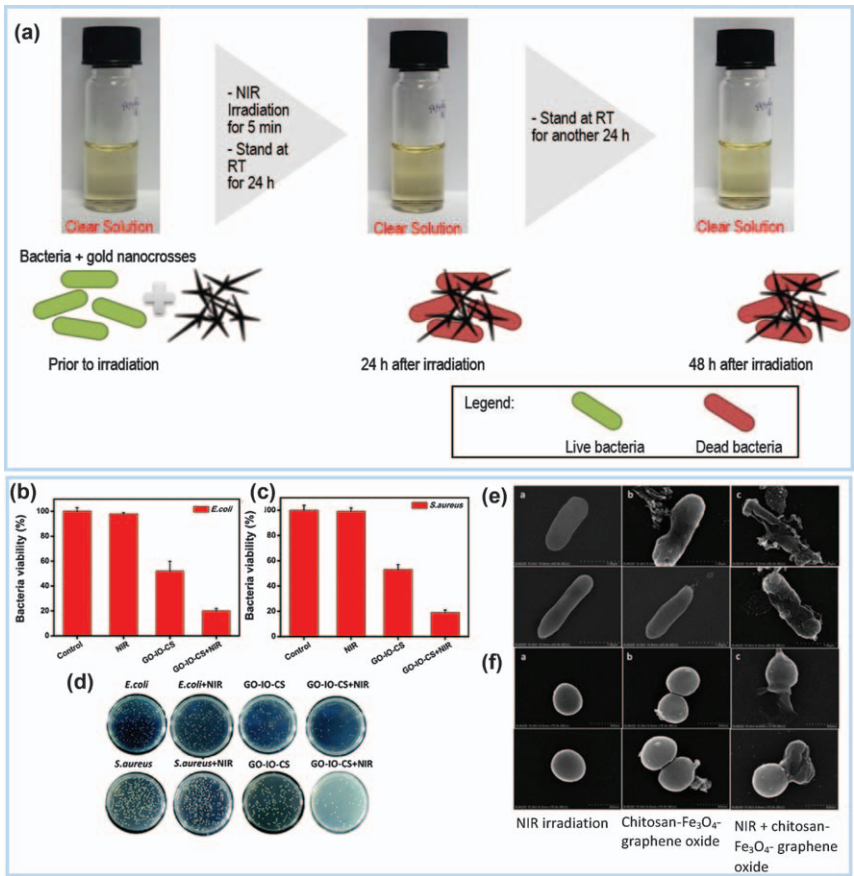

Figure 1.9 (a) Schematic illustration of the photothermal ablation of bacteria and their biofilms with gold nanocrosses. Reproduced from ref. 52 with permission from John Wiley and Sons, Copyright © 2016 WILEY-VCH Verlag GmbH & Co. KGaA, Weinheim. (b–f) The NIR-mediated photothermal antibacterial effect of chitosan and Fe_3O_4 functionalized graphene oxide on (b) *E. coli* and (c) *S. aureus*. (d) The corresponding bacterial colonies treated with chitosan and Fe_3O_4 functionalized graphene oxide, in the presence and absence of NIR. SEM images of (e) *E. coli* and (f) *S. aureus*, control experiment and treatment with chitosan and Fe_3O_4 functionalized graphene oxide under NIR radiation. Reproduced from ref. 171 with permission from the Royal Society of Chemistry.

Graphene derivatives such as graphene oxide, reduced graphene oxide, and other chemically modified graphene have been widely investigated in antibacterial applications.[169] In various graphene-based photothermal anti-infection agents, they are mostly integrated with other functional molecules or nanostructures to achieve more specific and effective photothermal sterilization. Hui *et al.* reported a polyelectrolyte-stabilized reduced graphene oxide antibacterial surface that is able to kill >90% airborne bacteria including antibiotic-tolerant persisters, on contact upon minutes of solar irradiation.[170] Jia *et al.* employed a photothermal antibiotic agent based on chitosan and Fe_3O_4 functionalized graphene oxide for capturing and inhibiting the growth of both *Staphylococcus aureus* and *Escherichia coli*, as well as destroying bacterial biofilms with NIR irradiation.[171] In the presence of nanocomposites and NIR radiation, the cell membranes of *E. coli* were broken down and lost their integrity while some intracellular components of *S. aureus* clearly leaked out, indicating effective sterilization through photothermal lysis (see Figure 1.9b).

1.4.3 Solar-driven Water Evaporation

Solar-driven evaporation is considered as a promising and sustainable approach for clean water production which is important to alleviate global water scarcity issues. In recent years, various types of NIR absorbing materials, including metallic nanostructures,[172–175] semiconductors,[176–178] and carbon-based materials[179–181] have been designed to optimize the solar spectrum absorption and achieve efficient light-to-vapor conversion. In particular, various gold solar absorbers including nanoparticles,[182] nanoshells,[172,183] and nanorods,[184] have been widely used in steam and clean water generation. Furthermore, gold nanostructures can be hybridized with other materials to improve photothermal efficiency or to form multifunctional composites.[185] Deng and co-workers introduced a surface evaporation approach *via* localized plasmonic heating by a self-assembled gold nanoparticle film[186] and an airlaid-paper-based gold nanoparticle film[187] at the air–water interface. When most of the thermal energy is confined and utilized directly at the evaporative surface, this localized heating system reduces heat loss and improves heat-to-evaporation conversion efficiency. With increased surface roughness and good thermal insulating properties, the paper substrate yielded high absorption of incident light and reduced heat loss, thus achieving a higher evaporation efficiency (77.8%) than free-standing plasmonic films (47.8%).

Successful examples of semiconductor-based solar adsorption materials with significant water evaporation efficiency include $WO_{2.72}$ nanoparticles,[188] magnetic microspheres (Fe_3O_4 and MFe_2O_4, M = Mn, Zn, Co),[66] and Cu_7S_4 nanocrystals.[189] As for carbon-based materials, they generally appear in black and are suitable for efficient broadband absorption.[190] With excellent light-to-heat conversion properties, carbon-based absorbers can induce rapid water evaporation upon illumination under different environmental conditions,

therefore they are widely used in a solar-driven steam generation system.[3,83,191] A comparative experiment was conducted by Ni *et al.* to study three different carbon-based nanofluids (graphite carbon black, carbon black, and graphene) in a solar-driven steam generation system.[83] The findings revealed that graphite carbon black and graphene nanofluids significantly outperformed the carbon black by 7% under 1.5 h of illumination. Wang *et al.* developed a solar thermal evaporation system based on reduced graphene oxide modified with magnetic Fe_3O_4 nanoparticles, aiming for desalination of seawater.[192] With high solar light absorption of over 95%, the evaporation efficiency yielded 70% in a 3.5% NaCl solution with dispersed nanocomposite, under solar illumination of 1 kW m^{-2} (see Figure 1.10). Moreover, this system offers the benefit of recyclability because magnetic nanoparticles can be easily separated from seawater.

1.5 Summary and Outlook

This book chapter provides a succinct review of the different classes of photothermal nanomaterials, such as plasmonic metal nanostructures, semiconductors, and carbon-, and polymer-based materials, which have been broadly explored as highly promising candidates for a variety of photothermal-related applications. The different photothermal materials along with their photothermal conversion mechanisms such as plasmonic localized heating of metals, electron–hole generation and relaxation of semiconductors as well as HOMO–LUMO excitation and lattice vibration of molecules are summarized. To realize a highly efficient photothermal material, the light absorbing capability is an essential factor. For the plasmonic light absorbing materials, the light absorption can be greatly improved through controlling the size, shape, and composition which in turn tune the LSPR peaks to the NIR region. On the other hand, enhancement of light absorption in a semiconductor can be obtained through element doping or introducing oxygen vacancies in the lattice. Also, carbon-based and organic polymeric materials are often assembled with other functional molecules or nanostructures to afford hybrid functional materials that can demonstrate better properties compared to their individual counterparts.

Apart from improving the light absorbing capability, the photothermal conversion performance of photothermal materials is discussed with respect to their application in biomedical and environmental fields. Due to the great advantages of PTT and the high demand for targeted cancer therapy, widespread studies on engineering photothermal materials have been reported and have demonstrated promising results in cancer treatment. When combined with NIR light, these inorganic and organic photothermal materials are capable of generating sufficient heat to raise the local temperature and thus result in tumor cell death. Among which, gold nanostructures have received great attention due to their strong optical absorption properties, outstanding photothermal conversion efficiencies, and good photo-stabilities. Moreover, they have achieved encouraging therapeutic efficacies in many *in vivo* animal

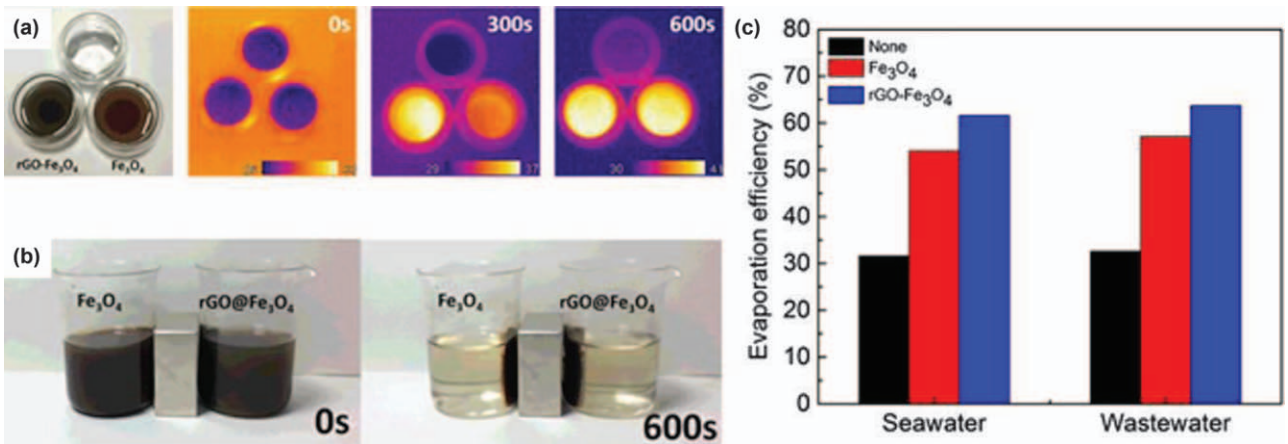

Figure 1.10 Photothermal performance of a solar-driven water evaporation system based on reduced graphene oxide modified Fe_3O_4 nanoparticles. (a) Photographs of saline solution, saline solution containing reduced graphene oxide-modified Fe_3O_4 nanoparticles, and saline solution containing Fe_3O_4 nanoparticles. IR images of different dispersions under solar irradiation of 1 $kW\,m^{-2}$ at 0, 300, and 600 s. (b) Recycling of Fe_3O_4 nanoparticles and reduced graphene oxide-modified Fe_3O_4 nanoparticles. (c) The corresponding evaporation efficiency in seawater and wastewater.
Reproduced from ref. 192 with permission from American Chemical Society, Copyright 2019.

studies, which make them promising photothermal materials in cancer treatment. Despite all the glaring prospects, application of photothermal materials is still associated with many challenges that may restrict their further application in clinical translation. For instance, thermal stability is a highly critical parameter particularly for gold nanostructures. When the heating rate far exceeds the cooling rate, the accumulated heat in the lattice will result in structural changes in terms of the shape or integrity of nanoparticles. Another concern of using photothermal materials in PTT is the possible long-term cytotoxicity of accumulated and aggregated nanomaterials, therefore, knowledge about their potential toxicity and health impact is essential before these nanomaterials can be used in real clinical settings.

Undoubtedly, photothermal material-based solar-driven water evaporation represents a green, efficient, low-cost, and environmentally benign technology for clean water generation. Material and structural design with favorable light absorption over the full solar spectrum and excellent photothermal conversion efficiencies are the prerequisites for a high-performance solar evaporation device. Although high conversion efficiencies of greater than 90% have been achieved in recently studied photothermal materials, more efforts are required to develop robust photothermal materials enabling good thermal/chemical stability and recyclability. Additionally, to facilitate practical applications of solar-driven water evaporation in different water quality (*e.g.* seawater and industrial wastewater), the properties of the photothermal materials, including photothermal stability, corrosion resistance, antibiofouling ability, as well as cost effectiveness, long-term stability, and durability should be taken into consideration. We anticipate that, in the coming years, more photothermal material and structural engineering strategies will be developed to effectively enhance the light absorption and light-to-heat conversion or even emerging new properties for a wider range of applications.

References

1. J. R. Melamed, R. S. Edelstein and E. S. Day, *ACS Nano*, 2015, **9**, 6.
2. J. Chen, C. Ning, Z. Zhou, P. Yu, Y. Zhu, G. Tan and C. Mao, *Prog. Mater. Sci.*, 2019, **99**, 1.
3. H. Ghasemi, G. Ni, A. M. Marconnet, J. Loomis, S. Yerci, N. Miljkovic and G. Chen, *Nat. Commun.*, 2014, **5**, 4449.
4. W. Shang and T. Deng, *Nat. Energy*, 2016, **1**, 16133.
5. L. Zhu, M. Gao, C. K. N. Peh and G. W. Ho, *Nano Energy*, 2019, **57**, 507.
6. Z. Wang, T. Horseman, A. P. Straub, N. Y. Yip, D. Li, M. Elimelech and S. Lin, *Sci. Adv.*, 2019, **5**, eaax0763.
7. C. Zhang, H. Q. Liang, Z. K. Xu and Z. Wang, *Adv. Sci.*, 2019, **6**, 1900883.
8. W.-S. Zhao, K. Fu, D.-W. Wang, M. Li, G. Wang and W.-Y. Yin, *Appl. Sci.*, 2019, **9**, 2174.
9. K. Geng, T. He, R. Liu, S. Dalapati, K. T. Tan, Z. Li, S. Tao, Y. Gong, Q. Jiang and D. Jiang, *Chem. Rev.*, 2020, **120**, 8814.
10. A. Furube and S. Hashimoto, *NPG Asia Mater.*, 2017, **9**, e454.

11. H. Yu, Y. Peng, Y. Yang and Z.-Y. Li, *Npj Comput. Mater.*, 2019, **5**, 45.
12. J. A. Webb and R. Bardhan, *Nanoscale*, 2014, **6**, 2502.
13. S. Link and M. A. El-Sayed, *J. Phys. Chem. B*, 1999, **103**, 8410.
14. S. Link and M. A. El-Sayed, *Int. Rev. Phys. Chem.*, 2000, **19**, 409.
15. M. Hu, J. Chen, Z. Y. Li, L. Au, G. V. Hartland, X. Li, M. Marquez and Y. Xia, *Chem. Soc. Rev.*, 2006, **35**, 1084.
16. E. S. Shibu, M. Hamada, N. Murase and V. Biju, *J. Photochem. Photobiol., C*, 2013, **15**, 53.
17. N. E. Motl, E. Ewusi-Annan, I. T. Sines, L. Jensen and R. E. Schaak, *J. Phys. Chem. C*, 2010, **114**, 19263.
18. A. Lalisse, G. Tessier, J. Plain and G. Baffou, *J. Phys. Chem. C*, 2015, **119**, 25518.
19. L. Zhou, Y. Tan, J. Wang, W. Xu, Y. Yuan, W. Cai, S. Zhu and J. Zhu, *Nat. Photonics*, 2016, **10**, 393.
20. A. Pujari and T. Thomas, *Mater. Chem. Phys.*, 2020, **253**, 123419.
21. K. Manthiram and A. P. Alivisatos, *J. Am. Chem. Soc.*, 2012, **134**, 3995.
22. H. Liang, H. Xi, S. Liu, X. Zhang and H. Liu, *Nanoscale*, 2019, **11**, 18183.
23. B. Li, X. Wang, X. Wu, G. He, R. Xu, X. Lu, F. R. Wang and I. P. Parkin, *Nanoscale*, 2017, **9**, 11012.
24. S. Ge, K. W. Wong and K. M. Ng, *New J. Chem.*, 2017, **41**, 677.
25. C. M. Hessel, V. P. Pattani, M. Rasch, M. G. Panthani, B. Koo, J. W. Tunnell and B. A. Korgel, *Nano Lett.*, 2011, **11**, 2560.
26. M. Gao, L. Zhu, C. K. Peh and G. W. Ho, *Energy Environ. Sci.*, 2019, **12**, 841.
27. W. W. Gärtner, *Phys. Rev.*, 1961, **122**, 419.
28. Q. Zou, M. Abbas, L. Zhao, S. Li, G. Shen and X. Yan, *J. Am. Chem. Soc.*, 2017, **139**, 1921.
29. Y. He, Y. Cao and Y. Wang, *Asian J. Org. Chem.*, 2018, **7**, 2201.
30. D. Xu, Z. Li, L. Li and J. Wang, *Adv. Funct. Mater.*, 2020, **30**, 2000712.
31. J. R. Vélez-Cordero and J. Hernández-Cordero, *Int. J. Therm. Sci.*, 2015, **96**, 12.
32. S. C. Boca, M. Potara, A. M. Gabudean, A. Juhem, P. L. Baldeck and S. Astilean, *Cancer Lett.*, 2011, **311**, 131.
33. S. Boca-Farcau, M. Potara, T. Simon, A. Juhem, P. Baldeck and S. Astilean, *Mol. Pharm.*, 2014, **11**, 391.
34. A. D'Agostino, A. Taglietti, P. Grisoli, G. Dacarro, L. Cucca, M. Patrini and P. Pallavicini, *RSC Adv.*, 2016, **6**, 70414.
35. A. D'Agostino, A. Taglietti, R. Desando, M. Bini, M. Patrini, G. Dacarro, L. Cucca, P. Pallavicini and P. Grisoli, *Nanomaterials*, 2017, **7**, 7.
36. C. E. A. Botteon, L. B. Silva, G. V. Ccana-Ccapatinta, T. S. Silva, S. R. Ambrosio, R. C. S. Veneziani, J. K. Bastos and P. D. Marcato, *Sci. Rep.*, 2021, **11**, 1974.
37. E. Ye, M. D. Regulacio, S. Y. Zhang, X. J. Loh and M. Y. Han, *Chem. Soc. Rev.*, 2015, **44**, 6001.
38. M. D. Regulacio, D.-P. Yang and E. Ye, *CrystEngComm*, 2020, **22**, 399.
39. S. Y. Tee and E. Ye, *Mater. Adv.*, 2021, **2**, 1507.

40. D. P. Yang, X. Liu, C. P. Teng, C. Owh, K. Y. Win, M. Lin, X. J. Loh, Y. L. Wu, Z. Li and E. Ye, *Nanoscale*, 2017, **9**, 15753.
41. X. Huang and M. A. El-Sayed, *Alexandria J. Med.*, 2019, **47**, 1.
42. Y. Wang, K. C. Black, H. Luehmann, W. Li, Y. Zhang, X. Cai, D. Wan, S. Y. Liu, M. Li, P. Kim, Z. Y. Li, L. V. Wang, Y. Liu and Y. Xia, *ACS Nano*, 2013, **7**, 2068.
43. A. Li Volsi, C. Scialabba, V. Vetri, G. Cavallaro, M. Licciardi and G. Giammona, *ACS Appl. Mater. Interfaces*, 2017, **9**, 14453.
44. M. Ji, X. Qiu, L. Hou, S. Huang, Y. Li, Y. Liu, S. Duan and Y. Hu, *Int. J. Nanomed.*, 2018, **13**, 1773.
45. D. Xu, J. Mao, Y. He and E. S. Yeung, *J. Mater. Chem. C*, 2014, **2**, 4989.
46. J. Liao, W. Li, J. Peng, Q. Yang, H. Li, Y. Wei, X. Zhang and Z. Qian, *Theranostics*, 2015, **5**, 345.
47. Q. Zhang, L. Wang, Y. Jiang, W. Gao, Y. Wang, X. Yang, X. Yang and Z. Liu, *Adv. Mater. Interfaces*, 2017, **4**, 1701166.
48. W. Xu, J. Qian, G. Hou, A. Suo, Y. Wang, J. Wang, T. Sun, M. Yang, X. Wan and Y. Yao, *ACS Appl. Mater. Interfaces*, 2017, **9**, 36533.
49. S. Wang, Q. Lin, W. Xu, Q. An, R. Zhou, C.-J. Yu, D. Xu and Z. Yuan, *RSC Adv.*, 2020, **10**, 12619.
50. E. Ye, K. Y. Win, H. R. Tan, M. Lin, C. P. Teng, A. Mlayah and M. Y. Han, *J. Am. Chem. Soc.*, 2011, **133**, 8506.
51. E. Ye, M. D. Regulacio, M. S. Bharathi, H. Pan, M. Lin, M. Bosman, K. Y. Win, H. Ramanarayan, S. Y. Zhang, X. J. Loh, Y. W. Zhang and M. Y. Han, *Nanoscale*, 2016, **8**, 543.
52. C. P. Teng, T. Zhou, E. Ye, S. Liu, L. D. Koh, M. Low, X. J. Loh, K. Y. Win, L. Zhang and M. Y. Han, *Adv. Healthcare Mater.*, 2016, **5**, 2122.
53. X. Huang, P. K. Jain, I. H. El-Sayed and M. A. El-Sayed, *Photochem. Photobiol.*, 2006, **82**, 412.
54. B. Panchapakesan, B. Book-Newell, P. Sethu, M. Rao and J. Irudayaraj, *Nanomedicine*, 2011, **6**, 1787.
55. E. C. Cho, C. Kim, F. Zhou, C. M. Cobley, K. H. Song, J. Chen, Z. Y. Li, L. V. Wang and Y. Xia, *J. Phys. Chem. C*, 2009, **113**, 9023.
56. X. Huang and M. A. El-Sayed, *J. Adv. Res.*, 2010, **1**, 13.
57. Q. Tian, J. Hu, Y. Zhu, R. Zou, Z. Chen, S. Yang, R. Li, Q. Su, Y. Han and X. Liu, *J. Am. Chem. Soc.*, 2013, **135**, 8571.
58. X. Wu, G. Y. Chen, G. Owens, D. Chu and H. Xu, *Mater. Today Energy*, 2019, **12**, 277.
59. C. J. Orendorff and C. J. Murphy, *J. Phys. Chem. B*, 2006, **110**, 3990.
60. X. Huang, S. Tang, X. Mu, Y. Dai, G. Chen, Z. Zhou, F. Ruan, Z. Yang and N. Zheng, *Nat. Nanotechnol.*, 2011, **6**, 28.
61. S. Tang, M. Chen and N. Zheng, *Small*, 2014, **10**, 3139.
62. X. Huang, S. Tang, J. Yang, Y. Tan and N. Zheng, *J. Am. Chem. Soc.*, 2011, **133**, 15946.
63. J. W. Xiao, S. X. Fan, F. Wang, L. D. Sun, X. Y. Zheng and C. H. Yan, *Nanoscale*, 2014, **6**, 4345.

64. G. Zhu, J. Xu, W. Zhao and F. Huang, *ACS Appl. Mater. Interfaces*, 2016, **8**, 31716.
65. J. Wang, Y. Li, L. Deng, N. Wei, Y. Weng, S. Dong, D. Qi, J. Qiu, X. Chen and T. Wu, *Adv. Mater.*, 2017, **29**, 1603730.
66. R. Chen, Z. Wu, T. Zhang, T. Yu and M. Ye, *RSC Adv.*, 2017, **7**, 19849.
67. Q. Huang, S. Hu, J. Zhuang and X. Wang, *Chem. – Eur. J.*, 2012, **18**, 15283.
68. C.-M. Wu, S. Naseem, M.-H. Chou, J.-H. Wang and Y.-Q. Jian, *Front. Mater.*, 2019, **6**, 49.
69. J. Yan, T. Wang, G. Wu, W. Dai, N. Guan, L. Li and J. Gong, *Adv. Mater.*, 2015, **27**, 1580.
70. S. Shen, S. Wang, R. Zheng, X. Zhu, X. Jiang, D. Fu and W. Yang, *Biomaterials*, 2015, **39**, 67.
71. X. Zhang, X. Xu, T. Li, M. Lin, X. Lin, H. Zhang, H. Sun and B. Yang, *ACS Appl. Mater. Interfaces*, 2014, **6**, 14552.
72. Q. Tian, M. Tang, Y. Sun, R. Zou, Z. Chen, M. Zhu, S. Yang, J. Wang, J. Wang and J. Hu, *Adv. Mater.*, 2011, **23**, 3542.
73. M. D. Regulacio, S. Y. Tee, S. H. Lim, C. P. Teng, L. D. Koh, S. Liu and M. Y. Han, *Nanoscale*, 2017, **9**, 17865.
74. Y. Xie, L. Carbone, C. Nobile, V. Grillo, S. D'Agostino, F. Della Sala, C. Giannini, D. Altamura, C. Oelsner, C. Kryschi and P. D. Cozzoli, *ACS Nano*, 2013, **7**, 7352.
75. S. Goel, F. Chen and W. Cai, *Small*, 2014, **10**, 631.
76. Q. Tian, F. Jiang, R. Zou, Q. Liu, Z. Chen, M. Zhu, S. Yang, J. Wang, J. Wang and J. Hu, *ACS Nano*, 2011, **5**, 9761.
77. B. Li, Q. Wang, R. Zou, X. Liu, K. Xu, W. Li and J. Hu, *Nanoscale*, 2014, **6**, 3274.
78. J. M. Luther, P. K. Jain, T. Ewers and A. P. Alivisatos, *Nat. Mater.*, 2011, **10**, 361.
79. X. Shao, T. Zhang, B. Li, M. Zhou, X. Ma, J. Wang and S. Jiang, *Dalton Trans.*, 2019, **48**, 4495.
80. T. Liu, C. Wang, W. Cui, H. Gong, C. Liang, X. Shi, Z. Li, B. Sun and Z. Liu, *Nanoscale*, 2014, **6**, 11219.
81. T. Liu, C. Wang, X. Gu, H. Gong, L. Cheng, X. Shi, L. Feng, B. Sun and Z. Liu, *Adv. Mater.*, 2014, **26**, 3433.
82. V. D. Dao and H. S. Choi, *Global Challenges*, 2018, **2**, 1700094.
83. G. Ni, N. Miljkovic, H. Ghasemi, X. Huang, S. V. Boriskina, C.-T. Lin, J. Wang, Y. Xu, M. M. Rahman, T. Zhang and G. Chen, *Nano Energy*, 2015, **17**, 290.
84. J. Lou, Y. Liu, Z. Wang, D. Zhao, C. Song, J. Wu, N. Dasgupta, W. Zhang, D. Zhang, P. Tao, W. Shang and T. Deng, *ACS Appl. Mater. Interfaces*, 2016, **8**, 14628.
85. X. Hu, W. Xu, L. Zhou, Y. Tan, Y. Wang, S. Zhu and J. Zhu, *Adv. Mater.*, 2017, **29**, 1604031.
86. C. Wang, X. Wang, Y. Chen and Z. Fang, *J. Photochem. Photobiol., B*, 2020, **204**, 111587.

87. N. Mauro, C. Scialabba, G. Cavallaro, M. Licciardi and G. Giammona, *Biomacromolecules*, 2015, **16**, 2766.
88. M. Hashemi, M. Omidi, B. Muralidharan, H. Smyth, M. A. Mohagheghi, J. Mohammadi and T. E. Milner, *ACS Appl. Mater. Interfaces*, 2017, **9**, 32607.
89. S. M. Mousavi, F. W. Low, S. A. Hashemi, N. A. Samsudin, M. Shakeri, Y. Yusoff, M. Rahsepar, C. W. Lai, A. Babapoor, S. Soroshnia, S. M. Goh, S. K. Tiong and N. Amin, *RSC Adv.*, 2020, **10**, 12851.
90. P. D. Dongare, A. Alabastri, S. Pedersen, K. R. Zodrow, N. J. Hogan, O. Neumann, J. Wu, T. Wang, A. Deshmukh, M. Elimelech, Q. Li, P. Nordlander and N. J. Halas, *Proc. Natl. Acad. Sci. U. S. A.*, 2017, **114**, 6936.
91. C. Chen, Y. Li, J. Song, Z. Yang, Y. Kuang, E. Hitz, C. Jia, A. Gong, F. Jiang, J. Y. Zhu, B. Yang, J. Xie and L. Hu, *Adv. Mater.*, 2017, **29**, 1701756.
92. N. Saifuddin, A. Z. Raziah and A. R. Junizah, *J. Chem.*, 2013, **2013**, 1.
93. R. Rao, C. L. Pint, A. E. Islam, R. S. Weatherup, S. Hofmann, E. R. Meshot, F. Wu, C. Zhou, N. Dee, P. B. Amama, J. Carpena-Nunez, W. Shi, D. L. Plata, E. S. Penev, B. I. Yakobson, P. B. Balbuena, C. Bichara, D. N. Futaba, S. Noda, H. Shin, K. S. Kim, B. Simard, F. Mirri, M. Pasquali, F. Fornasiero, E. I. Kauppinen, M. Arnold, B. A. Cola, P. Nikolaev, S. Arepalli, H. M. Cheng, D. N. Zakharov, E. A. Stach, J. Zhang, F. Wei, M. Terrones, D. B. Geohegan, B. Maruyama, S. Maruyama, Y. Li, W. W. Adams and A. J. Hart, *ACS Nano*, 2018, **12**, 11756.
94. X. Du, J. Xu, S. Deng, Z. Du, X. Cheng and H. Wang, *ACS Sustainable Chem. Eng.*, 2019, **7**, 17682.
95. C. Wang, L. Xu, C. Liang, J. Xiang, R. Peng and Z. Liu, *Adv. Mater.*, 2014, **26**, 8154.
96. Y. Ito, Y. Tanabe, J. Han, T. Fujita, K. Tanigaki and M. Chen, *Adv. Mater.*, 2015, **27**, 4302.
97. J. Yang, Y. Pang, W. Huang, S. K. Shaw, J. Schiffbauer, M. A. Pillers, X. Mu, S. Luo, T. Zhang, Y. Huang, G. Li, S. Ptasinska, M. Lieberman and T. Luo, *ACS Nano*, 2017, **11**, 5510.
98. J. T. Robinson, S. M. Tabakman, Y. Liang, H. Wang, H. S. Casalongue, D. Vinh and H. Dai, *J. Am. Chem. Soc.*, 2011, **133**, 6825.
99. M. Ioniță, G. M. Vlăsceanu, A. A. Watzlawek, S. I. Voicu, J. S. Burns and H. Iovu, *Composites, Part B*, 2017, **121**, 34.
100. P. Zhang, J. Li, L. Lv, Y. Zhao and L. Qu, *ACS Nano*, 2017, **11**, 5087.
101. L. Xiao, X. Chen, X. Yang, J. Sun and J. Geng, *ACS Appl. Polym. Mater.*, 2020, **2**, 4273.
102. J. Geng, C. Sun, J. Liu, L. D. Liao, Y. Yuan, N. Thakor, J. Wang and B. Liu, *Small*, 2015, **11**, 1603.
103. B. Guo, G. Feng, P. N. Manghnani, X. Cai, J. Liu, W. Wu, S. Xu, X. Cheng, C. Teh and B. Liu, *Small*, 2016, **12**, 6243.
104. P. Chen, Y. Ma, Z. Zheng, C. Wu, Y. Wang and G. Liang, *Nat. Commun.*, 2019, **10**, 1192.

105. C. Yu, L. Xu, Y. Zhang, P. S. Timashev, Y. Huang and X.-J. Liang, *ACS Appl. Polym. Mater.*, 2020, **2**, 4289.
106. J. Yang, J. Choi, D. Bang, E. Kim, E. K. Lim, H. Park, J. S. Suh, K. Lee, K. H. Yoo, E. K. Kim, Y. M. Huh and S. Haam, *Angew. Chem., Int. Ed.*, 2011, **50**, 441.
107. J. Zhou, Z. Lu, X. Zhu, X. Wang, Y. Liao, Z. Ma and F. Li, *Biomaterials*, 2013, **34**, 9584.
108. L. Cheng, K. Yang, Q. Chen and Z. Liu, *ACS Nano*, 2012, **6**, 5605.
109. H. Gong, L. Cheng, J. Xiang, H. Xu, L. Feng, X. Shi and Z. Liu, *Adv. Funct. Mater.*, 2013, **23**, 6059.
110. K. Yang, H. Xu, L. Cheng, C. Sun, J. Wang and Z. Liu, *Adv. Mater.*, 2012, **24**, 5586.
111. K. Ke, L. Lin, H. Liang, X. Chen, C. Han, J. Li and H. H. Yang, *Chem. Commun.*, 2015, **51**, 6800.
112. Y. Liu, K. Ai, J. Liu, M. Deng, Y. He and L. Lu, *Adv. Mater.*, 2013, **25**, 1353.
113. Y. Ding, S. Su, R. Zhang, L. Shao, Y. Zhang, B. Wang, Y. Li, L. Chen, Q. Yu, Y. Wu and G. Nie, *Biomaterials*, 2017, **113**, 243.
114. B. Guo, Z. Sheng, D. Hu, A. Li, S. Xu, P. N. Manghnani, C. Liu, L. Guo, H. Zheng and B. Liu, *ACS Nano*, 2017, **11**, 10124.
115. P. J. Waller, F. Gandara and O. M. Yaghi, *Acc. Chem. Res.*, 2015, **48**, 3053.
116. D. Bessinger, L. Ascherl, F. Auras and T. Bein, *J. Am. Chem. Soc.*, 2017, **139**, 12035.
117. B. J. Smith, A. C. Overholts, N. Hwang and W. R. Dichtel, *Chem. Commun.*, 2016, **52**, 3690.
118. A. P. Cote, A. I. Benin, N. W. Ockwig, M. O'Keeffe, A. J. Matzger and O. M. Yaghi, *Science*, 2005, **310**, 1166.
119. J. Tan, S. Namuangruk, W. Kong, N. Kungwan, J. Guo and C. Wang, *Angew. Chem., Int. Ed.*, 2016, **55**, 13979.
120. C. Hu, Z. Zhang, S. Liu, X. Liu and M. Pang, *ACS Appl. Mater. Interfaces*, 2019, **11**, 23072.
121. J. Espin, L. Garzon-Tovar, G. Boix, I. Imaz and D. Maspoch, *Chem. Commun.*, 2018, **54**, 4184.
122. J. Espin, L. Garzon-Tovar, A. Carne-Sanchez, I. Imaz and D. Maspoch, *ACS Appl. Mater. Interfaces*, 2018, **10**, 9555.
123. W. Wang, L. Wang, Y. Li, S. Liu, Z. Xie and X. Jing, *Adv. Mater.*, 2016, **28**, 9320.
124. F. Bray, J. Ferlay, I. Soerjomataram, R. L. Siegel, L. A. Torre and A. Jemal, *CA: Cancer J. Clin.*, 2018, **68**, 394.
125. R. K. Jain and T. Stylianopoulos, *Nat. Rev. Clin. Oncol.*, 2010, **7**, 653.
126. X. Huang, I. H. El-Sayed, W. Qian and M. A. El-Sayed, *J. Am. Chem. Soc.*, 2006, **128**, 2115.
127. Z. Xiao, C. Ji, J. Shi, E. M. Pridgen, J. Frieder, J. Wu and O. C. Farokhzad, *Angew. Chem., Int. Ed.*, 2012, **51**, 11853.
128. X. Cheng, R. Sun, L. Yin, Z. Chai, H. Shi and M. Gao, *Adv. Mater.*, 2017, **29**, 1604894.

129. J. Wang, G. Zhu, M. You, E. Song, M. I. Shukoor, K. Zhang, M. B. Altman, Y. Chen, Z. Zhu, C. Z. Huang and W. Tan, *ACS Nano*, 2012, **6**, 5070.
130. D. Yin, X. Li, Y. Ma and Z. Liu, *Chem. Commun.*, 2017, **53**, 6716.
131. Y. Wu, M. R. K. Ali, B. Dong, T. Han, K. Chen, J. Chen, Y. Tang, N. Fang, F. Wang and M. A. El-Sayed, *ACS Nano*, 2018, **12**, 9279.
132. S. Lal, S. E. Clare and N. J. Halas, *Acc. Chem. Res.*, 2008, **41**, 1842.
133. R. Vankayala, C. C. Lin, P. Kalluru, C. S. Chiang and K. C. Hwang, *Biomaterials*, 2014, **35**, 5527.
134. Y. Gao, Y. Li, Y. Wang, Y. Chen, J. Gu, W. Zhao, J. Ding and J. Shi, *Small*, 2015, **11**, 77.
135. J. Chen, C. Glaus, R. Laforest, Q. Zhang, M. Yang, M. Gidding, M. J. Welch and Y. Xia, *Small*, 2010, **6**, 811.
136. J. Qiu, M. Xie, T. Wu, D. Qin and Y. Xia, *Chem. Sci.*, 2020, **11**, 12955.
137. S. Wang, P. Huang, L. Nie, R. Xing, D. Liu, Z. Wang, J. Lin, S. Chen, G. Niu, G. Lu and X. Chen, *Adv. Mater.*, 2013, **25**, 3055.
138. D. Zhu, Y. Liu, M. Liu, X. Liu, P. N. Prasad and M. T. Swihart, *J. Mater. Chem. B*, 2020, **8**, 5491.
139. S. Liang, C. Li, C. Zhang, Y. Chen, L. Xu, C. Bao, X. Wang, G. Liu, F. Zhang and D. Cui, *Theranostics*, 2015, **5**, 970.
140. M. Song, N. Liu, L. He, G. Liu, D. Ling, X. Su and X. Sun, *Nano Res.*, 2018, **11**, 2796.
141. S. D. Lounis, E. L. Runnerstrom, A. Llordes and D. J. Milliron, *J. Phys. Chem. Lett.*, 2014, **5**, 1564.
142. H. Zheng, J. Z. Ou, M. S. Strano, R. B. Kaner, A. Mitchell and K. Kalantar-zadeh, *Adv. Funct. Mater.*, 2011, **21**, 2175.
143. N. Fernandes, C. F. Rodrigues, A. F. Moreira and I. J. Correia, *Biomater. Sci.*, 2020, **8**, 2990.
144. S. M. Sharker, S. M. Kim, J. E. Lee, K. H. Choi, G. Shin, S. Lee, K. D. Lee, J. H. Jeong, H. Lee and S. Y. Park, *J. Control. Release*, 2015, **217**, 211.
145. Z. Zhou, B. Kong, C. Yu, X. Shi, M. Wang, W. Liu, Y. Sun, Y. Zhang, H. Yang and S. Yang, *Sci. Rep.*, 2014, **4**, 3653.
146. Y. Tian, W. Yi, L. Bai, P. Zhang, J. Si, X. Hou, Y. Deng and J. Hou, *Int. J. Biol. Macromol.*, 2019, **137**, 904.
147. Z. Chen, Q. Wang, H. Wang, L. Zhang, G. Song, L. Song, J. Hu, H. Wang, J. Liu, M. Zhu and D. Zhao, *Adv. Mater.*, 2013, **25**, 2095.
148. W. Feng, W. Nie, Y. Cheng, X. Zhou, L. Chen, K. Qiu, Z. Chen, M. Zhu and C. He, *Nanomedicine*, 2015, **11**, 901.
149. L. Guo, D. D. Yan, D. Yang, Y. Li, X. Wang, O. Zalewski, B. Yan and W. Lu, *ACS Nano*, 2014, **8**, 5670.
150. L. Hou, X. Shan, L. Hao, Q. Feng and Z. Zhang, *Acta Biomater.*, 2017, **54**, 307.
151. S. Bharathiraja, P. Manivasagan, M. S. Moorthy, N. Q. Bui, K. D. Lee and J. Oh, *Photodiagn. Photodyn. Ther.*, 2017, **19**, 128.
152. Y. Li, W. Lu, Q. Huang, M. Huang, C. Li and W. Chen, *Nanomedicine*, 2010, **5**, 1161.

153. D. Wang, H. Dong, M. Li, Y. Cao, F. Yang, K. Zhang, W. Dai, C. Wang and X. Zhang, *ACS Nano*, 2018, **12**, 5241.
154. R. Marin, A. Skripka, L. V. Besteiro, A. Benayas, Z. Wang, A. O. Govorov, P. Canton and F. Vetrone, *Small*, 2018, **14**, e1803282.
155. N. Li, Q. Sun, Z. Yu, X. Gao, W. Pan, X. Wan and B. Tang, *ACS Nano*, 2018, **12**, 5197.
156. I. Marangon, C. Ménard-Moyon, A. K. A. Silva, A. Bianco, N. Luciani and F. Gazeau, *Carbon*, 2016, **97**, 110.
157. B. N. Eldridge, B. W. Bernish, C. D. Fahrenholtz and R. Singh, *ACS Biomater. Sci. Eng.*, 2016, **2**, 963.
158. B. Zhang, H. Wang, S. Shen, X. She, W. Shi, J. Chen, Q. Zhang, Y. Hu, Z. Pang and X. Jiang, *Biomaterials*, 2016, **79**, 46.
159. D. Wang, Y. Ren, Y. Shao, D. Yu and L. Meng, *Bioconjug. Chem.*, 2017, **28**, 2815.
160. L. Zhang, P. Rong, M. Chen, S. Gao and L. Zhu, *Nanoscale*, 2015, **7**, 16204.
161. G. Wang, F. Zhang, R. Tian, L. Zhang, G. Fu, L. Yang and L. Zhu, *ACS Appl. Mater. Interfaces*, 2016, **8**, 5608.
162. S. Gao, L. Zhang, G. Wang, K. Yang, M. Chen, R. Tian, Q. Ma and L. Zhu, *Biomaterials*, 2016, **79**, 36.
163. L. S. Lin, X. Yang, G. Niu, J. Song, H. H. Yang and X. Chen, *Nanoscale*, 2016, **8**, 2116.
164. D. de Melo-Diogo, E. C. Costa, C. G. Alves, R. Lima-Sousa, P. Ferreira, R. O. Louro and I. J. Correia, *Eur. J. Pharm. Biopharm.*, 2018, **131**, 162.
165. J. Wu, Z. Li, Y. Li, A. Pettitt and F. Zhou, *Technol. Cancer Res. Treat.*, 2018, **17**, 1533034618768637.
166. Z. Li, Y. Chen, Y. Yang, Y. Yu, Y. Zhang, D. Zhu, X. Yu, X. Ouyang, Z. Xie, Y. Zhao and L. Li, *Front. Bioeng. Biotechnol.*, 2019, **7**, 293.
167. L. Zou, H. Wang, B. He, L. Zeng, T. Tan, H. Cao, X. He, Z. Zhang, S. Guo and Y. Li, *Theranostics*, 2016, **6**, 762.
168. H. Yu, Z. Cui, P. Yu, C. Guo, B. Feng, T. Jiang, S. Wang, Q. Yin, D. Zhong, X. Yang, Z. Zhang and Y. Li, *Adv. Funct. Mater.*, 2015, **25**, 2489.
169. J. W. Xu, K. Yao and Z. K. Xu, *Nanoscale*, 2019, **11**, 8680.
170. L. Hui, J. T. Auletta, Z. Huang, X. Chen, F. Xia, S. Yang, H. Liu and L. Yang, *ACS Appl. Mater. Interfaces*, 2015, **7**, 10511.
171. X. Jia, I. Ahmad, R. Yang and C. Wang, *J. Mater. Chem. B*, 2017, **5**, 2459.
172. N. J. Hogan, A. S. Urban, C. Ayala-Orozco, A. Pimpinelli, P. Nordlander and N. J. Halas, *Nano Lett.*, 2014, **14**, 4640.
173. L. Zhou, S. Zhuang, C. He, Y. Tan, Z. Wang and J. Zhu, *Nano Energy*, 2017, **32**, 195.
174. J. Fang, Q. Liu, W. Zhang, J. Gu, Y. Su, H. Su, C. Guo and D. Zhang, *J. Mater. Chem. A*, 2017, **5**, 17817.
175. M. Zhu, Y. Li, F. Chen, X. Zhu, J. Dai, Y. Li, Z. Yang, X. Yan, J. Song, Y. Wang, E. Hitz, W. Luo, M. Lu, B. Yang and L. Hu, *Adv. Energy Mater.*, 2018, **8**, 1701028.

176. F. Yu, Z. Guo, Y. Xu, Z. Chen, M. S. Irshad, J. Qian, T. Mei and X. Wang, *ACS Appl. Mater. Interfaces*, 2020, **12**, 57155.
177. N. Wei, Z. Li, Q. Li, E. Yang, R. Xu, X. Song, J. Sun, C. Dou, J. Tian and H. Cui, *J. Colloid Interface Sci.*, 2020, **588**, 369.
178. X. Wu, M. E. Robson, J. L. Phelps, J. S. Tan, B. Shao, G. Owens and H. Xu, *Nano Energy*, 2019, **56**, 708.
179. Y. Wang, L. Zhang and P. Wang, *ACS Sustainable Chem. Eng.*, 2016, **4**, 1223.
180. G. Liu, J. Xu and K. Wang, *Nano Energy*, 2017, **41**, 269.
181. Z. Zhao, G. Jia, Y. Liu, Q. Zhang, Y. Zhou and K. Chang, *ACS Omega*, 2020, **5**, 13482.
182. H. Jin, G. Lin, L. Bai, A. Zeiny and D. Wen, *Nano Energy*, 2016, **28**, 397.
183. M. S. Zielinski, J. W. Choi, T. La Grange, M. Modestino, S. M. Hashemi, Y. Pu, S. Birkhold, J. A. Hubbell and D. Psaltis, *Nano Lett.*, 2016, **16**, 2159.
184. L. Tian, J. Luan, K. K. Liu, Q. Jiang, S. Tadepalli, M. K. Gupta, R. R. Naik and S. Singamaneni, *Nano Lett.*, 2016, **16**, 609.
185. Y. Liu, J. Lou, M. Ni, C. Song, J. Wu, N. P. Dasgupta, P. Tao, W. Shang and T. Deng, *ACS Appl. Mater. Interfaces*, 2016, **8**, 772.
186. Z. Wang, Y. Liu, P. Tao, Q. Shen, N. Yi, F. Zhang, Q. Liu, C. Song, D. Zhang, W. Shang and T. Deng, *Small*, 2014, **10**, 3234.
187. Y. Liu, S. Yu, R. Feng, A. Bernard, Y. Liu, Y. Zhang, H. Duan, W. Shang, P. Tao, C. Song and T. Deng, *Adv. Mater.*, 2015, **27**, 2768.
188. T. F. Chala, C. M. Wu, M. H. Chou and Z. L. Guo, *ACS Appl. Mater. Interfaces*, 2018, **10**, 28955.
189. C. Zhang, C. Yan, Z. Xue, W. Yu, Y. Xie and T. Wang, *Small*, 2016, **12**, 5320.
190. A. B. Kuzmenko, E. van Heumen, F. Carbone and D. van der Marel, *Phys. Rev. Lett.*, 2008, **100**, 117401.
191. Z. Deng, J. Zhou, L. Miao, C. Liu, Y. Peng, L. Sun and S. Tanemura, *J. Mater. Chem. A*, 2017, **5**, 7691.
192. X. Wang, G. Ou, N. Wang and H. Wu, *ACS Appl. Mater. Interfaces*, 2016, **8**, 9194.

CHAPTER 2

Engineered Gold Nanoparticles for Photothermal Applications

TABITHA JONES,[a] GEMMA DAVISON,[a] HYEON-HO JEONG[b] AND TUNG-CHUN LEE*[a,c]

[a] Department of Chemistry, University College London (UCL), London WC1H 0AJ, UK; [b] School of Electrical Engineering and Computer Science, Gwangju Institute of Science and Technology, Cheomdangwagiro 123, 61005 Gwangju, Republic of Korea; [c] Institute for Materials Discovery, University College London (UCL), London WC1H 0AJ, UK
*Email: tungchun.lee@ucl.ac.uk

2.1 Introduction

Gold nanoparticles (Au NPs) are arguably the most versatile and widely studied nanomaterials to date.[1] Typically defined as particles of 1–100 nm in size,[2] which is in the sub-wavelength regime of visible light,[3] Au NPs offer a multitude of unique physiochemical features. These include uniform and tailorable size and shape, high chemical stability and biocompatibility, availability *via* scalable liquid-phase synthesis and surface modification, and unique optical properties.[4,5]

Similar to their bulk analog, Au NPs are famous for their chemical stability and specificity. On one hand, they are generally stable against oxidation under a range of conditions, including variable pH, ionic strength, and temperature, without major concerns regarding leaching of toxic chemical species.[6] On the other hand, their surface can be readily modified with high fidelity by a range of thiol- or amine-containing ligands, to produce colloidally stable NPs with various surface charges (including positive, negative,

Nanoscience & Nanotechnology Series No. 54
Photothermal Nanomaterials
Edited by Enyi Ye and Zibiao Li

Published by the Royal Society of Chemistry, www.rsc.org

zwitterionic, and neutral) and functional groups. The combination of the above two properties enables Au NPs to be exploited as an ideal nanoscale platform for drug and gene delivery among other nanocarriers.[7]

Notably, however, the distinguishing feature that allows Au NPs to top the ''hall of fame of nanomaterials'' is their unique optical properties underpinned by a physical phenomenon known as localized surface plasmon resonance (LSPR),[8] which is mediated by nanostructures of plasmonic metals, *e.g.* gold, silver, copper, and aluminum. LSPR involves the coherent oscillation and excitation of free electrons on the surface of plasmonic nanostructures, under exposure to electromagnetic waves (*i.e.* photons) in the ultraviolet–visible–near infrared (UV–VIS–NIR) spectral region.[9]

LSPR typically allows stronger light–matter interaction than that of small molecules due to a better match in length scale between the propagation distance of localized surface plasmons and the wavelength of UV–VIS–NIR light, as well as the large polarizability of plasmonic materials at optical frequency. Under resonance conditions, the electric field around an Au NP will be significantly enhanced which facilitates light–matter interaction of the medium surrounding a nanoparticle *via* near-field effects. The resultant oscillating electric dipole and multipoles can also impact the associated far-field spectral scattering signal; meanwhile, part of their energy will be dissipated as heat *via* Joule heating due to the increased frequency of collisions between the electrons and lattice atoms.[10]

Early research in plasmonics in the 1900s mainly focused on the gigantic light intensity enhancement around a nanoparticle by LSPR, which has resulted in a range of promising photonic advances in biosensing, trace chemical detection, photovoltaics, and plasmon-enhanced spectroscopy. In this context, energy dissipation as heat will weaken the optical signal and is therefore considered an undesired loss that has to be minimized.

The emergence of thermoplasmonics research can be traced back to 1999, when Au NPs were first utilized to generate heat from light to investigate the denaturation of proteins.[11] More importantly, the main benefits of using metal nanoparticles over commonly used dyes have been identified, which include enhanced light–matter interactions, high achievable temperatures, localized heating with high spatiotemporal resolution, and strong resistance against thermal and photo-bleaching of absorbers. Subsequent seminal work of the field includes plasmonic photothermal imaging,[12] plasmonic photothermal therapy (PPTT),[13,14] photothermal-triggered drug and gene delivery,[15] as well as photoacoustic imaging.[16]

Following the ground-breaking initial developments in the early 2000s, the field of thermoplasmonics, where plasmonic nanoparticles are used to generate localized heat, has been growing rapidly.[10,17] The scope of research has also been extended from heat generation to heat quantification and management. Along the course, a plethora of applications for photothermal gold nanostructures have been discovered from cancer therapy[18–21] to nanofabrication[22–25] to solar steam generation.[26–29]

The main motivation of utilizing plasmonic nanoparticles as photothermal agents is to efficiently convert light into heat in a highly localized fashion at the nanoscale. Plasmonic nanoparticles can significantly outperform molecular dyes due to their strong light–matter interaction and their resistance to thermal and photo-bleaching. The combination of these two properties also underpins their ability to generate heat under tight temporal confinement, typically down to the nanosecond scale, using high-power pulse lasers that can achieve temperatures as high as 300 °C. In contrast, the niche of plasmonic nanoparticles will fade in macroscale heating scenarios because the absorption cross section (C_{abs}) and the absorber size are no longer the only parameters of interest. Under this circumstance, the overall absorbance (A) of the entire system becomes relevant, where $A = C_{abs}cl$, c is the concentration of the absorber, and l is the optical path length. Thus, concentrated black paint or carbon black can be used to cost-effectively achieve almost 100% absorption. Furthermore, these black materials exhibit high absorbance across a wide spectral range compared to plasmonic nanoparticles and are therefore more suitable for applications involving broadband light sources, such as the sun.

Regarding selection among plasmonic metals, gold is the most commonly used material in thermoplasmonics.[30] This is despite the fact that theoretically, silver should exhibit more efficient photothermal light-to-heat conversion due to its superior optical properties, such as larger absorption cross section.[31,32] However, in practical terms, the oxidation of silver by sulfur atoms of the ligands significantly dampens and weakens the plasmonic resonances.[30] In general, silver nanoparticles (Ag NPs) are prone to oxidation by atmospheric oxygen, especially in aqueous media of acidic or alkaline pH and/or in the presence of ammonia and compounds containing amino groups. This oxidation results in the generation and dissolution of Ag^+ cations which are mainly responsible for the observed cytotoxicity and low biocompatibility of Ag NPs.[33,34] On the contrary, Au NPs are chemically stable and highly biocompatible. In the material selection and design process, it is important to consider other requirements, and hence the material with the highest absorption cross section may not always win. For instance, biological and biomedical applications call for a combination of high biocompatibility, NPs of sizes between 10 nm and 150 nm for prolonged blood circulation,[35] as well as LSPR in the NIR biological transparency window. In this context, gold nanoparticles outperform silver nanoparticles.

This chapter aims to provide an overview of the landscape in state-of-the-art thermoplasmonics research and to propose a framework for classifying and designing novel photothermal gold nanoparticles, illustrated by selected examples and applications. In Section 2.1 we discuss the background of gold nanoparticle research in the context of thermoplasmonics (see Table 2.1 for a summary of the strengths and weaknesses of Au NPs in various contexts). We note the competitive edge of plasmonic NPs as efficient and highly localized heat sources at the nanoscale, and the multiple constraints that have to be considered when optimizing NP design for a specific application.

Table 2.1 Strengths and weaknesses of Au NPs in various application contexts.

	Strength	Weakness
General	– Chemical stability against oxidation	– Low chemical stability toward species containing soft atoms, incl. I, Br, S, P, N
	– Ease of synthesis into NPs of controllable size and shapes	– Some shape-directing ligands (*e.g.* CTAB) are toxic and difficult to remove
	– Facile functionalization to form colloidally stable NPs with a range of functional groups	– Prone to aggregation in high ionic strength media (*e.g.* PBS)
	– High biocompatibility	– Actual toxicity remains less characterized, as it depends on the surface ligands and the means of administering
Photonics	– Strong and tunable optical signal *via* optimizing their size, shape, and arrangements	– Instability in optical signal which is sensitive to aggregation of NPs
	– Optical signals that are highly sensitive to the surrounding environment	– Optical signal susceptible to contamination
Thermo-plasmonics	– High photo-conversion efficiency due to a high density of free electrons and thus large absorption cross-section and Joule number	– Less suitable for macroscale photothermal heating due to limitation on NP concentration in the media
	– Resistance to thermal and photo-bleaching	– Non-spherical Au NPs reshape into spheres from 150 °C, altering their optical properties
	– Highly localized heating at the nanoscale	– Less suitable for broadband illumination due to sharp LSPR absorption
	– Fast photothermal response (milliseconds)	
	– Ultrahigh temperature can be achieved (up to 300 °C by pulse laser, 220 °C by continuous-wave laser)	
	– Heating beyond the fluid boiling point without boiling it	
	– LSPR can be in the NIR biological transparency window	
	– LSPR can be tuned to achieve wavelength-specific photothermal effects	

In Section 2.2 the physical origin of photothermal effects in Au NPs *via* the Joule heating mechanism is briefly discussed, setting a theoretical background for the fundamental structural dimensions employed in the next section. In Section 2.3 we propose a classification framework for gold nanostructures based on three fundamental structural dimensions (length scale, anisotropy, and complexity) for classifying and designing photothermal Au NPs. In Section 2.4 we review representative examples of potential applications of thermoplasmonics, featuring brand-new functions that are unachievable using conventional photothermal agents, for instance, performing nanosurgery based on selective localized heating of subcellular compartments or single organelles,[36] and breaking the Shockley–Queisser limit of photovoltaic conversion of 41% by using the approach of thermophotovoltaics to achieve a theoretical limit of 80% photoconversion efficiency.[37] Last but not least, in Section 2.5 we attempt to distil the high-level message based on recent developments and to propose possible directions of future research in thermoplasmonics.

2.2 Physical Mechanism

Here we introduce the basic mechanism of the photothermal effect of gold nanoparticles, which stems from the optical property of metals in the nanoscale, known as localized surface plasmon resonance (LSPR). We explore the physics of LSPR by first considering the interaction of a metallic nanosphere with an electromagnetic wave. Subsequent subsections discuss how LSPR changes in nanoparticles of different sizes and shapes, and how they are associated with heat generation.

2.2.1 Localized Surface Plasmon Resonance

The optical properties of metals highly depend on the motion of electrons within them, which can give rise to new exciting optical effects when their motion is restricted by the dimensions of the nanoparticles with a size smaller than the wavelength of the incident light, typically 10–100 nm. This is due to the fact that, when the size of an Au NP is <10 nm, the mean free path of the oscillating electrons in the nanoparticle can be longer than the particle size, resulting in quantum effects[38] (see ref. 38 for quantum plasmonics). Meanwhile Au NPs over *ca.* 100 nm in diameter begin to violate the simple quasi-static approximation where the higher mode resonance including radiation damping becomes effective.

We begin with the simplest case in terms of geometry and analytical treatment; a homogeneous, isotropic nanosphere of gold in the range of 10–100 nm. When visible light is illuminated onto a gold nanosphere, the free electrons on its surface are excited and lead to the displacement of the electron cloud relative to the nuclei. This causes the Coulombic restoring force between the nuclei and the electron cloud, which leads to the continuous oscillations of the electron cloud. Such collective coherent

oscillation can be maximized when the oscillation frequency matches that of the incoming light. This phenomenon is termed localized surface plasmon resonance (LSPR). Under this condition, the excited electrons strongly enhance the optical field surrounding the gold nanosphere and then follow two decay processes: i) scattering, where the energy is radiatively emitted as photons with the same frequency as the incident light, and ii) absorption, where the energy is converted into phonons which is the source of heat. The sum of these two processes is known as extinction. Hence, the LSPR for a spherical nanoparticle can be expressed in terms of:

$$C_{\text{ext}} = C_{\text{sca}} + C_{\text{abs}} \tag{2.1}$$

where C_{ext}, C_{sca}, and C_{abs}, respectively, denote the extinction, scattering, and absorption cross sections. When this LSPR is caused by the interaction of a plane wave with a spherical gold nanoparticle, in a quasi-static approximation, the absorption and scattering cross sections can be described in terms of the particle's polarizability α.[39]

$$C_{\text{abs}} = \frac{2\pi}{\lambda}\text{Im}(\alpha) \tag{2.2}$$

$$C_{\text{sca}} = \frac{8\pi^3}{3\lambda^4}[\alpha]^2 \tag{2.3}$$

where α describes the electromagnetic response of the particle given by the Clausius–Mossotti relation:[39]

$$\alpha(\omega) = 4\pi R^3 \frac{\varepsilon(\omega) - \varepsilon_{\text{m}}}{\varepsilon(\omega) + 2\varepsilon_{\text{m}}} \tag{2.4}$$

where ε_{m} and $\varepsilon(\omega)$ are, respectively, the frequency-dependent dielectric constants of the surrounding medium and nanoparticle. This shows that the polarizability rises with the increasing radius R of the gold nanoparticle and also shows that $|\alpha|$ is maximized when $|\varepsilon(\omega) + 2\varepsilon_{\text{m}}|$ is a minimum (the Fröhlich condition).[39] Crucially, these affect eqn (2.2) and (2.3), such that the absorption and scattering (and thus extinction) can be resonantly enhanced due to the increase in the polarizability (α), which originates from the increase in size of the nanoparticle (R) (Figure 2.1b) and/or the dielectric constant of the surrounding media (ε_{m}), specifically refractive index (n) here (Figure 2.1c).

We now consider another special case of absorption, an ellipsoidal shaped Au NP with semi-axes $a_1 \leq a_2 \leq a_3$, so $\frac{x^2}{a_1^2} + \frac{y^2}{a_2^2} + \frac{z^2}{a_3^2} = 1$. This leads to the general form of the polarizabilities α_i along the principal axes ($i = 1, 2, 3$):

$$\alpha_i = 4\pi a_1 a_2 a_3 \frac{\varepsilon(\omega) - \varepsilon_{\text{m}}}{3\varepsilon_{\text{m}} + 3L_i(\varepsilon(\omega) - \varepsilon_{\text{m}})} \tag{2.5}$$

where L_i is a geometrical factor that satisfies $\Sigma L_i = 1$ and for a sphere $L_1 = L_2 = L_3 = \frac{1}{3}$. The depolarization factor is also often used to define the

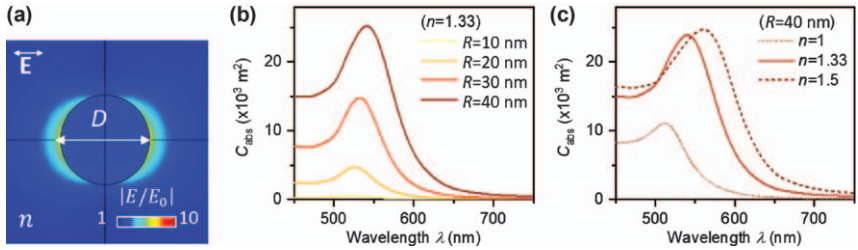

Figure 2.1 (a) Optical near-field enhancement and (b–c) absorption cross-sections of spherical gold nanoparticles when changing (b) the Au NP radius (R) and (c) the surrounding medium refractive index (n).

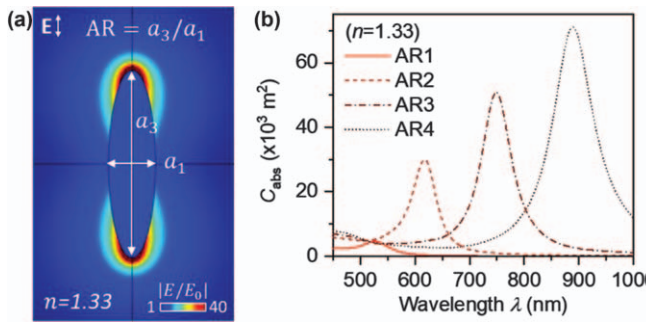

Figure 2.2 (a) Optical near-field enhancement and (b) absorption cross-sections of spheroidal gold nanoparticles with aspect ratios (AR) of 1–4. a_1 and a_2 are fixed at 20 nm and a_3 is varied from 20 nm to 80 nm with 20 nm intervals.

shape effect (see ref. 40 for details).[40] These equations can be used to describe the absorption cross-section for non-spherical particles. Based on the Mie solution, Figure 2.2 shows the numerical simulation of the important case of ellipsoids; spheroids that change absorption cross-section and resonance wavelength according to an increase in their aspect ratio.[30] The incident linear polarization is along the long axis (a_3) of the spheroid which results in the largest absorption.

2.2.2 Plasmonic Heating

The localized surface plasmon resonance generates heat *via* the Joule effect, so here we show that they are related.[30] The time-averaged heat power density q is given as:

$$q = \frac{1}{2}\mathrm{Re}(\mathbf{J} \cdot \mathbf{E}^{*}) \tag{2.6}$$

where **J** is the electronic current density and **E** is the electric field inside the nanostructure. Utilizing the relationship between the current density and

the polarization vector ($\mathbf{P}$), $\mathbf{J} = \partial\mathbf{P}/\partial t$ and $\mathbf{P} = \varepsilon_0(\varepsilon - 1)\mathbf{E}$, eqn (2.6) can also be expressed as:

$$q = \frac{\omega}{2}\varepsilon_0 \mathrm{Im}(\varepsilon)|\mathbf{E}|^2 \tag{2.7}$$

where ω is the angular frequency of the light. It is important to note that the heat power density within a nanoparticle is proportional to the square of the amplitude of the electric field. According to Poynting's theorem, the total heat power (Q) delivered by a nanoparticle is simply the integral of q over the nanoparticle volume V:

$$Q = \frac{\omega}{2}\varepsilon_0 \mathrm{Im}(\varepsilon) \iiint |\mathbf{E}_\omega|^2 \, \mathrm{d}\mathbf{V} \tag{2.8}$$

The heat generated by a gold nanoparticle results in a temperature increase in the nanoparticle and the surrounding medium due to heat diffusion. This can be expressed *via* the general heat transfer equation:

$$\rho C_\mathrm{p} \frac{\partial T(\mathbf{r})}{\partial t} = \nabla \cdot [\kappa \nabla T(\mathbf{r})] + Q \tag{2.9}$$

where ρ, C_p, and κ are the density, specific heat capacity, and thermal conductivity at constant pressure, respectively. $T(\mathbf{r})$ is the absolute temperature. To determine the heat generated by a nanoparticle and the subsequent temperature rise in the surroundings, the electric field inside the particle must be determined. This can be done by solving Maxwell's equation numerically using finite element modeling (FEM).[10]

$$\nabla \times \mu_\mathrm{r}^{-1}(\nabla \times \mathbf{E}) - \frac{\omega^2}{c^2}\left(\varepsilon - i\frac{\sigma}{\omega\varepsilon_0}\right)\mathbf{E} = 0 \tag{2.10}$$

where μ_r is the relative magnetic permeability and c is the speed of light. The electric field, and consequently the heat power density, within a spherical nanoparticle is considered to be uniform for particles smaller than the plasmon resonance wavelength.[10] This leads to the optical absorption cross-section (C_abs) defined in eqn (2.2), so Q can be described as:

$$C_\mathrm{abs} = \frac{Q}{I_0} \tag{2.11}$$

where I_0 is the intensity of the incident light given by $I_0 = \frac{c\varepsilon_0}{2}|\mathbf{E}|^2$. This highlights why C_abs is one of the most important quantities to consider when evaluating a particular nanostructure for plasmonic heating.

The temperature distribution around the particle is governed by eqn (2.9) which reaches a steady state within tens of nanoseconds and therefore

satisfies Laplace's equation. The general solution of the temperature gradient outside a spherical nanoparticle is:

$$\Delta T(r) = \frac{Q}{4\pi\kappa r}, \quad r \geq R \tag{2.12}$$

where r is the distance from the center of a nanoparticle with radius R. $\Delta T(r)$ is at its maximum at the surface of the nanoparticle (where $r = R$). From eqn (2.8), $Q \propto R^3$, therefore substituting $r = R$ into eqn (2.12) gives $\Delta T(\max) \propto R^2$.[31] However, since there is an upper limit of LSPR where the radiation damping becomes effective, $R \approx 50$ nm might present as the upper size limit for wavelength-selective plasmonic heating.

2.2.3 Au for Plasmonic Heating

For macroscale heating, the absorbance (A) of the sample plays a key role, defined as:

$$A = C_{\text{abs}} cl \tag{2.13}$$

where c is the molecular concentration (in molecules per m^3) and l is the thickness of the system. This means that the absorption cross-section is not a single parameter to increase the absorption, so the plasmonic nanoparticles may not be the best solution when aiming for macroscale heating because other cheap materials, *e.g.* carbon black, can reach almost 100% absorption over the whole visible range by increasing their concentration (Figure 2.3a).[41]

However, the key advantage of using plasmonic nanoparticles for heating is their ability to generate heat in extremely small volumes at a specific

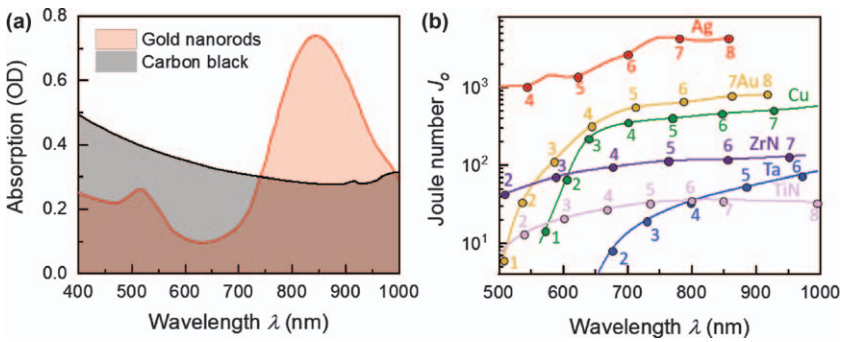

Figure 2.3 (a) Absorption spectra of 0.01 $g\,L^{-1}$ solutions of carbon black and silica-coated gold nanorods (12.5 nm×50 nm), suspended in ethanol. Reproduced from ref. 41 with permission from American Chemical Society, Copyright 2018. (b) Calculated Joule numbers of ellipsoids made of different materials, and for different aspect ratios, from 1 to 8. Reproduced from ref. 42 with permission from American Chemical Society, Copyright 2015.

wavelength, making them the best candidates for applications requiring spatially confined heating with a restricted spectral window (*e.g.,* in the human body). In this context, it is important to identify or design the most suitable plasmonic nanoparticles for a specific application. A common goal for plasmonic heating applications is to maximize the light-to-heat conversion, which can be achieved by engineering the nanoparticle's physical geometry (size and shape) and material composition. Details of these effects will be discussed in the following section, but the majority of material composition will be fixed to Au due to the following reasons. Figure 2.3b shows values of the Joule number (J_o) at the plasmonic resonance for nanospheroids of different aspect ratios (for simplicity) and made of various materials.[42]

$$J_o = \frac{C_{abs}\lambda_{ref}}{2\pi V} \tag{2.14}$$

where λ_{ref} is 1240 nm (an arbitrary reference to make J_o dimensionless) and V is the volume of the nanospheroid. J_o is proportional to C_{abs}, which stems from the material permittivity in the current circumstance of the given geometry. Hence the material with the best J_o, Ag here, could be considered as the best among the given materials in Figure 2.3b.[42] However, as discussed in Section 2.1, the oxidation of silver can significantly dampen the plasmonic resonance.[30] Furthermore, in practice, Ag is not always suitable as it has to compromise with other requirements depending on the application. For instance, in biomedical applications, the nanoparticles should be a few tens of nanometers in size for cellular uptake while presenting the resonance in the NIR transparency window. Furthermore, physicochemical stability is crucial for low toxicity. Thus, in this context, gold is superior to silver (although it has a lower J_o), as it not only exhibits resonance in a longer wavelength regime while remaining sufficiently small to favor cellular penetration but is also intrinsically stable in various biological fluids.

2.3 Classification Framework

Gold nanoparticles exhibit vast structural diversity, ranging from simple nanospheres to highly complex assemblies of Au NPs on a DNA Origami scaffold, made of more than 200 molecularly precise components. Enabled by advances in synthesis, fabrication, and self-assembly approaches, the number of novel hybrid gold nanostructures, tailored to perform a specific function, is growing at an impressive rate (see Section 2.5 for details). Perhaps ironically, we might be the victims of our own success because the huge and fast-growing number of gold nanostructures reported in the literature could become incomprehensible and intractable for many researchers who would like to select the ''best'' gold nanostructure for their system without going too deep into the physics and chemistry of Au NPs. This humiliating scenario is like trying to select the ''best'' dish of food for dinner from a long

and unfamiliar menu written in a foreign language. An easy way out for this scenario is indeed to go for the classics, *i.e.*, gold nanospheres, with the risk of missing out on other far more promising options.

Another issue that could impede the nanomaterial design and selection process is that the majority of gold nanostructures in the literature were designed for purposes other than thermoplasmonics. Is there a systematic way of quickly assessing the transferability of gold nanostructures optimized for other photonic applications, and repurposing them for thermoplasmonics without the need for reinventing the wheel?

In this section, we propose a classification framework based on three fundamental structural dimensions, namely length scale, anisotropy, and complexity, with an aim to gain a clear overview of the highly diverse range of gold nanostructures. Meanwhile, gold nanostructures are grouped into three main classes, (1) homogeneous Au NPs, (2) heterogeneous Au NPs, and (3) Au NP assemblies, according to their length scale and material complexity. Representative subclasses can then be organized with respect to each other according to structural dimensions, as shown in Figure 2.4.

This framework can offer a means to visualize the materials space defined by the independent structural dimensions, and thereby aiding comparison and design of nanomaterials in a systematic fashion. While many existing examples of gold nanomaterials are not featured in the scheme owing to limitation of space, other nanostructures can be readily inserted into the framework by benchmarking against examples in the scheme based on fundamental structural parameters. For instance, gold nanocubes are made of pure gold and with anisotropy between that of a sphere and a rod, thus they can be positioned between spheres (Figure 2.4a) and elongated NPs (Figure 2.4b).

The relevance of the structural dimensions to the potential thermoplasmonic applications of a nanomaterial and the corresponding consideration about nanomaterial design will be briefly discussed in the subsections below. It is noted that a similar classification framework for Au NPs in biomedical applications has been proposed in ref. 1. By comparing and contrasting the two frameworks, we can identify structural features that are generally critical to most applications, as well as those that are specific to thermoplasmonics.

2.3.1 Length Scale

2.3.1.1 Isolated Nanoparticles

The length scale of an individual gold nano-object typically lies in the range of 1–100 nm, and those of composite and self-assembled nanostructures generally span a much wider range up to the micron regime. While length scale in this context refers to the overall size of a nano-object, it is noted that, in the case of hierarchical nanostructures, a nano-object can have a feature size much smaller than the overall length scale of the NP. For instance, the

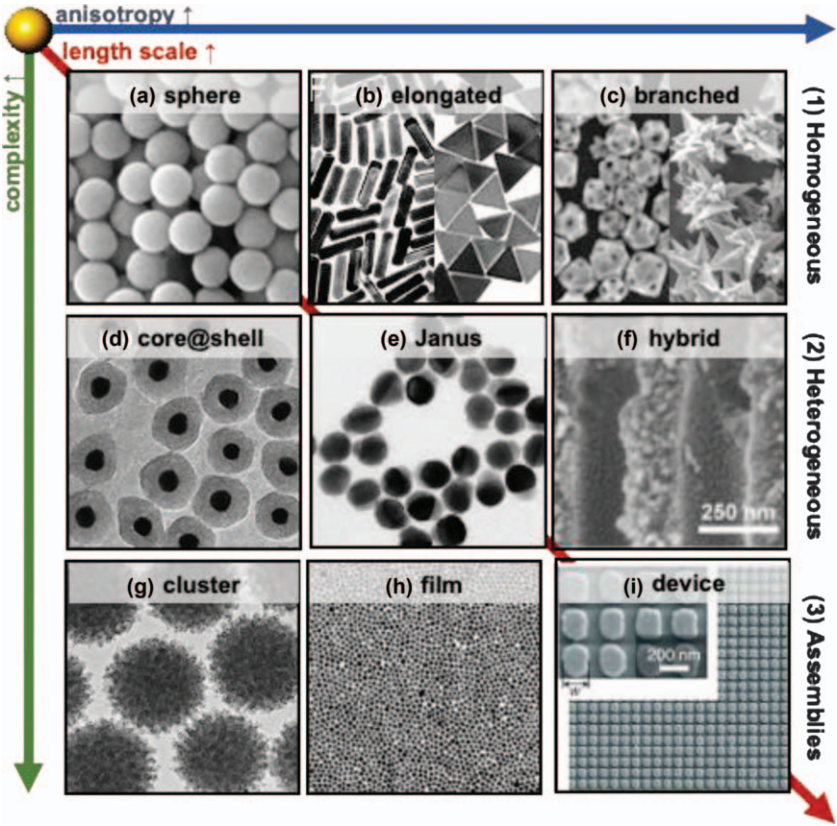

Figure 2.4 Classification framework of Au NPs for thermoplasmonics. (a) Nanospheres,[56] (b) single crystal nanorods[58] and triangular nanoplates,[59] (c) nano-cages[60] and nano-stars,[61] (d) core@shell NPs,[62] (e) Janus NPs,[44] (f) a hybrid NP system, illustrated by an aluminum porous structure decorated with Au NPs,[68] (g) clusters of Au NPs,[69] (h) a nanofilm,[72] and (i) a device, as illustrated by Au nanopads on an Au–Al_2O_3 substrate.[50] (a) Reproduced from ref. 56 with permission from American Chemical Society, Copyright 2013. (b) Reproduced from ref. 58 and 59 with permission from American Chemical Society, Copyright 2008 and 2018. (c) Reproduced from ref. 60 and 61 with permission from American Chemical Society and AIP Publishing, Copyright 2008 and 2018 American Vacuum Society. (d) Reproduced from ref. 62 with permission from the Royal Society of Chemistry. (e) Reproduced from ref. 44, https://doi.org/10.1186/s11671-019-3185-6, under the terms of the CC BY 4.0 license, https://creativecommons.org/licenses/by/4.0/. (f) Reproduced from ref. 68 with permission from Elsevier, Copyright 2017. (g) Reproduced from ref. 69, https://doi.org/10.3390/nano9091202, under the terms of the CC BY 4.0 license, https://creativecommons.org/licenses/by/4.0/. (h) Reproduced from ref. 72 with permission from Elsevier, Copyright 2018. (i) Reproduced from ref. 50 with permission from AIP Publishing, Copyright 2010.

hybrid gold–aluminum nanostructure consists of aluminum nanopores ($d \sim 300$ nm) decorated with gold nanoparticles ($d \sim 20$ nm) as shown in Figure 2.4f.

Length scale is the most important structural dimension in the context of thermoplasmonics, since the polarizability ($\alpha(\omega)$) and the total heat power (Q) of an isolated nanoparticle are proportional to the cube of its radius (R^3), *i.e.*, its volume V, as shown in eqn (2.4) and (2.8) respectively. Nevertheless, there is an upper limit of LSPR where the radiation damping becomes effective, $d \approx 100$ nm might present as the upper limit of particle size for wavelength-selective plasmonic heating. Beyond this size, the extinction spectrum of Au NPs will suffer from significant broadening due to radiation damping as well as multipolar LSPR modes, resulting in ineffective absorption under narrow-band illumination.

To the first approximation, by considering only the direct effect of size in eqn (2.8), a large nanoparticle (*e.g.*, $V = 10^5$ nm^3) exhibits the same total heat power as a group of isolated smaller nanoparticles with the same total volume (*e.g.*, 100 NPs of $V = 10^3$ nm^3 per NP). Hence, a large NP can be ''chopped up'' into smaller NPs without compromising the total heat power. However, the real situation is more complicated, since a change in particle size will impact the LSPR wavelength and intensity as a function of the imaginary part of the dielectric function, Im(ε). In addition, collective effects from interparticle plasmonic coupling in the short range and collective thermoplasmonic effects based on temperature diffusion in the long range could not be omitted for ensembles of NPs (see Section 2.3.1.2).

Application-driven design requirements should also be carefully considered. For instance, *in vivo* biomedical applications typically call for NPs of size between 10–150 nm for prolonged blood circulation or smaller than 10 nm for rapid renal clearance. At the same time, the LSPR should be in the NIR biological transparency window. The combination of these requirements already implies the NP size to be close to 100 nm in the case of spherical NPs, while a further red-shift in LSPR can be achieved by engineering the shape and aspect ratio of the NPs (see Section 2.3.2).

For solution-based applications, larger nanoparticles tend to exhibit lower colloidal stability owing to the large van der Waals interactions between them. The attractive interactions can be screened by appropriate coating of the Au NPs by either polymers or inorganic materials (see Section 2.3.3).

2.3.1.2 *Collective Effects*

On the upper end of the length scale structural dimension reside different groups of hierarchical structures made of large ensembles of Au NPs, including clusters, films, and devices (Figure 2.4g–i) where collective effects cannot be omitted.

In the short range (*i.e.*, interparticle spacing $\lesssim 0.1$ particle size), coupling between localized surface plasmon on neighboring NPs occurs and gives rise to new modes of resonance, typically known as the cavity mode or

charge-transfer mode.[43] The new modes will result in new broad peaks in the extinction response at longer wavelengths. If properly designed and engineered, the new LSPR modes can enhance absorption in the NIR range. For uncontrolled aggregation, however, the extinction response will be severely broadened, accompanied by precipitation of NPs out of solution which is a commonly encountered scenario.

In the long range, collective photothermal effects can take place *via* the coupling of the temperature diffusion profile of neighboring NPs. Interestingly, this cumulative effect can occur for a sparse nanoparticle distribution depending on the area of the illuminated region and will result in a strong overall temperature increase of several orders of magnitude higher than the prediction based on a single NP. In addition, it will lead to a highly uniform temperature distribution in the media. This phenomenon can potentially be applied to focusing heat within the interior of an Au NP cluster (Figure 2.4g).

2.3.2 Anisotropy

2.3.2.1 Shape Anisotropy

Shape anisotropy is considered the second key dimension in the engineering of photothermal Au NPs. It can be quantitatively described in terms of the aspect ratio of a nanostructure, which is equal to the ratio between their major and their shortest minor axes. For instance, the aspect ratio of a sphere is equal to 1 (*i.e.*, no shape anisotropy), while that of an ellipsoid or rod is equal to its length divided by its cross-sectional diameter (Figure 2.2), while that of a triangular plate is equal to its length divided by its thickness.

Elongation of a spherical NP into a nanorod is accompanied by an increase in aspect ratio and appearance of new LSPR modes, namely the transverse mode (*i.e.*, resonance across the nanorod) and the longitudinal mode (*i.e.*, resonance along the nanorod). The increase in length of the NP relaxes the confinement of the surface plasmon and increases the polarizability α along the major axis (see eqn (2.5) for the general form of the polarizabilities α_i along the principal axes of an ellipsoid). As a result, the longitudinal mode gives rise to a new absorption band that is significantly red-shifted with respect to that of the transverse mode, allowing modulation of the LSPR wavelength *via* aspect ratio optimization (see Figure 2.2b for the simulated absorption cross-section of ellipsoidal NPs of various aspect ratios). This approach of tuning the LSPR wavelength is considered more robust and reliable than that *via* aggregation of NPs which is prone to the formation of aggregates with undesired shape and rapid degradation over time.

Red-shifting of the LSPR to the NIR spectral region shows benefits in biomedical applications and in additive manufacturing where Au NPs can be used as transparent photothermal agents.[41] Furthermore, by employing NPs of different aspect ratios within the same system, it becomes possible to selectively generate heat in a specific photothermal agent by matching the wavelength of illumination with that of the NP.

In addition to impacting the LSPR wavelength, the aspect ratio of a NP also affects its heat power. Since the total heat power (Q) depends on the volume (V) of the NP (eqn (2.8)), it is important to first normalize the heat power of a NP against its volume before extracting the effect of anisotropy. The normalized heat power at the LSPR of an ellipsoidal NP with different aspect ratios can be described by a dimensionless term known as the Joule number (J_o) (eqn (2.14) and Figure 2.3b). The wavelength dependence of J_o mainly reflects the trend in the imaginary part of the dielectric function (Im(ε)) across different photothermal materials, where J_o generally shows a monotonic increase upon an increase in LSPR wavelength which corresponds to an increase in aspect ratio.

2.3.2.2 Material Anisotropy

Material anisotropy of a NP refers to the asymmetric distribution of materials and/or molecules within its construct and/or on its surface. A classic example of materials anisotropy involves the formation of a nano-shell of one material (*e.g.* Au, Co, Fe, or a semiconductor) on the surface of one hemisphere of a nanoparticle made of a different material (*e.g.* Au or SiO_2) to yield a Janus NP (Figure 2.4e), which is named after the two-faced ancient Roman God.[44–46] The break of mirror symmetry allows photothermal heating to be concentrated on only the gold-coated face of the Janus NP which subsequently generates a thermal gradient across the Janus NP. If the Janus NP is in contact with liquid media, the resultant thermal gradient can then produce a phoretic force under illumination, which can then be harnessed for fuel-free self-propulsion of the Janus NP if it is suspended in the liquid,[47,48] or for light-powered microfluidic pumping if there is an array of Janus NPs aligned and fixed on the wall of a microfluidic channel.[49]

Materials anisotropy can also be utilized to guide the flow of photothermal energy. For instance, in thermophotovoltaics, solar irradiation can be efficiently down-converted into IR irradiation (heat) and then to electricity by coupling a cascade of thermal emitters and a narrow-bandgap photovoltaic cell (0.8–1.1 eV) at the back of an Au NP array (Figure 2.4i).[50]

2.3.3 Material Complexity

Complexity refers to the number of types of materials and molecules within a given nanostructure and the degree of order among individual components. Simple systems typically consist of homogeneous Au NPs stabilized by a single type of ligand, whereas complex systems can involve more than 200 molecularly precise components as found in DNA-origami templated Au NP assemblies.[51]

In the context of thermoplasmonics, the purpose of incorporating other materials and molecular components in a gold nanostructure is to address the basic design requirements of a given photothermal application, as well as to introduce multiple functionalities within a single nanostructure. For applications that

involve working temperatures from a few 100 to 1000 °C, such as thermophotovoltaics and catalysis, thermal stability of Au NPs becomes a primary consideration, as non-spherical Au NPs are known to reshape into nanospheres above 150 °C, impacting their optical properties. This design requirement can be addressed by coating the Au NPs with thermally robust materials, such as Al_2O_3[52] and HfO_2,[53] to form core@shell NPs (Figure 2.4d). The oxide coatings can also increase the chemical and colloidal stability of core@shell NPs for solution-based applications. It is noted that coating an Au NP with another material will modify the refractive index around the Au NP and thereby shift the LSPR wavelength, usually to a larger value (see eqn (2.4)). Nevertheless, the shift is typically insignificant compared to that resulting from modulating the aspect ratio (Figure 2.1c and 2.2b).

The dielectric function of gold can be directly engineered *via* doping or alloying with another material, which provides a handle for optimizing the LSPR wavelength and the Joule number. In particular, when a plasmonic metal (*e.g.* Au, Ag, and Cu) is alloyed with a non-plasmonic metal (*e.g.* Ti and Fe), the LSPR typically becomes damped due to increased lattice scattering, which results in the alloyed material being more ''lossy'' and potentially exhibiting a larger Joule number. Despite being applied in photonics,[54] this approach of dispersion engineering has not been implemented in thermoplasmonics and careful evaluation is needed to assess its applicability. In particular, the damped LSPR could be significantly broadened which could lead to a notable decrease in absorption cross-section at the LSPR wavelength.

Furthermore, entirely new properties and functions can arise by carefully combining functional materials. For instance, in a seminal work on plasmonic hot-carrier chemistry, silver nanocubes are coupled to NPs of a wide-bandgap semiconductor (TiO_2) which are proposed to be capable of extracting the hot electrons from the LSPR of silver nanocubes to enhance photocatalytic water splitting reactions.[55] This is not possible with either material alone.

Designing hybrid Au NPs with multiple functionalities is of particular interest in biomedical fields, where service life cycle design is crucial for *in vivo* applications. In particular, non-negotiable requirements have to be fulfilled, including high solubility in aqueous media and high biocompatibility. On top of that, the NPs have to perform the predefined function specifically and efficiently. Since biological systems are highly complex in nature, the ideal NPs will be able to cope with the complex environment while being transported to the target region and triggering a specific task on-demand. This can only be achieved by incorporating and optimizing multiple functionalities from various functional molecular, polymeric, and material components on the NP platform, *e.g.* targeting cells, evading immune response, generating heat, and delivering drugs.[1]

2.3.4 Classification of Hybrid Gold Nanoparticles

Gold nanostructures can be generally classified into three main categories, namely (1) homogeneous Au NPs, (2) heterogeneous Au NPs, and (3) Au NP

assemblies. While categories (1) and (2) mainly concern individual NPs, category (3) includes assemblies of Au NPs exhibiting collective properties that are not found in their disassembled counterparts. From (1) to (3), there is a general increase in length scale and material complexity owing to the increase in the number of components made of different materials across the categories. The dimension of anisotropy varies rather independently both across and within the categories, with the exception of NPs of very low symmetry, which can only be found in the larger length scale regime (Figure 2.4c, f and i). This is due to the relatively low stability of NPs of low symmetry in the small length scale regime owing to surface and lattice effects. It is noted that a similar classification framework for Au NPs in biomedical applications has been proposed in ref. 1. By comparing and contrasting the two frameworks, we can identify structural features that are generally critical to most applications, as well as those that are specific to thermoplasmonics.

2.3.4.1 Homogeneous Au NPs

Homogeneous Au NPs refer to NPs that contain only gold within the construct. This is the simplest class of Au NPs, which are chemically stable, highly biocompatible, and easy to functionalize using thiol and amine chemistry. The Au NPs are typically stabilized by a self-assembled monolayer of ligand molecules, which prevents them from aggregation and sintering. With the actual wavelength depending on their size and shape, they exhibit well-defined LSPR owing to the absence of other LSPR-damping materials.

Spherical Au NPs (Figure 2.4a) are commercially available with $d = 2$–200 nm and a wide range of ligands. They remain the most popular choice for thermoplasmonics and many other applications. Moving up along the anisotropy dimension, there exists a wide variety of Au nanocrystals with different shapes (Figure 2.4b–c), ranging from classical spheres[56] to cubes,[57] rods,[58] plates,[59] cages,[60] and stars.[61] As discussed in Section 2.3.2.1, engineering the shape anisotropy is an effective means to modulate the LSPR wavelength, particularly shifting it to the NIR range, which is beneficial to *in vivo* applications.

2.3.4.2 Heterogeneous Au NPs

Heterogeneous Au NPs are NPs consisting of gold and at least one other material. As a classical example in this category, core@shell NPs (Figure 2.4d) are NPs with a core of typically gold encapsulated inside a shell of various materials.[62,63] The shell layer can be made of polymers[64] or inorganic materials[65] and can be used to enhance the thermal, chemical, and colloidal stability, biocompatibility, and anti-fouling properties of the NPs. Furthermore, it can be used to load and release drugs on-demand upon chemical stimuli, as well as to anchor cell targeting moieties for hyperthermia therapy.

Moving up along the anisotropy dimension, Janus NPs (JNPs, Figure 2.4e) emerge as the next representative subclass that exhibits material anisotropy.

A JNP consists of a core that is only partially coated on one side or coated by a different material on each of the two faces, which results in a break of mirror symmetry on the NP. As discussed in Section 2.3.2.2, photothermal effects can be concentrated on only the gold-coated face of an Au-SiO_2 JNP and thus give rise to thermophoretic effects for fuel-free self-propulsion[47,48] and microscale pumping applications.[49] As a basic asymmetric NP, JNPs can also serve as key intermediates toward more complex asymmetric NPs, such as Au NP@SiO_2 nanocups[66] and other advanced nanomachinery.[67]

At the higher end of the complexity dimension, heterogeneous Au NPs consist of multiple materials (including metals, alloys, ceramics, magnetics, and polymers) with different material composition and distribution, which are broadly classified as hybrid Au NP systems, as illustrated by the self-assembled aluminum porous structure decorated with Au NPs for broadband absorption in solar steam generation and desalination (Figure 2.4f).[68]

2.3.4.3 Au NP Assemblies

Au NP assemblies are ensembles of Au NPs exhibiting collective properties and behaviors that are different from the individual building blocks. Additional structural parameters are often required to describe the arrangement of NPs within the assemblies, including interparticle spacing, number of NPs per assembly, and degree of ordering.

Clusters of Au NPs (Figure 2.4g) represent ensembles of Au NPs that are aggregated to form a well-defined secondary nanostructure, which can span a wide range of morphologies from spherical clusters[69] to three-dimensional open networks,[70,71] two-dimensional nano-films[72] (Figure 2.4h), and even one-dimensional nano-chains. Hybrid clusters can be formed by self-assembly or co-aggregation of Au NPs and other nanomaterials. As discussed in Section 2.3.1.2, aggregation of NPs can give rise to plasmonic coupling effects and collective photothermal effects, impacting the photothermal properties and performance of the system.

Devices made of multiple components of different materials arranged in a hierarchical, highly ordered, pre-designed fashion reside at the higher ends of all three fundamental structural dimensions. In the context of thermoplasmonics, Au or other plasmonic nanostructures will be employed as the active photothermal component, as illustrated by an array of Au nanopads on an Au–Al_2O_3 substrate for thermophotovoltaics (Figure 2.4i).[50]

2.4 Applications

The ability to rapidly generate localized heat is very useful and, as a result, there are a wide range of potential applications for photothermal Au nanostructures. Some of these applications are well established and have been researched extensively, such as cancer treatment and drug delivery, while others are only just starting to be explored. This section attempts to give an overview of the key applications and to highlight how the characteristics of

the classification framework influence the performance of Au nanostructures in the areas of biomedicine, nanofabrication, solar steam generation, catalysis, thermophoresis, and functional materials.

2.4.1 Biomedical Applications

Biomedical applications have been the primary area of research for photothermal Au nanostructures thus far. Consequently, it is also the field in which the widest range of different Au nanostructures has been studied. Here we summarize the use of Au NPs for hyperthermia, drug delivery, photoacoustic imaging, cancer therapy, cell fusion, and some of the new emerging applications.

2.4.1.1 Hyperthermia

It was first reported that heat could be a potential cancer treatment in 1866, when Wilhelm Busch discovered that a high fever in one of his patients had resulted in the disappearance of a sarcoma.[10] Current cancer treatment methods include chemotherapy, radiotherapy, immunotherapy, and surgery. These methods can have inadvertent side effects, and risk damaging healthy cells. Hyperthermic cancer therapy can be used to cause apoptosis of cancer cells, in conjunction with radiation or chemotherapy. However, there are side effects of hyperthermia if the heat generation is not specific.[21] Therefore it is beneficial to deliver localized hyperthermia using photothermal NPs, particularly plasmonic NPs which can be engineered so that their resonant wavelength is within the ''biological window'' (650–1100 nm), where the least blood and tissue attenuation occurs.[21]

There are two methods by which Au NPs can be delivered to a tumor site for photothermal therapy: local injection and delivery by the enhanced permeability and retention (EPR) effect.[10,73–75] The EPR effect is the process by which Au NPs accumulate at tumor locations due to leaky immature vasculature (Figure 2.5a and b). They are then brought into the tumor cells *via* non-specific receptor-mediated endocytosis. To enhance this passive cellular uptake, Au NPs can have surface modifications (*i.e.* increase in complexity, 3rd structural dimension (SD3)). For example, binding thiol or amine groups to the surface of Au NPs can enhance cellular uptake due to their affinity for cellular membranes. When looking at the tumor penetrating abilities, Au NPs with sizes ranging from 20 to 100 nm have been tested (*i.e.* length scale, SD1).[76,77] The smaller Au NPs (<20 nm) are cleared from the extracellular fluid environment too quickly, and the larger Au NPs (>100 nm) have a limit on the distance they can travel from the blood vessels to the tumors, therefore an optimal size needs to be determined.[76,77]

When the Au NPs are positioned at the target site and illuminated, the absorbed light energy is converted into heat, which induces necrosis or apoptosis of cancer cells. Due to their ease of synthesis and ligand conjugation, spherical Au NPs were among the first classification to be studied for photothermal therapy.[21] The surface of Au NPs can be modified, for example

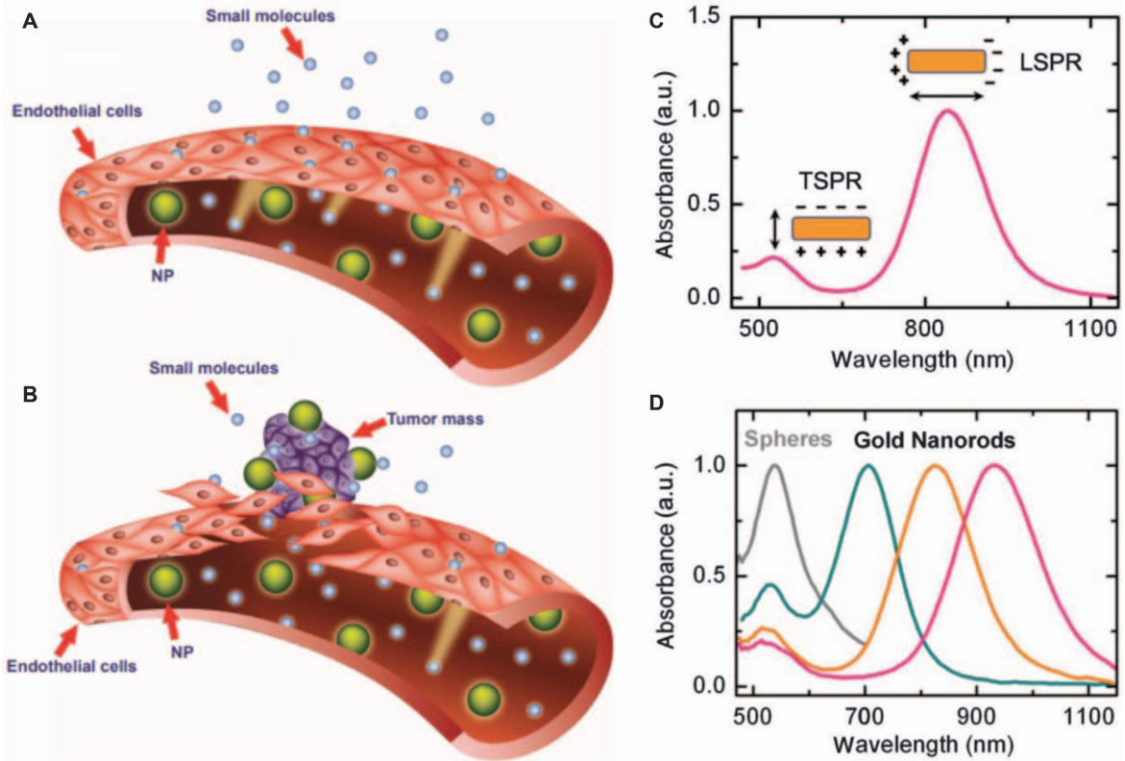

Figure 2.5 (A–B) Illustration of nanoparticle delivery by the enhanced permeability and retention (EPR) effect. Tumor vessel walls (B) are more permeable than normal vessel walls (A) due to gaps between the endothelial cells. This allows nanoparticles to accumulate at tumor sites. Reproduced from ref. 75 with permission from Dove Medical Press, Copyright 2015. (C) Absorbance spectra of an Au nanorod solution. The inset shows a schematic of the transverse and longitudinal surface plasmon resonance (SPR) modes, which correspond to the two absorption peaks, respectively. (D) Comparison of the absorbance spectra of Au nanospheres and rods. The LSPR increases as the aspect ratio of the nanorod increases (blue < orange < pink). Reproduced from ref. 80 with permission from Chinese Laser Press, Copyright 2013.

with single-stranded DNA and cytochrome c, for pH-responsive Au NPs.[78] However, the absorbance peak of Au NPs is in the visible region, which cannot penetrate deep tumors, making them less ideal for *in vivo* studies.[79] Since near-infrared (NIR) light has good transparency through the body, it is beneficial for the LSPR of the Au NPs to be within the NIR window. Consequently, increasing the anisotropy (SD2) should be considered to achieve the maximal absorption at the desired wavelength regime (Figure 2.5c and d).[80] The temperature needed for full destruction of cancer cells *in vitro* can vary depending on the type of cell but is generally in the region of 70–80 °C. This can be readily achieved *via* plasmonic heating.

The increase in length scale (SD1) and/or anisotropy (SD2) (in part) permits more absorption of light and hence results in stronger plasmonic heating. In particular, Au nanorods (NRs), with higher anisotropy than spherical Au NPs, have been investigated in a range of studies, due to the fact that they can extend the resonant wavelength into the NIR region.[21] Au NRs have been modified with porphyrin and conjugated with trastuzumab to increase the targeting selectivity and amplify the detecting effectiveness to selectively destroy breast cancer cells under NIR laser.[81] Alternative methods for the targeted photothermal therapy treatment of cancer include conjugating the Au NR surface with polymeric networks,[82] carbonic anhydrase IX,[83] sialic acid,[84] and a cyclic peptide.[85] It has also been demonstrated that Au NRs can inhibit cancer cell migration by altering the actin filaments and cell junction proteins. Gold nanoplates[86] and nanocages[87] have also been shown to be successful candidates for photothermal therapy.

Conversely, increasing the length and/or anisotropy of the NPs affects the rate of clearance from the body.[88] So, as an alternative, Au nanoshells which are either hollow or have different core materials such as silica or Au–sulfide can be synthesized to increase the absorption cross-section in the NIR region.[88–102] Alternative ways in which the length scale (SD1) has been increased are by forming gold nanoparticle clusters[103–107] and gold nanoraspberries.[108–110] Research has found that Au nanoraspberries have a high heating efficiency in both NIR regions, compared to Au nanospheres and NRs.[19] To obtain further tip-enhanced plasmonic properties, branched Au NPs, especially Au nanostars, have been used for photothermal therapy, including photothermal immunotherapy for brain tumor treatment,[111] in uveal (eye) melanoma cells,[112] and hippocampal cells,[113] among many others.[114–123] Additionally, when compared to gold nanorods and nanocages, gold nanohexapods demonstrated the lowest cytotoxicity and highest cellular uptake, possibly due to their pure Au composition and the absence of toxic surface-capping ligands, making them promising nanostructures for photothermal cancer therapy (Figure 2.6).[124]

2.4.1.2 Drug Delivery

There has been significant interest in using plasmonic heating for light-triggered drug delivery. Au NPs can enable targeted drug delivery using two main methods (Figure 2.7). The first approach is to fabricate a capsule, often a lipid vesicle, which contains gold nanoparticles and the therapeutic

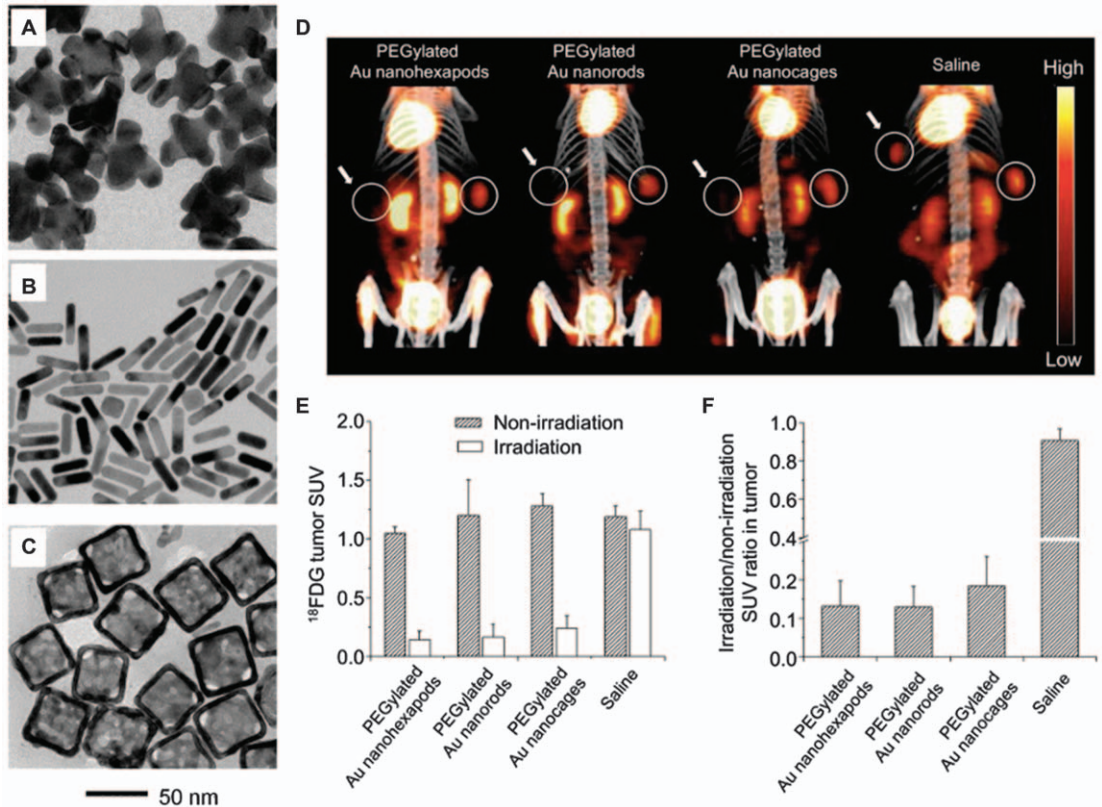

Figure 2.6 Comparison of the performance of different Au NPs for photothermal cancer treatment. (A–C) TEM images of Au nanohexapods (A), Au nanorods (B) and Au nanocages (C). The 50 nm scale bar applied to all images. (D) 18F-flourodeoxyglucose positron emission tomography/computed tomography (18F-FDG PET/CT) co-registered images of mice injected with aqueous suspensions of PEGylated nanohexapods, nanorods, nanocages, or saline. Tumors were treated either with (left, circled and arrow) or without (right, circled) laser irradiation. (E) Plot showing 18F-FDG PET/CT standardized uptake values (SUVs) in laser-treated and nontreated tumors. (F) Plot showing the ratios of laser-treated tumors to nontreated tumors 18F-FDG SUVs.
Adapted from ref. 124 with permission from American Chemical Society, Copyright 2013.

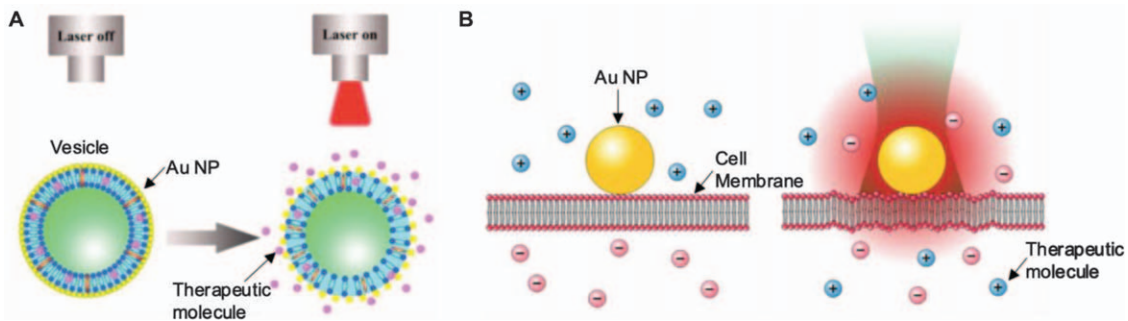

Figure 2.7 Illustration of the two main methods of plasmonic nanostructure triggered drug delivery. (A) Therapeutic molecules are encapsulated in a vesicle modified with Au nanostructures. Laser light is used to generate heat which ruptures the capsule and releases the drugs. Adapted from ref. 133 with permission from Elsevier, Copyright 2017. (B) Plasmonic heating is used to alter the permeability of the cell membrane and enable the transport of therapeutic molecules into the cell.
Reproduced from ref. 139, https://doi.org/10.1038/srep22686, under the terms of the CC BY 4.0 license, https://creativecommons.org/licenses/by/4.0/.

molecule.[125–135] This could be a nucleic acid, protein, gene, or drug, such as doxorubicin, dipyridamole, curcumin, or insulin.[136] Heat generated from irradiating the Au NP can then be used to rupture the wall of the capsule and release the therapeutic molecule at the target location. The temperature at which the capsule starts to rupture depends on the structure but it can be as low at 33 °C for lipid membranes.[128] The second approach is to use plasmonic heating to alter the permeability of cell membranes to allow the injection of molecules that are normally unable to pass into cells.[131,137–139] This method has recently been used to selectively inject fluorescently tagged siRNAs and isothiocyanate–dextran dye into rat retinal ganglion cells *in vivo*.[137] The process did not result in any cell death and opens up new opportunities for the treatment of retinal degenerative diseases. Thus far, research in this area has focused on small, simple nanostructures such as spherical nanoparticles and nanorods. However, there has been an attempt to encapsulate gold nanoclusters within reconstituted phospholipid bilayers to facilitate cellular uptake, which induce larger temperature rises within cells.[140] Furthermore, increasing the complexity (SD3) of the nanostructures could lead to additional functionalities such as hyperthermia, imaging, or self-propulsion.[141]

2.4.1.3 Photoacoustic Imaging

Photoacoustic imaging (PAI) is a biomedical imaging technique which combines optical irradiation and ultrasound detection (Figure 2.8a).[16,142–144] In PAI, light-absorbing materials (either endogenous chromophores or exogenous contrast agents) are irradiated with a short-pulse laser which induces a rapid thermoelastic expansion of the surrounding tissue.[16,143] This thermoelastic expansion generates wide-band ultrasound waves which can be detected with a transducer and processed to form an image. Au nanostructures are popular photoacoustic contrast agents because of their strong and tunable optical absorption and efficient heat generation. A wide range of different Au nanostructures have been investigated with the aim of increasing the absorption efficiency and tuning the resonant frequency to the wavelength range of the biological window.[16,143,145–152] As discussed previously, increasing the anisotropy allows maximal absorption in the desired wavelength regime (SD2).[16,149] For this reason and due to their facile synthesis, Au NRs have been used extensively in PAI research,[16,148–152] while Au nanostars have been highlighted as superior photoacoustic contrast agents due to their geometry, which offers long-term stability as well as high absorption efficiency in the NIR spectral range.[149] The surface of Au nanostructures can also be modified to enhance their affinity for particular cells (Figure 2.8b).[153]

2.4.1.4 Multimodal Cancer Therapy

To make photothermal cancer therapy more effective, hyperthermia can be combined with other features such as drug delivery and imaging *via* the formation of multifunctional nanostructures (*i.e.* increase in complexity, SD3).[154]

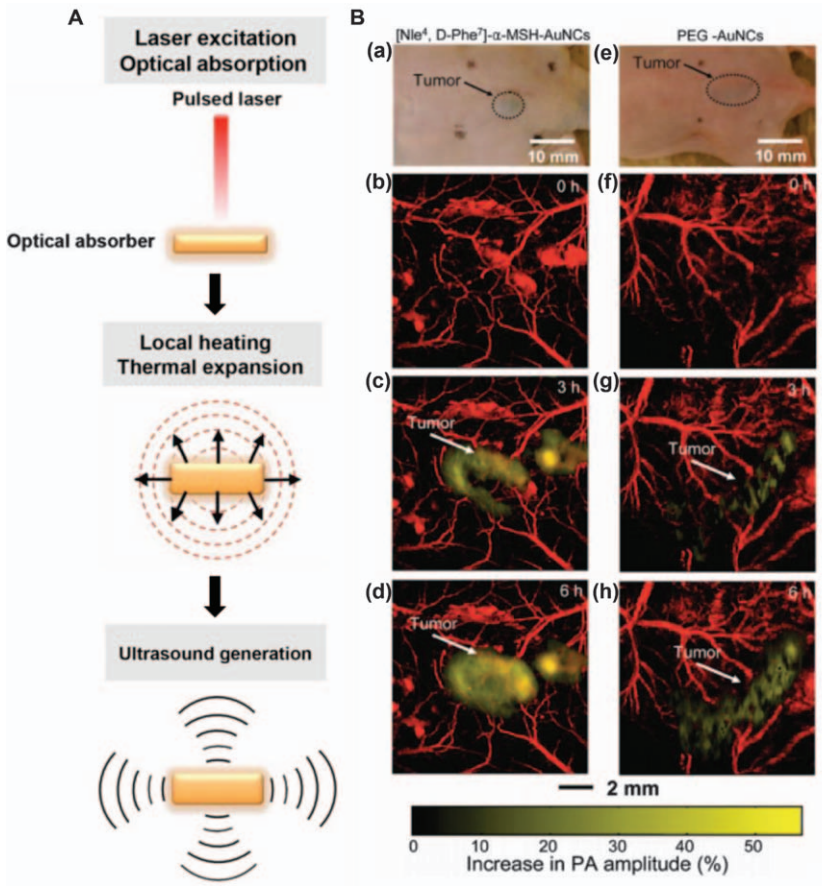

Figure 2.8 (A) Illustration of photoacoustic (PA) signal generation. A short-pulse laser is used to irradiate an optical absorber (Au NR here), which causes an increase in the local temperature. An ultrasonic pressure wave is then generated by the thermal expansion of the absorber. Reproduced from ref. 143, https://doi.org/10.1186/s12929-019-0594-x, under the terms of the CC BY 4.0 license, https://creativecommons.org/licenses/by/4.0/. (B) *In vivo* non-invasive PA time-course coronal maximum amplitude projection images of B16 melanomas using Au nanocages (NCs) bioconjugated with a [Nle4, D-Phe7]-α-melanocyte-stimulating hormone. (a and e) Photographs of nude mice transplanted with B16 melanomas before injection of (a) [Nle4, D-Phe7]-α-MSH- and (e) PEG-Au NCs. Time-course PA images of the B16 melanomas after intravenous injection with (b–d) [Nle4, D-Phe7]-α-MSH- (f–h) PEG-Au NCs. Reproduced from ref. 153 with permission from American Chemical Society, Copyright 2010.

For example, successful drug delivery has been achieved by coating triangular Au nanoplates with thiolated, hairpin-forming oligonucleotides and/or thiolated AS1411, which are then loaded with doxorubicin (DOX), a chemotherapeutic agent.[155] The triangular Au nanoplates are heated upon NIR

illumination, which causes the hairpin sequences to denature, releasing the DOX.[155]

More complex nanostructures can be synthesized to enable simultaneous hyperthermia and drug release.[156] For example, Janus nanoparticles have been used by combining Au NPs with a hydrophobic polydivinylbenzene (PDVB) matrix,[157] and silica.[158,159] This enables hyperthermia to be achieved through the photothermal effect of the Au NPs and drug release from the additional material. The complexity can be further increased by using multishell NPs. For instance, Au NRs coated with mesoporous silica and then a thermosensitive polymer have been shown to release DOX upon NIR exposure.

Photothermal therapy can also be combined with imaging, to allow visual guidance of the treatment. Peptide-conjugated PEGylated Au nanotriangles have been used for hyperthermia combined with computed tomography (CT) and photoacoustic imaging (Figure 2.9).[59] Triangular Au nanoplates have also been used to enhance optical coherence tomography imaging while thermally damaging Hela cancer cells.[160] Additionally, Au nanocubes have been used as fluorescence probes for cell imaging.[57]

Gold nanostars can be used for photothermal therapy combined with magnetic resonance imaging (MRI) when decorated on MnO_2 nanosheets,[161] for photoacoustic imaging,[162] and CT imaging.[163] MRI, multispectral photoacoustic tomography (MSOT), and CT can also be combined with photothermal therapy by using Au–Fe_2C Janus NPs.[164] Additionally, polydopamine-coated and perfluorohexane-filled Au core/hollow mesoporous silica shell particles can combine photothermal therapy with a range of different imaging techniques.[165] These different nanostructures all show great promise for multimode photothermal therapy for the treatment of cancer.

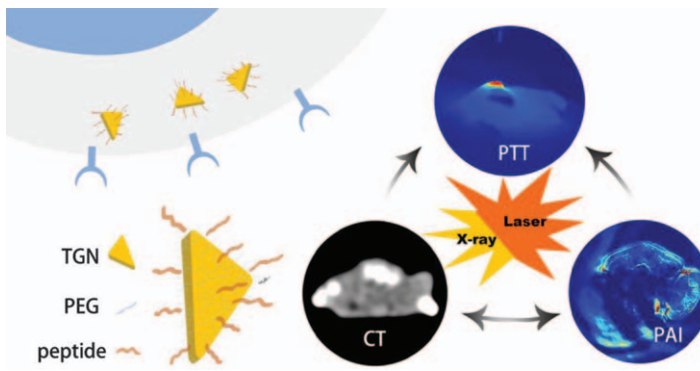

Figure 2.9 Schematic illustration of peptide-conjugated PEGylated triangular gold nanoplates (TGN) and potential use as a targeting photothermal therapy agent to treat non-small cell lung cancer under the guidance of computed tomography (CT) and photoacoustic imaging.
Reproduced from ref. 59 with permission from American Chemical Society, Copyright 2018.

2.4.1.5 Cell Fusion

Plasmonic heating can be used to fuse single cells or vesicles.[10,166–171] Fusion enables the transfer of genetic material between cells and the transfer of molecular content between vesicles.[169] This has a wide variety of applications from fundamental research into membrane biophysics[172] to the formation of novel hybrid cells.[166,167] To fuse cells or vesicles, they first need to be positioned next to each other. This can be achieved using an optical trap or by coating nanoparticles in antibodies which have a high affinity to the target cells and using these NPs to bind the cells together.[10,169] Once the cells or vesicles are in place, an Au nanostructure positioned in the contact area is irritated, generating heat which results in fusion of the cells or vesicles (Figure 2.10). In 2016, two living cells were successfully fused using optical trapping and laser irradiation of a 150 nm Au NP located between the cells.[173] After fusion, the syncytium created contained two nuclei and a cytoplasm that consisted of a mixture of the cytoplasms of the two original cells. The syncytium remained viable with a healthy metabolism for at least 4 hours after fusion. This field of research has received particular attention in recent years because of its potential to enable reprogramming of somatic cells by fusion to stem cells.[169]

2.4.1.6 Other Biomedical Applications

A diverse range of other biomedical applications for photothermal Au nanostructures have also been proposed.[5,32,166,174–180] These include modulating

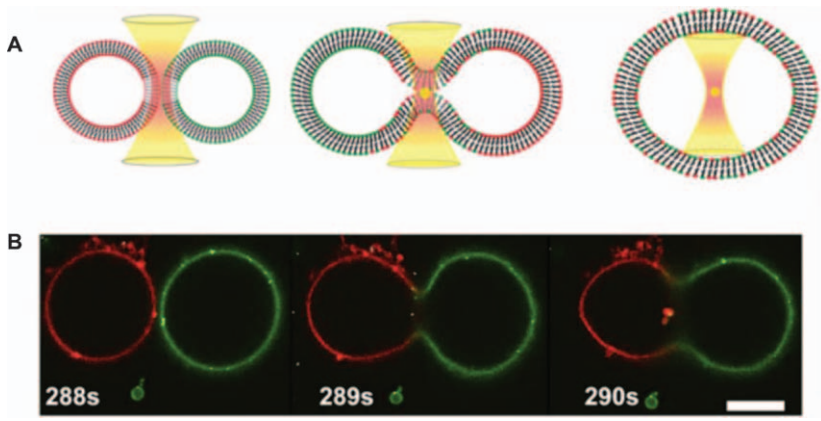

Figure 2.10 Vesicle fusion mediated by plasmonic Au NPs. (A) Illustration showing how two adjacent vesicles are fused by laser-induced heating of an Au NP trapped between the vesicles. Fusion causes complete mixing of the lipids and cargos. (B) Confocal images showing the same stages as depicted in A. The scale bar is 10 μM.
Reproduced from ref. 168 with permission from American Chemical Society, Copyright 2015.

neural activity,[175,176] accelerating wound healing,[177] preventing biofilm formation on medical devices,[177,181] and treating acne.[174] Most of these technologies are still at the early stages of development. However, there has been a successful in-man trial of plasmonic photothermal therapy for the treatment of coronary atherosclerosis.[179] Silica core–Au shell NPs were delivered to the target coronary artery *via* a bioengineered on-artery patch, and the site was illuminated with NIR light after 7 days. The patients who had been treated with the photothermal therapy displayed significant regression in coronary atherosclerosis after 12 months and a lower risk of cardiovascular death compared to patients who did not receive the treatment.

2.4.2 Nanofabrication

The ability of photothermal Au nanostructures to rapidly generate localized heat has opened up a number of promising developments in the field of nanofabrication. These include plasmon-assisted chemical vapor deposition, nanopatterning, and additive manufacture.

2.4.2.1 Plasmon-assisted Chemical Vapor Deposition (PACVD)

Chemical vapor deposition (CVD) is a widely used thin-film deposition technique in which a substrate is placed in a vacuum at high temperature and exposed to one or more volatile precursors that react and adsorb onto the surface. In traditional CVD, the entire substrate is kept at high temperatures (400–1000 °C) for the whole process. In PACVD, Au NPs are arranged on the substrate before it is exposed to the CVD precursor and a low power visible-wavelength laser is used to initiate plasmonic heating (Figure 2.11a).[182] This enables controlled, localized deposition of the material. This technique has been used to fabricate PbO[182] and Si nanowires,[25] TiO_2 microstructures,[182] and carbon nanotubes.[25,183]

2.4.2.2 Nanopatterning

Plasmonic heating can also be employed to create nanoscale patterns in materials.[23,24,184] When a tightly focused laser beam is applied to a nanoparticle, optical forces are exerted onto the particle which can cause it to move.[23,184] Combining this effect with plasmonic heating can result in controlled, localized phase changes. This idea has been used to mill precise grooves in a PVA film *via* localized thermal decomposition of the polymer layer, which occurs at 520 °C.[184] The melting point of glass is too high (1400–1600 °C) to use this technique to produce nanopatterned glass substrates. However, an alternative method has been developed which combines plasmonic heating and chemical etching. In this method, an Au NP is placed on a glass surface and surrounded by aqueous tetrabutylammonium hydroxide.[23] When the Au NP is illuminated by a laser, the heat generated causes structural modifications in the glass that result in localized etching

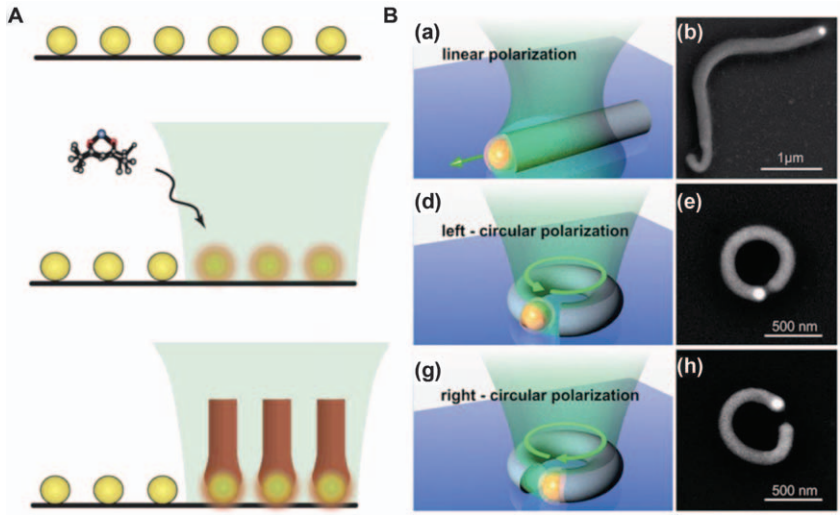

Figure 2.11 (A) Schematic of the plasmon-assisted chemical vapor deposition process (PACVD). A template of nanoscale Au structures laid down on a substrate (top). The substrate is exposed to a gaseous environment containing the CVD precursor in a carrier gas, and a laser is focused on the surface heating the NPs (middle). Growth is initiated only on the heated NPs (bottom). Reproduced from ref. 182 with permission from American Chemical Society, Copyright 2006. (B) Fabrication of PDMS nanowires using plasmonic Au NPs. (a, d, and g) Schematic illustrations of the nanowire formation with linear (a), left circularly (d), and right circularly (g) polarized light. (b, e, and h) SEM images of the PDMS wires. The NPs that were used to form the wires are visible as bright spots at the end of the structures. Reproduced from ref. 24 with permission from American Chemical Society, Copyright 2013.

and the formation of nanocavities. The shape of the nanocavity depends on the nanoparticle. In this work, spherical nanoparticles and nanotriangles were used but more intricate patterns could be produced by increasing the complexity of the NPs. This idea can also be used in the opposite way to create patterns *via* the formation of solid or crystalline sections in polymers.[24,185] For example, Au NPs have been used to form nanoscale polydimethylsiloxane (PDMS) particles and wires through localized thermal curing. The 82 nm Au NPs were heated up to 340 °C upon irradiation with a 2 mW laser. Optical forces were used to move the particle through the fluid polymer precursor, and it was possible to form PDMS rings by applying circularly polarized light (Figure 2.11b).

2.4.2.3 Additive Manufacturing

Further to nanofabrication and patterning, plasmonic heating can be used to enhance conventional manufacturing processes by reducing reaction times or improving material quality.[22,41,186,187] Carbon-based photothermal

sensitizers are commonly used to enhance the sintering of polymer powders in additive manufacturing. However, their broad absorption spectrum means that they can only produce black or gray objects. In 2018, Au nanorods were coated with silica and mixed with polyamide powders to create stable powders which were used to produce white and brightly colored 3D printed objects.[41] The shape of the NRs was engineered to maximize the photothermal efficiency (maximum efficiency of 0.86 ± 0.6) and the composite powder displayed significantly improved light-to-heat conversion compared to conventional carbon-black sensitizers.

2.4.3 Solar Steam Generation

Plasmonic heating with Au NPs can be used for solar steam generation, which has a range of applications. One of the most promising of these applications is the production of clean water. 97% of the world's water is salt water, therefore desalination of salt water is an effective way to provide people with fresh water.[26] The current methods of steam generation rely on either burning coal or other biological material to heat bulk water, which causes pollution, or the use of optical devices to concentrate sunlight to boil water, which is inefficient and expensive.[188] Therefore, a clean and efficient method is needed. Another application of solar steam generation is energy production. Solar steam generation provides the possibility of a renewable and accessible energy source, with potential for large-scale power supply.[28] Other possible uses include purification of wastewater, steam sterilization, and for photo-heat-catalysts.[27]

There are two systems which can be used for solar steam generation: the suspending system where plasmonic NPs are dispersed in the water, and the floating system in which the nanoparticles float on the surface of the water (Figure 2.12).[188] In both set-ups the plasmonic NPs absorb sunlight and heat up the water due to the photothermal effect, producing steam.

2.4.3.1 Suspending System

The effect of increasing the size of Au NPs on the photothermal conversion efficiency for solar steam generation has been investigated. Au NPs from 3 nm to 40 nm have been synthesized, and it was found that the photothermal conversion efficiency was the highest for the largest Au NPs, which agrees with the theoretical relationship between the Au NP size and the photothermal power.[28]

SiO_2 core–Au shell nanoshells have also been used in suspending photothermal solar steam generation systems.[29] Compared to a solution containing carbon NPs, the solution containing SiO_2 core–Au shell nanoshells started increasing in temperature much sooner (5 s *vs* 20 s) and reached a higher temperature (steam temperatures of up to 140 °C after 10 minutes).[29] Au NPs within the size range of 10–30 nm have also been shown to have a higher photothermal conversion efficiency for solar steam generation than spherical graphite particles, and carbon nanotubes.[189]

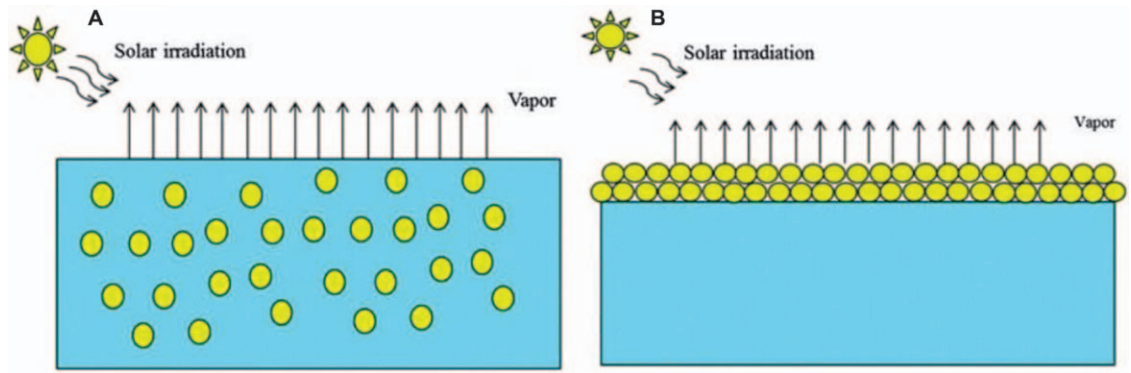

Figure 2.12 Schematic illustration of the two main methods of solar steam generation. (A) The suspending system where plasmonic NPs are dispersed in the water. (B) The floating system where the NPs float on the surface of the water. Reproduced from ref. 188 with permission from the Royal Society of Chemistry.

2.4.3.2 *Floating System*

To reduce loss of heat to the bulk of the water and improve the water vapor conversion efficiency, the development of floating Au NP films began. Inspired by skin and plant leaves, a self-assembling Au NP film at the air–water interface was developed.[190] In this system the thermal energy from the Au NPs is directly applied to the evaporative surface, resulting in a large evaporation rate while the bulk liquid temperature remains relatively undisturbed.[190] A reusable film has been fabricated by depositing an Au NP film onto air-laid paper which can be recycled many times while maintaining a high (78%) evaporation efficiency.[191]

2.4.4 Catalysis

Catalysis is an area in which photothermal gold nanostructures could make a significant impact. The rate of a chemical reaction typically depends exponentially on temperature, as described by the Arrhenius equation $\left(k \propto \exp\left(\frac{E_a}{RT}\right)\right)$, where k is the rate constant, E_a is the activation energy, R is the gas constant, and T is the temperature. Consequently, plasmonic heating can quickly and efficiently speed up thermally activated chemical reactions.[180,192] However, in recent years there has been significant debate over the underlying mechanism of photothermal catalysis.[193–202] The discussion has focused on whether heat generation or hot charge-carriers play a more significant role in the catalysis. Hot carrier catalysis was first proposed in 2004.[203] Hot carriers are formed when a metal nanoparticle absorbs a photon and promotes one electron from below the Fermi level to a state high above the Fermi level.[180,192] The energy gained by the electron is equal to that of the incident photon (a few electron volts in the visible–NIR range). The electron–hole pair formed in this process only exists for tens of femtoseconds due to collisions with other unexcited electrons in the particle. However, in that time they can be transferred to molecules adsorbed on the surface of the NP and activate chemical reactions.[198,200] Plasmonic hot-carrier chemistry has been an area of substantial interest over the last few years with researchers suggesting it has applications in nanochemistry,[202,204] water splitting[55,205,206] and artificial photosynthesis.[207–209] Regardless of the exact mechanism, photothermal Au nanostructures are an exciting prospect for the field of catalysis for a number of key reasons. Firstly, Au NPs are already used as heterogeneous catalysts and incorporating plasmonic heating would enhance their performance.[210] Secondly, they can absorb light with a broad range of wavelengths unlike traditional semiconducting photocatalytic materials, such as TiO_2, where the absorption is determined by the bandgap of the material.[192] Lastly, the localized nature of photothermal catalysis offers a very high level of spatial control over the reaction that occurs.

2.4.5 Thermophoresis

Thermophoresis is the migration of solutes in fluids in response to a temperature gradient.[211] Photothermal Au nanostructures can be employed to induce thermophoresis due to their ability to rapidly generate localized heat.[212,213] Thus far this idea has been exploited in two main ways. It can be used to move and position plasmonic NPs themselves which enables the formation of hot spots for optical sensing.[214,215] Alternatively, by arranging Au nanostructures on a surface, thermophoresis can be used to transport and manipulate objects across the surface.[216–220] In 2016, this idea was utilized to enhance the performance of a microfluidic sensing chip.[219] An Au nanorod array was used to generate convective flow within the microchannel which increased the transport velocity of a test analyte, immunoglobulin G, through the chip. The current interest in microfluidics and lab-on-a-chip devices is likely to result in significant research into plasmonic thermophoresis.

2.4.6 Functional materials

Research into photothermal gold nanostructures has led to the development of some novel materials. These fit into three main categories: shape memory, self-healing, and sterilizing.

2.4.6.1 Shape Memory Polymers

Shape memory polymers (SMPs) are a class of polymers that can be deformed into a temporary shape and recovered to their original shape upon external stimulus, most often a temperature change. Normally, the shape change is initiated by direct heating of the material. However, researchers have now started to incorporate Au nanostructures inside SMPs and exploit plasmonic heating to trigger the shape change.[221–226] Both spherical NPs[222–225] and NRs[221,222,227] have been successfully incorporated into SMPs. However, Au NRs have been shown to achieve faster responses in polyurethane-based SMPs than Au nanospheres.[222] This is due to their superior photothermal efficiency which is a result of their increased anisotropy (SD2). The additional benefit of using plasmonic heating to trigger a shape change rather than general heating is that the temperature rise can be localized. This enables spatially selective shape recovery which can generate a number of intermediate shapes. This has been demonstrated using a composite material consisting of poly(3-caprolactone)-surface functionalized Au NPs loaded in a matrix of branched oligo(3-caprolactone) cross-linked with hexamethylene diisocyanate (Figure 2.13a and b).[224]

2.4.6.2 Self-healing Materials

Self-healing materials which contain photothermal Au nanostructures aim to repair cracks or fractures in a way that mimics human skin.[225,228–230]

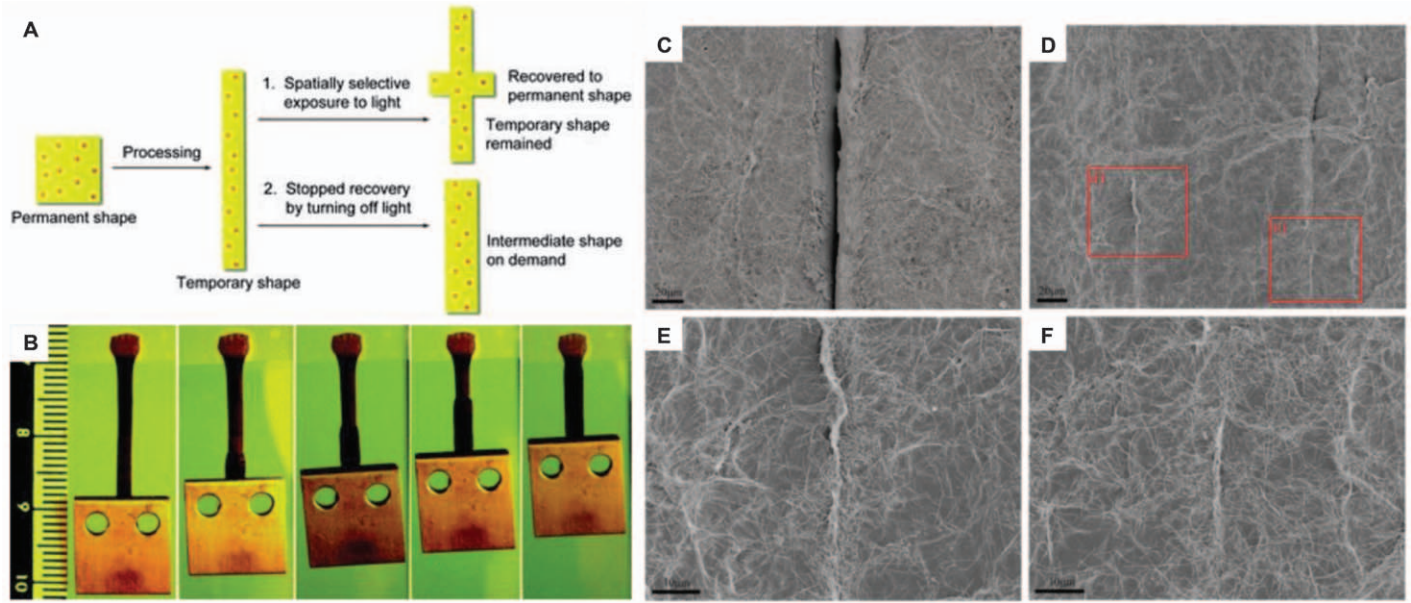

Figure 2.13 (A–B) Spatially selective shape memory polymer. (A) Schematic illustration of spatially selective shape recovery and the process of achieving intermediate shapes on demand. (B) Photographs showing a spatially selective shape recovery process at room temperature by separate laser exposures on four sections of an Au NP-loaded polymer film stretched to 100% deformation, with the film stepwise lifting a load 350 times its weight. Reproduced from ref. 224 with permission from the Royal Society of Chemistry. (C–F) Tri-layered, light-triggered healable, conductive membranes made from reduced graphene oxide and silver nanowires deposited on an electrospun fibrous composite of Au nanoparticle-incorporated polycaprolactone (Au@PCLx/rGO/Ag FM). SEM images of Au@PCLx/rGO/Ag FM with a typical crack (C) and two cracks after local heating (D–F). Reproduced from ref. 229 with permission from the Royal Society of Chemistry.

The Au NPs are embedded in a thermoplastic polymer and when damage occurs, laser light is shone on the affected area to initiate plasmonic heating. This softens or melts the surrounding polymer and allows it to heal the crack. In 2016, a flexible, conductive membrane was fabricated by depositing reduced graphene oxide and silver nanowires onto an electrospun fibrous composite of Au nanoparticle-incorporated polycaprolactone (Figure 2.13c–f).[229] After being cut with a scalpel, the membrane was irradiated with 532 nm light and was able to regain its structural and electrical properties without any loss in surface conductivity. This type of self-healing behavior has also been incorporated into shape memory polymers to create multi-functional materials.[225] So far, only spherical NPs have been used for plasmonic heating-controlled self-healing but increasing the length scale, anisotropy, or complexity of the particles could result in improved performance or enhanced functionality. However, cost and ease of synthesis are also important considerations when developing novel materials.

2.4.6.3 Sterilizing Materials

Bacterial biofilm formation on surgical equipment and implants is an increasing problem as antibiotic resistance grows. As discussed in Section 2.4.1.1, plasmonic Au nanostructures can cause hyperthermia and thus kill bacteria. Therefore, there has recently been interest in adding Au NPs to the surface of surgical materials to prevent biofilm formation.[231–235] In 2019, a proof-of-principle study was published in which polypropylene surgical meshes were coated with Au NRs and then exposed to a biofilm of *Staphylococcus aureus* bacteria.[234] After applying a train of light pulses to the Au-modified mesh, the number of viable bacteria decreased by 99.5%.

2.5 Conclusions and Outlook

Remarkable recent advances in nanoparticle synthesis and nanofabrication, underpinned by progress in characterization techniques and fundamental theories, have resulted in novel gold nanoparticles (Au NPs) that possess unprecedented physicochemical properties and multi-functionality. In particular, their ability to convert light to heat, a.k.a. plasmonic heating, promises great potential for diverse applications including biomedicine, nanofabrication, solar steam generation, catalysis, thermophoresis, and functional materials.

The development trend of thermoplasmonics in academia can be reflected in the number of publications containing Au NPs and other closely related keywords (Figure 2.14a). Overall, this area of research is booming with the number of publications reaching 10^3 per year (over 20% possession rate among all types of thermophotonics). It is interesting to note that one-third of publications (*i.e.* 30% possession rate) were thermoplasmonics in the field of thermophotonics by 2015. Recently the possession rate decreased down to 20%, but the number of publications remains *ca.* 10^3 per year.

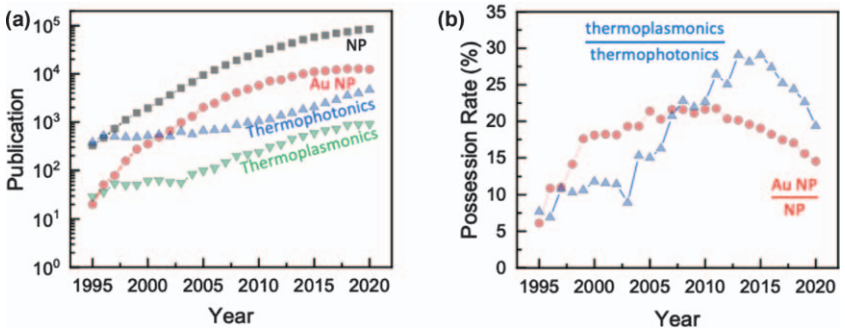

Figure 2.14 Growing popularity of thermophotonics and thermoplasmonics. (a) Number of academic articles published containing the terms "nanoparticles" (NPs, black), "gold nanoparticles" (Au NPs, red), "thermophotonics" (blue), and "thermoplasmonics" (green) since 1995. (b) Possession rate of Au NPs *vs* NPs (red) and thermoplasmonics *vs.* thermophotonics (blue).
Source: Web of Science, as assessed on 23rd February 2021.

This can be attributed to the growing diversity of material systems and energy conversion mechanisms in the research field of thermophotonics, while thermoplasmonics has been positioned as a steady seller. Furthermore, the trend of diversification is also reflected in nanoparticle research. In particular, the possession rate of Au NPs within the NP literature has declined slightly over the past decade, but the number of publications has remained around 10^4 per year. This is accompanied by the raise in the share of hybrid Au NPs as well as alternative plasmonic materials (*e.g.* Cu, Ag, Al, and Mg) and dielectric resonators (*e.g.* Si and TiO_2) in the NP literature (Figure 2.14b). This observation indicates that the focus of the field is shifting toward the development of diverse photothermal NPs, but the plasmonic heating with Au NPs still holds great interest in academia.

The rapid evolution of thermophotonic nanomaterials, especially thermoplasmonic nanoparticles, motivated us to shape a new classification framework for primary nanomaterials, *i.e.* Au NPs based on their fundamental dimensions (length scale, anisotropy, and complexity, Figure 2.4). Categorization systems such as this demystify the wide range of geometries available and provide a systematic tool for designing new shape engineered Au NPs. In the practical aspects, the framework can facilitate convenient comparison and benchmarking of novel Au NPs against well-established Au NP systems. Moreover, it could also aid reflection on the future direction of Au NPs for research in thermophotonics with regard to the balance between exploring complex new materials and exploiting well understood existing materials in both fundamental and practical contexts.

In the latter part of this chapter, we discussed how plasmonic heating can be utilized for various applications based on the axis of the classification framework. In particular, we have extensively discussed the role of plasmonic

heating for biomedical applications, illustrated by the proof-of-concept experiments of cell therapy (including hyperthermia, drug delivery), photoacoustic imaging, and cell fusion. However, we point out that, despite the huge volume of research on this topic, the number of Au NP systems finding their way into general use remains insignificant.[236] Especially, *in vivo* use of Au NPs in humans has not been approved by the Food and Drug Administration (FDA).[237]

Moreover, photothermal Au NPs find a multitude of uses in other new emerging applications, such as nanofabrication, solar steam generation, thermophoresis, catalysis, and functional materials, although there are still several challenges that need to be addressed. For instance, the ongoing 'hot' discussion in photocatalysis needs to be clarified experimentally and theoretically. Another interesting, and perhaps useful, study is hybrid nanomaterial systems comprising two or more functional materials. For instance, Au–Fe nanoparticles can be plasmonically as well as magnetically active, where both functions can be used for heating. In addition to utilizing them as nano-rheology probes,[238] it might be interesting to explore orthogonal or dual heating activation.

The field of thermoplasmonics has witnessed an impressive growth from its humble beginning, where heating effects were considered an undesirable phenomenon, to a promising diverse branch of study under light–matter interactions, where control over ubiquitous photothermal effects becomes a unique handle to trigger and modulate physiochemical events at the nanoscale. Throughout the course of development, gold nanoparticles have played an indispensable role in both fundamental studies and proof-of-concept applications.

Advancement of the field will benefit from versatile nanofabrication technologies that can materialize design of complex hybrid NPs. For instance, recent development in nanoscale glancing angle deposition (nanoGLAD) enables rapid prototyping of three-dimensional hybrid NPs with programmable shape and composition.[239–241] Meanwhile, research in thermoplasmonics will also be facilitated by state-of-the-art nanoscale thermometry. For instance, temperature-gradient control and mapping at the subcellular level can be achieved by introducing Au NPs and N-doped diamond nanocrystals into a single human embryonic fibroblast.[242] The combination of nanoscale plasmonic heating and thermometry unlocks huge potential applications in life science and beyond.

References

1. H.-H. Jeong, E. Choi, E. Ellis and T.-C. Lee, *J. Mater. Chem. B*, 2019, **7**, 3480–3496.
2. Y. Xia, Y. Xiong, B. Lim and S. E. Skrabalak, *Angew. Chem. Int. Ed. Engl.*, 2009, **48**, 60–103.
3. E. C. Le Ru and P. G. Etchegoin, *Principles of Surface-enhanced Raman Spectroscopy: and Related Plasmonic Effects*, Elsevier, Amsterdam; Boston, 1st edn, 2009.

4. D. A. Giljohann, D. S. Seferos, W. L. Daniel, M. D. Massich, P. C. Patel and C. A. Mirkin, *Angew. Chem. Int. Ed. Engl.*, 2010, **49**, 3280–3294.
5. L. Dykman and N. Khlebtsov, *Chem. Soc. Rev.*, 2012, **41**, 2256–2282.
6. H. Kim, S. Beack, S. Han, M. Shin, T. Lee, Y. Park, K. S. Kim, A. K. Yetisen, S. H. Yun, W. Kwon and S. K. Hahn, *Adv. Mater.*, 2018, **30**, 1701460.
7. X. J. Loh, T.-C. Lee, Q. Dou and G. R. Deen, *Biomater. Sci.*, 2016, **4**, 70–86.
8. K. M. Mayer and J. H. Hafner, *Chem. Rev.*, 2011, **111**, 3828–3857.
9. S. Schlücker, *Angew. Chem., Int. Ed.*, 2014, **53**, 4756–4795.
10. L. Jauffred, A. Samadi, H. Klingberg, P. M. Bendix and L. B. Oddershede, *Chem. Rev.*, 2019, **119**, 8087–8130.
11. G. Huttmann and R. Birngruber, *IEEE J. Sel. Top. Quantum Electron.*, 1999, **5**, 954–962.
12. D. Boyer, P. Tamarat, A. Maali, B. Lounis and M. Orrit, *Science*, 2002, **297**, 1160–1163.
13. C. M. Pitsillides, E. K. Joe, X. Wei, R. R. Anderson and C. P. Lin, *Biophys. J.*, 2003, **84**, 4023–4032.
14. L. R. Hirsch, R. J. Stafford, J. A. Bankson, S. R. Sershen, B. Rivera, R. E. Price, J. D. Hazle, N. J. Halas and J. L. West, *Proc. Natl. Acad. Sci. U. S. A.*, 2003, **100**, 13549–13554.
15. P. Ghosh, G. Han, M. De, C. K. Kim and V. M. Rotello, *Adv. Drug Delivery Rev.*, 2008, **60**, 1307–1315.
16. W. Li and X. Chen, *Nanomedicine*, 2015, **10**, 299–320.
17. G. Baffou and R. Quidant, *Laser Photonics Rev.*, 2013, **7**, 171–187.
18. C. Vilches and R. Quidant, in *Frontiers of Nanoscience*, ed. W. J. Parak and N. Feliu, Elsevier, 2020, vol. 16, pp. 307–352.
19. A. P. Sangnier, A. V. de Walle, R. Aufaure, M. Fradet, L. Motte, E. Guénin, Y. Lalatonne and C. Wilhelm, *Adv. Biosyst.*, 2020, **4**, 1900284.
20. S. Hwang, J. Nam, S. Jung, J. Song, H. Doh and S. Kim, *Nanomedicine*, 2014, **9**, 2003–2022.
21. J. B. Vines, J.-H. Yoon, N.-E. Ryu, D.-J. Lim and H. Park, *Front. Chem.*, 2019, **7**, 167.
22. R. J. Fortenbaugh and B. J. Lear, *Nanoscale*, 2017, **9**, 8555–8559.
23. Y. Osaka, S. Sugano and S. Hashimoto, *Nanoscale*, 2016, **8**, 18187–18196.
24. M. Fedoruk, M. Meixner, S. Carretero-Palacios, T. Lohmüller and J. Feldmann, *ACS Nano*, 2013, **7**, 7648–7653.
25. L. Cao, D. N. Barsic, A. R. Guichard and M. L. Brongersma, *Nano Lett.*, 2007, **7**, 3523–3527.
26. F. Liu, Y. Lai, B. Zhao, R. Bradley and W. Wu, *Front. Chem. Sci. Eng.*, 2019, **13**, 636–653.
27. Y. Lin, H. Xu, X. Shan, Y. Di, A. Zhao, Y. Hu and Z. Gan, *J. Mater. Chem. A*, 2019, **7**, 19203–19227.
28. A. Guo, Y. Fu, G. Wang and X. Wang, *RSC Adv.*, 2017, **7**, 4815–4824.
29. O. Neumann, A. S. Urban, J. Day, S. Lal, P. Nordlander and N. J. Halas, *ACS Nano*, 2013, **7**, 42–49.

30. G. Baffou, *Thermoplasmonics: Heating Metal Nanoparticles Using Light*, Cambridge University Press, Cambridge, 2017.
31. A. O. Govorov and H. H. Richardson, *Nano Today*, 2007, **2**, 30–38.
32. M. Kim, J.-H. Lee and J.-M. Nam, *Adv. Sci.*, 2019, **6**, 1900471.
33. D. McShan, P. C. Ray and H. Yu, *J. Food Drug Anal.*, 2014, **22**, 116–127.
34. M. Ema, H. Okuda, M. Gamo and K. Honda, *Reprod. Toxicol.*, 2017, **67**, 149–164.
35. N. Hoshyar, S. Gray, H. Han and G. Bao, *Nanomedicine*, 2016, **11**, 673–692.
36. H. M. L. Robert, J. Savatier, S. Vial, J. Verghese, B. Wattellier, H. Rigneault, S. Monneret, J. Polleux and G. Baffou, *Small*, 2018, **14**, e1801910.
37. Z. Zhou, E. Sakr, Y. Sun and P. Bermel, *Nanophotonics*, 2016, **5**, 1–21.
38. M. S. Tame, K. R. McEnery, Ş. K. Özdemir, J. Lee, S. A. Maier and M. S. Kim, *Nat. Phys.*, 2013, **9**, 329–340.
39. C. Louis and O. Pluchery, *Gold Nanoparticles For Physics, Chemistry And Biology*, World Scientific, 2nd edn, 2017.
40. M. Kim, J. Lee and J. Nam, *Adv. Sci.*, 2019, **6**, 1900471.
41. A. W. Powell, A. Stavrinadis, I. de Miguel, G. Konstantatos and R. Quidant, *Nano Lett.*, 2018, **18**, 6660–6664.
42. A. Lalisse, G. Tessier, J. Plain and G. Baffou, *J. Phys. Chem. C*, 2015, **119**, 25518–25528.
43. R. W. Taylor, T.-C. Lee, O. A. Scherman, R. Esteban, J. Aizpurua, F. M. Huang, J. J. Baumberg and S. Mahajan, *ACS Nano*, 2011, **5**, 3878–3887.
44. X.-D. Liu, K. Chen, S. Ma, Z.-H. Hao, S. Liang, L. Zhou and Q.-Q. Wang, *Nanoscale Res. Lett.*, 2019, **14**, 349.
45. Z. Li, A. Lopez-Ortega, A. Aranda-Ramos, J. L. Tajada, J. Sort, C. Nogues, P. Vavassori, J. Nogues and B. Sepulveda, *Small*, 2018, **14**, 1800868.
46. A. Kirillova, C. Marschelke and A. Synytska, *ACS Appl. Mater. Interfaces*, 2019, **11**, 9643–9671.
47. Y. Wu, T. Si, J. Shao, Z. Wu and Q. He, *Nano Res.*, 2016, **9**, 3747–3756.
48. M. Xuan, Z. Wu, J. Shao, L. Dai, T. Si and Q. He, *J. Am. Chem. Soc.*, 2016, **138**, 6492–6497.
49. T. Yu, A. G. Athanassiadis, M. N. Popescu, V. Chikkadi, A. Güth, D. P. Singh, T. Qiu and P. Fischer, *ACS Nano*, 2020, **14**, 13673–13680.
50. J. Hao, J. Wang, X. Liu, W. J. Padilla, L. Zhou and M. Qiu, *Appl. Phys. Lett.*, 2010, **96**, 251104.
51. A. Kuzyk, R. Schreiber, Z. Fan, G. Pardatscher, E.-M. Roller, A. Högele, F. C. Simmel, A. O. Govorov and T. Liedl, *Nature*, 2012, **483**, 311–314.
52. G. Albrecht, S. Kaiser, H. Giessen and M. Hentschel, *Nano Lett.*, 2017, **17**, 6402–6408.
53. H.-H. Jeong, M. Alarcón-Correa, A. G. Mark, K. Son, T.-C. Lee and P. Fischer, *Adv. Sci.*, 2017, **4**, 1700234.
54. H.-H. Jeong, A. G. Mark, M. Alarcón-Correa, I. Kim, P. Oswald, T.-C. Lee and P. Fischer, *Nat. Commun.*, 2016, **7**, 11331.

55. D. B. Ingram and S. Linic, *J. Am. Chem. Soc.*, 2011, **133**, 5202–5205.
56. Y.-J. Lee, N. B. Schade, L. Sun, J. A. Fan, D. R. Bae, M. M. Mariscal, G. Lee, F. Capasso, S. Sacanna, V. N. Manoharan and G.-R. Yi, *ACS Nano*, 2013, **7**, 11064–11070.
57. X. Wu, T. Ming, X. Wang, P. Wang, J. Wang and J. Chen, *ACS Nano*, 2010, **4**, 113–120.
58. H. Chen, X. Kou, Z. Yang, W. Ni and J. Wang, *Langmuir*, 2008, **24**, 5233–5237.
59. Y. Zhao, W. Liu, Y. Tian, Z. Yang, X. Wang, Y. Zhang, Y. Tang, S. Zhao, C. Wang, Y. Liu, J. Sun, Z. Teng, S. Wang and G. Lu, *ACS Appl. Mater. Interfaces*, 2018, **10**, 16992–17003.
60. S. E. Skrabalak, J. Chen, Y. Sun, X. Lu, L. Au, C. M. Cobley and Y. Xia, *Acc. Chem. Res.*, 2008, **41**, 1587–1595.
61. H. I. Khan, M. U. Khalid, A. Abdullah, A. Ali, A. S. Bhatti, S. U. Khan and W. Ahmed, *J. Vac. Sci. Technol. B Microelectron. Nanometer. Struct. Process Meas. Phenom.*, 2018, **36**, 03E101.
62. N. Pazos-Pérez, B. Rodríguez-González, M. Hilgendorff, M. Giersig and L. M. Liz-Marzán, *J. Mater. Chem.*, 2010, **20**, 61–64.
63. R. Ghosh Chaudhuri and S. Paria, *Chem. Rev.*, 2012, **112**, 2373–2433.
64. E. Ellis, K. Zhang, Q. Lin, E. Ye, A. Poma, G. Battaglia, X. Jun Loh and T.-C. Lee, *J. Mater. Chem. B*, 2017, **5**, 4421–4425.
65. A. D. Celiz, T.-C. Lee and O. A. Scherman, *Adv. Mater.*, 2009, **21**, 3937–3940.
66. M. Alarcón-Correa, T.-C. Lee and P. Fischer, *Angew. Chem.*, 2015, **127**, 6834–6838.
67. E. Ellis, S. Moorthy, W.-I. Katherine Chio and T.-C. Lee, *Chem. Commun.*, 2018, **54**, 4075–4090.
68. L. Zhou, S. Zhuang, C. He, Y. Tan, Z. Wang and J. Zhu, *Nano Energy*, 2017, **32**, 195–200.
69. Y. Yu, Y. Xie, P. Zeng, D. Zhang, R. Liang, W. Wang, Q. Ou and S. Zhang, *Nanomaterials*, 2019, 9, 1202.
70. T.-C. Lee and O. A. Scherman, *Chem. Commun.*, 2010, **46**, 2438–2440.
71. T.-C. Lee and O. A. Scherman, *Chem. – Eur. J.*, 2012, **18**, 1628–1633.
72. Y. Xu, Z. Ye, C. Li, H. McCabe, J. Kelly and S. E. J. Bell, *Appl. Mater. Today*, 2018, **13**, 352–358.
73. K. Greish, in *Cancer Nanotechnology: Methods and Protocols*, ed. S. R. Grobmyer and B. M. Moudgil, Humana Press, Totowa, NJ, 2010, pp. 25–37.
74. S. K. Golombek, J.-N. May, B. Theek, L. Appold, N. Drude, F. Kiessling and T. Lammers, *Adv. Drug Delivery Rev.*, 2018, **130**, 17–38.
75. G. Bozzuto and A. Molinari, *Int. J. Nanomedicine*, 2015, **10**, 975–999.
76. V. Guerrero-Florez, S. C. Mendez-Sanchez, O. A. Patrón-Soberano, V. Rodríguez-González, D. Blach and F. Martínez, *J. Mater. Chem. B*, 2020, **8**, 2862–2875.
77. S. D. Perrault, C. Walkey, T. Jennings, H. C. Fischer and W. C. W. Chan, *Nano Lett.*, 2009, **9**, 7.

78. S. Park, W. J. Lee, S. Park, D. Choi, S. Kim and N. Park, *Sci. Rep.*, 2019, **9**, 20180.
79. L. C. Kennedy, L. R. Bickford, N. A. Lewinski, A. J. Coughlin, Y. Hu, E. S. Day, J. L. West and R. A. Drezek, *Small*, 2011, **7**, 169–183.
80. J. Li, H. Guo and Z.-Y. Li, *Photon. Res*, 2013, **1**, 28.
81. X. Kang, X. Guo, X. Niu, W. An, S. Li, Z. Liu, Y. Yang, N. Wang, Q. Jiang, C. Yan, H. Wang and Q. Zhang, *Sci. Rep.*, 2017, **7**, 42069.
82. H. J. Moon, M. Ku, H. Lee, N. Yoon, J. Yang and K. W. Bong, *Sci. Rep.*, 2018, **8**, 13683.
83. Y. Chen, X. Bian, M. Aliru, A. A. Deorukhkar, O. Ekpenyong, S. Liang, J. John, J. Ma, X. Gao, J. Schwartz, P. Singh, Y. Ye, S. Krishnan and H. Xie, *Oncotarget*, 2018, **9**, 26556–26571.
84. D. Yin, X. Li, Y. Ma and Z. Liu, *Chem. Commun.*, 2017, **53**, 6716–6719.
85. Y.-T. Liao, C.-H. Liu, Y. Chin, S.-Y. Chen, S. H. Liu, Y.-C. Hsu and K. C.-W. Wu, *J. Mater. Chem. B*, 2019, **7**, 4451–4460.
86. F. Gao, G. He, H. Yin, J. Chen, Y. Liu, C. Lan, S. Zhang and B. Yang, *Nanoscale*, 2019, **11**, 2374–2384.
87. J. Chen, C. Glaus, R. Laforest, Q. Zhang, M. Yang, M. Gidding, M. J. Welch and Y. Xia, *Small*, 2010, **6**, 811–817.
88. S. Abbasi, M. Servatkhah and M. M. Keshtkar, *Chin. Phys. B*, 2016, **25**, 087301.
89. I. Grabowska-Jadach, D. Kalinowska, M. Drozd and M. Pietrzak, *Biomed. Pharmacother.*, 2019, **111**, 1147–1155.
90. F. Majidi, E. Mohammadi, B. Mehravi, S. Nouri, K. Ashtari and A. Neshasteh-riz, *Artif. Cells, Nanomed., Biotechnol.*, 2019, **47**, 2161–2170.
91. S. Nouri, E. Mohammadi, B. Mehravi, F. Majidi, K. Ashtari, A. Neshasteh-Riz and S. Einali, *Artif. Cells, Nanomed., Biotechnol.*, 2019, **47**, 2316–2324.
92. A. R. Rastinehad, H. Anastos, E. Wajswol, J. S. Winoker, J. P. Sfakianos, S. K. Doppalapudi, M. R. Carrick, C. J. Knauer, B. Taouli, S. C. Lewis, A. K. Tewari, J. A. Schwartz, S. E. Canfield, A. K. George, J. L. West and N. J. Halas, *Proc. Natl. Acad. Sci. U. S. A.*, 2019, **116**, 18590–18596.
93. A. J. Coughlin and J. L. West, in *Nanomedicine*, ed. and T. J. Webster, Woodhead Publishing, 2012, pp. 326–355.
94. J. Zhang, T. Zhao, F. Han, Y. Hu and Y. Li, *J. Nanobiotechnol.*, 2019, **17**, 80.
95. T. Nunes, T. Pons, X. Hou, K. Van Do, B. Caron, M. Rigal, M. Di Benedetto, B. Palpant, C. Leboeuf, A. Janin and G. Bousquet, *J. Exp. Clin. Cancer Res.*, 2019, **38**, 306.
96. M. P. Melancon, W. Lu, Z. Yang, R. Zhang, Z. Cheng, A. M. Elliot, J. Stafford, T. Olson, J. Z. Zhang and C. Li, *Mol. Cancer Ther.*, 2008, **7**, 1730–1739.
97. K. M. Mayle, K. R. Dern, V. K. Wong, S. Sung, K. Ding, A. R. Rodriguez, Z. Taylor, Z. H. Zhou, W. S. Grundfest, T. J. Deming and D. T. Kamei, *SLAS Technol.: Transl. Life Sci. Innovation*, 2017, **22**, 18–25.

98. U. S. Chung, J.-H. Kim, B. Kim, E. Kim, W.-D. Jang and W.-G. Koh, *Chem. Commun.*, 2016, **52**, 1258–1261.
99. M. Wang, Y. Liu, X. Zhang, L. Luo, L. Li, S. Xing, Y. He, W. Cao, R. Zhu and D. Gao, *J. Mater. Chem. B*, 2017, **5**, 2161–2171.
100. S.-Y. Lee and M.-J. Shieh, *ACS Appl. Mater. Interfaces*, 2020, **12**, 4254–4264.
101. E. S. Day, P. A. Thompson, L. Zhang, N. A. Lewinski, N. Ahmed, R. A. Drezek, S. M. Blaney and J. L. West, *J. Neuro-Oncol.*, 2011, **104**, 55–63.
102. S. H. Kang, Y. K. Lee, I. S. Park, I.-K. Park, S. M. Hong, S. Y. Kwon, Y. H. Choi, S. J. Madsen, H. Hirschberg and S. J. Hong, *BioMed Res. Int.*, 2020, **2020**, 1–14.
103. J. Kim, S. H. Chun, L. Amornkitbamrung, C. Song, J. S. Yuk, S. Y. Ahn, B. W. Kim, Y. T. Lim, B.-K. Oh and S. H. Um, *Nano Convergence*, 2020, **7**, 5.
104. C. Iodice, A. Cervadoro, A. Palange, J. Key, S. Aryal, M. R. Ramirez, C. Mattu, G. Ciardelli, B. E. O'Neill and P. Decuzzi, *Opt. Lasers Eng.*, 2016, **76**, 74–81.
105. B. Khlebtsov, V. Zharov, A. Melnikov, V. Tuchin and N. Khlebtsov, *Nanotechnology*, 2006, **17**, 5167–5179.
106. L. Amornkitbamrung, J. Kim, Y. Roh, S. H. Chun, J. S. Yuk, S. W. Shin, B.-W. Kim, B.-K. Oh and S. H. Um, *Langmuir*, 2018, **34**, 2774–2783.
107. S. Wang, K.-J. Chen, T.-H. Wu, H. Wang, W.-Y. Lin, M. Ohashi, P.-Y. Chiou and H.-R. Tseng, *Angew. Chem., Int. Ed.*, 2010, **49**, 3777–3781.
108. J. Depciuch, M. Stec, B. Klebowski, J. Baran and M. Parlinska-Wojtan, *J. Nanobiotechnol.*, 2019, **17**, 107.
109. N. Gandra, C. Portz, S. Z. Nergiz, A. Fales, T. Vo-Dinh and S. Singamaneni, *Sci. Rep.*, 2015, **5**, 10311.
110. A. P. Sangnier, R. Aufaure, S. Cheong, L. Motte, B. Palpant, R. D. Tilley, E. Guenin, C. Wilhelm and Y. Lalatonne, *Chem. Commun.*, 2019, **55**, 4055–4058.
111. Y. Liu, P. Chongsathidkiet, B. M. Crawford, R. Odion, C. A. Dechant, H. R. Kemeny, X. Cui, P. F. Maccarini, C. D. Lascola, P. E. Fecci and T. Vo-Dinh, *Immunotherapy*, 2019, **11**, 1293–1302.
112. R. Ahijado-Guzmán, N. Sánchez-Arribas, M. Martínez Negro, G. González, M. Santiago-Varela, M. Pardo, A. Piñeiro Ces, I. Lopez-Montero, E. Junquera and A. Guerrero-Martínez, *Nanomaterials*, 2020, **10**, 590.
113. F. Santamaria and X. G. Peralta, in *Use of Nanoparticles in Neuroscience*, ed. F. Santamaria and X. G. Peralta, Springer, New York, NY, 2018, pp. 69–87.
114. C. Song, F. Li, X. Guo, W. Chen, C. Dong, J. Zhang, J. Zhang and L. Wang, *J. Mater. Chem. B*, 2019, **7**, 2001–2008.
115. Y. Zhu, Q. Sun, Y. Liu, T. Ma, L. Su, S. Liu, X. Shi, D. Han and F. Liang, *R. Soc. Open Sci.*, 2018, **5**, 180159.

116. H. Chatterjee, D. S. Rahman, M. Sengupta and S. K. Ghosh, *J. Phys. Chem. C*, 2018, **122**, 13082–13094.
117. Y. Li, X. Wang, L. Gao, P. Hu, L. Jiang, T. Ren, R. Fu, D. Yang and X. Jiang, *J. Mater. Sci.*, 2018, **53**, 14138–14148.
118. A. Espinosa, A. K. A. Silva, A. Sánchez-Iglesias, M. Grzelczak, C. Péchoux, K. Desboeufs, L. M. Liz-Marzán and C. Wilhelm, *Adv. Healthcare Mater.*, 2016, **5**, 1040–1048.
119. Y. Liu, J. R. Ashton, E. J. Moding, H. Yuan, J. K. Register, A. M. Fales, J. Choi, M. J. Whitley, X. Zhao, Y. Qi, Y. Ma, G. Vaidyanathan, M. R. Zalutsky, D. G. Kirsch, C. T. Badea and T. Vo-Dinh, *Theranostics*, 2015, **5**, 946–960.
120. T. Vo-Dinh, *J. Immunol. Sci.*, 2018, **2**, 1–8.
121. M. Borzenkov, G. Chirico, M. Collini, A. Määttänen, P. Ihalainen, E. Cabrini, G. Dacarro and P. Pallavicini, *Biophotonics: Photonic Solutions for Better Health Care V*, 2016, **9887**, 98872C.
122. W. Lu, A. K. Singh, S. A. Khan, D. Senapati, H. Yu and P. C. Ray, *J. Am. Chem. Soc.*, 2010, **132**, 18103–18114.
123. L. Wang, D. Meng, Y. Hao, Y. Zhao, D. Li, B. Zhang, Y. Zhang and Z. Zhang, *J. Biomater. Appl.*, 2015, **30**, 547–557.
124. Y. Wang, K. C. L. Black, H. Luehmann, W. Li, Y. Zhang, X. Cai, D. Wan, S.-Y. Liu, M. Li, P. Kim, Z.-Y. Li, L. V. Wang, Y. Liu and Y. Xia, *ACS Nano*, 2013, **7**, 2068–2077.
125. B. V. Parakhonskiy, W. J. Parak, D. Volodkin and A. G. Skirtach, *Langmuir*, 2019, **35**, 8574–8583.
126. S. Carregal-Romero, M. Ochs, P. Rivera-Gil, C. Ganas, A. M. Pavlov, G. B. Sukhorukov and W. J. Parak, *J. Controlled Release*, 2012, **159**, 120–127.
127. A. Ambrosone, V. Marchesano, S. Carregal-Romero, D. Intartaglia, W. J. Parak and C. Tortiglione, *ACS Nano*, 2016, **10**, 4828–4834.
128. A. Kyrsting, P. M. Bendix, D. G. Stamou and L. B. Oddershede, *Nano Lett.*, 2011, **11**, 888–892.
129. L. Anderson, E. Hansen, E. Y. Lukianova-Hleb, J. H. Hafner and D. O. Lapotko, *J. Controlled Release*, 2010, **144**, 151–158.
130. A. Wijaya, S. B. Schaffer, I. G. Pallares and K. Hamad-Schifferli, *ACS Nano*, 2009, **3**, 80–86.
131. M. Delcea, N. Sternberg, A. M. Yashchenok, R. Georgieva, H. Bäumler, H. Möhwald and A. G. Skirtach, *ACS Nano*, 2012, **6**, 4169–4180.
132. W. Xiong, R. Mazid, L. W. Yap, X. Li and W. Cheng, *Nanoscale*, 2014, **6**, 14388–14393.
133. Y. Liu, X. Zhang, Z. Liu, L. Wang, L. Luo, M. Wang, Q. Wang and D. Gao, *Nanomed.: Nanotechnol., Biol. Med.*, 2017, **13**, 1891–1900.
134. S. Jiang, K. Wang, Y. Dai, X. Zhang and F. Xia, *Macromol. Mater. Eng.*, 2019, **304**, 1900087.
135. S. Xing, X. Zhang, L. Luo, W. Cao, L. Li, Y. He, J. An and D. Gao, *Nanotechnology*, 2018, **29**, 405101.

136. M. Molina, M. Asadian-Birjand, J. Balach, J. Bergueiro, E. Miceli and M. Calderón, *Chem. Soc. Rev.*, 2015, **44**, 6161–6186.
137. A. M. Wilson, J. Mazzaferri, É. Bergeron, S. Patskovsky, P. Marcoux-Valiquette, S. Costantino, P. Sapieha and M. Meunier, *Nano Lett.*, 2018, **18**, 6981–6988.
138. M. E. Muroski, O. Nag, E. Oh, A. L. Huston and J. B. Delehanty, in *Colloidal Nanoparticles for Biomedical Applications XIV*, International Society for Optics and Photonics, 2019, vol. 10892, p. 108920M.
139. P. Urban, S. R. Kirchner, C. Mühlbauer, T. Lohmüller and J. Feldmann, *Sci. Rep.*, 2016, **6**, 22686.
140. J. Nam, Y.-T. Kim, A. Kang, K.-H. Kim, K. Lee, W. S. Yun and Y. H. Kim, *J. Nanomater.*, 2016, **2016**, 1–7.
141. J. Seaberg, H. Montazerian, M. N. Hossen, R. Bhattacharya, A. Khademhosseini and P. Mukherjee, *ACS Nano*, 2021, **15**, 2099–2142.
142. X. Yang, E. W. Stein, S. Ashkenazi and L. V. Wang, *WIREs Nanomed. Nanobiotechnol.*, 2009, **1**, 360–368.
143. W.-W. Liu and P.-C. Li, *J. Biomed. Sci.*, 2020, **27**, 3.
144. A. B. E. Attia, G. Balasundaram, M. Moothanchery, U. S. Dinish, R. Bi, V. Ntziachristos and M. Olivo, *Photoacoustics*, 2019, **16**, 100144.
145. J. Song, J. Kim, S. Hwang, M. Jeon, S. Jeong, C. Kim and S. Kim, *Chem. Commun.*, 2016, **52**, 8287–8290.
146. X. Cheng, R. Sun, L. Yin, Z. Chai, H. Shi and M. Gao, *Adv. Mater.*, 2017, **29**, 1604894.
147. S. Han, R. Bouchard and K. V. Sokolov, *Biomed. Opt. Express*, 2019, **10**, 3472–3483.
148. Y.-S. Chen, Y. Zhao, S. J. Yoon, S. S. Gambhir and S. Emelianov, *Nat. Nanotechnol.*, 2019, **14**, 465–472.
149. R. García-Álvarez, L. Chen, A. Nedilko, A. Sánchez-Iglesias, A. Rix, W. Lederle, V. Pathak, T. Lammers, G. von Plessen, K. Kostarelos, L. M. Liz-Marzán, A. J. C. Kuehne and D. N. Chigrin, *ACS Photonics*, 2020, **7**, 646–652.
150. J. V. Jokerst, A. J. Cole, D. Van de Sompel and S. S. Gambhir, *ACS Nano*, 2012, **6**, 10366–10377.
151. K. Cai, W. Zhang, M. F. Foda, X. Li, J. Zhang, Y. Zhong, H. Liang, H. Li, H. Han and T. Zhai, *Small*, 2020, **16**, 2002748.
152. X. Ge, Q. Fu, L. Su, Z. Li, W. Zhang, T. Chen, H. Yang and J. Song, *Theranostics*, 2020, **10**, 4809–4821.
153. C. Kim, E. C. Cho, J. Chen, K. H. Song, L. Au, C. Favazza, Q. Zhang, C. M. Cobley, F. Gao, Y. Xia and L. V. Wang, *ACS Nano*, 2010, **4**, 4559–4564.
154. J. Seaberg, H. Montazerian, M. N. Hossen, R. Bhattacharya, A. Khademhosseini and P. Mukherjee, *ACS Nano*, 2021, **15**, 2099–2142.
155. T. Brann, D. Patel, R. Chauhan, K. T. James, P. J. Bates, M. T. Malik, R. S. Keynton and M. G. O'Toole, *J. Nanomater.*, 2016, **2016**, 1–11.
156. Z. Wang, Z. Chang, D. Shao, F. Zhang, F. Chen, L. Li, M. Ge, R. Hu, X. Zheng, Y. Wang and W. Dong, *ACS Appl. Mater. Interfaces*, 2019, **11**, 34755–34765.

157. Y. Wang, X. Ji, P. Pang, Y. Shi, J. Dai, J. Xu, J. Wu, T. B. Kirk and W. Xue, *J. Mater. Chem. B*, 2018, **6**, 2481–2488.
158. Y.-S. Wang, D. Shao, L. Zhang, X.-L. Zhang, J. Li, J. Feng, H. Xia, Q.-S. Huo, W.-F. Dong and H.-B. Sun, *Appl. Phys. Lett.*, 2015, **106**, 173705.
159. Z. Wang, Y. Wang, M. Lu, L. Li, Y. Zhang, X. Zheng, D. Shao, J. Li and W. Dong, *RSC Adv.*, 2016, **6**, 44498–44505.
160. X. Jiang, R. Liu, P. Tang, W. Li, H. Zhong, Z. Zhou and J. Zhou, *RSC Adv.*, 2015, **5**, 80709–80718.
161. J. Liu, H. Cui, S. Yan, X. Jing, D. Wang and L. Meng, *Mater. Today Commun.*, 2018, **16**, 97–104.
162. S. Liang, C. Li, C. Zhang, Y. Chen, L. Xu, C. Bao, X. Wang, G. Liu, F. Zhang and D. Cui, *Theranostics*, 2015, **5**, 970–984.
163. L. Zhang, X.-Q. Yang, J.-S. Wei, X. Li, H. Wang and Y.-D. Zhao, *Theranostics*, 2019, **9**, 5424–5442.
164. Y. Ju, H. Zhang, J. Yu, S. Tong, N. Tian, Z. Wang, X. Wang, X. Su, X. Chu, J. Lin, Y. Ding, G. Li, F. Sheng and Y. Hou, *ACS Nano*, 2017, **11**, 9239–9248.
165. C. Cai, X. Li, Y. Wang, M. Liu, X. Shi, J. Xia and M. Shen, *Chem. Eng. J.*, 2019, **362**, 842–850.
166. A. Bahadori, L. B. Oddershede and P. M. Bendix, *Nano Res.*, 2017, **10**, 2034–2045.
167. D. Yeheskely-Hayon, L. Minai, L. Golan, E. J. Dann and D. Yelin, *Small*, 2013, **9**, 3771–3777.
168. A. Rørvig-Lund, A. Bahadori, S. Semsey, P. M. Bendix and L. B. Oddershede, *Nano Lett.*, 2015, **15**, 4183–4188.
169. A. Bahadori, G. Moreno-Pescador, L. B. Oddershede and P. M. Bendix, *Rep. Prog. Phys.*, 2018, **81**, 032602.
170. G. Bolognesi, M. S. Friddin, A. Salehi-Reyhani, N. E. Barlow, N. J. Brooks, O. Ces and Y. Elani, *Nat. Commun.*, 2018, **9**, 1882.
171. A. Vivek, G. Bolognesi and Y. Elani, *Micromachines*, 2020, **11**, 388.
172. A. Bahadori, A. R. Lund, S. Semsey, L. B. Oddershede and P. M. Bendix, in *Optical Trapping and Optical Micromanipulation XIII*, International Society for Optics and Photonics, 2016, vol. 9922, p. 992211.
173. A. Bahadori, L. B. Oddershede and P. M. Bendix, *Nano Res.*, 2017, **10**, 2034–2045.
174. D. Y. Paithankar, F. H. Sakamoto, W. A. Farinelli, G. Kositratna, R. D. Blomgren, T. J. Meyer, L. J. Faupel, A. N. B. Kauvar, J. R. Lloyd, W. L. Cheung, W. D. Owczarek, A. M. Suwalska, K. B. Kochanska, A. K. Nawrocka, E. B. Paluchowska, K. M. Podolec, M. M. Pirowska, A. B. Wojas-Pelc and R. R. Anderson, *J. Invest. Dermatol.*, 2015, **135**, 1727–1734.
175. J. W. Lee, H. Jung, H. H. Cho, J. H. Lee and Y. Nam, *Biomaterials*, 2018, **153**, 59–69.
176. S. Yoo, S. Hong, Y. Choi, J.-H. Park and Y. Nam, *ACS Nano*, 2014, **8**, 8040–8049.

177. X. Xu, X. Liu, L. Tan, Z. Cui, X. Yang, S. Zhu, Z. Li, X. Yuan, Y. Zheng, K. W. K. Yeung, P. K. Chu and S. Wu, *Acta Biomater.*, 2018, **77**, 352–364.
178. T. Cui, S. Wu, Y. Sun, J. Ren and X. Qu, *Nano Lett.*, 2020, **20**, 7350–7358.
179. A. N. Kharlamov, A. E. Tyurnina, V. S. Veselova, O. P. Kovtun, V. Y. Shur and J. L. Gabinsky, *Nanoscale*, 2015, **7**, 8003–8015.
180. G. Baffou, F. Cichos and R. Quidant, *Nat. Mater.*, 2020, **19**, 946–958.
181. T. Cui, S. Wu, Y. Sun, J. Ren and X. Qu, *Nano Lett.*, 2020, **20**, 7350–7358.
182. D. A. Boyd, L. Greengard, M. Brongersma, M. Y. El-Naggar and D. G. Goodwin, *Nano Lett.*, 2006, **6**, 2592–2597.
183. W. H. Hung, I.-K. Hsu, A. Bushmaker, R. Kumar, J. Theiss and S. B. Cronin, *Nano Lett.*, 2008, **8**, 3278–3282.
184. M. Fedoruk, A. A. Lutich and J. Feldmann, *ACS Nano*, 2011, **5**, 7377–7382.
185. C. D. Jones and L. A. Lyon, *J. Am. Chem. Soc.*, 2003, **125**, 460–465.
186. K. M. Haas and B. J. Lear, *Chem. Sci.*, 2015, **6**, 6462–6467.
187. A. W. Powell, A. Stavrinadis, S. Christodoulou, R. Quidant and G. Konstantatos, *Nano Lett.*, 2020, **20**, 3485–3491.
188. Z. Deng, J. Zhou, L. Miao, C. Liu, Y. Peng, L. Sun and S. Tanemura, *J. Mater. Chem. A*, 2017, **5**, 7691–7709.
189. H. Zhang, H.-J. Chen, X. Du and D. Wen, *Sol. Energy*, 2014, **100**, 141–147.
190. Z. Wang, Y. Liu, P. Tao, Q. Shen, N. Yi, F. Zhang, Q. Liu, C. Song, D. Zhang, W. Shang and T. Deng, *Small*, 2014, **10**, 3234–3239.
191. Y. Liu, S. Yu, R. Feng, A. Bernard, Y. Liu, Y. Zhang, H. Duan, W. Shang, P. Tao, C. Song and T. Deng, *Adv. Mater.*, 2015, **27**, 2768–2774.
192. C. Kuppe, K. R. Rusimova, L. Ohnoutek, D. Slavov and V. K. Valev, *Adv. Opt. Mater.*, 2020, **8**, 1901166.
193. L. Zhou, D. F. Swearer, C. Zhang, H. Robatjazi, H. Zhao, L. Henderson, L. Dong, P. Christopher, E. A. Carter, P. Nordlander and N. J. Halas, *Science*, 2018, **362**, 69–72.
194. Y. Sivan, J. Baraban, I. Un and Y. Dubi, *Science*, 2019, **364**, eaaw9367.
195. L. Zhou, D. F. Swearer, H. Robatjazi, A. Alabastri, P. Christopher, E. A. Carter, P. Nordlander and N. J. Halas, *Science*, 2019, **364**, eaaw9545.
196. Y. Dubi, I. W. Un and Y. Sivan, *Chem. Sci.*, 2020, **11**, 5017–5027.
197. E. L. Keller and R. R. Frontiera, *ACS Nano*, 2018, **12**, 5848–5855.
198. G. Baffou, I. Bordacchini, A. Baldi and R. Quidant, *Light: Sci. Appl.*, 2020, **9**, 108.
199. C. Zhan, B.-W. Liu, Y.-F. Huang, S. Hu, B. Ren, M. Moskovits and Z.-Q. Tian, *Nat. Commun.*, 2019, **10**, 2671.
200. H.-H. Shin, J. Koo, K. Lee and Z. Kim, *Appl. Mater. Today*, 2019, **16**, 112–119.
201. Y. Dubi and Y. Sivan, *Light: Sci. Appl.*, 2019, **8**, 89.
202. J. Qiu and W. D. Wei, *J. Phys. Chem. C*, 2014, **118**, 20735–20749.
203. Z.-Q. Tian, B. Ren and D.-Y. Wu, *J. Phys. Chem. B*, 2002, **106**, 9463–9483.
204. S. Mukherjee, F. Libisch, N. Large, O. Neumann, L. V. Brown, J. Cheng, J. B. Lassiter, E. A. Carter, P. Nordlander and N. J. Halas, *Nano Lett.*, 2013, **13**, 240–247.

205. J. Lee, S. Mubeen, X. Ji, G. D. Stucky and M. Moskovits, *Nano Lett.*, 2012, **12**, 5014–5019.
206. C. Gomes Silva, R. Juárez, T. Marino, R. Molinari and H. García, *J. Am. Chem. Soc.*, 2011, **133**, 595–602.
207. M. Moskovits, *Nat. Nanotechnol.*, 2015, **10**, 6–8.
208. K. Ueno, T. Oshikiri, X. Shi, Y. Zhong and H. Misawa, *Interface Focus*, 2015, **5**, 20140082.
209. S. Mubeen, J. Lee, N. Singh, S. Krämer, G. D. Stucky and M. Moskovits, *Nat. Nanotechnol.*, 2013, **8**, 247–251.
210. M. Stratakis and H. Garcia, *Chem. Rev.*, 2012, **112**, 4469–4506.
211. R. Piazza, *Soft Matter*, 2008, **4**, 1740–1744.
212. J. S. Donner, G. Baffou, D. McCloskey and R. Quidant, *ACS Nano*, 2011, **5**, 5457–5462.
213. B. Roxworthy, A. Bhuiya, S. Vanka and K. Toussaint, *Nat. Commun.*, 2014, **5**, 3173.
214. L. Lin, X. Peng, M. Wang, L. Scarabelli, Z. Mao, L. M. Liz-Marzán, M. F. Becker and Y. Zheng, *ACS Nano*, 2016, **10**, 9659–9668.
215. U. Khadka, V. Holubec, H. Yang and F. Cichos, *Nat. Commun.*, 2018, **9**, 3864.
216. M. Braun and F. Cichos, *ACS Nano*, 2013, **7**, 11200–11208.
217. M. Braun, A. P. Bregulla, K. Günther, M. Mertig and F. Cichos, *Nano Lett.*, 2015, **15**, 5499–5505.
218. J. C. Ndukaife, A. V. Kildishev, A. G. A. Nnanna, V. M. Shalaev, S. T. Wereley and A. Boltasseva, *Nat. Nanotechnol.*, 2016, **11**, 53–59.
219. J. Garcia-Guirado, R. A. Rica, J. Ortega, J. Medina, V. Sanz, E. Ruiz-Reina and R. Quidant, *ACS Photonics*, 2018, **5**, 3673–3679.
220. L. Lin, M. Wang, X. Peng, E. N. Lissek, Z. Mao, L. Scarabelli, E. Adkins, S. Coskun, H. E. Unalan, B. A. Korgel, L. M. Liz-Marzán, E.-L. Florin and Y. Zheng, *Nat. Photonics*, 2018, **12**, 195–201.
221. Q. Shou, K. Uto, M. Iwanaga, M. Ebara and T. Aoyagi, *Polym. J.*, 2014, **46**, 492–498.
222. Z. Xiao, Q. Wu, S. Luo, C. Zhang, J. Baur, R. Justice and T. Liu, *Part. Part. Syst. Charact.*, 2013, **30**, 338–345.
223. S. Li, X. Jin, Y. Shao, X. Qi, J. Yang and Y. Wang, *Eur. Polym. J.*, 2019, **116**, 302–310.
224. H. Zhang, H. Xia and Y. Zhao, *J. Mater. Chem.*, 2011, **22**, 845–849.
225. H. Zhang and Y. Zhao, *ACS Appl. Mater. Interfaces*, 2013, **5**, 13069–13075.
226. C. J. Ward, R. Tonndorf, A. Eustes, M. L. Auad and E. W. Davis, *J. Nanomater.*, 2020, **2020**, 1–8.
227. C. J. Ward, R. Tonndorf, A. Eustes, M. L. Auad and E. W. Davis, *Efficacy of Gold Photothermal-Activated Shape Memory Polyurethane*, https://www.hindawi.com/journals/jnm/2020/5189434/, (accessed 3 July 2020).
228. H. Qin, T. Zhang, H.-N. Li, H.-P. Cong, M. Antonietti and S.-H. Yu, *Chem*, 2017, **3**, 691–705.
229. L. Chen, L. Si, F. Wu, S. Y. Chan, P. Yu and B. Fei, *J. Mater. Chem. C*, 2016, **4**, 10018–10025.

230. P. Peng, B. Zhang, Z. Cao, L. Hao, F. Yang, W. Jiao, W. Liu and R. Wang, *Compos. Sci. Technol.*, 2016, **133**, 165–172.
231. V. P. Zharov, K. E. Mercer, E. N. Galitovskaya and M. S. Smeltzer, *Biophys. J.*, 2006, **90**, 619–627.
232. M. Zhu, G. Baffou, N. Meyerbröker and J. Polleux, *ACS Nano*, 2012, **6**, 7227–7233.
233. M. Pihl, E. Bruzell and M. Andersson, *Mater. Sci. Eng.: C*, 2017, **80**, 54–58.
234. I. de Miguel, I. Prieto, A. Albornoz, V. Sanz, C. Weis, P. Turon and R. Quidant, *Nano Lett.*, 2019, **19**, 2524–2529.
235. M. Borzenkov, M. Moros, C. Tortiglione, S. Bertoldi, N. Contessi, S. Faré, A. Taglietti, A. D'Agostino, P. Pallavicini, M. Collini and G. Chirico, *Beilstein J. Nanotechnol.*, 2018, **9**, 2040–2048.
236. A. C. Anselmo and S. Mitragotri, *Bioeng. Transl. Med.*, 2016, **1**, 10–29.
237. D. Bobo, K. J. Robinson, J. Islam, K. J. Thurecht and S. R. Corrie, *Pharm. Res.*, 2016, **33**, 2373–2387.
238. H.-H. Jeong, A. G. Mark, T.-C. Lee, M. Alarcón-Correa, S. Eslami, T. Qiu, J. G. Gibbs and P. Fischer, *Nano Lett.*, 2016, **16**, 4887–4894.
239. H.-H. Jeong, A. G. Mark, T.-C. Lee, K. Son, W. Chen, M. Alarcón-Correa, I. Kim, G. Schütz and P. Fischer, *Adv. Sci.*, 2015, **2**, 1500016.
240. J. G. Gibbs, A. G. Mark, T.-C. Lee, S. Eslami, D. Schamel and P. Fischer, *Nanoscale*, 2014, **6**, 9457–9466.
241. A. G. Mark, J. G. Gibbs, T.-C. Lee and P. Fischer, *Nat. Mater.*, 2013, **12**, 802–807.
242. G. Kucsko, P. C. Maurer, N. Y. Yao, M. Kubo, H. J. Noh, P. K. Lo, H. Park and M. D. Lukin, *Nature*, 2013, **500**, 54–58.

CHAPTER 3

Branched Metallic Nanocrystals: Synthesis, Properties, and Photothermal Applications

KAREN YUANTING TANG,[a] JERRY ZHI XIONG HENG,[a] KHIN YIN WIN,[b] SI YIN TEE,[a] ZIBIAO LI*[a,c] AND ENYI YE*[a]

[a] Institute of Materials Research and Engineering, Agency for Science, Technology & Research, 2 Fusionopolis Way, Singapore 138634, Singapore; [b] Singapore Institute of Food and Biotechnology Innovation, Agency for Science, Technology & Research, 31 Biopolis Way, Singapore 138669, Singapore; [c] Department of Materials Science and Engineering, National University of Singapore, 9 Engineering Drive 1, Singapore 117576, Singapore
*Emails: lizb@imre.a-star.edu.sg; yeey@imre.a-star.edu.sg

3.1 Introduction

Metal nanostructures have distinctive and captivating properties which enable them to be used in an extensive range of applications across multiple research disciplines. The size and shape of such materials are crucial parameters that affect their properties and specific functions for different applications. In many cases, shape offers much better flexibility in tuning the properties of metal nanostructures as different nanocrystal shapes exhibit different physical and chemical properties. For example, the surface plasmon resonance (SPR) characteristics of gold nanoparticles can change dramatically due to their different shapes, resulting in a change in color.[1] This can give rise to various applications like sensing, imaging, surface-enhanced Raman scattering, and

Nanoscience & Nanotechnology Series No. 54
Photothermal Nanomaterials
Edited by Enyi Ye and Zibiao Li

Published by the Royal Society of Chemistry, www.rsc.org

photothermal therapy.[2–4] The type of facets exposed on the surface also affects the catalytic activity and selectivity of Pt and Pd nanoparticles.[5,6] This has gained great interest and been used in major catalytic reactions, such as the oxygen reduction reaction and formic acid oxidation.[3] Different bactericidal properties of silver nanostructures against *E. coli* due to shape variation have also been reported.[7] Synthesis of metal nanostructures with controllable shapes had become an extensive area of research, as the demand for specific metal nanostructures with a particular morphology grows.

Nanostructured metals with controlled morphologies can be easily prepared as colloids through wet-chemical synthetic methods. For the past century, synthetic protocols have been developed for preparations of colloidal metal nanostructures with various shapes, dating back to 1857, when spherical Au nanoparticles were synthesized and documented.[8] But it was not until the last two decades that fabrication of highly complex geometrical metal nanostructures was achieved. Of all synthetic methods, the solution-based approach to synthesize nanocrystals emerged, as it is able to produce nanostructures with a wide variety of shapes, from simple geometries like rods and cubes, to more complicated morphologies like cages and highly branched architectures.[9–12]

In this book chapter, we will be focusing on metallic nanostructures with anisotropically branched morphologies. This is a special class of metal nanostructures, which can be effectively modified to suit the various applications. We will discuss the various synthesis strategies of these anisotropic branched metallic nanostructures in Section 3.2. We will investigate how the morphologies affect the optical properties in Section 3.3, and the various photothermal therapeutic applications in Section 3.4. Lastly, the conclusions and a future perspective are appended in the final section.

3.2 Strategies for the Synthesis of Anisotropic Branched Metallic Nanostructures

Through appropriate choice of the synthetic method and finetuning of the experimental conditions, one can obtain nanostructured materials of the targeted size and shape. For branched metallic nanostructures, the mechanism of branch formation depends greatly on the type of synthetic approach used. In this section, we focus on the different synthetic protocols based on wet chemistry, which have been reported to successfully prepare anisotropic branched metallic nanostructures. We classify the protocols into 5 main strategies, (1) seeded growth, (2) seedless growth, (3) templated growth, (4) chemical etching, and (5) green methods.

3.2.1 Seeded Growth

The seeded growth methodology is one of the approaches used in traditional crystal growing.[13] It utilizes pre-synthesized seeds as nucleation points for growth of anisotropic branched metallic nanostructures. This method requires an additional step of synthesis, as it distinctly separates the nucleation

event from the growth. This separation might be considered as inconvenient, but it allows precise control of the size of the nanocrystals.[14] The morphology of the targeted nanostructures can also be controlled with the change of size, shape, and composition of the seeds, with this strategy.

One of the classical examples of the seeded growth methodology is by reducing $HAuCl_4$ in the presence of cetyl-trimethylammoinium bromide (CTAB) as a surfactant and silver salt, to form gold nanorods. A thin layer of silver bromide (from silver salt with CTAB) is formed epitaxially on Au {111} and promotes the growth of gold nanorods with {111} facets. Through careful tuning of the concentration of the different reagents, Murphy's group was able to synthesize short Au nanorods, ranging from 20 to 100 nm (aspect ratio from 2 to 4) in high yield.[15,16]

Xia and co-workers[17] also reported the successful formation of Au nanohexapods from Au nanocrystal seeds. They synthesized the gold nanohexapods by reducing $HAuCl_4$ using dimethylformamide (DMF) in water, in the presence of octahedral-shaped Au seeds. The Au atoms nucleated and grew favorably from the 6 vertices of the nano-octahedra, forming the Au nanohexapods. The arm lengths of the nanohexapods can be controlled by varying certain experimental parameters such as temperature and the amount of $HAuCl_4$ added. Another group, Skrabalak *et al.*[18–20] managed to produce an Au–Pd bimetallic nanocrystal that has an Au-rich interior with Pd-rich exterior (Figure 3.1A). This was done by co-reduction of $HAuCl_4$ and H_2PdCl_4 using ascorbic acid, in the presence of pre-synthesized Au nano-octahedra. As the reduction potential of $HAuCl_4$ is higher than H_2PdCl_4, Au was deposited on the Au seeds first, followed by the deposition of Pd at the tip of the branches. Interestingly, the branches grow from the eight {111}c facets, rather than the 6 vertices, as mentioned above. Through further investigation, the octahedral Au seeds undergo restructuring to form a cubic structure before the formation of the arms. Hence, the eight branches were grown from the eight vertices of the intermediate cubic structure. Another noteworthy observation is that the morphology of the bimetallic nanocrystal can be tuned by a simple change in the pH, resulting in nano-octapods, concave nanostructures, and nano-octahedra.

Stabilizers like poly(vinylpyrrolidone) (PVP) are also sometimes used in the synthesis of branched anisotropic nanostructures. The addition of PVP controls the reduction kinetics of $AuCl_4^-$ ions on the Au seed surfaces. Hence, the rapid, kinetically controlled growth along the preferred crystal facets enables the formation of branched Au nanostructures with pointed tips. For example, gold nanostars can be obtained through this method, through careful control of PVP and DMF ratio.[21,22] Khoury and co-worker[22] reported the use of PVP and DMF with $HAuCl_4$ to obtain high-yield gold nanostars. Figure 3.1B shows the growth of the nanostars from the gold seeds. They suggested that the growth mechanism involves two stages: first, a rapid growing phase after nucleation of Au seeds. This rapid growth phase allows the formation of shallow protrusions that originate from the surface and develop distinct branches. Second, a gradual growth which mainly involves the deposition of gold on the protrusions, forming the branches of the nanostars.

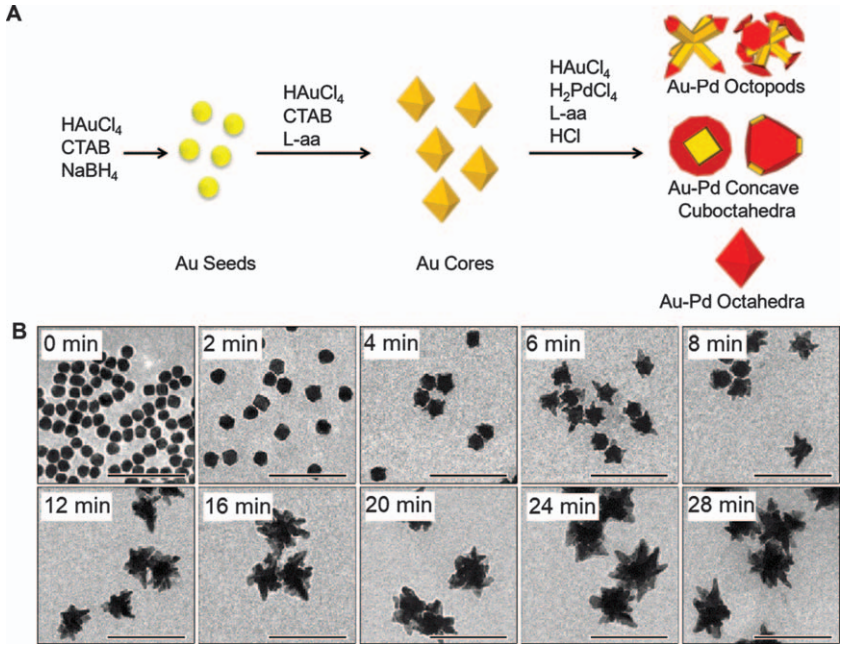

Figure 3.1 Seeded growth of anisotropically branched metal nanocrystals. (A) Schematic representation that illustrates the synthesis of Au–Pd nanocrystals from Au seeds. Adapted from ref. 19 with permission from American Chemical Society, Copyright 2014. (B) TEM images of nanostar formation over time. Reproduced from ref. 22 with permission from American Chemical Society, Copyright 2008.

3.2.2 Seedless Growth

Seedless growth is also another commonly used strategy for anisotropic branching of metal nanostructures. It has gained its popularity due to its facile one-pot approach, as well as its high versatility and capability. However, the size and morphology of the nanostructures may be affected by the *in situ* formation of the metal core and subsequent branching, as the rates of nucleation and growth compete with each other. Another critical challenge is the need to break the highly symmetrical fcc structure of metals for the formation of these anisotropically branched structures. In this subsection, we will discuss how twin defects, ions, ligands, and polymorphs have been used to facilitate the growth of such nanostructures *via* the seedless route.

3.2.2.1 Twin-determined Branching

A twinned crystal is formed when two or more separate crystals intergrow together symmetrically. This could happen when there is erroneous attachment of adatoms, resulting in crystals separated by the twin boundary. Metals with low stacking fault energy are most vulnerable to twinning. For example, fcc metals are more prone to forming thermodynamically favored

nanocrystals with five-fold symmetry in very small sizes. However, the twinned structure should not be sustained when the crystal grows bigger, due to the dramatic increase of the strain energy, and single crystal structures like truncated octahedrons are formed. With careful manipulation and control of the growth conditions, a wide array of shapes can also be obtained at larger sizes.

Yang and co-workers[23] explored the roles of twin defects in the formation of platinum multipod nanostructures. They determined that the number of twinned planes formed at the initial stage of crystal growth will affect the final morphology of the Pt nanostructures. Without the twin plane, the initial cuboctahedral nanocrystals evolve slowly into octapods under conditions promoting growth along the ⟨111⟩ directions (Figure 3.2(i)). However, the presence of twin planes in the initial nanocrystal leads to different end morphologies. In Figure 3.2(ii)–(iv), the initial nanocrystals with single, five-fold, and multiply twinned planes transform into planar tripods, multipod structures with a rod like center, and monopod/multipod structures with a sphere-like core, respectively. Notably, the twining events and growth kinetics along the given directions can be drastically altered by changing the

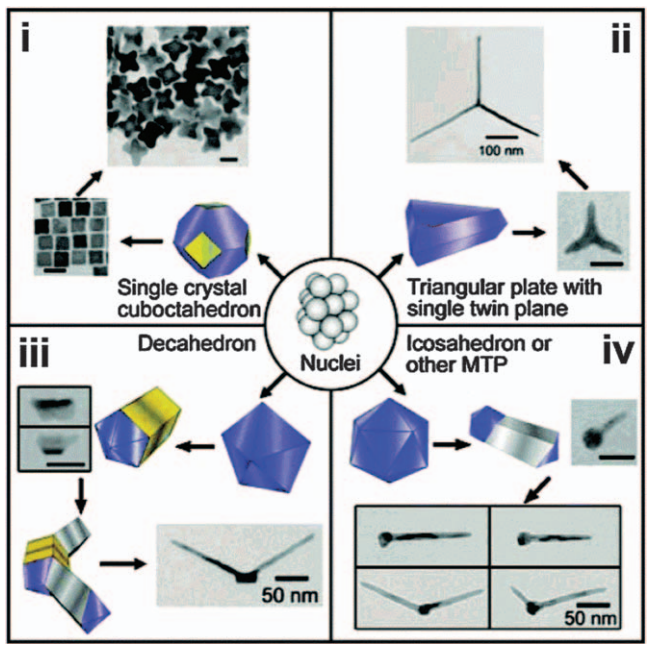

Figure 3.2 Twin-determined branching. Schematic illustration that shows the evolution of Pt nuclei to nanostructures with various branched morphologies. The number of twin planes in the initially formed nanocrystals is the determinant of the final morphology of the nanocrystal.
Reproduced from ref. 23 with permission from American Chemical Society, Copyright 2007.

reaction conditions (*e.g.* reaction temperature). This can trigger formation of various branched nanostructures.

Xia's group[24] showed that the five-fold twinned Rh decahedral structure that was formed initially evolved into a starfish-like morphology under desirable conditions. Using $[\{Rh(CF_3COO)_2\}_2]$ as the Rh precursor, ethylene glycol as the reductant and PVP as stabilizers, the reaction mixture is heated to 180 °C, and samples are collected at different intervals. At the initial stage, the Rh nanocrystals formed are multiply-twinned five-fold structures, mostly in a decahedron shape. The arms started to grow from the twin boundary corners along the ⟨110⟩ direction, with further heating. Interestingly, this is normally not observed in other noble metal systems, as the initial decahedral nanocrystals typically grow axially along the five-fold twin junction, forming elongated nanostructures, like nanorods and nanowires, with a pentagonal cross-section.[9,10,25] The preferred elongation is due to preferential binding of capping agents on the {100} facets of the growing nanostructures. However, in the Rh decahedral nanocrystals, the PVP is not able to effectively bind on the {100} side faces, hence, leading to a different growth behavior. It is also noteworthy that irregularly shaped nanocrystals are obtained instead of starfish-shaped ones when $[\{Rh(CF_3COO)_2\}_2]$ is replaced with Na_3RhCl_6 as the Rh precursor. The Cl ions in Na_3RhCl_6 will be released during the reaction and cause oxidative etching during the nucleation and growth processes when oxygen is present. This oxidative etching makes it difficult to obtain a twinned nanocrystal as twin defects are highly susceptible to oxidation and dissolution.

3.2.2.2 *Ion-assisted Branching*

Ion-assisted branching occurs whereby specific ions, which can be either cationic or anionic, are added to direct and mediate branching. Han *et al.*[26] used copper species as the reducing agent, instead of classical reducing agents such as citric acid or hydrazine, in the colloidal preparation of Au nanocrosses. The copper species also plays an important role during the nucleation stage. They direct the gold branches to grow along the ⟨110⟩ and ⟨001⟩ directions and secondary branching along ⟨111⟩, forming nanocrosses. With the careful choice of the Cu species, the size of the cross-shaped Au obtained can be controlled, due to the difference in the reduction rate. Cheng's group[27] revealed that spiky, urchin-like Au nanostructures can be obtained with the use of Ag^+ to induce branching, shown in Figure 3.3A. The Au nanostructures are produced from mixing $HAuCl_4$ and $AgNO_3$ with moderate amounts of ascorbic acid in water. The ascorbic acid favorably reduces $[AuCl_4]^-$, due to its higher reduction potential, to form Au nanocrystals. Small amounts of Ag^+ are then reduced and deposited on the surface of the Au nanocrystals. These Ag^0 atoms function as active sites and promote the growth of branches from the nanocrystals, resulting in the formation of anisotropic Au nanostructures. Fewer and larger spikes on the Au nanostructures can be observed when a decreasing amount of Ag^+ is

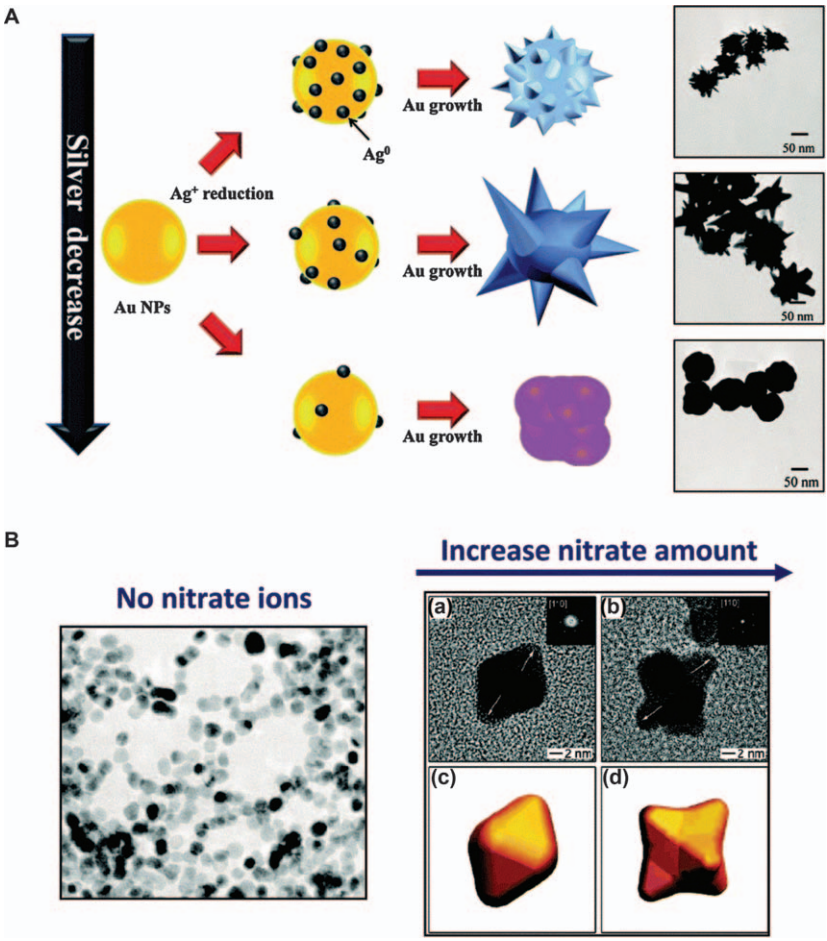

Figure 3.3 Ion-assisted branching. (A) Schematic illustration of the Ag^+-mediated growth of branched Au nanocrystals. By varying the Ag^+ concentration, the size and shape can be controlled. The TEM images of the resulting nanostructures are shown on the right. Reproduced from ref. 27 with permission from the Royal Society of Chemistry. (B) NO_3^- mediated growth of branched Pt nanocrystals. The TEM image on the left shows the spheroidal Pt nanocrystals that were obtained in the absence of NO_3^-. The effect of increasing the NO_3^- concentration is seen on the right. The HRTEM images (a and b) and the corresponding models (c and d) show that the growth of Pt nanocrystals was substantially enhanced at the ridges and corners to form multipods. Reproduced from ref. 28 with permission from American Chemical Society, Copyright 2004.

used. Conversely, when the Ag^+ concentration is too low, no spikes are obtained, resulting in popcorn-like nanostructures.

Other than cations, anions can also be used to assist in branching for anisotropic nanocrystals. Xia's group,[28] for instance, reported that the formation of such anisotropic Pt nanocrystals can be controlled by the addition

of nitrate ions (NO_3^-) to the polyol system. The concentration of nitrate ions present in the system has a shape-directing effect, as shown in Figure 3.3B. When no nitrate ions are present, only irregular spheroidal Pt nanocrystals were obtained. As the concentration increases, the facets get more defined and eventually, with sufficiently high concentrations, multipods are formed. It was suggested that the Pt^{4+} reduction pathway was altered by the NO_3^-, leading to the formation of anisotropic nanostructures. Absorption spectroscopy data show that there is an *in situ* reduction of NO_3^- to NO_2^-, which has a strong binding affinity with Pt ions, forming nitroplaninate complexes. This substantially decelerates the reduction of Pt ions to Pt^0, which alters the reaction kinetics and growth rates associated with different crystallographic facets of the Pt nanostructures, resulting in anisotropically branched nanostructures.

3.2.2.3 Ligand Directed Branching

Ligands (*e.g.* PVP) are well-known to be added to control the shape and sizes of nanostructured materials. They have functional groups that can be chemically bound to the nanocrystal structures. This binding helps to facilitate the formation of branches, as it lowers the energy and slows the growth rate of the bound facet relative to others. Zheng *et al.*[29] were able to generate octapod-shaped Pt nanocrystals with exposed {411} high-index facets by introducing a surface-controlling ligand, methylamine. Both PVP and methylamine are used in the synthesis system as capping agents. When only methylamine is present, highly aggregated Pt octapods are obtained, showing that the main role of PVP is to prevent such aggregation of Pt nanocrystals (Figure 3.4A). Meanwhile, when only PVP is used, mixed morphologies of Pt nanocrystals are obtained, showing that methylamine plays a crucial role in the octapod fabrication. Their results show that the methylamine can bind selectively to the high-index {411} facets of Pt during growth. The degree of concavity is also observed to be lowered significantly when the amount of methylamine is reduced. Chen and co-workers[30] showed that synthesis of Pd tetrapods is possible by using the amino acid arginine. Arginine is able to favorably chemisorb on Pd {111} facets and modifies the reduction kinetics of the Pd precursor.

Tilley's group[31] was able to demonstrate that the final morphology of the Pd nanocrystals can be modified through varying the nature of surface capping ligands. The icosahedral Pd nanostructures were obtained when oleylamine (OM) was used exclusively, suggesting that growth happens thermodynamically. Yet when oleic acid (OA) is introduced with oleylamine (1 : 1 ratio of OA : OM), anisotropically branched Pd nanostructures are formed. As the carboxylic acid functionality of OA has weaker bonding to Pd than the amine moiety of OM, the presence of OA destabilizes the system, allowing kinetic growth of nanostructures, leading to branched morphology. It is noted that the multipod arms grow in the direction where OA molecules bind themselves weakly to the faces of the structure.

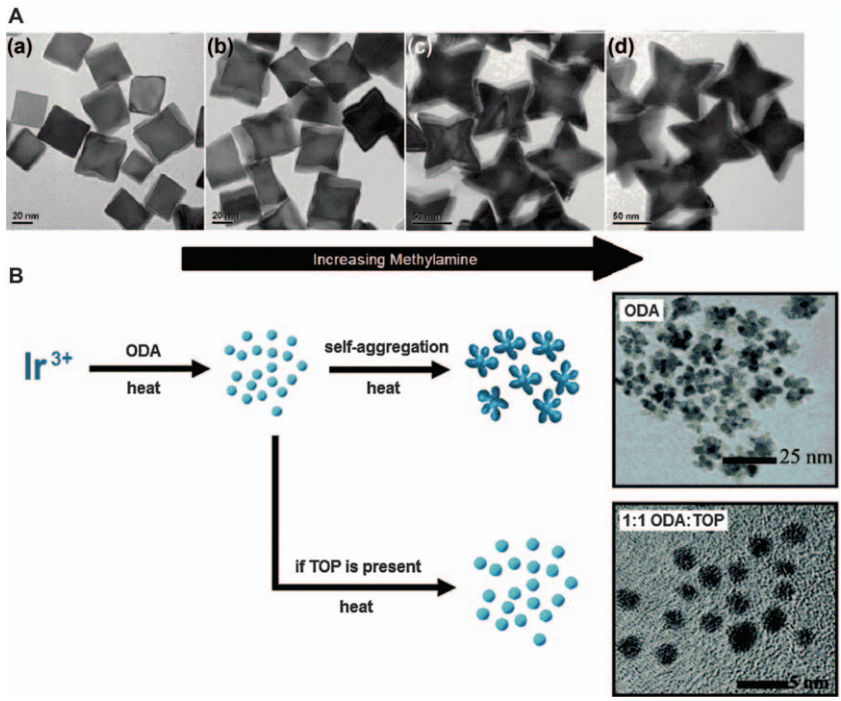

Figure 3.4 Ligand-directed branching. (A) TEM images of Pt nanocrystals. The concavity of the Pt nanocrystals increases with more methylamine (ligand) added. Reproduced from ref. 29 with permission from American Chemical Society, Copyright 2011. (B) Schematic depiction and TEM images showing the ligand-controlled self-aggregation of Ir nanocrystals. Octadecylamine (ODA), a ligand with weak binding affinity toward Ir, promotes the self-aggregation of the weakly passivated Ir nanocrystals into nanodendrites. In the presence of trioctylphosphine (TOP), the growth of well-passivated quasi-spherical nanocrystals is favored. Reproduced from ref. 34 with permission from the Royal Society of Chemistry.

The biological buffer molecule, HEPES (2-[4-(2-hydroxyethyl)-1-piperazinyl]ethanesulfonic acid), can be used as both a reducing and shape-directing agent to synthesize high yielding anisotropic Au nanostructures, as demonstrated by Lee *et al.*[32] The Au multipods fabricated have a selective tip growth along ⟨111⟩ directions. From the results, it is deduced that the piperazine group in HEPES is responsible for the adsorption of the molecule to the Au facets, binding most weakly at the {111} planes. Another study revealed that the HEPES molecules are able to self-assemble into long-range ordered structures at high concentrations, aiding the formation of branched Au nanostructures.[33] Based on theoretical calculations from experimental results, the HEPES molecule's sulfonate group preferably binds to the Au surface, and the free hydroxyl groups help with the self-assembly and bilayer formation through hydrogen bonding.

Choosing the appropriate ligands is also significant in the aggregation-based assembly of small metal nanocrystals into anistropically branched nanostructures. Ligands with weak to intermediate binding affinity to the metal ion precursor or small metal nanocrystals generally work best in forming highly branched nanostructures through this method. For example, formation of dendritic Ir nanocrystals is demonstrated by Zou and co-workers,[34] by using octadecylamine (ODA) as both the reductant and capping agent (Figure 3.4B). The Ir dendrites are synthesized simply by mixing $IrCl_3$ and ODA at 290 °C under a nitrogen flow for 15 minutes. Ir^{3+} was gradually reduced to Ir^0 at the initial stage of the reactions, enabling the formation of small Ir nanocrystals. With further heating, the Ir nanocrystals gradually self-aggregate and evolve into nanodendrites. The gradual reduction is regulated by ODA due to their weak binding affinity. As the stabilization by ODA is ineffective, Ir^0 coalescences and self-aggregates themselves into Ir nanocrystals. Only quasi-spherical Ir nanocrystals were obtained when a more effective stabilizer, trioctylphosphine (TOP), was added with ODA. The strong binding affinity of TOP enables the formation of a stable Ir^{3+} complex and delays the nucleation process due to ODA impeding the reduction of Ir^{3+}. Adding on, TOP enables the growth of nanocrystals to proceed through atomic addition rather than self-assembly due to its ability to effectively cap the surface of the initially formed nanocrystals. Such fabrication of anisotropically branched nanostructures through ligand-controlled self-aggregation is also reported in Pd nanodendrite synthesis.[35]

3.2.2.4 Polymorphism-induced Branching

When the solid metal compound exists in more than one crystalline form, polymorphism occurs. Hence, when the single crystal has more than one polymorph, growth will occur in different directions and branching occurs. Tilley's group[36] adopted the approach in synthesizing branched Ni nanostructures, exploiting Ni metal's inherent fcc–hcp polymorphism. Thermal decomposition and reduction of nickel acetylacetonate in mesitylene, in the presence of hexadecylamine (HDA) and trioctylphosphine (TOP) as capping ligands, under a hydrogen atmosphere, yield Ni nanostructures that consist of a fcc Ni core and alternating fcc and hcp phase arms. It is also noteworthy that the TOP ligand plays a crucial role in enhancing the growth of the branched structure. From the study, truncated octahedral fcc Ni nanocrystals are formed initially, which are bound by six {100} and eight {111} facets. Out of the 2 types of facets, growth occurs only with {111} facets due to the preferential binding of TOP molecules to the {100} facets, leading to arms formation. The {111} fcc facets will grow to become {001} hcp facets due to the presence of stacking faults along the [111] direction. Kinetic growth conditions, phase stability, and surface energies are some factors that are believed to contribute to the alternating fcc and hcp phases in the arms.

3.2.3 Templated Growth

Anisotropic branching of nanostructures can also be synthesized through a template-assisted growth approach. The template provides a structural scaffold for the nanostructures to grow into the templates' complementary shape. Xia *et al.*[37] successfully fabricated branched Au nanostructures by using an array of magnetic Fe nanoparticles as templates. From their study, it is shown that the Fe nanoparticles sis not only serves as a framework, but also plays a part in the reaction and falls apart naturally to release the desired product. The uniform quasi-spherical Fe nanoparticles self-assembled on a magnetic stir bar to form a three-dimensional (3D) porous lattice template. A galvanic replacement reaction between Fe and Au^+ takes place upon addition of AuCl, producing Au atoms. These Au atoms begin to nucleate and grow into multipods within the void spaces of the porous lattice. The magnetic attraction between the Fe nanoparticles is gradually weakened due to the consumption of Fe and the volume expansion from Au replacing Fe. This results in the eventual self-destruction of the template and releases the Au multipods naturally. Any residual Fe nanoparticles can be removed by acid washing of samples.

Liu and co-workers[38] reported the use of graphene oxide (GO) nanosheets as a scaffold to form highly branched Au nanostructures. GO is a two-dimensional (2D) honeycomb lattice of carbon atoms with various oxygen-containing moieties like carboxyl, hydroxyl, and epoxyl. *In situ* nucleation of Au atoms happens at these functionality sites during ethanol-assisted reduction. Subsequently, these oxygen-containing moieties also aid in directing the growth of the nanostructures, leading to a well-defined structure being formed. Only irregular Au nanocrystals, without a well-defined structure, were obtained when GO nanosheets were absent. Maroneze's group[39] also successfully obtained asymmetrical 2D gold nanostructures by using GO nanosheets as a template (Figure 3.5). The GO was first treated with cationic alkoxysilane to allow for adsorption of $AuCl_4^-$ onto GO, followed by *in situ* reduction of $AuCl_4^-$ to form Au nanoparticles, which then grow along the GO to form anisotropic 2D Au nanostructures. When the reaction proceeds, the nanostructures get larger and start to coalesce together to form a complete layer, resulting in anisotropic nanosheets. One issue noted is that these Au nanosheets contain some defects, such as holes and slits, as a result of a coalescence process.

Another template that has been used for this kind of synthesis in solution is deep eutectic solvent (DES). DES is a type of ionic solvent that can form an extended network through hydrogen bonding, allowing it to be used as a template for nanostructure growth. For example, Sun's group[40] demonstrated a method to synthesize branched Au nanostructures by reducing $HAuCl_4$ with ascorbic acid in DES at 30 °C. It is noteworthy that the DES has a triple role in the system, being a solvent, stabilizer, and liquid template. The water content in DES can be carefully controlled to modify the morphology of the Au nanocrystals, as it alters the structural features of the

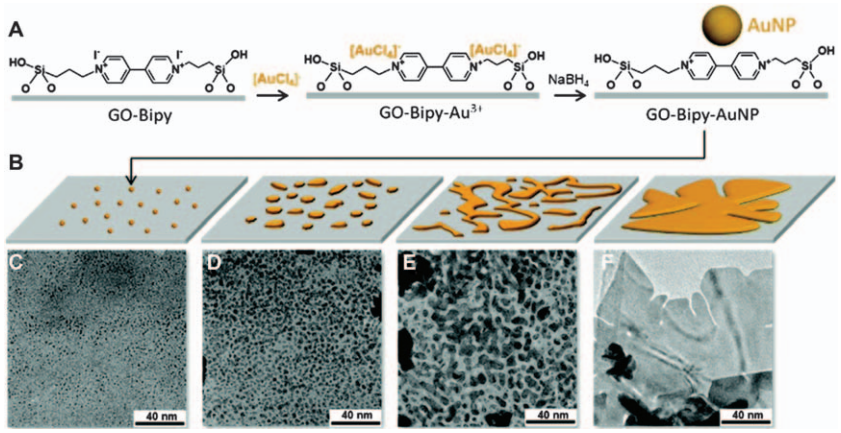

Figure 3.5 Templated growth of branched metal nanostructures. Schematic diagram of (A) functionalization of graphene oxide (GO) and the formation of the gold nanoseeds and (B) the evolution of the asymmetric 2D gold nanostructure and (C–F) the respective TEM images.
Reproduced from ref. 39 with permission from the Royal Society of Chemistry.

template. The morphology can transform from snowflake-like to star-shaped to thorny when different water levels (no water, 5000 ppm, and >10 000 ppm respectively) are present.

3.2.4 Chemical Etching

Branched nanostructures fabricated from a chemical etching approach are created through selective dissolution of certain crystallographic facets using etchants. Preparation of high yield and purity nanostructures with different morphologies is possible with careful tuning of the etchant strength. As an example, Yang *et al.*[41] were able to fabricate a series of Ag nanocrystals with different shapes using their highly selective etchant formulation. They use a 9 : 1 NH_4OH/H_2O_2 solution that enables etching of {100} facets over {111} facets of Ag nano-octahedra, with a high degree of selectivity. With increasing concentration of the etchant, the preferential etching in the [100] direction increases, converting the initial octahedral to octapod nanocrystals, as shown in Figure 3.6A.

The amount of branching on Pt nanocrystals can be manipulated by precise control of HCl, by oxidative etching, as demonstrated by Xiong and co-workers.[42] A mixture of H_2PtCl_6, PVP (as the stabilizer), KBr, ethylene glycol (as the reducing agent), and water were heated in air for the Pt nanocrystals preparations. With the addition of different HCl concentrations to the reaction mixture, the crystallinity of the initial Pt nanocrystals and the modes of atomic addition can be modified. The Pt nanocrystals formed initially are singly-twinned triangular nanoplates which transform into nanotripods, when HCl is not present. However, single-crystal cuboctahedral Pt nanocrystals are formed

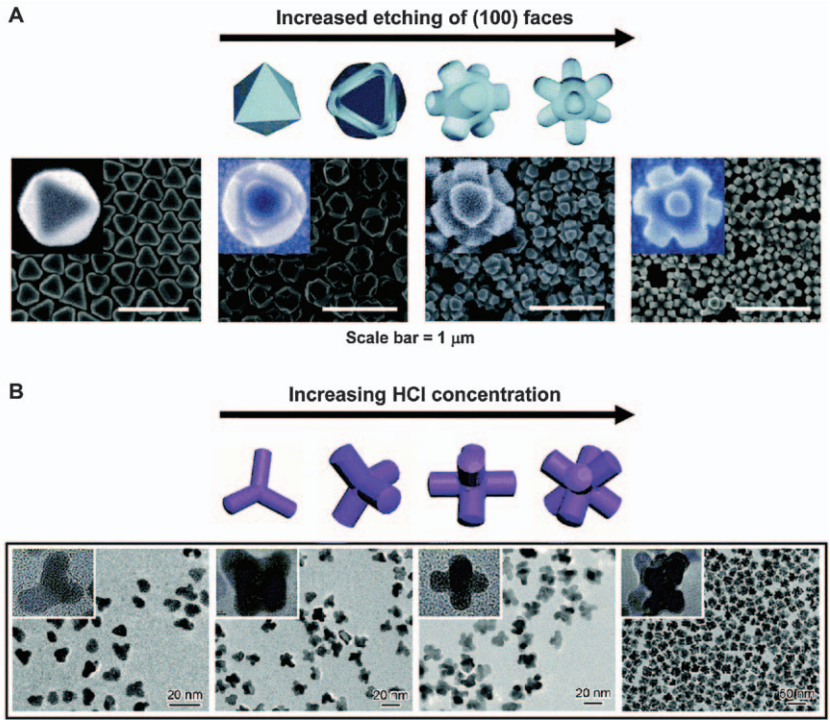

Figure 3.6 Chemical etching approach for branched metal nanostructures. (A) Schematic depiction and SEM images showing the etching progress of octahedral-shaped Ag nanocrystals using an etchant formulation that preferentially etches in the [100] direction. Reproduced from ref. 41 with permission from American Chemical Society, Copyright 2010. (B) Schematic depiction and TEM images that show the effect of varying amounts of HCl on the extent of oxidative etching of Pt nanocrystals. Reproduced from ref. 42 with permission from American Chemical Society, Copyright 2012.

initially in the presence of HCl. These initial cuboctahedra then transform into multiply branched structures, with an increasing number of branches when increasing amounts of HCl are used (Figure 3.6B). This is explained as the etching strength of O_2 and Cl^- are greatly enhanced by the acidity of HCl, hence, more facets are etched oxidatively.

A unique etching process was observed by Tilley's group,[43] during the fabrication of branched Pt nanostructures in a hydrogenated atmosphere. From the study, Pt nano-octapods were obtained with the usage of a high concentration of $Pt(acac)_2$ as the metal precursor. Synchrotron-based results showed that the initial cuboctahedral nanocrystals underwent an etching process, dissolving the {100} facets and simultaneously growing along the {111} directions, to obtain the octapods. It was believed that the acetylacetonate group acts as an etchant species, as its enol form is able to etch metal surfaces *via* chelation, since traditional etchants like O_2 and halides are absent.

3.2.5 Green Synthesis

In recent years, synthesis *via* greener methods has been growing, as research is moving towards sustainability. Additionally, conventional wet-chemical synthetic methods might also use chemicals that have adverse effects on human health and the environment. Hence, prompting the research community to explore the use of biogenic materials like plant extracts, microorganisms, and biomolecules in the synthesis of branched metallic nanostructures.[44–56] Biogenic substances have their own advantages. As they are obtained from biological sources, they are considered to be environmentally benign and are biocompatible. Hence, there are suitable substitute reagents to replace toxic chemicals and ones that are considered safer to use for biomedical applications. These biogenic materials are also relatively inexpensive as compared to the chemicals used in conventional colloidal syntheses. This section will be divided into 3 subsections, which will describe how each biogenic substance is used in the synthesis of anisotropically branched nanostructures: 1) plant extracts; 2) microorganism; and 3) biomolecules.

3.2.5.1 Plant Extracts

In the past decade, researchers have been using a wide array of plant extracts for metal nanostructures. The phytochemicals in the plant extracts allow phytosynthesis and formation of metallic nanostructures.[44,46–48,51,54] Phytosynthesis is normally carried out in an aqueous medium under ambient conditions, which is a rapid and cheap approach that is easily scalable for bulk production. However, the exact mechanism of metal nanostructure formation *via* this kind of synthesis has not yet been fully established. Particularly, ass plant extracts have a large number of compositions, making it difficult to identify their role played in the synthesis. Nonetheless, it is generally agreeable that formation of metal nanostructures from plant extracts is a result of the synergistic action of the phytochemicals in them. Spherical nanoparticles are typically produced when phytochemicals are used.[57–61] However, in recent years, there has been an increasing number of reports on anisotropic metallic nanostructures synthesized from plant extracts.[62–74]

One of the most commonly produced branched nanostructures through a phytochemical-mediated approach is nano-flowers. For example, Thakur's group[68] used *Syzygium cumini* fruit extract to synthesize 3D flower-like Au nanostructures, with a proposed aggregation-based formation mechanism as depicted in Figure 3.7A. The two-step reaction involves a first step of phytochemical-mediated reduction of a Au precursor to obtain Au nanocrystals that are capped with the phytochemicals with conjugatable hydroxyl moieties. The nanocrystals then gradually aggregate together to form the reported multi-branched nanoflowers. Ye and co-workers[69] also reported obtaining Au nanocrystals with flower-like structures, using a similar aggregation-induced mechanism (Figure 3.7B) with star fruit juice (*Averrhoa carambola*). The fruit is rich in vitamin C and polyphenolic antioxidants,

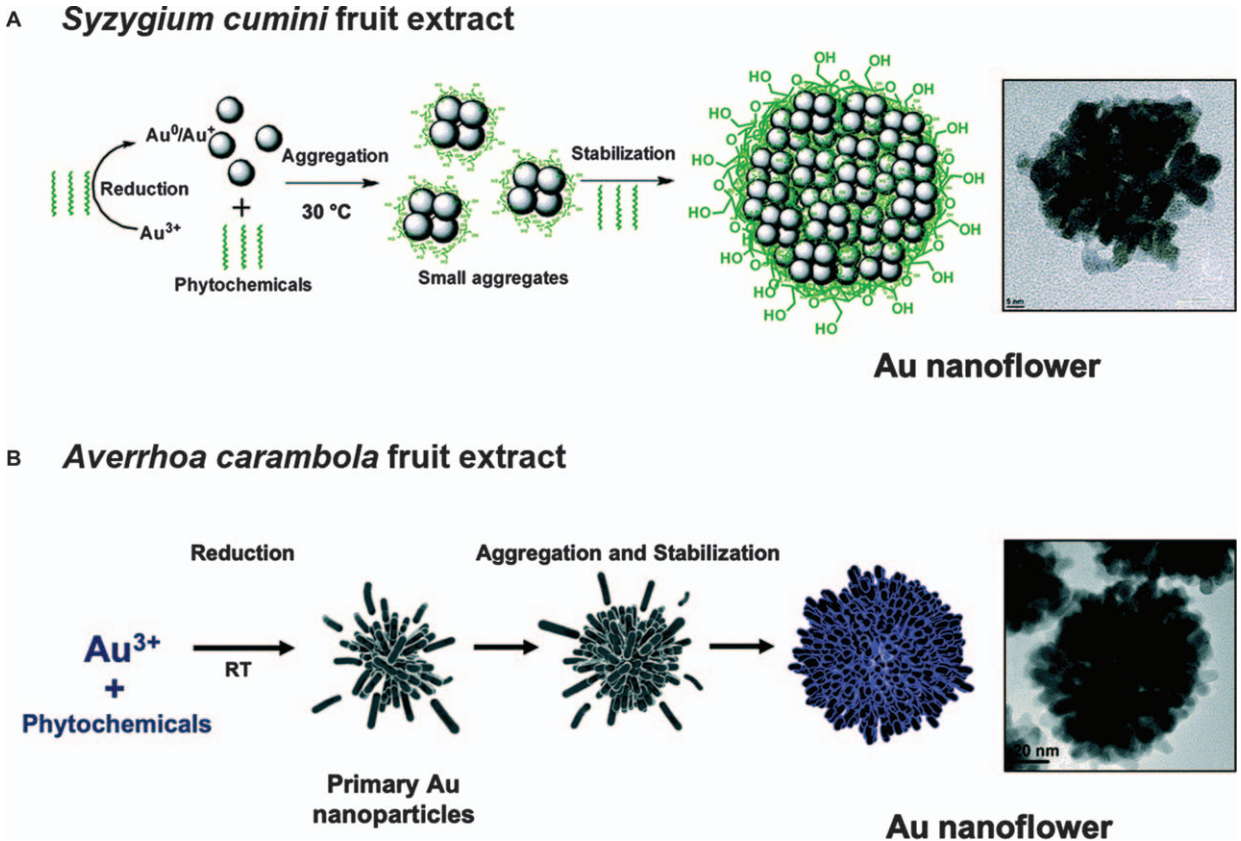

Figure 3.7 Phytochemical-mediated fabrication of nanoflowers using plant extracts. (A) Schematic illustration of the synthesis of multi-branched Au nanoflowers using *Syzygium cumini*. Reproduced from ref. 68 with permission from American Chemical Society, Copyright 2017. (B) Schematic depiction of the fabrication of Au flower-like nanostructures using *Averrhoa carambola*. Reproduced from ref. 69 with permission from the Royal Society of Chemistry.

which are good reducing and capping agents. Interestingly, Wang's group[62] was able to prepare a variety of 3D multi-branched Au nanocrystals (*e.g.* flower, urchin, and confeito structures) through reduction of an Au precursor with gum arabic. The hydroxyproline-rich gum arabic acts as a capping agent, which is critical to the growth of nanostructures through a successive aggregation model.

Bimetallic flower-like nanostructures are also reported by using plant extracts. For instance, Sun *et al.*[64] reported the formation of such a material with an Au core and Pd petals through a seeded growth approach that involves successive reduction of the Au and Pd precursors and room temperature. The Au precursor was first reduced using ascorbic acid to form Au seeds. The Pd precursor was then added gradually, followed by the introduction of *Cacumen platyclade* leaf extract. The Au seeds formed acted as nucleation points for the aggregation and growth of Pd petals, obtaining the Au–Pd core–petal nanoflowers. The gradual introduction of the Pd precursor and usage of plant extract as a mild reductant and capping agent are essential for controlling the nucleation rates of Pd. These ensured that the Pd are deposited on the Au seeds and not forming separate Pd nanostructures. The low temperature used also prohibited interdiffusion of atoms between the Au core and Pd petals. Intriguingly, alloyed AuPd nanoflowers were obtained instead of a core–petal structure when reduction of Au and Pd precursors occur simultaneously.[65]

3.2.5.2 Microorganisms

As microorganisms (bacteria and fungi) have the ability to detoxify heavy metals, they have sparked substantial interest in applications in metal nanostructure synthesis *via* a biomimetic approach.[75,76] They have metal-binding proteins that are efficient in reducing metal ions through both intracellular and extracellular reduction mechanisms. Additionally, metal nanostructures can grow into intricate morphologies as the surface structure of microorganisms can serve as an excellent templating medium.[77–79]

Li and co-workers[66] reported using *Escherichia coli* bacteria to synthesize dendritic and horn-like Au nanostructures. In the presence of cationic surfactant, the Au ions are first biosorbed and reduced by the microbial surface, forming tiny Au nanoparticle nuclei. Ascorbic acid was added to enhance the reduction process as the microbial reduction was slow even when the biosorption happens readily. The Au nanoparticle nuclei linked themselves together through linear fusion and grew progressively on the microbial surface, forming dendritic Au nanostructures. The dendritic nanostructures then eventually grow into nanofilms as the Au nanoparticles filled the gap in between the branches. Ultimately, the two Au nanofilms formed between the adjacent bacterial cells merge and form a unique horn-like morphology, which is rarely seen *via* traditional wet-chemical synthesis. Au nanohorns were also synthesized *via* a similar microorganisim-mediated mechanism, using yeast *Pichia pastoris*.[80]

Pd and Pt nanoflower fabrication with the use of fungal mycelia of *Rhizopus oryzae* was reported without additional reducing agent.[81] The cell surface proteins of the mycelia have various functionalities which allow the fungi to serve several roles (reducing, capping, and shape-directing agents) during the fabrication. A similar Pd nanoflower structure was also obtained using *Pichia pastoris*, but with ascorbic acid present.[82] *Pichia pastoris* is also capable of being utilized for the fabrication of alloyed AuPd nanoflowers with H_2 as the reductant (Figure 3.8).[83] The Au ions reduce on the cell surface, followed by a reduction of Pd ions, which aggregate on the Au surfaces. This sequence leads to a flower-like nanostructure with an Au core and Pd petals initially. However, due to the interdiffusion process, homogeneously alloyed AuPd nanoflowers are obtained.

3.2.5.3 Biomolecules

Biomolecules can be broadly termed as molecules that are present in organisms that are typically essential to biological processes. They can be of large molecules such as proteins, carbohydrates, lipids, and nucleic acids, or small molecules like vitamins and other metabolites.

The most commonly used biomolecule for synthesis of metallic nanocrystals is vitamin C (or ascorbic acid). Vitamin C is not only a potent antioxidant (reducing agent), but is also non-toxic and biocompatible, making it a superior candidate for synthesis of nanostructures with biological applications. Typically, ascorbic acid acts exclusively as the reducing agent and does not participate in morphological control. For example, both Vo's[84] and Lv's[85] teams used ascorbic acid as a reducing agent in a one-pot synthesis of branched Au nanoparticles. However, some studies suggest that ascorbic acid is able to do morphological directing. For instance, Wang and co-workers[86] reported the synthesis of hyperbranched Pt nanostructures using only Pt precursors (K_2PtCl_4) and ascorbic acid. The resultant branched morphology of the Pt nanocrystals was attributed to 2,3-diketo-1-gulonic acid (DGA), which is an oxidation by-product of ascorbic acid. As shown in Figure 3.9A, ascorbic acid undergoes an oxidation process and forms dehydroascorbic acid (DHA). However, DHA is not stable and converts to DGA spontaneously through hydrolysis of the lactone ring. The DGA molecules can selectively bind to specific facets of the growing Pt nanocrystals through their carboxyl functionality. The theoretical calculations supported the proposed mechanism, which revealed the preferential binding of DGA onto Pt (100) and (110) facets. As a result, the growth in these two directions was restricted and only growth of Pt (111) was observed, and anisotropically branched Pt nanostructures are formed. Yang's group[87] also reported a similar method for their Au nanourchin growth, using only Au precursor and ascorbic acid. The schematic diagram of the proposed mechanism is shown in Figure 3.9B. Nanoflowers with an Au core and Pt petals were also reported by addition of ascorbic acid and Pt precursor into a boiling solution of pre-formed Au seeds.[88]

Another class of biomolecules that are used frequently is deoxyribonucleic acid (DNA). Due to its well-defined and sequence-specific structure, it is

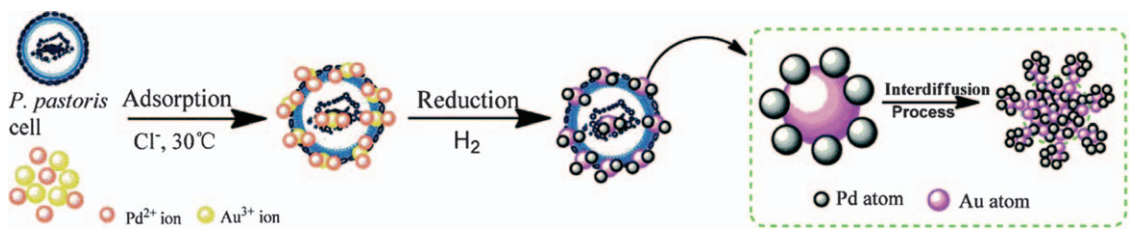

Figure 3.8 Microorganism-assisted formation. Schematic illustration of the fabrication of AuPd nanoflowers using *Pichia pastoris*. Reproduced from ref. 83 with permission from the Royal Society of Chemistry.

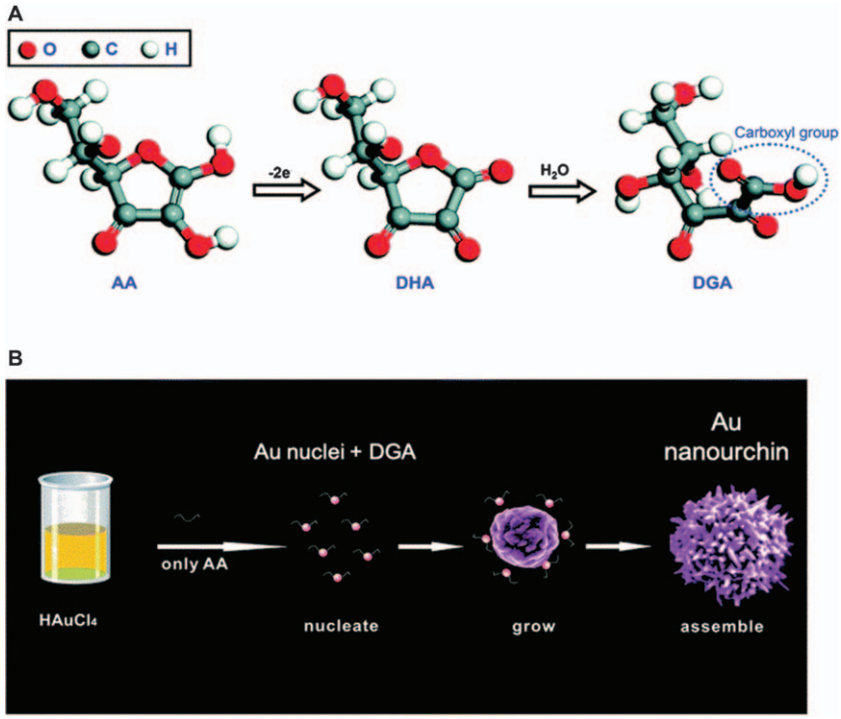

Figure 3.9 (A) Synthetic scheme of ascorbic acid (AA) to 2,3-diketo-1-gulonic acid (DGA). Firstly oxidation of AA to dehydroascorbic acid (DHA), followed by hydrolysis to DGA. Reproduced from ref. 86 with permission from American Chemical Society, Copyright 2010. (B) Schematic representation of the DGA-mediated growth of Au nanourchins. Reproduced from ref. 87 with permission from the Royal Society of Chemistry.

usually used to provide a skeletal framework for template directing synthesis of metal nanostructures with unique morphology. For instance, Song *et al.*[89] reported synthesizing X- and Y-shaped Au nanocrystals using similarly shaped DNA templates (Figure 3.10A). Single-stranded oligonucleotides, that are half-block complementary to each other, were annealed together to form the DNA templates. Either a four-armed DNA (X-DNA) or a Y-armed DNA (Y-DNA) were obtained from the hybridization of four or three strands of oligonucleotides, respectively. When Au precursor was added, complexation of the Au ions with the DNA templates occurred. The bound Au ions were then reduced and X- and Y-shaped Au nanostructures were formed.

Lu's group[90] examined the effect of three types of single-stranded 30-mer DNAs comprised of poly A, poly C, and poly T (A30, C30 and T30) on the growth of Au nanocrystals from pre-synthesized nanospheres. A30 and C30 have a much higher binding affinity to Au nanospheres which promotes inhomogeneous growth and Au nanoflowers are obtained. On the other hand, T30 has a lower binding affinity with the Au nanospheres, hence, is not able to induce growth of

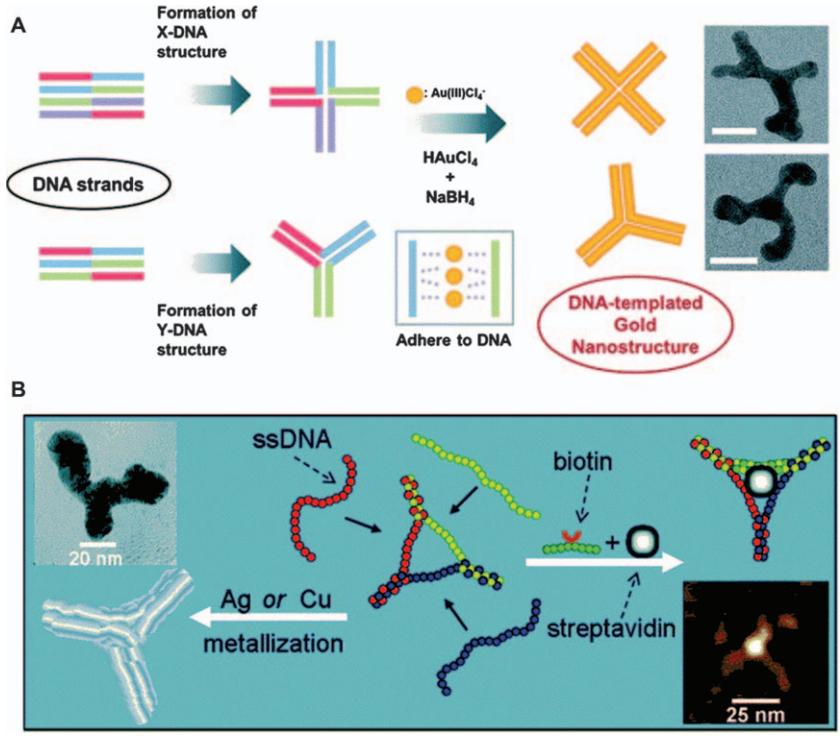

Figure 3.10 Branched nanostructure synthesis using DNA as a template. (A) Schematic depiction of the DNA-templated synthesis of four-armed (X-shaped) and three-armed (Y-shaped) Au nanostructures. The TEM images of the final branched structures are also shown (scale bar: 20 nm). Reproduced from ref. 89 with permission from the Royal Society of Chemistry. (B) Schematic depiction of the formation of branched Ag and Cu nanostructures using a branched template based on DNA–protein assemblies. Reproduced from ref. 92 with permission from American Chemical Society, Copyright 2005.

anisotropic nanostructures, resulting in only bigger nanospheres. In a subsequent study, they investigated the effect of different DNA sequences on the growth of Au nanostructures using pre-synthesized Au nanoprisms.[91] The Au nanoprisms used were planar twinned crystals with {111} facets on both the top and bottom surfaces, with stacking faults at the side faces. The resulting Au nanocrystals have varying morphologies, including multi-tipped nanoflowers and six-tipped nanostars, as the DNA sequences bind differently to the exposed facets of the nanoprisms, leading to the growth of the seeds in different directions. Branched Ag and Cu nanostructures were synthesized using DNA–protein assemblies as templates (Figure 3.10B).[92,93] The DNA–protein template has a streptavidin protein core that is conjugated to a biotinylated DNA molecule. Metallization of the template results in branched metal nanostructures forming, and the lengths of the branches can be controlled by the size of DNA. Meanwhile, Huang and co-workers used the nucleotide guanosine

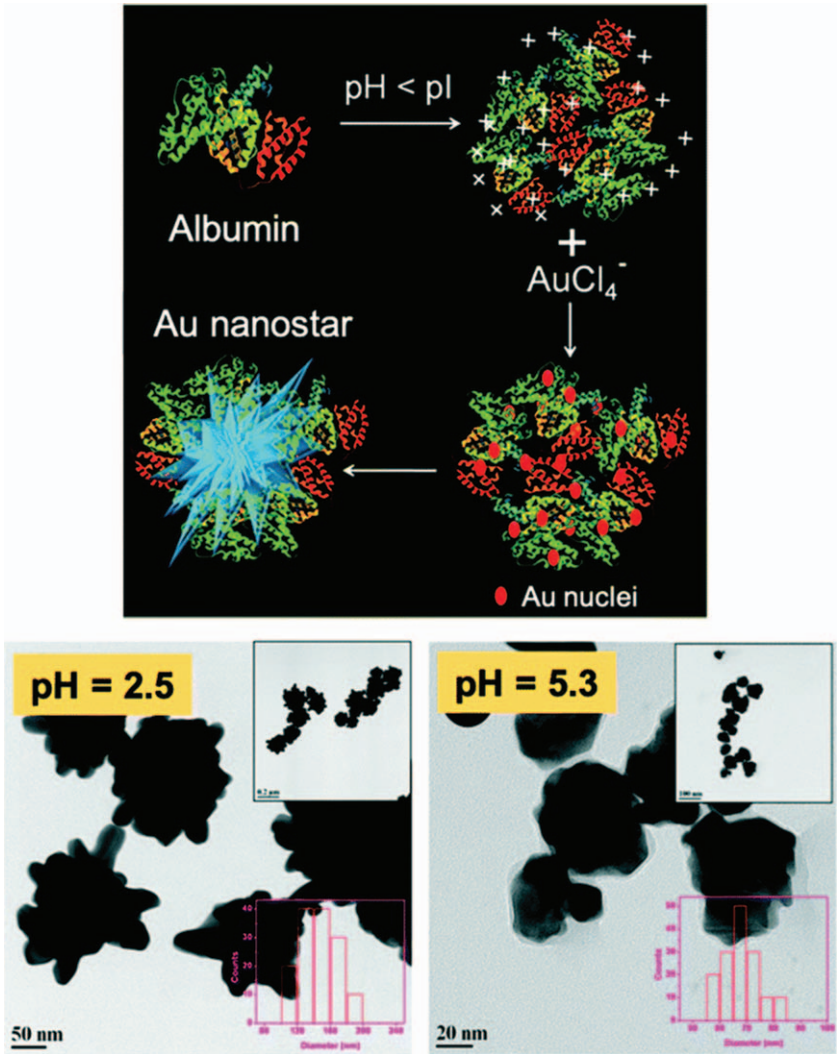

Figure 3.11 Schematic illustration of the albumin-directed synthesis of multi-tipped Au nanostars. The formation of a nanostar is promoted when the solution pH is less than the isoelectric point (pI) of albumin, which is 4.7 (for bovine serum albumin).
Reproduced from ref. 95 with permission from American Chemical Society, Copyright 2017.

5′-monophosphate (5′-GMP) as the capping agent to control the synthesis and Au nanoflowers with abundant tips are obtained.[94]

Just like DNA, protein is also a good candidate as a template for directing the shape of metal nanostructures. For example, Srivastava *et al.*[95] reported the use of albumin as a template for the fabrication of multi-tipped Au nanostars, as shown in Figure 3.11. To generate the star-shaped morphology, the pH of the

reaction mixture plays a critical role. pH values lower than the isoelectric point (pI) of albumin are especially favored as the net positive charge will allow the attachment of the Au precursor ions ($AuCl_4^-$) to it. Additionally, at such a low pH value, the α helices in albumin are stretched in such a way that they transform into β sheets, hence easing the access to attach the Au precursor to the functional groups. The β sheet conformation also allows the reduced Au nuclei to be readily evolved to the spiked nanostars. In a separate study, the same group uses poly(L-arginine)-albumin core–shell nanoparticles as seeds to prepare albumin-stabilized Au nanostars.[96] And on a separate paper, albumin is used primarily as a stabilizing agent.[97] The as-synthesized Au nanostars had inherit stability, functionality, and biocompatibility due to albumin's non-toxicity and binding capabilities. As a result, these albumin-stabilized Au nanostars showed compatibility toward cells and human blood.

Anisotropically branched metal nanostructures can also be synthesized through enzymatic synthesis pathways. Li's group[98] demonstrated the fabrication of Au nanoflowers through such a pathway using trypsin, which is a proteolytic enzyme that is present in the human digestive system. Similar to albumin, the attachment of $AuCl_4^-$ to trypsin is favorable when the reaction mixture has a lower pH than trypsin's pI. These $AuCl_4^-$ ions that are bound to trypsin were then reduced by ascorbic acid to form Au nanoparticles. The cysteine residues in trypsin have thiol functional groups which readily bind to the different crystallographical facets on the Au nanoparticles, resulting in anisotropic growth into nanoflowers. Ma *et al.*[99] reported the synthesis of Ag nanoflowers with the use of only the amino acid L-cysteine and $AgNO_3$. L-cysteine is believed to have a triple role of reducing, capping, and shape-directing capabilities.

Carbohydrates can also be employed in the synthesis of anisotropic metal nanocrystals. For instance, Nhung and co-worker used chitosan to mediate the synthesis of both Au[100] and Ag[101] nanoflowers. A schematic of the chitosan-mediated growth process is shown in Figure 3.12A. The process involves mixing of the metal precursor with ascorbic acid (as a reductant) and 50 kDa chitosan (as a template). Chitosan has amino and hydroxyl moieties that can bind to specific facets of the nucleated metal nanocrystals, leading to selective facet growth. Additionally, its flexible molecular conformation enables adjacent chains to trigger aggregation of the nucleated metal nanocrystals and support the growth into Au nanostructures with hierarchical flower-like morphology. Carrageenan, a liner sulfated polysaccharide present in some seaweeds, is utilized for the preparation of Pd nanoflowers with thorn-like petals.[102] As shown in Figure 3.12B, the Pd precursor was reduced using ascorbic acid, in the presence of carrageenan (as a capping agent). Carrageenan has hydroxyl and sulfate functional groups which can interact with specific facets of the growing nuclei, directing them to form Pd nanoflowers.

Monosaccharides like fructose are also reported being utilized in a hydrothermal process to obtain dendritic Pt nanostructures.[103] The hydrothermal reaction was performed at 180 °C, in which a thermolytic reduction had occurred. It has been hypothesized that fructose not only serves as a reductant,

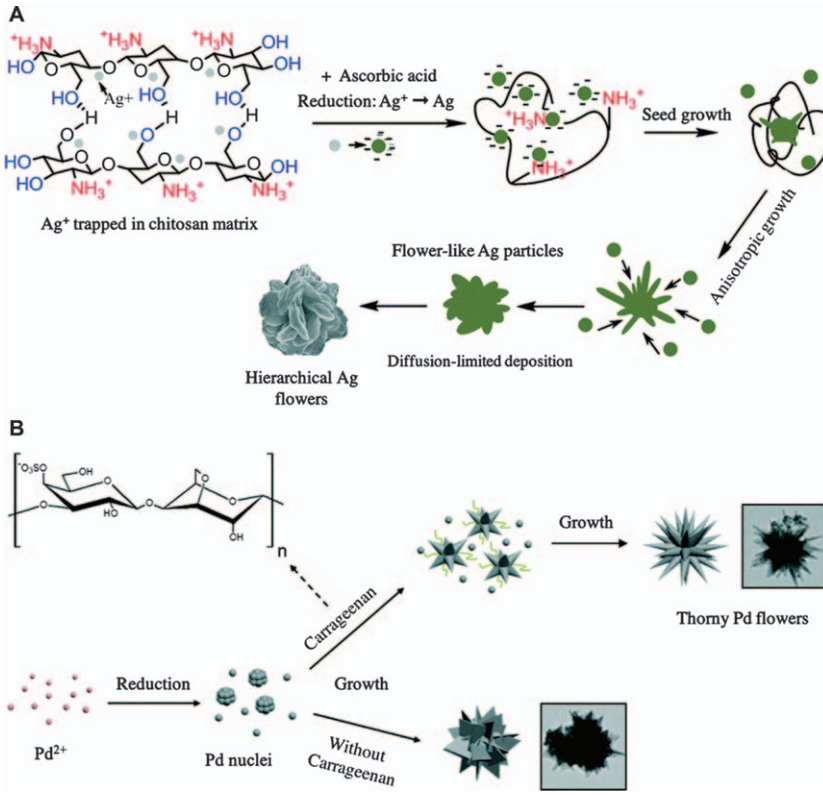

Figure 3.12 Formation of anisotropic metal nanostructures using carbohydrates as shape-directing agents. (A) Schematic depiction of chitosan-directed formation of hierarchical flower-like Ag architectures. Reproduced from ref. 100 with permission from American Chemical Society, Copyright 2014. (B) Schematic illustration of the carrageenan-assisted formation of thorny flower-like Pd structures. Reproduced from ref. 102 with permission from American Chemical Society, Copyright 2018.

but also acts as a source of hydrothermal carbon (HTC). HTC can bind onto the Pt surface and promote anisotropic growth into dendritic structures.

3.3 Optical and Photothermal Properties

Metallic nanostructures of varying morphologies have been vastly employed in an array of applications today for their optical properties. When certain metals are diminished to a size smaller than the wavelength of light, the light–metal interactions occurring can lead to a phenomenon known as the localized surface plasmon resonance (LSPR) effect. LSPR is commonly observed in noble metals such as gold and silver, and to a smaller extent in other non-noble metals such as aluminum and palladium. Notably, the LSPR absorption bands of Au and Ag lie in the visible region. Alongside other favorable properties such as chemical stability, good biocompatibility, and ease of surface

functionalization, they can be employed in various advanced applications such as sensing,[104,105] alternative medical treatment, and photocatalysis.[106] For this reason, the bulk of this chapter will be based on Au nanostructures.

When these metallic nanoparticles (NP) are irradiated with light, the surface electrons will be excited and cause a polarization of charges between the metal surface and the nuclei. This is counteracted with a coulombic restoring force that consequently affects the oscillation of these conduction band electrons, commonly termed as surface plasmon.[107] However, when this oscillation frequency coincides with the frequency of light that is irradiated, the absorption of (resonant) incident light produces intense and localized electric fields in its immediate surrounding, giving rise to the LSPR effect.

As LSPR activities are conducted at the surface, it is highly susceptible to changes in the morphology of the metallic NPs and/or its contagious medium.[107] The LSPR absorption band (and therefore its optical properties) of the metallic NPs can thus easily be tuned by altering its size or shape. The variation in sizes of metallic NPs can be a very simple approach to modulate its optical properties, but a variation in shape offers more versatility in many situations due to the prospect of having different physiochemical properties at different facets of the nanostructure. This has spurred material chemists to innovate distinctive anisotropically branched nanocomposites with unique and complex configurations:[108] nanocrosses,[109] nanoflowers, and nanohexapods, to name but a few. These nanostructures are designed and verified to be excellent light absorbers and scatterers due to enhancements that are brought about by their structural features.

After the absorption of light by the metallic nanostructures, the excited electrons would tend to liberate the additional energy they come to possess through a couple of relaxation pathways. One possible outcome of such relaxation is localized heating of metallic nanostructures. Upon the photoexcitation of conduction electrons, non-thermal hot carriers that are generated *via* Landau damping proceed to disseminate their energy through electron–electron scattering, resulting in internal electron thermalization.[110] Following this is the diffusion of thermal energy to its vicinity (*i.e.* the photothermal effect), while the metallic nanostructure cools down and stabilizes.

The inclusion of branched features in a metallic nanostructure's morphology can be remarkably beneficial as they can strengthen the photothermal effect. With the existence of branches, plasmonic hot spots can be established where the electromagnetic fields would be intensely magnified in small pockets of space (*i.e.* the tips of the branches). These hot spots are quintessential in producing increased hot carriers from the disruption of linear momentum of the electron in the hotspots[111] and hence an amplification in the photothermal effect. When a considerable amount of heat can be generated in its locality, the photothermal effect can be effectively exploited for practical applications,[105] notably in minimal invasive cancer treatments such as photothermal therapy and photothermal-induced chemotherapy. In the following sub-sections, selected branched metallic nanostructures that make excellent photothermal transducers are showcased and elaborated on.

3.3.1 Nanoflowers, Nano-urchins, and Nanodendrites

Ideally, a good photothermal transducing agent should not only absorb light proficiently in the NIR region but also maintain appropriate sizes for therapeutic applications. This cannot be achieved with just Au NPs as their LSPR absorbance lie in the visible region and they absorb poorly in the NIR region. Hupp *et al.*[112] and Gao *et al.*[113] reported a red shift in SPR absorption bands when branched features were introduced to Au NPs. Hence, branched variants of the Au NPs, such as nanoflowers, nano-urchins and nanodendrites can be attractive candidates in the making of a good photothermal transducer. In an instance, the optical and photothermal properties of Au nanoflowers have been explored by Ye and co-workers[69] (Figure 3.13). By simply adding an Au precursor ($AuCl_3$) to star fruit juice, Au nanoflowers (GNFs) of average diameters ~100 nm were synthesized (Figure 3.13B). Next, the absorption spectrum

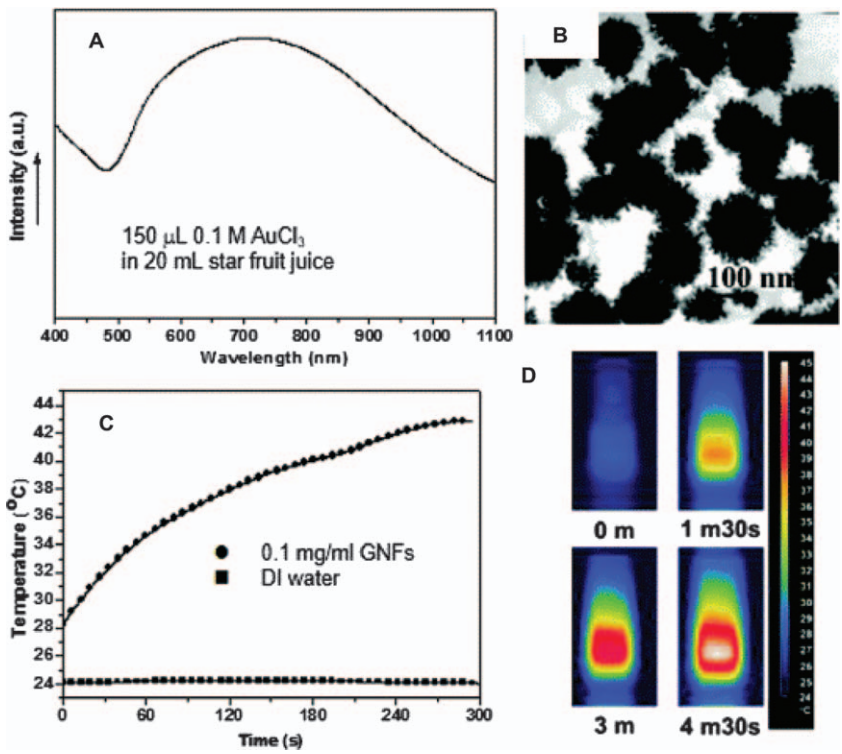

Figure 3.13 Characterization of GNFs for their optical and photothermal properties: (A) Absorption spectrum of GNFs after the reaction of a gold precursor in star fruit juice; (B) corresponding TEM image of the GNFs; (C) temperature elevation of water by GNFs upon irradiation with an 808 nm laser with a power density of 1 W cm^{-2}; (D) Corresponding thermographic images recorded at different time intervals.
Reproduced from ref. 69 with permission from the Royal Society of Chemistry.

of the GNFs was obtained and a broad absorption peak that spans from 500 nm to 1100 nm is observed in Figure 3.13A, peaking at around 725 nm. This is in contrast with typical Au nanospheres which have an absorption peak at ~570 nm and absorb poorly in the NIR region. With an establishment of its absorption spectrum, the GNFs were further subjected to a simple setup where they were shorn with an 808 nm NIR laser with a power density of 1 W cm^{-2} to evaluate their suitability as photothermal agents for therapeutic purposes. By measuring the temperature of the aqueous medium with an infrared camera, it can be seen that there is a significant increase in temperature (~14 °C) when compared to a control setup of pure water (Figure 3.13C and D). This underscores the GNFs ability to act as a photothermal transducer upon absorption of NIR light and release heat to its locality.

The photothermal stability of GNFs was additionally conducted by Wang *et al.*[114] and Gao *et al.*[115] In Wang and co-workers' study, the irradiation of a 785 nm laser with 1.5 W cm^{-2} power for 10 min resulted in a 10 °C increase in its aqueous medium (3 °C for pure water). After 5 cycles of recurred heating, the GNFs did not experience any change in their morphology. Conjugates of the GNF were also verified to be stable after 30 min of laser irradiation. The results were mirrored in Gao and co-workers' study where their conjugated GNFs were able to achieve rapid thermalization under 2 min of 808 nm laser irradiation. After 30 min of laser irradiation, the conjugated GNFs remained stable, as its spectral profile, hydrodynamic size, and morphology remained almost unperturbed. Hence, from the mentioned studies, GNFs exhibit desirable optical and photothermal properties for photothermal transducing applications.

In the same vein, Au nano-urchins (GNU)[116–118] and Au nanodendrites (GND) have multiple branches like GNFs that enable tuning of their LSPR absorption bands for effective photothermal applicability (Figure 3.14 and 3.15). For example, Djaker *et al.*[116] experimented with the irradiation of 808 nm laser on Au NPs and GNUs and reported an increase in temperature elevation speed in water of about 80% when GNU was compared with Au NPs (Figure 3.14C and D). They attributed this finding to the closer proximity of GNU's LSPR absorption peak to the laser irradiation and a greater absorption cross-section (σ_{abs}). Based on experimental results and the Mie theory, the growth in σ_{abs} was estimated to be in the range of 60–80%. Meanwhile, Ong and co-workers demonstrated tunability in controlling the morphology of their Au nanostructure between GNF and GNU *via* Ag^{+} which acted as a shape-directing agent.[117] In this, they were able to fabricate GNUs were "pointier spikes" that were accompanied with a red shift in LSPR absorption from the visible to the NIR region. The GNUs were also robust when tested for their photothermal effect and any changes in their structural integrity after 808 nm laser irradiation.

On the topic of GNDs, the studies of Wang *et al.*[119] and Mao *et al.*[120] have demonstrated the complexity in tuning the absorbance spectrum of GNDs where it is influenced by various factors such as aspect ratio, inter-branching gaps, dendritic length, and density, *etc.* Both studies reported a red shift of

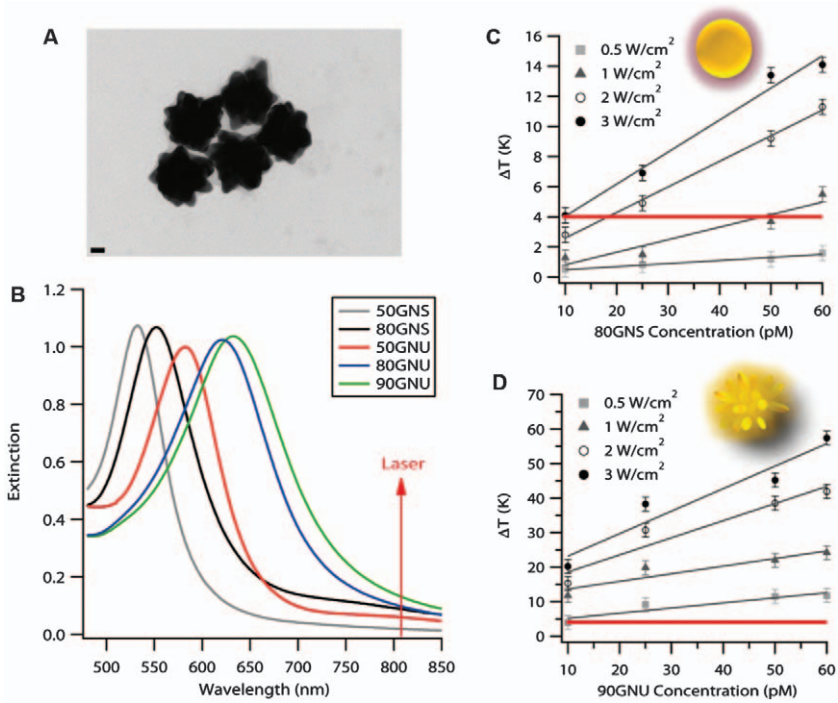

Figure 3.14 Characterization of Au nanourchins (GNU) for their optical and photothermal properties: (A) TEM images of the GNUs; (B) absorption spectra of Au nanospheres (GNS) and GNUs of different sizes; (C and D) temperature elevation of water by GNS and GNU after 15 min of irradiation with an 808 nm laser at different power densities.
Reproduced from ref. 116 with permission from American Chemical Society, Copyright 2019.

LSPR absorption bands with increases in dendritic length. This is analogous to the concept of red shifting the absorption band of a nanorod by extending its length. However, a difference in results was observed with regard to altering the dendritic density. In Wang and co-workers' study, the increase in dendritic density resulted in slight increases in the GND's size and brought about a red-shift in its absorption band to 1064 nm as compared to GNDs of lower densities or Au NPs (Figure 3.15A and B). On the other hand, in Mao and co-workers' study, the increase in dendritic density resulted in a blue shift in the absorption maxima to about 700 nm with poorer extinction coefficients at longer wavelengths. It was elucidated that the increase in dendritic density was compensated with shorter dendritic length, resulting in the sparser GND having a red-shifted absorption peak compared with the denser ones. Hence, the mentioned references showcase the utility of branched elements in tuning the optical profile of Au nanostructures for photothermal applications.

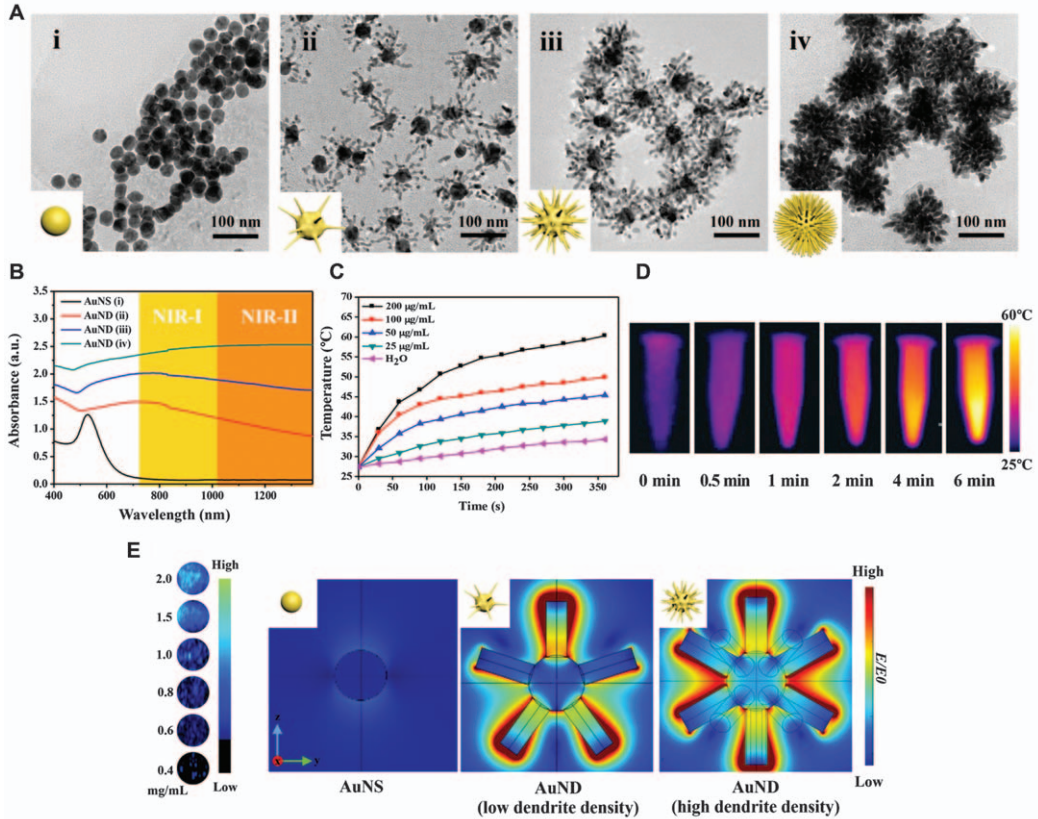

Figure 3.15 Characterization of Au nanodendrites (GND) for their optical and photothermal properties: (A) TEM images of the Au nanoseed (i) and GNDs with different branch densities (ii–iv); (B) absorption spectra of GNDs with different branch densities; (C) temperature elevation curve of water by GNDs under 1064 nm laser irradiation with a power density of 1.0 W cm^{-2} for 360 s); (D) representative photothermal images of GND solution (100 μg mL^{-1}) under 1064 nm laser irradiation with power density of 1.0 W cm^{-2} at various irradiation time points; (E) COMSOL simulation with a 785 nm laser irradiation which illustrates the hotspots of the GND at the dendritic tips.
Reproduced from ref. 119 with permission from American Chemical Society, Copyright 2021.

3.3.2 Nanocrosses

Besides Au NPs, the nanorod is another morphology that is ubiquitously utilized for photothermal applications.[121–124] While nanorods can achieve NIR absorption at large aspect ratios, the introduction of branched features can conceivably give rise to augmented capabilities. The nanocross is one such adaptation that possesses a cross-like morphology extending in transverse and longitudinal directions, unlike nanorods which only extend in one direction. The plasmonic properties of Au nanocrosses have been investigated by Han *et al.*[109] Figure 3.16A exhibits the TEM images of their fabricated Au nanocrosses, and it can be discerned that the Au nanocrosses are shaped by two longer branches along the ⟨110⟩ direction and two shorter ones along the ⟨001⟩ direction. In its absorption spectrum (Figure 3.16B), two distinct signals were observed – a gentler peak in the visible region at around 550 nm and an intense but broad absorption band enveloping over the NIR region (*i.e.* 800 nm to 1200 nm). The two signals are ascribed to the transverse and longitudinal branches, respectively. By altering the growth conditions of the Au nanocrosses, *i.e.* time for growth of the crystal and use of different reducing agents, the absorption peaks in the spectrum could be tuned accordingly.[26,125] For instance, a shift in absorption peak toward shorter wavelengths was seen when smaller Au nanocrosses were fabricated.

Further investigations on the influence of shape on the optical properties of nanocrosses were performed using monochromated electron energy-loss spectroscopy (EELS).[126] Figure 3.16C illustrates the scanning TEM (STEM) dark field image of a sample Au nanocross, overlaid with monochromated energy filtered TEM (EFTEM) maps of the plasmonic modes in the nanocross. In addition, a 1 mm electron probe was placed at the five locations of the right image in Figure 3.16D to give the corresponding monochromated EELS spectra in Figure 3.16D. It was revealed that there exist three main plasmonic modes in the nanocross, represented in Figure 3.16C, and that radiation damping is prevalent at NIR energy ranges below 1.6 eV where the aspect ratios are large. The enumerated spectra of the plasmonic modes in Figure 3.16D reiterate the pronounced NIR absorption of the nanocross. Discrete dipole approximation studies were also conducted to probe the synergistic coupling of the four branches in the Au nanocross.[109] It was discerned that any of the branches could act as reception points for the excitation of the entire nanocross. The proficient absorption of NIR light and ability to activate the entire nanocross at any ''receptor'' branches allow the nanocrosses to serve as bi-directional nanoantennas that can efficaciously harvest incident light for succeeding purposes, *i.e.* photothermal transduction.

3.3.3 Nanohexapods

The general favorability toward multiple branched configurations can be understood due to plasmonic modes occurring at the tips of the branches.[107]

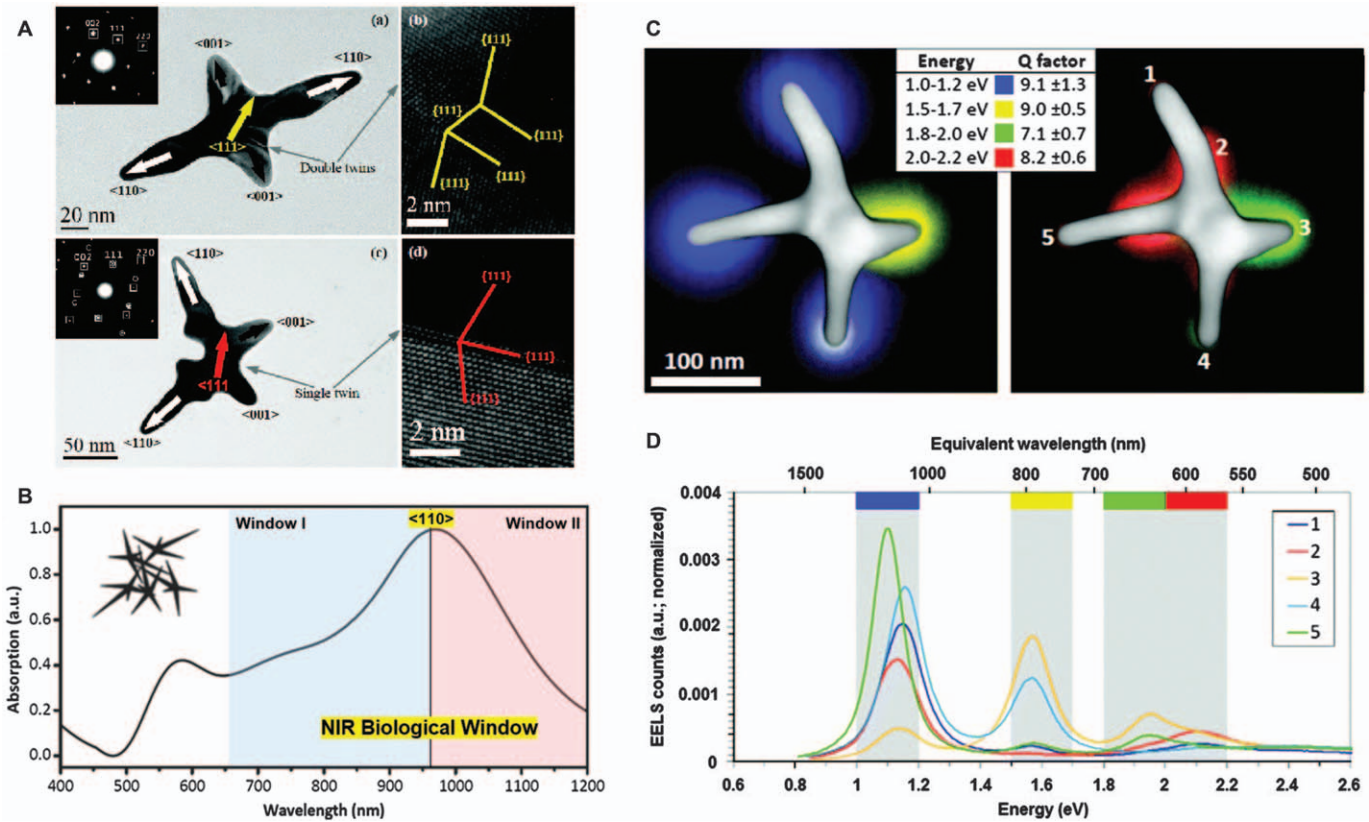
A
(a)
<001>
<110>
<111>
Double twins
<110>
<001>
20 nm
(b)
{111}
{111}
{111}
{111}
{111}
2 nm
<110>
(c)
<001>
<111
Single twin
<001>
50 nm
<110>
(d)
{111}
{111}
{111}
2 nm
B
Window I
<110>
Window II
NIR Biological Window
Absorption (a.u.)
Wavelength (nm)
C
Energy
Q factor
1.0-1.2 eV
9.1 ±1.3
1.5-1.7 eV
9.0 ±0.5
1.8-2.0 eV
7.1 ±0.7
2.0-2.2 eV
8.2 ±0.6
100 nm
1
2
3
4
5
D
Equivalent wavelength (nm)
EELS counts (a.u.; normalized)
Energy (eV)

However, many of these nanostructures possess an arbitrary number of arms with a span of differing arm lengths. Specificity in shape design could be desirable in enabling us to control the optical properties of the nanostructure at will. In this aspect, Xia *et al.* fabricated Au nanostructures with six designated arms – Au nano-hexapods (GNH).[17,127] The arm length and correspondingly the spectral profile of these GNHs can be tuned by adjusting the concentration of Au precursor ($HAuCl_4$) and reaction temperature. When the GNH is pitted against Au nanorods and nanocages of similar spectral profiles (Figure 3.17), a relatively similar photothermal effect was observed among the three nanostructures. However, the GNHs and nanocages had better photothermal stability than the nanorods, where exposure to an 805 nm laser at a power density of 15 $mW\,cm^{-2}$ for 15 min melted the nanorods but not the GNHs and nanocages. In addition, DDA studies identified several plasmonic peaks between 700 and 900 nm which correspond to GNH in various orientations.

3.3.4 Other Branched Metallic Nanostructures with Strong NIR Absorption

Besides the above nanostructures, there exist a diverse range of anisotropically branched nanostructures with strong NIR absorption that could potentially be used for photothermal applications. For example, Au bellflowers (GBF) were synthesized by Chen *et al.* using a liquid–liquid–gas triphase interface system.[128] The GBFs have a unique morphology which consist of a V shape dome for intensification of acoustic signals while there are also numerous branched petals for strong NIR absorption and photothermal effect (photothermal efficiency, η ~74%). Au nanostars[129–133] have also been prevalently studied for photothermal transducing purposes, attributed to their strong LSPR absorbance band in the NIR region (Figure 3.18B).

Figure 3.16 Characterization of Au nanocrosses. (A) TEM images showing the Au nanocrosses existing as (top) double twin and (bottom) single twin. Reproduced from ref. 109 with permission from American Chemical Society, Copyright 2011. (B) Vis–NIR absorption spectra of the Au nanocrosses, where there is a strong absorption peak in the NIR region. Reproduced from ref. 125 with permission from John Wiley and Sons, Copyright © 2016 WILEY-VCH Verlag GmbH & Co. KGaA, Weinheim. (C) Visualization of plasmonic modes using monochromated EELS maps where (left) maps the modes at 1.1 eV and 1.6 eV and (right) maps the modes at 1.9 eV and 2.1 eV; (C) monochromated EELS taken in STEM mode, by placing a 1 nm electron probe at locations 1–5 indicated in the panel (C, right). All five spectra were normalized at the 'zero-loss peak' maximum, after which a pre-measured background was subtracted. The spectral peaks represent the plasmon modes, around which the color-coded, gray 0.2 eV energy windows were placed for the EFTEM experiments, giving the maps in (C). Reproduced from ref. 26 with permission from the Royal Society of Chemistry.

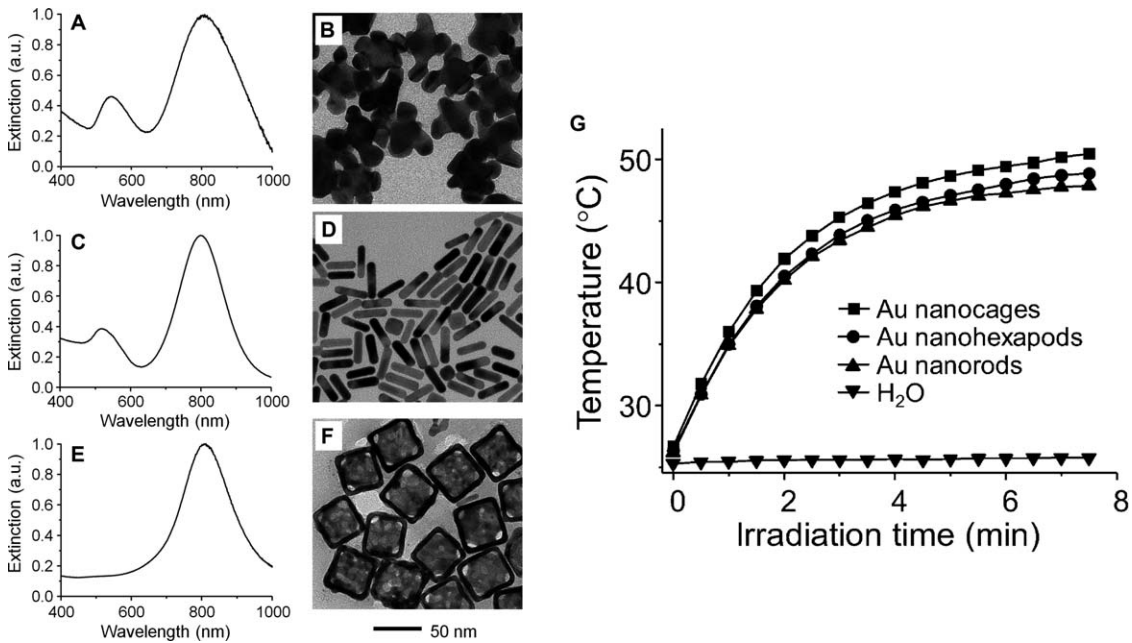

Figure 3.17 Absorption spectra and TEM images of Au nanohexapod (A and B), Au nanorods (C and D) and Au nanocages (E and F) for comparison of photothermal effect; (G) temperature elevation of water when the nanostructures are subjected to irradiation of an 805 nm laser at 0.8 $W\,cm^{-2}$ power density.
Reproduced from ref. 127 with permission from American Chemical Society, Copyright 2013.

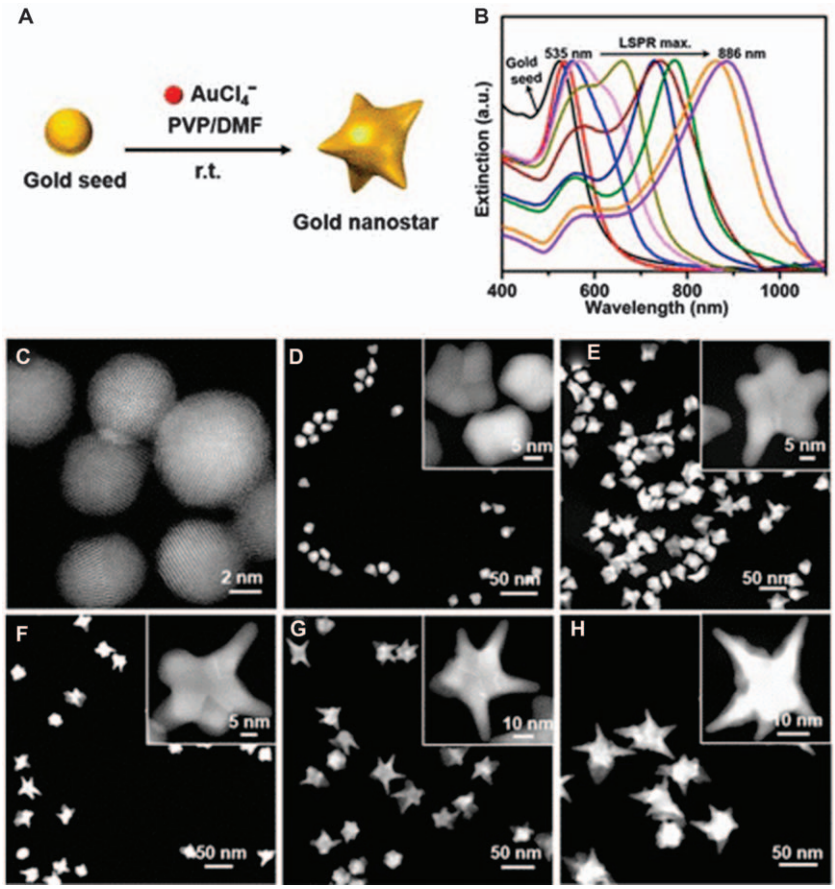

Figure 3.18 (A) Schematic illustration of the preparation of Au nanostars. Gold seeds serve as the nucleation site for the anisotropic growth of Au nanostars through the reduction of $AuCl_4^-$ in the presence of PVP and DMF. (B) Absorption spectra for the gold seed and Au nanostars with various concentrations of gold seeds and their corresponding HAADF-STEM images (C–H). Insets in (D–H) show STEM images of Au nanostars at a higher magnification.
Reproduced from ref. 133 with permission from American Chemical Society, Copyright 2018.

3.4 Applications of Branched Metallic Nanocrystals in Photothermal Therapy (PTT)

With the advancement of nanotechnology, the idea of using heat as a treatment option has been re-evaluated and modified to progress into next generation therapeutics. In this development, inorganic nanostructures have attracted special interest due to their high thermal conversion efficiency, application in bio-imaging, ease of synthesis and surface modification. Among these, plasmonic noble metallic nanostructures distinguish themselves from

other nanostructures such as semiconductor quantum dots, and magnetic and polymeric nanoparticles by their unique surface plasmon resonance (SPR). This SPR, resulting from photon confinement to a small particle size, enhances all the radiative and nonradiative properties of the nanoparticles.

The conventional cancer treatment regimens include surgical resection, radiation therapy, and chemotherapy, where the latter two tend to have side-effects and damage normal tissues. On the other hand, multidrug-resistant organisms (MDROs) are on the rise at an alarming rate around the world. Infections due to MDROs are extremely hard to treat as MDROs are resistant to many antibiotics in the frontline, making treatments ineffective. These problems call for attention and alternative treatment options. To reduce risks/side effects and avoid drug resistance, new medical strategies such as photothermal sensitization and photothermal ablation therapy have been explored for cancer management and infection treatment. Nanotechnology brings excitement for cancer diagnosis and therapy as well as MDRO infection treatment through heat generated from light to destroy cancer or MDRO cells, without affecting the surrounding healthy normal tissues. For the success of photothermal treatment, strong optical absorption of metallic nanostructures and their high efficiency of photothermal conversion, as well as their active accumulation at the sites are critical.

Plasmonic photothermal therapy involving gold-based nanoparticle contrast agents was first reported by Pitsillides and group in 2003.[134] They used anti-CD8 immunogold nanospheres in combination with a nanosecond visible pulsed laser. These nanoparticles specifically bound to T lymphocyte cells and subsequent laser irradiation resulted in destruction of over 90%. Later, Zharov *et al.*[135] reported that cancer cell death could be induced by a single nanosecond pulse at an energy of 2–3 $J\,cm^{-2}$ with 10–15 gold nanoparticles per cell. However, visible light does not penetrate tissue optimally in clinical applications. Thus, NIR light is required for its deep penetration due to minimal absorption of the hemoglobin and water molecules in tissues in this spectral region. Along with it, NIR-absorbing metal nanoparticles are required. Extensive studies have addressed the issue through various perspectives including but not limited to tuning shape, size, and composition to develop metal nanostructures to achieve optimal structural and photothermal properties, as discussed in previous sections. Great efforts have been made to develop photothermal therapy strategies as alternative or combinational treatment options for diseases including cancer and infections caused by multi-drug-resistant bacteria and bacterial biofilm.[136]

Due to unique strong surface plasmon resonance (SPR) absorption, noble metals such as gold and silver nanostructures can significantly enhance photothermal conversion and are promising for photothermal therapy applications. Ideally, metal nanostructures should have strong and tunable SPR, be easy to deliver, have low toxicity, and be convenient for bioconjugation for actively targeting specific cells.[137] Here, we would highlight the importance of shape in achieving photothermal properties with the focus on gold branched nanostructures for photothermal applications in cancer and infection management.

3.4.1 Cancer Management

Most chemotherapeutic drugs are not specific to tumor cells, but are also able to cause harm to other cells and consequently are associated with side effects such as compromised immunity, hair loss, nausea, *etc.* In the pursuit of therapies capable of reducing undesired side effects and enhancing efficacy, there has been growing interest in utilizing hyperthermia (heat) to achieve these goals.[138] The history of using hyperthermic cancer therapy originated in 1893 by Coley; cancer patients infected by erysipelas had high fevers and resulted in either reduced cancer symptoms or complete regression of tumors.[139] Since then, studies have been performed applying hyperthermia to cancerous tumors to maintain tissue temperatures of 42 to 45 °C for treatment.[140] As whole body hyperthermia would cause cardiovascular and gastrointestinal side effects, a favorable modality for cancer treatment would require a targeted, nanoparticle-mediated localized hyperthermia.

One of the unconventional approaches is the use of NIR irradiation and heat-absorbing metal nanostructures to selectively and effectively eradicate cancer cells.[69,109] Such treatment using NIR light absorption to incite thermal damage is an established means of destroying cancer tissues since tissues heated beyond a certain thermal threshold undergo various mechanisms of cellular damage such as protein structural changes or carbonization of tissues.[141] Metal nanostructures perform as nanoscale heaters for photothermal therapy. Under specific light irradiation, photothermal therapy can be applied to localize heat focused on the target site to kill cancer cells at a specific part of the body in a non-invasive manner.

Gold nanostructures have found numerous medical applications in recent years because of their facile synthesis and surface modification, strongly enhanced and tunable optical properties, and most importantly their excellent biocompatibility making it feasible for clinical settings. Besides these attractive properties, synthesis methods of gold nanostructures have also been modified to be more favorable. High quality, high yield, and size controllable colloidal branched gold nanostructures can be quickly prepared by greener synthesis methods.[142]

The successful fabrication of structurally more complex metal nanostructures such as semi-shells, multi-shells, split rings, helixes, and gammadions has created greatly enriched surface plasmonic properties.[143] Metallic nanostructures with their geometry-dependent optical resonances are of great interest due to their ability to manipulate light in ways not possible with conventional optical materials.[144] The morphology and size of the nanostructures strongly affect their surface plasmon resonance (SPR) properties and subsequently influence their applications.[145] For instance, gold nanorods or nanostars are more suitable for photothermal therapy than spherical gold nanoparticles, owing to their shape. As they comprise branches, they can absorb incident NIR light more efficiently and thus achieve higher light-to-heat conversion, giving rise to better heat generation.

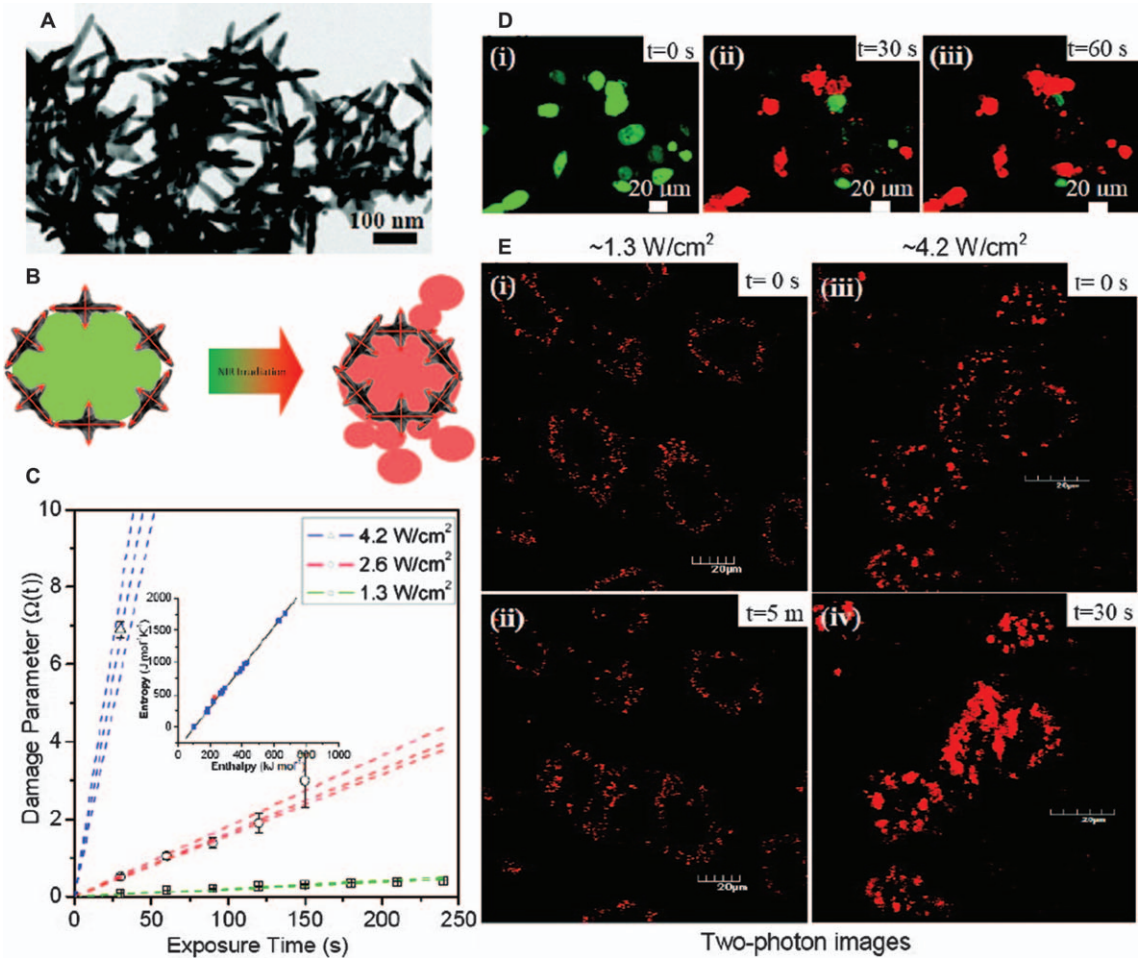
A
100 nm
B
NIR Irradiation
C
Damage Parameter (Ω(t))
Exposure Time (s)
4.2 W/cm2
2.6 W/cm2
1.3 W/cm2
Entropy (J/mol K)
Enthalpy (kJ mol-1)
D
(i) t=0 s
(ii) t=30 s
(iii) t=60 s
20 µm
E
~1.3 W/cm2
~4.2 W/cm2
(i) t= 0 s
(iii) t= 0 s
(ii) t=5 m
(iv) t=30 s
20µm
Two-photon images

The branched gold nanostructures have inspired wide research interests due to their good biocompatibility and excellent photothermal property. Taking these factors into consideration in the design and development of photothermal tools, Ye and colleagues[109] devised free-standing multiple-branched gold nanocrosses which exhibit a pronounced near- and mid-IR localized surface plasmon resonance (LSPR). Structural analysis showed singly and doubly twinned gold nanocrosses (see Figure 3.16). These highly multiple-branched gold nanocrosses, as seen in Figure 3.19A, produced a rich surface plasmon spectrum, demonstrating that the effective conversion of NIR light into heat mainly relied on their branched features. Notably, gold nanocrosses act as an octopus antenna in efficiently capturing the incident light along any branches and convert it into heat which is then rapidly transmitted to the localized area and destroys cancer cells effectively.

A comprehensive study revealed the effect of laser intensity and exposure time on the destruction of cells *via* irradiation of human lung cancer cells (A549 cells) associated with gold nanocrosses using a 900 nm laser at intensities of 1.3, 2.6, and 4.2 $W\,cm^{-2}$ (see Figure 3.19C). Remarkably, all the cancer cells were killed under laser irradiation within 30 s at 4.2 $W\,cm^{-2}$ while ~95% of the cells were killed after laser irradiation for 150 s at 2.6 $W\,cm^{-2}$. However, cell death was not observed in control experiments in the absence of gold nanocrosses, where the cancer cells remained alive even after 10 min of irradiation. For qualitative study of the photothermal treatment, cells were also observed under a confocal microscope. At a lower laser intensity of ~1.3 $W\,cm^{-2}$, gold nanocrosses associated primarily on the A549 cells and were observed to have minimal changes in shape after 5 min of irradiation. But at a higher laser intensity of 4.2 $W\,cm^{-2}$, the cells started to shrink immediately upon laser exposure. These observations are well correlated to the quantitative study (see Figure 3.19D). After 30 s irradiation at 4.2 $W\,cm^{-2}$, the cells had drastically been changed in both shape and size. The resulting collapsed cell membranes affected the gold nanocrosses and agglomerates were observed. Furthermore, the time-dependent damage process under irradiation at a middle laser intensity of 2.6 $W\,cm^{-2}$ (see Figure 3.19E) illustrated a slower destruction rate, as predicted.

Figure 3.19 Photothermal damage, Arrhenius model, and two-photon luminescence imaging of A549 cancer cells associated with gold nanocrosses. (A) TEM image of gold nanocrosses. (B) A schematic of the destruction of cancer cells by gold nanocrosses under NIR laser irradiation. Gold nanocrosses accumulate on the surface of cancer cells, then convert the incident light into heat and destroy cancer cells upon NIR irradiation. (C) Photothermal damage of A549 cancer cells associated with gold nanocrosses as a function of time at 900 nm laser intensities of 1.3, 2.6, and 4.2 $W\,cm^{-2}$. (D) Confocal images showing the time-dependent damage process at 2.6 $W\,cm^{-2}$ after 900 nm irradiation for 0, 30, and 60 s. (E) Two-photon luminescence images of gold nanocrosses associated with cells under 900 nm laser excitation at 1.3 and 4.2 $W\,cm^{-2}$. Reproduced from ref. 109 with permission from American Chemical Society, Copyright 2011.

The study indicates that the shape of nanostructures significantly influences their absorption efficiency and photothermal profile. Similarly, laser intensity and irradiation time greatly affect the success of photothermal treatment. The synergistic coupling between the branches facilitates the highly branched gold nanocrosses to efficiently capture IR light for effective photothermal destruction of cancer cells. The enhanced hyperthermia properties of the gold nanocrosses proved to be a very promising tool for cancer therapy. An effective targeted-therapy method, combined with laser-induced hyperthermia therapy, could be an alternative way to treat solid tumors.[146–148]

As the temperature elevation is directly related to the absorption of light by plasmonic nanostructures, the absorption cross-section of nanostructures of different shapes is important criteria in the design of plasmonic nanostructures. Gold nanostructures with controlled assembly could bring in tunable optical and photothermal properties. Gold nanoflowers (GNF) using 'green' L-ascorbic acid has caught attention as they have abundant petals giving a large absorption cross-section and these nanoflower petals play an important role in Raman signal enhancement allowing signal improvement in the order of 10^6. This enhancement was explained in terms of the electromagnetic enhancement mechanism of the metal nanomaterials.[149] These gold nanoflowers demonstrated high biocompatibility and improved signals when using a confocal microscope, indicating its applicability as a multimodal *in vitro* SERS-based sensor and imaging tag. In another study, GNF produced using starfruit juice showed interesting NIR photothermal properties.[69] This suggests that the GNFs produced can be used as a photothermal therapy agent as the biomolecules in the starfruit juice cap the GNFs and make them more biocompatible. Next, irradiation time effect on the photothermal destruction of the MCF-7 cancer cells was investigated by confocal microscopy throughout the laser irradiation. Obviously, the cells started to bleb after a few seconds of irradiation and were destroyed after 30 s (see Figure 3.20A). Dead cells with a blebbing membrane indicate that the destruction of the cancer cells might be due to localized heat at their membrane which was in direct contact with GNFs. The highly efficient *in vitro* photothermal therapy led to further investigation of the *in vivo* photothermal therapy using MCF-7 tumor-induced BALB/c mice and 808 nm NIR laser irradiation at a power density of 0.5 $W\,cm^{-2}$ for 6 min. Tumors shrank and eventually disappeared in the mice with GNF injection and laser irradiation while tumors grew rapidly in the mice with either NIR irradiation without GNF injection, or GNF injection without NIR irradiation (see Figure 3.20B–D). The results indicate that either NIR irradiation or GNF injection alone did not provide any therapeutic effect on the tumor, demonstrating an excellent *in vivo* photothermal therapeutic efficacy of GNFs. Gold nanoflowers present great potential in photothermal cancer therapy.

The shape-dependency of photothermal properties is well pronounced. The highly branched gold nanostructures with sharp tips – nano-snowflakes hold the highest photothermal conversion efficiency, and gold nanostructures with blunt tips – nanoflowers hold the lowest.[150] Gold nano-snowflakes could absorb light with a wide range of wavelengths from 500 nm to more

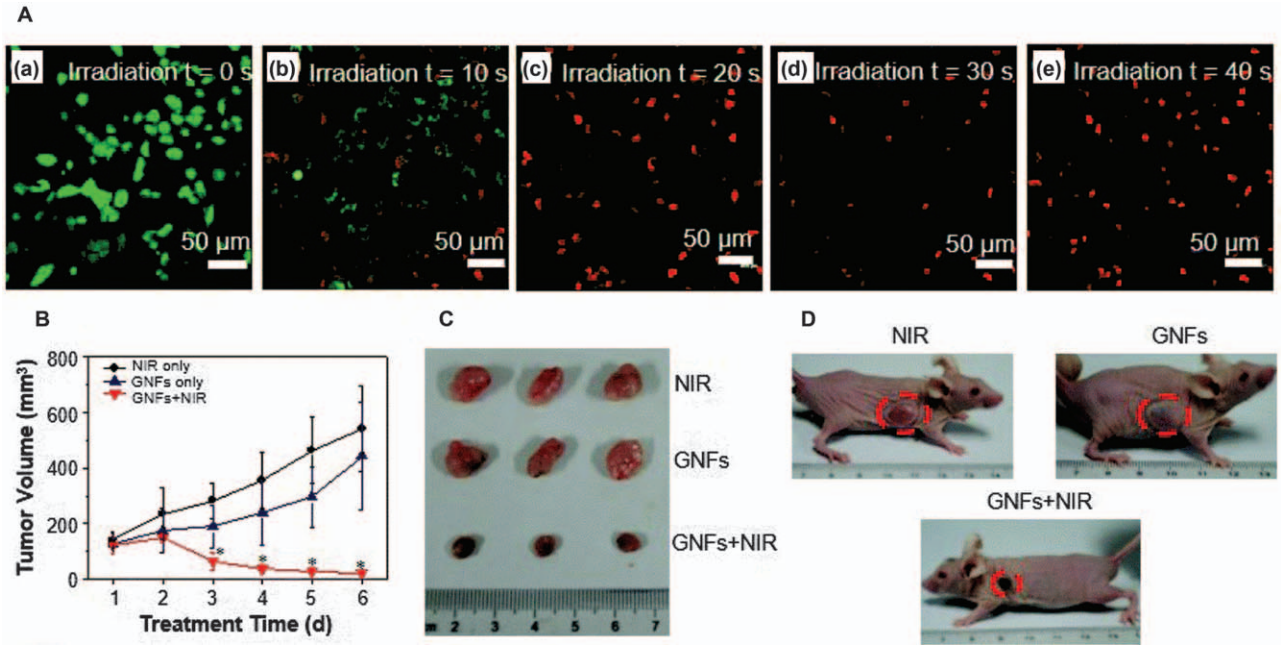

Figure 3.20 Photothermal destruction of MCF-7 cancer cells using GNFs. (A) Confocal microscope images demonstrating the effect of irradiation time on the photothermal destruction of MCF-7 cells incubated with GNFs under irradiation with an 808 nm CW laser. (B) *In vivo* evaluation of the photothermal therapy of tumor by GNFs under NIR irradiation. Initial dorsal subcutaneous tumor implantation was conducted by injecting MCF-7 cancer cells into mice. The experiments started when the tumor size reached ~110 mm^3. The experimental results are shown as a mean with the SD error bars ($n = 5$). (C) The images of excised tumors from different groups after treatment for 6 days. (D) Representative photographs of mice with treatment of the NIR laser only, GNFs only, and GNFs under NIR laser irradiation after 6 days.
Reproduced from ref. 69 with permission from the Royal Society of Chemistry.

than 1000 nm which covered the visible light to near infrared region due to their highly branched structure. The highest photothermal conversion efficiency of gold nano-snowflakes may be attributed to: the wider SPR absorption peak with high absorption around 808 nm and highly branched nanostructure for enhancing the local electromagnetic field of petals on the surface. The red-shift and much wider SPR absorption peak is consistent with the shape evolution from gold nanoflowers to nanostars and finally to nano-snowflakes. Gold nanostars have two localized SPR (LSPR) peaks in the visible and infrared regions; their Raman signal enhancement and SERS ability greatly depend on the infrared absorption from the plasmon resonance along the aligned branches. The lightning rod effect and creation of hot spots could be enhanced with the length and number of gold branches.[151]

Besides the shape, the size of nanostructures strongly influences their photothermal effects on cells.[134,135] Nanostructures with sizes from 10 to 30 nm have the strongest effect.[152] Although theoretical calculations may indicate that the photothermal effect of larger nanostructures is more significant, the lower cellular uptake might have reduced overall efficiency. Also, the size of 10–30 nm is very well correlated to microbubble formation, a cause of cell damage, induced by the nanostructures.

With high interest in developing innovative smart nanomedicines, there could be a whole range of different shapes and sizes of plasmonic branched nanostructures exhibiting strong photothermal efficacy, to emerge for evaluation in clinical settings. There are also hybrid photothermal nanostructures, incorporating different materials for improved stability, synergistic effects, enhanced efficacy, *etc.* For instance, by incorporating silver into gold, Ag–Au nanostructures exhibit a high SERS activity while incorporating an aptamer into Ag–Au nanostructures enables targeting the surface of human breast cancer cells (MCF-7 cells) with high affinity and specificity.[153] Collectively, the aptamer–Ag–Au nanostructures have a high adsorption of NIR irradiation and capability to execute photothermal therapy of MCF-7 cells at a very low irradiation power density (0.25 $W\,cm^{-2}$) without destroying the healthy cells and the surrounding normal tissue. These nanostructures may offer a protocol to specifically recognize and sensitively detect the cancer cells, and great potential for application in the photothermal therapy of the cancers.

As bimetallic nanostructures draw attention as exciting materials for effective photothermal therapy, Joseph *et al.*[154] reported gold–silver (AuAg) spiky branched nanostars with gold (90%) being the major component, possessing two distinct intense localized surface plasmon resonances in the NIR and short-wavelength infrared ranges. AuAg nanostars with evenly spaced spikes and low branching expressed great potential for photothermal therapy, active in both the visible and NIR regions. McGrath and coworkers[155] developed palladium–gold (Pd–Au) nanostructures containing multiple gold nanocrystals on highly branched palladium seeds. Pd–Au heterostructures caused destruction of HeLa cancer cells *in vitro*, as well as complete destruction of tumor xenographs in mouse models *in vivo* under

808 nm laser irradiation at an intensity of 3 W cm^{-2} for 30 min, demonstrating effective photothermal therapy (see Figure 3.21A–C). In contrast, there was no significant effect on cell viability or tumor site in the absence of the nanostructures or exposure to laser light.

To achieve biocompatibility, Xia's group[127] coated gold nanohexapods with polyethylene glycol and demonstrated application in photothermal therapy and diagnosis. The PEGylated Au nanohexapods achieved high cellular uptake and low cytotoxicity *in vitro* as well as significant blood circulation and tumor accumulation after intravenous injection *in vivo*. The PEGylated Au nanohexapods exhibited the highest photothermal conversion efficiency *in vivo* when

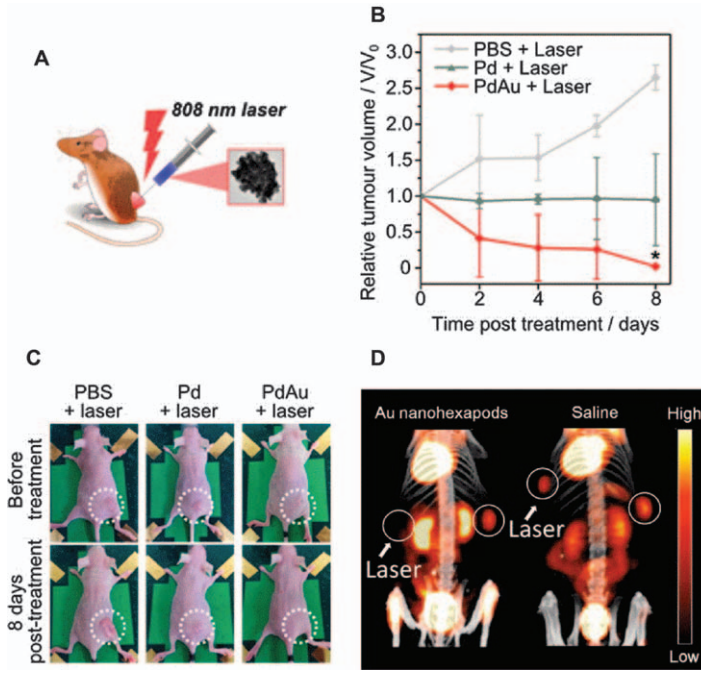

Figure 3.21 *In vivo* photothermal treatment using branched nanostructures. (A) Schematic of *in vivo* photothermal treatment. (B) *In vivo* photothermal hyperthermia efficacy of Pd–Au, as compared to laser treatment with Pd seeds and with PBS only. A quantity of 100 μL of either PBS, Pd, or Pd–Au (at 50 μg mL^{-1} Pd concentration) in PBS was injected into HeLa xenographs in mice ($n = 3$ for each group; $^{*}p < 0.05$). (C) Representative images taken of the mice immediately before and 8 days after laser irradiation of the tumor site for 30 min at 3 W cm^{-2}. The dashed white circles indicate the tumor regions. Reproduced from ref. 155 with permission from American Chemical Society, Copyright 2015. (D) ^{18}F-FDG PET/CT co-registered images of mice intravenously administrated with an aqueous suspension of Au nanohexapods and saline solution. Tumor locations are marked with white circles. Irradiated tumors are highlighted with white arrows. Reproduced from ref. 127 with permission from American Chemical Society, Copyright 2013.

compared with PEGylated Au nanocages and Au nanorods, possibly due to branched features. When the photothermal treatment effect on tumor metabolic activity was assessed using ^{18}F-flourodeoxyglucose positron emission tomography combined with computed tomography (^{18}F-FDG PET/CT), significantly reduced ^{18}F-FDG uptake was found in the irradiated tumors in contrast to the contralateral non-irradiated tumors (see Figure 3.21D). Photothermal treatment presented 90% reduction of tumor metabolism in mice treated with Au nanohexapods. This indicates branched Au nanostructures as promising photothermal materials achieving almost complete destruction of tumor glycolic activity.

For high stability in an isotonic solution, Lin *et al.*[156] linked branched-gold nanoparticles with thiol-modified mannoside (Man@BAu NPs). Man@BAu NPs showed low cytotoxicity, broad NIR absorption in the biological window, and good photothermal conversion killing ~36–55% of the MDA-MB-231 cells under 808 nm laser irradiation (1.08 W) for 10 min.

3.4.2 Bacterial and Biofilm Treatment

The widespread use of antibiotics has resulted in the ongoing and ever-increasing occurrences of antibiotic-resistant bacteria. Antibiotic resistance is a continually evolving process and has become a serious problem of global public health. Relying on existing drugs to treat the bacterial diseases will not be able to circumvent the development of resistance by bacteria.[157] Also, bacteria may be developed into biofilm which can physically block the access of drugs to the bacterial cells, making treatment even more difficult.[158] Therefore, treatment of the emerging antibiotic-resistant bacteria requires a totally new strategy that is conceptually different from the traditional small-molecule drugs.[159] There is a strong interest in the use of plasmonic metal nanoparticles for bacterial infection treatments through photothermal therapy. As NIR light is reported to penetrate the subcutaneous cell layer up to a depth of 10 mm to a few centimeters, the structural dimensions of metal nanostructures are specifically designed to ensure that they maximally absorb NIR light for subsequent effective conversion into heat.[160] These significant properties have drawn attention to develop gold nanostructures as novel and competent nano-photothermal vectors to destroy bacteria at the molecular level, circumventing drug-resistant issues.

Plasmonic gold nanostructures are promising nanomedicines for combating drug resistant bacterial infections as they can absorb light efficiently in the NIR region where light penetration in tissues is optimal and convert it to local heat by photo-exciting the conduction electrons to induce surface plasmon oscillations followed by non-radiative relaxation.[161] A significant photothermal effect can be obtained using gold nanostructures at fluences below the medical laser safety threshold[162] which is of the order of 20 to 100 mJ cm^{-2} depending on the method of application. While NIR wavelengths harmlessly pass through the human body, they heat plasmonic materials such as gold nanoshells to a high temperature of more than 70 °C and will thermally ablate any cell

(bacteria or eukaryotic) in close proximity to these plasmonic materials. The advantage of this treatment method is selective killing of the cells in direct contact with gold nanostructures but leaving surrounding healthy cells unaffected, owing to the rapid dissipation of thermal energy over short distances.

Heat radiation is very promising to effectively address the issue of antibiotic resistance because it can be easily delivered to the infected sites for physically destroying bacteria instead of inhibiting their growth like drugs. The temperature at the targeted region has to reach between 40 and 50 °C in order to kill cancer cells while for bacteria and biofilm the temperature has to reach between 50 and 80 °C as bacteria have double cell walls which need higher energy for their destruction.[163] Various types of gold nanostructures were explored for ablation of multidrug-resistant bacteria and biofilms at the infected area.[125,164–167]

Thermal ablation of bacteria using plasmonic gold nanostructures depends largely on the efficiency of NIR light absorption, distribution of nanostructures at the target site, and temperature profile upon laser irradiation.[168] To enhance stability and targeting ability, gold nanostructures can easily be modified with appropriate surface ligands *via* the surface chemistry of gold. Teng and colleagues[125] conjugated NIR-absorbing gold nanocrosses with biologically active moieties to achieve targeting to the pathogenic bacteria *P. aeruginosa* PAO1 selectively for complete destruction of the bacteria and their biofilm. When exposed to 800 nm light with a low power density of 3.0 $W\,cm^{-2}$ for 5 min, the conjugated gold nanocrosses were heated up promptly and destructed the superbug bacteria completely (see Figure 3.22). The local hyperthermia is achieved *via* functionalized plasmonic gold nanocrosses which efficiently convert optical energy into thermal energy upon irradiation with light for photo-ablation of bacteria in a short time, and all the cells deceased under 70 °C for 5 min or 80 °C for 2 min. Complete ablation was observed in the irradiated region of the biofilm marked with a dashed line, while the surrounding cells beyond the laser-exposed area remained alive. It shows that all the biofilm cells in the area irradiated with the laser were killed while the biofilm cells beyond the laser-exposed area have no noticeable effect, indicating the localized photothermal effect. Even after 48 h post-irradiation, there was no live bacteria present. This indicates that the hyperthermia is a promising tool for ablating bacteria and inhibiting the development of biofilm.

The localized hyperthermia is shown to be highly shape- and composition-dependent and can be tuned to achieve efficient photothermal activities in the desired applications. The gold nanostars in colloidal solutions demonstrated efficient photothermal properties of 3 and 100 times higher than gold nanorods and iron oxide nanoparticles, respectively.[169] Borzenkov and co-workers[170] embedded gold nanostars in thin PVA films to display improved mechanical properties and an enhanced photothermal activity. The films showed promising photothermal activities upon exposure to NIR light, offering novel bactericidal films with a protective function. Similarly, monolayers of gold nanostars were attached onto mercaptopropyltrimethoxysilane-modified

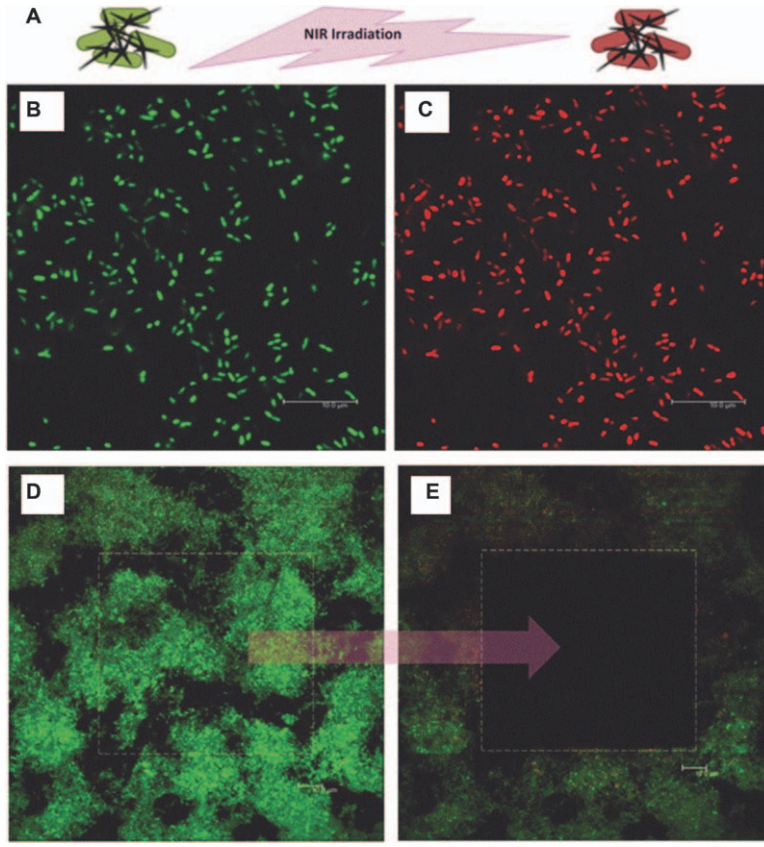

Figure 3.22 Photothermal effect of the conjugated gold nanocrosses on the growth of PAO1 bacteria and biofilm. (A) Schematic of photothermal treatment of bacterial infection using conjugated gold nanocrosses and NIR laser irradiation. Confocal images of PAO1 bacteria preincubated with the conjugated gold nanocrosses (B) before irradiation and (C) after irradiation for 5 min with a multiphoton laser at 800 nm at a power density of $\approx$3.0 W cm^{-2}. Bacteria destruction was indicated by red staining with propidium iodide and no destruction (no adverse effect) was indicated by green staining with syto 9. Confocal images of the biofilm treated with gold nanocrosses (D) before irradiation and (E) after irradiation at its central rectangular region for 5 min with a multiphoton laser at 800 nm at a power density of $\approx$3.0 W cm^{-2}. Localized photothermal effect and ablation of the biofilm were observed in the irradiated region. Confocal imaging was performed at 100$\times$ magnification. Scale bar = 10 μm. Reproduced from ref. 125 with permission from John Wiley and Sons, Copyright © 2016 WILEY-VCH Verlag GmbH & Co. KGaA, Weinheim.

glass substrates to provide a photothermal platform for generating local hyperthermia and effectively destroying *S. aureus* biofilms.[171]

Gold nanoflowers with a strong NIR plasmon may serve as an efficient photothermal agent in antibacterial applications. Gold nanoflowers with

their surface protrusions offer a larger surface area for surface functionalization. These would direct them to bacteria, resulting in cell death and other cellular damage *via* the rupture of the cellular membrane of bacteria. When comparing the bactericidal effects of gold nanoparticles, nanostars, and nanoflowers toward *S. aureus* bacteria, it is evident that antibacterial activity is dependent on the shape of the gold nanostructures. Gold nanoflowers exhibited the most promising performance in various anti-infection applications accompanied with non-cytotoxic function to mammalian cells.[172] Stable Dap-Au nanoflowers were prepared with daptomycin (Dap) micelles as the template and reducing agents to generate a photothermal conversion efficiency of ~40% from light to heat and effectively inhibit the growth of bacteria in the assistance of 808 nm light.[173]

Although silver is known as a highly-effective and broad-spectrum antibacterial agent, its severe cytotoxicity to mammalian cells and noticeable reduction in antibacterial activity with time restrict their practical applications. For better application prospects, bimetallic gold–silver particles were recently developed for improved application in photothermal and antibiotic-based treatment as compared to pure gold or silver particles. This enhanced bactericidal activity without increasing their cytotoxicity guarantees the clinical applications of silver.[174] Encouraged by this, the development of many other hybridized photothermal nanostructures is in the pipeline to serve in photothermal therapy applications.

3.5 Conclusion, Perspective, and Outlook

In recent years, there has been mounting interest in using branched metallic nanocrystals for photothermal applications. As the shape, size, and morphology of the nanocrystals have a vast impact on their properties and applications, interest in the synthetic routes that ensure careful control of such nanostructures is also growing rapidly. In this chapter, four traditional solution-based strategies (seeded growth, seedless growth, templated growth, and chemical etching), with a recent growing green method are discussed. Seeded growth, the oldest method of the lot, involves a two-step process that first grows small metal nanocrystals. They are then used as seeds for further formation of branches on the nanocrystals due to the different surfaces. This strategy allows precise control in size due to the splitting of nucleation and growth stages. Moreover, the final morphology of the anisotropic nanostructures can also be controlled by the shape, size, and composition of the seed. This approach also allows the formation of bimetallic nanostructures easily. Seedless growth, on the other hand, does not use pre-synthesized seeds to facilitate the subsequent branching, instead, foreign ions or capping agents are added to mediate its growth. Crystal twinning and polymorphism are also exploited for such growth, hence, seedless growth is a convenient one-pot synthetic strategy. The templated growth strategy, as the name

implies, uses a template to facilitate the nucleation and direct the growth of branched nanostructures. Materials like deep eutectic solvents and nanoparticle arrays are some examples that are used as such templates. The chemical etching route uses chemical etchants to selectively dissolve certain crystallographic facets to achieve branched nanoarchitectures. Lastly, there has been a tremendous development in using green methods for anisotropic growth of branched nanostructures. Biogenic substances like plant extracts, microorganisms, and biomolecules are used in the synthesis for reasons such as being more environmentally friendly and biocompatible. This allows the synthesized branched metallic nanocrystals to be a safer option for biomedical applications.

With the synthesized anisotropically branched nanostructures, the properties of the nanocrystals were studied for better fit for various applications. For example, branched Au nanostructures provide pronounced absorption in the NIR region, which could be further exploited for photothermal ablation or photothermal-modulated drug release applications. While novel metallic nanostructures with superseding capabilities are increasingly developed, it is important to appreciate how the introduction of branched features could induce stronger NIR absorption and the corresponding photothermal effect.

As discussed, the applications of photothermal therapy for cancer and bacterial and biofilm treatments are almost limited to the use of Au and Ag nanostructures. They both have superior plasmonic and photothermal properties but can be costly as they are noble metals. However, Au is mostly preferred due to its stability even though Ag is relatively cheaper and has a stronger plasmonic response. It is postulated that Ag will make a good alternative to Au by functionalizing the branched Ag nanostructures, making them more stable. Alloyed anisotropic nanocrystals containing Au and Ag could also be further studied to capture the advantages of both metals.

Prospectively, we envision that more versatile and facile methods will be developed for the synthesis of anisotropic metal nanostructures. This allows more cutting-edge nanostructures to be designed for explicit applications with particular properties. However, growth mechanisms and structure-to-property correlations need to be studied in depth to be accelerated for wider applications of such materials. Additionally, the formation of nanostructures using different types of metals can also be explored. Currently, the most commonly used metals include Au, Ag, Pt, and Pd. With more different types of branched metallic nanocrystals, new properties and applications may be viable. Furthermore, we foresee a huge growth in synthesis of anisotropic metallic nanocrystals *via* biogenic methods. Biogenic synthesis ensures that the nanostructures are benign and safe for biomedical application. Last but not least, challenges related to stability and scaling-up need to be overcome to enable branched metallic nanocrystals to be commercialized for such applications.

References

1. E. C. Dreaden, A. M. Alkilany, X. Huang, C. J. Murphy and M. A. El-Sayed, *Chem. Soc. Rev.*, 2012, **41**, 2740–2779.
2. M. Hu, J. Chen, Z. Y. Li, L. Au, G. V. Hartland, X. Li, M. Marquez and Y. Xia, *Chem. Soc. Rev.*, 2006, **35**, 1084–1094.
3. P. K. Jain, X. Huang, I. H. El-Sayed and M. A. El-Sayed, *Acc. Chem. Res.*, 2008, **41**, 1578–1586.
4. K. Xia, L. Zhang, Y. Huang and Z. Lu, *J. Nanosci. Nanotechnol.*, 2015, **15**, 63–73.
5. S. Cheong, J. D. Watt and R. D. Tilley, *Nanoscale*, 2010, **2**, 2045–2053.
6. H. Zhang, M. Jin, Y. Xiong, B. Lim and Y. Xia, *Acc. Chem. Res.*, 2013, **46**, 1783–1794.
7. S. Pal, Y. K. Tak and J. M. Song, *Appl. Environ. Microbiol.*, 2007, **73**, 1712–1720.
8. M. Faraday, *Philos. Trans. R. Soc.*, 1857, **147**, 145–181.
9. A. R. Tao, S. Habas and P. Yang, *Small*, 2008, **4**, 310–325.
10. Y. Xia, Y. Xiong, B. Lim and S. E. Skrabalak, *Angew. Chem., Int. Ed.*, 2009, **48**, 60–103.
11. B. Lim and Y. Xia, *Angew. Chem., Int. Ed.*, 2011, **50**, 76–85.
12. H. You, S. Yang, B. Ding and H. Yang, *Chem. Soc. Rev.*, 2013, **42**, 2880–2904.
13. W. Niu, L. Zhang and G. Xu, *Nanoscale*, 2013, **5**, 3172–3181.
14. C. Gao, J. Goebl and Y. Yin, *J. Mater. Chem. C*, 2013, **1**, 3898–3909.
15. N. R. Jana, L. Gearheart and C. J. Murphy, *Adv. Mater.*, 2001, **13**, 1389–1393.
16. T. K. Sau and C. J. Murphy, *Langmuir*, 2004, **20**, 6414–6420.
17. D. Y. Kim, T. Yu, E. C. Cho, Y. Ma, O. O. Park and Y. Xia, *Angew. Chem., Int. Ed.*, 2011, **50**, 6328–6331.
18. C. J. Desantis, A. A. Peverly, D. G. Peters and S. E. Skrabalak, *Nano Lett.*, 2011, **11**, 2164–2168.
19. C. J. DeSantis, A. C. Sue, M. M. Bower and S. E. Skrabalak, *ACS Nano*, 2012, **6**, 2617–2628.
20. R. G. Weiner, C. J. DeSantis, M. B. T. Cardoso and S. E. Skrabalak, *ACS Nano*, 2014, **8**, 8625–8635.
21. P. Senthil Kumar, I. Pastoriza-Santos, B. Rodriguez-Gonzalez, F. Javier Garcia de Abajo and L. M. Liz-Marzan, *Nanotechnology*, 2008, **19**, 015606.
22. C. G. Khoury and T. Vo-Dinh, *J. Phys. Chem. C*, 2008, **112**, 18849–18859.
23. S. Maksimuk, X. Teng and H. Yang, *J. Phys. Chem. C*, 2007, **111**, 14312–14319.
24. H. Zhang, X. Xia, W. Li, J. Zeng, Y. Dai, D. Yang and Y. Xia, *Angew. Chem., Int. Ed.*, 2010, **49**, 5296–5300.
25. J. L. Elechiguerra, J. Reyes-Gasga and M. J. Yacaman, *J. Mater. Chem.*, 2006, **16**, 3906.
26. E. Ye, M. D. Regulacio, M. S. Bharathi, H. Pan, M. Lin, M. Bosman, K. Y. Win, H. Ramanarayan, S. Y. Zhang, X. J. Loh, Y. W. Zhang and M. Y. Han, *Nanoscale*, 2016, **8**, 543–552.

27. L.-C. Cheng, J.-H. Huang, H. M. Chen, T.-C. Lai, K.-Y. Yang, R.-S. Liu, M. Hsiao, C.-H. Chen, L.-J. Her and D. P. Tsai, *J. Mater. Chem.*, 2012, **22**, 2244–2253.
28. T. Herricks, J. Chen and Y. Xia, *Nano Lett.*, 2004, **4**, 2367.
29. X. Huang, Z. Zhao, J. Fan, Y. Tan and N. Zheng, *J. Am. Chem. Soc.*, 2011, **133**, 4718–4721.
30. G. T. Fu, X. Jiang, R. Wu, S. H. Wei, D. M. Sun, Y. W. Tang, T. H. Lu and Y. Chen, *ACS Appl. Mater. Interfaces*, 2014, **6**, 22790–22795.
31. J. Watt, N. Young, S. Haigh, A. Kirkland and R. D. Tilley, *Adv. Mater.*, 2009, **21**, 2288–2293.
32. J. Xie, J. Y. Lee and D. I. C. Wang, *Chem. Mater.*, 2007, **19**, 2823.
33. H. Liu, Y. Xu, Y. Qin, W. Sanderson, D. Crowley, C. H. Turner and Y. Bao, *J. Phys. Chem. C*, 2013, **117**, 17143–17150.
34. C. Wang, G. Xiao, Y. Sui, X. Yang, G. Liu, M. Jia, W. Han, B. Liu and B. Zou, *Nanoscale*, 2014, **6**, 15059–15065.
35. N. Ortiz and S. E. Skrabalak, *Angew. Chem., Int. Ed.*, 2012, **51**, 11757–11761.
36. A. P. LaGrow, S. Cheong, J. Watt, B. Ingham, M. F. Toney, D. A. Jefferson and R. D. Tilley, *Adv. Mater.*, 2013, **25**, 1552–1556.
37. Z. Li, W. Li, P. H. Camargo and Y. Xia, *Angew. Chem., Int. Ed.*, 2008, **47**, 9653–9656.
38. M. Zhu, B. Lei, F. Ren, P. Chen, Y. Shen, B. Guan, Y. Du, T. Li and M. Liu, *Sci. Rep.*, 2014, **4**, 5259.
39. V. S. Marangoni, L. D. Germano, C. C. C. Silva, E. A. de Souza and C. M. Maroneze, *Nanoscale*, 2018, **10**, 13315–13319.
40. H. G. Liao, Y. X. Jiang, Z. Y. Zhou, S. P. Chen and S. G. Sun, *Angew. Chem., Int. Ed.*, 2008, **47**, 9100–9103.
41. M. J. Mulvihill, X. Y. Ling, J. Henzie and P. Yang, *J. Am. Chem. Soc.*, 2010, **132**, 268.
42. L. Ma, C. Wang, M. Gong, L. Liao, R. Long, J. Wang, D. Wu, W. Zhong, M. J. Kim, Y. Chen, Y. Xie and Y. Xiong, *ACS Nano*, 2012, **6**, 9797.
43. S. Cheong, J. Watt, B. Ingham, M. F. Toney and R. D. Tilley, *J. Am. Chem. Soc.*, 2010, **131**, 14590.
44. M. S. Akhtar, J. Panwar and Y.-S. Yun, *ACS Sustainable Chem. Eng.*, 2013, **1**, 591–602.
45. M. A. Faramarzi and A. Sadighi, *Adv. Colloid Interface Sci.*, 2013, **189–190**, 1–20.
46. H. P. Borase, B. K. Salunke, R. B. Salunkhe, C. D. Patil, J. E. Hallsworth, B. S. Kim and S. V. Patil, *Biotechnol. Appl. Biochem.*, 2014, **173**, 1–29.
47. A. D. Brumbaugh, K. A. Cohen and S. K. St Angelo, *ACS Sustainable Chem. Eng.*, 2014, **2**, 1933–1939.
48. R. I. Iyer and T. Panda, *J. Nanosci. Nanotechnol.*, 2014, **14**, 2024–2037.
49. S. Poulose, T. Panda, P. P. Nair and T. Theodore, *J. Nanosci. Nanotechnol.*, 2014, **14**, 2038–2049.
50. J. Huang, L. Lin, D. Sun, H. Chen, D. Yang and Q. Li, *Chem. Soc. Rev.*, 2015, **44**, 6330–6374.

51. P. Dauthal and M. Mukhopadhyay, *Ind. Eng. Chem. Res.*, 2016, **55**, 9557–9577.
52. F. Qazi, Z. Hussain and M. N. Tahir, *RSC Adv.*, 2016, **6**, 60277–60286.
53. R. S. Varma, *ACS Sustainable Chem. Eng.*, 2016, **4**, 5866–5878.
54. P. Vishnukumar, S. Vivekanandhan and S. Muthuramkumar, *Chem-BioEng Rev.*, 2017, **4**, 18–36.
55. J. Singh, T. Dutta, K. H. Kim, M. Rawat, P. Samddar and P. Kumar, *J. Nanobiotechnol.*, 2018, **16**, 84.
56. G. A. Kahrilas, L. M. Wally, S. J. Fredrick, M. Hiskey, A. L. Prieto and J. E. Owens, *ACS Sustainable Chem. Eng.*, 2014, **2**, 367–376.
57. Y. Liu, S. Kim, Y. J. Kim, H. Perumalsamy, S. Lee, E. Hwang and T. H. Yi, *Int. J. Nanomed.*, 2019, **14**, 2945–2959.
58. N. Thangamani and N. Bhuvaneshwari, *Chem. Phys. Lett.*, 2019, **732**, 136587.
59. P. Vijaya Kumar, S. Mary Jelastin Kala and K. S. Prakash, *Mater. Lett.*, 2019, **236**, 19–22.
60. Y. Zheng, H. Zhang and L. Fu, *Inorg. Nano-Met. Chem.*, 2019, **48**, 449–453.
61. M. Zhou, J. Yin, X. Zhao, Y. Fu, X. Jin, X. Liu and T. Jiao, *Colloids Surf., A*, 2020, **603**, 125293.
62. L. Wang, M. Imura and Y. Yamauchi, *CrystEngComm*, 2012, **14**, 7594.
63. L. Wu, W. Wu, X. Jing, J. Huang, D. Sun, T. Odoom-Wubah, H. Liu, H. Wang and Q. Li, *Ind. Eng. Chem. Res.*, 2013, **52**, 5085–5094.
64. D. Sun, G. Zhang, J. Huang, H. Wang and Q. Li, *Materials*, 2014, **7**, 1360–1369.
65. D. Sun, G. Zhang, X. Jiang, J. Huang, X. Jing, Y. Zheng, J. He and Q. Li, *J. Mater. Chem. A*, 2014, **2**, 1767–1773.
66. X. Jing, D. Huang, H. Chen, T. Odoom-Wubah, D. Sun, J. Huang and Q. Li, *J. Chem. Technol. Biotechnol.*, 2015, **90**, 678–685.
67. I. Fierascu, M. I. Georgiev, A. Ortan, R. C. Fierascu, S. M. Avramescu, D. Ionescu, A. Sutan, A. Brinzan and L. M. Ditu, *Sci. Rep.*, 2017, **7**, 12428.
68. N. S. Thakur, J. Bhaumik, S. Kirar and U. C. Banerjee, *ACS Sustainable Chem. Eng.*, 2017, **5**, 7950–7960.
69. D. P. Yang, X. Liu, C. P. Teng, C. Owh, K. Y. Win, M. Lin, X. J. Loh, Y. L. Wu, Z. Li and E. Ye, *Nanoscale*, 2017, **9**, 15753–15759.
70. D. Borah, M. Hazarika, P. Tailor, A. R. Silva, B. Chetia, G. Singaravelu and P. Das, *Appl. Nanosci.*, 2018, **8**, 241–253.
71. S. Sasidharan, R. Poojari, D. Bahadur and R. Srivastava, *ACS Sustainable Chem. Eng.*, 2018, **6**, 10562–10577.
72. M. Klekotko, K. Brach, J. Olesiak-Banska, M. Samoc and K. Matczyszyn, *Mater. Chem. Phys.*, 2019, **229**, 56–60.
73. G. A. Molina, R. Esparza, J. L. Lopez-Miranda, A. R. Hernandez-Martinez, B. L. Espana-Sanchez, E. A. Elizalde-Pena and M. Estevez, *Colloids Surf., B*, 2019, **180**, 141–149.

74. R. Y. Parapat, F. A. Yudatama, M. R. Musadi, M. Schwarze and R. Schomäcker, *Ind. Eng. Chem. Res.*, 2019, **58**, 2460–2470.
75. K. B. Narayanan and N. Sakthivel, *Adv. Colloid Interface Sci.*, 2010, **156**, 1–13.
76. T. J. Park, K. G. Lee and S. Y. Lee, *Appl. Microbiol. Biotechnol.*, 2016, **100**, 521–534.
77. D.-P. Yang, S. Chen, P. Huang, X. Wang, W. Jiang, O. Pandoli and D. Cui, *Green Chem.*, 2010, **12**, 2038.
78. R. Selvakumar, N. Seethalakshmi, P. Thavamani, R. Naidu and M. Megharaj, *RSC Adv.*, 2014, **4**, 52156–52169.
79. M. W. Ullah, Z. Shi, X. Shi, D. Zeng, S. Li and G. Yang, *ACS Sustainable Chem. Eng.*, 2017, **5**, 11163–11175.
80. M. Wang, T. Odoom-Wubah, H. Chen, X. Jing, T. Kong, D. Sun, J. Huang and Q. Li, *Nanoscale*, 2013, **5**, 6599–6606.
81. S. K. Das, T. Parandhaman, N. Pentela, A. K. M. Maidul Islam, A. B. Mandal and M. Mukherjee, *J. Phys. Chem. C*, 2014, **118**, 24623–24632.
82. T. Odoom-Wubah, M. Du, W. B. Osei, D. Sun, J. Huang and Q. Li, *Chin. J. Chem. Eng.*, 2015, **23**, 1907–1915.
83. H. Chen, D. Sun, X. Jiang, X. Jing, F. Lu, T. Odoom-Wubah, Y. Zheng, J. Huang and Q. Li, *RSC Adv.*, 2013, **3**, 15389.
84. Q. K. Vo, M. N. Nguyen Thi, P. P. Nguyen Thi and D. T. Nguyen, *Processes*, 2019, **7**, 631.
85. W. Lv, C. Gu, S. Zeng, J. Han, T. Jiang and J. Zhou, *Biosensors*, 2018, **8**, 113.
86. L. Wang, C. Hu, Y. Nemoto, Y. Tateyama and Y. Yamauchi, *Cryst. Growth Des.*, 2010, **10**, 3454–3460.
87. X. Wang, D. P. Yang, P. Huang, M. Li, C. Li, D. Chen and D. Cui, *Nanoscale*, 2012, **4**, 7766–7772.
88. J. Zhang, Q. Yu, W. Qiu, K. Li, L. Qian, X. Zhang and G. Liu, *Microchim. Acta*, 2019, **186**, 357.
89. J. Song, S. Hwang, S. Park, T. Kim, K. Im, J. Hur, J. Nam, S. Kim and N. Park, *RSC Adv.*, 2016, **6**, 51658–51661.
90. Z. Wang, J. Zhang, J. M. Ekman, P. J. Kenis and Y. Lu, *Nano Lett.*, 2010, **10**, 1886–1891.
91. Z. Wang, L. Tang, L. H. Tan, J. Li and Y. Lu, *Angew. Chem., Int. Ed.*, 2012, **51**, 9078–9082.
92. H. c. A. Becerril, R. M. Stoltenberg, D. R. Wheeler, R. C. Davis, J. N. Harb and A. T. Woolley, *J. Am. Chem. Soc.*, 2005, **127**, 2828.
93. S. Rudiuk, A. Venancio-Marques, G. Hallais and D. Baigl, *Soft Matter*, 2013, **9**, 9146.
94. P. Huang, O. Pandoli, X. Wang, Z. Wang, Z. Li, C. Zhang, F. Chen, J. Lin, D. Cui and X. Chen, *Nano Res.*, 2012, **5**, 630–639.
95. S. Sasidharan, D. Bahadur and R. Srivastava, *ACS Sustainable Chem. Eng.*, 2017, **5**, 10163–10175.
96. S. Sasidharan, D. Bahadur and R. Srivastava, *ACS Appl. Mater. Interfaces*, 2016, **8**, 15889–15903.

97. S. Sasidharan, D. Bahadur and R. Srivastava, *RSC Adv.*, 2016, **6**, 84025–84034.
98. L. Li and J. Weng, *Nanotechnology*, 2010, **21**, 305603.
99. X. Ma, Q. Guo, Y. Xie and H. Ma, *Chem. Phys. Lett.*, 2016, **652**, 148–151.
100. T. T. Nhung, Y. Bu and S.-W. Lee, *J. Cryst. Growth*, 2013, **373**, 132–137.
101. T. T. Nhung and S. W. Lee, *ACS Appl. Mater. Interfaces*, 2014, **6**, 21335–21345.
102. N. Ma, X. Liu, Z. Yang, G. Tai, Y. Yin, S. Liu, H. Li, P. Guo and X. S. Zhao, *ACS Sustainable Chem. Eng.*, 2017, **6**, 1133–1140.
103. S. Ouyang, L. Wang, J. Cui, H. Shi, T. Wang and S. Wang, *NANO*, 2015, **10**, 1550106.
104. C. Caucheteur, T. Guo and J. Albert, *Anal. Bioanal. Chem.*, 2015, **407**, 3883–3897.
105. J.-F. Masson, *ACS Sens.*, 2017, **2**, 16–30.
106. K. Y. Tang, J. X. Chen, E. D. R. Legaspi, C. Owh, M. Lin, I. S. Y. Tee, D. Kai, X. J. Loh, Z. Li, M. D. Regulacio and E. Ye, *Chemosphere*, 2021, **265**, 129114.
107. M. Kim, J.-H. Lee and J.-M. Nam, *Adv. Sci.*, 2019, **6**, 1900471.
108. E. Ye, M. D. Regulacio, S. Y. Zhang, X. J. Loh and M. Y. Han, *Chem. Soc. Rev.*, 2015, **44**, 6001–6017.
109. E. Ye, K. Y. Win, H. R. Tan, M. Lin, C. P. Teng, A. Mlayah and M. Y. Han, *J. Am. Chem. Soc.*, 2011, **133**, 8506–8509.
110. M. L. Brongersma, N. J. Halas and P. Nordlander, *Nat. Nanotechnol.*, 2015, **10**, 25–34.
111. G. V. Hartland, L. V. Besteiro, P. Johns and A. O. Govorov, *ACS Energy Lett.*, 2017, **2**, 1641–1653.
112. E. Hao, R. C. Bailey, G. C. Schatz, J. T. Hupp and S. Li, *Nano Lett.*, 2004, **4**, 327–330.
113. H. Yuan, W. Ma, C. Chen, J. Zhao, J. Liu, H. Zhu and X. Gao, *Chem. Mater.*, 2007, **19**, 1592–1600.
114. C. Song, Y. Dou, L. Yuwen, Y. Sun, C. Dong, F. Li, Y. Yang and L. Wang, *J. Mater. Chem. B*, 2018, **6**, 3030–3039.
115. Y. Liu, X. Zhang, L. Luo, L. Li, Y. He, J. An and D. Gao, *ACS Biomater. Sci. Eng.*, 2018, **4**, 2911–2921.
116. H. Moustaoui, J. Saber, I. Djeddi, Q. Liu, A. T. Diallo, J. Spadavecchia, M. Lamy de la Chapelle and N. Djaker, *J. Phys. Chem. C*, 2019, **123**, 17548–17554.
117. Z. Y. Ong, S. Chen, E. Nabavi, A. Regoutz, D. J. Payne, D. S. Elson, D. T. Dexter, I. E. Dunlop and A. E. Porter, *ACS Appl. Mater. Interfaces*, 2017, **9**, 39259–39270.
118. B. Zhang, J. Wang, J. Sun, Y. Wang, T. Chou, Q. Zhang, H. R. Shah, L. Ren and H. Wang, *Adv. Ther.*, 2020, **3**, 2000114.
119. J. Sun, J. Wang, W. Hu, Y. Wang, T. Chou, Q. Zhang, B. Zhang, Z. Yu, Y. Yang, L. Ren and H. Wang, *ACS Appl. Mater. Interfaces*, 2021, **13**, 10778–10795.

120. P. Qiu, M. Yang, X. Qu, Y. Huai, Y. Zhu and C. Mao, *Biomaterials*, 2016, **104**, 138–144.
121. M.-F. Tsai, S.-H. G. Chang, F.-Y. Cheng, V. Shanmugam, Y.-S. Cheng, C.-H. Su and C.-S. Yeh, *ACS Nano*, 2013, **7**, 5330–5342.
122. M. A. Mackey, M. R. K. Ali, L. A. Austin, R. D. Near and M. A. El-Sayed, *J. Phys. Chem. B*, 2014, **118**, 1319–1326.
123. B. Jang, J.-Y. Park, C.-H. Tung, I.-H. Kim and Y. Choi, *ACS Nano*, 2011, **5**, 1086–1094.
124. P. Zijlstra, P. M. R. Paulo and M. Orrit, *Nat. Nanotechnol.*, 2012, **7**, 379–382.
125. C. P. Teng, T. Zhou, E. Ye, S. Liu, L. D. Koh, M. Low, X. J. Loh, K. Y. Win, L. Zhang and M. Y. Han, *Adv. Healthcare Mater.*, 2016, **5**, 2122–2130.
126. M. Bosman, E. Ye, S. F. Tan, C. A. Nijhuis, J. K. W. Yang, R. Marty, A. Mlayah, A. Arbouet, C. Girard and M.-Y. Han, *Sci. Rep.*, 2013, **3**, 1312.
127. Y. Wang, K. C. L. Black, H. Luehmann, W. Li, Y. Zhang, X. Cai, D. Wan, S.-Y. Liu, M. Li, P. Kim, Z.-Y. Li, L. V. Wang, Y. Liu and Y. Xia, *ACS Nano*, 2013, **7**, 2068–2077.
128. P. Huang, P. Rong, J. Lin, W. Li, X. Yan, M. G. Zhang, L. Nie, G. Niu, J. Lu, W. Wang and X. Chen, *J. Am. Chem. Soc.*, 2014, **136**, 8307–8313.
129. X. Li, L. Xing, K. Zheng, P. Wei, L. Du, M. Shen and X. Shi, *ACS Appl. Mater. Interfaces*, 2017, **9**, 5817–5827.
130. Y. Liu, J. R. Ashton, E. J. Moding, H. Yuan, J. K. Register, A. M. Fales, J. Choi, M. J. Whitley, X. Zhao, Y. Qi, Y. Ma, G. Vaidyanathan, M. R. Zalutsky, D. G. Kirsch, C. T. Badea and T. Vo-Dinh, *Theranostics*, 2015, **5**, 946–960.
131. A. Espinosa, A. K. A. Silva, A. Sánchez-Iglesias, M. Grzelczak, C. Péchoux, K. Desboeufs, L. M. Liz-Marzán and C. Wilhelm, *Adv. Healthcare Mater.*, 2016, **5**, 1040–1048.
132. C. Bi, J. Chen, Y. Chen, Y. Song, A. Li, S. Li, Z. Mao, C. Gao, D. Wang, H. Möhwald and H. Xia, *Chem. Mater.*, 2018, **30**, 2709–2718.
133. Y. Pu, Y. Zhao, P. Zheng and M. Li, *Inorg. Chem.*, 2018, **57**, 8599–8607.
134. C. M. Pitsillides, E. K. Joe, X. Wei, R. R. Anderson and C. P. Lin, *Biophys. J.*, 2003, **84**, 4023–4032.
135. V. P. Zharov, J.-W. Kim, D. T. Curiel and M. Everts, *Nanomedicine*, 2005, **1**, 326–345.
136. K. P. Miller, L. Wang, Y.-P. Chen, P. J. Pellechia, B. C. Benicewicz and A. W. Decho, *Front. Microbiol.*, 2015, **6**, 189.
137. J. Z. Zhang, *J. Phys. Chem. Lett.*, 2010, **1**, 686–695.
138. J. B. Vines, J.-H. Yoon, N.-E. Ryu, D.-J. Lim and H. Park, *Front. Chem.*, 2019, **7**, 167.
139. H. R. Moyer and K. A. Delman, *Int. J. Hyperthermia*, 2008, **24**, 251–261.
140. K. H. Luk, R. M. Hulse and T. L. Phillips, *West. J. Med.*, 1980, **132**, 179–185.
141. Q. Zhao, L. Wang, R. Cheng, L. Mao, R. D. Arnold, E. W. Howerth, Z. G. Chen and S. Platt, *Theranostics*, 2012, **2**, 113–121.

142. M. D. Regulacio, D.-P. Yang and E. Ye, *CrystEngComm*, 2020, **22**, 399–411.
143. J. K. Gansel, M. Wegener, S. Burger and S. Linden, *Opt. Express*, 2010, **18**, 1059–1069.
144. N. A. Mirin and N. J. Halas, *Nano Lett.*, 2009, **9**, 1255–1259.
145. L. Jauffred, A. Samadi, H. Klingberg, P. M. Bendix and L. B. Oddershede, *Chem. Rev.*, 2019, **119**, 8087–8130.
146. N. S. Abadeer and C. J. Murphy, *J. Phys. Chem. C*, 2016, **120**, 4691–4716.
147. H. Chen, X. Zhang, S. Dai, Y. Ma, S. Cui, S. Achilefu and Y. Gu, *Theranostics*, 2013, **3**, 633–649.
148. D. H. M. Dam, J. H. Lee, P. N. Sisco, D. T. Co, M. Zhang, M. R. Wasielewski and T. W. Odom, *ACS Nano*, 2012, **6**, 3318–3326.
149. A. S. Patel, S. Juneja, P. K. Kanaujia, V. Maurya, G. V. Prakash, A. Chakraborti and J. Bhattacharya, *Nano-Struct. Nano-Objects*, 2018, **16**, 329–336.
150. H. Ma, Z. Liu, Y. Wei and L. Jiang, *Colloids Surf., A*, 2019, **582**, 123889.
151. J. Zhu, M.-J. Liu, J.-J. Li and J.-W. Zhao, *Eur. Phys. J. B*, 2017, **90**, 216.
152. J. l. Li and M. Gu, *IEEE J. Sel. Top. Quantum Electron.*, 2010, **16**, 989–996.
153. P. Wu, Y. Gao, H. Zhang and C. Cai, *Anal. Chem.*, 2012, **84**, 7692–7699.
154. D. Joseph, R. Baskaran, S. G. Yang, Y. S. Huh and Y.-K. Han, *J. Colloid Interface Sci.*, 2019, **542**, 308–316.
155. A. J. McGrath, Y.-H. Chien, S. Cheong, D. A. J. Herman, J. Watt, A. M. Henning, L. Gloag, C.-S. Yeh and R. D. Tilley, *ACS Nano*, 2015, **9**, 12283–12291.
156. H.-C. Lin, K.-F. Hsu, C.-L. Lai, T.-C. Wu, H.-F. Chen and C.-H. Lai, *Molecules*, 2020, **25**, 1853.
157. A. Bassegoda, K. Ivanova, E. Ramon and T. Tzanov, *Appl. Microbiol. Biotechnol.*, 2018, **102**, 2075–2089.
158. L. Hall-Stoodley, J. W. Costerton and P. Stoodley, *Nat. Rev. Microbiol.*, 2004, **2**, 95–108.
159. R. Smith and J. Coast, *Br. Med. J.*, 2013, **346**, f1493.
160. R. Weissleder, *Nat. Biotechnol.*, 2001, **19**, 316–317.
161. J. Olson, S. Dominguez-Medina, A. Hoggard, L.-Y. Wang, W.-S. Chang and S. Link, *Chem. Soc. Rev.*, 2015, **44**, 40–57.
162. A. N. S. Insitute, Washington, 2005, vol. ANSI-Z136.3.
163. A. O'Toole, E. B. Ricker and E. Nuxoll, *Biofouling*, 2015, **31**, 665–675.
164. V. P. Zharov, K. E. Mercer, E. N. Galitovskaya and M. S. Smeltzer, *Biophys. J.*, 2006, **90**, 619–627.
165. N. W. S. Kam, M. Connell, J. A. Wisdom and H. Dai, *Proc. Natl. Acad. Sci. U. S. A.*, 2005, **102**, 11600.
166. X. Li, S. M. Robinson, A. Gupta, K. Saha, Z. Jiang, D. F. Moyano, A. Sahar, M. A. Riley and V. M. Rotello, *ACS Nano*, 2014, **8**, 10682–10686.
167. P. Yuan, X. Ding, Z. Guan, N. Gao, R. Ma, X.-F. Jiang, Y. Y. Yang and Q.-H. Xu, *Adv. Healthcare Mater.*, 2015, **4**, 674–678.
168. V. Knittel, M. P. Fischer, T. de Roo, S. Mecking, A. Leitenstorfer and D. Brida, *ACS Nano*, 2015, **9**, 894–900.

169. S. Freddi, L. Sironi, R. D'Antuono, D. Morone, A. Donà, E. Cabrini, L. D'Alfonso, M. Collini, P. Pallavicini, G. Baldi, D. Maggioni and G. Chirico, *Nano Lett.*, 2013, **13**, 2004–2010.
170. M. Borzenkov, M. Moros, C. Tortiglione, S. Bertoldi, N. Contessi, S. Fare, A. Taglietti, A. D'Agostino, P. Pallavicini, M. Collini and G. Chirico, *Beilstein J. Nanotechnol.*, 2018, **9**, 2040–2048.
171. P. Pallavicini, A. Donà, A. Taglietti, P. Minzioni, M. Patrini, G. Dacarro, G. Chirico, L. Sironi, N. Bloise, L. Visai and L. Scarabelli, *Chem. Commun.*, 2014, **50**, 1969–1971.
172. J. Penders, M. Stolzoff, D. J. Hickey, M. Andersson and T. J. Webster, *Int. J. Nanomed.*, 2017, **12**, 2457–2468.
173. J. Wang, J. Zhang, K. Liu, J. He, Y. Zhang, S. Chen, G. Ma, Y. Cui, L. Wang and D. Gao, *Int. J. Pharm.*, 2020, **580**, 119231.
174. X. Jiang, X. Fan, W. Xu, R. Zhang and G. Wu, *ACS Biomater. Sci. Eng.*, 2020, **6**, 680–689.

CHAPTER 4

Metal–Oxide Semiconductor Nanomaterials for Photothermal Catalysis

CHEN YE,*[a] ZIBIAO LI[b,c] AND ENYI YE[b]

[a] School of Chemistry and Chemical Engineering, University of Jinan, No. 336, West Road of Nan Xinzhuang, Jinan 250022, Shandong, China; [b] Institute of Materials Research and Engineering, Agency for Science, Technology & Research, 2 Fusionopolis Way, Singapore 138634, Singapore; [c] Department of Materials Science and Engineering, National University of Singapore, 9 Engineering Drive 1, Singapore 117576, Singapore
*Email: yechen-chem@hotmail.com

4.1 Introduction

In previous decades, energy demand has gradually increased with economic development. The depletion of non-renewable resources and environmental issues have meant that people have started to pay more attention to the development of renewable energy sources. These energies include carbon neutral sources like sunlight, wind, rain, tides, waves, and geothermal heat. Among these, solar energy has attracted a lot of attention due to its wide application in green energy technologies such as solar heating, photovoltaics, solar thermal energy, solar architecture, and artificial photosynthesis. Previous studies using solar energy as a power source are mainly focused on the utilization of UV light and a tiny portion of visible light. How to extend the spectrum to respond to the whole visible light region, even to the infrared (IR) region, is a meaningful challenge.[1,2]

Nanoscience & Nanotechnology Series No. 54
Photothermal Nanomaterials
Edited by Enyi Ye and Zibiao Li

Published by the Royal Society of Chemistry, www.rsc.org

In many kinds of chemical reactions, catalysts are used to increase the reaction rate. Indeed, around 95% of chemical products, especial everyday goods, are manufactured through catalytic routes. In the meantime, many of these processes require external energy supplied by non-renewable sources.[3,4] Thermal catalysis is one of the most common forms of catalysis in conventional industrial processes, such as ammonia synthesis and reforming. The critical advantages of industrial dependence on thermally driven catalysis are the high efficiency and applicability for large scale processes. With growing concerns about the energy shortage problem, using sustainable energy sources to drive energetically demanding catalytic processes is urgently needed.

Photocatalysis has been widely investigated for the conversion of solar energy to chemical energy. In photocatalysis processes, solar light can be used ''directly'' to drive the reactions. The mechanism of photocatalysis involves light absorption, charge carrier generation and separation, followed by the migration of carriers to the active surface site for reactions. Photocatalysts are often heterostructures that involve a semiconductor material with another semiconductor material or metal nanoparticle. In this kind of material structure design, only photons with equal or higher energy than the bandgap can be absorbed and used to generate electron–hole pairs. These charge carriers then migrate to the material surface and initiate reduction or oxidation processes. It is therefore only light with high energy, normally UV and a tiny region of visible light that can be utilized for photocatalysis reactions. Thus, the efficiency of most photocatalysis reactions is very low.

Recently, photothermal catalysis, which involves both photocatalysis and thermal catalysis processes, has attracted significant attention. In 2014, Meng *et al.* demonstrated the application of the photothermal effect for the conversion of CO_2.[5] Photothermal catalysis combines photocatalysis and thermal catalysis. It uses both the light and heat components of solar energy. The heat can be obtained directly from solar light and/or generated from the light-to-heat effect. Thus, the utilization of sustainable energy – solar light (as photocatalysis) and the attainment of thermally-driven catalysis reactions are both achieved in photothermal enhanced processes.

4.2 Overview of Photothermally-enhanced Catalysis

To discuss the importance of photothermal catalysis, it is essential to explain the relationship between photocatalysis and solar-powered thermal catalysis. In photocatalysis, upon absorption of light, electron–hole pairs are generated and subsequently undergo reduction and oxidation reactions. To ensure the reactions take place successfully, the energy should be higher than the activation energy of the reactions. This is the key factor to achieving an efficient photocatalysis reaction. Accordingly, the light that can be used to drive a photocatalysis reaction should have relatively high energy, normally UV and partially visible light. Most visible light, especially infrared light, cannot be absorbed and used in photocatalysis processes.[6–9] Different from this, in

photothermal catalysis, the catalyst materials have been engineered to absorb almost the whole solar spectrum. In brief, the high energy light can be used directly to catalyze the reaction, while the rest of the light is used to generate heat *via* the light-to-heat effect. The heat generated directly from the inside reaction system contributes to raising the temperature at the active sites on the material surface. Thus, photothermal catalysis is a combination process consisting of photocatalysis and solar-driven thermal catalysis.

Based on the discussion of M. Ghoussoub *et al.*, the photothermal effect affects both the reaction kinetics and energy efficiency in catalytic reactions.[6] But the effect is different on the endothermic reaction and exothermic reaction. In endothermic catalytic reactions, the processes include the adsorption of the reagents at active sites on the catalyst surface, activation of chemical bonds, formation of intermediate species, conversion of intermediates to products, and the desorption of product molecules. These steps can be described by a free energy profile, as shown in Figure 4.1. In this profile, the initial, intermediate, and final thermodynamic states are presented along with the reaction coordinate pathway. Each state is separated by an activation barrier, which dictates the kinetics of the surface chemical reaction.

In the photothermal catalysis reaction, both photochemical and thermochemical processes can contribute to the overall reaction rate. The photocatalysis process in the catalytic reaction contributes to increasing the rate of reaction. There are two possibilities related to this effect. First, the photocatalysis effect directly occurs in the rate-limiting steps of the reaction and

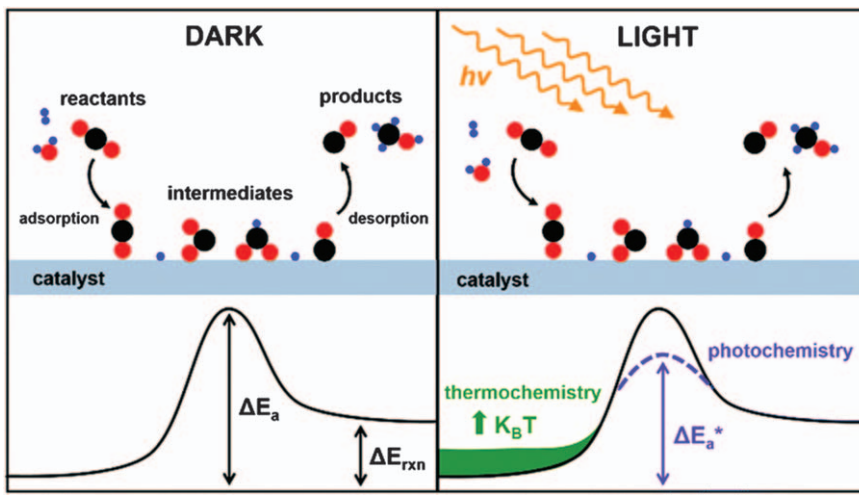

Figure 4.1 Effect of solar irradiation on the endothermic reaction profile of a photothermal catalyst. Photochemistry has the effect of reducing the activation energy barrier, while temperature enhances the probability of reactants overcoming the barrier by providing additional thermal energy.
Reproduced from ref. 6 with permission from the Royal Society of Chemistry.

therefore lowers the measured activation energy barrier. This reduction in energy barrier normally attributes to a charge transfer to the catalyst surface or an energy transfer to the transition state.[10,11]

Secondly, the photocatalysis effect does not affect the rate-limiting steps but affects the earlier steps, which causes the reduction of the earlier energetic barrier and results in the formation of more intermediate products for the coming rate-limiting step. In this possibility, the measured activation barrier is not changed although the reaction speeded up obviously.

Besides, the selectivity of the reaction is also an important factor that needs to be attended to. The intermediate steps that occur on the catalyst surface are very complicated. The change of electronic or structural properties of the active sites on the catalyst surface can potentially vary the selectivity of the reaction by altering the reaction mechanism. The changes in surface properties can be achieved by electronic charge transfer or surface reconstruction. As discussed above, the effects, such as charge transfer, may also induce a change in activation energy. But there is no visual information that indicates the direct relationship between activation energy and selectivity of the reaction. The reaction may simply proceed in the same mechanism, albeit at a faster rate.

In thermal catalysis, the increase in temperature effectively increases the reaction rate. In terms of a reaction profile, this corresponds to an increase in k_BT and then increases the probability of overcoming the activation energy by skewing the Boltzmann distribution toward higher energies.[12] Specifically, upon the thermal energy input into the system, the formation of products is increased, and also the unwanted species (including unreacted reagents and final products) are easy to be desorbed from the active sites. The same effects can be found in the photothermal catalysis processes. In particular, the heat energy is directly generated at the active sites *via* the light-to-heat effect in the photothermal catalysis process. This could reduce the heat loss and efficiently use the heat to enhance the catalytic effect.

Different from endothermic reactions, the situation about the photothermal catalysis exothermic reactions is not so clear. The higher temperature generated by the photothermal catalytic effect cannot help to drive the exothermic reactions. Still, there are also some advantages to exothermic reactions *via* the photothermal catalytic effect. These include: (1) improving selectivity of the reaction and (2) offering direct local heating of the active site of the catalyst, and thereby circumventing unnecessary heating of reactor equipment.

Given the above, photothermal catalysis shows definitive advantages compared to traditional photo- and/or thermal catalysis. First, photothermal catalysis involves more highly efficient harvesting and utilization of the solar spectrum, especial the low energy visible and infrared light that would be insufficient to excite photocatalysis reactions. Secondly, there is no requirement for external thermal energy supply while the heat is generated directly on the surface of the catalyst *via* the light-to-heat effect. The temperature of the catalytic active sites on the surface rises instantaneously while operating under

mild conditions. This could speed up the reaction, refrain from the deactivation of the catalyst, and increase the selectivity for products.

4.3 Semiconductor Nanomaterials as the Photothermal Catalyst

Intensive efforts have been devoted to developing high-performance light-to-heat converting materials in the past decades. One of the key factors that determine the converting efficiency is the light harvest ability of the catalyst materials. In a photothermal catalytic system, light absorbing materials should show highly optical absorption efficiency and broad light absorption across the solar spectrum (250 to 2500 nm). Thus, an overall high solar absorption of the catalyst material is the crucial point to achieve high solar-to-thermal conversion. Common materials that have been used as photocatalysts include metals, semiconductor materials, and hybrid combinations of semiconductor–metal materials and organic–inorganic materials.

4.3.1 Material Selection

Nanoscale metallic or semiconducting materials show high optical absorption across much of the solar spectrum and high surface area. These properties make them ideal photothermal catalyst materials. The broadband optical absorption results from electronic transitions occurring in narrow bandgap semiconductors. The semiconducting materials with such broad optical absorption properties include non-stoichiometric metal oxides with mid-gap defect states, mixed valence states, and/or conduction electrons; semiconductor nanomaterials exhibiting the localized surface plasmon resonance (LSPR) effect; and hybrid materials in which both metallic and semiconducting systems are present.[7,13–15]

According to Ozin's work, defects in nanoscale metal oxides create mid-bandgap states that can enable materials to perform photothermal catalysis. These states exist in non-stoichiometric materials containing oxygen and/or metal vacancies and interstitials, mixed metal valences, and conduction electrons that can enhance the optical absorption in the visible and near-infrared spectra. In general, the nanoscale metal oxide materials should contain at least one of these three defect types to perform photothermal catalytic reactions. It is also possible that the three types of defects can exist in one material.

Another key approach to enhancing the photothermal effect is to fabricate a hybrid architecture to tailor the electronic, chemical, and thermal properties of the catalyst materials. A metal oxide decorated with metal nanoparticles (NPs) is a common structure that has been widely used as a photothermal catalyst material. In many examples, one component in this kind of hybrid structure is considered as the principal catalyst while another component as a nanoheater.[9,12,16–19]

4.3.2 Bandgap Engineering

It has been demonstrated that the band structure of semiconductor materials can be modified *via* adding impurities, self-doping, or introducing disorder to the surface layers. As mentioned above, the smaller bandgap, mid-gap energy states, mixed valence states, and/or conduction electrons are the dominant control for optical excitation and relaxation, causing the widening of the light absorption of metal oxide materials.[20] For instance, Ye *et al.* observed broad absorption in magnesium-reduced TiO_2 nanoparticles populated with oxygen vacancies.[21] The resulting TiO_x exhibited light absorption from the UV to the NIR range. Moreover, with more magnesium added to the reactions, the optical absorption ability increased. This can be attributed to the decrease of the oxygen content in TiO_x. Wang *et al.* presented Ti_2O_3 nanoparticles with 100% internal and 92% external solar–thermal conversion efficiency. The narrow bandgap structure of Ti_2O_3 nanoparticles enables light absorption across the whole solar spectrum. Relevant studies have also been reported by Qi *et al.* They fabricated 2D black In_2O_{3-x} nanosheets by photoinduced defect engineering for photothermal catalytic CO production. The bifunctional oxygen vacancies in these nanosheets enhanced light-harvesting and chemical adsorption of CO_2 molecules and achieved a 103.21 mmol g_{cat}^{-1} h^{-1} CO production efficiency.[22]

4.3.3 Localized Surface Plasmon Resonance (LSPR) Effect

Surface plasmon resonance (SPR) is a resonant oscillation of conduction electrons at the interface between negative and positive permittivity materials excited by the electromagnetics of incident light. When this phenomenon is generated at the nanoscale material surface, we call it the localized surface plasmon resonance (LSPR) effect. LSPR has been known since 400 A.D. Metal material, like gold and silver, was one of the earliest known objects that exhibit LSPR properties. So far, our understanding of LSPR metal materials, especially their optical properties, which lie in the visible spectral range and have already been well established. Now, what is most interesting is the new LSPR materials and their differences from the classical metals.

Semiconductor nanomaterials have been actively explored due to their excellent optical and thermal properties. LSPR in semiconductor nanocrystals results in resonant absorption, scattering, and near field enhancement across a wide optical range from the visible to far-infrared spectral range. This makes semiconductor NCs promising materials for therapy, imaging, photochemical, photothermal, heat transfer, catalysis, and some other applications. The most familiar LSPR semiconductor NCs include metal oxides, metal chalcogenides, metal nitride, and silicon.

In LSPR metals, natural resonance frequencies are normally in the visible spectrum range which is caused by the high carrier concentration of metals themselves. To shift their optical response to the infrared (IR) spectrum, particle size or morphology modification is required. Unlike LSPR metals, the LSPR response of semiconductor NCs can also be tuned and even the

crystal structure has already been constructed. In semiconductor NCs, the carrier concentration can be tuned by chemical doping, post-synthetic reactions or photochemical and electrochemical reactions. These strategies allow tuning the optical response of LSPR NCs from the visible to far-infrared spectrum. Furthermore, there are no strict limits on the size and shape of those LSPR semiconductor materials.

The LSPR properties of semiconductor NCs depend on the shape, size, dopant type, dopant concentration and distribution, and doping method of NCs. Based on the summary by Agrawal *et al.*, three guidelines can help when designing LSPR semiconductor materials: (1) increase the free carrier concentration by increasing the dopant concentration, which will cause a blue shift of the LSPR response spectrum; (2) dopant choice and distribution structure changes the electron scattering and the near field enhancement around NCs; (3) refer the intrinsic dielectric properties of NCs with different shapes and sizes, thereby determining the LSPR characteristics of the desired NCs.[23]

From the above information, other than designing new nanostructures, doping becomes a very helpful process to tailor the LSPR properties of semiconductor NCs. Doping is an essential process to develop semiconductor materials by introducing impurity atoms into the host crystals. It can efficiently adjust the optical and electronic properties of semiconductor NCs. The different types of chemical doping include vacancy doping, and aliovalent substitutional doping, interstitial doping.[24–29] In vacancy doping, for example, O doped WO_{3-x}, the charge carrier density changes as the stoichiometry changes in semiconductor NCs. This type of doping can introduce either free holes or free electrons without introducing any extrinsic ions. For aliovalent doping, impurity atoms are introduced *via* substitutional or interstitial doping. This mechanism can donate free holes or electrons to the valence band or conduction band, respectively.[27,30–32] Aliovalent doping could occur during the synthesis process to affect the crystal structure of NCs, it can also be utilized for the modification of pre-synthesized NCs. In the synthesis of doped metal oxide NCs, the presence of dopant ions can significantly affect the nucleation and growth processes and then further affect the NCs' size and shape. The control of dopant concentration and spatial distribution has been proved to play a vital role in the determination of the LSPR response of metal oxides. During the past few years, various plasmonic metal oxide NCs have been developed, such as tin-doped In_2O_3,[33–36] indium-doped CdO,[29,37–39] aluminum-doped ZnO,[40,41] copper-doped ZnO[42] NCs, and so on. Alternatively, chemical transformation of pre-synthesized metal oxide NCs could control the chemical properties, concentration, and distribution of dopants *via* "conversion chemistry" strategies like cation-exchange.[43–47]

4.3.4 Size and Shape Effect

When designing a photothermal catalyst material, it is necessary to understand the relation between the catalytic rate, selectivity, and not only the size of particles but also their morphologies.

The size of the nanoparticles plays an important role in the photothermal catalytic reaction system. Basically, the smaller particles show a relatively larger surface area in which more active sites on the surface are provided. In the meantime, nanostructured morphologies also have a significant influence on the electronic structures of the materials attributed to the quantum confinement effect. For instance, charge carrier separation is able to be enhanced in small, especially nanoscale, particles. Besides, nanostructuring can also affect the thermal conductivity of materials. In this case, the increase in the surface area has direct consequences for the increase in surface roughness of the catalytic component. This offers an effective strategy for reducing the thermal conductivity of a material and, hence, promoting heat generation near the active sites on the surface. This conclusion has been demonstrated by Ozin and co-workers in their review article.[6,47–49]

On the other hand, overall photothermal catalytic performance can be weakened by using smaller size particles. Due to the spatial confinement effect, reducing lattice dimensions could lead to poor charge carrier separation. And, as mentioned before, reducing size can also result in a blue shift in the resonant frequency which narrows the light absorption range. Thus, a holistic approach should be taken when designing photothermal catalysts, especial the nanoheater component. For instance, one study based on the $Pd@Nb_2O_5$ catalyst investigated the effect of nanoheater size on photothermal CO_2 catalysis. Pd nanoparticles with different sizes (from 5 to 20 nm) were used as nanoheaters in these hybrid catalyst materials. The results revealed that different reactions show different selectivity on different sized nanoheaters. In particular, the smaller Pd nanoparticles exhibited a higher photothermal catalytic ability and selectivity upon a CO_2 to CO conversion reaction. With a smaller Pd nanoheater, the CO production rate could reach 18.8 mol g_{cat}^{-1} h^{-1} with 99.5% selectivity.[50]

The shape of nanomaterials directly affects their optical and thermal properties. In a photothermal catalytic system, it is possible to improve the catalytic performance by tailoring the morphologies of catalyst materials, especially the particles with an LSPR effect. In plasmonic semiconductor nanomaterials, symmetrical structures, such as nanorods, nanocubes, nanowires, and nanostars, show efficient absorption in the near-IR region of the solar spectrum. For example, Chen *et al.* reported a $W_{18}O_{49}$ nanowire material that exhibits enhanced absorption with wavelengths from 510 to 1100 nm.[51] Hua *et al.*'s HCuPO nanosheets show high photothermal catalysis at 808 nm.[52] In addition, non-symmetrical and hollow geometries have been demonstrated to show increased broadband absorption which makes good use of the whole visible spectrum.[53,54]

Theoretically, localized heating can be enhanced by sharp geometric structures, such as tips, corners, and edges. This will result in a higher heating efficiency in the photothermal catalytic system. Based on Baffou's results, this is due to increased electromagnetic field intensity at sharp positions.[55] Thus, the nanostructures with a high concentration of edges and corners would be a better choice for maximizing the nanoheating effect.

Another kind of catalyst structure that is also worth mentioning is porous structures. A porous structure can reduce thermal transport properties, to be more precise, the thermal conductivity of catalyst materials.[56] As discussed before, relatively lower thermal conductivity is a benefit for the enhancement of localized heat generation within the catalyst at surface active sites. Thus, the use of a porous structure can efficiently promote thermally driven reactions in the photothermal catalytic reaction system.

4.3.5 Hybrid Structures

As mentioned earlier, most photothermal catalytic reaction systems comprise a metal oxide decorated with metal NPs. In this kind of structure, one component, often the metal oxide, functions as the catalyst with active sites on the material surface, while another component, metal NPs, functions as a nanoheater to assist the reactions on the surface. Actually, the surface reactions often happen on both components. For instance, the C–O bond activation and H_2 dissociation reactions in the CO_2 reduction system are normally present on different active sites.

The physical properties of catalysts are directly related to their nanostructures. A hybrid nanostructure offers several advantages on the optical, electronic, and chemical properties compared to a single component nanostructure.[57] For example, the heat generated in a photothermal catalysis system can be transferred from the source component to the active sites located on another component, which could enhance the heat effect in hybrid nanostructured catalysts. Besides, the charge carrier generation and transport can be boosted in semiconductor-based hybrid nanocatalysts, for both photocatalysis and photothermal catalysis systems, rather than single component semiconductor nanomaterials. Several examples of possible hybrid architectures are presented in Scheme 4.1, which have been demonstrated in the literature. The most common hybrid nanomaterials for photothermal catalysis reactions include metal oxide–metal NP heterostructures and core/shell nanostructures.

4.3.5.1 Metal/Semiconductor Heterostructures

Metal/semiconductor heterostructure materials are one of the most studied systems. An ideal semiconductor material as a photothermal catalyst should have important properties including high surface area, broadband optical absorption, and effective charge carrier separation structure. The strong broadband optical absorption can cause the generation of charge carriers and/or high local temperature at active sites. These types of materials are generally nonstoichiometric metal oxides with oxygen/metal vacancies, mixed metal valence electrons, and/or conduction electrons.[6,58–60] Ozin and co-workers reported an example of this kind of material using Pd NPs supported on Nb_2O_5 for the photocatalytic reduction of CO_2.[50] According to their results, Pd NPs acted as nanoheaters that effectively enhance the local temperature of Nb_2O_5-based catalysts for the CO_2 hydrogenation reaction. The deposited Pt NPs could assist the trapping of excited electrons from the conduction band of semiconductor

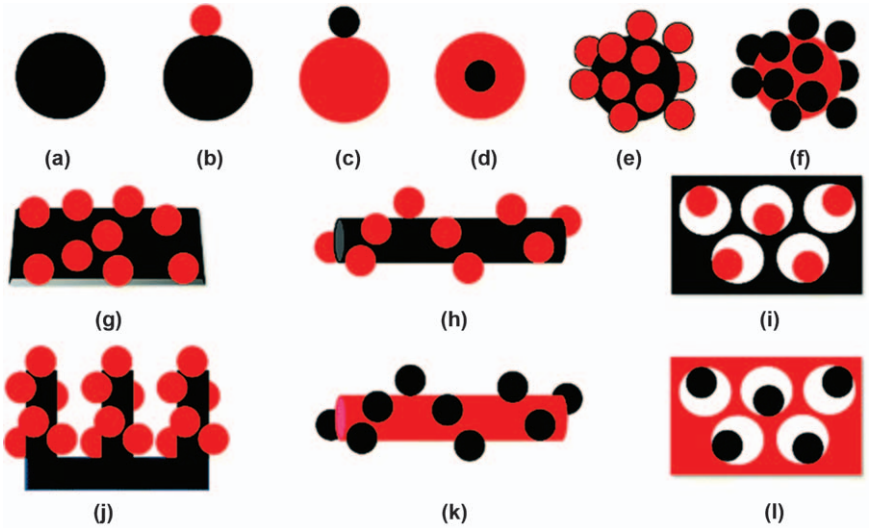

Scheme 4.1 Illustration of a library of photothermal nanoscale architectures where the black objects refer to a broadband light absorber that can function as a nanoheater/catalyst and the red objects are the catalyst. Reproduced from ref. 6 with permission from the Royal Society of Chemistry.

oxides (*e.g.* TiO_2), thus preventing electron–hole recombination, and then enhancing the overall reaction rate.[61] Another appealing material that has also been studied widely is In_2O_3-based catalyst materials. Also by Ozin *et al.*, a non-stoichiometric black In_2O_{3-x}/In_2O_3 material was used for the photothermal hydrogenation of CO_2. In their results, the In_2O_{3-x} component was generated in stoichiometric In_2O_3 crystals to form In_2O_{3-x}/In_2O_3 heterostructures.[62] These heterostructured materials displayed broad light absorption properties across almost the entire solar spectrum and then provided excellent photothermal catalytic performances. Firstly, the photogenerated charge carriers could induce the photochemical reduction of CO_2 due to the photocatalytic effect. Secondly, the absorption of irradiation light could cause strong local heating which also promotes the catalytic performance attributed to the thermal-catalytic effect in photothermal catalysis systems. The combined use of both catalytic effects efficiently catalyzes the entire reaction and shows 100% selectivity towards the CO production pathway. Therefore, the use of broadband absorption semiconductors, alone or in combination with metallic active sites, offers the possibility for an incredibly high photothermal catalytic activity and relatively good product/pathway selectivity.

4.3.5.2 Core/Shell Structures

Core–shell structured hybrid materials present the advantages of tunable optical, electronic, and thermal properties because of their bifunctional structure. This could also be a very attractive strategy to develop new materials that exhibit

good photo-thermal performances.[63,64] On the one hand, it is possible to achieve a high photothermal catalytic performance by creating a new core/shell structured nanocatalyst. For instance, Kumar and co-workers designed a Pt@TiO_2–AuNPs core/shell structure for the photothermal catalysis CO_2 reduction. In their work, the introduction of the TiO_2 layer results in a higher quantum yield compared with bare Au NPs. This is due to the combination of positive effects like the enlargement of surface area, the red-shift and broadening of the LSPR peak, and the enhancement of light absorption. On the other hand, the tuning of metal shell thickness could control the local heating in the thermal catalytic process and the hot-carrier injection in the photocatalytic process. Xiong and co-workers demonstrated that the thickness of the metal shell seems to be a crucial parameter to determine the surface plasmon decay pathways for local heating and/or electron transfer processes in photothermal catalytic systems.[65]

4.4 Photothermal Catalytic Applications

A photothermal catalytic reaction is the combined action of solar energy and thermal energy. This enables some reactions to operate under relatively milder conditions, like lower temperature and/or pressure. So far, the reactions or processes that have already been improved by using photothermal catalysis include CO_2 conversion, Fischer–Tropsch process, NH_3 synthesis, and so on. Here we will give a brief review of the development of these reactions.

4.4.1 CO_2 Conversion

The utilization of CO_2 normally includes two kinds of synthesis processes. The first one is called the non-reductive route since the chemical state of carbon remains at +4 before and after the reaction. This process can produce products like urea, carboxylic acids, polymers, and so on. The other synthesis process is often called the reductive route in which the chemical state of carbon is lowered, as its name suggests. Methane (CH_4), carbon oxide (CO), and alcohols are the most common products in the CO_2 reduction processes. The reduction of CO_2 has attracted significant attention in the past decades. It has been considered as a solution for the energy shortage and environmental deterioration since it can produce green fuels.

H_2 and H_2O are the primary reductants that have been used to assist the reduction of CO_2. By using H_2, CH_4, CO and ethanol, methanol are produced *via* methane production, reverse water gas shift (RWGS), and alcohol synthesis reactions, respectively. The reduction of CO_2 by H_2O could produce solar fuels, normally hydrocarbons, such as CH_4 and methanol. This synthesis process is commonly called artificial photosynthesis.[66–70] And this has been recognized as the most promising technique to achieve carbon neutrality, especial in the chemical industry and energy production.

Generally, in the reduction of CO_2, the number of electrons that participate in the reactions is the crucial point to determine the final products. Thus, the

use of photocatalysis or photothermal catalysis, which could promote the generation of hot electrons, will speed up these reactions effectively.

4.4.1.1 Reverse Water Gas Shift (RWGS)

Reverse water gas shift (RWGS) is an endothermic reaction that can produce CO through the hydrogenation of CO_2.[16,71] This reaction uses H_2 as a reducing agent and is considered to be a sustainable strategy for CO_2 capture and conversion (eqn (4.1)). The chemical state of carbon is reduced from +4 to +2 which indicates that this is a 2 electron reduction reaction. It is remarkable that, by working together with a sustainable and renewable hydrogen source, the produced CO can form syngas (CO/H_2) and further transform it into useful fuels, like alkanes, alcohols, gasoline, and so on.[72,73]

$$Co_2 + H_2 \rightarrow CO + H_2O \ (\Delta H_{298\ K} = 41.1\ \text{kJ mol}^{-1}) \tag{4.1}$$

In previous research, RWGS reactions were catalyzed by the thermal-catalytic effect. Common catalysts that have been well studied include noble metals, transition metals, and metal oxide materials. In photothermal catalysis RWGS reactions, the major concerns are focused on the light-harvesting and solar–thermal conversion abilities of catalyst materials, which means the catalysts with photocatalytic properties become promising alternatives.

The most traditional photothermal catalyst is TiO_2 support catalyst materials. By composing with metal particles, the catalytic activity increased quite a lot. When Pd nanoparticles were loaded on TiO_2, the CO production rate increased more than 7 times compared to pristine TiO_2 nanomaterials (P25).[74] The induced Pd particles not only increase the number of photo-generated hot carriers but also enlarge the specific area which enhances the CO_2 adsorption. Au is another famous plasmonic particle that has been widely used as a catalyst or co-catalyst.[75–77] The use of Au/TiO_2 resulted in a CO_2 reduction rate of 2.7 mmol g_{cat}^{-1} h^{-1} under visible light irradiation. When Au works together with ZnO, the light-to-thermal effect induces a high temperature reaching up to 600 °C.[78] Interesting results were obtained with Au/CeO_2. The catalysis activity is extremely high under the illumination, while less than 4% of CO_2 was converted at the same temperature under thermal conditions.[75]

Another attractive material was developed by Ozin and co-workers—indium oxides. The $In_2O_{3-x}(OH)y$ materials they studied in 2014 show a CO production rate of 153 μmol g_{cat}^{-1} h^{-1} which was 4.3 times higher than in the dark.[79] Very recently, they reported a black indium oxide material In_2O_{3-x}/In_2O_3.[80] This In_2O_{3-x}/In_2O_3 material could drive the reaction at 23882.75 μmol g_{cat}^{-1} h^{-1} for CO production. This indium oxide material shows the best catalytic activities of all reported indium oxide-based photothermal catalyst materials.

4.4.1.2 Methane Production

CO_2 methanation, also known as the Sabatier reaction, is one of the most studied processes based on the hydrogenation of CO_2 (eqn (4.2)). Similar to

RWGS reactions, with H_2 from renewable sources, CH_4 can be produced from CO_2. Considering the wide application of CH_4 as a fuel source, this CO_2 methanation reaction has attracted substantial attention for use in energy conversion and storage projects.[70,81,82]

$$CO_2 + 4H_2 \rightarrow CH_4 + 2H_2O \ (\Delta H_{298\ K} = -165.1\ kJ\ mol^{-1}) \quad (4.2)$$

The kinetic barrier of this reduction reaction is extremely high. Thus, to achieve a favorable CH_4 yield, appropriate energy input, catalysts, and reaction conditions are required. This reaction was discovered in 1897, occurring at high temperatures (300–400 °C) and pressures (around 30 bar) in the presence of a nickel catalyst. Besides Ni-, Ru-, and Rh-based catalysts also exhibit excellent catalytic abilities for the reduction of CO_2.

Many examples can be found in the literature on the production of CH_4 from CO_2, like oxide/graphene, metal/oxide, or semiconductor heterostructures with/without extra metal loaded.[83–87] Since this methanation reaction is also one process of CO_2 reduction by using H_2 as a reducing agent, the product selectivity needs to be determined. Both methanation and RWGS reactions occur over Rh-based catalysts, with CH_4 and CO as the main products, respectively. Everitt and Liu's groups discovered that product selectivity can be tuned with Rh/Al_2O_3 catalysts.[88] Experimental results indicated that production rates of CH_4 and CO were similar in the dark. After introducing UV light, the rate of CH_4 production increased significantly, whereas the rate of CO production was enhanced only very slightly (see Figure 4.2). This is attributed to the better selectivity of CH_4 in this Rh/Al_2O_3 catalyzed photothermal catalytic CO_2 hydrogenation system.

4.4.1.3 Methanol and Ethanol Synthesis

Methanol (CH_3OH) is an important material that either can be used directly as a solvent or fuel or be used as a raw material for the synthesis of hydrocarbons and other compounds.[89] The traditional production strategy to produce methanol is from syngas (CO/H_2). As mentioned before, syngas can be formed *via* an RWGS process, thus methanol also can be formed directly from a thermal-catalytic CO_2 and H_2 reaction. From this, it seems possible to achieve a photothermal catalytic methanol production strategy as an alternative.

$$CO_2 + 3H_2 \rightarrow CH_3OH + H_2O \ (\Delta H_{298\ K} = -49.9\ kJ\ mol^{-1}) \quad (4.3)$$

$$CO + 2H_2 \rightarrow CH_3OH \quad (4.4)$$

In traditional methanol production (eqn (4.4)), CO reacts with two H_2 to form methanol. Adding eqn (4.1) and (4.4) together, the overall reaction is the same as the above eqn (4.3). Thus, replacing CO with CO_2 as the carbon source in the methanol formation strategy could obtain methanol directly.[90–92] This is another successful sample that can produce liquid fuel directly from the reduction of CO_2. And of course, the development of an

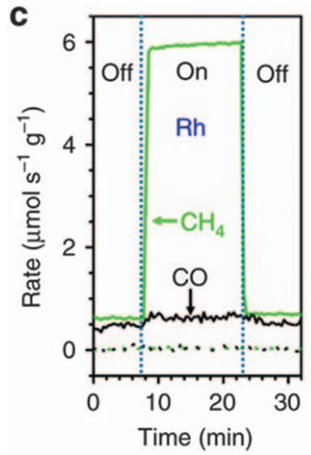

Figure 4.2 Photo-thermo CO_2 hydrogenation over a Rh/Al_2O_3 catalyst. Rates of CH_4 (green) and CO (black) production at 350 °C in the dark and in the light. Reproduced from ref. 88, https://doi.org/10.1038/ncomms14542, under the terms of the CC BY 4.0 license, https://creativecommons.org/licenses/by/4.0/.

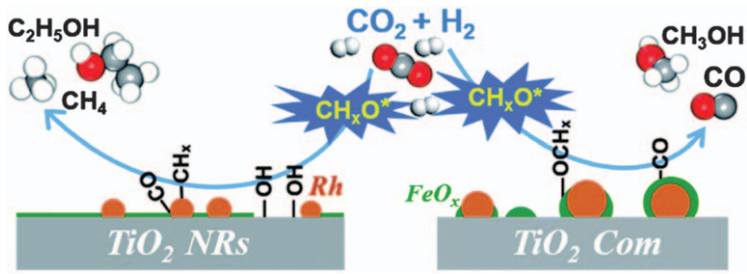

Scheme 4.2 Schematic of CO_2 hydrogenation over a Rh-based catalyst with or without hydroxyl groups on TiO_2. The hydroxyls play an important role in accelerating the scission of CH_x–O* and promote the formation of ethanol.
Reproduced from ref. 93 with permission from the Royal Society of Chemistry.

efficient catalyst is the true part that takes much effort. Additionally, ethanol also can be produced by this hydrogenation of CO_2 over a proper catalyst.[93]

Only a few studies have been done on the synthesis of methanol and ethanol from the reduction of CO_2, especial the formation of ethanol.[93] The difficulties lie in CO_2 activation, dissociation of the C–O bond and the formation of C1 by-products.[94] In 2019, Gong and co-workers reported hydroxyl-mediated ethanol production from CO_2. The RhFeLi alloy-loaded TiO_2 nanorods were used as catalysts (see Scheme 4.2). The crucial point of this system is the surface functionalization with hydroxyls which can protonate methanol and proceed to the formation of ethanol.[95–98]

4.4.1.4 Artificial Photosynthesis

Artificial photosynthesis is the most direct approach to convert CO_2. It was replicated and developed from natural photosynthesis. This technique provides a valuable solution for CO_2 reduction because fuels can be directly synthesized using CO_2 and H_2O which are both easy to acquire from nature. Various kinds of carbon-based fuels or compounds, such as CO, CH_3OH, or CH_4, can be produced *via* this technique by using sunlight as the energy source.[66,67,70]

Several semiconductor oxide-based catalyst materials have been studied for use in artificial photosynthesis reactions, such as TiO_2, ZnO, Cu_2O, WO_3, MoO_3, or Fe_xO_y.[18,99,100] These oxides exhibit some common properties such as high light-harvesting ability, low charge recombination rate, and stability at high temperature, which make them adaptable to becoming photothermal catalysts. In this particular case of CO_2 conversion, good CO_2 adsorption is also desired. These catalysts have already been evaluated for working in different reactions at different temperatures and/or different ranges of light.

4.4.2 Fischer–Tropsch Process

The Fischer–Tropsch process is a series of chemical reactions that convert carbon monoxide into liquid hydrocarbons by working together with hydrogen or water. This process was first developed in 1925 by Franz Fischer and Hans Tropsch. These reactions typically occur at high temperature (150–300 °C) and pressure (one to several tens bar) in the presence of catalysts. In 2015, Guo's group and Su's group both published interesting results about the photothermal catalyzed Fischer–Tropsch process. Theoretically, the use of photothermal catalysts instead of traditional metal catalysts should not only lower the cost but also, and most importantly, enhance the catalytic activity. In Guo's work, a ruthenium/graphene nano-heterostructure was used as the photothermal catalyst for the formation of C_{20+} hydrocarbons from a mixture of $CO:H_2$ (1 : 1).[101] Based on their results, the catalytic activity is around 7.8 mol mol_{cat}^{-1} h^{-1} while the reaction is carried out in a dark environment and reaches up to 14.4 mol mol_{cat}^{-1} h^{-1} while visible light (400–800 nm) irradiation is supplied. And beyond that, the 150 °C reaction temperature with 10–20 bar gas pressure is also a relatively mild condition compared to the traditional Fischer–Tropsch process. As shown in Figure 4.3, the reaction rate is enhanced by increasing the irradiation intensity. While maintaining the reaction temperature unchanged at 150 °C, the contribution of thermal effect from direct heating should be consistent. Thus, the increase in reaction rate should be attributed to the photocatalytic and solar–thermal effects.

Su and co-workers reported another catalytic system in 2018. In this design, TiO_2 nanotube supported Co catalysts were used to catalyze the FT reactions ($CO:H_2 = 1:2$) under the irradiation of UV light.[102] The thermal only and irradiation only experiments have also been investigated as comparison experiments. From their results, there are a few points that are worth specifying.

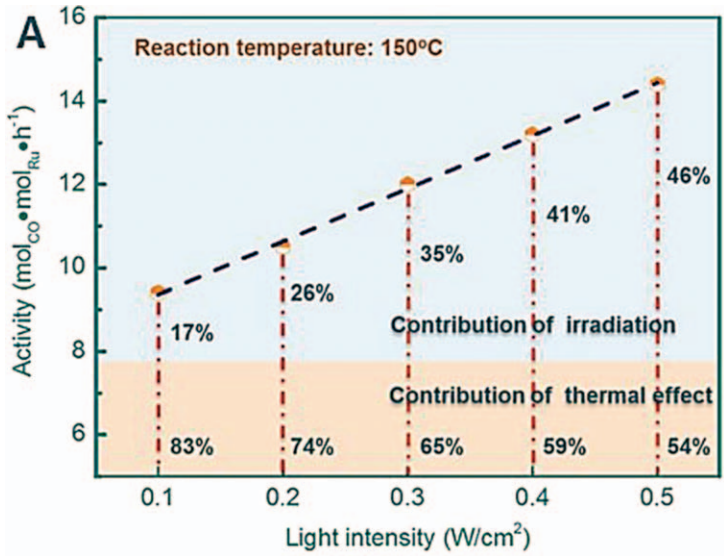

Figure 4.3 Dependence of the catalytic activity of Ru/graphene for PFTS on the light intensity shows that the activity linearly decreases with decreasing light intensity.
Reproduced from ref. 101 with permission from American Chemical Society, Copyright 2015.

First, the UV irradiation alone does not have enough energy to overcome the reaction energy barrier, the assistance from solar converting heat is required. Secondly, the CO conversion value increased from 9.2% to 63.9% by inducing UV irradiation. And thirdly, *in situ* Raman spectroscopy results proved the adsorption of CO on metal particles and the weakening of the C–O bond. The electrons that attended the dissociation of the C–O bond are generated and transferred from the support materials, such as graphene in Guo's work, to TiO_2, MnO, ZnO and so on.[102–104] This makes the support material a key part in the development of photothermal catalytic systems.

In addition, to improve the CO conversion efficiency, product selectivity is another parameter that needs to be investigated in the Fischer–Tropsch process. In the Fischer–Tropsch process, the most used catalysts contain group VIIIB transition metals, especial ruthenium, iron, nickel, and so on. These catalysts show differences in CO hydrogenation product selectivity. They can be used alone or together as an alloy to enhance selectivity.[104] According to the published data, iron-based catalysts show good selectivity toward light olefins,[105,106] Co-based catalysts suitable for the production of higher hydrocarbons,[107] while Ni-based catalysts exhibit efficient methanation production.[108] Although these typical experiences could apply to most of the reactions, changing the composition of metal and oxide could promote the reaction toward a quite different product. For instance, Ni-based catalysts are commonly considered unsuitable for the synthesis of olefins. However, a very

recent publication reviewed that, by cooperation with MnO material, Ni/MnO catalyzed Fischer–Tropsch reactions present olefin selectivity up to 33.0%.[104]

This Fischer–Tropsch process is a complicated reaction system. It can be used for the production of olefins, hydrocarbons, alcohols, dimethyl ether, and so on.[109–112] Thus, to develop the photothermal catalytic Fischer–Tropsch process, both CO conversion efficiency and product selectivity need to be considered.

4.4.3 NH_3 Synthesis

The Haber–Bosch process is an artificial nitrogen fixation process to produce ammonia (eqn (4.5)).[113] This process has already been applied for the industrial production of ammonia under extreme reaction conditions: high temperatures (400 °C to 500 °C) and pressures (100 bar to 200 bar). How to carry out this reaction under a mild condition became one of the most challenging research aims of the 20th century.

$$N_2 + 3H_2 \rightarrow 2NH_3 \ (\Delta H_{298\ K} = -91.8\ \text{kJ mol}^{-1}) \tag{4.5}$$

In 2018, Zhang's group was successfully introducing sunlight into the ammonia synthesis reaction as the only energy source.[114] In their work, a Ru-loaded $TiO_{2-x}H_x$ catalyst material was constructed, and by using it, the reaction could occur at atmospheric pressure without any external heating supply. The temperature inside the reactor has been measured reaching 360 °C under irradiation. Their results directly indicate the existence of a photothermal catalytic effect inside the reaction system. The ammonia generation rate of this process is up to 112.6 μmol g_{cat}^{-1} h^{-1}, which is much higher than the Ru-based catalyst supported thermal-catalytic process. Another interesting work that is worth mentioning was carried out by Liu's group in 2019.[115] They proposed the existence of thermal gradients in photothermal catalytic systems. The thermal gradients could act as a thermodynamic pump to shift the global equilibrium to improve the catalytic activities and product yield simultaneously. The short penetration depth of light, especially UV light, considered a weakness in light-driven catalysis previously, has now become an advantage to achieve thermal gradients. This strategy explained another possibility about what happened after the photothermal heat energy was generated at a catalyst surface.

4.5 Outlook

The combination of photocatalytic and thermal-catalytic effects makes the photothermal catalytic system an excellent strategy to promote reactions. With the help of photothermal catalysts, the Fischer–Tropsch process and ammonia synthesis can be carried out under relatively mild conditions. Solar energy is sustainable energy, and by using this instead of heat energy, the environmental problems can, and will, be greatly eased. From another perspective, photothermal catalysis of CO_2 conversion to fuels could also relieve us from

greenhouse gas. And the most important thing is, another raw material for CO_2 treatment is H_2 or H_2O, which are either easy to obtain or produce. The successful construction of CO_2 conversion systems and artificial photosynthesis processes brings us one step closer to achieving the carbon cycle.

Of course, what we have done is just the beginning. There are still too many problems that need to be solved and too many challenges that need to be faced. First is the catalytic performance. The performance of catalysts consists of three parts: activity, selectivity, and stability. (1) Although we already developed many kinds of materials and structures, only a few catalyst materials show higher catalytic activity. For most of the system, CO_2 conversion is still lower than 10%. (2) According to the three photothermal catalytic systems that have been reviewed in this chapter, product selectivity is still a problem. The product selectivity is limited by the catalysts themselves. This means we still cannot control the direction of the reactions except by changing the catalyst materials. The working mechanism of catalysts is not clear yet. (3) The stability problem is what we care about. It is not only related to how many times we can use a catalyst or to how long we can use it but also how to recycle it completely. The leaking of these catalysts, especial nanoscale catalysts will cause a more serious environmental problem. Secondly, the construction of photothermal catalytic devices is in demand. A proper device could make use of and recycle catalysts conveniently and safely. Thirdly, the supporting theories of the whole photothermal catalytic system are insufficient. The *in situ* study or characterization of photothermal catalytic processes lags far behind. Insight into the catalysis mechanism will help us know how the catalyst acts in a system, and make it possible to design a really meaningful catalyst material/device.

References

1. P. Christopher, H. Xin and S. Linic, *Nat. Chem.*, 2011, **3**, 467–472.
2. F. Liu, M. Zeng, Y. Li, Y. Yang, M. Mao and X. Zhao, *Adv. Funct. Mater.*, 2016, **26**, 4518–4526.
3. R. Schloegl, *ChemSusChem*, 2010, **3**, 209–222.
4. Y. Zhao, W. Gao, S. Li, G. R. Williams, A. H. Mahadi and D. Ma, *Joule*, 2019, **3**, 920–937.
5. X. Meng, T. Wang, L. Liu, S. Ouyang, P. Li, H. Hu, T. Kako, H. Iwai, A. Tanaka and J. Ye, *Angew. Chem., Int. Ed.*, 2014, **53**, 11478–11482.
6. M. Ghoussoub, M. Xia, P. N. Duchesne, D. Segal and G. Ozin, *Energy Environ. Sci.*, 2019, **12**, 1122–1142.
7. P. G. O'Brien, A. Sandhel, T. E. Wood, A. A. Jelle, L. B. Hoch, D. D. Perovic, C. A. Mims and G. A. Ozin, *Adv. Sci.*, 2014, **1**, 1400001.
8. S. I. Nikitenko, T. Chave, C. Cau, H.-P. Brau and V. Flaud, *ACS Catal.*, 2015, **5**, 4790–4795.
9. J. Jia, P. G. O'Brien, L. He, Q. Qiao, T. Fei, L. M. Reyes, T. E. Burrow, Y. Dong, K. Liao, M. Varela, S. J. Pennycook, M. Hmadeh, A. S. Helmy, N. P. Kherani, D. D. Perovic and G. A. Ozin, *Adv. Sci.*, 2016, **3**, 1600189.

10. A. Corma and H. Garcia, *J. Catal.*, 2013, **308**, 168–175.
11. X. Chang, T. Wang and J. Gong, *Energy Environ. Sci.*, 2016, **9**, 2177–2196.
12. F. Wang, Y. Huang, Z. Chai, M. Zeng, Q. Li, Y. Wang and D. Xu, *Chem. Sci.*, 2016, **7**, 6887–6893.
13. J. Jia, C. Qian, Y. Dong, Y. F. Li, H. Wang, M. Ghoussoub, K. T. Butler, A. Walsh and G. A. Ozin, *Chem. Soc. Rev.*, 2017, **46**, 4631–4644.
14. L. Nagarajan, R. A. De Souza, D. Samuelis, I. Valov, A. Boerger, J. Janek, K.-D. Becker, P. C. Schmidt and M. Martin, *Nat. Mater.*, 2008, **7**, 391–398.
15. K. Szot, W. Speier, G. Bihlmayer and R. Waser, *Nat. Mater.*, 2006, **5**, 312–320.
16. J. Ren, S. Ouyang, H. Xu, X. Meng, T. Wang, D. Wang and J. Ye, *Adv. Energy Mater.*, 2017, **7**, 1601657.
17. X. Meng, T. Wang, L. Liu, S. Ouyang, P. Li, H. Hu, T. Kako, H. Iwai, A. Tanaka and J. Ye, *Angew. Chem., Int. Ed.*, 2014, **53**, 11478–11482.
18. L. Wang, Y. Wang, Y. Cheng, Z. Liu, Q. Guo, H. Minh Ngoc and Z. Zhao, *J. Mater. Chem. A*, 2016, **4**, 5314–5322.
19. Y. F. Li, N. Soheilnia, M. Greiner, U. Ulmer, T. Wood, A. A. Jelle, Y. Dong, A. P. Y. Wong, J. Jia and G. A. Ozin, *ACS Appl. Mater. Interfaces*, 2019, **11**, 5610–5615.
20. X. Chen, L. Liu, P. Y. Yu and S. S. Mao, *Science*, 2011, **331**, 746–750.
21. M. Ye, J. Jia, Z. Wu, C. Qian, R. Chen, P. G. O'Brien, W. Sun, Y. Dong and G. A. Ozin, *Adv. Energy Mater.*, 2017, **7**, 1601811.
22. Y. H. Qi, L. Z. Song, S. X. Ouyang, X. C. Liang, S. B. Ning, Q. Q. Zhang and J. H. Ye, *Adv. Mater.*, 2020, **32**, 1903915.
23. A. Agrawal, S. H. Cho, O. Zandi, S. Ghosh, R. W. Johns and D. J. Milliron, *Chem. Rev.*, 2018, **118**, 3121–3207.
24. S. C. Erwin, L. J. Zu, M. I. Haftel, A. L. Efros, T. A. Kennedy and D. J. Norris, *Nature*, 2005, **436**, 91–94.
25. A. M. Schimpf, K. E. Knowles, G. M. Carroll and D. R. Gamelin, *Acc. Chem. Res.*, 2015, **48**, 1929–1937.
26. E. Sachet, C. T. Shelton, J. S. Harris, B. E. Gaddy, D. L. Irving, S. Curtarolo, B. F. Donovan, P. E. Hopkins, P. A. Sharma, A. L. Sharma, J. Ihlefeld, S. Franzen and J.-P. Maria, *Nat. Mater.*, 2015, **14**, 414–420.
27. E. L. Runnerstrom, A. Bergerud, A. Agrawal, R. W. Johns, C. J. Dahlman, A. Singh, S. M. Selbach and D. J. Milliron, *Nano Lett.*, 2016, **16**, 3390–3398.
28. D. S. Bhachu, D. O. Scanlon, G. Sankar, T. D. Veal, R. G. Egdell, G. Cibin, A. J. Dent, C. E. Knapp, C. J. Carmalt and I. P. Parkin, *Chem. Mater.*, 2015, **27**, 2788–2796.
29. B. F. Donovan, E. Sachet, J.-P. Maria and P. E. Hopkins, *Appl. Phys. Lett.*, 2016, **108**, 021901.
30. M. K. H. Taha, O. Boisron, B. Canut, P. Melinon, J. Penuelas, M. Gendry and B. Masenelli, *RSC Adv.*, 2017, **7**, 28677–28683.
31. P. Agoston, P. Erhart, A. Klein and K. Albe, *J. Phys.: Condens. Matter*, 2009, **21**, 455801.
32. A. Agrawal, R. W. Johns and D. J. Milliron, *Annu. Rev. Mater. Res.*, 2017, **47**, 1–31.

33. S. Q. Li, P. Guo, L. Zhang, W. Zhou, T. W. Odom, T. Seideman, J. B. Ketterson and R. P. H. Chang, *ACS Nano*, 2011, **5**, 9161–9170.
34. J. Lee, S. Lee, G. Li, M. A. Petruska, D. C. Paine and S. Sun, *J. Am. Chem. Soc.*, 2012, **134**, 13410–13414.
35. D. Ito, S. Yokoyama, T. Zaikova, K. Masuko and J. E. Hutchison, *ACS Nano*, 2014, **8**, 64–75.
36. M. Kanehara, H. Koike, T. Yoshinaga and T. Teranishi, *J. Am. Chem. Soc.*, 2009, **131**, 17736–17737.
37. R. J. Mendelsberg, Y. Zhu and A. Anders, *J. Phys. D: Appl. Phys.*, 2012, **45**, 425302.
38. T. R. Gordon, T. Paik, D. R. Klein, G. V. Naik, H. Caglayan, A. Boltasseva and C. B. Murray, *Nano Lett.*, 2013, **13**, 2857–2863.
39. X. Ye, J. Fei, B. T. Diroll, T. Paik and C. B. Murray, *J. Am. Chem. Soc.*, 2014, **136**, 11680–11686.
40. R. Buonsanti, A. Llordes, S. Aloni, B. A. Helms and D. J. Milliron, *Nano Lett.*, 2011, **11**, 4706–4710.
41. E. Della Gaspera, A. S. R. Chesman, J. van Embden and J. J. Jasieniak, *ACS Nano*, 2014, **8**, 9154–9163.
42. F. Liu, L. Song, S. Ouyang and H. Xu, *Catal. Sci. Technol.*, 2019, **9**, 2125–2131.
43. D. H. Son, S. M. Hughes, Y. D. Yin and A. P. Alivisatos, *Science*, 2004, **306**, 1009–1012.
44. L. De Trizio and L. Manna, *Chem. Rev.*, 2016, **116**, 10852–10887.
45. B. Sadtler, D. O. Demchenko, H. Zheng, S. M. Hughes, M. G. Merkle, U. Dahmen, L.-W. Wang and A. P. Alivisatos, *J. Am. Chem. Soc.*, 2009, **131**, 5285–5293.
46. S. Han, X. Qin, Z. An, Y. Zhu, L. Liang, Y. Han, W. Huang and X. Liu, *Nat. Commun.*, 2016, **7**, 13059.
47. Z. Liu, Y. Zhong, I. Shafei, R. Borman, S. Jeong, J. Chen, Y. Losovyj, X. Gao, N. Li, Y. Du, E. Sarnello, T. Li, D. Su, W. Ma and X. Ye, *Nat. Commun.*, 2019, **10**, 1394.
48. J. Lim, K. Hippalgaonkar, S. C. Andrews, A. Majumdar and P. Yang, *Nano Lett.*, 2012, **12**, 2475–2482.
49. H. Wu, J. Carrete, Z. Zhang, Y. Qu, X. Shen, Z. Wang, L.-D. Zhao and J. He, *NPG Asia Mater.*, 2014, **6**, e108.
50. J. Jia, H. Wang, Z. Lu, P. G. O'Brien, M. Ghoussoub, P. Duchesne, Z. Zheng, P. Li, Q. Qiao, L. Wang, A. Gu, A. A. Jelle, Y. Dong, Q. Wang, K. K. Ghuman, T. Wood, C. Qian, Y. Shao, C. Qiu, M. Ye, Y. Zhu, Z.-H. Lu, P. Zhang, A. S. Helmy, C. V. Singh, N. P. Kherani, D. D. Perovic and G. A. Ozin, *Adv. Sci.*, 2017, **4**, 1700252.
51. Z. G. Chen, Q. Wang, H. L. Wang, L. S. Zhang, G. S. Song, L. L. Song, J. Q. Hu, H. Z. Wang, J. S. Liu, M. F. Zhu and D. Y. Zhao, *Adv. Mater.*, 2013, **25**, 2095–2100.
52. Z. Hua, B. Li, L. Li, X. Yin, K. Chen and W. Wang, *J. Phys. Chem. C*, 2017, **121**, 60–69.

53. L. Zhu, M. Gao, C. K. N. Peh and G. W. Ho, *Mater. Horiz.*, 2018, **5**, 323–343.
54. A. Aubry, D. Y. Lei, A. I. Fernandez-Dominguez, Y. Sonnefraud, S. A. Maier and J. B. Pendry, *Nano Lett.*, 2010, **10**, 2574–2579.
55. G. Baffou, R. Quidant and C. Girard, *Appl. Phys. Lett.*, 2009, **94**, 153109.
56. Y. Zhao, L. Yang, L. Kong, M. H. Nai, D. Liu, J. Wu, Y. Liu, S. Y. Chiam, W. K. Chim, C. T. Lim, B. Li, J. T. L. Thong and K. Hippalgaonkar, *Adv. Funct. Mater.*, 2017, **27**, 1702824.
57. D. F. Swearer, H. Zhao, L. Zhou, C. Zhang, H. Robatjazi, J. M. P. Martirez, C. M. Krauter, S. Yazdi, M. J. McClain, E. Ringe, E. A. Carter, P. Nordlander and N. J. Halas, *Proc. Natl. Acad. Sci. U. S. A.*, 2016, **113**, 8916–8920.
58. K. Manthiram and A. P. Alivisatos, *J. Am. Chem. Soc.*, 2012, **134**, 3995–3998.
59. Z. Fang, S. Jiao, Y. Kang, G. Pang and S. Feng, *ChemistryOpen*, 2017, **6**, 261–265.
60. R. Du, W. Liu, H. Bai, H. Wang and G. Xi, *RSC Adv.*, 2020, **10**, 2075–2084.
61. D. Kumar, C. H. Park and C. S. Kim, *ACS Sustainable Chem. Eng.*, 2018, **6**, 8604–8614.
62. L. Wang, Y. Dong, T. Yan, Z. Hu, A. A. Jelle, D. M. Meira, P. N. Duchesne, J. Y. Y. Loh, C. Qiu, E. E. Storey, Y. Xu, W. Sun, M. Ghoussoub, N. P. Kherani, A. S. Helmy and G. A. Ozin, *Nat. Commun.*, 2020, **11**, 2432.
63. S. Das, J. Perez-Ramirez, J. Gong, N. Dewangan, K. Hidajat, B. C. Gates and S. Kawi, *Chemical Society Reviews*, 2020, **49**, 2937–3004.
64. D. Mateo, J. L. Cerrillo, S. Durini and J. Gascon, *Chemical Society Reviews*, 2021, **50**, 2173–2210.
65. H. Huang, L. Zhang, Z. Lv, R. Long, C. Zhang, Y. Ling, K. Wei, C. Wang, L. Chen, Z.-Y. Li, Q. Zhang, Y. Luo and Y. Xiong, *J. Am. Chem. Soc.*, 2016, **138**, 6822–6828.
66. G. Zhao, X. Huang, X. Wang and X. Wang, *J. Mater. Chem. A*, 2017, **5**, 21625–21649.
67. K. Li, B. Peng and T. Peng, *ACS Catal.*, 2016, **6**, 7485–7527.
68. C. Sonnichsen, T. Franzl, T. Wilk, G. von Plessen, J. Feldmann, O. Wilson and P. Mulvaney, *Phys. Rev. Lett.*, 2002, **88**, 077402.
69. M. J. Kale and P. Christopher, *Science*, 2015, **349**, 587–588.
70. M. A. A. Aziz, A. A. Jalil, S. Triwahyono and A. Ahmad, *Green Chem.*, 2015, **17**, 2647–2663.
71. S. Kattel, W. Yu, X. Yang, B. Yan, Y. Huang, W. Wan, P. Liu and J. G. Chen, *Angew. Chem., Int. Ed.*, 2016, **55**, 7968–7973.
72. L. Pastor-Perez, F. Baibars, E. Le Sache, H. Arellano-Garcia, S. Gu and T. R. Reina, *J. CO2 Util.*, 2017, **21**, 423–428.
73. X. Yang, X. Su, X. Chen, H. Duan, B. Liang, Q. Liu, X. Liu, Y. Ren, Y. Huang and T. Zhang, *Appl. Catal., B*, 2017, **216**, 95–105.

74. C. Xu, W. Huang, Z. Li, B. Deng, Y. Zhang, M. Ni and K. Cen, *ACS Catal.*, 2018, **8**, 6582–6593.
75. B. Lu, F. Quan, Z. Sun, F. Jia and L. Zhang, *Catal. Commun.*, 2019, **129**, 105724.
76. A. A. Upadhye, I. Ro, X. Zeng, H. J. Kim, I. Tejedor, M. A. Anderson, J. A. Dumesic and G. W. Huber, *Catal. Sci. Technol.*, 2015, **5**, 2590–2601.
77. I. Tanabe, T. Ryoki and Y. Ozaki, *RSC Adv.*, 2015, **5**, 13648–13652.
78. C. Wang, O. Ranasingha, S. Natesakhawat, P. R. Ohodnicki, Jr, M. Andio, J. P. Lewis and C. Matranga, *Nanoscale*, 2013, **5**, 6968–6974.
79. L. B. Hoch, P. G. O'Brien, A. Jelle, A. Sandhel, D. D. Perovic, C. A. Mims and G. A. Ozin, *ACS Nano*, 2016, **10**, 9017–9025.
80. L. Wang, Y. Dong, T. Yan, Z. Hu, A. A. Jelle, D. M. Meira, P. N. Duchesne, J. Y. Y. Loh, C. Qiu, E. E. Storey, Y. Xu, W. Sun, M. Ghoussoub, N. P. Kherani, A. S. Helmy and G. A. Ozin, *Nat. Commun.*, 2020, **11**, 2432.
81. J. Sun, Y. Wang, H. Zou, X. Guo and Z.-J. Wang, *J. Energy Chem.*, 2019, **29**, 3–7.
82. A. J. Martin, G. O. Larrazabal and J. Perez-Ramirez, *Green Chem.*, 2015, **17**, 5114–5130.
83. L. Lin, K. Wang, K. Yang, X. Chen, X. Fu and W. Dai, *Appl. Catal., B*, 2017, **204**, 440–455.
84. D. Mateo, A. M. Asiri, J. Albero and H. Garcia, *Photochem. Photobiol. Sci.*, 2018, **17**, 829–834.
85. D. Mateo, J. Albero and H. Garcia, *Appl. Catal., B*, 2018, **224**, 563–571.
86. E. T. Kho, S. Jantarang, Z. Zheng, J. Scott and R. Amal, *Engineering*, 2017, **3**, 393–401.
87. S. Jantarang, E. C. Lovell, T. H. Tan, J. Scott and R. Amal, *Prog. Nat. Sci.: Mater. Int.*, 2018, **28**, 168–177.
88. X. Zhang, X. Li, D. Zhang, N. Q. Su, W. Yang, H. O. Everitt and J. Liu, *Nat. Commun.*, 2017, **8**, 14542.
89. G. A. Olah, *Angew. Chem., Int. Ed.*, 2005, **44**, 2636–2639.
90. M. D. Porosoff, B. Yan and J. G. Chen, *Energy Environ. Sci.*, 2016, **9**, 62–73.
91. X. Yang, S. Kattel, S. D. Senanayake, J. A. Boscoboinik, X. Nie, J. Graciani, J. A. Rodriguez, P. Liu, D. J. Stacchiola and J. G. Chen, *J. Am. Chem. Soc.*, 2015, **137**, 10104–10107.
92. J. Bao, G. Yang, Y. Yoneyama and N. Tsubaki, *ACS Catal.*, 2019, **9**, 3026–3053.
93. C. Yang, R. Mu, G. Wang, J. Song, H. Tian, Z.-J. Zhao and J. Gong, *Chem. Sci.*, 2019, **10**, 3161–3167.
94. M. Aresta, A. Dibenedetto and A. Angelini, *Chem. Rev.*, 2014, **114**, 1709–1742.
95. Y. Dai, S. Liu and N. Zheng, *J. Am. Chem. Soc.*, 2014, **136**, 5583–5586.
96. J.-D. Lin, Q.-Y. Bi, L. Tao, T. Jiang, Y.-M. Liu, H.-Y. He, Y. Cao and Y.-D. Wang, *ACS Catal.*, 2017, **7**, 1720–1727.
97. F. Liu, W. Kong, C. Qi, L. Zhu and F.-S. Xiao, *ACS Catal.*, 2012, **2**, 565–572.

98. Q. Sun, B. Aguila, G. Verma, X. Liu, Z. Dai, F. Deng, X. Meng, F.-S. Xiao and S. Ma, *Chem*, 2016, **1**, 628–639.
99. Q. Guo, Q. Zhang, H. Wang, Z. Liu and Z. Zhao, *Catal. Commun.*, 2016, **77**, 118–122.
100. J. Li, Y. Ye, L. Ye, F. Su, Z. Ma, J. Huang, H. Xie, D. E. Doronkin, A. Zimina, J.-D. Grunwaldt and Y. Zhou, *J. Mater. Chem. A*, 2019, **7**, 2821–2830.
101. X.-N. Guo, Z.-F. Jiao, G.-Q. Jin and X.-Y. Guo, *ACS Catal.*, 2015, **5**, 3836–3840.
102. L. Wang, Y. Zhang, X. Gu, Y. Zhang and H. Su, *Catal. Sci. Technol.*, 2018, **8**, 601–610.
103. L. Liu, A. V. Puga, J. Cored, P. Concepcion, V. Perez-Dieste, H. Garcia and A. Corma, *Appl. Catal., B*, 2018, **235**, 186–196.
104. Y. Wang, Y. Zhao, J. Liu, Z. Li, G. I. N. Waterhouse, R. Shi, X. Wen and T. Zhang, *Adv. Energy Mater.*, 2020, **10**, 1902860.
105. X. Zhou, J. Ji, D. Wang, X. Duan, G. Qian, D. Chen and X. Zhou, *Chem. Commun.*, 2015, **51**, 8853–8856.
106. J. Lu, L. Yang, B. Xu, Q. Wu, D. Zhang, S. Yuan, Y. Zhai, X. Wang, Y. Fan and Z. Hu, *ACS Catal.*, 2014, **4**, 613–621.
107. L. Zhong, F. Yu, Y. An, Y. Zhao, Y. Sun, Z. Li, T. Lin, Y. Lin, X. Qi, Y. Dai, L. Gu, J. Hu, S. Jin, Q. Shen and H. Wang, *Nature*, 2016, **538**, 84–87.
108. V. P. Ananikov, *ACS Catal.*, 2015, **5**, 1964–1971.
109. X. Liu, M. Wang, C. Zhou, W. Zhou, K. Cheng, J. Kang, Q. Zhang, W. Deng and Y. Wang, *Chem. Commun.*, 2018, **54**, 140–143.
110. K. Cheng, B. Gu, X. Liu, J. Kang, Q. Zhang and Y. Wang, *Angew. Chem. Int. Ed.*, 2016, **55**, 4725–4728.
111. Z.-J. Wang, H. Song, H. Pang, Y. Ning, T. D. Dao, Z. Wang, H. Chen, Y. Weng, Q. Fu, T. Nagao, Y. Fang and J. Ye, *Appl. Catal., B*, 2019, **250**, 10–16.
112. S. Xie, Z. Shen, J. Deng, P. Guo, Q. Zhang, H. Zhang, C. Ma, Z. Jiang, J. Cheng, D. Deng and Y. Wang, *Nat. Commun.*, 2018, **9**, 1181.
113. V. Smil, *Nature*, 1999, **400**, 415.
114. C. Mao, L. Yu, J. Li, J. Zhao and L. Zhang, *Appl. Catal., B*, 2018, **224**, 612–620.
115. X. Li, X. Zhang, H. O. Everitt and J. Liu, *Nano Lett.*, 2019, **19**, 1706–1711.

CHAPTER 5

Copper Sulfide-based Nanomaterials for Photothermal Applications

MICHELLE D. REGULACIO

Institute of Chemistry, University of the Philippines Diliman, Quezon City 1101, Philippines
Email: mdregulacio@up.edu.ph

5.1 Introduction

Binary copper sulfides are an interesting class of metal chalcogenide semiconductors that have become a topic of intense research among nanomaterials scientists over the last decade. They are generally represented by the chemical formula $Cu_{2-x}S$, with x values ranging from 0 to 1.[1] Notable examples include CuS (covellite), $Cu_{1.12}S$ (or Cu_9S_8, yarrowite), $Cu_{1.75}S$ (or Cu_7S_4, anilite), $Cu_{1.8}S$ (or Cu_9S_5, digenite), $Cu_{1.81}S$ (or $Cu_{29}S_{16}$, roxbyite), $Cu_{1.94}S$ (or $Cu_{31}S_{16}$, djurleite), and Cu_2S (chalcocite).[2] The vast interest in these compounds is rooted from the desire to find suitable alternatives to cadmium and lead chalcogenides (*i.e.*, CdE and PbE, where E = S, Se, Te), which are technologically promising but are hounded by toxicity issues that limit their use in practical settings. Because they are composed of nontoxic and earth-abundant elements, copper sulfides are environmentally benign and low-cost. With their various stoichiometries, they also have the advantage of being compositionally and structurally diverse, which can be exploited in the manipulation of their properties.[3] Moreover, the binary Cu–S system can be easily doped or alloyed to yield multinary compounds having

Nanoscience & Nanotechnology Series No. 54
Photothermal Nanomaterials
Edited by Enyi Ye and Zibiao Li

Published by the Royal Society of Chemistry, www.rsc.org

composition-dependent properties that can be readily tuned to suit the desired functions.[3–6] When prepared in nanosized dimensions, the size and morphology of these materials can also be engineered to tailor their properties and enhance their performance in a given application. This renders them useful in a broad range of applications that span across multiple areas of research, including optoelectronics, catalysis, photovoltaics, thermoelectrics, energy storage, and biomedicine.[7–9]

Research over the past decade has shown that $Cu_{2-x}S$ nanomaterials are ideal photothermal transduction materials because they are capable of intense photon absorption and can efficiently transform the absorbed light into heat.[10–13] Their ability to absorb light is attributed to their strong localized surface plasmon resonance (LSPR) with frequencies within the near-infrared (NIR) spectral window.[4] First reported in 2009, the LSPR in $Cu_{2-x}S$ nanomaterials arises from the collective oscillation of free charge carriers, particularly free holes, which are generated by copper vacancies in the valence band.[14] This is different from the case of nanosized noble metals (*e.g.* Au, Ag), where the LSPR originates from the collective oscillation of free electrons in the conduction band. As the LSPR frequency is determined by the concentration of free charge carriers, $Cu_{2-x}S$ nanomaterials absorb light of longer wavelengths compared to noble metal nanomaterials because they have a lower density of free charge carriers (*i.e.*, the number of free holes in $Cu_{2-x}S$ is considerably lower than the number of free electrons in metals).[15] Thus, while the LSPR absorption band for Au and Ag nanospheres can be found in the visible spectral range, the LSPR absorption band for similar-sized $Cu_{2-x}S$ nanospheres lies in the NIR region. In spite of the difference in LSPR origin, there are similarities in the plasmonic behavior of metals and copper sulfides. For both types of materials, the LSPR frequency is dependent on the size and shape of the plasmonic nanostructures.[16,17] In the case of shape (or morphology), nanostructures with anisotropic morphologies exhibit spectral features that differ from those observed for spherical-shaped nanocrystals.[18,19] The reduced shape symmetry in anisotropic nanostructures gives rise to additional resonance on account of the different ways in which light can be polarized.[20] For example, nanorods display longitudinal and transverse plasmon resonances that correspond to the rod's long and short axes, respectively. The local environment is another factor that can influence the plasmon-induced optical response of both metals and $Cu_{2-x}S$. Red-shifting of the LSPR maximum is observed with increasing refractive index of the surrounding media.[16,21]

When comparing the different $Cu_{2-x}S$ phases, CuS ($x = 1$) has the highest density of free holes because it is the most copper-deficient, and so, it has the strongest plasmonic absorption in the NIR region. The absorption peak becomes less intense and shifts to longer wavelengths as x decreases (see Figure 5.1a) due to the reduction in the concentration of free holes as the $Cu_{2-x}S$ phase becomes less copper deficient.[22] This demonstrates that the stoichiometry-dependent free carrier concentration of $Cu_{2-x}S$ nanomaterials could enable modulation of their absorption properties through composition

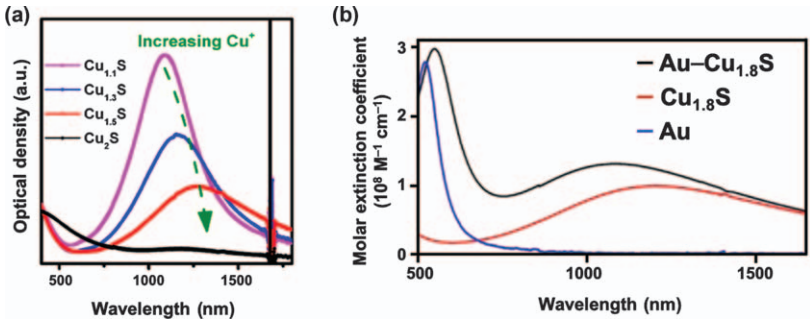

Figure 5.1 (a) Evolution of the optical extinction spectra for $Cu_{2-x}S$ nanocrystals with increasing copper content (or decreasing hole concentration). Reproduced from ref. 22 with permission from American Chemical Society, Copyright 2013. (b) Optical extinction spectra of Au–$Cu_{1.8}S$ nanocomposites and their corresponding components: Au and $Cu_{1.8}S$ nanoparticles. Reproduced from ref. 26 with permission from American Chemical Society, Copyright 2014.

control. For Cu_2S ($x = 0$), plasmonic absorption is not observed because the number of free holes is not abundant enough to generate LSPR. However, it has been noted that nanostructured Cu_2S is unstable in air.[17] When exposed to oxygen at ambient conditions, it can transform to other $Cu_{2-x}S$ phases with sufficient free holes that can allow for LSPR-induced NIR absorption. Aside from adjusting the $Cu_{2-x}S$ stoichiometry, the composition can also be modified by doping or alloying since the copper-deficient $Cu_{2-x}S$ lattice can readily accommodate additional metal cations.[4,23] The incorporation of extrinsic metal cations fills the copper vacancies, thereby reducing the concentration of free holes. This leads to red-shifting of the LSPR absorption band. For example, when In^{3+} was increasingly integrated into $Cu_{2-x}S$ nanocrystals, progressive red-shifting from 1341 to 1533 nm was observed as the indium cation fraction increased from 0 to 47%.[24] However, this is accompanied by weakening of the LSPR response due to filling of the cation vacancies by indium. The LSPR band eventually disappeared when the indium cation fraction reached 60%, implying that the free hole concentration had been greatly diminished.

In an effort to enhance the LSPR absorption cross-section of $Cu_{2-x}S$ nanomaterials, the construction of nanocomposites that combine $Cu_{2-x}S$ with another plasmonic material has been pursued. Particular attention has been directed toward Au–$Cu_{2-x}S$, a dual plasmonic hybrid that exhibits LSPR in both the visible and the NIR region.[25] As seen in Figure 5.1b, two well-defined absorption peaks are present in the extinction spectrum of Au–$Cu_{1.8}S$ hybrid nanostructures.[26] The peak in the visible region is attributed to the LSPR absorption of the Au domain, whereas the NIR absorption band is from the LSPR of the $Cu_{2-x}S$ component. Interestingly, when compared to $Cu_{1.8}S$ nanoparticles synthesized under similar conditions, the Au–$Cu_{1.8}S$ hybrid nanostructures displayed a substantially stronger NIR

absorption, indicating that the plasmonic absorption of $Cu_{2-x}S$ can be improved through coupling with Au. Theoretical simulations showed that this observed absorption enhancement is a result of the influence of the surface-enhanced near-field at the Au surface on the collective oscillation of holes in $Cu_{1.8}S$. This increased absorption ultimately translates to better photothermal transduction efficiency of the nanocomposite.

Because copper sulfide-based nanomaterials are strong NIR-absorbers, they are regarded as promising photothermal transduction agents in biomedical applications, where the use of NIR light is desired to achieve deeper penetration into tissues and better localized heating. In fact, their potential use as photothermal materials in cancer therapy has already been documented in numerous publications, which will be extensively reviewed later in this chapter. Different compositions, morphologies, and hybrids have been synthesized with the object of enhancing the NIR absorbance and the photothermal transduction efficiency. In the following section, the synthetic strategies by which these photothermally active copper sulfide-based nanomaterials can be prepared are presented.

5.2 Synthesis of Copper Sulfide-based Nanomaterials

5.2.1 $Cu_{2-x}S$ Nanostructures

Nanostructured materials of binary copper sulfides can be prepared through solution-phase (or wet chemical) synthesis. The most commonly used methods are the colloidal chemical method, the solvothermal (or hydrothermal) approach, and the microwave-assisted technique. In fabricating $Cu_{2-x}S$ nanostructures with the desired properties for photothermal applications, judicious selection of experimental parameters and conditions is essential. This subsection discusses the different strategies that have been employed in synthesizing photothermal $Cu_{2-x}S$ nanostructures of varying compositions and morphologies.

5.2.1.1 Composition Control

As the crystal structure, band gap, and LSPR of $Cu_{2-x}S$ nanomaterials vary as a function of x, composition control can be used to regulate their optical and electronic properties. It is therefore crucial to establish synthetic methodologies that would enable the preparation of $Cu_{2-x}S$ nanostructures with tunable composition. Using colloidally-prepared $Cu_{1.1}S$ nanocrystals as the starting copper sulfide material, Xie *et al.* were able to synthesize a series of samples with increasing Cu : S ratios (up to Cu_2S) through incorporation of increasing amounts of Cu(I) ions.[22] The complex $[Cu(CH_3CN)_4]PF_6$ was employed as the source of cuprous ions. It was noted that the reaction of the starting nanocrystals with the Cu(I) complex is a reduction reaction, where the sulfur sublattice is gradually reduced with rising amounts of Cu(I). The increase in copper content equates to a decrease in the concentration of

free holes, and this resulted in the red-shifting and damping of the LSPR band (see Figure 5.1a). Meanwhile, Kriegel *et al.* started with pre-synthesized Cu_2S nanocrystals and transformed them into nonstoichiometric $Cu_{1.97}S$ by exposing them to air for 6 days.[27] The starting Cu_2S is not plasmonic, but an LSPR band developed and progressively intensified with continuous oxygen exposure due to accelerated formation of copper vacancies. Considering that the vacancy-induced LSPR bands of copper sulfides can change spontaneously with oxygen exposure, Georgieva *et al.* sought a way to stabilize the copper vacancy concentration in these materials at ambient conditions.[28] They showed that surface passivation with tetrathiomolybdate (MoS_4^{2-}) can provide the necessary protection against oxidation in air because it can strongly chelate to copper ions. As a result, the NIR absorption behavior is stabilized. However, the MoS_4^{2-} concentration should not be too high as to avoid the formation of ternary Cu_2MoS_4.

The reducing ability of the solvent has also been found to be a critical factor in the composition-tunable synthesis of $Cu_{2-x}S$ nanocrystals.[29,30] The observed trend is that the copper vacancy in the resultant $Cu_{2-x}S$ increases with decreasing reducing ability of the solvent. For example, in their colloidal synthesis of $Cu_{2-x}S$ nanocrystals with different stoichiometries, Freymeyer *et al.* made use of a mixture of oleic acid (OA) and dodecanethiol (DDT) with variable ratios as the solvent system (see Figure 5.2).[30] With its thiol functionality, DDT can serve as a reducing agent. Thus, increasing the OA : DDT ratio (*i.e.* decreasing the DDT content) lowers the reducing ability of the solvent system, and this leads to increasing copper deficiency of the product from the most copper-rich Cu_2S to the most copper-deficient CuS.

5.2.1.2 Morphological Design

Shape or morphology is another important parameter that dictates the plasmonic absorption profile of $Cu_{2-x}S$ nanomaterials. For example, Tao and co-workers have shown that the plasmonic behavior of $Cu_{2-x}S$ nanocrystals with disk-like (or platelet-like) morphology is markedly different from that of spherical nanocrystals.[31] As shown in Figure 5.3, only one NIR absorption band is present in the extinction spectrum of $Cu_{2-x}S$ nanospheres, whereas there are two distinct bands for the nanodisks. These two plasmon bands are ascribed to the excitation of shape-dependent dipolar LSPR modes, where excitation occurs for incident radiation polarized in two directions: parallel and perpendicular to the plane of the disk. The position and relative intensities of these bands can be adjusted by controlling the aspect ratio (*i.e.*, diameter-to-height ratio) of the disk. Several protocols can be used to prepare $Cu_{2-x}S$ nanodisks (or nanoplates), and the disks that are formed are usually hexagonal in shape. Many of the reported methodologies make use of single-source precursors that are able to decompose to $Cu_{2-x}S$ when heated in suitable solvents. For instance, when CuSCN was heated in oleylamine at 240 °C, hexagonal $Cu_{1.94}S$ nanodisks (Figure 5.4a) were generated.[32] Another useful precursor is the copper dithiocarbamate complex,

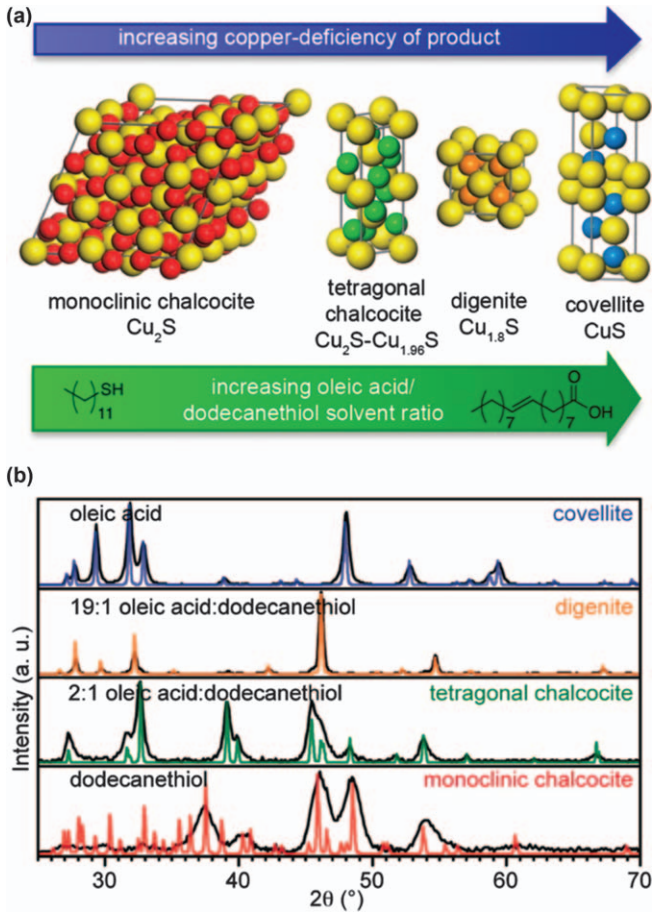

Figure 5.2 Influence of solvent reducing ability on the $Cu_{2-x}S$ phase and stoichiometry. (a) The $Cu_{2-x}S$ crystal structures and (b) the corresponding X-ray diffraction patterns of the $Cu_{2-x}S$ nanocrystals obtained by varying the oleic acid/dodecanethiol ratio. The copper ions are color-coded in the different phases, while the sulfur ions are depicted as yellow spheres. Reproduced from ref. 30 with permission from American Chemical Society, Copyright 2013.

$Cu(S_2CNEt_2)_2$, which can also produce hexagonal $Cu_{1.94}S$ nanodisks when heated in a solvent mixture of hexadecanethiol and trioctylamine at 250 °C.[33] On the other hand, Liu *et al.* showed that room-temperature synthesis is possible as they were able to prepare CuS nanodisks at ambient conditions by reacting $(NH_4)_2S$ with a Cu(II)–oleylamine complex in toluene.[34] Furthermore, through a multiple injection approach, they were able to vary the lateral dimensions of the CuS nanodisks over a wide range while maintaining the thickness at 4 nm, resulting in nanodisks with different aspect ratios. As the LSPR wavelength is sensitive to the aspect ratio, tunable plasmonic absorption was achieved.

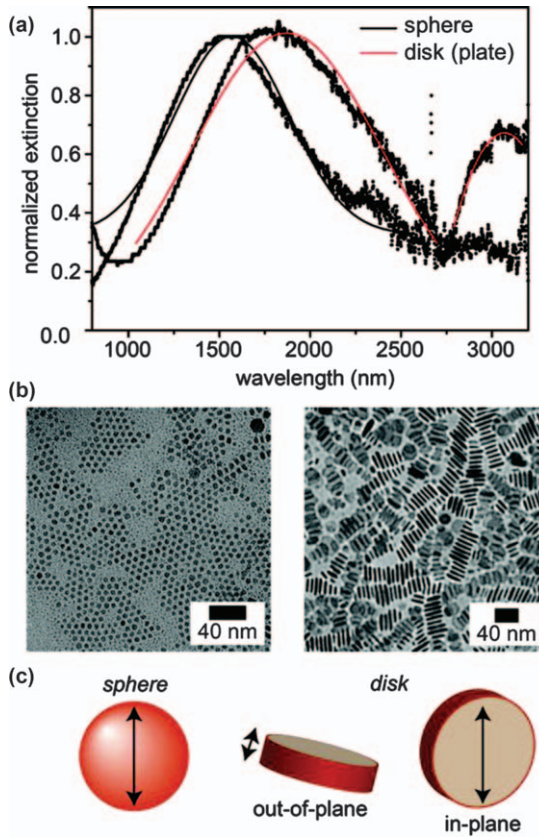

Figure 5.3 Shape-dependent LSPR of $Cu_{2-x}S$ nanocrystals. (a) Optical extinction spectra, (b) TEM images, and (c) schematic illustrations of LSPR polarizations for spherical and disk-shaped nanocrystals. The black and red solid lines in (a) are the best fits of the extinction peaks.
Reproduced from ref. 31 with permission from American Chemical Society, Copyright 2011.

A morphological characteristic that is desirable in photothermal applications is porosity. The incorporation of porous features in nanomaterials affords several advantages over nonporous counterparts of similar size, and these benefits include lower density, larger surface area, and better surface permeability.[35] Moreover, since photothermal activity heavily relies on the light harnessing ability of the material, a porous architecture is advantageous because it allows for stronger photon absorption. The pores can function as optical cavity mirrors that can trap light and enable multiple light reflection and scattering.[36] This eventually leads to improved light–material interaction and high light utilization efficiency. The formation of porous nanostructures usually follows an aggregation-based mechanism, where smaller colloidal nanostructures spontaneously aggregate in solution to form hierarchical superstructures. Multiple cavities are generated as the initial nanostructures self-assemble, and

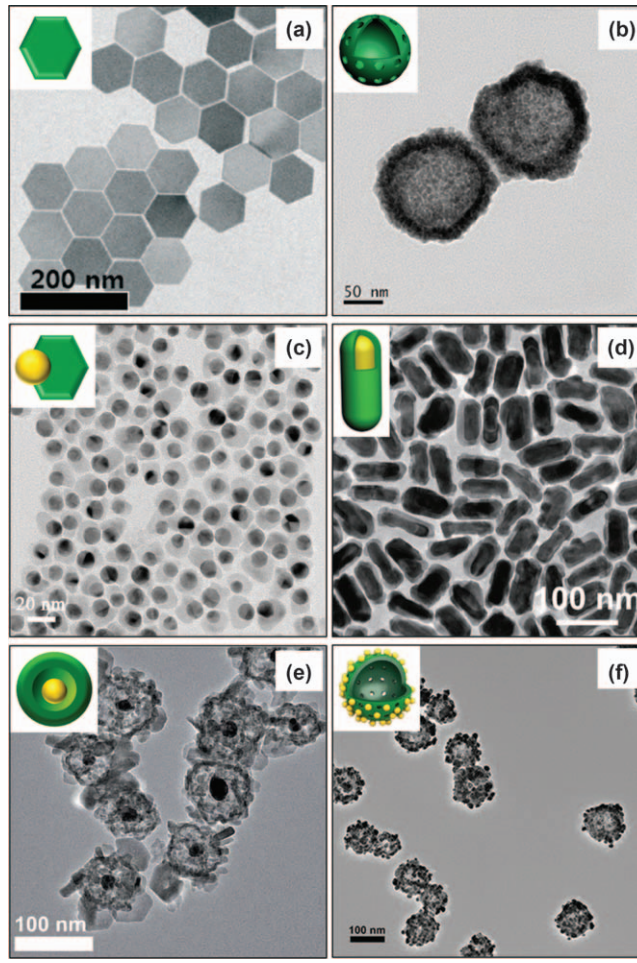

Figure 5.4 TEM images and schematic illustrations (shown as insets) of different $Cu_{2-x}S$-based nanostructures. (a) Hexagonal $Cu_{1.94}S$ nanodisks. Reproduced from ref. 32 with permission from the Royal Society of Chemistry. (b) Hollow-porous CuS nanospheres. Reproduced from ref. 39 with permission from Elsevier, Copyright 2016. (c) Au–CuS nanoheterodimers. Reproduced from ref. 41 with permission from the Royal Society of Chemistry. (d) Core–shell Au–$Cu_{1.75}S$ nanorods. Reproduced from ref. 44 with permission from John Wiley and Sons, Copyright © 2018 WILEY-VCH Verlag GmbH & Co. KGaA, Weinheim. (e) Yolk–shell Au–$Cu_{1.75}S$ nanostructures. Reproduced from ref. 46 with permission from the Royal Society of Chemistry. (f) Core–satellite CuS/Cu_2S–Au nanostructures. Reproduced from ref. 51 with permission from John Wiley and Sons, Copyright © 2017 WILEY-VCH Verlag GmbH & Co. KGaA, Weinheim.

this accounts for the porosity of the final superstructures. Mu *et al.* used the microwave irradiation method to prepare porous CuS microspheres with a hierarchical flower-like configuration.[37] The precursor solution was first

prepared by mixing $CuCl_2$, thiourea, NaOH, and EDTA, which served as both a chelating agent and a surface-capping agent. This solution was then subjected to microwave irradiation for several minutes under a N_2 atmosphere. From transmission electron microscopy (TEM) images, it was found that the flower-like spheres are made up of petal-like nanosheets as assembly units.

In certain cases, porous superstructures with a huge void at the center (*i.e.*, hollow) are produced, such as in the case of the acanthosphere-like CuS superstructures that were reported by Zhang and co-workers.[38] Synthesis was performed through solvothermal heating of a methanolic solution containing $Cu(CH_3COO)_2$, thiourea, and CH_3COOH at 100 °C for 8 h. TEM analysis revealed that the hollow-porous structure consists of 10 nm nanoflakes and nanorods as building blocks. This type of architecture is suitable for loading and transport of drugs, and can thus be utilized in photothermal-controlled drug delivery. The use of a template is another means of constructing hollow nanostructure morphologies. Hollow-porous nanospheres of CuS (Figure 5.4b) and $Cu_{1.12}S$ have been fabricated through this strategy using pre-synthesized Cu_2O nanospheres as the starting template material.[39,40] In this template-mediated approach, the sulfidation of the sacrificial Cu_2O template is achieved through addition of Na_2S, which reacts with the template surface to form a thin layer of copper sulfide shell. As sulfidation proceeds, interior voids are generated due to the Kirkendall effect since the outward diffusion of copper cations is faster than the inward diffusion of sulfur anions.

5.2.2 Copper Sulfide-based Nanocomposites

As the popularity of plasmonic $Cu_{2-x}S$ nanomaterials started to rise, scientists have begun to delve deeper into the modification and enhancement of their properties to allow for multimodal applications. Several studies have focused on the creation of composites or hybrids (also called heterostructures), where $Cu_{2-x}S$ is coupled with another material with equally interesting properties. The synthetic protocols that have been used in constructing such hybrids are reviewed in this subsection.

5.2.2.1 Au–$Cu_{2-x}S$ Hybrid

The combination of $Cu_{2-x}S$ with another plasmonic material can enable the creation of a dual-plasmonic system with multiple optical resonance modes. Au, being the most widely studied plasmonic metal, is the most commonly paired plasmonic material with $Cu_{2-x}S$. A wide range of Au–$Cu_{2-x}S$ hybrid configurations have already been reported (*e.g.* heterodimer, core–shell, yolk–shell), examples of which are shown in the TEM images in Figure 5.4c–f. Sun *et al.* demonstrated the synthesis of Au–CuS nanocomposites with a heterodimer (or Janus) configuration (Figure 5.4c).[41] They employed a seed-mediated growth technique, where colloidal Au nanocrystals are synthesized first and then used as seeds for the subsequent growth of CuS. The reaction between the pre-synthesized Au seeds and the CuS precursors

(*i.e.*, $Cu(acac)_2$ and S) was carried out at 100 °C under N_2, with combined dichlorobenzene and oleylamine as the solvating medium. It was noted that oleylamine is essential as the activating agent for the formation of CuS. However, its concentration in the reaction mixture should be kept low to avoid rapid nucleation of CuS as this can result in homogeneous nucleation of free CuS nanocrystals. The resulting two-faced hybrid consists of quasi-spherical Au on one side and plate-like CuS on the other side. A similar configuration was achieved by Ding *et al.* in their synthesis of Au–$Cu_{1.8}S$ nanocomposites by also using the seeded growth method.[26] On the other hand, Wang *et al.* were able to prepare Au–CuS nanoheterodimers through the galvanic exchange route.[42] In this case, CuS nanoplates were prepared first and were later mixed with $HAuCl_4$ in water under magnetic stirring at ambient conditions. Galvanic replacement of Cu by Au enabled the *in-situ* growth of Au nanocrystals on the CuS nanoplates. Moreover, increasing the reaction time was found to increase the size and the number of Au nanocrystals on each plate.

Sun and co-workers recently reported the synthesis of Au–$Cu_{2-x}S$ nanocomposites with a core–shell structure that consists of a quasi-spherical Au core and a polycrystalline $Cu_{2-x}S$ shell.[43] They utilized a seeded growth protocol, where pre-synthesized Au seeds are coated entirely with $Cu_{2-x}S$ when heated in ethylene glycol (EG). $Cu(NO_3)_2$ and thiourea were used as the Cu and S precursors, respectively, and the reaction with Au seeds was performed at the boiling temperature of EG. By adjusting the precursor molar ratios, the $Cu_{2-x}S$ shell was able to grow in a phase-selective and thickness-controlled manner. Keeping the Cu : S precursor molar ratio at 1 : 3 enabled the selective growth of CuS shells without forming other $Cu_{2-x}S$ phases. On the other hand, a 3 : 1 Cu : S precursor molar ratio led to the exclusive formation of $Cu_{1.8}S$ shells. In both cases, the thickness of the shell can be tuned by adjusting the amount of the Cu precursor relative to that of the Au seeds. The TEM images and the extinction spectra of the core–shell Au–CuS nanostructures with varying shell thickness are displayed in Figure 5.5. The broad NIR absorption band peaking at around 1000 nm is attributed to the plasmonic hole oscillations in the CuS shells. This peak becomes more intense with increasing shell thickness because of the increasing CuS content. Meanwhile, the distinct absorption peak at around 540–620 nm in the visible region is due to the plasmonic electron oscillations in the Au cores. As the LSPR of Au is highly sensitive to the surrounding environment, a systematic red-shifting of the Au plasmon peak is observed with the thickening of the CuS shells due to the high refractive index of CuS. Aside from the two plasmon-induced absorption bands, there exists another band at around 400 nm, which is ascribed to the interband electronic transitions from the valence band to the conduction band of CuS. The intensity of this band strengthens with increasing thickness of the CuS shell.

A core–shell hybrid arrangement was also created by Leng *et al.* in their synthesis of Au–$Cu_{1.75}S$ nanorods (Figure 5.4d).[44] Pre-synthesized Au nanorods were used as the starting seeds, and the $Cu_{1.75}S$ shell was grown through hydrothermal reaction of the Au seeds with $Cu(NO_3)_2$ and $Ni(PhCOS)_2$

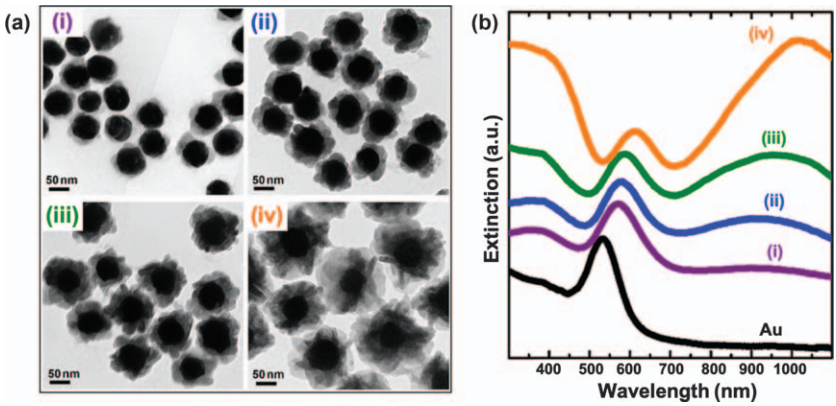

Figure 5.5 (a) TEM images and (b) optical extinction spectra of core–shell Au–CuS nanostructures that are composed of 62 nm Au cores and CuS shells with various thicknesses. The four samples were labeled as (i), (ii), (iii), and (iv) in the order of increasing CuS shell thickness.
Reproduced from ref. 43 with permission from American Chemical Society, Copyright 2020.

at 140 °C in the presence of the cationic surfactant, cetyltrimethylammonium bromide (CTAB). Interestingly, when thinner Au nanorods were used as seeds, site-selective growth of $Cu_{1.75}S$ occurred, in which the nanorod ends were preferentially capped. As a consequence, hybrid nanostructures with a dumbbell-like morphology were primarily obtained. The inhomogeneous shell growth in thinner nanorods is likely due to their more curved ends, which are favorable sites for nucleation. In a recent study by Wang *et al.*, it was found that the growth of $Cu_{2-x}S$ on Au nanorods can be regulated by adjusting the amount of CTAB and bovine serum albumin (BSA) in the reaction mixture.[45] The authors noted that when CTAB and BSA are surface-bound to the Au nanorod seeds, Cu-coordination sites are created, which can facilitate the formation of $Cu_{2-x}S$. At low concentrations of these capping agents, $Cu_{2-x}S$ nucleates and grows only on one side of the rod, resulting in a heterodimer configuration. On the other hand, high concentrations of these reagents allow for multiple nucleation of $Cu_{2-x}S$ islands, which eventually grow and merge into a shell that covers the nanorod entirely.

An emerging hybrid configuration is the yolk–shell (or rattle-type) structure, which is composed of a core that is encased within a hollow shell. The main feature that distinguishes it from the core–shell structure is the interstitial space between the inner core and the outer shell. Because of this interior void, there can be multiple reflections of light between the core and the shell, and this is beneficial for maximum utilization of light energy. Zhang *et al.* carefully designed a yolk–shell structure that consists of an interior Au core and a hollow-porous $Cu_{1.75}S$ (or Cu_7S_4) shell (Figure 5.4e).[46] They employed a template-mediated synthetic strategy using core–shell Au–Cu_2O nanostructures as the template material. When Na_2S was added to the template, sulfidation of

the Cu_2O shell readily occurred due to the lower solubility product of $Cu_{1.75}S$ ($K_{sp} = 1 \times 10^{-48}$) as compared to Cu_2O ($K_{sp} = 2 \times 10^{-15}$).[47] During the sulfidation process, Kirkendall voids were created and this enabled the transformation of the initial core–shell structure into a yolk–shell architecture. This type of templating technique was also employed by Chang *et al.* in their synthesis of a yolk–shell composite comprising a central Au core and a hollow-porous CuS shell.[48] A series of Au cores were utilized, from nanospheres to differently-sized nanorods. As shown in Figure 5.6, the different Au cores resulted in LSPR absorption peaks at 520, 700, 808, 860, and 980 nm. Meanwhile, Yu *et al.* prepared a yolk–shell hybrid that is composed of a rod-shaped Au core and an octahedral-shaped hollow $Cu_{1.75}S$ shell.[49] The template that was used was a core–shell hybrid where the Au nanorod is entirely coated with a solid Cu_2O nanooctahedron. This template was converted into the yolk–shell product after reacting with Na_2S. The thickness of the $Cu_{1.75}S$ shell was varied by adjusting the Cu_2O : Na_2S molar ratios, where an increase in the amount of Na_2S led to thicker shells. With the increase in shell thickness, the LSPR absorption peaks become less intense, indicating that the LSPR response of Au can be negatively impacted by thick $Cu_{1.75}S$ shells.

In applications where the surface-enhanced Raman scattering (SERS) effect of Au is essential, a hybrid configuration where Au is the exterior component is more ideal. Lv *et al.* described the synthesis of a unique core–shell hybrid

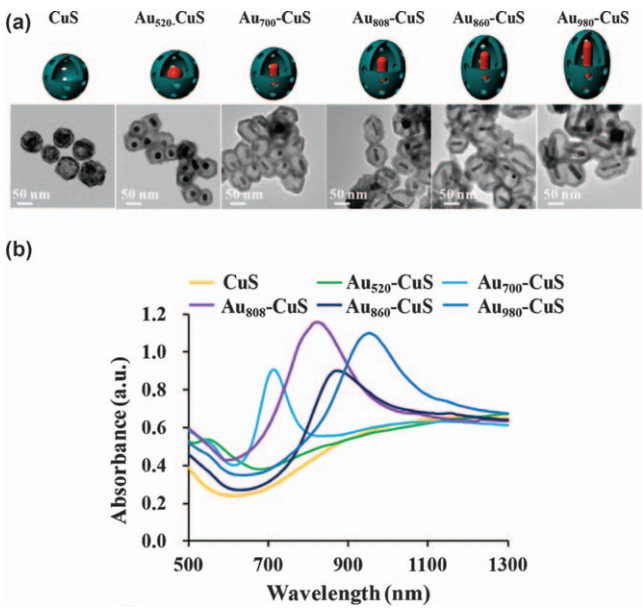

Figure 5.6 (a) TEM images with schematic illustrations and (b) optical extinction spectra of yolk–shell Au–CuS nanostructures with varying sizes. The samples were labeled according to the LSPR absorption peak of their Au core. Reproduced from ref. 48 with permission from American Chemical Society, Copyright 2018.

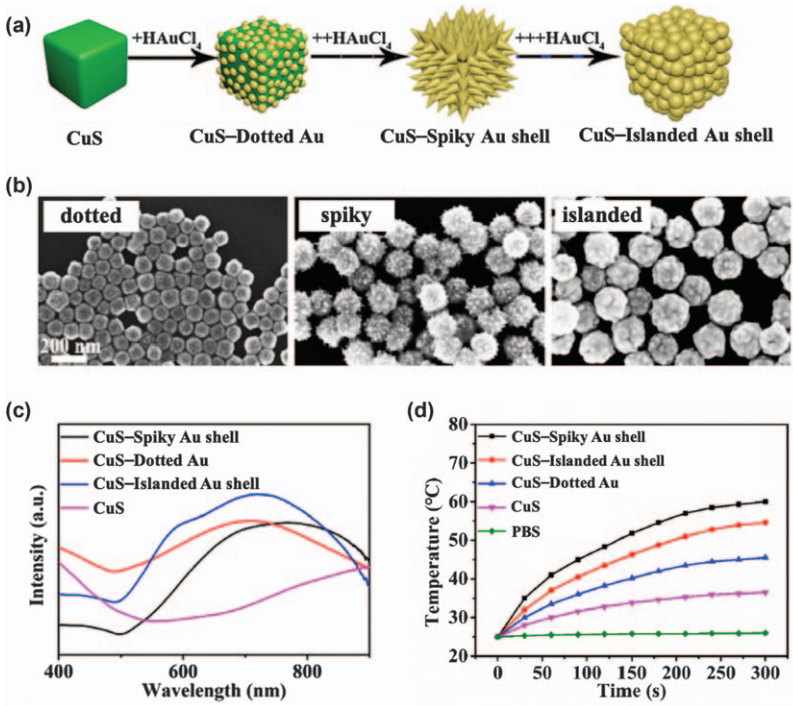

Figure 5.7 (a) Schematic illustrations, (b) SEM images, (c) optical extinction spectra, and (d) photothermal profiles of CuS–Au nanostructures, where cubic CuS cores are coated with Au shells of various morphologies (*i.e.*, dotted, spiky, and islanded).
Reproduced from ref. 50 with permission from the Royal Society of Chemistry.

consisting of a hollow CuS nanocube core that is enclosed by a spiky Au shell.[50] First, hollow CuS nanocubes were synthesized from Cu_2O nanocubes through the template-assisted method. Ascorbic acid (AA) and $HAuCl_4$ were then added successively for the growth of the Au shell. It was noted that the Au shell morphology can be varied by adjusting the molar ratio of $HAuCl_4$ to AA. The shell morphology evolved from dotted to spiky to islanded with increasing amount of $HAuCl_4$ (Figure 5.7). In the dotted configuration, the hollow CuS cubic core is decorated with tiny spherical Au satellites. This type of core–satellite arrangement has also been reported by Deng *et al.* but with a hollow-porous two-layered CuS/Cu_2S spherical core (Figure 5.4f).[51]

5.2.2.2 *Other $Cu_{2-x}S$ Hybrids*

Aside from Au, other plasmonic noble metals such as Ag and Pt have been coupled with $Cu_{2-x}S$ for the enhancement of the photothermal conversion efficiency.[52,53] In the case of Pt, its catalase-like activity can be utilized to aid

in cancer therapy. Liang *et al.* recently reported a Pt–CuS hybrid with a hollow-porous Janus architecture.[53] In their synthesis, pre-synthesized hollow-porous CuS nanospheres were spread evenly onto a clean silicon wafer to form a monolayer, and then a catalytic Pt layer was deposited onto the top surface of the nanospheres through a vacuum metal sputter deposition method. The resultant Pt–CuS Janus nanostructures were released from the substrate after ultrasonic treatment in water.

Other $Cu_{2-x}S$ hybrids that have been reported make use of materials with properties that are not exhibited by $Cu_{2-x}S$ so as to integrate additional functionalities that cannot be provided by $Cu_{2-x}S$ alone. For example, to endow the hybrid with magnetic capability, Wu *et al.* developed a yolk–shell composite where ferromagnetic Fe_3O_4 nanoparticles are delocalized inside hollow-porous CuS nanostructures.[54] CTAB-coated Fe_3O_4 nanoparticles were prepared first, and these were coated with Cu_2O by mixing with $Cu(NO_3)_2$, hydrazine, and PVP. It was noted that the electrostatic interactions between positively-charged CTAB and negatively-charged PVP facilitated the formation of the Fe_3O_4–Cu_2O core–shell structure. Sulfidation of the Cu_2O shell by addition of $(NH_4)_2S$ yielded the final yolk–shell Fe_3O_4–CuS hybrid. Meanwhile, Chen and co-workers demonstrated the pairing of CuS with chromium-doped persistent luminescence nanoparticles (PLNPs) to create an activatable photothermal nanoprobe with an ultralow background for *in vivo* luminescence imaging.[55] Peptide-functionalized PLNPs and citrate-capped CuS nanoparticles were first prepared separately. They were then mixed together in the dark with constant stirring for 3 h to form the composite. The peptide-functionalized PLNPs have terminal –SH groups that can conjugate to the CuS nanoparticles *via* Cu–S bonds and thus facilitate the formation of a core–satellite hybrid structure, where a PLNP core is surrounded with multiple CuS nanoparticles. Further surface modification was performed to enable the nanoprobe for tumor-targeted luminescence imaging-guided photothermal therapy.

5.3 Applications in Photothermal Therapy (PTT)

Photothermal therapy (PTT) is a minimally-invasive treatment approach that relies on the ability of an optically active material to absorb light and convert it into heat (*i.e.*, the photothermal effect). The heat that is generated is then used for therapeutic purposes. $Cu_{2-x}S$ nanomaterials are suitable photothermal agents for biomedical applications because their photothermal effect is stimulated by light in the NIR spectral window, which is often referred to as the biological transparency window or the therapeutic window. With wavelengths that range from 700 to 1400 nm, NIR light is less energetic than visible light and is less absorbed by tissue components (*e.g.* water and blood).[56,57] Thus, it allows for deeper tissue penetration and improved spatial/temporal tissue resolution. In addition, it enables better localization of heat, which ensures that only the targeted cells are thermally damaged during PTT.

The photothermal behavior is typically assessed by monitoring the change in temperature (ΔT) over time when an aqueous dispersion of the nanostructures is exposed to NIR light. A positive ΔT is expected for photothermal nanostructures because the light-to-heat conversion causes a rise in temperature. In terms of magnitude, a larger ΔT is indicative of better photon absorption capability, which translates to enhanced photothermal activity because the more light that is absorbed, the greater the heat that will be produced. The magnitude of ΔT is concentration-dependent as exemplified in Figure 5.8a for 11 nm CuS nanoparticles.[58] While there is no marked change in temperature for pure water upon exposure to NIR light, an increase in ΔT is observed with increasing amounts of CuS nanoparticles in water. The nanostructure morphology also influences the magnitude of ΔT. For example, Tian *et al.* compared the photothermal conversion capability of CuS nanoplates and their hierarchical flower-like superstructures.[59] As depicted in Figure 5.8b, the superstructures can serve as excellent laser-cavity

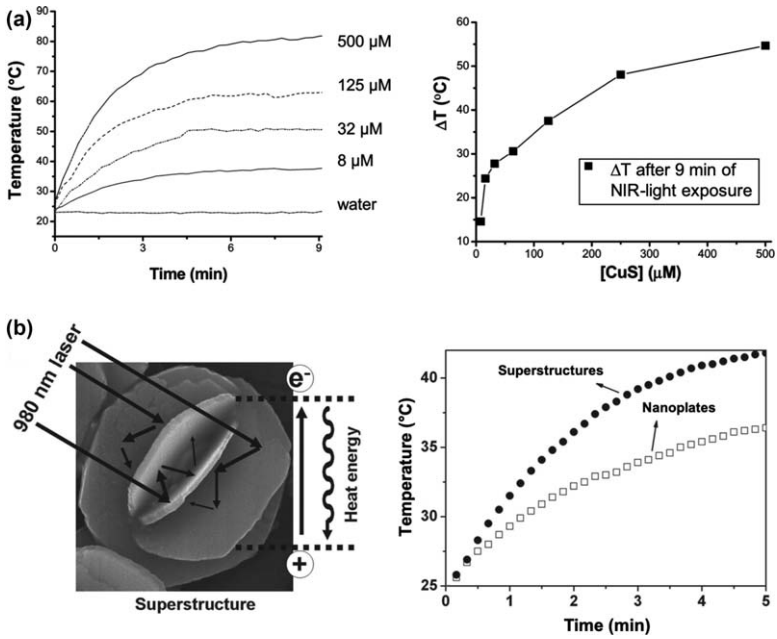

Figure 5.8 (a) Concentration-dependent temperature elevation (ΔT) of aqueous dispersions of CuS nanoparticles induced by NIR laser irradiation at 808 nm with a power density of 16 W cm^{-2}. Reproduced from ref. 58 with permission from American Chemical Society, Copyright 2010. (b) Morphology-dependent photothermal profiles of CuS superstructures and their nanoplate building blocks (sample concentration: 0.25 g L^{-1}; NIR laser: 980 nm with a power density of 0.51 W cm^{-2}). The figure on the left shows a schematic representation of a CuS superstructure serving as laser-cavity mirrors and its photothermal conversion. Reproduced from ref. 59 with permission from John Wiley and Sons, Copyright © 2011 WILEY-VCH Verlag GmbH & Co. KGaA, Weinheim.

mirrors that allow for enhanced light–material interaction, thereby promoting stronger photon absorption. Thus, the superstructures induced a larger temperature rise relative to their plate-like building blocks upon irradiation with a 980 nm laser. Hybrid formation can also lead to a larger ΔT as demonstrated in Figure 5.7d for the coupling of CuS with Au.[50] This is due to the hybrid's ability to absorb more NIR photons than the uncoupled CuS.

5.3.1 Cancer Therapy

In utilizing the photothermal effect for cancer treatment, the heat that is produced upon NIR-light stimulation is exploited in the destruction of cancer cells through the hyperthermia effect. Table 5.1 provides a list of the various copper sulfide-based nanostructures that have been examined as photothermal therapeutic agents for the ablation of cancer cells. Prior to their use, the nanostructures are typically subjected to surface functionalization with amphiphilic macromolecules or polymers (*e.g.* polyethylene glycol (PEG) and its derivatives) to improve their biocompatibility and water-dispersibility.[60,62] For instance, Huang *et al.* modified the surface of their hydrophobic CuS nanoparticles with a phospholipid–PEG coating to transfer them to the aqueous phase.[63] When intravenously injected into mice, no noticeable signs of organ damage were observed (Figure 5.9a), implying that the PEGylated CuS nanoparticles exhibit good biocompatibility. Moreover, infrared (IR) thermal imaging showed that when the nanoparticle-injected tumor-bearing mice were exposed to 808 nm light, the tumor surface temperature increased rapidly within 5 min of irradiation (Figure 5.9b). This demonstrates the excellent photothermal conversion capability of the CuS nanoparticles. Motivated by these results, additional *in vivo* studies were conducted, where effective tumor elimination was achieved after 6 days for photothermally-treated mice.

Guo and co-workers rationally engineered a CuS-based therapeutic agent for combinatorial therapy that involves both PTT and immunotherapy.[64] Their design consists of chitosan-coated hollow-porous CuS nanospheres that are conjugated to oligodeoxynucleotides containing cytosine–guanine (CpG) motifs, which are known immunoadjuvants that can trigger specific antitumor immunity. After NIR-light excitation, these structures break down, releasing smaller CuS nanoparticles as well as chitosan–CpG complexes. While the CuS component was able to treat local tumors at the primary site through photothermal ablation, the chitosan–CpG complex was found effective in inducing systemic immunity against both primary treated and distant untreated tumors. Thus, a more potent anticancer effect was achieved. Furthermore, it was shown that the disintegrated CuS nanostructures are biodegradable and can be cleared from the body through both hepatobiliary and renal excretion.

Photothermally responsive $Cu_{2-x}S$-based nanomaterials are also deemed suitable for controlled drug delivery because they are able to regulate the release of drugs through NIR light-induced heating. This makes it possible to construct a bimodal therapeutic system based on $Cu_{2-x}S$ that combines PTT and chemotherapy. For efficient loading and delivery of drugs, a hollow-porous

Table 5.1 Photothermally responsive copper sulfide-based nanostructures for cancer treatment.

Composition	Morphology and size	Therapeutic modality	Diagnostic modality	Reference
CuS	Spherical, 3.8 nm	PTT		63
CuS	Flower-like superstructures, 1–2 μm	PTT		59
CuS	Hollow-porous spherical superstructures, 85 nm	PTT and Immunotherapy		64
CuS	Hollow-porous acanthosphere-like superstructures, 160 nm, wall thickness of 35 nm	PTT and Chemotherapy	PAI	38
CuS	Hollow-porous spheres, 100 nm, wall thickness of 20 nm	PTT, PDT and Chemotherapy	PAI	39
$Cu_{1.12}S$	Hollow spheres, 18 nm, wall thickness of 3.5 nm	PTT and CDT	PAI	40
$Cu_{1.8}S$	Spherical, 20 nm	PTT		60
$Cu_2S + Cu_{1.94}S$	Spherical, 6.5 nm	PTT and PDT		62
$Cu_{2-x}S$	Spherical, 2 nm	PTT	PAI	61
$Cu_{2-x}S$	Spherical, 5 nm	PTT and CDT	PAI	65
[^{64}Cu]CuS	Spherical, 5.6 nm	PTT	PET/CT imaging	70
[^{64}Cu]CuS	Spherical, 11 nm	PTT and Radiotherapy	PET/CT imaging	58, 69
CuS–Au	Core–shell Core: hollow-porous CuS cube, 78 nm Shell: spiky Au shell, varied thickness	PTT	SERS intracellular imaging	50
CuS/Cu_2S–Au	Core–satellite, 100 nm Core: hollow-porous spherical CuS/Cu_2S Satellites: tiny Au dots	PTT and Chemotherapy	PAI	51
Au–CuS	Yolk–shell, 101 nm Core: Au rod/sphere, size was varied Shell: hollow-porous elliptical CuS, 15 nm thick	PTT, PDT and Chemotherapy		48

Au–CuS	Heterodimer Au quasi-sphere (size was varied) + CuS hexagonal plate, ~70 nm	PTT	CT imaging	42
Au–$Cu_{1.75}S$	(a) Core–shell nanorods Core: Au rods, 37×84 nm Shell: CuS shell, thickness of 5–12 nm (b) Dumbbell-like $Cu_{1.75}S$-tipped Au rods, 21×61 nm	PTT		44
Au–$Cu_{1.8}S$	Heterodimer, ~20 nm Au quasi-sphere + $Cu_{1.8}S$ plate	PTT	CT imaging	26
Au–$Cu_{2-x}S$	Heterodimer (Au rod + $Cu_{2-x}S$ sheet) Au rod: 17×60 nm $Cu_{2-x}S$ sheet: 28×64 nm, 12 nm thick	PTT and CDT		45
Ag–CuS	Heterodimer, spherical, 10–20 nm	PTT		52
Pt–CuS	Hollow-porous Janus spheres, 120 nm	PTT and SDT	PAI	53
Fe_3O_4–CuS	Yolk–shell, 139 nm Core: octahedral Fe_3O_4, 28 nm Shell: hollow-porous spherical CuS, 27 nm thick	PTT	MRI	54
PLNP–CuS	Core–satellite, 141 nm Core: irregularly shaped PLNP, 79 nm Satellites: CuS quasi-spheres, 12 nm	PTT	Luminescence imaging	55

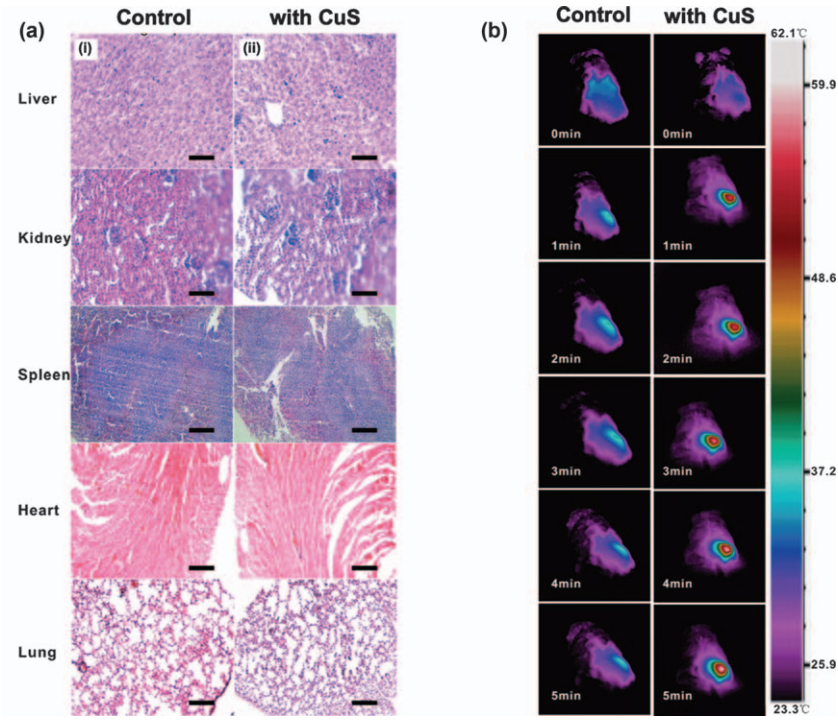

Figure 5.9 (a) Histochemical study of the organs harvested from mice 24 h after injection of PEGylated CuS nanoparticles (Scale bars: 100 mm). (b) Infrared thermal imaging 24 h after intravenous injection of CuS nanoparticles into mice (NIR laser: 808 nm with a power density of 1 W cm^{-2}). For both (a) and (b), results from the control group (*i.e.*, no CuS injected) are also shown.
Reproduced from ref. 63 with permission from John Wiley and Sons, Copyright © 2015 WILEY-VCH Verlag GmbH & Co. KGaA, Weinheim.

architecture is usually desired, such as the acanthosphere-like morphology of the CuS superstructures that were developed by Zhang *et al.*[38] With their mesoporous shell and hollow interior, these CuS superstructures were found to exhibit high drug loading capacity for doxorubicin (DOX), a widely used chemotherapeutic drug (Figure 5.10a). Moreover, it was demonstrated that the release of the loaded DOX molecules is NIR- and pH-sensitive, allowing for controlled drug release. Both *in vitro* (Figure 5.10b) and *in vivo* (Figure 5.10c) experiments showed that when compared to either PTT or chemotherapy alone, the combination of PTT and chemotherapy presented better anticancer efficacy owing to synergistic effects. In addition, it was noted that the superstructures can break apart into smaller particles that can be readily excreted by the body after therapy is completed. Deng *et al.* also reported a synergistically enhanced antitumor efficacy for their hollow-porous CuS/Cu_2S–Au hybrid nanostructures due to combined PTT and chemotherapy effects.[51] To endow the hybrid with photoactivated targeting capability, the surface was

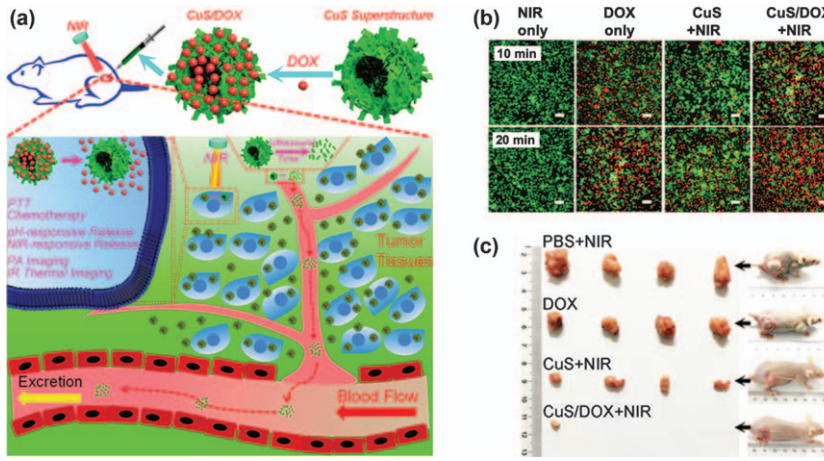

Figure 5.10 (a) Schematic depiction of acanthosphere-like CuS superstructures and their use as a clearable multimodal theranostic agent for cancer treatment. (b) Fluorescence images of HeLa cells subjected to different treatment conditions (Scale bars: 100 μm). The cells were co-stained with calcein AM (green, living cells) and propidium iodide (red, dead cells). (c) Photographs of tumor-bearing mice and tumors after 20 days of treatments.
Reproduced from ref. 38 with permission from the Royal Society of Chemistry.

functionalized with a thermosensitive copolymer and a photoswitchable tumor targeting ligand. This promoted tumor cellular uptake and reduced off-target toxicity as nonspecific binding to normal cells is prevented.

Very recently, the potential utility of $Cu_{2-x}S$ nanostructures for combined PTT and chemodynamic therapy (CDT) has been explored.[40,45,65] CDT is an emerging cancer treatment approach with minimal invasiveness, high tumor specificity and selectivity, and low systemic toxicity and side effects.[66] It operates through Fenton chemistry, where endogenous H_2O_2 that is overproduced in the tumor microenvironment is converted to hydroxyl radicals ($^{\bullet}OH$) in the presence of a suitable catalyst. The generated $^{\bullet}OH$, which is a reactive oxygen species (ROS), causes oxidative stress that leads to the destruction of tumor cells. $Cu_{2-x}S$-based nanomaterials can serve as CDT agents because the copper ions can effectively catalyze the decomposition of H_2O_2 to produce $^{\bullet}OH$ radicals. Moreover, when photothermally active $Cu_{2-x}S$ nanostructures are irradiated with NIR light, the resulting temperature elevation can promote tumor eradication in two ways: (i) by PTT-induced tumor cell death and (ii) by accelerating the production of $^{\bullet}OH$ radicals, which enhances the CDT effect.[65] Thus, the $Cu_{2-x}S$-enabled coupling of PTT and CDT can result in a superadditive therapeutic performance. As the catalytic efficiency is largely dependent on the number of catalytic active sites, a nanostructure morphology that has a large surface area can further enhance the therapeutic effect. This has been demonstrated by Wang *et al.* through

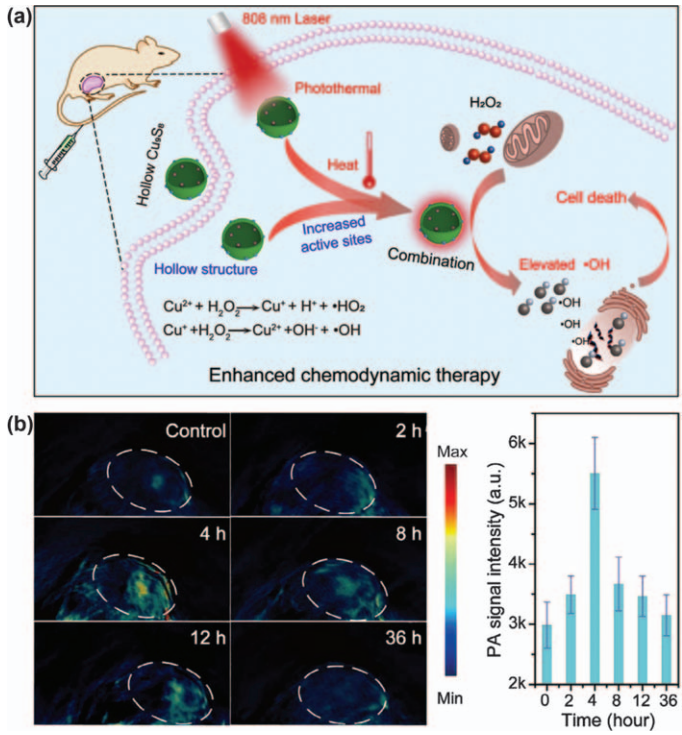

Figure 5.11 (a) Schematic diagram showing the combined PTT and CDT capabilities of hollow $Cu_{1.12}S$ (or Cu_9S_8) nanospheres. (b) *In vivo* photoacoustic images of tumor-bearing mice (tumors are marked by white circles) at different time points after intravenous injection of hollow $Cu_{1.12}S$ nanospheres. The corresponding photoacoustic signal intensities are shown on the right.
Reproduced from ref. 40 with permission from Elsevier, Copyright 2020.

the use of hollow-porous $Cu_{1.12}S$ nanospheres, as schematically illustrated in Figure 5.11a.[40] They observed that the hollow-porous $Cu_{1.12}S$ nanospheres displayed better CDT effect than their solid counterparts in both *in vitro* and *in vivo* experiments, and this was attributed to the increased number of catalytic active sites in the hollow-porous structure.

A bimodal therapeutic system can also be achieved through coupling of PTT with photodynamic therapy (PDT). Similar to PTT, PDT is a low-invasive cancer treatment method that requires light irradiation. However, it is more akin to CDT in terms of the mechanism by which cancer cells are destroyed as it is also ROS-mediated. In general, PDT utilizes a light-responsive agent (*i.e.*, a photosensitizer) and endogenous molecular oxygen (O_2) to produce cytotoxic ROS when exposed to light.[67] Many of the photosensitizers that have been initially explored can be excited only by visible light. In the case of $Cu_{2-x}S$ nanocrystals, Wang *et al.* found that activation by NIR light did not only result in heat

generation but also led to elevated levels of ROS, which can cause a high degree of irreversible damage to diseased cells.[62] Thus, they ascribed the overall antitumor efficacy of their $Cu_{2-x}S$ nanocrystals to combined hyperthermia (PTT) and ROS-induced (PDT) effects. For $Cu_{2-x}S$-based nanomaterials with a hollow-porous architecture, a multimodal therapeutic platform that integrates chemotherapy with PTT and PDT becomes possible as this type of morphology enables encapsulation of chemotherapeutic drugs.[39,48]

Sonodynamic therapy (SDT) is another promising ROS-mediated curative modality that can be coupled with PTT to produce synergistic therapeutic effects. Unlike PDT, which relies on light stimulation, SDT makes use of ultrasound to trigger the generation of cytotoxic ROS. The main advantage of SDT over PDT is that ultrasound can penetrate tissues more deeply than light, and this is beneficial for treatment of deeply located tumors.[68] The SDT agent, which reacts with endogenous O_2 to produce ROS when activated by ultrasound cavitation, is called a sonosensitizer. The role of nanomaterials in SDT is broadly classified into two types: (1) as the actual sonosensitizer and (2) as the sonosensitizer carrier. In the work of Liang *et al.*, hollow-porous Pt–CuS Janus nanostructures were used as carriers for the delivery of sonosensitizers to diseased cells.[53] The large inner cavity of the nanostructures is advantageous for loading the organic porphyrin-based sonosensitizer, tetra-(4-aminophenyl)porphyrin. *In vivo* studies showed that the combination of PTT and SDT can lead to complete tumor eradication without an obvious recurrence. The presence of Pt was credited for the remarkable antitumor efficacy as it can enhance the PTT effect by increasing hot electron generation, which increases the photothermal conversion efficiency. In addition, Pt can catalyze the decomposition of endogenous H_2O_2 to produce O_2 that can relieve tumor hypoxia and augment the SDT-induced production of ROS.

Ionizing radiation can also be utilized to induce tumor cell death in a process called radiation therapy (or radiotherapy). To combine PTT with radiotherapy, Zhou *et al.* incorporated ^{64}Cu, a beta-emitting radionuclide, to produce [^{64}Cu]CuS nanoparticles that are both photothermally active and radioactive.[69] They found that the use of PTT in conjunction with radiotherapy can effectively suppress breast tumor metastasis through eradication of tumor-initiating cells (TICs). These TICs are self-renewing cells that are involved in tumor initiation and maintenance; hence, their complete elimination can prevent the dreaded tumor recurrence and metastasis.

5.3.2 Cancer Theranostics

Apart from exhibiting photothermal properties, many of the $Cu_{2-x}S$-based nanomaterials discussed in this chapter also possess imaging capabilities. Because of this, they can be an ideal multimodal system for cancer theranostics, where they function not only as therapeutic agents but also as diagnostic agents. Photoacoustic imaging (PAI) is one of the imaging modalities where $Cu_{2-x}S$ nanomaterials can be used as a photothermally activatable contrast agent. In PAI, the biological tissues and contrast agent

are irradiated with short laser pulses to generate thermoelastic expansion and ultrasonic signals, which are then detected and analyzed to produce images.[10] The information that can be obtained from the photoacoustic images can be used to guide PTT. For instance, Wang *et al.* used PAI to monitor the time at which the maximum accumulation of hollow-porous $Cu_{1.12}S$ nanospheres occurred at the tumor site after intravenous administration to a tumor-bearing mouse.[40] As seen in Figure 5.11b, the photoacoustic signal intensity reached its highest value at 4 h, which indicates that $Cu_{1.12}S$ is maximally enriched in the tumor site 4 h post-injection.

Radiolabeled [^{64}Cu]CuS nanoparticles can be employed as radiotracers for positron emission tomography (PET), a highly sensitive diagnostic tool that utilizes radioactive substances to serve as tracers that can detect changes in metabolic processes in the body.[58,69,70] A PET scan is typically combined with a computed tomography (CT) scan to obtain superimposed images that can help provide more detailed and accurate information. Zhou *et al.* used PET/CT imaging to investigate how the size of CuS nanoparticles can influence their pharmacokinetics and biodistribution.[70] The PET/CT images in Figure 5.12 revealed that the 5.6 nm particles had lower uptake in most major organs at 24 h after intravenous injection as compared to the larger 19 nm particles. Moreover, it can be deduced from the images that the smaller nanoparticles initially accumulated in the kidney and the bladder, but renal clearance was nearly completed at 2 h post-injection. Meanwhile, the 19 nm particles were largely taken up by the liver and most remained even after 24 h. This indicates that small-sized CuS nanoparticles (<6 nm) exhibit a shorter elimination half-life and faster systemic clearance, which are desirable in minimizing long-term risk of adverse side effects.

In many cases, the imaging functionality is integrated by creating a hybrid of $Cu_{2-x}S$ with a material with diagnostic properties. With its high atomic number, Au has shown excellent X-ray attenuation ability, and this has motivated the study of Au–$Cu_{2-x}S$ nanocomposites as a contrast enhancing

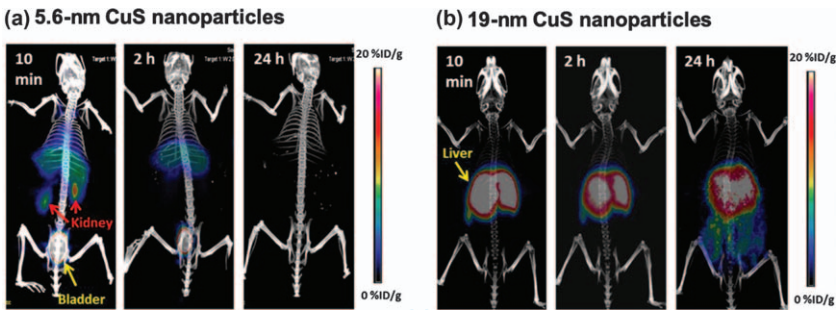

Figure 5.12 Representative micro-PET/CT maximum intensity projection images after intravenous injection of (a) 5.6 nm and (b) 19 nm [^{64}Cu]CuS nanoparticles into tumor-free Swiss mice.
Reproduced from ref. 70 with permission from American Chemical Society, Copyright 2015.

agent for CT imaging. When comparing the CT images of a tumor-bearing mouse that were taken before and after intratumoral injection of the Au–$Cu_{1.8}S$ nanocomposites, Ding *et al.* observed a significantly enhanced contrast in the tumor region in the images taken after injection, indicating that the Au–$Cu_{1.8}S$ hybrid possesses a CT contrast enhancing effect.[26] Meanwhile, Lv and co-workers found that their composite, which consists of a hollow-porous cubic CuS core enclosed in a spiky Au shell, exhibits enhanced SERS sensitivity owing to the multiple Au tips that can act as plasmonic hot spot regions.[50] With the strong SERS activity of their hybrid, they demonstrated its use for real-time monitoring of biochemical responses during PTT of living cancer cells.

In constructing a hybrid with magnetic resonance imaging (MRI) capability, Wu and co-workers synthesized a yolk–shell composite where CuS is coupled to ferromagnetic Fe_3O_4.[54] *In vivo* MR imaging of transplanted tumors in mice showed substantial reduction in the MRI signal intensity of the tumor region at 1 h post-injection. This implies that the Fe_3O_4-containing hybrid is potentially useful as a T_2-weighted (negative) MRI contrast agent. Chen *et al.* explored the combination of CuS and PLNPs to create an activatable nanoprobe that can be utilized for luminescence imaging.[55] They used a chromium-doped zinc germanogallate ($Zn_{1.1}Ga_{1.8}Ge_{0.1}O_4$:$Cr^{3+}$) as the PLNP material, which exhibits strong NIR luminescence with a long-lasting afterglow. The PLNPs and CuS nanoparticles were linked together by a peptide substrate that is specific to matrix metalloproteinases (MMPs), which are enzymes that are overexpressed in tumor microenvironments and are associated with cancer progression. As CuS is a strong NIR-light absorber, its coupling with NIR-light-emitting PLNPs resulted in considerable luminescence quenching due to the fluorescence resonance energy transfer (FRET) effect. However, when incubated with MMP-positive cancer cells, the MMP-specific peptide substrate that bridges the two components is cleaved, and this restores the luminescence of the PLNPs. Thus, this MMP-activatable hybrid does not only offer effective PTT by the CuS nanoparticles but also provides the capability to image cancer cells by the activated PLNPs.

5.4 Summary and Outlook

In summary, plasmonic $Cu_{2-x}S$ nanomaterials are emerging as one of the most promising classes of photothermal nanomaterials due to their strong NIR-light absorption and remarkable light-to-heat conversion efficiency. Because their photothermal activity operates in the therapeutic NIR optical window, they are often studied as photothermal agents for biomedical applications, particularly in the treatment of cancer. A wide variety of compositions, morphologies, and hybrids have already been explored to enhance their photothermal performance and/or to incorporate additional functionalities. Through rational design, several $Cu_{2-x}S$-based nanomaterials were found to exhibit synergistic therapeutic effects and excellent imaging capabilities, making them prime candidates as multimodal theranostic

agents in imaging-guided cancer therapy. However, there are certain challenges that need to be overcome before they can be adopted for clinical use. First, serious concerns regarding nanomaterial toxicity may hinder their practical use if not addressed accordingly. Further *in vivo* studies are therefore necessary to gain a better understanding of their pharmacokinetics and to assess their potential long-term toxicological effects. Another major challenge is the development of synthetic protocols that would allow for large-scale manufacturing as the current synthetic procedures are limited to laboratory-scale production. Aside from scalability, factors such as cost-effectiveness, simplicity, and reliability must also be considered when developing methodologies for producing $Cu_{2-x}S$-based nanomaterials that are targeted for real-world applications.

With the rising popularity of $Cu_{2-x}S$-based nanomaterials for photothermal applications, it is foreseen that more related materials will be examined for their photothermal properties in the coming years. In fact, recent years have witnessed an increasing number of papers reporting the photothermal behavior of doped (*e.g.* Gd-doped and Mn-doped CuS)[71,72] and multinary (*e.g.* $CuCo_2S_4$, $Cu_{12}Sb_4S_{13}$)[73,74] derivatives of $Cu_{2-x}S$. Considering the numerous compositional variations that can be realized when other elements are incorporated into the binary Cu–S system, it is anticipated that the library of photothermally active $Cu_{2-x}S$-based nanomaterials will continue to expand. Their performance as photothermal conversion agents should be evaluated not only in PTT but also in other important applications, such as in photothermal antibacterial treatment, solar-driven water purification, and photoactuation.

Acknowledgements

The author acknowledges funding support from the UP System Balik-PhD Program (OVPAA-BPhD-2019-07).

References

1. P. Roy and S. K. Srivastava, *CrystEngComm*, 2015, **17**, 7801.
2. D. J. Chakrabarti and D. E. Laughlin, *Bull. Alloy Phase Diagrams*, 1983, **3**, 254.
3. C. Coughlan, M. Ibáñez, O. Dobrozhan, A. Singh, A. Cabot and K. M. Ryan, *Chem. Rev.*, 2017, **117**, 5865.
4. Y. Liu, M. Liu and M. T. Swihart, *J. Phys. Chem. C*, 2017, **121**, 13435.
5. M. D. Regulacio and M.-Y. Han, *Acc. Chem. Res.*, 2016, **49**, 511.
6. O. Stroyuk, A. Raevskaya and N. Gaponik, *Chem. Soc. Rev.*, 2018, **47**, 5354.
7. S. Sun, P. Li, S. Liang and Z. Yang, *Nanoscale*, 2017, **9**, 11357.
8. X. Chen, J. Yang, T. Wu, L. Li, W. Luo, W. Jiang and L. Wang, *Nanoscale*, 2018, **10**, 15130.
9. W. van der Stam, A. C. Berends and C. de Mello Donega, *Chem. Phys. Chem.*, 2016, **17**, 559.

10. M. Zhou, M. Tian and C. Li, *Bioconjug. Chem.*, 2016, **27**, 1188.
11. X. Huang, W. Zhang, G. Guan, G. Song, R. Zou and J. Hu, *Acc. Chem. Res.*, 2017, **50**, 2529.
12. B. Yun, H. Zhu, J. Yuan, Q. Sun and Z. Li, *J. Mater. Chem. B*, 2020, **8**, 4778.
13. A. N. Nikam, A. Pandey, G. Fernandes, S. Kulkarni, S. P. Mutalik, B. Singh Padya, S. D. George and S. Mutalik, *Coord. Chem. Rev.*, 2020, **419**, 213356.
14. Y. Zhao, H. Pan, Y. Lou, X. Qiu, J. Zhu and C. Burda, *J. Am. Chem. Soc.*, 2009, **131**, 4253.
15. W. Xu, H. Liu, D. Zhou, X. Chen, N. Ding, H. Song and H. Ågren, *Nano Today*, 2020, **33**, 100892.
16. P. K. Jain, X. Huang, I. H. El-Sayed and M. A. El-Sayed, *Acc. Chem. Res.*, 2008, **41**, 1578.
17. J. M. Luther, P. K. Jain, T. Ewers and A. P. Alivisatos, *Nat. Mater.*, 2011, **10**, 361.
18. M. Hu, J. Chen, Z.-Y. Li, L. Au, G. V. Hartland, X. Li, M. Marquez and Y. Xia, *Chem. Soc. Rev.*, 2006, **35**, 1084.
19. R. Lesyuk, E. Klein, I. Yaremchuk and C. Klinke, *Nanoscale*, 2018, **10**, 20640.
20. N. E. Motl, A. F. Smith, C. J. DeSantis and S. E. Skrabalak, *Chem. Soc. Rev.*, 2014, **43**, 3823.
21. X. Liu, X. Wang, B. Zhou, W.-C. Law, A. N. Cartwright and M. T. Swihart, *Adv. Funct. Mater.*, 2013, **23**, 1256.
22. Y. Xie, A. Riedinger, M. Prato, A. Casu, A. Genovese, P. Guardia, S. Sottini, C. Sangregorio, K. Miszta, S. Ghosh, T. Pellegrino and L. Manna, *J. Am. Chem. Soc.*, 2013, **135**, 17630.
23. A. Agrawal, S. H. Cho, O. Zandi, S. Ghosh, R. W. Johns and D. J. Milliron, *Chem. Rev.*, 2018, **118**, 3121.
24. X. Wang and M. T. Swihart, *Chem. Mater.*, 2015, **27**, 1786.
25. C. Yan, Q. Tian and S. Yang, *RSC Adv.*, 2017, **7**, 37887.
26. X. Ding, C. H. Liow, M. Zhang, R. Huang, C. Li, H. Shen, M. Liu, Y. Zou, N. Gao, Z. Zhang, Y. Li, Q. Wang, S. Li and J. Jiang, *J. Am. Chem. Soc.*, 2014, **136**, 15684.
27. I. Kriegel, C. Jiang, J. Rodríguez-Fernández, R. D. Schaller, D. V. Talapin, E. da Como and J. Feldmann, *J. Am. Chem. Soc.*, 2012, **134**, 1583.
28. Z. N. Georgieva, M. A. Tomat, C. Kim and K. E. Plass, *Chem. Commun.*, 2016, **52**, 9082.
29. M. D. Regulacio, S. Y. Tee, S. H. Lim, Z. Zhang and M.-Y. Han, *CrystEngComm*, 2018, **20**, 6803.
30. N. J. Freymeyer, P. D. Cunningham, E. C. Jones, B. J. Golden, A. M. Wiltrout and K. E. Plass, *Cryst. Growth Des.*, 2013, **13**, 4059.
31. S.-W. Hsu, K. On and A. R. Tao, *J. Am. Chem. Soc.*, 2011, **133**, 19072.
32. D. Yoon, H. Jin, S. Ryu, S. Park, H. Baik, S. J. Oh, S. Haam, C. Joo and K. Lee, *CrystEngComm*, 2015, **17**, 4627.
33. M. D. Regulacio, C. Ye, S. H. Lim, M. Bosman, L. Polavarapu, W. L. Koh, J. Zhang, Q.-H. Xu and M.-Y. Han, *J. Am. Chem. Soc.*, 2011, **133**, 2052.

34. M. Liu, X. Xue, C. Ghosh, X. Liu, Y. Liu, E. P. Furlani, M. T. Swihart and P. N. Prasad, *Chem. Mater.*, 2015, **27**, 2584.
35. M. D. Regulacio, Y. Wang, Z. W. Seh and M.-Y. Han, *ACS Appl. Nano Mater.*, 2018, **1**, 3042.
36. D. Wu, J. Duan, C. Zhang, K. Guo and H. Zhu, *J. Phys. Chem. C*, 2013, **117**, 9121.
37. C.-F. Mu, Q.-Z. Yao, X.-F. Qu, G.-T. Zhou, M.-L. Li and S.-Q. Fu, *Colloids Surf., A*, 2010, **371**, 14.
38. W. Zhang, J. Xiao, Q. Cao, W. Wang, X. Peng, G. Guan, Z. Cui, Y. Zhang, S. Wang, R. Zou, X. Wan, H. Qiu and J. Hu, *Nanoscale*, 2018, **10**, 11430.
39. Q. Feng, Y. Zhang, W. Zhang, X. Shan, Y. Yuan, H. Zhang, L. Hou and Z. Zhang, *Acta Biomater.*, 2016, **38**, 129.
40. Y. Wang, L. An, J. Lin, Q. Tian and S. Yang, *Chem. Eng. J.*, 2020, **385**, 123925.
41. C. Sun, M. Liu, Y. Zou, J. Wei and J. Jiang, *RSC Adv.*, 2016, **6**, 26374.
42. Z. Wang, N. Yu, X. Li, W. Yu, S. Han, X. Ren, S. Yin, M. Li and Z. Chen, *Chem. Eng. J.*, 2020, **381**, 122613.
43. M. Sun, X. Fu, K. Chen and H. Wang, *ACS Appl. Mater. Interfaces*, 2020, **12**, 46146.
44. C. Leng, X. Zhang, F. Xu, Y. Yuan, H. Pei, Z. Sun, L. Li and Z. Bao, *Small*, 2018, **14**, 1703077.
45. B. Wang, R. Li, G. Guo and Y. Xia, *Chem. Commun.*, 2020, **56**, 8996.
46. J. Zhang, G. Liu, F. He, L. Chen and Y. Huang, *RSC Adv.*, 2015, **5**, 87903.
47. Y.-H. Chiu, S. B. Naghadeh, S. A. Lindley, T.-H. Lai, M.-Y. Kuo, K.-D. Chang, J. Z. Zhang and Y.-J. Hsu, *Nano Energy*, 2019, **62**, 289.
48. Y. Chang, Y. Cheng, Y. Feng, H. Jian, L. Wang, X. Ma, X. Li and H. Zhang, *Nano Lett.*, 2018, **18**, 886.
49. X. Yu, J. Bi, G. Yang, H. Tao and S. Yang, *J. Phys. Chem. C*, 2016, **120**, 24533.
50. Q. Lv, M.-Y. Gao, Z.-H. Cheng, Q. Chen, A.-G. Shen and J.-M. Hu, *Chem. Commun.*, 2018, **54**, 13399.
51. X. Deng, K. Li, X. Cai, B. Liu, Y. Wei, K. Deng, Z. Xie, Z. Wu, P. Ma, Z. Hou, Z. Cheng and J. Lin, *Adv. Mater.*, 2017, **29**, 1701266.
52. C. Yang, L. Ma, X. Zou, G. Xiang and W. Chen, *Cancer Nanotechnol.*, 2013, **4**, 81.
53. S. Liang, X. Deng, Y. Chang, C. Sun, S. Shao, Z. Xie, X. Xiao, P. Ma, H. Zhang, Z. Cheng and J. Lin, *Nano Lett.*, 2019, **19**, 4134.
54. Z.-C. Wu, W.-P. Li, C.-H. Luo, C.-H. Su and C.-S. Yeh, *Adv. Funct. Mater.*, 2015, **25**, 6527.
55. L.-J. Chen, S.-K. Sun, Y. Wang, C.-X. Yang, S.-Q. Wu and X.-P. Yan, *ACS Appl. Mater. Interfaces*, 2016, **8**, 32667.
56. C. Dong, W. Feng, W. Xu, L. Yu, H. Xiang, Y. Chen and J. Zhou, *Adv. Sci.*, 2020, **7**, 2001549.
57. C. Wu, Y. Wu, X. Zhu, J. Zhang, J. Liu and Y. Zhang, *Nano Today*, 2021, **36**, 100963.
58. M. Zhou, R. Zhang, M. Huang, W. Lu, S. Song, M. P. Melancon, M. Tian, D. Liang and C. Li, *J. Am. Chem. Soc.*, 2010, **132**, 15351.

59. Q. Tian, M. Tang, Y. Sun, R. Zou, Z. Chen, M. Zhu, S. Yang, J. Wang, J. Wang and J. Hu, *Adv. Mater.*, 2011, **23**, 3542.
60. B. Li, Q. Wang, R. Zou, X. Liu, K. Xu, W. Li and J. Hu, *Nanoscale*, 2014, **6**, 3274.
61. J. Mou, P. Li, C. Liu, H. Xu, L. Song, J. Wang, K. Zhang, Y. Chen, J. Shi and H. Chen, *Small*, 2015, **11**, 2275.
62. S. Wang, A. Riedinger, H. Li, C. Fu, H. Liu, L. Li, T. Liu, L. Tan, M. J. Barthel, G. Pugliese, F. De Donato, M. S. D'Abbusco, X. Meng, L. Manna, H. Meng and T. Pellegrino, *ACS Nano*, 2015, **9**, 1788.
63. Y. Huang, Y. Lai, S. Shi, S. Hao, J. Wei and X. Chen, *Chem. – Asian J.*, 2015, **10**, 370.
64. L. Guo, D. D. Yan, D. Yang, Y. Li, X. Wang, O. Zalewski, B. Yan and W. Lu, *ACS Nano*, 2014, **8**, 5670.
65. R. Hu, Y. Fang, M. Huo, H. Yao, C. Wang, Y. Chen and R. Wu, *Biomaterials*, 2019, **206**, 101.
66. X. Wang, X. Zhong, Z. Liu and L. Cheng, *Nano Today*, 2020, **35**, 100946.
67. J. Chen, T. Fan, Z. Xie, Q. Zeng, P. Xue, T. Zheng, Y. Chen, X. Luo and H. Zhang, *Biomaterials*, 2020, **237**, 119827.
68. H. Xu, X. Zhang, R. Han, P. Yang, H. Ma, Y. Song, Z. Lu, W. Yin, X. Wu and H. Wang, *RSC Adv.*, 2016, **6**, 50697.
69. M. Zhou, J. Zhao, M. Tian, S. Song, R. Zhang, S. Gupta, D. Tan, H. Shen, M. Ferrari and C. Li, *Nanoscale*, 2015, **7**, 19438.
70. M. Zhou, J. Li, S. Liang, A. K. Sood, D. Liang and C. Li, *ACS Nano*, 2015, **9**, 7085.
71. H. Shi, Y. Sun, R. Yan, S. Liu, L. Zhu, S. Liu, Y. Feng, P. Wang, J. He, Z. Zhou and D. Ye, *Nano Lett.*, 2019, **19**, 937.
72. B. Zhou, J. Zhao, Y. Qiao, Q. Wei, J. He, W. Li, D. Zhong, F. Ma, Y. Li and M. Zhou, *Appl. Mater. Today*, 2018, **13**, 285.
73. X. Huang, G. Deng, L. Liao, W. Zhang, G. Guan, F. Zhou, Z. Xiao, R. Zou, Q. Wang and J. Hu, *Nanoscale*, 2017, **9**, 2626.
74. M. D. Regulacio, S. Y. Tee, S. H. Lim, C. P. Teng, L.-D. Koh, S. Liu and M.-Y. Han, *Nanoscale*, 2017, **9**, 17865.

CHAPTER 6

Two-dimensional Nanomaterials and Hybrids

X. YAO,[a] G. GUAN,*[a] M. Y. HAN,*[a,b] Z. LI[b,c] AND E. YE[b]

[a] Institute of Molecular Plus, Tianjin University, Tianjin 300072, P.R. China; [b] Institute of Materials Research and Engineering, Agency for Science, Technology & Research (A*STAR), 2 Fusionopolis Way, Singapore 138634, Singapore; [c] Department of Materials Science and Engineering, National University of Singapore, 9 Engineering Drive 1, Singapore 117576, Singapore
*Emails: guijianguan@tju.edu.cn; han_mingyong@tju.edu.cn

6.1 Introduction

With the wide exploration and fast development of nanoscience/nanotechnology, nanostructured materials with different dimensions have been readily synthesized and utilized as ideal agents in various applications.[1,2] Among them, two-dimensional (2D) materials with ultrathin thickness (*i.e.*, nanosheets) have been attracting extensive research attention because their superb physical and chemical features provide some promising applications in various fields such as energy conversion, electronics, and optoelectronics.[3,4] As a milestone for developing 2D materials, graphene was mechanically produced in 2004 to exhibit a honeycomb lattice structure of carbon,[5] which possesses a large specific surface area, high Young's modulus, and intrinsic mobility.[6–8] The pioneering discovery and extensive investigation of graphene subsequently inspired extensive exploration on 2D nanomaterials. As a typical example, a single layer of transition metal dichalcogenide (TMD) like MoS_2, $MoSe_2$, WS_2, *etc.* is formed *via* sandwiching a transition metal layer between two chalcogen layers.[9] In 2014, black phosphorus (BP) nanosheets were

Nanoscience & Nanotechnology Series No. 54
Photothermal Nanomaterials
Edited by Enyi Ye and Zibiao Li

Published by the Royal Society of Chemistry, www.rsc.org

fabricated to demonstrate a puckered honeycomb morphology, in which sp^3-hybridized phosphorus atoms are arranged along two directions of armchair and zig-zag *via* the formation of tetrahedral bonding.[10]

Through quantum confinement in the vertical direction, ultrathin 2D materials with a large sheet size exhibit strong light–matter interactions. When irradiated by incident light with an appropriate wavelength in the visible region, some special 2D nanomaterials can generate lots of free electron–hole pairs and possess an extraordinary catalytic activity for photocatalytic degradation of organic pollutants, which was systematically demonstrated in our recent review.[11–13] As the wavelength of incident light is increased into the near infrared (NIR) range, 2D nanomaterials with narrower bandgaps can be employed as emerging photothermal agents for high-efficiency conversion of light to heat.[14] In the past five years, photothermal conversion from NIR light has been attracting significant interest owing to its promising applications in selective ablation of tumor cells and bacteria.[15] Typically, electron–hole pairs are generated in graphene after exposure to NIR light and result in a great heating of electrons. Through slow scattering between electrons and phonons, the hot electrons and the lattice reach the equilibrium of heat (*i.e.*, temperature increment).[16] For MoS_2 nanosheets, the decrease in layer number to a single layer makes its bandgap change from "indirect" to "direct",[17] so that the photons are absorbed more rapidly by single-layer MoS_2 to radiate the heat through the robust interactions of electrons with holes.[2,18] More recently, BP nanosheets have been proved to have a direct bandgap that is larger than the zero-bandgap of graphene but smaller than the one of TMDs.[19] The physical features make 2D nanomaterials exceedingly desirable in photothermal applications compared to some traditional materials, which not only exhibit adjustable optical properties by controlling the thickness of sheets or the introduction of plasmonic metals/other functional species but also provide good surface-modifiable platforms and new opportunities for utilization in broader fields.[14]

As shown in Figure 6.1, 2D nanomaterials have been obtained experimentally *via* "top-down" and "bottom-up" strategies and successfully hybridized with

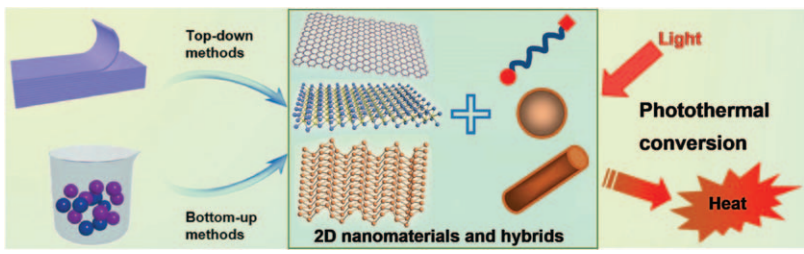

Figure 6.1 The "top-down" and "bottom-up" preparation strategies of 2D nanomaterials and their hybridization with special species and functional nanostructures, which can achieve excellent conversion from light to heat. Reproduced from ref. 20 with permission from John Wiley and Sons, Copyright © 2020 Wiley-VCH Verlag GmbH & Co. KGaA, Weinheim.

special species and functional nanostructures for photothermal conversion with a higher efficiency.[20] Herein, we first demonstrate the usual preparation methods of 2D nanomaterials and then use graphene, TMD, and BP nanosheets as typical examples to summarize the photothermal properties of surface-modified and functional species-hybridized 2D nanomaterials. Meanwhile, their novel photothermal applications are also involved, particularly the photothermal therapies against cancer and bacterial infections. Finally, the merits and disadvantages of several types of 2D nanomaterials are further discussed, and some suggestions are given for guiding their further developments in photothermal applications.

6.2 Preparation and Functionalization of 2D Nanomaterials

To produce high-quality 2D nanomaterials in large yields, various fabrication methods of 2D nanomaterials have been facilely developed in recent decades, which can be divided into two different routes: top-down and bottom-up. The top-down route is used to exfoliate ultrathin nanosheets from layered crystals *via* breaking the weak van der Waals forces between the interlayers, including mechanical cleavage, ion intercalation- and sonication-assisted liquid exfoliations.[3] While the bottom-up route is used to chemically produce ultrathin nanosheets through physical/chemical deposition on substrates or controlled reactions of specific precursors under special conditions, *i.e.*, physical/chemical vapor deposition and chemical synthesis.[21]

For layered crystals with weak bonding forces between adjacent layers, their 2D nanosheets can be readily produced *via* exfoliating the parent bulks by top-down approaches (see Figure 6.2). Typically, Scotch tape is conveniently used to provide a mechanical force to cleave bulky crystals into nanosheets and then transfer them onto substrates (*e.g.*, SiO_2/Si), which can obtain high-purity sheets with varied thickness but that lack the ability to produce nanosheets on a large scale.[22] To this end, exfoliation methods in the liquid phase have been developed to obtain large-scale nanosheets and provide easier approaches for engineering the obtained nanosheets. Particularly, ion-intercalated exfoliation is carried out by the (electro)chemical intercalation of ions in organic solvent

Figure 6.2 The top-down approaches for producing 2D nanomaterials *via* exfoliation of layered bulky crystals by utilizing different formats of forces. Reproduced from ref. 21 with permission from Elsevier, Copyright 2019.

and then exfoliation in water owing to the generation of hydrogen gas, which is very appealing to produce single-layer nanosheets with structural and electronic deformations.[23] Alternatively, 2D nanomaterials are also obtained by sonication-driven exfoliation of bulky crystal after adding surfactants, polymers, or proteins in exfoliation solution.[24]

At the same time, 2D nanomaterials can also be fabricated by using chemical synthetic processes under certain reaction conditions by bottom-up techniques (see Figure 6.3). Among them, physical vapor deposition (PVD) is an important method for producing large area and thickness uniform 2D nanomaterials with low toxicity.[25] However, it is difficult to form monolayer nanosheets *via* PVD methods. Alternatively, chemical vapor deposition (CVD) can fabricate sheets on preselected substrates in a high vacuum and with high-temperature, in which the sheet size and thickness are tuned simply by controlling the time of deposition and the rate of gas flow, and it is also convenient to hybridize diverse 2D sheets at vertical and horizontal orientations.[26] In addition, chemical synthesis through hydrothermal and solvothermal reactions has been employed to produce various nanosheets, in which the sheet size and thickness can be controlled *via* changing the precursors used and/or by adjusting the reaction conditions, and the nanosheets can be directly functionalized or hybridized with other functional components.[27]

To increase the dispersity of nanosheets and/or improve their biocompatibility, 2D nanomaterials are usually modified physically or chemically with other special species, which not only increases their chemical/physical stability but also improves their targeting ability and adjusts their optical properties for better applications.[28] As reported, polyethylene glycol (PEG), polyvinylpyrrolidone (PVP), and polydopamine (PDA) are some widely-used functional molecules for improving the dispersity of 2D nanomaterials while some biological molecules like bovine serum albumin (BSA) are frequently utilized as both exfoliating and stabilizing agents to increase their biocompatibility.[20] Additionally, the hybrid of 2D nanosheets with other nanostructured materials can exhibit more promising performances in broader applications *via* a great synergistic effect.[29] As indicated, this surface engineering on nanosheets is especially important for utilizing the photothermal conversion of 2D nanomaterials in practical applications. To this end, we will demonstrate the

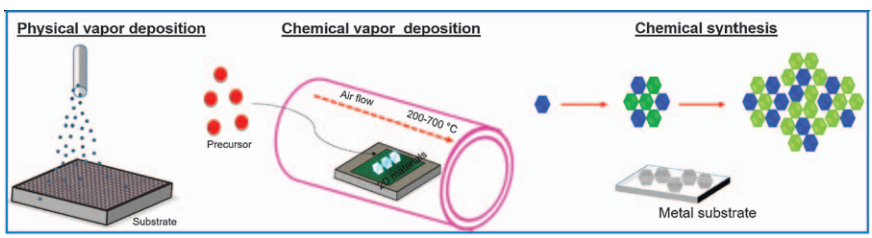

Figure 6.3 The bottom-up approaches for synthesizing 2D nanomaterials from various reactive precursors by using different reaction conditions. Reproduced from ref. 21 with permission from Elsevier, Copyright 2019.

photothermal conversion and applications of diversified 2D nanomaterials after surface modification or/and hybridization.

6.3 Graphene

Besides the direct production of graphene *via* exfoliation of graphite or chemical synthesis, another high-efficient preparation method is to first oxidize graphite into graphene oxide (GO) and then produce reduced graphene oxide (rGO) *via* further reduction reaction. As 2D photothermal materials, graphene, GO and rGO have been attracting great attention due to their strong absorbance of NIR radiation, which means that graphene-based nanosheets can be successfully utilized in photothermal therapy (PTT) for selectively ablating cancer cells and efficiently inhibiting tumor growth.[16]

6.3.1 Modified Graphene

Small Molecules: For bare graphene, there are no hydrophilic groups at its surface, so the direct use of graphene faces a challenge of poor stability in aqueous environments. To this end, surface modification is extremely important for various applications of graphene. Typically, the introduction of arginine onto a rGO surface not only improves its stability and cancer cell uptake but also results in higher NIR absorbance by 3.2 times than GO.[30] After being conjugated with alanine *via* π–π interactions, the stability of GO sheets was doubly improved and its photothermal conversion efficiency (PCE) under 808 nm irradiation was enhanced by 89% and 33% as compared to GO and RGO.[31] In Chen's work, GO sheets were firstly oxidized by nitronium ion (NO_2^+) solution under microwave heating to form smaller sheets and were then reduced by glucose to obtain functionalized rGO sheets.[32] For the resultant rGO, the absorption of 808 nm light was increased by 10-fold, and the loaded doxorubicin (DOX) could be released controllably by three different stimuli: decreasing pH, yielding glutathione (GSH) and increasing temperature. Alternatively, Mei *et al.* synthesized amino-functionalized GO (GO–NH_2) *via* grafting ethylenediamine to obtain excellent photothermal efficiency (see Figure 6.4A).[33] As shown in Figure 6.4B and C, the GO–NH_2 nanosheets can yield 80 °C after white light irradiation for 10 min. Through electrostatic attraction, GO–NH_2 sheets exhibited excellent antibacterial ability to prevent the development of Gram-negative and positive bacteria, which was 32-times higher than that of pure GO (see Figure 6.4D). Similarly, Wang's group used porphyrin to functionalize GO nanosheets through π–π interactions, which can significantly absorb 808 nm light to result in PCE increases by 89% and 33% compared to GO and rGO.[34] In addition, Wang's group demonstrated a dual-targeted antibacterial platform by using boronic acid- and quaternary ammonium salt-functionalized graphene, which can reach ∼50 °C under irradiation with an 808 nm laser.[35] *Via* electrostatic adhesion and covalent coupling, the resultant graphene is specifically bound to the bacteria and their biofilms to improve bactericidal efficacy owing to the synergy of hyperthermia.

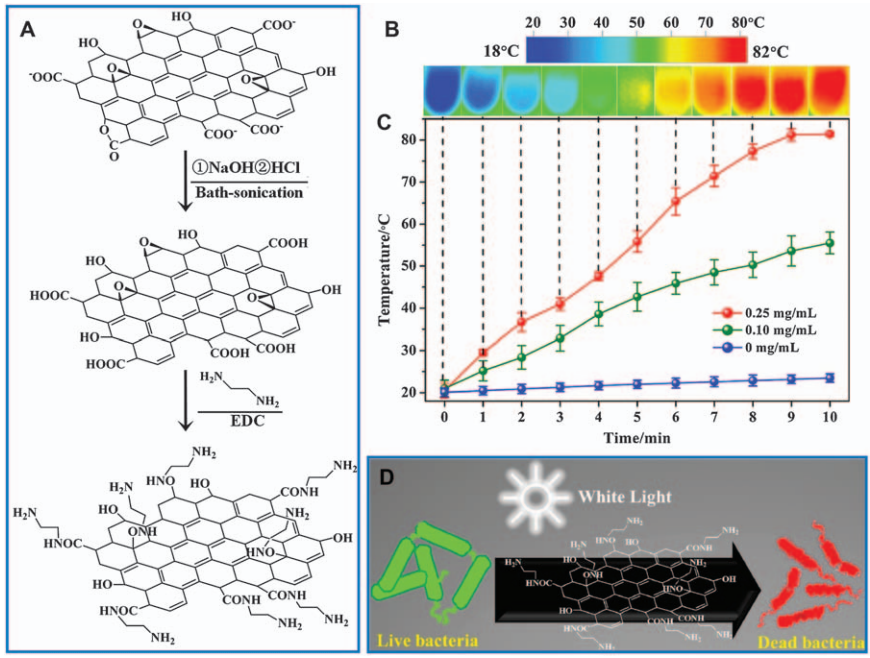

Figure 6.4 (A) Schematic figure for synthesizing GO–NH_2. (B) Heating images at different irradiation times by using 0.25 mg mL^{-1} GO–NH_2 and (C) heating curves of different concentrations of GO–NH_2 sheets after irradiation by white light (159 mW cm^{-2}). (D) The capture of bacteria and subsequent photothermal ablation by GO–NH_2 nanosheets.
Reproduced from ref. 33 with permission from American Chemical Society, Copyright 2019.

Polymers: Compared with small molecules, more research studies have used polymer materials to modify graphene for higher stability and better functionalization. In recent years, there have still been lots of studies involving the usage of PEG for developing graphene-based photothermal agents. For instance, the simple mixing of GO and $[NP(MPEG750)(GlyPheLeu)Et]_3$ (CP750) can produce rGO/CP750 assembly with good water-dispersibility and strong NIR absorbance.[36] Under 808 nm laser irradiation, the rGO/CP750 nanosheets exhibited a large generation of heat and the temperature changed from 34.1 to 78.0 °C. Ma *et al.* synthesized GO–amino(polyethyleneglycol) (GO–PEG–NH_2) *via* the hydrophobic binding of heptadecyl end groups in 1,2-distearoyl-*sn*-glycero-3-phosphoethanolamine-*N*-[amino-(polyethyleneglycol)] onto the surface of GO sheets, which enabled the efficient photothermal ablation of the captured bacteria under NIR irradiation.[37] Alternatively, folic acid (FA) functionalized PEGylated GO sheets of ~30 nm in size were prepared by using non-equilibrium plasma to etch GO and subsequently amidic coupling and azide–alkyne click cycloaddition were utilized to functionalize the obtained GO sheets with FA-terminated PEG2000 chains.[38]

The GO–PEG–FA sheets loaded a large amount of DOX (>33%) and behaved as an NIR-driven heater. Similarly, the rGO–PEG–FA nanosheets were synthesized to deliver an indoleamine-2,3-dioxygenase inhibitor to trigger PTT destruction of primary tumors and release tumor-associated antigens.[39] In addition, PEGylated GO sheets were also utilized as a gene delivery system to combine NIR light thermotherapy and gene therapy for significant anticancer efficacy.[40]

Like PEG, PDA is another widely-used polymer for modifying graphene in photothermal applications. Typically, PDA-modified rGO was used as a substrate to immobilize antiarrhythmic peptide 10 (AAP10) to form PDA/rGO nanocomposites, which facilitated cancer therapy *via* NIR-driven PTT after its tremendous absorption for NIR light.[41] Similarly, indocyanine green-loaded PDA/rGO was fabricated to effectively enhance their optical absorption at 780 nm to exhibit better PTT efficiency and higher photoacoustic contrast as compared to GO and rGO–PDA.[42] More interestingly, Fu's group integrated DNA aptamers on PDA/rGO nanosheets to develop a dual stimuli-responsive nanoplatform.[43] As shown in Figure 6.5, an acidic intracellular environment and NIR light can control the release of drug from the rGO–PDA sheets, and the rGO–PDA sheets simultaneously serve as a photothermal agent to yield heating for PTT under NIR irradiation.

Beyond PEG and PDA, other polymers were also reported to modify graphene for photothermal applications. Typically, the functionalization of rGO with a hyaluronic acid (HA)-based amphiphilic polymer improved their stability and cytocompatibility in targeted cancer therapy.[44] Poly(allylamine hydrochloride)-functionalized rGO was synthesized to show superb photothermal conversion and pH-controlled drug release for chemo-photothermal therapy at high efficiency.[45] Zhang's group first loaded methylene blue (MB) on GO sheets and then coated PF127 to fabricate GO–MB/PF127 nanocomposites, which were successively achieved by self-assembly of molecules and thin-film hydration techniques.[46] When 808 nm and 660 nm light were used individually, GO in GO–MB/PF127 nanocomposites led to the photothermal destruction of cancer cells while MB yielded singlet oxygen to inhibit the growth of cancer cells due to the generation of oxidative stress. Recently, Geng's group reported a grafting strategy for modifying polythiophenes onto the surface of rGO nanosheets, which provided the water-dispersible rGO nanosheets with a high PCE value at ~88%.[47] As a result, the increased temperature killed 100% of *E. coli via* combining the photothermal effect together with an electrostatic targeted process.

Biological Macromolecules: In Fang's work, *Memecylon edule* leaf extracts were used to reduce GO and form oxidized polyphenol-coated rGO, which exhibited exceptional NIR ablation of the lung cancer cells.[48] Deng's group modified glycol chitosan on carboxyl graphene to exhibit an increment amount of heat in the NIR irradiation and an interesting self-adaptive targeting ability in the acidic tissues without destroying the healthy cells (pH 7.4).[49] Similarly, Chung's group reported loading DOX onto BSA-coated rGO sheets for NIR-controlled chemo-photothermal therapy.[50]

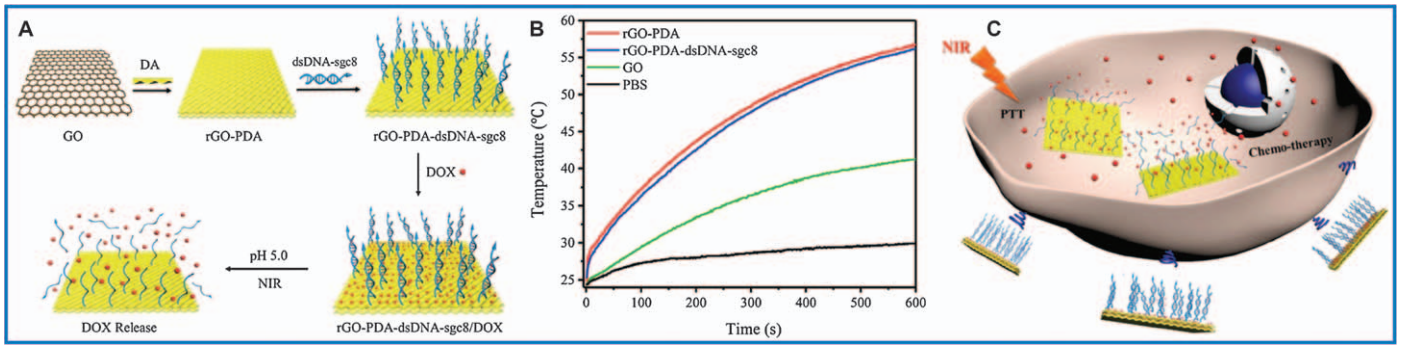

Figure 6.5 (A) Schematic demonstration for preparing an rGO–PDA–dsDNA–sgc8/DOX nanoplatform. (B) Photothermal curves of the GO, rGO–PDA, rGOPDA–dsDNA–sgc8, and PBS solution under irradiation of an 808 nm laser (2.0 W cm^{-2}). (C) The chemo–photothermal synergetic therapy of using the rGO–PDA–dsDNA–sgc8/DOX nanoplatform.
Reproduced from ref. 43 with permission from the Royal Society of Chemistry.

6.3.2 Nano-hybridized Graphene

For developing graphene-based photothermal agents toward combined applications, some special nanostructures are usually introduced to fabricate nano-hybridized graphene, such as fullerene, metal nanostructures, metal oxides, and so on.

Fullerene: As reported, GO and C_{60} are two types of good nanomaterials for PTT and photodynamic therapy (PDT), respectively. For that, a hybrid of GO–PEG and C_{60} was synthesized by a step-wise conjugation method.[51] Experimentally, the grafting of C_{60} onto GO sheets did not compromise the photothermal ability of GO, while the presence of GO enhanced the activity of C_{60} to produce more singlet oxygen under NIR irradiation. In another work, γ-cyclodextrin (γ-CD) was comprised on GO–FA sheets to further host pure C_{60} molecules for the production of GO–FA/γ-CD/C_{60} nanohybrids with enhanced phototherapy effects, benefiting from the higher stability of C_{60}, greater light absorption, and better cellular uptake of nanohybrids.[52]

Gold Nanostructures: With superb photothermal properties *via* plasmon absorbance,[15] gold nanostructures such as particles, stars, and rods have been frequently reported to hybridize with graphene to achieve synergistic photothermal conversion. Typically, gold nanoparticles (AuNPs) were modified by α-synuclein and then introduced to GO nanosheets to sandwich them between two AuNP monolayers, which strongly adhered onto the cell surface and exhibited an excellent photothermal ability (see Figure 6.6).[53]

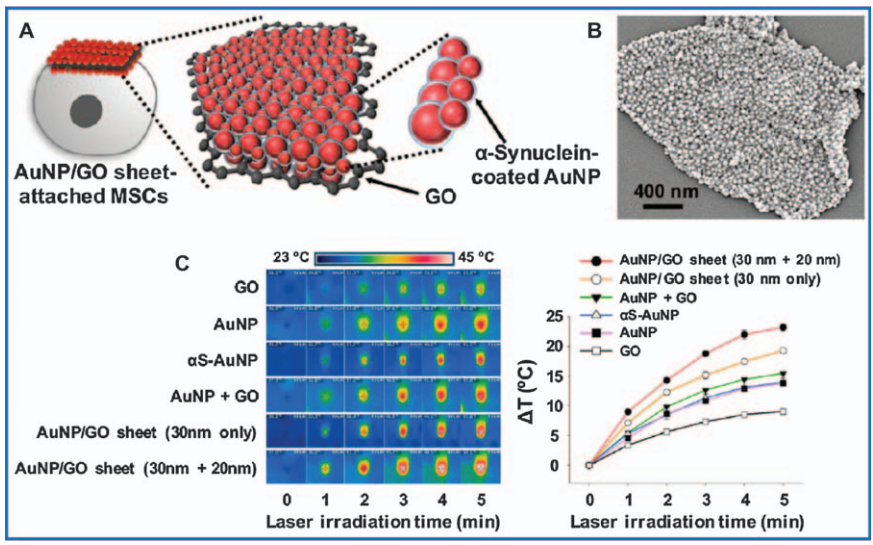

Figure 6.6 (A) Attaching an AuNPs/GO hybrid onto mesenchymal stem cells (MSCs) for the fast photothermal treatment of cancer. (B) SEM image of AuNPs/GO hybrid sheets. (C) Photothermal effects of various samples under different conditions, which were obtained by using an 808 nm-emitting laser. Reproduced from ref. 53 with permission from American Chemical Society, Copyright 2017.

When the AuNP/GO-attached mesenchymal stem cells were injected into tumor-bearing mice, the photothermal therapeutic performance was greatly improved because large amounts of AuNPs were delivered to the tumor and generated lots of heat at the tumor area. Alternatively, a one-step route was developed to reduce GO sheets and simultaneously coat rGO with 5–30 nm-sized AuNPs *via* employing nisin peptides with a thermostable and antimicrobial ability to fabricate AuNP–rGO nanocomposites.[54] The photothermal conversion of AuNP–rGO nanocomposites on MCF7 breast cancer cells inhibited the growth of ~80% cells after irradiation by NIR light ($0.5\ W\,cm^{-2}$) for 5 min. Similarly, Yang *et al.* synthesized a nanocomposite of aptamer–AuNP–GO for facilitating targeted ablation of tumor cells by NIR-activated PTT, which exhibited therapeutic effects on MCF-7 cells at an ultralow sample concentration without an adverse effect on healthy cells.[55] Furthermore, the aptamer–modified GO–AuNP composites were loaded with DOX for heat-stimulative and sustained drug release.[56]

In Wang's work,[57] AuNPs were uniformly coated onto rGO nanosheets in a mixed solvent of water/*n*-butylamine and further incorporated in cross-linked poly(ε-caprolactone) to form a rapid light-controlled shape memory polymer, which exhibited a significantly increased photothermal efficiency and greatly improved mechanical stiffness. In a similar work, quaternized carboxymethyl chitosan (QCCS) was utilized to reduce Au^{3+} ions and served as coupling species to hybridize the formed AuNPs on GO sheets, and then the resultant Au–QCCS–GO nanohybrids were added into the solution of nanocellulose to fabricate photothermal paper after vacuum filtration.[58] After exposure to NIR light, the Au–QCCS–GO paper increased the temperature to ~80 °C, which was adequate for heating ablation upon Gram-positive and Gram-negative bacteria. In addition, Au core/GO shell composites with an amphiphilic surface were one-pot synthesized by utilizing GO as the reducing agent, which provided desirable functions for improving the photothermal ability and enhancing Raman scattering.[59]

Like AuNPs, gold nanostars (AuNSs) were grown *in situ* on GO sheets and further coated with a positively-charged lipid bilayer film accompanied with the reduction of GO.[60] The rGO@AuNSs were used in gene/photothermal treatments that were guided by photoacoustic and photothermal images, respectively. In Zhang's work,[61] PDA–GO, AuNSs, PEG, and DOX were integrated to form a novel nanoplatform for combined therapy of metastatic breast cancer under irradiation of NIR light (see Figure 6.7). In another work, AuNSs were first grown on GO and then modified with PEG and linked with Chlorin e6 (Ce6) to form a photosensitizer-assembled graphene/AuNS hybrid.[62] Owing to the increased optical absorption for NIR light, the composite of graphene and AuNS–PEG exhibited a high PCE and outstanding performance in synergistic PDT and PTT of cancer under the assistance of photothermal imaging.

Gold nanorods (AuNRs) have been demonstrated as efficient photothermal nanomaterials for converting light energy into heat,[15] so AuNRs are of importance for the PTT of various cancers. In Szunerits's work,[63] AuNRs

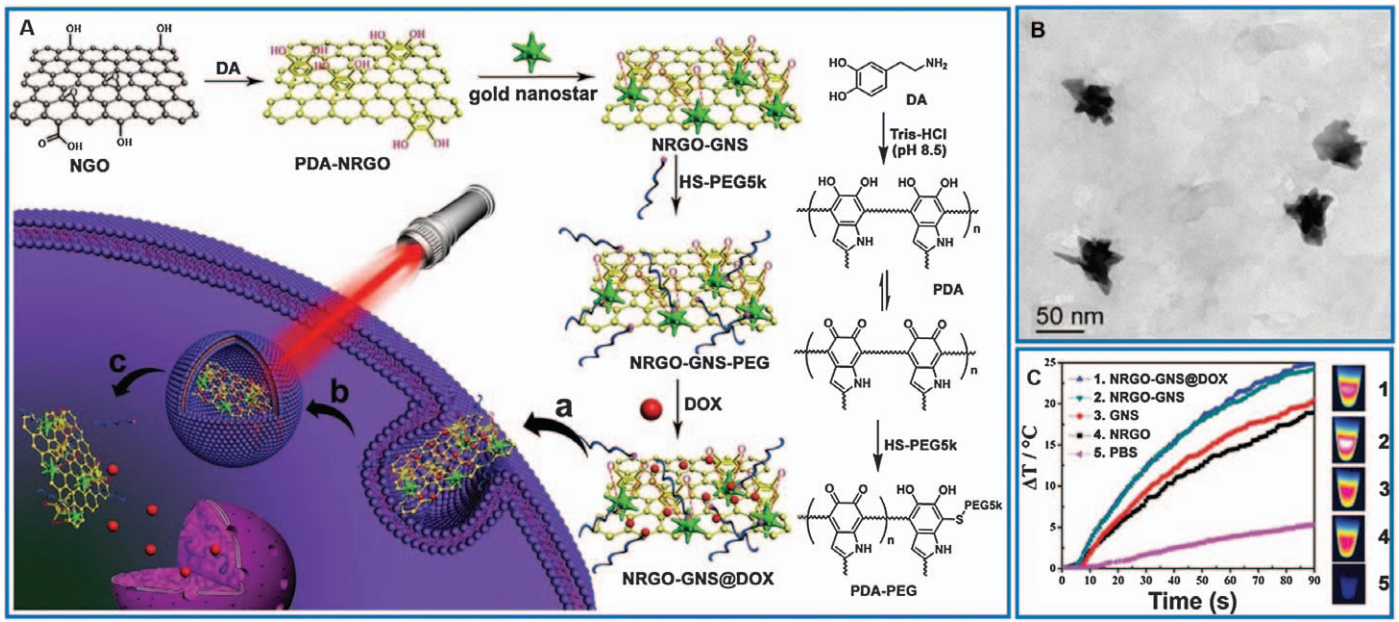

Figure 6.7 (A) Schematic illustration for synthesizing NRGO–GNS@DOX nanocomposites and chemo-photothermal treatment of breast cancer: (a) internalization of an NRGO–GNS@DOX nanohybrid, (b) entrapment inside the lysosome vesicles, and (c) release of DOX after NIR irradiation. (B) TEM images of NRGO–GNS@DOX. (C) Temperature elevation of different samples when the laser photo-density was set to 4.0 W cm^{-2}.
Reproduced from ref. 61 with permission from John Wiley and Sons, Copyright © 2016 WILEY-VCH Verlag GmbH & Co. KGaA, Weinheim.

were enrobed with rGO–PEG nanosheets to exert effective photothermal ablation of tumors under irradiation of NIR light at low doses and to act as fluorescent markers in cells by integrating NIR dyes onto the rGO shells. Upon irradiation with 800 nm at 0.7 W cm^{-2}, the growth of a U87MG tumor was inhibited. Alternatively, Song's group synthesized rGO-loaded AuNR vesicles with a greatly improved photoacoustic ability and photothermal activity, which also exhibited a large loading amount of drug due to the presence of cavities on the vesicle and large surface area of rGO.[64] Then, an NIR-driven photothermal process induced the release of DOX from the vesicular cavity, and the acidic intracellular microenvironment induced drug release from the rGO surface.

Silver and Palladium Nanostructures: To combine the superb photothermal activity of graphene and the antibacterial ability of silver nanoparticles (AgNPs), Tan *et al.* prepared rGO/Ag nanocomposites to effectively kill multi-drug resistant (MDR) bacteria.[65] Compared to individual components, the rGO/Ag nanocomposites exhibited significantly higher antibacterial ability for killing regular and MDR bacteria, indicating that the photothermal process resulted in a greatly synergetic antibacterial performance. Alternatively, Liu's groups developed an effective and simple approach for generating AgNPs directly on rGO nanosheets by using GSH as a co-reducing agent, and the AgNP/GSH–rGO nanohybrid was demonstrated to exhibit highly-efficient antibacterial activity for reducing wound infection or improving cancer therapy *via* photothermal ablation.[66] In Wang's work,[67] AgNPs were grown *in situ* on polyethylenimine (PEI)-modified magnetic rGO to form Ag@rGO–Fe_3O_4–PEI composites, which exhibited an outstanding antibacterial ability. After irradiation by a 785 nm laser for 0.5 min (50 mW cm^{-2}), an ablating rate of 99.9% was attained for *E. coli O157*:*H7* (1×10^7 cfu mL^{-1}) at a dosage of 0.1 μg mL^{-1}. Recently, silver modified mesoporous silica/rGO sheets with a sandwiched structure (rGO/MS/Ag) were successfully synthesized as an interesting antibacterial agent, in which the rGO and AgNPs were reduced *in situ* without adding any other reductants.[68] As a result, the rGO/MS/Ag hybrid exhibited an excellent photothermal conversion ability and antibacterial activities against various bacteria upon NIR irradiation using only a relatively low dosage.

Palladium nanoparticles (PdNPs) were another excellent metal nanomaterial that was used to hybridize graphene in photothermal applications. Experimentally, GO–PdNP nanosheets were prepared in CTAB solution by reducing H_2PdCl_4 with $NaBH_4$ and ascorbic acid.[69] In Zhang's work,[70] well-dispersed Pd crystals were successfully synthesized in nitrogen-doped graphene (Pd/N–graphene) in the format of a single atom *via* a freeze-drying-based approach, which exhibited exceptional capability and selectivity to hydrogenize C_2H_2 in the presence of H_2 under photothermal heating. A highly-efficient conversion was achieved for acetylene (99%) and its selectivity to ethylene was 93.5% at 125 °C.

Metal Oxide Nanostructures: To enhance the DOX loading amount, MS nanoparticles were hybridized with dopamine-functionalized GO and further conjugated by the targeting HA molecules.[71] As a result, the

pH-controlled and NIR-activated DOX release improved the performance of chemo-photothermal therapy. Alternatively, iron oxide nanoparticle-modified GO nanosheets (GO–IONP) were modified with chitosan (CS) and dextran (DEX) by layer-by-layer self-assembly for producing GO–IONP–CS/DEX composites with the abilities of targeting drug and photothermal effects.[72] Similarly, a ternary composite of rGO–Fe_3O_4–PANI with excellent photothermal performance was prepared *via* co-reducing GO and iron nitrate in solvothermal reactions, and *in situ* polymerization of PVA-linked polyaniline.[73] At a light power density of 2.0 W cm^{-2}, a PCE value of 86.3% was achieved by using 100 μg mL^{-1} of nanocomposites, and the temperature difference can be up to 56.7 °C.

Beyond silica and Fe_3O_4, TiO_2 nanostructures were also used to hybridize graphene for a greatly enhanced photothermal effect in the photocatalytic reduction of CO_2, which benefited from the synergetic process of the increased electron mobility and dramatically enhanced surface temperature.[74] Alternatively, rice-shaped ZnO nanoparticles were anchored on graphene and then sensitized with cobalt phthalocyanine (CoPc) to form a NIR-activated photothermal nanohybrid, which can increase the temperature to 68 °C after irradiation by a 980 nm laser for 7 min (see Figure 6.8).[75] In comparison, the PCE value from graphene–ZnO–CoPc was higher than the ones from gold- and CuS-involved photothermal materials. Recently, manganese dioxide (MnO_2) nanoparticles were functionalized on FA-modified GO sheets for utilization in the targeted PTT under NIR irradiation.[76] Also, the graphene–MnO_2 nanohybrid was investigated to catalytically oxidize gaseous formaldehyde with the assistance of a xenon lamp.[77] As a result, the transferring rate of formaldehyde to CO_2 was increased by 80% compared to bare MnO_2, which was attributed to the dual generation of heat from both MnO_2 and graphene. Moreover, graphene has a high conducting process for heat, so that the yielded heat was quickly moved from the graphene to MnO_2

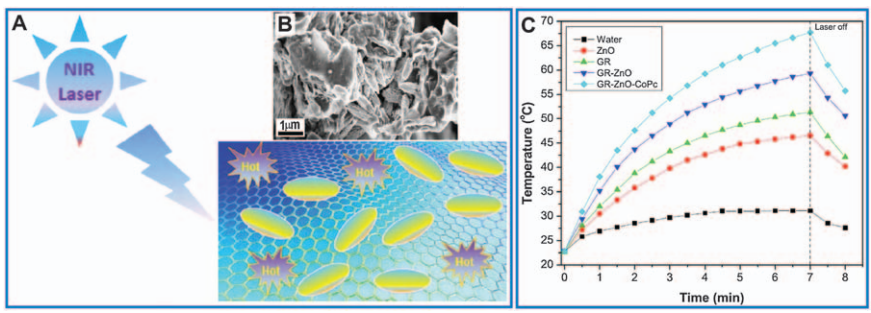

Figure 6.8 (A) Cobalt phthalocyanine (CoPc)-modified graphene–ZnO nanocomposite used as a NIR-responsive photothermal system. (B) SEM image of graphene–ZnO–CoPc. (C) Rise in temperature for different samples with the increment of illumination time.
Reproduced from ref. 75 with permission from American Chemical Society, Copyright 2019.

and the surface temperature of MnO_2 was even higher than that of graphene, which was beneficial for facilitating the activation of surface lattice oxygen.

Other Functional Nanomaterials: GO/$NaYF_4$: Yb,Er nanocomposites were fabricated through a hydrothermal reaction, in which cubic phase $NaYF_4$: Yb,Er nanoparticles were loaded onto the surface of GO nanosheets.[78] Under irradiation by a NIR light of 980 nm, the PCE value over hybrids reached 71.1% to reveal that the PCE of GO could be increased by 13.9% due to the doping of $NaYF_4$: Yb,Er nanocrystals. With the assistance of PEG, $BaGdF_5$ particles were stably loaded on the surface of GO sheets through a solvothermal process to fabricate GO/$BaGdF_5$/PEG nanocomposites.[79] Under irradiation by 808 nm light (0.5 W cm^{-2}), the photothermal ablation of tumors *in vivo* was achieved at high efficiency through enhanced NIR absorption, improved photothermal activity, and excellent tumor targeting ability by using GO/$BaGdF_5$/PEG.

6.3.3 Graphene-based Films, 3D Structures, and Devices

For a simple synergistic enhanced antimicrobial therapy, GO and poly-(allylamine hydrochloride) (PAH) were alternately deposited to form hybrid films, which exhibited an excellent photothermal property with an NIR laser of 1064 nm.[80] The enhanced antimicrobial performance was attributed to the synergistic functions of membrane-stress induced on bacteria and photothermal effect by irradiation with an NIR laser. With a large surface area, open sharp edges, and non-stacking 3D structure, vertically-oriented graphene (VG) nanosheets were directly synthesized on traditional soda-lime glass by a plasma-enhanced CVD method at 580 °C.[81] The fabricated VG nanosheets/glass hybrid exhibited excellent solar thermal conversion, which led to a 70–130% increment for the surface temperature. In Lin's work,[82] adhesive graphene was fabricated at the surface of β-tricalcium phosphate bioceramics using CVD instrument, and the resultant composites exhibited superb photothermal effects to kill most of the osteosarcoma cells (>90%). In addition, ultrahigh photothermal temperature was successfully achieved by using a hybrid foam of graphene/polypyrrole (rGO/PPy), which increased the surface temperature as high as 380 °C under irradiation of 808 nm light at 2.6 W cm^{-2}.[83]

Although the unique 2D nanostructure endows nanosheets with outstanding features, the lack of colloidal stability remains a great challenge to deeply develop their biomedical applications *in vivo*. For that, Ji *et al.* developed an effective method for incorporating GO sheets *in situ* into a thermosensitive matrix to obtain hybridized nanogels with an enhanced photothermal effect and improved loading efficiency toward anticancer drugs.[84] Similarly, a NIR- and pH-controlled carboxymethyl chitosan (CCS)-modified rGO/aldehyde modified PEG hydrogel was synthesized to exhibit outstanding delivery performance of DOX.[85] The functionalization with CCS achieved high NIR absorbing ability and uniform distribution of rGO, contributing to the enhanced photothermal performance. Alternatively, Gao *et al.* developed a photothermal miniature reactor based on graphene liquid marbles, which can exactly control the temperature for modulating reaction kinetics.[86]

With the power increment of the used laser, the surface temperature of graphene liquid marble was regulated between 21–135 °C and its surrounding water temperature was between 21–74 °C. Through temperature regulation, a 12-fold increased reaction rate was achieved for degrading methylene blue as compared to that value at room temperature.

As indicated, the solar energy can break viscosity. For utilizing this process, a 3D $CuFeSe_2$-modified graphene aerogel (GA–$CuFeSe_2$) was produced to exhibit an outstanding photothermal conversion activity with a PCE value of 79.62%.[87] Experimentally, the GA–$CuFeSe_2$ heated the crude oil to ~100 °C within 10 s, indicating the practical application of this nanohybrid for oil spills. In Chen's work, polyacrylic acid-*g*-polylactic acid (PAA-*g*-PLLA) was functionalized onto GO sheets *via* cleavable bonds and finally fabricated a stimuli-responsive scaffold to be embedded with adipose-derived stem cells (ADSCs) for breast cancer therapy (see Figure 6.9).[88] As reported, the GO–polymer scaffolds were able to simultaneously achieve pH-controlled PTT at low temperature for selectively inducing apoptosis of tumor cells and greatly improving ADSC growth, which caused the death of >95% cells in a human breast cancer (MCF-7) model *in vitro* and completely eliminated tumor tissue in mice. To combine the volumetric absorption of nanofluids and high latent storage density of phase change materials (PCMs), Yang *et al.* used melamine sponge as the supporting structures, paraffin wax as solid–liquid PCMs, rGO and zirconium carbide as solar absorbing agents and thermal conduction materials to fabricate novel form-stable PCM systems, which showed a high thermal storage ability and superb heat transferring process, and the PCE was up to 81% when 0.01 wt% zirconium carbide was doped into the PCM system.[89]

To deal with the global water crisis, solar energy has been used to purify wastewater and desalinate seawater *via* the generation of vapor. To avoid salt deposition on the evaporation surface and ensure long-term work for water evaporation, Zhu's group used rGO and ultralong hydroxyapatite nanowires (HNs) to fabricate a salt-rejecting photothermal paper, which had a hierarchical

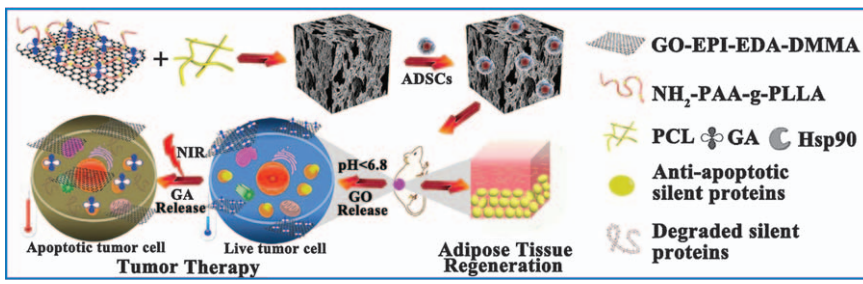

Figure 6.9 Schematic demonstration for synthesizing and utilizing an ADSC-embedded GO–GA-polymer scaffold in breast cancer therapy, which releases GO and GA *via* a pH-triggered process, and combines tumor selective PTT and adipose tissue regeneration.
Reproduced from ref. 88 with permission from John Wiley and Sons, Copyright © 2019 WILEY-VCH Verlag GmbH & Co. KGaA, Weinheim.

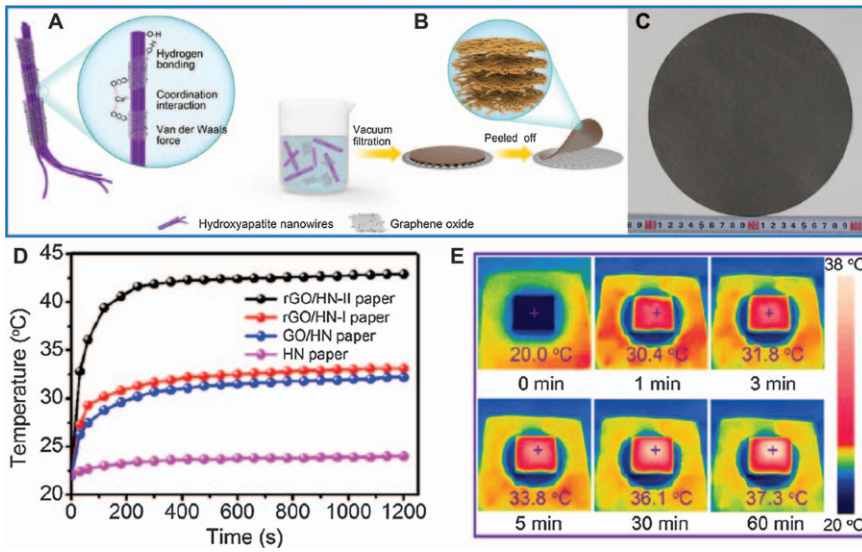

Figure 6.10 Synthesis and photothermal properties of GO-hydroxyapatite nanowire (HN) paper. (A) Hierarchical deposition of GO and HNs by vacuum-driven filtration. (B) Structure of layered GO/HN paper. (C) Optical image of the GO/HN paper. (D) Average paper surface temperature under 1 sun illumination. (E) NIR thermal images of the rGO/HN paper at different irradiation times by 1 sun.
Reproduced from ref. 90 with permission from American Chemical Society, Copyright 2020.

porous structure, interconnected channels, and high mechanical strength (see Figure 6.10).[90] Moreover, the length of time of the thermal treatment can adjust the hydrophilicity and hydrophobicity of the photothermal paper. Under irradiation of 1 sun ($1\ kW\,m^{-2}$), the evaporation rate of water and energy conversion efficiency over the hydrophilic rGO/HN paper were $1.48\ kg\,m^{-2}\,h^{-1}$ and 89.2%, respectively. Very recently, Li's group deposited graphene onto non-woven masks *via* a laser-driven forward transfer route, which can functionalize commercially available surgical masks with good self-cleaning and excellent photothermal performances.[91] After exposure to sunlight, the surface temperature of the functionalized mask can be rapidly increased to >80 °C, so that the masks can be reused after sunlight irradiation. More importantly, this graphene-modified mask can be reused directly in solar-trigged desalination and exhibit a good salt-rejecting property for long-term usage.

6.4 TMD Nanosheets

In recent years, TMD nanosheets have been reported frequently to develop photothermal materials for various biomedical applications.[2] As the most widely-used TMD nanosheets, the photothermal properties of MoS_2 nanosheets were first demonstrated, followed by other TMD nanosheets such as $MoSe_2$, $MoTe_2$, WS_2, and WSe_2.

6.4.1 MoS_2 Nanosheets

With a unique bandgap structure and various excellent optical properties, MoS_2 nanosheets have attracted wide research attention in the fields of energy storage, biosensors, and other biomedical fields.[18,92,93] Particularly, MoS_2 nanosheets have been usually utilized as novel photothermal agents for efficient PTT of cancer and improved antibacterial efficacy *via* their high absorption of NIR light.[94] As reported, the normal MoS_2 sheets with interlayer spacing of ~0.65 nm exhibited a PCE at ~45%, while interlayer-expanded MoS_2 nanosheets (~0.94 nm) were demonstrated to show a higher PCE at ~62%.[95] For further increasing the PCE or/and improving the stability of MoS_2 nanosheets, more and more research has reported the preparation of surface-modified and nano-hybridized MoS_2 nanosheets in the past five years.

Polymers-modified MoS_2 Nanosheets: To improve the dispersibility and stability of MoS_2 nanosheets in water, the surface of MoS_2 is usually modified with linear polymer PEG *via* physical adsorption. As a typical example, PEG was readily modified on MoS_2 nanoflakes in a hydrothermal synthesis *via* the assistance of PAA, and the PEGylated MoS_2 flakes had superb stability in various solutions and high photothermal conversion activity, which was used for effectively ablating cancer cells and suppressing the tumor growth.[96] Similarly, a one-pot solvothermal synthesis was developed for the convenient fabrication of PEGylated MoS_2 sheets *via* an ''integrated'' precursor with Mo and S elements.[97] In Jia's work,[98] erlotinib (Er) was modified to MoS_2 sheets *via* the linkage of PEG in click chemistry and the subsequent incorporation of DOX resulted in a multifunctional MoS_2 platform for performing co-delivery of Er and DOX in a more effective cancer therapy. In the presence of NIR light, the usage of MoS_2–PEG–Er/DOX can achieve the synergetic chemo-photothermal therapy of cancer and efficiently suppressed tumor growth in lung cancer-bearing mice. In Han's work,[99] MoS_2 sheets were produced by chemical exfoliation together with probe sonication and further modified with cytosine–phosphate–guanine (CPG) and PEG to fabricate MoS_2–PEG–CPG nanosheets as a multifunctional platform for photothermal immunotherapy, which was further enhanced by photothermal treatment. As indicated, the branched polymers are more slowly cleared from blood circulation as compared to linear ones. For that, Zhou's group presented a surface-initiated ring-opening polymerization-based strategy to modify the surface of MoS_2 sheets with multihydroxy hyperbranched polyglycerol (HPG), which possessed an outstanding photothermal ability for converting light into heat in PTT.[100] Similarly, Wang *et al.* fabricated HPG-functionalized MoS_2 nanosheets by the physical absorption of HPG onto the MoS_2 surface, forming a novel photothermal nanocarrier with a high PCE for chemo-photothermal therapy.[101] In addition, block copolymer-MoS_2 nanocomposites (BCP-MoS_2) were also synthesized as a novel self-monitoring photothermal agent for simultaneous photothermal heating and temperature profile imaging.[102] After exposure to NIR laser, photothermal energy generated by MoS_2 effectively increased the local temperature and simultaneously induced conformational transitions of

the BCP over MoS_2, so that a distance-dependent Förster resonance energy transfer occurred between the BCP and MoS_2 to cause the change of fluorescent signal correspondingly. Experimentally, the usage of BCP-MoS_2 in photothermal heating and optical imaging was fully reversible with good stability. Recently, Zhang *et al.* reported a general polyphenol-based approach for facilely exfoliating various TMD sheets at the monolayer or multilayer.[103] In the optimized experiment of exfoliating MoS_2 nanosheets, the yield and concentration of MoS_2 sheets were as high as 60.5% and 1.21 mg mL^{-1}, respectively. Moreover, the as-obtained MoS_2 sheets possessed excellent biological stability for loading antibiotic drugs and showed a high photothermal conversion capability for a synergetic application of chemotherapy and PTT (see Figure 6.11).

Biomacromolecule-modified MoS_2 Nanosheets: In Jin's work,[104] MoS_2 nanosheets were linked with positively-charged quaternized chitosan (QCS) for improving the dispensability/stability and enhancing the binding force of MoS_2 on a bacterial membrane. Through π–π stacking and hydrophobic interaction, a first-line antibiotic, ofloxacin (OFLX), was further loaded onto QCS–MoS_2 nanosheets for excellent bactericidal activity *via* combining antibiotic–photothermal therapy, which can be performed at a mild temperature of 45 °C and low concentration of antibiotic. Similarly, HA was modified onto MoS_2 sheets *via* the formation of disulfide to synthesize a sheddable HA shell on the MoS_2 surface, which was used as a functionalized nanoplatform to achieve targeted delivery of camptothecin and controlled drug release in the presence of tumor-associated GSH or/and NIR irradiation.[105]

In recent years, more and more biomacromolecules have been employed to develop MoS_2-based photothermal materials. For instance, Deng *et al.* prepared MoS_2 nanosheets using protein BSA to exhibit a strong NIR absorbing capability and high drug loading ratio for better tumor therapy.[106] For the loaded resveratrol (RV) on MoS_2 sheets (MoS_2–RV), the MoS_2–RV nanosheets can passively target and accumulate to the tumor region, and RV molecules can be released from the surface of MoS_2 nanosheets *via* irradiation with an NIR laser (1 W cm^{-2}). Furthermore, Zhang *et al.* modified PEI, PEG, and BSA on MoS_2 nanosheets *via* the linking of FA to form a novel nanoplatform with dual stimuli-trigged (pH and NIR) targeted drug delivery and chemo-photothermal functions.[107] Alternatively, regenerated silk fibroin (RSF) can self-assemble and bind at the surface of MoS_2 sheets through simply adding MoS_2 dispersion into RSF aqueous solution.[108] The resultant RSF/MoS_2 nanohybrids demonstrated higher photothermal capability/stability and less cytotoxicity as compared to the bare MoS_2, resulting in outstanding photothermal activity to ablate HeLa cells *in vitro*. In another work, Xie *et al.* fabricated an egg yolk phospholipid connected MoS_2 carrier by simple physical adsorption for treating tumors in chemotherapy and PTT.[109] As indicated, the lipid functionalization significantly increased the accumulating ability of the modified carrier in mice tumors, leading to a better photothermal application than that of pure MoS_2 sheets. For enhancing the photothermal capability of the MoS_2 nanosheets, melanin (Mel) as a new type of photothermal material was modified on HA-targeted MoS_2

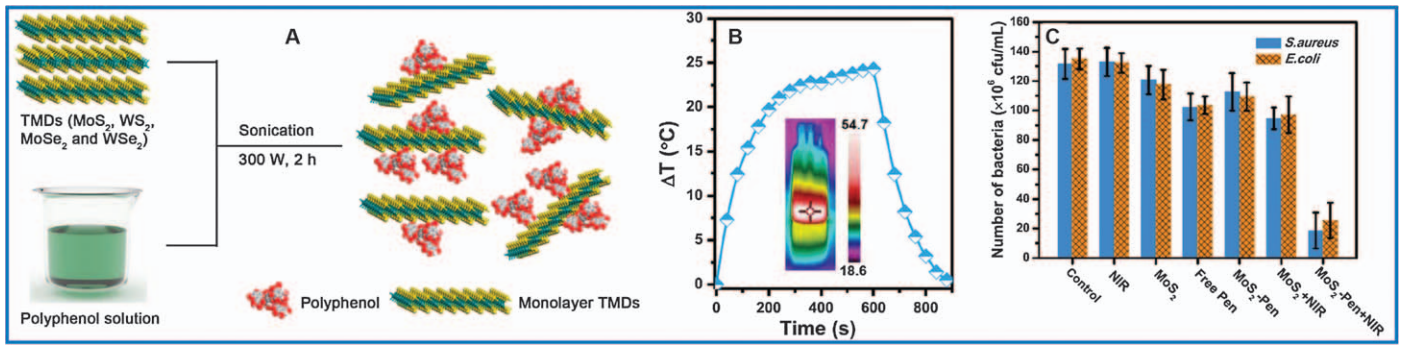

Figure 6.11 (A) Schematic of TMD nanosheet exfoliation *via* polyphenol-assisted sonication. (B) Photothermal characterization of a MoS_2–penicillin solution under irradiation of NIR light (3 W cm^{-2}). (C) Number of *S. aureus* and *E. coli* bacteria when using various antibacterial materials.
Reproduced from ref. 103 with permission from American Chemical Society, Copyright 2018.

sheets to form a multifunctional drug delivery system with strong interaction toward CD44 receptor-positive MCF-7 cells.[110] The prepared nanocomposite had a high photothermal capability (PCE at 55.3%) and good biocompatibility. Moreover, the drug release can be precisely controlled by employing the low pH in the tumor cells and exposing to NIR irradiation. Recently, antibody (anti-protein A IgG), PDA, and PEG–SH-functionalized MoS_2 nanosheets were synthesized to serve as an *S. aureus*-targeted PTT nanoagent.[111] The PDA served as a bio-nano interface to be beneficial for the covalent binding of antibody and PEG–SH to MoS_2 sheets *via* catechol chemistry. As a result, the targeted PTT showed the superb killing ability of larger than 4 log (>99.99%) against *S. aureus* both in biofilms and infected tissues and did not cause damage to normal mammalian cells.

Nano-hybridized MoS_2 Nanosheets: The decoration of nanostructured materials on MoS_2 sheets has been established for improving their PCE, biocompatibility, and photostability in cancer PTT. Typically, Shen's group used 0D N-doped carbon dots (CDs) and 2D MoS_2 sheets as the assembled units to construct 0D/2D/0D sandwich heterojunctions, which endowed an additional increment for NIR absorption *via* the combination of CDs and MoS_2 sheets and obtained a much higher PCE (78.2%) than that of the individual components (CDs: 37.6%; MoS_2: 38.3%).[112] In Liu's work,[113] an effective approach was demonstrated to selectively induce the epitaxial growth of Au nanocrystals on MoS_2 sheets for increased NIR absorbance and better photoelectric application, which can be used as a multifunctional theranostic nanoplatform for imaging-guided photothermal and radiation therapy. After modification of PEG, the obtained hybrid showed strong X-ray attenuation and high photothermal conversion capability and achieved synergistic tumor inhibition *via* hyperthermia elevated oxygenation levels and sensitized radiation therapy. Alternatively, multifunctional FePt/MoS_2–FA nanocomposites (FPMF) were synthesized by hybridizing FePt nanocrystals and FA onto MoS_2 sheets.[114] In an experiment, FePt nanocrystals can catalyze the Fenton reaction to generate reactive oxygen species. Moreover, tumor cells were effectively ablated by the produced heat *via* photothermal conversion of MoS_2 sheets.

Beyond metal nanostructures, metal oxides and sulfides were also utilized to fabricate hybrid systems for various photothermal exploitations. Typically, Shao *et al.* wrapped MoS_2 layers around DOX-loaded periodic mesoporous organosilicas (PMOs) and then decorated them with PEG to obtain a PMO–DOX@MoS_2–PEG platform as a NIR-induced drug nanocarrier.[115] The resultant hybrid nanoplatforms had a large drug loading capacity (160 $\mu g\ mg^{-1}$), superb photothermal conversion activity, and good dispersibility in physiological solution. Moreover, the photothermal heat from the MoS_2 sheets can control the release of DOX by using an 808 nm laser, which achieved a combined chemotherapy and PTT for liver cancer cells and breast cancer cells. In Zhao's work,[116] MoS_2 sheets and Fe_3O_4 particles were integrated into a magnetic targeted photothermal system, in which MoS_2 can convert light energy into heat while Fe_3O_4 acted as a targeted unit toward the tumor site guided by an additional magnetic field. After functionalization with PEG, the

MoS_2/Fe_3O_4 composite was successfully employed as a dual-functional system for T_2-weighted magnetic resonance (MR) and photoacoustic tomography (PAT) imaging. Similarly, Fe_3O_4 nanoparticles were loaded onto the surface of MoS_2 sheets through a sulfur-based reaction to form MoS_2–Fe_3O_4 nanocomposites,[117] which were then conjuncted with two kinds of PEG to achieve improved stability for PAT and MR imaging. In Rajasekar's work,[118] a robust route was developed to deposit tantalum (TaO_2) onto a CS-coated MoS_2 nanosheet *via* electrostatic interaction for improving cancer PTT efficiency. The prepared TaO_2–CS–MoS_2 nanomaterial showed low toxicity and high photostability and PCE, which increased the environmental temperature from 26 to 47.2 °C under 808 nm light for 5 min.

For achieving the hybridization of MoS_2 with metal sulfides, single-layer MoS_2 nanosheets were modified with different fluorescent semiconductor quantum dots (QDs) and arginine–glycine–aspartic (RGD)-containing peptides to form novel multifunctional 0D/2D RGD–QD–MoS_2 sheets with superb fluorescence, photothermal activity, and cancer-targeted ability.[119] As indicated, HeLa tumor cells in mice can be imaged in fluorescence and completely eliminated by photothermal ablation using NIR light at low power, which resulted from the rapid accumulation of RGD–QD–MoS_2 at the tumor sites owing to the RGD-integrin targeting function and the enhanced penetration and retention effect. In Zhu's work,[120] MoS_2 nanosheets were connected with copper sulfide (CuS) and modified with PEG to form a multifunctional nanoplatform. The presence of both MoS_2 and CuS led to a high PCE at ~59.3%. After loading with DOX, the synergistic usage of chemo-photothermal therapy resulted in more cell death than either chemotherapy or PTT. More interestingly, MoS_2/Bi_2S_3–PEG (MBP) nanosheets were produced by using a one-pot, solvothermal method for image-guided diagnosis of tumors and combined tumor PTT and radiotherapy (RT) (see Figure 6.12).[121] The MoS_2 nanosheets endowed MBP with excellent PTT performance and

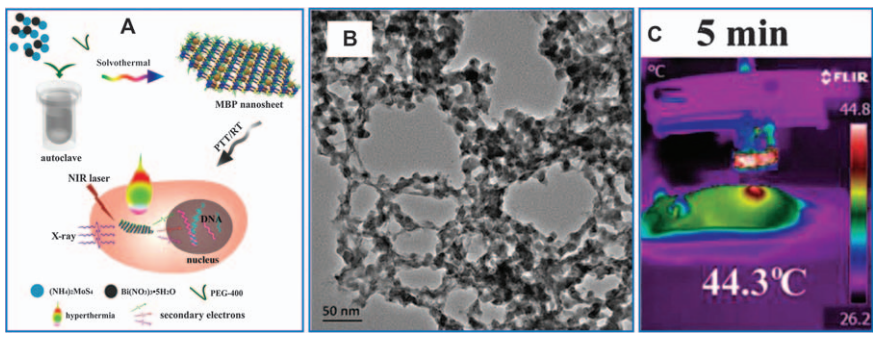

Figure 6.12 (A) Schematic figure for the solvothermal preparation of MoS_2/Bi_2S_3–PEG (MBP) sheets and their PTT and radiotherapy (RT) of tumors. (B) TEM image of MBP nanosheets. (C) *In vivo* photothermal image of MBP-injected mice after irradiation for 5 min.
Reproduced from ref. 121 with permission from John Wiley and Sons, Copyright © 2015 WILEY-VCH Verlag GmbH & Co. KGaA, Weinheim.

photoacoustic imaging property, and such 2D MBP nanostructures exhibited desirable photothermal capability, good colloidal stability, and biocompatibility in biomedical applications.

6.4.2 $MoSe_2$ and $MoTe_2$ Nanosheets

Similar to MoS_2, ultrathin $MoSe_2$ and $MoTe_2$ were also reported as good 2D photothermal agents. As shown in Figure 6.13, a PVP-assisted exfoliation was developed to produce and simultaneously functionalize $MoSe_2$ sheets.[122] The $MoSe_2$–PVP nanosheets with a hydrophilic surface were found to be biocompatible and used as a promising PTT material. Furthermore, the resultant nanosheets were also encapsulated into a hydrogel matrix for developing some smart devices. Alternatively, a red blood cell (RBC) membrane was utilized for camouflaging $MoSe_2$ sheets to attain enhanced hemocompatibility and circulation time due to the prevention of macrophage phagocytosis.[123] In Zhang's work,[124] $MoTe_2$ sheets were modified with PEG–cyclic arginine–glycine aspartic acid tripeptide (PEG–cRGD) to exhibit wider NIR absorption. After loading with DOX, $MoTe_2$–PEG–cRGD/DOX was employed in the combined PTT and chemotherapy. Owing to the high PCE, $MoTe_2$–PEG–cRGD/DOX showed an excellent killing ability for tumor cells in the presence of NIR light. Through the cRGD-guided targeted process, $MoTe_2$–PEG–cRGD/DOX efficiently accumulated at tumor sites to cause a strong ablation of tumor cells.

6.4.3 WS_2 and WSe_2 Nanosheets

Stable 1T-WS_2 ultrathin nanosheets were prepared *via* intercalation with NH_4^+ by employing a hydrothermal method and were used in the PTT of cancer.[125] The resultant 150 nm-sized nanosheets were highly hydrophilic and had strong light absorbance and superb photostability in a broad NIR region. Under irradiation of an 808 nm laser, the 1T-WS_2 sheets could successfully ablate tumor cells *via* the photothermal process. Alternatively, Qu's group demonstrated the photothermal application of WS_2 sheets for not only effectively inhibiting Aβ aggregation and but also dissociating the formed Aβ aggregates (of note, to inhibit Aβ aggregation and destabilize the formed Aβ fibrils has a promising function against Alzheimer's disease).[126] As indicated, Aβ40 molecules can selectively bind onto the WS_2's surface through van der Waals and electrostatic forces and thus inhibit the aggregation of Aβ40. More importantly, the high NIR absorbing capability of WS_2 enabled amyloid aggregates to be re-dissolved in the presence of NIR light. In Shen's work,[127] WS_2 nanosheets were connected with a biomimetic liposome (WS_2-lipid) to achieve a combined chemo and photothermal therapeutic therapy owing to excellent photothermal amount and high drug loading capability. In addition, Geng *et al.* synthesized biocompatible, positively-charged CDs and modified them on both sides of negatively-charged WS_2 sheets *via* electrostatically driven assembly.[128] The 0D/2D heterostructure was readily utilized to trigger an

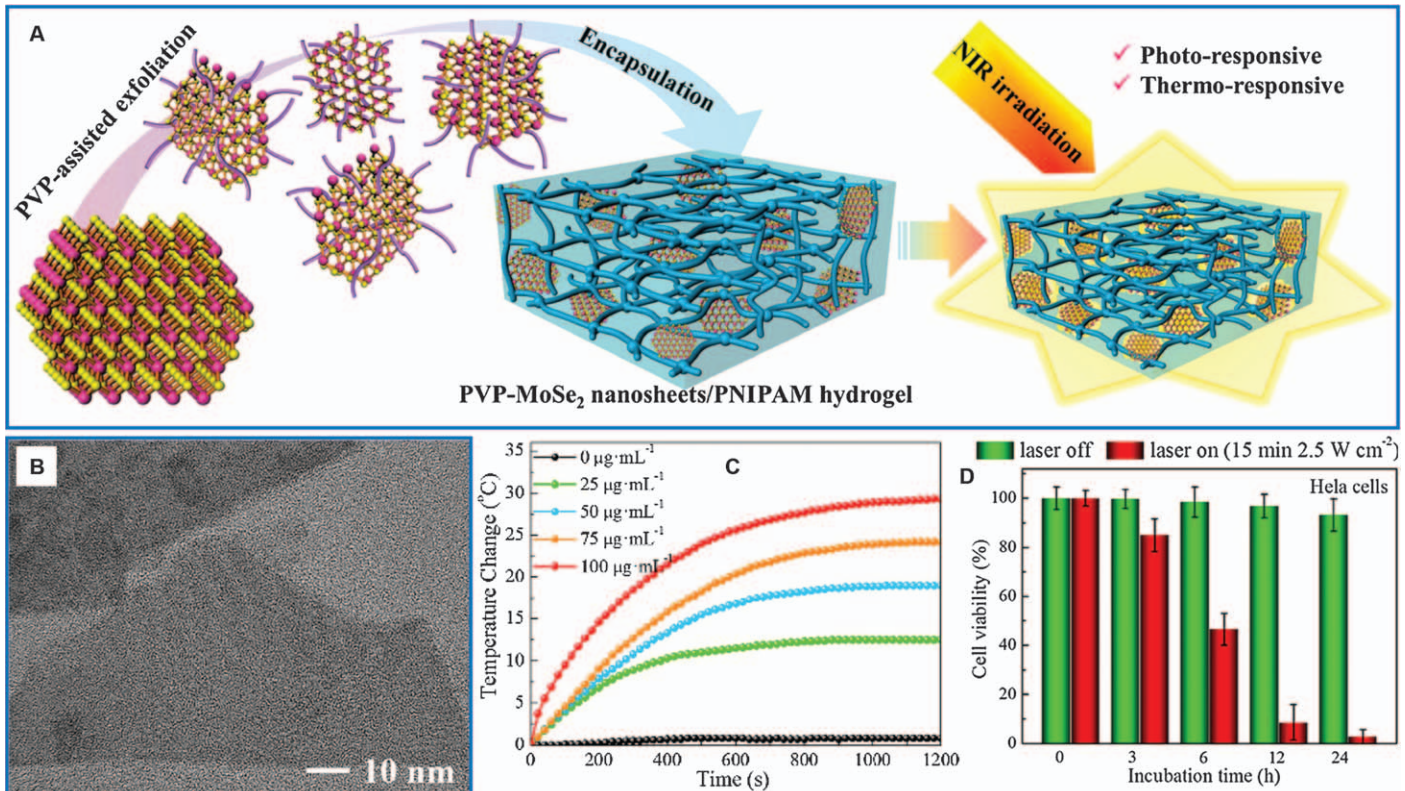

Figure 6.13 (A) Schematic of PVP–$MoSe_2$ sheets/PNIPAM hydrogel preparation. (B) TEM image of $MoSe_2$ sheets. (C) Temperature elevation of the solution with different concentrations of PVP–$MoSe_2$ when using an 808 nm laser at 2.5 W cm^{-2}. (D) Viability of HeLa cells after incubation with PVP–$MoSe_2$ for different amounts of time with or without NIR treatment. Reproduced from ref. 122 with permission from American Chemical Society, Copyright 2016.

effective photothermal process with NIR irradiation of 1064 nm, which can simultaneously achieve osteosarcoma treatment and bone regeneration.

By using BSA as both exfoliating and stabilizing agents, WSe_2 sheets were produced *via* a simple and efficient liquid-phase exfoliation to endow the WSe_2–BSA nanosheets with high chemical stability and desirable biocompatibility.[129] The obtained WSe_2–BSA nanosheets were utilized not only as an efficient photothermal material but also as a nanocarrier for loading photosensitive methylene blue. In another work, PVP-intercalated WSe_2 nanosheets were facilely synthesized by a solvothermal reaction of selenourea crystals and WCl_6 along with a PVP polymeric nanogel.[130] The resultant PVP-inserted WSe_2 sheets showed a high PCE, greatly improved biocompatibility, and physiological stability.

6.4.4 Other TMD Nanosheets

As a new TMD nanomaterial, TiS_2 nanosheets were produced by a chemically synthetic approach and then connected with PEG to obtain TiS_2–PEG nanosheets with high stability in physiological environments and no clear toxicity (see Figure 6.14).[131] With high absorbance of NIR light, the TiS_2–PEG sheets could provide a strong contrast in photoacoustic imaging, which revealed the high tumor uptake and retention of sheets after systemic administration into tumor-bearing mice. Moreover, the TiS_2–PEG sheets were further applied for *in vivo* PTT to completely eliminate the tumors in mice under NIR laser irradiation. Similarly, another new kind of TMD, 2D rhenium disulfide (ReS_2) with strong NIR absorbance and X-ray attenuation, was successfully produced and modified with PEG.[132] The resultant ReS_2–PEG sheets were stable in physiological environment and the synergistic photothermal radiotherapy achieved an extraordinary destruction of tumors. In another work, a probe sonication-driven exfoliation was used to synthesize ReS_2–PVP sheets at scale.[133] With strong NIR absorbance and high PCE (79.2%), ReS_2 sheets served as a therapeutic agent for complete ablation of tumors without no obvious toxicity. Recently, ultrathin ReS_2 were also prepared through ultrasonic exfoliation in BSA solution to show good biocompatibility and high NIR absorbing ability.[134] For better performance, the anti-cancer drug resveratrol (RSV) and targeted molecule FA was successively connected on the ReS_2 surface to fabricate ReS_2@RSV–FA nanocomposites. Without NIR irradiation but $pH = 6.5$, ~16.5% of the RSV molecules were released after 24 h, whereas the value was increased to 55.3% in the presence of NIR light (1 $W\,cm^{-2}$). This indicated that this hybridized 2D structure provided a dual-stimuli-sensitive drug delivery and had the potential to be utilized for combining chemo-photothermal therapy in cancer treatment.

6.5 Black Phosphorus Nanosheets

With a direct bandgap, broad optical absorbance from the visible to NIR region, and superb photothermal capability, BP-based nanostructured

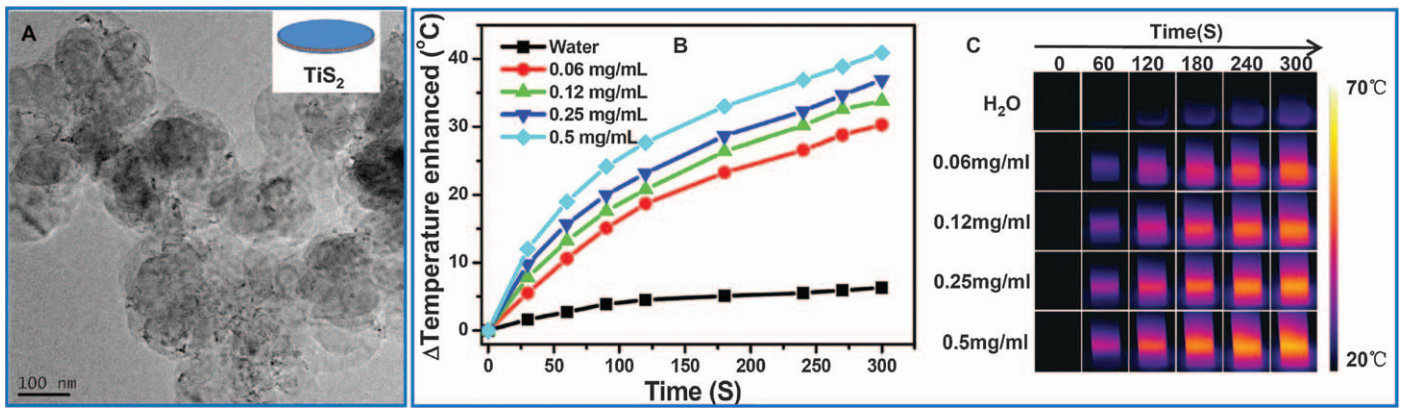

Figure 6.14 (A) TEM image of TiS_2 nanosheets. (B) Photothermal curves and (C) IR thermal images of solutions with different TiS_2 concentrations under irradiation of 808 nm light (0.8 W cm^{-2}).
Reproduced from ref. 131 with permission from the Royal Society of Chemistry, Copyright 2015.

materials have exhibited various promising applications as effective photothermal systems.[19] As reported, the BP sheets with a larger size are confirmed to have a higher PCE in the ablation of cancer cells.[135] And, the photothermal effect of BP nanosheets was used for developing a novel immunofiltration strip that can readout the change of temperature.[136] In addition, BP nanosheets are also a highly-efficient drug delivery system with a large loading capacity, which can be attributed to its puckered honeycomb structure and ultra large surface area. Therefore, BP-based PTT and PDT have emerged and exhibited outstanding anti-tumor therapeutic abilities. Particularly, BP nanosheets have recently been reported as an intriguing photothermal material in PTT against cancer. Before the practical utilization of BP sheets, their poor stability should first be improved greatly. For that, some effective approaches have been developed to protect BP layers from rapid degradation in an ambient environment, including surface modification and hybridization with other functional materials.

6.5.1 Surface-modified BP Nanosheets

In recent years, various functional species have been modified onto BP nanosheets for improving their stability or/and introducing new functions. For instance, Nile Blue (NB) dye was modified onto BP nanosheets *via* diazonium chemistry, which not only enhanced the stability of BP sheets but also endowed them with NIR fluorescence.[137] As indicated, the dye-modified BP system was a novel multifunctional nanomedicine with good biocompatibility, strong PTT and NIR imaging capabilities. Moreover, the NB@BP sheets marked the tumor sites with red fluorescence and caused the efficient ablation of tumor cells in the presence of NIR light. In Liu's work,[138] exfoliated BP nanosheets were linked with PEI and PEG to serve as the NIR-responsive nanoagent to trigger PTT. Meanwhile, Xu *et al.* used the effective protection of poly(lactic-*co*-glycolic acid) (PLGA) to improve the defect of BP nanosheets, which preserved the stable PTT effect of BP sheets and biodegradability of the material.[139] Meanwhile, DOX was loaded on BP/PLGA for further chemotherapy and preventing the recurrence of tumors after PTT. In Chen's work,[140] BP sheets were proved to possess an exceptionally larger loading capacity for DOX than graphene and MoS_2. As a result, drug release was increased in the acidic environment and further quickened *via* the photothermal process of BP sheets by using 808 nm light. Meanwhile, the intrinsic feature of BP sheets allowed them to simultaneously be used in PDT and PTT.

Recently, Yang's group synthesized Ce6-connected BP sheets for synergistic PTT and PDT of cancer under the guidance of fluorescence and thermal imaging.[141] As indicated, the loading of Ce6 endowed BP nanosheets good biocompatibility, physiological stability, and tumor-targeted ability, and an increased PCE was achieved as compared to BP@PEG (43.6% *vs.* 28.7%). In another work, BP nanosheets were modified with PDA and then covalently connected with both Ce6 and triphenyl phosphonium (TPP) *via* carbodiimide reaction of amino with carboxyl groups (see Figure 6.15).[142]

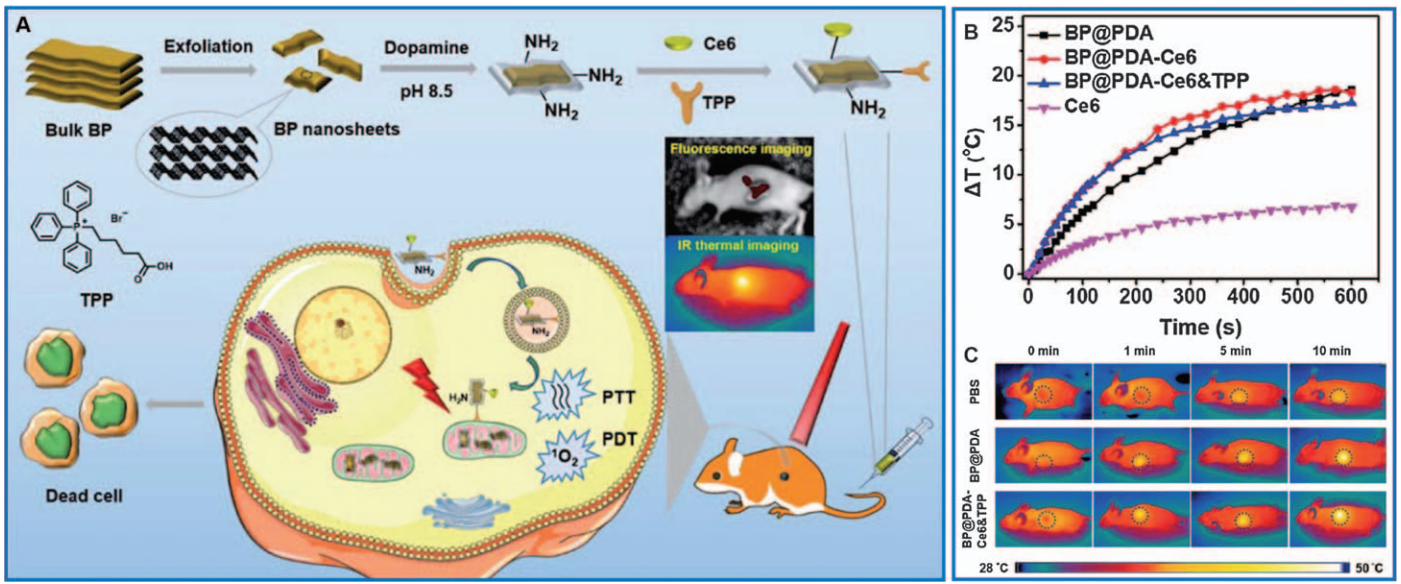

Figure 6.15 (A) Schematic figure for preparing BP@PDA–Ce6&TPP sheets and their therapeutic applications. (B) Photothermal response of different samples under irradiation with a 660 nm laser for 10 min (1.0 W cm^{-2}). (C) IR thermal images of mice after injecting BP@PDA NSs or BP@PDA–Ce6&TPP sheets under different times of laser irradiation.
Reproduced from ref. 142 with permission from the Royal Society of Chemistry, Copyright 2019.

Through the strong absorption of BP@PDA for NIR light and the rapid generation of reactive oxygen species by Ce6, the resultant nanosystems showed significantly enhanced efficiency in the killing of cancer cells. Alternatively, Deng's group demonstrated that platinum-involved anticancer drugs (DACHPt or $Pt(NH_3)_2$) were coordinated onto BP sheets for forming BP/DACHPt and BP/$Pt(NH_3)_2$ composites with improved stability.[143] Interestingly, BP sheets were found to bind DACHPt twice their weight and release it in an acid- and NIR-sensitive manner. *Via* combined photothermal and chemo therapy, BP/DACHPt can completely kill the tumor cells. In Zhang's work,[144] the BP sheets were produced *via* a liquid-phase exfoliation approach and combined with gemcitabine into the thermo-sensitive Pluronic F127 hydrogel by a ''cold method'' for intratumoral injection. The BP-based hydrogel will result in phase translation at near body temperature and exhibited high photothermal efficacy *in vitro* and good biodegradability for better applications. In another interesting work, BP sheets were successfully exfoliated by a self-made ultrasonic route and then were electrostatically modified with mitoxantrone hydrochloride (MTX) and HA at their surface.[145] The resultant BP@MTX–HA nanosheets not only had good physical stability and high PCE but also exhibited pH/NIR-responsive release abilities. Experimentally, the temperature can increase to >45 °C after irradiation by 808 nm light for 3 min (1.0 W cm^{-2}).

For achieving a better performance, more combined formats of BP and polymers have been developed for stabilizing BP nanosheets. Typically, polypyrrole (PPy) particles were loaded onto BP nanosheets to fabricate nanohybrids with high-performance for PTT, which benefited from the enhanced NIR absorbing capability of the two components.[146] Compared to the bare BP nanosheets, the nanocomposites exhibited good biocompatibility and superior PCE in the NIR region. In Hai's work,[147] a multifunctional liposome (MFL) as both the targeting ligands and imaging units was produced and then connected at the surface of BP nanosheets to fabricate a sandwiched BP@MFL platform, which effectively improved the stability of BP nanosheets in water and selectively entered into cancer cells for their photothermal ablation. Alternatively, a PDA functionalized approach was employed to improve the stability and photothermal capability of BP sheets through the formation of nanocapsules (see Figure 6.16), which were utilized as multifunctional delivery systems for targeted chemo, gene, and PTT in cancer treatment.[148] Furthermore, poly(vinyl alcohol) hydrogels based on PDA modified BP were conveniently produced *via* a freezing/thawing strategy.[149] With a high PCE, the composited hydrogels exhibited a NIR-trigged drug release process and also showed enhanced mechanical strength due to the strong hydrogen bonding interaction of BP nanosheets and the PVA matrix. Similarly, BP nanosheets were incorporated into a thermosensitive hydrogel of poly(D,L-lactide)–poly(ethylene glycol)–poly(D,L-lactide) (PLEL) to fabricate an interesting PTT nanosystem for postoperative therapy of cancer.[150] As indicated, the BP@PLEL hydrogels were biodegradable and biocompatible and exhibited superb photothermal capability in the NIR region and NIR-trigged sol–gel

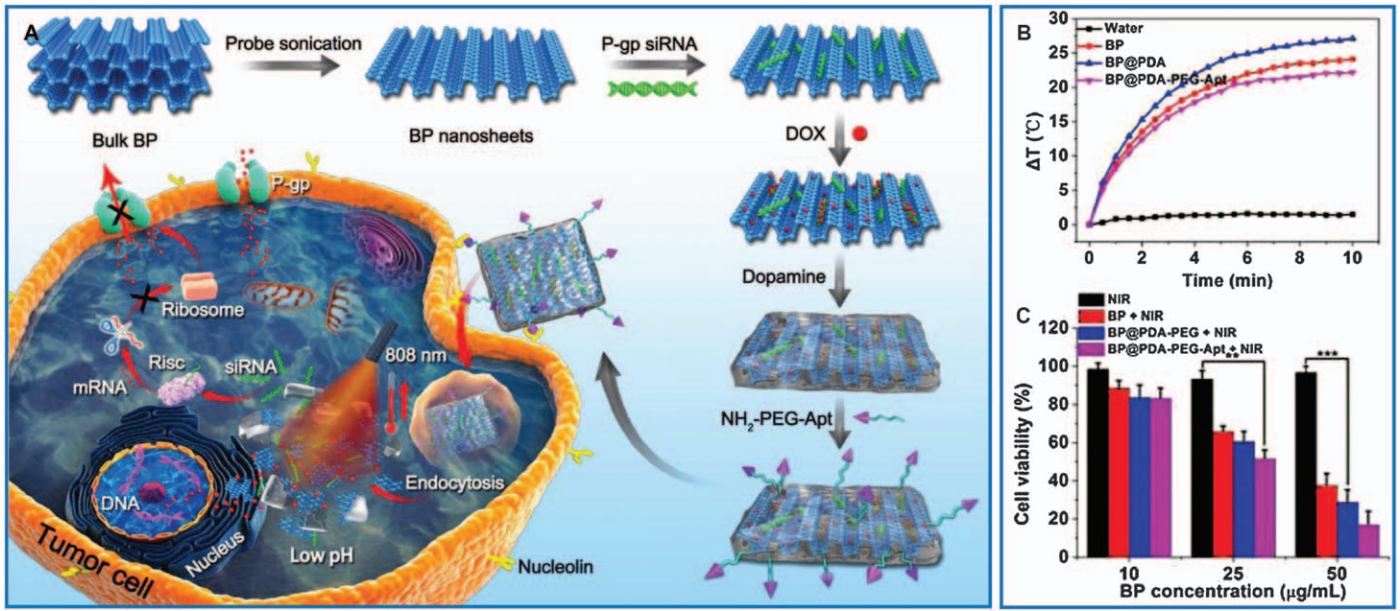

Figure 6.16 (A) Schematic for fabricating BP-based nanosheets and combined chemo/gene/photothermal therapy on tumor cells. (B) Temperature elevation curves of different samples after irradiation with an 808 nm laser (1 W cm^{-2}). (C) The relative cell viabilities of MCF-7 cells after incubation with different concentrations of BP samples and irradiation with an NIR laser for 10 min.
Reproduced from ref. 148, https://doi.org/10.1002/advs.201800510, under the terms of the CC BY 4.0 license, https://creativecommons.org/licenses/by/4.0/.

transition. Therefore, the BP@PLEL hydrogels enabled fast gelation to form a gelled membrane on wounds in the presence of NIR light and offered high PTT efficacy for eliminating tumor tissues. Recently, Xing *et al.* demonstrated that the combination of cellulose and BP sheets can be utilized to form green and injectable composite hydrogels for PTT against cancer.[151] The 3D cellulose/BP network had micrometer-sized pores and thin, strong cellulose walls in it, and thus exhibited outstanding photothermal conversion, improved stability, and flexibility.

6.5.2 Au Nanostructure-hybridized BP Nanosheets

As shown in Figure 6.17, BP bulks were exfoliated with the assistance of sonication into BP sheets in deoxygenated water or hexane, and then monodisperse AuNPs were assembled onto formed BP sheets to fabricate BP/Au hybrid nanomaterals.[152] Thanks to the high PCE of BP/Au composites after irradiation with an NIR laser, they ablated the bacterial membrane more efficiently than pure BP with a biofilm inhibition rate of 58%. Alternatively, BP nanosheets loaded with AuNPs were achieved by a one-step synthetic approach, in which the Au nanocrystals not only enhanced the PCE of the composites but also endowed BP–Au with the ability to serve as a SERS substrate for Raman biodetection.[153] Under 808 nm irradiation, BP–Au sheets were capable of generating sufficient hyperthermia to ablate cancer cells, and the transplanted tumor cells were not found in most of the tumor-bearing mice. In Wang's work,[154] AuNP-enhanced BP sheets were used as the signal component to develop an immunochromatographic sensor (PT-ICS) as the antibody probe for quantitative photothermal sensing process. As indicated, the PCE of the BP–Au sheet was increased by 12.9% as compared to the bare BP sheets at 808 nm irradiation. Moreover, the antibody was more easily connected to the hybrid sheets owing to the strong physical adsorption of AuNPs. Recently, Liu *et al.* fabricated BP–Au hybrids in the solution of BP flakes and gold salt by using BP as the sole reducing agent, which was revealed to have an extraordinary PCE and drug delivery amount.[155] For achieving a broad light absorption band, a novel hybrid was produced by assembling Fe_3O_4 and AuNPs on BP sheets (BPs@Au@Fe_3O_4), which were highly biocompatible and exhibited an outstanding inhibition efficacy for tumors *via* the synergistic PTT and PDT.[156] Moreover, the BP@Au@Fe_3O_4 nanohybrid can precisely detect the growth and inhibition of tumor with the assistance of magnetic resonance imaging.

6.5.3 BP Nanosheets Hybridized with Other Species Beyond Au

Hu *et al.* reported that BP nanosheets can capture Cu^{2+} to accelerate the degradation of BP and enhance its photothermal stability, and achieve chemodynamic therapy-improved PTT.[157] Furthermore, when $^{64}Cu^{2+}$ was employed, positron emission tomography (PET) imaging can be developed to quantitatively track the nanosheets *in vivo* at real time. In another work, FePt

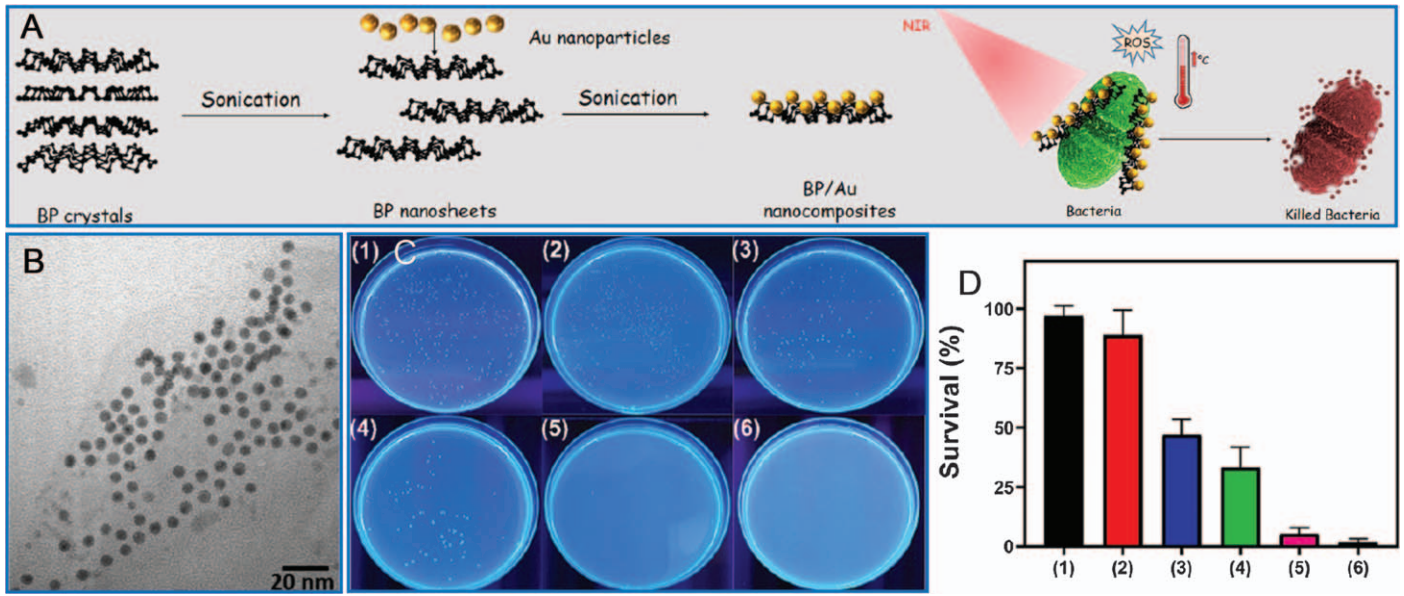

Figure 6.17 (A) The exfoliation/hybridization of BP nanosheets and their photothermal antibacterial applications under NIR light. (B) TEM image of BP/Au nanocomposites. (C) Agar petri dish images of *E. faecalis* bacterial colonies after treatment with BP/Au nanocomposites and (D) their corresponding survival rates: (1) bacteria only, (2) NIR laser, (3) BP, (4) BP + NIR laser, (5) BP/Au, and (6) BP/Au + NIR laser.
Reproduced from ref. 152 with permission from American Chemical Society, Copyright 2020.

nanocrystals were decorated on BP sheets to form a FePt/BP–PEI–FA hybrid platform, which can provide the synergistic tumor treatments from PTT, PDT, and chemodynamic therapy (CDT).[158] Alternatively, Lv's group used ultrathin BP nanosheets as nanocarriers and equipped them with upconversion NYF particles ($NaYF_4$:Yb^{3+},Tm^{3+}) as imaging agents, which can exhibit photothermal and photodynamic functions for efficiently treating tumors after combining with immunotherapy (see Figure 6.18).[159] As indicated, the PCE can reach 30.84% by using 980 nm light, higher than common Au nanostructures such as AuNSs (22.63%) and AuNRs (23.33%). More recently, Xu *et al.* used upconversion nanoparticles as cores to synthesize SiO_2 shells and CuS nanocrystals were coated onto the SiO_2 shells. After further modifying with PEG, the CuS-involved nanoparticles were finally conjugated onto the surface of BP sheets *via* electrostatic interaction.[160] Through further loading of anticancer drugs, the synergistic therapy of PTT, PDT, and chemotherapy was performed for greatly improved performance.

6.6 Summary and Outlook

With an ultrathin thickness and thickness-dependent bandgaps, 2D nanostructured materials can greatly absorb visible or infrared light and subsequently generate considerable heat *via* high-efficiency photothermal conversion. Herein, we first demonstrate the usual preparation methods of 2D nanomaterials and then used graphene, TMD, and BP nanosheets as typical examples to summarize the photothermal properties of surface-modified and nano species-hybridized 2D nanomaterials. Meanwhile, their novel photothermal applications are also involved, particularly the photothermal therapies on cancer and bacterial infections. Beyond the 2D nanomaterials demonstrated here, another two types of nanosheets also have the unique photothermal-conversion property for being utilized in PTT and combined therapies, *i.e.*, MXenes[161] and metal Pd nanosheets.[162] To understand their photothermal properties more easily, the merits and drawbacks of different 2D nanomaterials are summarized in Table 6.1, which also demonstrate the representative PCE values of typical nanosheets reported in previous studies.

With excellent photothermal capability and promising potential applications as photothermal nanomaterials, 2D nanomaterials and their hybridized composites are developed at a rapid rate, however, they still cannot meet the requirements for clinical translation. Firstly, the biosafety of 2D nanosystems has not been investigated exhaustively and deeply to indicate their systemic toxicity, ablating uncertainty in processes, and long-term consequences on humans. Secondly, the physicochemical features of 2D nanomaterials are strongly dependent on their sheet size, layer thickness, and surface structure/ligands. To this end, a standardized operating protocol is needed for significantly facilitating and/or exploiting the practical applications of superb 2D nanomaterials in clinical medicine. Thirdly, 2D nanomaterials are difficult to naturally degrade in physiological solution

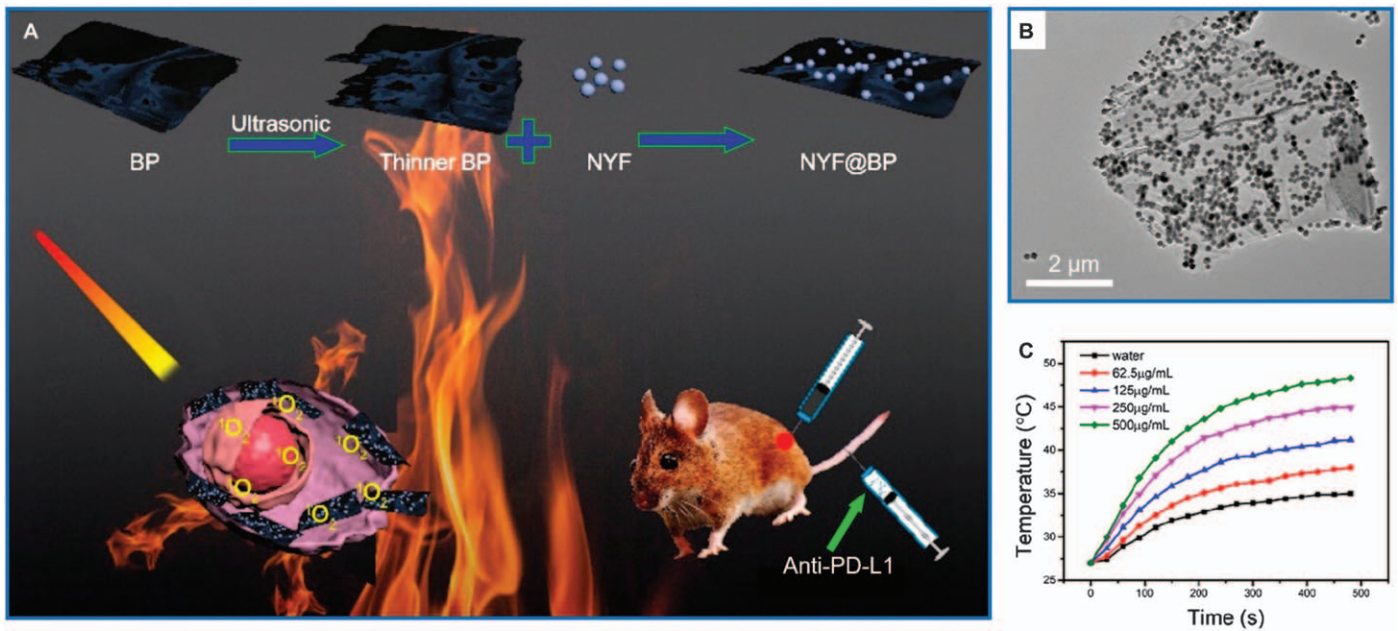

Figure 6.18 (A) Schematic illustration of NYF@BP for photothermal, photodynamic, and immunotherapy. (B) TEM images of NYF@BP. (C) Photothermal curves of NYF@BP solution with different concentrations after exposure to a 980 nm laser (0.7 W cm^{-2}). Reproduced from ref. 159 with permission from American Chemical Society, Copyright 2020.

Table 6.1 The performances of different 2D nanomaterials and their PCE. Reproduced from ref. 20 with permission from John Wiley and Sons, Copyright © 2020 Wiley-VCH Verlag GmbH & Co. KGaA, Weinheim.

Type	Merits	Drawbacks	Materials	PCE (%)
Graphene	High NIR absorbance, high stability, high flexibility, controlled chemical modification	Difficult biodegradation	Graphene GO rGO	79.62 89 89.2
TMDs	High stability in liquid and air, low cytotoxicity, diverse composition	Poor water solubility, relatively low extinction coefficients and PCE in the NIR region	MoS_2 $MoSe_2$ WS_2 ReS_2 TaS_2	62.5 57.9 32.83 79.2 39
BP	Biodegradation, high extinction coefficient and PCE	Instability, uncontrollable synthesis, difficult storage, and surface modification	BP	43.6
MXenes	Strong absorption in the NIR-I and NIR-II, enzyme-triggered biodegradation	Difficult large-scale production, difficult control of morphology and structure	Ti_3C_2 Nb_2C Ta_4C_3	100 45.65 44.7
Pd nanosheets	Highly tunable diameter, high PCE	High cost	Pd	52

owing to their good crystallinity with few defects, and only biodegradable materials really have the desirable biological safety required for entering clinical experiments. Overall, a lot of effort is still required to improve the photothermal applications of 2D nanomaterials for making more significant progress in future exploitations.

References

1. G. Guan, M. Wu and M. Y. Han, *Adv. Funct. Mater.*, 2019, 1903439.
2. H. Chen, T. Liu, Z. Su, L. Shang and G. Wei, *Nanoscale Horiz.*, 2018, **3**, 74.
3. G. Guan and M. Y. Han, *Adv. Sci.*, 2019, 1901837.
4. Z. Mohammadpour and K. Majidzadeh-A, *ACS Biomater. Sci. Eng.*, 2020, **6**, 1852.
5. K. S. Novoselov, A. K. Geim, S. V. Morozov, D. Jiang, Y. Zhang, S. V. Dubonos, I. V. Grigorieva and A. A. Firsov, *Science*, 2004, **306**, 666.
6. Y. Zhu, S. Murali, W. Cai, X. Li, J. W. Suk, J. R. Potts and R. S. Ruoff, *Adv. Mater.*, 2010, **22**, 3906.
7. C. N. R. Rao, A. K. Sood, K. S. Subrahmanyam and A. Govindaraj, *Angew. Chem., Int. Ed.*, 2009, **48**, 7752.
8. H. Tang, C. M. Hessel, J. Wang, N. Yang, R. Yu, H. Zhao and D. Wang, *Chem. Soc. Rev.*, 2014, **43**, 4281.
9. M. Chhowalla, H. S. Shin, G. Eda, L. J. Li, K. Loh and H. Zhang, *Nat. Chem.*, 2013, **5**, 263.

10. X. Zhang, H. M. Xie, Z. D. Liu, C. L. Tan, Z. M. Luo, H. Li, J. D. Lin, L. Q. Sun, W. Chen and Z. C. Xu, *Angew. Chem., Int. Ed.*, 2015, **54**, 3653.
11. G. Guan, E. Ye, M. You and Z. Li, *Small*, 2020, **16**, 1907087.
12. G. Guan, J. Xia, S. Liu, Y. Cheng, S. Bai, S. Y. Tee, Y. W. Zhang and M. Y. Han, *Adv. Mater.*, 2017, **29**, 1700326.
13. G. Guan, M. Wu, Y. Cai, S. Liu, Y. Cheng, S. Y. Tee, Y. W. Zhang and M. Y. Han, *Chem. Mater.*, 2018, **30**, 5108.
14. C. Lin, H. Hao, L. Mei and M. Wu, *Smart Mater. Med.*, 2020, **1**, 150.
15. G. Guan, K. Y. Win, X. Yao, W. Yang and M. Y. Han, *Adv. Healthcare Mater.*, 2020, 2001158.
16. Y. W. Chen, Y. L. Su, S. H. Hu and S. Y. Chen, *Adv. Drug Delivery Rev.*, 2016, **105**, 190.
17. G. Guan, S. Zhang, S. Liu, Y. Cai, M. Low, C. P. Teng, I. Y. Phang, Y. Cheng, K. L. Duei, B. M. Srinivasan, Y. Zheng, Y. W. Zhang and M. Y. Han, *J. Am. Chem. Soc.*, 2015, **137**, 6152.
18. J. Lu, M. Chen, L. Dong, L. Cai, M. Zhao, Q. Wang and J. Li, *Colloids Surf., B*, 2020, **194**, 111162.
19. M. Qiu, W. X. Ren, T. Jeong, M. Won, G. Y. Park, D. K. Sang, L. P. Liu, H. Zhang and J. S. Kim, *Chem. Soc. Rev.*, 2018, **47**, 5588.
20. S. Liu, X. Pan and H. Liu, *Angew. Chem., Int. Ed.*, 2020, **59**, 5890.
21. C. Murugan, V. Sharma, R. K. Murugan, G. Malaimegu and A. Sundaramurthy, *J. Controlled Release*, 2019, **299**, 1.
22. K. S. Novoselov and A. H. C. Neto, *Phys. Scr.*, 2012, **T146**, 014006.
23. X. Cai, Y. Luo, B. Liu and H. M. Cheng, *Chem. Soc. Rev.*, 2018, **47**, 6224.
24. N. Liu, P. Kim, J. H. Kim, J. H. Ye, S. Kim and C. J. Lee, *ACS Nano*, 2014, **8**, 6902.
25. C. Muratore, A. A. Voevodin and N. R. Glavin, *Thin Solid Films*, 2019, **688**, 137500.
26. Y. Zhang, Y. Zhang, Q. Ji, J. Ju, H. Yuan, J. Shi, T. Gao, D. Ma, M. Liu, Y. Chen, X. Song, H. Y. Hwang, Y. Cui and Z. Liu, *ACS Nano*, 2013, **7**, 8963.
27. X. Guo, Y. Wang, F. Wu, Y. Ni and S. Kokot, *Analyst*, 2015, **140**, 1119.
28. A. Zhang, A. Li, W. Zhao and J. Liu, *Chem. – Eur. J.*, 2018, **24**, 4215.
29. X. Wang and L. Cheng, *Nanoscale*, 2019, **11**, 15685.
30. M. Hashemi, M. Omidi, B. Muralidharan, H. Smyth, M. A. Mohagheghi, J. Mohammadi and T. E. Milner, *ACS Appl. Mater. Interfaces*, 2017, **9**, 32607.
31. X. Chen, C. Li, X. Wang and X. Zhao, *Mater. Res. Express*, 2019, **6**, 085080.
32. H. Liu, T. Li, Y. Liu, G. Qin, X. Wang and T. Chen, *Nanoscale Res. Lett.*, 2016, **11**, 211.
33. L. Mei, C. Lin, F. Cao, D. Yang, X. Jia, S. Hu, X. Miao and P. Wu, *ACS Appl. Nano Mater.*, 2019, **2**, 2902.
34. S. Su, J. Wang, J. Wei, R. Martínez-Zaguilán, J. Qiu and S. Wang, *New J. Chem.*, 2015, **39**, 5743.

35. H. Wang, B. Zhao, W. Dong, Y. Zhong, X. Zhang, Y. Gong, R. Zhan, M. Xing, J. Zhang, G. Luo and W. Qian, *Chem. Eng. J.*, 2020, **393**, 124595.
36. A. Chae, S. Jo, Y. Choi, B. Ryu, C. A. Choi, S. Y. Park and I. In, *App. Surf. Sci.*, 2019, **474**, 111.
37. G. Ma, J. Qi, Q. Gui, X. Bao, D. Gao and C. Xing, *Polymers*, 2020, **12**, 1116.
38. N. Mauro, C. Scialabba, S. Agnello, G. Cavallaro and G. Giammona, *Mater. Sci. Eng., C*, 2020, **107**, 110201.
39. M. Yan, Y. Liu, X. Zhu, X. Wang, L. Liu, H. Sun, C. Wang, D. Kong and G. Ma, *ACS Appl. Mater. Interfaces*, 2019, **11**, 1876.
40. F. Yin, K. Hu, Y. Chen, M. Yu, D. Wang, Q. Wang, K. T. Yong, F. Lu, Y. Liang and Z. Li, *Theranostics*, 2017, **7**, 1133.
41. J. Yu, Y. H. Lin, L. Yang, C. C. Huang, L. Chen, W. C. Wang, G. W. Chen, J. Yan, S. Sawettanun and C. H. Lin, *Adv. Healthcare Mater.*, 2017, **6**, 1600804.
42. D. Hu, J. Zhang, G. Gao, Z. Sheng, H. Cui and L. Cai, *Theranostics*, 2016, **6**, 1043.
43. W. Jiang, F. Mo, Y. Lin, X. Wang, L. Xu and F. Fu, *J. Mater. Chem. B*, 2018, **6**, 4360.
44. R. Lima-Sousa, D. de Melo-Diogo, C. G. Alves, E. C. Costa, P. Ferreira, R. O. Louro and I. J. Correia, *Carbohydr. Polym.*, 2018, **200**, 93.
45. S. Roy, A. Sarkar and A. Jaiswal, *Nanomedicine*, 2019, **14**, 255.
46. M. Ma, L. Cheng, A. Zhao, H. Zhang and A. Zhang, *Photodiagn. Photodyn.*, 2020, **29**, 101640.
47. L. Xiao, J. Sun, L. Liu, R. Hu, H. Lu, C. Cheng, Y. Huang, S. Wang and J. Geng, *ACS Appl. Mater. Interfaces*, 2017, **9**, 5382.
48. C. Wang, X. Wang, Y. Chen and Z. Fang, *J. Photochem. Photobiol., B*, 2020, **204**, 111587.
49. W. Qian, C. Yan, D. He, X. Yu, L. Yuan, M. Liu, G. Luo and J. Deng, *Acta Biomater.*, 2018, **69**, 256.
50. Y. A. Cheon, J. H. Bae and B. G. Chung, *Langmuir*, 2016, **32**, 2731.
51. Q. Li, L. Hong, H. Li and C. Liu, *Biosens. Bioelectron.*, 2017, **89**, 477.
52. Z. Hu, C. Wang, F. Zhao, X. Xu, S. Wang, L. Yu, D. Zhang and Y. Huang, *Nanoscale*, 2017, **9**, 8825.
53. S. Kang, J. Lee, S. Ryu, Y. Kwon, K. H. Kim, D. H. Jeong, S. R. Paik and B. S. Kim, *Chem. Mater.*, 2017, **29**, 3461.
54. S. V. Otari, M. Kumar, M. Z. Anwar, N. D. Thorat, S. K. S. Patel, D. Lee, J. H. Lee, J. K. Lee, Y. C. Kang and L. Zhang, *Sci. Rep.*, 2017, **7**, 10980.
55. L. Yang, Y. T. Tseng, G. Suo, L. Chen, J. Yu, W. J. Chiu, C. C. Huang and C. H. Lin, *ACS Appl. Mater. Interfaces*, 2015, **7**, 5097.
56. X. Wang, Q. Han, N. Yu, J. Li, L. Yang, R. Yang and C. Wang, *J. Mater. Chem. B*, 2015, **3**, 4036.
57. S. Li, X. Jin, Y. Shao, X. Qi, J. Yang and Y. Wang, *Eur. Polym. J.*, 2019, **116**, 302.

58. J. Luo, W. Deng, F. Yang, Z. Wu, M. Huang and M. Gu, *Carbohydr. Polym.*, 2018, **198**, 206.
59. Y. K. Kim, H. K. Na, S. Kim, H. Jang, S. J. Chang and D. H. Min, *Small*, 2015, **11**, 2527.
60. X. Jia, W. Xu, Z. Ye, Y. Wang, Q. Dong, E. Wang, D. Li and J. Wang, *Small*, 2020, **16**, 2003707.
61. F. Wang, Q. Sun, B. Feng, Z. Xu, J. Zhang, J. Xu, L. Lu, H. Yu, M. Wang, Y. Li and W. Zhang, *Adv. Healthcare Mater.*, 2016, **5**, 2227.
62. C. Wu, D. Li, L. Wang, X. Guan, Y. Tian, H. Yang, S. Li and Y. Liu, *Acta Biomater.*, 2017, **53**, 631.
63. K. Turcheniuk, T. Dumych, R. Bilyy, V. Turcheniuk, J. Bouckaert, V. Covk, V. Chopyak, V. Zaitsev, P. Mariot, N. Prevarskaya, R. Boukherroub and S. Szunerits, *RSC Adv.*, 2016, **6**, 1600.
64. J. Song, X. Yang, O. Jacobson, L. Lin, P. Huang, G. Niu, Q. Ma and X. Chen, *ACS Nano*, 2015, **9**, 9199.
65. S. Tan, X. Wu, Y. Xing, S. Lilak, M. Wu and J. X. Zhao, *Colloids Surf., B*, 2020, **185**, 110616.
66. M. Li, L. Huang, X. Wang, Z. Song, W. Zhao, Y. Wang and J. Liu, *J. Colloid Interface Sci.*, 2018, **529**, 444.
67. N. Wang, B. Hu, M. L. Chen and J. H. Wang, *Nanotechnology*, 2015, **26**, 195703.
68. R. Liu, X. Wang, J. Ye, X. Xue, F. Zhang, H. Zhang, X. Hou, X. Liu and Y. Zhang, *Nanotechnology*, 2018, **29**, 105704.
69. R. K. Thapa, Z. C. Soe, W. Qu, K. Poudel, J. H. Jeong, S. G. Jin, S. K. Ku, H. G. Choi, Y. M. Lee, C. S. Yong and J. O. Kim, *Colloids Surf., B*, 2018, **169**, 429.
70. S. Zhou, L. Shang, Y. Zhao, R. Shi, G. I. N. Waterhouse, Y. C. Huang, L. Zheng and T. Zhang, *Adv. Mater.*, 2019, **31**, 1900509.
71. L. Shao, R. Zhang, J. Lu, C. Zhao, X. Deng and Y. Wu, *ACS Appl. Mater. Interfaces*, 2017, **9**, 1226.
72. F. Zhang, M. Xie, Y. Zhao, Y. Zhang, M. Yang, N. Yang, T. Deng, M. Zhang and J. Xie, *Ceram. Int.*, 2019, **45**, 5996.
73. F. Soysal, Z. Çıplak, B. Getiren, C. Gökalp and N. Yıldız, *Mater. Res. Bull.*, 2020, **124**, 110763.
74. M. Xu, X. Hu, S. Wang, J. Yu, D. Zhu and J. Wang, *J. Catal.*, 2019, **377**, 652.
75. G. M. Neelgund and A. Oki, *ACS Omega*, 2019, **4**, 5696.
76. J. H. Lim, D. E. Kim, E. J. Kim, C. D. Ahrberg and B. G. Chung, *Macromol. Res.*, 2018, **26**, 557.
77. J. Wang, G. Zhang and P. Zhang, *Appl. Catal., B*, 2018, **239**, 77.
78. Z. Li, O. Johnson, J. Huang, T. Feng, C. Yang, Z. Liu and W. Chen, *Mater. Res. Bull.*, 2018, **106**, 365.
79. H. Zhang, H. Wu, J. Wang, Y. Yang, D. Wu, Y. Zhang, Y. Zhang, Z. Zhou and S. Yang, *Biomaterials*, 2015, **42**, 66.
80. R. Kurapati, M. Vaidyanathan and A. M. Raichur, *RSC Adv.*, 2016, **6**, 39852.

81. H. Ci, H. Ren, Y. Qi, X. Chen, Z. Chen, J. Zhang, Y. Zhang and Z. Liu, *Nano Res.*, 2018, **11**, 3106.
82. A. Shen, C. Zhao, L. Mao, Y. Wu, B. Zhao and K. Lin, *Mater. Today Chem.*, 2020, **17**, 100322.
83. Y. Chai, H. Ma, X. Ma, X. Zhang, Y. He, Y. Wang, Q. Jiang, X. Wang, J. Ji and M. Xue, *J. Mater. Chem. A*, 2020, **8**, 10891.
84. P. Ji, W. Zhang, S. Ai, Y. Zhang, J. Liu, J. Liu, P. He and Y. Li, *Nanotechnology*, 2019, **30**, 115701.
85. W. Liu, X. Zhang, L. Zhou, L. Shang and Z. Su, *J. Colloid Interface Sci.*, 2019, **536**, 160.
86. W. Gao, H. K. Lee, J. Hobley, T. Liu, I. Y. Phang and X. Y. Ling, *Angew. Chem., Int. Ed.*, 2015, **54**, 3993.
87. A. Sun, X. Hou and X. Hu, *Nano Energy*, 2020, **70**, 104511.
88. G. Bai, P. Yuan, B. Cai, X. Qiu, R. Jin, S. Liu, Y. Li and X. Chen, *Adv. Funct. Mater.*, 2019, **29**, 1904401.
89. J. Yang, Y. Jia, N. Bing, L. Wang, H. Xie and W. Yu, *Appl. Therm. Eng.*, 2019, **163**, 114412.
90. Z. C. Xiong, Y. J. Zhu, D. D. Qin and R. L. Yang, *ACS Appl. Mater. Interfaces*, 2020, **12**, 32556.
91. H. Zhong, Z. Zhu, J. Lin, C. F. Cheung, V. L. Lu, F. Yan, C. Y. Chan and G. Li, *ACS Nano*, 2020, **14**, 6213.
92. G. Guan, M. You, X. Liu, Y. L. Wu, E. Ye and Z. Li, *Adv. Mater. Interfaces*, 2019, 1900585.
93. G. Guan, S. Liu, Y. Cheng, Y. W. Zhang and M. Y. Han, *Nanoscale*, 2018, **10**, 10911.
94. J. Shi, J. Li, Y. Wang, J. Cheng and C. Y. Zhang, *J. Mater. Chem. B*, 2020, **8**, 5793.
95. C. Fu, L. Tan, X. Ren, Q. Wu, H. Shao, J. Ren, Y. Zhao and X. Meng, *Chem. Commun.*, 2018, **54**, 13989.
96. L. Chen, Y. Feng, X. Zhou, Q. Zhang, W. Nie, W. Wang, Y. Zhang and C. He, *ACS Appl. Mater. Interfaces*, 2017, **9**, 17347.
97. S. Wang, K. Li, Y. Chen, H. Chen, M. Ma, J. Feng, Q. Zhao and J. Shi, *Biomaterials*, 2015, **39**, 206.
98. J. Liu, J. Zheng, H. Nie, H. Chen, B. Li and L. Jia, *Chem. Eng. J.*, 2020, **381**, 122541.
99. Q. Han, X. Wang, X. Jia, S. Cai, W. Liang, Y. Qin, R. Yang and C. Wang, *Nanoscale*, 2017, **9**, 5927.
100. B. Huang, D. Wang, G. Wang, F. Zhang and L. Zhou, *J. Colloid Interface Sci.*, 2017, **508**, 214.
101. K. Wang, Q. Chen, W. Xue, S. Li and Z. Liu, *ACS Biomater. Sci. Eng.*, 2017, **3**, 2325.
102. C. H. Park, H. Yun, H. Yang, J. Lee and B. J. Kim, *Adv. Funct. Mater.*, 2017, **27**, 1604403.
103. C. Zhang, D. F. Hu, J. W. Xu, M. Q. Ma, H. Xing, K. Yao, J. Ji and Z. K. Xu, *ACS Nano*, 2018, **12**, 12347.

104. Y. Huang, Q. Gao, X. Li, Y. Gao, H. Han, Q. Jin, K. Yao and J. Ji, *Nano Res.*, 2020, **13**, 2340.
105. J. Liu, F. Li, J. Zheng, B. Li, D. Zhang and L. Jia, *J. Nanobiotechnol.*, 2019, **17**, 78.
106. R. Deng, H. Yi, F. Fan, L. Fu, Y. Zeng, Y. Wang, Y. Li, Y. Liu, S. Ji and Y. Su, *RSC Adv.*, 2016, **6**, 77083.
107. X. Zhang, J. Wu, G. R. Williams, S. Niu, Q. Qian and L. M. Zhu, *Colloids Surf., B*, 2019, **173**, 101.
108. Z. Li, Y. Yang, J. Yao, Z. Shao and X. Chen, *Mater. Sci. Eng., C*, 2017, **79**, 123.
109. M. Xie, N. Yang, J. Cheng, M. Yang, T. Deng, Y. Li and C. Feng, *Colloids Surf., B*, 2020, **187**, 110631.
110. Y. Yang, J. Wu, D. H. Bremner, S. Niu, Y. Li, X. Zhang, X. Xie and L. M. Zhu, *Colloids Surf., B*, 2020, **185**, 110585.
111. Y. Zhang, W. Xiu, S. Gan, J. Shan, S. Ren, L. Yuwen, L. Weng, Z. Teng and L. Wang, *Front. Bioeng. Biotechnol.*, 2019, **7**, 218.
112. B. Geng, H. Qin, F. Zheng, W. Shen, P. Li, K. Wu, X. Wang, X. Li, D. Pan and L. Shen, *Nanoscale*, 2019, **11**, 7209.
113. T. Liu, S. Shen, Y. Huang, X. Zhang, Z. Lai, T. H. Tran, Z. Liu and L. Cheng, *Nanoscale*, 2019, **11**, 22788.
114. D. Zhang, P. Cui, Z. Dai, B. Yang, X. Yao, Q. Liu, Z. Hu and X. Zheng, *Nanoscale*, 2019, **11**, 19912.
115. T. Shao, J. Wen, Q. Zhang, Y. Zhou, L. Liu, L. Yuwen, Y. Tian, Y. Zhang, W. Tian, Y. Su, Z. Teng, G. Lu and J. Xu, *J. Mater. Chem. B*, 2016, **4**, 7708.
116. J. Yu, W. Yin, X. Zheng, G. Tian, X. Zhang, T. Bao, X. Dong, Z. Wang, Z. Gu, X. Ma and Y. Zhao, *Theranostics*, 2015, **5**, 931.
117. T. Liu, S. Shi, C. Liang, S. Shen, L. Cheng, C. Wang, X. Song, S. Goel, T. E. Barnhart, W. Cai and Z. Liu, *ACS Nano*, 2015, **9**, 950.
118. S. Rajasekar, E. M. Martin, S. Kuppusamy and C. Vetrivel, *Arabian J. Chem.*, 2020, **13**, 4741.
119. Y. Zhang, W. Xiu, Y. Sun, D. Zhu, Q. Zhang, L. Yuwen, L. Weng, Z. Teng and L. Wang, *Nanoscale*, 2017, **9**, 15835.
120. X. Zhang, J. Wu, G. R. Williams, Y. Yang, S. NIu, Q. Qian and L. M. Zhu, *J. Colloid Interface Sci.*, 2019, **539**, 433.
121. S. Wang, X. Li, Y. Chen, X. Cai, H. Yao, W. Gao, Y. Zheng, X. An, J. Shi and H. Chen, *Adv. Mater.*, 2015, **27**, 2775.
122. Z. Lei, W. Zhu, S. Xu, J. Ding, J. Wan and P. Wu, *ACS Appl. Mater. Interfaces*, 2016, **8**, 20900.
123. L. He, T. Nie, X. Xia, T. Liu, Y. Huang, X. Wang and T. Chen, *Adv. Funct. Mater.*, 2019, **29**, 1901240.
124. N. Ma, M. K. Zhang, X. S. Wang, L. Zhang, J. Feng and X. Z. Zhang, *Adv. Funct. Mater.*, 2018, **28**, 1801139.
125. Q. Liu, C. Sun, Q. He, A. Khalil, T. Xiang, D. Liu, Y. Zhou, J. Wang and L. Song, *Nano Res.*, 2015, **8**, 3982.

126. M. Li, A. Zhao, K. Dong, W. Li, J. Ren and X. Qu, *Nano Res.*, 2015, **8**, 3216.
127. M. Xie, M. Yang, X. Sun, N. Yang, T. Deng, Y. Li and H. Shen, *J. Mater. Chem. B*, 2020, **8**, 2331.
128. B. Geng, H. Qin, W. Shen, P. Li, F. Fang, X. Li, D. Pan and L. Shen, *Chem. Eng. J.*, 2020, **383**, 123102.
129. X. Jia, J. Bai, Z. Ma and X. Jiang, *J. Mater. Chem. B*, 2017, **5**, 269.
130. O. A. Moses, M. I. Khan, Q. Fang, L. Qin, Z. ur Rehman, Y. Zhang, C. D. Feng, Y. Ma, X. Tang, C. Wu, M. L. Adam, D. Huang, H. Liu and L. Song, *Nanotechnology*, 2019, **30**, 065102.
131. X. Qian, S. Shen, T. Liu, L. Cheng and Z. Liu, *Nanoscale*, 2015, **7**, 6380.
132. S. Shen, Y. Chao, Z. Dong, G. Wang, X. Yi, G. Song, K. Yang, Z. Liu and L. Cheng, *Adv. Funct. Mater.*, 2017, **27**, 1700250.
133. Z. H. Miao, L. X. Lv, K. Li, P. Y. Liu, Z. Li, H. Yang, Q. Zhao, M. Chang, L. Zhen and C. Y. Xu, *Small*, 2018, **14**, 1703789.
134. Q. Huang, S. Wang, J. Zhou, X. Zhong and Y. Huang, *RSC Adv.*, 2018, **8**, 4624.
135. H. Fu, Z. Li, H. Xie, Z. Sun, B. Wang, H. Huang, G. Han, H. Wang, P. K. Chu and X. F. Yu, *RSC Adv.*, 2017, **7**, 14618.
136. L. Lu, M. Wang, D. Zhang and H. Zhang, *Analyst*, 2019, **144**, 6647.
137. Y. Zhao, L. Tong, Z. Li, N. Yang, H. Fu, L. Wu, H. Cui, W. Zhou, J. Wang, H. Wang, P. K. Chu and X. F. Yu, *Chem. Mater.*, 2017, **29**, 7131.
138. H. Zhao, H. Chen, Z. Guo, W. Zhang, H. Yu, Z. Zhuang, H. Zhong and Z. Liu, *Chem. Eng. J.*, 2020, **394**, 124314.
139. X. Xu, Y. Jiang, M. Wang, H. Wang, C. Lu and H. Yang, *Part. Part. Syst. Charact.*, 2020, 2000243.
140. W. Chen, J. Ouyang, H. Liu, M. Chen, K. Zeng, J. Sheng, Z. Liu, Y. Han, L. Wang, J. Li, L. Deng, Y. N. Liu and S. Guo, *Adv. Mater.*, 2017, **29**, 1603864.
141. X. Yang, D. Wang, Y. Shi, J. Zou, Q. Zhao, Q. Zhang, W. Huang, J. Shao, X. Xie and X. Dong, *ACS Appl. Mater. Interfaces*, 2018, **10**, 12431.
142. X. Yang, D. Wang, J. Zhu, L. Xue, C. Ou, W. Wang, M. Lu, X. Song and X. Dong, *Chem. Sci.*, 2019, **10**, 3779.
143. G. Liu, H. Tsai, X. Zeng, J. Qi, M. Luo, X. Wang, L. Mei and W. Deng, *Chem. Eng. J.*, 2019, **375**, 121917.
144. L. Qin, G. Ling, F. Peng, F. Zhang, S. Jiang, H. He, D. Yang and P. Zhang, *J. Colloid Interface Sci.*, 2019, **556**, 232.
145. F. Zhang, F. Peng, L. Qin, D. Yang, R. Li, S. Jiang, H. He and P. Zhang, *Colloids Surf., B*, 2019, **180**, 353.
146. C. Su, H. Zhong, H. Chen, Y. Guo, Z. Guo, D. Huang, W. Zhang, Q. Wu, B. Yang and Z. Liu, *New J. Chem.*, 2019, **43**, 8620.
147. L. Hai, A. Zhang, X. Wu, H. Cheng, D. He, T. Wang, X. He and K. Wang, *ACS Appl. Nano Mater.*, 2020, **3**, 563.
148. X. Zeng, M. Luo, G. Liu, X. Wang, W. Tao, Y. Lin, X. Ji, L. Nie and L. Mei, *Adv. Sci.*, 2018, **5**, 1800510.

149. G. Yang, X. Wan, Z. Gu, X. Zeng and J. Tang, *J. Mater. Chem. B*, 2018, **6**, 1622.
150. J. Shao, C. Ruan, H. Xie, Z. Li, H. Wang, P. K. Chu and X. F. Yu, *Adv. Sci.*, 2018, **5**, 1700848.
151. C. Xing, S. Chen, M. Qiu, X. Liang, Q. Liu, Q. Zou, Z. Li, Z. Xie, D. Wang, B. Dong, L. Liu, D. Fan and H. Zhang, *Adv. Healthcare Mater.*, 2018, **7**, 1701510.
152. İ. Aksoy, H. Küçükkeçeci, F. Sevgi, Ö. Metin and I. H. Patir, *ACS Appl. Mater. Interfaces*, 2020, **12**, 26822.
153. G. Yang, Z. Liu, Y. Li, Y. Hou, X. Fei, C. Su, S. Wang, Z. Zhuang and Z. Guo, *Biomater. Sci.*, 2017, **5**, 2048.
154. S. Li, Y. Zhang, W. Wen, W. Sheng, J. Wang, S. Wang and J. Wang, *Biosens. Bioelectron.*, 2019, **133**, 223.
155. Z. Liu, H. Chen, Y. Jia, W. Zhang, H. Zhao, W. Fan, W. Zhang, H. Zhong, Y. Ni and Z. Guo, *Nanoscale*, 2018, **10**, 18795.
156. D. Yang, G. Yang, P. Yang, R. Lv, S. Gai, C. Li, F. He and J. Lin, *Adv. Funct. Mater.*, 2017, **27**, 1700371.
157. K. Hu, L. Xie, Y. Zhang, M. Hanyu, Z. Yang, K. Nagatsu, H. Suzuki, J. Ouyang, X. Ji, J. Wei, H. Xu, O. C. Farokhzad, S. H. Liang, L. Wang, W. Tao and M. R. Zhang, *Nat. Commun.*, 2020, **11**, 2778.
158. X. Yao, B. Yang, S. Wang, Z. Dai, D. Zhang, X. Zheng and Q. Liu, *J. Mater. Chem. B*, 2020, **8**, 8010.
159. D. Xu, J. Liu, Y. Wang, Y. Jian, W. Wu and R. Lv, *ACS Biomater. Sci. Eng.*, 2020, **6**, 4940.
160. M. Xu, G. Yang, H. Bi, J. Xu, S. Dong, T. Jia, Z. Wang, R. Zhao, Q. Sun, S. Gai, F. He, D. Yang and P. Yang, *Chem. Eng. J.*, 2020, **382**, 122822.
161. Z. Xie, Y. Duo, Z. Lin, T. Fan, C. Xing, L. Yu, R. Wang, M. Qiu, Y. Zhang, Y. Zhao, X. Yan and H. Zhang, *Adv. Sci.*, 2020, **7**, 1902236.
162. Y. Chen, L. Wang and J. Shi, *Nano Today*, 2016, **11**, 292.

CHAPTER 7

Polymer–Quantum Dot Hybrid Materials

MAE JOANNE B. AGUILA,*[a] VAN KHIEM NGUYEN,[b,d] DUY KHANH PHAM,[b,d] NGOC QUYEN TRAN,[b,d] VAN TOAN NGUYEN,[c,d] THANH MIEN NGUYEN[e] AND BICH THI LUONG*[b,d]

[a] Institute of Chemistry, University of the Philippines Los Baños, Los Baños 4031, Laguna, Philippines; [b] Institution of Applied Materials Science – Vietnam Academy of Science and Technology, Ho Chi Minh City, Vietnam; [c] Duy Tan University, Da Nang City, Vietnam; [d] Graduate University of Science and Technology, Vietnam Academy of Science and Technology, Vietnam; [e] Pusan National University, Korea
*Emails: mbaguila@up.edu.ph; marialuongbich@gmail.com

7.1 Introduction

Quantum dots (QDs) or semiconductor nanocrystals are materials that exhibit optical and electronic properties that are intermediate between those in the bulk and distinct molecular systems.[1] Both the size and shape of these QDs dictate their properties, and because of their highly tunable optoelectronic properties, these materials are being explored in many biological applications such as in biosensing and as diagnostic and therapeutic agents.[2] For practical utilization of these semiconductor nanocrystals, these materials are generally implanted into a solid matrix such as glass or another crystal, or surface-modified in suspensions.[3] Polymers make ideal coating materials for QDs as they usually do not

Nanoscience & Nanotechnology Series No. 54
Photothermal Nanomaterials
Edited by Enyi Ye and Zibiao Li

Published by the Royal Society of Chemistry, www.rsc.org

absorb at the visible region, can impart mechanical and chemical stability to the nanocrystals, and prevent the formation of QD clusters.[1,2] As such, these polymer–quantum dot hybrids can be formed more easily into thin films or spheres. Unfortunately, incorporation of QDs into the polymers results in the decline of the optical and electronic properties. Current research studies are exploring the enhancement of the encapsulation process and the use of biocompatible polymers, while improving the properties of the polymer–QD hybrids.

This chapter summarizes the development in the synthesis, structure, and properties of QDs, along with the preparation of polymer–QD hybrid materials. The discussion is focused on QDs based on binary metal chalcogenides (*e.g.* CdSe, CdS). Finally, the application of these materials as photothermal agents for cancer therapy is presented.

7.2 Quantum Dots: Synthesis, Structures, and Properties

Quantum dots are interesting materials well known for their unique optoelectronic properties. The most studied QDs are those prepared from the elements of (i) groups II and VI (*e.g.* CdSe, ZnS), (ii) groups IV and VI (*e.g.* PbTe, PbS), or (iii) groups III and V (*e.g.* InAs, InP) in the periodic table.[1,4] QDs based on carbon (*e.g.* graphene) and on multinary combinations of elements (*e.g.* $CuInS_2$) have also been prepared.[5–11]

7.2.1 General Synthetic Routes for Quantum Dots

Most methods for the preparation of QDs involve colloid chemistry, organometallic chemistry, or confined matrices chemistry.[12] The seminal work done by Bawendi and co-workers paved the way for preparing high-quality QDs.[13] The synthesis involved the breakdown of organometallic precursors into an organic-based coordinating ligand as the solvent at high temperatures. This synthetic route generally results in high quantum yields for the QDs with a narrow size distribution. Because of their small sizes, QDs have high surface areas, which make for unstable colloidal QD mixtures. Coordinating organic ligands, such as trioctylphosphine oxide (TOPO), are usually added to coat the surface of the QDs for functionalization.[13–15] The coordinating solvent is important in controlling the discrete homogeneous nucleation and slow growth and annealing of the QDs.[13] Still, the use of expensive and hazardous organometallic reagents and the conditions of high temperature are some of the disadvantages of the synthesis of QDs in organic media.[16] While the coordinating organic ligands passivate the surface of the QDs, these render the as-synthesized QDs hydrophobic and insoluble in aqueous media. This limits the application of such QDs in biological systems. Subsequent surface encapsulation or ligand exchange steps are needed to convert these coated QDs into hydrophilic materials.

However, these added steps also impart a decreasing effect on the photoluminescence quantum yields (PLQYs) of the QDs.[17,18]

The aqueous synthesis of QDs entails less toxic and inexpensive reagents and results in QDs with better solubility in water and biocompatibility. For instance, Rajh *et al.* reported the synthesis of CdTe crystals from salts containing Cd^{2+} and HTe^{-} ions, with 3-mercapto-1,2-propanediol as the stabilizing ligand.[19] Other thiol-containing ligands, including glutathione,[20] arginine,[21] 3-mercaptopropane-1-sulfonic acid, 2-mercaptosuccinic acid, 3-mercaptoacetic acid, and 2-mercaptoacetic acid[22] were also explored as stabilizing compounds. Unfortunately, QDs derived from aqueous media have low stability and low PLQY.[16] Since the surface of the QDs is very reactive, the QD particles tend to clump together when exposed to heat, light, air, or some ions. This results in surface deterioration, hence the decrease in PLQY. The initial report of Bhargava *et al.* on Mn-doped ZnS (Mn:ZnS) showed that doping of the QDs can influence the morphology and improve the properties of the QDs.[23,24] The PL of doped QDs depends on the dopant, and not on the host or parent material. Different dopants such as metals, transition metals, or halides have been used to dope QDs to vary their emitted colors[25–27] or for use in photocatalysis[28,29] and bioimaging.[30] Rare earth metal ions have also been used as dopants for QDs.[31,32]

7.2.2 Band Structures and Optical Properties

The light-emitting properties of QDs resemble those from discrete electronic transitions.[1–3] When the electron in the valence band is excited to the conduction band, a hole is created in the valence band. Luminescence comes from the reconciliation of the previously excited electron and the positive hole in the valence band. The wavelength of the emitted light corresponds to the energy band gap (E_g) between the valence and the conduction bands. As the size of the QDs decreases, the energy band gap increases. There is a greater percentage of atoms on the surface of the QDs; hence those with a smaller size have a higher surface area. Having a wider surface area leads to the recombination of the electron and hole in the traps on the surface.

Increasing the PLQY of the QDs can be done by attaching another layer of semiconductor onto the original one, resulting in core/shell structures of the QDs.[3,33,34] This additional inorganic layer enhances the photoluminescence of QDs. The types of core/shell structures are differentiated based on the band gap alignments of the valence and conduction bands of the core layer with those of the shell layer. Schematic representations are displayed in Figure 7.1. For a type I core/shell structure, the band gap of the core layer is smaller than that of the shell, which is the opposite for the inverse type I structure. The charge carriers are restrained in the core layer only for the type I structure. The shell layer acts as a barrier between the optically active core layers from its surrounding medium. This reduces the effects of the changes in the local environment of the QDs on the optical properties and makes the core/shell structure less prone to photodegradation. A small red

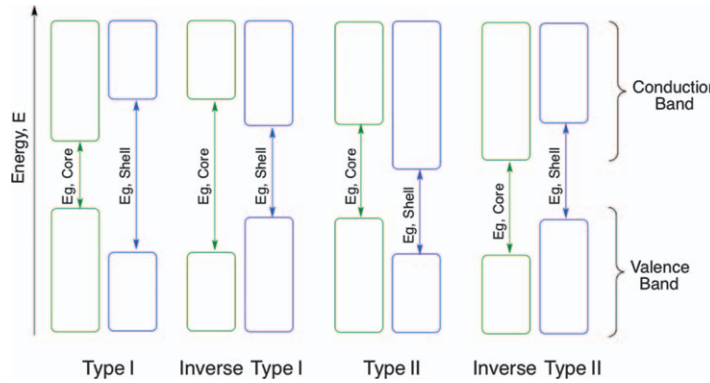

Figure 7.1 Energy level diagrams of the different types of core/shell structures of quantum dots.

shift is observed in the PL wavelength. Examples of this type I structure include CdSe/ZnS, CdSe/CdS, and CdS/ZnS. On the other hand, for the inverse type I form, the electron and hole may be partially or totally restricted into the shell, depending on the thickness of the shell. As such, the red shift in the PL wavelength also depends on the thickness of the shell. QDs of CdS/HgS, CdS/CdSe, and ZnSe/CdSe belong to the inverse type I structure.

The conduction band edge of the shell is located within the band gap of the core for the type II structure. For the inverse type II structure, the valence band edge of the shell is within the band gap of the core. This staggered alignment of the bands for these materials causes spatial distribution of the charge carriers into the core and shell regions of the structure, making it easier to tune the color of the light emitted by changing the thickness of the shell. Examples of type II core/shell structures are CdTe/CdSe, CdSe/ZnTe, and CdSe/ZnSe. Meanwhile, inverse type II structures include InP/CdS and PbS/CdS.

7.2.3 Biocompatible Polymer-decorated Quantum Dots

The desired characteristics for biological applications of QDs include aqueous solubility, low toxicity, and stable PL activity.[35–38] The as-synthesized QDs tend to aggregate in water, losing their PL. Doping or layering with another inorganic material minimizes the PL degradation but often increases metal toxicity. Coating the QD surface with organic ligands prevents the conglomeration of the particles, although the usual long organic chains limit the solubility of QDs in water. In recent years, many research studies on the use of polymer molecules as coating ligands for QDs are reported. Polymer coating makes QDs more stable even in wider pH and ionic strength ranges, through the multivalent interactions between the polymer and QD. The polymer acts as a separation between the QD and the local surroundings, decreasing possible metal leakage. Polymers also

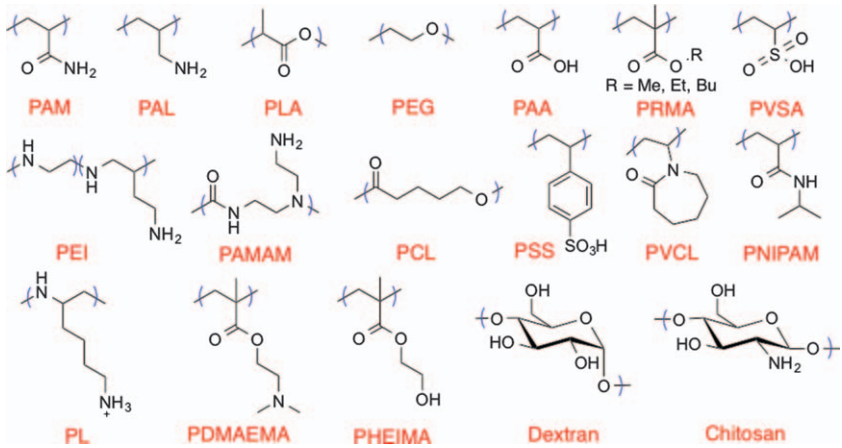

Figure 7.2 Representative polymers that are often used for the fabrication of biocompatible polymer–QD hybrid materials.

provide sites for functionalization in QDs, allowing for easier modifications of the structure appropriate for a certain application. Biocompatible polymers with low toxicity are used for polymer–QD composites for biological applications. Examples of which are shown in Figure 7.2.

7.3 Strategies for Encapsulating Quantum Dots with Organic Polymers

There are several approaches for the introduction of polymeric molecules into QD structures. These methods may involve direct surface modification of QDs with the polymer and incorporation of the QDs into polymer colloids or films. The primary fabrication procedures for polymer–QD hybrid materials include (i) ligand exchange between the polymer and the coordinated ligand, (ii) the polymer "grafting to" the QDs, (iii) the polymer "grafting from" the QDs, (iv) capping the QD with polymer, and (v) growing QDs in the polymeric material.

7.3.1 Ligand Exchange Between the Original Ligand and the Polymer

Ligand exchange is a direct way of introducing polymer molecules into QDs. This requires the dissociation of the original hydrophobic ligand (usually TOPO) that is attached to the QD with the polymer (Figure 7.3). The polymeric molecule contains functionality that can attach to the QD, such as thiol, carboxyl, or amine. A disadvantage of doing a ligand exchange reaction is that it is quite difficult to control, which may sometimes lead to colloidally less stable QDs with lower QY.

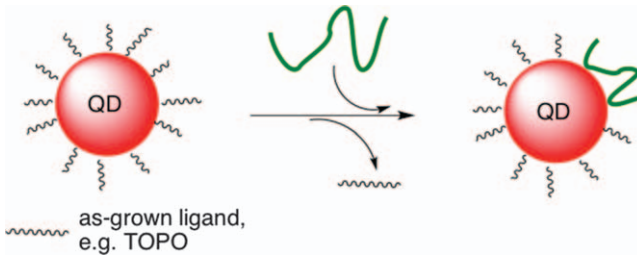

Figure 7.3 General scheme for the fabrication of polymer–QD hybrids through a ligand exchange reaction.

The thiol group is the most studied and commonly utilized appendage to a polymer because of its high affinity for soft metals. Thiolated polyethylene glycol (PEG) has been used to coat CdSe/ZnS, using monodentate or bidentate thiols.[39–43] Wu *et al.* reported the synthesis of pH-responsive CdSe/CdZnS QDs by modifying the surface with the peptide–polymer denatured human serum albumin–PEG–thioctic acid (dHSA–PEG–TA).[44] Dendritic thiol-terminated OH-poly(amidoamine) (OH-PAMAM) polymer was conjugated to CdSe nanocrystals to improve the photochemical stability of the QDs in an aqueous system.[45]

The amine functionality is also explored as an anchor for polymers in ligand exchange reactions. Polymer–CdSe/ZnS[46] and CdTe[47] QD hybrids with increased colloidal stability were prepared with octylamine-modified polyacrylic acid (PAA) polymer. Surface modification of CdSe QDs was also carried out with hexylamine modified poly(acryloyloxysuccinimide) (PAAS)[48] and PEG–poly(ethyleneimine) (PEI) and PEG–diethylenetriamine (DETA).[49] Poly(*N,N*-dimethylaminoethyl methacrylate) (PDAEMA), a thermo- and pH-sensitive polymer with a tertiary amine group, was used to passivate the surface of CdSe and CdSe/ZnS to make the QDs.[50–52] In addition, PAMAM–CdSe,[53] PEI–CdSe/ZnS,[54] PEG–PEI–CdSe/CdS/ZnS,[55] poly(allylamine)CdSe,[56] imidazole–poly(*N*-isopropylacrylamide) (PNIPAM)–CdSe and imidazole–acetoacetylethyl methacrylate–*N*-vinylcaprolactam copolymer (PVCL)–CdSe,[57] and imidazole–PEG–CdSe/CdZnS[58] were among the amine-functionalized polymer–QD hybrids synthesized through a ligand exchange process. Wang *et al.* also used a ligand exchange method to replace the bound octylamine with poly(styrene-*co*-acrylonitrile)–NH_2 (PSAN–NH_2) on the surface of ZnO QDs.[59]

Polymers with multidentate phosphine[60] and phosphine oxide[61] groups as anchors were used to prepare a polymer–CdSe/ZnS hybrid. The QDs of γ-Fe_2O_3, CdSe, TiO_2, and PbS were modified with PAA, a carboxyl-based polymer, to make them more hydrophilic.[62,63] Ehlert *et al.* studied ligand exchange reactions for the preparation of polymethylmethacrylate-*co*-polymethacrylic acid (PMMA-*co*-PMAc)-ZnO, as well as the hybrids polystyrene–pentaethylenehexamine (PS–PEHA)–CdSe, PS–PEHA–Fe_2O_3, and polyisoprene (PI)–PEHA–PbS.[64]

7.3.2 "Grafting to" Procedure

In the "grafting to" method (Figure 7.4), the surface of the QD is modified with linear or hyperbranched pre-synthesized polymers which have end-functionalizations that can bind strongly to the QD through covalent interactions. This is a more complex procedure and may be considered as a higher-level modification after a ligand exchange reaction. This procedure is a suitable technique for attaching macromolecules into QDs, although the number of attached macromolecules cannot be controlled. Since the polymers to be used are already preformed, these chains can be properly characterized.[65]

The Peng group used dendron ligands in the synthesis of surface-modified QDs.[66] They prepared hydrophilic CdSe nanocrystals from dendron ligands with thiol as the focal anchor and containing amide, carboxylic acid, ester, and alcohol as the terminal groups. The succeeding reaction with ethylcarbodiimide (EDC) reagent gave amide functional groups at the terminals. In another report, two dendrimer ligands were included into CdSe and CdSe/CdS QDs.[67] The native QDs were coated first with OH-functionalized dendritic polymers with thiol as the anchor. An NH_2-end-functionalized bridging dendrimer was then attached through the hydroxyl groups. The resulting amino box product was tested in several coupling reactions. They also reported the formation of CdSe and CdSe/CdS dendron QDs using a ligand that has thiol as the focal anchor and alkene as the terminal groups.[68] The alkene groups in the modified QDs underwent ring closing metathesis (RCM), improving the thermal and photochemical stability of the dendron nanocrystal.

PEG-based polymer–QD hybrids were also synthesized following this "grafting to" method. For instance, core/shell CdSe/ZnS QDs coated with PAA polymer were conjugated with methoxy- and carboxy-terminated PEG amine through EDC coupling.[69] On the other hand, a labeling probe was prepared when the amino-terminated PEG–CdSe/$Zn_xCd_{1-x}S$ hybrid was covalently conjugated with a fluorescence resonance energy transfer (FRET) acceptor dye and streptavidin.[70] In another example, CdSe/ZnS modified with dihydrolipoic acid (DHLA)–PEG: DHLA–PEG–COOH was conjugated with dye and biotin.[71] Furthermore, Tan *et al.* presented the reaction of

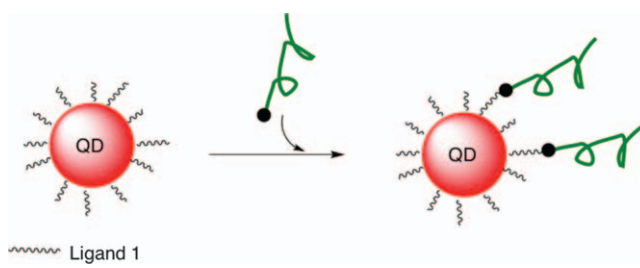

Figure 7.4 General scheme for the fabrication of a polymer–QD hybrid through the "grafting to" QD method.

methoxy–PEG and PEG–oleylamide with polyacrylate/polyacrylamide-modified CdSe/ZnS.[72] Meanwhile, Jennings *et al.* showed the incorporation of formylbenzamide into a PEG-lipid derivatized 1,2-distearoyl-*sn*-glycero-3-phosphoethanolamine (DSPE)–PEG–CdSe/ZnS polymer QD hybrid.[73]

7.3.3 "Grafting from" Procedure

The "grafting from" method is the construction of a polymer chain on the surface of QDs (Figure 7.5). The QD surface has ligands with initiating or linking groups, from which the polymerization can be grown. While this method is trickier and more difficult than grafting the end-functionalized polymers to QDs, it results in higher grafting ratios because of the lower steric hindrance around the polymerization site. This method is generally referred to as surface-initiated polymerization.

Through atom transfer radical polymerization (ATRP), core/shell CdS/SiO_2 was modified with a silane initiator 3-(2-bromopropionyloxy)propyl dimethylethoxysilane (BIDS).[74] A poly(methyl methacrylate) (PMMA)–CdS/SiO_2 hybrid was formed from the $NiBr_2(PPh_3)_2$-catalyzed reaction of modified nanocrystal and methyl methacrylate. Carrot *et al.* presented the surface modification of CdS with thioglycerol, which later served as the initiator for ring opening polymerization (ROP) of the lactone ε-caprolactone, in the presence of $AlEt_3$.[75] Quantum dot-oligo(phenylene vinylene) (OPV) nanostructures were prepared from bulk film OPV and dioctyl-*para*-bromobenzylphosphine oxide (DOPO-Br)-covered CdSe QDs.[76,77] The OPV ligands were grown to about six phenylene vinylene repeating units, from the chain-end phosphine oxides.

The Emrick group utilized this "grafting from" procedure to generate a variety of polymer–CdSe hybrids.[78] Polymerization of cyclic olefins onto the 4-vinylbenzyl group of the phosphine oxide ligands of the CdSe nanoparticles was done through ruthenium-catalyzed ring-opening metathesis polymerization (ROMP). In another report, TOPO–CdSe nanocrystals were ligand exchanged with phosphine oxide functionalized with a 2,2,6,6-tetramethylpiperidinyloxy (TEMPO) benzyl group.[79] The TEMPO moiety facilitated the nitroxide-mediated controlled free radical polymerization for the growth of PS and poly(styrene-*r*-methyl methacrylate) copolymer on the CdSe

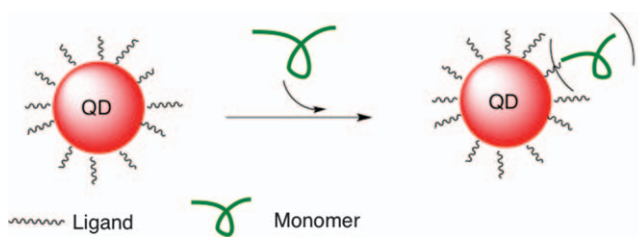

Figure 7.5 General scheme for the fabrication of a polymer–QD hybrid through the polymer "grating from" QD method.

surface. The polymer poly(*para*-phenylene vinylene) was also grafted onto the CdSe surface, through the palladium-catalyzed Heck coupling reaction for the copolymerization of divinylbenzene, dibromobenzene, and the benzylbromide group of the phosphine oxide ligand of CdSe.[80] CdSe surface-grafted with poly(styrene-*b*-methyl acrylate) was generated from the two-step free-radical reversible addition fragmentation chain transfer (RAFT) polymerization.[81]

Zhou *et al.* showed that multihydroxyl hyperbranched polyglycerol (HPG)–CdTe nanohybrids can be derived from *in situ* anionic ring opening polymerization (ROP) of thiol-functionalized CdTe and glycidol.[82] With the same native QDs, they also presented the synthesis of poly(2-(dimethylamino)ethyl methacrylate) (PDMAEMA)–CdTe through direct surface-initiated oxyanionic vinyl polymerization (OAVP) involving the hydroxyl groups of the modified QDs and 2-(dimethylamino)ethyl methacrylate.[83] Esteves *et al.* reported the regulated growth of poly(*n*-butyl acrylate) (P*n*-BA) from a CdS surface using activators generated by electron transfer (AGET) ATRP in miniemulsions.[84] The Mecking group prepared polyfluorene–CdSe/CdS hybrid particles through Suzuki–Miyaura polycondensation[85] or *via* Pd(II)-mediated polymerization[86] of dioxaborolan-substituted fluorine.

7.3.4 Capping Polymer onto Quantum Dots

The capping method (Figure 7.6) involves the attachment of polymers to the as-grown QDs through noncovalent interactions, such as hydrophobic or electronic interactions. Amphiphilic copolymers and polyelectrolytes are typically used to couple with the original ligands on the QDs, without the need for ligand exchange. Polymer–QD hybrids derived from this type of synthesis are generally more resistive and colloidally stable, although they have larger diameters.

Dubertret *et al.* first reported the use of PEG phosphatidylethanolamine (PE) copolymerized with phosphatidylcholine (PC) to encapsulate unmodified CdSe/ZnS QDs.[87] The alkyl groups on the PEG–PE formed the hydrophobic micelle surrounding the QD, with the hydrophobic PEG extending to the water phase. An amphiphilic triblock polymer consisting of hydrophobic polybutyacrylate and polyethylacrylate and hydrophilic polymethacrylic acid

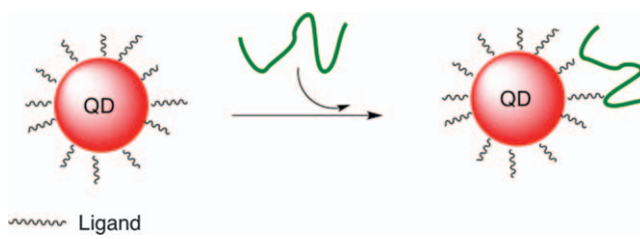

Figure 7.6 General scheme for the fabrication of a polymer–QD hybrid through capping a polymer onto the QDs.

segments was used to cap TOPO–CdSe/ZnS QDs.[88] The hydrophilic carboxylic acid ends were further crosslinked with amine–PEG. The reaction of hydrophobic CdSe/ZnS with 3,4,5-tris(*n*-dodecan-1-yloxy)benzoxy-substituted PEG[89] or with poly(maleic anhydride-*alt*-1-octadecene) (PMAO)–PEG[90] afforded micellar encapsulated CdSe/ZnS nanocrystals. Debnath *et al.* reported the coating of CdSe/ZnS QDs with the polymer polysuccimide conjugated with octylamine and PEG (ODA–PSI–PEG).[91]

Octylamine-terminated alkyl-modified PAA polymeric molecules were shown to cap TOPO–CdSe-based nanoparticles to increase their water solubility.[92–96] Alkyl-substituted poly(maleic anhydride) (PMA) copolymers have been widely used as coating ligands, and the micellar cores were formed with the interactions of the alkyl groups of PMA and the hydrophobic ligands on QDs.[97–103] The anhydride is an excellent functionality that can serve as sites for crosslinking or can be hydrolyzed to give the water compatible carboxylic group, allowing for further modification of the polymer encapsulating the QDs.

Rizvi *et al.* prepared a nanocomposite polymer emulsion to coat CdTe/CdS/ZnS QDs.[104] They combined the hydrophobic cage-like molecule, polyhedral oligomeric silsesquioxane (POSS), with hydrophilic poly(carbonateurea) urethane (PCU). Chen and co-workers synthesized photostable, water-soluble encapsulated $Cd_xSe_y/Zn_{1-x}S_{1-y}$ QDs.[105] Here, the mercaptopropionic acid-modified QDs were successfully encapsulated with two surfactants, oleic acid and sodium bis(2-ethylhexyl)-sulfosuccinate.

Polyelectrolytes have charged groups that can attach to functionalized, charged QDs through electrostatic interactions. Mercaptoacetic carboxylic acid-modified CdSe/ZnS, bearing negative charges upon deprotonation, was coated with a multifunctional poly(acrylamide) (PAM) polymer with positively-charged alkylammonium and phosphonium side groups.[106] Poly(*N*-isopropylacrylamide)–acrylic acid (PNIPAM–AAc) was used to cap the positively-charged cetylammonium-modified CdTe, affording a pH-dependent microgel.[107] On the other hand, the negatively-charged CdTe nanocrystals were stabilized by electrostatic interactions with the octadecyl-*p*-vinylbenzyldimethylammonium-styrene copolymer, where the nanocrystal also served as branching or crosslinking sites.[108]

Several biopolymers have also been used as special kinds of polyelectrolyte capping ligands. Mattoussi *et al.* incorporated negatively-charged CdSe/ZnS particles into two-domain model maltose binding protein-basic zipper (MBP-zb) fusion protein, through its electrostatic interactions with the positively-charged leucine C-terminus.[109] The protonated amino groups of chitosan directly bonded to the charged CdSe/ZnS and Gd–diethylene triamine pentaacetate (DTPA) to afford magnetic chitosan–QD nanobeads.[110] Hybrid cholesterol–QD nanogels were prepared with the use of an amino-modified cholesterol-bearing pullulan.[111]

A unique way of preparing a polymer–QD hybrid material is through layer-by-layer assembly (LbL) where nanocrystals are conjugated with oppositely-charged polyelectrolytes, affording a multilayer organic inorganic

architecture.[112] CdTe QDs have been deposited into a layered film made up of cationic poly(allylamine hydrochloride) (PAH) and the poly(styrenesulfonate) (PSS),[113,114] or of the biocompatible cationic poly-L-lysine hydrobromide (PLL) and the anionic poly-D-glutamic acid sodium salt (PGA).[114] Carboxylic acid (*e.g.* thioacetic acid (TAA)), DHLA-capped CdSe/ZnS nanoparticles were encapsulated into a freely-suspended membrane composed of PAH and PSS,[115] or into the weak electrolyte pair of PAH and anionic PAA.[116] Self-assembled heterostructures on hyaluronic acid (HAA) patterned glass substrates were constructed from the sequential deposition of cationic PAA-coated and anionic mercaptoacetic acid-treated CdSe/ZnS QDs.[117] Nifontova *et al.* fabricated CdSe/ZnS-encoded polyelectrolyte microcapsules by LbL deposition of the oppositely-charged polycation PAH and polyanion PSS or PAA polymers and the carboxylated thiol-PEG functionalized QDs.[118,119] Surface-modified QDs bearing a positive charge from the protonated amino group of cysteamine (Cam) and negative charge from the depronated carboxyl group of mercaptopropionic acid (MPA) were assembled to form $(QD–Cam/QD–MPA)_n$ multilayer films.[120] Wang *et al.* prepared CdTe/polyelectrolyte (PAH, PSS) multilayers through LbL assembly, and onto which a layer of the anti-immunoglobulin G (anti-IgG) was absorbed.[121] CdSe/ZnS–glyconanospheres were derived from the electrostatic attraction between charged mercaptosuccinic acid-modified QDs and the negatively-charged carboxymethyldextran and positively-charged polylysine ligands.[122] An ultrathin film was made from multilayers of chitosan and organophosphorus hydrolase as layers and TGA-capped CdSe QDs as negative layers.[123]

7.3.5 Growth of QDs Within a Polymer

Another way to synthesize polymer–QD hybrids is to use the polymer as a template on which to grow the QDs directly (Figure 7.7). Typically, metal cations are embedded first in the linear, hyperbranched, or nanospherical polymers. Then, the anions are introduced to precipitate the QDs. The nanocrystals are grown on the surface or the interior of the polymer.

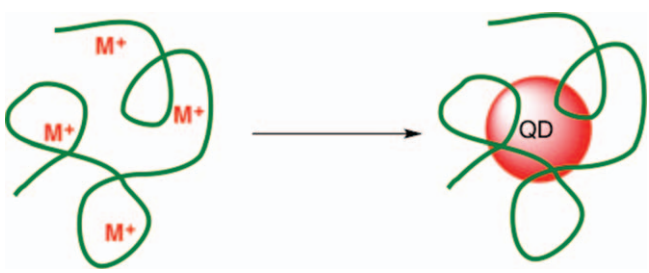

Figure 7.7 General scheme for the fabrication of polymer–QD hybrids through the growth of QDs within the polymer.

Dendrimers of hydroxyl-terminated PAMAM were used to encapsulate CdS QDs through the alternating addition of Cd^{2+} and S^{2-} solutions in the dendrimer solution.[124] ZnS and CdS QDs were prepared with the multihydroxy hyperbranched polyglycerol (HPG) as the stabilizer, in the polar organic solvent dimethylformamide (DMF) at room temperature.[125] The Kumacheva group explored the *in situ* synthesis of CdS nanocrystals on the surface of poly(methyl methacrylate)–poly(methacrylic acid) (PMMA–PMAA).[126,127] The carboxylic groups were deprotonated, and K^+ ions in the electrical double layer were ion-exchanged with Cd^{2+} ions. The S^{2-} ion source was then added, and the CdS QDs were dispersed into the polymer latex particles. A shell of PMMA–PMAA was assembled onto the polymer–CdS hybrid through the surfactant-free emulsion polymerization of MMA and MAA. They further reported the synthesis of CdS through the same approach, but this time using the polymer poly(*N*-isopropyl acrylamide–acrylic acid–2-hydroxyethyl acrylate) (poly(NIPAM–AA–HEA)) as the stabilizer and poly(MMA–butyrate acrylate (BA)–AA) as the shell.[128,129] Wang *et al.* used the polymers poly(methyl acrylate–glycidyl methacrylate–iminodiacetic acid) (poly(MA-*co*-GMA–IDA)[130] and poly(MA-*co*-MMA-*co*-GMA–IDA)[131] to chelate Cd^{2+} through $-N(CH_2COOH)_2$ groups. The S^{2-} ions came from H_2S, which was generated from the reaction of Na_2S and HCl. ZnS was then added as the shell onto the hybrid CdS/poly(MA-*co*-MMA-*co*-GMA–IDA).[131] The metal-chelating polymers poly(styrene-*co*-GMA–IDA) (poly(St-*co*-GMA–IDA)[132] and partially sulfonated polystyrene (PSS)[133] were also employed in the polymer–CdS composite. Spherical polyelectrolyte brushes (SPBs) were prepared from the photoemulsion polymerization of PS@2[*p*-(2-hydroxy-2-methylpropiophenone)]-ethyleneglycol methacrylate (HMEM) and AA.[134] These SPBs were then used as the template for CdS synthesis. Zhang *et al.* described the preparation of poly(arylene ether ketone) (PAEK)–ZnS and PAEK–CdS hybrids through the incorporation of the acetate salts of Cd^{2+} or Zn^{2+} in the polymer, followed by the reaction with thiourea in DMF.[135,136] A composite of cellulose nanofibrils (CNFs) and CdS QDs were fabricated from the *in situ* reaction of the Cd^{2+} suspension in TEMPO-oxidized CNFs and the S^{2-} ions.[137]

7.4 Photothermal Applications of Polymer-decorated Quantum Dots

The inherent optical properties of QDs mark these materials as excellent fluorophores for biological applications.[35,138,139] These materials are utilized in various applications, such as immunohistochemical detection, drug delivery and therapeutics, biosensing, small animal imaging, and single-quantum dot tracking of targets intra- and extracellularly. Furthermore, these materials are being designed to promote the death of cancerous tissues through targeted photothermal therapy.[140–145]

7.4.1 Photothermal Therapy

Photothermal therapy (PTT) is a non-invasive means of treating cancerous cells and has gained tremendous attention in recent years.[140–147] Higher temperatures are found to be detrimental to cancer cells. Normal cells can survive at 44 °C, but cancer cells are destroyed at 42.5 °C. The blood flow in these cancer cells is restricted at higher temperatures, lessening the ability of these cells to dissipate heat. The induced thermal energy, typically generated through a near-infrared (NIR) laser, leads to necrosis or apoptosis of these cells.[142] While NIR laser light can diffuse through skin, it is not absorbed by the tissue components (*e.g.* water, hemoglobin, melanin). Generally, PTT functions through the use of light only, or in conjunction with endogenous molecules or metal nanostructures.[145] The use of QDs as PTT agents promotes a more targeted mode of hyperthermia of cancerous cells. The small size of the QDs (<100 nm) makes these materials easier to move through the cancerous cells.[141] In addition, using polymer–QD hybrids as PTT agents provides the additional advantages of having low toxicity, being easily dispersible in aqueous medium, and having highly modifiable functional groups on the surface.

The proposed mechanism for the conversion of light to heat through nanocrystals is *via* surface plasmon resonance (SPR).[142,147] SPR is usually reported for metal nanocrystals due to their high free electron concentrations, but it can also occur in semiconductor nanocrystals with substantial free carrier concentrations. When nanosized metals absorb light, electrons in the conduction band oscillate around the surface and charge separation occurs.[147] This results in rapid non-equilibrium heating of the system. In addition, relaxation of the electrons through electron–electron scattering further increases the temperature of the surface. Upon cooling back to equilibrium, the electrons and lattice phonons couple, allowing energy exchange between these particles. Furthermore, the cooling of the nanocrystal lattice through phonon–phonon coupling is accompanied by the dissipation of heat into the surrounding medium.

In semiconductor nanocrystals, carrier separation occurs upon light absorption as electrons are excited from the valence to the conduction band, leaving holes in the valence band. The photothermal effect primarily results from the nonradiative phonons.[148] The energy from the absorbed light can be transferred to phonons that leads to temperature elevation. In the case of core/shell semiconductor nanocrystals, the carrier lifetime and optical transition rate are heavily dependent on the band alignment. For type I core/shell structures, the carrier lifetime is short, and this limits the photothermal effect. In core/shell structures with type II band alignment, the free carriers are confined in the two different regions (the core and shell regions), and so, the lifetime of electron–hole pairs can be very long. Consequently, most of the absorbed photon energy can be converted into the phonon system, leading to highly efficient photothermal conversion. For example,

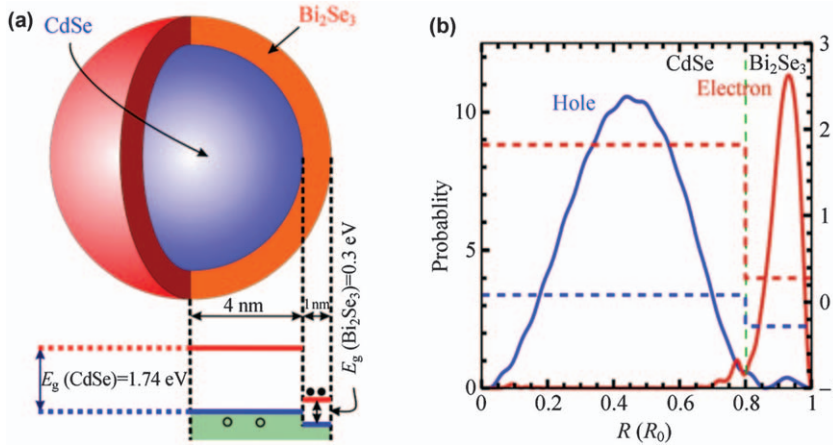

Figure 7.8 (a) Schematic band profile of type II core/shell QDs and (b) the spatial distribution of electron and hole states in the core/shell QDs. Reproduced from ref. 148 with permission from Springer Nature, Copyright 2015.

type II core/shell QDs composed of TGA-modified CdSe/Bi_2Se_3 were shown to have an efficient photothermal conversion when irradiated with an 808 nm laser, and this is attributed to the spatial separation of photogenerated electrons and holes (Figure 7.8).[148]

7.4.1.1 Polymer–QD Hybrids as Photothermal Agents

A key challenge in the development of nanomaterial-based photothermal agents (PTAs) is the design of robust QDs. The extent of the photothermal conversion by QDs depends on the morphology and thermal stability of the nanocrystals.[144] For this purpose, nanocrystals can be used as selective photothermal absorbers, targeted drug delivery vehicles, photo-immunological agents, and theranostic tools.[143] Red/brown, brown, or close to black CdTe and CdSe QDs were shown to have efficient photothermal transduction upon irradiation at 671 nm.[149] These QDs were injected into melanoma tumor-bearing mice and underwent irradiation at 671 nm for 20 min, significantly inhibiting the growth of the tumors.

Volsi *et al.* reported the encapsulation of Au–SiO_2/CdSe/CdS QDs with the polymer α,β-poly(*N*-hydroxyethyl)-DL-aspartamide (PHEA) functionalized with lipoic acid (LA), PEG, and folic acid (FA) pendant molecules.[150] Aqueous dispersion of this QD–polymer micelle showed an increase in temperature when irradiated at 810 nm. The polymer coating had no effect on the hyperthermic properties of the inorganic Au–SiO_2/CdSe/CdS QDs. Under *in vitro* conditions using human breast cancer cells MCF7, this hybrid was successfully incorporated mostly into the cytoplasm of the cell (Figure 7.9, top). Irradiating with an 810 nm laser showed that there was a high cell death *via* hyperthermia (Figure 7.9, bottom). There was also a higher

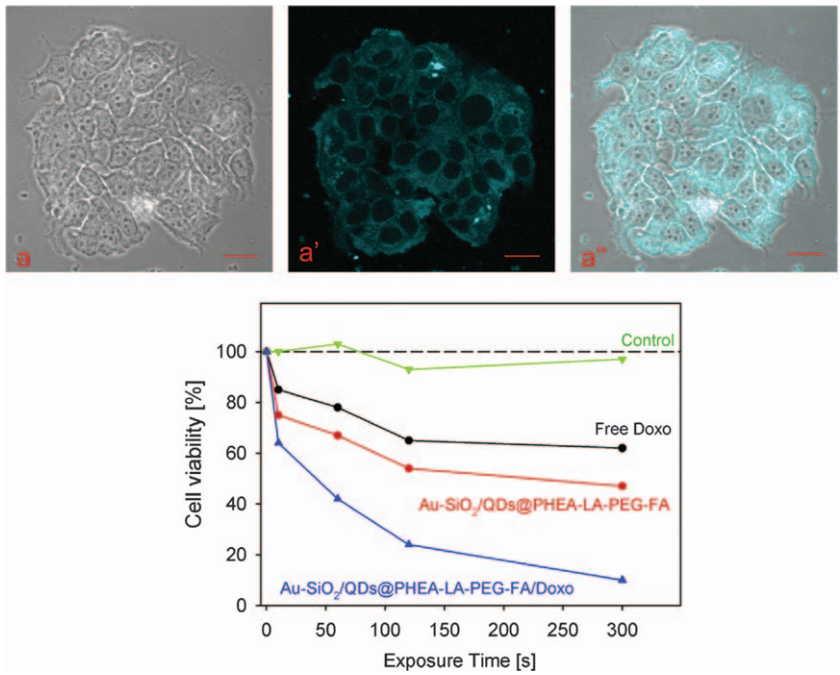

Figure 7.9 Top: Confocal fluorescence images of the MCF7 cells loaded with Au–SiO_2/CdSe/CdS–(PHEA–LA–PEG–FA) for 24 h; (a) bright side, (a′) fluorescent, and (a″) merged. Bottom: Photothermal studies of the MCF7 cells with different treatments.
Reproduced from ref. 150 with permission from Elsevier, Copyright 2018.

decrease in the viability of the cells when the photothermal effect of the hybrid is combined with the anti-tumor properties of the drug doxorubicin.

Hydrophobic core/shell MnSe/Bi_2Se_3 QDs that are capped with oleylamine were prepared through the cation-exchange reaction of MnSe in solution with Bi sources.[151] To make them water-dispersible and physiologically compatible, an amphiphilic polymer was introduced to coat these QDs through hydrophobic interactions. The polymer used was PEG-grafted poly(maleicanhydride-*alt*-1-octadecene) (C18PMH-PEG). When applied to 4T1 cancer cells, the MnSe/Bi_2Se_3–PEG hybrid was found to exhibit both strong NIR ablation upon irradiation at 808 nm and enhanced X-ray induced DNA damage. More remarkably, the polymer–QD hybrid served as a multi-functional agent, playing a synergistic PTT and radiation therapy effect in 4T1 tumor-bearing mice, with a 4 mg kg^{-1} hybrid dose, and irradiation at 808 nm and 4 Gy X-ray dose (Figure 7.10).

WS_2 QDs were synthesized from liquid exfoliation of commercially available WS_2 bulk with H_2SO_4, followed by coating of lipoic acid (LA)–PEI.[152] When irradiated with an 808 nm NIR laser, the temperature of the hybrids increased with the concentration of the hybrid or with irradiation time,

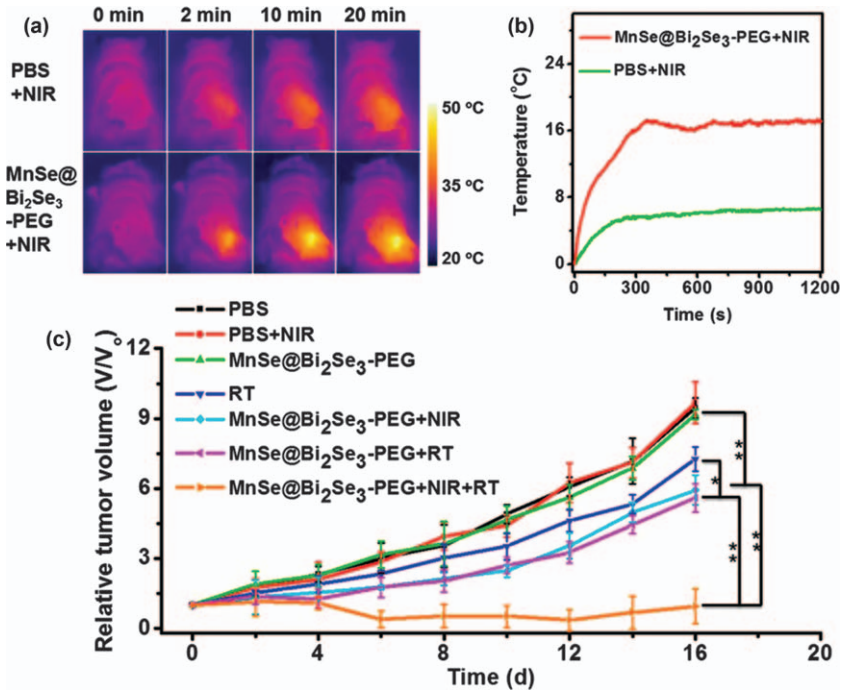

Figure 7.10 (a) Thermal images. (b) Temperature monitoring of the 4T1 cells in mice after photothermal treatment with 808 nm irradiation. (c) Cell growth increase for the 4T1 cells after different treatments.
Reproduced from ref. 151 with permission from John Wiley and Sons, Copyright © 2015 WILEY-VCH Verlag GmbH & Co. KGaA, Weinheim.

proving its potential as a PTT agent. To test for its efficiency as a gene therapy (GT) agent, the LA–PEI-coated WS_2 hybrids were then loaded with the surviving-siRNA molecules, to facilitate cell death. The movement of the siRNA molecules was totally minimized by their strong binding to the hybrids, preventing their degradation, and they were only release when heparin was added. This suggests that the hybrid is a good gene loading and release carrier. *In vitro* studies using BEL-7402 and HeLa cells showed the synergistic therapeutic effect as a PTT agent and as a gene therapy agent (Figure 7.11). Even in animal modeling experiments using Balb/c nude mice bearing BEL 7402 cancer cells, there was an excellent tumor growth inhibition ratio of 91.7% when the WS_2–PEI–siRNA hybrid was used for combined GT + PTT.

Ag_2S QDs were prepared *via* template synthesis with the genetically engineered polypeptide $RGDPC_{10}A$ (CPCC) as the template. This CPCC–Ag_2S hybrid was found to have a superior photothermal conversion efficiency (21%) when compared to other photothermal materials and organic dyes. When injected with CPCC–Ag_2S hybrids, followed by irradiation with an 808 nm laser, the HeLa tumor-bearing mice showed a significant decrease in tumor cells (Figure 7.12). The temperature of the tumor changed to 51.5 °C,

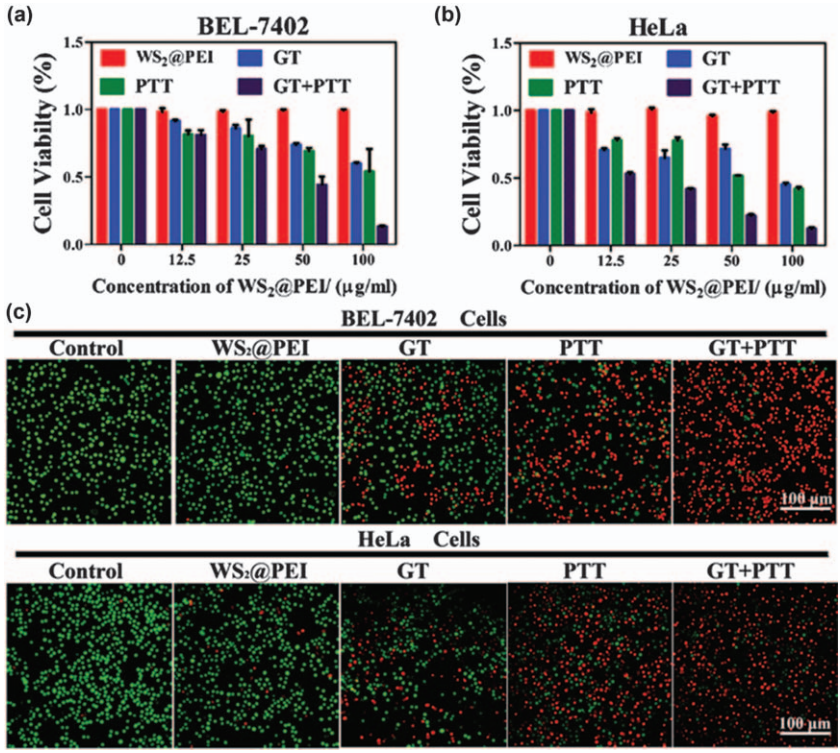

Figure 7.11 (a and b) Cell viability data after different treatments. (c) Staining images indicating the relative number of live (green) and dead (red) cells. Reproduced from ref. 152 with permission from John Wiley and Sons, Copyright 2016 © 2016 WILEY-VCH Verlag GmbH & Co. KGaA, Weinheim.

plateauing at 61.2 °C after 10 min, establishing that the cell death was due to hyperthermia. The tumors were isolated, showing the shrinkage in size after the photothermal treatment with CPCC–Ag_2S QDs.

7.5 Conclusions

Significant progress has been achieved in the development and applications of well-defined polymer–QD hybrids. Research efforts have focused on the synthetic approaches for the incorporation of QDs into polymeric molecules. The ease of preparation, effects on inherent properties of QDs, and the intended application of the material are among the important considerations in choosing which strategy is to be used for the preparation of polymer–QD hybrids. For applications in biological and medical fields, the biocompatibility of the QDs is still the main challenge. Polymeric coating on QDs not only increases the stability and solubility of QDs but also provides responsive sites for environmental stimuli affording a more functional and smart

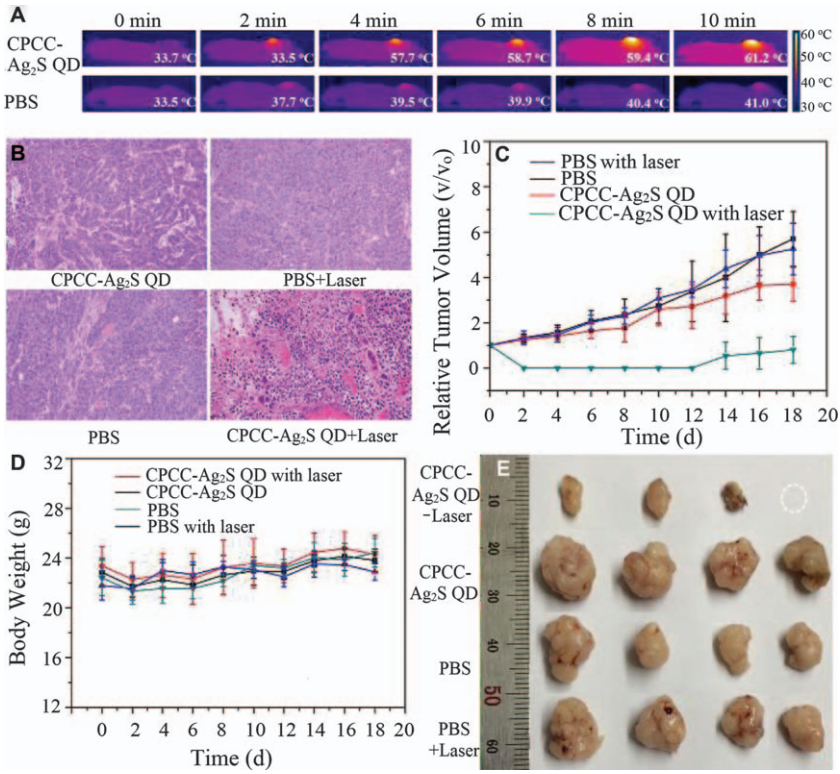

Figure 7.12 (a) Thermal images of the tumors, (b) stained tumor slices, (c) tumor growth plots, (d) body weight change curves, and (e) comparative slices of the tumors, in HeLa tumor-bearing mice after different treatments. Reproduced from ref. 153 with permission from the Royal Society of Chemistry.

material. With this, the design of the functional groups of the polymer, in terms of types and number, would be a significant area to address. Furthermore, post-synthesis functionalization could open a wider selection of simpler polymers that can be used, since functional groups can be introduced after the preparation of the polymer–QD hybrids.

Photothermal therapy is one of the exciting applications of the biocompatible polymer–QD hybrids. These materials offer localized and targeted treatment of cancer cells, preventing adverse effects on the surrounding healthy cells. Development of polymer–QD hybrids with improved photothermal conversion efficiency even at lower dosages could clearly widen the utilization of this technique. Aside from promoting hyperthermia of cancer cell, these hybrids can be used for other types of therapy. As such, exploiting the synergistic effects of combined therapies should be explored. With all the promising leads in pursuing polymer–QDs as PTT agents, the pharmacokinetics and degradation behavior of these materials in biological systems should also be studied more aggressively.

The synthesis of polymers and QDs is still developing as individual areas. Use of biodegradable polymers and more earth-abundant, less toxic metals should be investigated. With this, novel polymer–QD hybrids can still be fabricated, with even better and more exceptional properties.

References

1. N. Tomczak, D. Jańczewski, M. Han and G. J. Vancso, *Prog. Polym. Sci.*, 2009, **34**, 393.
2. N. Tomczak, R. Lu and J. G. Vancso, *Nanoscale*, 2013, **5**, 12018.
3. A. M. Smith and S. Nie, *Acc. Chem. Res.*, 2010, **43**, 190.
4. O. Oluwafemi, N. Revaprasadu and A. Ramirez, *J. Cryst. Growth*, 2008, **310**, 3230.
5. R. Wang, K.-Q. Lu, Z.-R. Tang and Y.-J. Xu, *J. Mater. Chem. A*, 2017, **5**, 3717.
6. C. Sakdaronnarong, A. Sangjan, S. Boonsith, D. C. Kim and H. S. Shin, *Catalysts*, 2020, **10**, 320.
7. D. Raeyani, S. Shojaei, S. A. Kandjani and W. Wlodarski, *Procedia Eng.*, 2016, **168**, 1312.
8. X. Kang, Y. Yang, L. Huang, Y. Tao, L. Wang and D. Pan, *Green Chem.*, 2015, **17**, 4482.
9. P. Tian, L. Tang, K. S. Teng and S. P. Lau, *Mater. Today Chem.*, 2018, **10**, 221.
10. Y. Chen, S. Li, L. Huang and D. Pan, *Inorg. Chem.*, 2013, **52**, 7819.
11. P.-H. Chuang, C. C. Lin and R.-S. Liu, *ACS Appl. Mater. Interfaces*, 2014, **6**, 15379.
12. M. Green and P. O'Brien, *Chem. Commun.*, 1999, 2235.
13. C. B. Murray, D. J. Norris and M. G. Bawendi, *J. Am. Chem. Soc.*, 1993, **115**, 8706.
14. M. A. Hines and P. Guyot-Sionnest, *J. Phys. Chem.*, 1996, **100**, 468.
15. B. O. Dabbousi, J. Rodriguez-Viejo, F. V. Mikulec, J. R. Heine, H. Mattoussi, R. Ober, K. F. Jensen and M. G. Bawendi, *J. Phys. Chem. B*, 1997, **101**, 9463.
16. S. Parani, N. Tsolekile, B. M. May, K. Pandian and O. S. Oluwafemi, in *Nonmagnetic and Magnetic Quantum Dots*, ed. V. N. Stavrou, IntechOpen Limited, London, 2018, ch. 12, pp. 201–219.
17. G. J. J. Draaisma, D. Reardon, A. P. H. J. Schenning, S. C. J. Meskers and C. W. M. Bastiaansen, *J. Mater. Chem. C*, 2016, **4**, 5747.
18. A. S. Karakoti, R. Shukla, R. Shanker and S. Singh, *Adv. Colloid Interface Sci.*, 2015, **215**, 28.
19. T. Rajh, O. I. Micic and A. J. Nozik, *J. Phys. Chem.*, 1993, **97**, 11999.
20. O. S. Oluwafemi, O. A. Daramola and V. Ncapayi, *Mater. Lett.*, 2014, **133**, 9.
21. V. Ncapayi, S. Parani, S. P. Songca, T. Kodama and O. S. Oluwafemi, *Mater. Lett.*, 2017, **189**, 168.

22. S. Parani, N. Tsolekile, K. Pandian and O. S. Oluwafemi, *J. Mater. Sci.: Mater. Electron.*, 2017, **28**, 11151.
23. R. N. Bhargava, D. Gallagher, X. Hong and A. Nurmikko, *Phys. Rev. Lett.*, 1994, **72**, 416.
24. A. K. Guria and N. Pradhan, *Chem. Mater.*, 2016, **28**, 5224C.
25. C. Rajesh, C. Phadnis, K. G. Sonawane and S. Mahamuni, *J. Exp. Nanosci.*, 2015, **10**, 1082.
26. C. Rajesh, C. Phadnis, K. Sonawane and S. Mahamuni, *Phys. Scr.*, 2015, **90**, 015803.
27. J. C. Aphesteguy, G. V. Kurlyandskaya, J. P. de Celis, A. P. Safronov and N. N. Schegoleva, *Mater. Chem. Phys.*, 2015, **161**, 243.
28. R. Saleh and N. F. Djaja, *Spectrochim. Acta, Part A*, 2014, **130**, 581.
29. D. Schelonka, J. Tolasz and V. Štengl, *Photochem. Photobiol.*, 2015, **91**, 1071.
30. O. A. Aleksandrova, D. S. Mazing, L. B. Matyushkin, S. F. Musikhin, A. V. Nikiforova, V. A. Moshnikov and V. Barzda, *2015 Photonics North*, 2015, p. 1, DOI: 10.1109/PN.2015.7292477.
31. Y. Wang, X. Liang, E. Liu, X. Hu and J. Fan, *Nanotechnology*, 2015, **26**, 375601.
32. S. Sureshkumar, B. Jothimani, T. M. Sridhar and B. Venkatachalapathy, *RSC Adv.*, 2016, **6**, 16081.
33. P. Reiss, M. Protière and L. Li, *Small*, 2009, **5**, 154.
34. A. R. AbouElhamd, K. A. Al-Sallal and A. Hassan, *Energies*, 2019, **12**, 1058.
35. A. Hezinger, J. Teßmar and A. Göpferich, *Eur. J. Pharm. Biopharm.*, 2008, **68**, 138.
36. S. J. Rosenthal, J. C. Chang, O. Kovtun, J. R. McBride and I. D. Tomlinson, *Chem. Biol.*, 2011, **18**, 10.
37. L. Shen, *J. Funct. Biomater.*, 2011, **2**, 355.
38. A. M. Wagner, J. M. Knipe, G. Orive and N. A. Peppas, *Acta Biomater.*, 2019, **94**, 44.
39. A. M. Derfus, W. C. W. Chan and S. N. Bhatia, *Adv. Mater.*, 2004, **16**, 961.
40. E.-C. Kang, A. Ogura, K. Kataoka and Y. Nagasaki, *Chem. Lett.*, 2004, **33**, 840.
41. H. T. Uyeda, I. L. Medintz, J. K. Jaiswal, S. M. Simon and H. Mattoussi, *J. Am. Chem. Soc.*, 2005, **127**, 3870.
42. I. Yildiz, B. McCaughan, S. F. Cruickshank, J. F. Callan and F. M. Raymo, *Langmuir*, 2009, **25**, 7090.
43. K. Susumu, B. C. Mei and H. Mattousi, *Nat. Protoc.*, 2009, **4**, 424.
44. Y. Wu, S. Chakrabortty, R. A. Gropeanu, J. Wilhelmi, Y. Xu, K. S. Er, S. L. Kuan, K. Koynov, Y. Chan and T. Weil, *J. Am. Chem. Soc.*, 2010, **132**, 5012.
45. Y. A. Wang, J. J. Li, H. Chen and X. Peng, *J. Am. Chem. Soc.*, 2002, **124**, 2293.
46. L. C. Mattheakis, J. M. Dias, Y.-J. Choi, J. Gong, M. P. Bruchez, J. Liu and E. Wang, *Anal. Biochem.*, 2004, **327**, 200.

47. A. M. Smith and S. Nie, *J. Am. Chem. Soc.*, 2008, **130**, 11278.
48. I. Potapova, R. Mruk, C. Hübner, R. Zentel, T. Basché and A. Mews, *Angew. Chem. Int. Ed.*, 2005, **44**, 2437.
49. M. S. Nikolic, M. Krack, V. Aleksandrovic, A. Kornowski, S. Förster and H. Weller, *Angew. Chem. Int. Ed.*, 2006, **45**, 6577.
50. X.-S. Wang, T. E. Dykstra, M. R. Salvador, I. Manners, G. D. Scholes and M. A. Winnik, *J. Am. Chem. Soc.*, 2004, **126**, 7784.
51. M. Wang, J. K. Oh, T. E. Dykstra, X. Lou, G. D. Scholes and M. A. Winnik, *Macromolecules*, 2006, **39**, 3664.
52. L. Shen, R. Soong, M. Wang, A. Lee, C. Wu, G. D. Scholes, P. M. Macdonald and M. A. Winnik, *J. Phys. Chem. B*, 2008, **112**, 1626.
53. C. Zhang, S. O'Brien and L. Balogh, *J. Phys. Chem. B*, 2002, **106**, 10316.
54. T. Nann, *Chem. Commun.*, 2005, 1735.
55. H. Duan and S. Nie, *J. Am. Soc.*, 2007, **129**, 3333.
56. J. Lee, B. Yang, R. Li, T. A. P. Seery and F. Papadimitrakopoulos, *J. Phys. Chem. B*, 2007, **111**, 81.
57. L. Shen, A. Pich, D. Fava, M. Wang, S. Kumar, C. Wu, G. D. Scholes and M. A. Winnik, *J. Mater. Chem.*, 2008, **18**, 763.
58. W. Liu, A. B. Greytak, J. Lee, C. R. Wong, J. Park, L. F. Marshall, W. Jiang, P. N. Curtin, A. Y. Ting, D. G. Nocera, D. Fukumura, R. K. Jain and M. G. Bawendi, *J. Am. Soc.*, 2010, **132**, 472.
59. Z. Wang, C. Mahoney, J. Yan, Z. Lu, R. Ferebee, D. Luo, M. R. Bockstaller and K. Matyjasewksi, *Langmuir*, 2016, **32**, 13207.
60. S. Kim and M. G. Bawendi, *J. Am. Soc.*, 2003, **125**, 14652.
61. S.-W. Kim, S. Kim, J. B. Tracy, A. Jasanoff and M. G. Bawendi, *J. Am. Soc.*, 2005, **127**, 4556.
62. T. Zhang, J. Ge, Y. Hu and Y. Yin, *Nano Lett.*, 2007, **7**, 3203.
63. W. Lin, K. Fritz, G. Guerin, G. R. Bardajee, S. Hinds, V. Sukhovatkin, E. H. Sargent, G. D. Scholes and M. A. Winnik, *Langmuir*, 2008, **24**, 8215.
64. S. Ehlert, S. M. Taheri, D. Pirner, M. Dreschsler, H.-W. Schmidt and S. Förster, *ACS Nano*, 2014, **8**, 6114.
65. R. Zentel, *Inorganics*, 2020, **8**, 20.
66. Y. A. Wang, J. J. Li, H. Chen and X. Peng, *J. Am. Chem. Soc.*, 2002, **124**, 2293.
67. W. Guo, J. J. Li, Y. A. Wang and X. Peng, *Chem. Mater.*, 2003, **15**, 3125.
68. W. Guo, J. J. Li, Y. A. Wang and X. Peng, *J. Am. Soc.*, 2003, **125**, 3901.
69. B. Ballou, B. C. Lagerholm, L. A. Ernst, M. P. Bruchez and A. S. Waggoner, *Bioconjugate Chem.*, 2004, **15**, 79.
70. W. Liu, M. Howarth, A. B. Greytak, Y. Zheng, D. G. Nocera, A. Y. Ting and M. G. Bawendi, *J. Am. Soc.*, 2008, **130**, 1274.
71. K. Susumu, H. T. Uyeda, I. L. Medintz, T. Pons, J. B. Delehanty and H. Mattoussi, *J. Am. Soc.*, 2007, **129**, 13987.
72. S. J. Tan, N. R. Jana, S. Gao, P. K. Patra and J. Y. Ying, *Chem. Mater.*, 2010, **22**, 2239.

73. (a) T. L. Jennings, S. G. Becker-Catania, R. C. Triulzi, G. Tao, B. Scott, K. E. Sapsford, S. Spindel, E. Oh, V. Jain, J. B. Delehanty, D. E. Prasuhn, K. Boeneman, W. R. Algar and I. L. Medintz, *ACS Nano*, 2011, **5**, 5579; (b) X. Huang, J. Hu, Y. Li, F. Xin, R. Qiao and T. P. Davis, *Biomacromolecules*, 2019, **20**, 4243.
74. S. C. Farmer and T. E. Patten, *Chem. Mater.*, 2001, **13**, 3920.
75. G. Carrot, D. Rutot-Houzé, A. Pottier, P. Degée, J. Hilborn and P. Dubois, *Macromolecules*, 2002, **35**, 8400.
76. M. Y. Odoi, N. I. Hammer, K. Sill, T. Emrick and M. D. Barnes, *J. Am. Chem. Soc.*, 2006, **128**, 3506.
77. N. I. Hammer, K. T. Early, K. Sill, M. Y. Odoi, T. Emrick and M. D. Barnes, *J. Phys. Chem. B*, 2006, **110**, 14167.
78. H. Skaff, M. F. Ilker, E. B. Coughlin and T. Emrick, *J. Am. Chem. Soc.*, 2002, **124**, 5729.
79. K. Sill and T. Emrick, *Chem. Mater.*, 2004, **16**, 1240.
80. H. Skaff, K. Sill and T. Emrick, *J. Am. Chem. Soc.*, 2004, **126**, 11322.
81. H. Skaff and T. Emrick, *Angew. Chem. Int. Ed.*, 2004, **43**, 5383.
82. L. Zhou, C. Gao, W. Xu, X. Wang and Y. Xu, *Biomacromolecules*, 2009, **10**, 1865.
83. L. Zhou, C. Gao and W. Xu, *J. Mater. Chem.*, 2009, **19**, 5655.
84. A. C. C. Esteves, L. Bombalski, T. Trindade, K. Matyjaszewski and A. Barros-Timmons, *Small*, 2007, **3**, 1230.
85. C. Nagele, J. Haase, A. Leitenstirfer and S. Mecking, *ACS Macro Lett.*, 2012, **1**, 1343.
86. T. de Roo, S. Huber and S. Mecking, *ACS Macro Lett.*, 2016, **5**, 786.
87. B. Dubertret, P. Skourides, D. J. Norris, V. Noireaux, A. H. Brivanlou and A. Libchaber, *Science*, 2002, **298**, 1759.
88. X. Gao, Y. Cui, R. M. Levenson, L. W. Chung and S. Nie, *Nat. Biotechnol.*, 2004, **22**, 969.
89. F. Boulmedais, P. Bauchat, M. J. Brienne, I. Arnal, F. Artzner, T. Gacoin, M. Dahan and V. Marchi-Artzner, *Langmuir*, 2006, **22**, 9797.
90. W. W. Yu, E. Chang, J. C. Falkner, J. Zhang, A. M. Al-Somali, C. M. Sayes, J. Johns, R. Drezek and V. L. Colvin, *J. Am. Chem. Soc.*, 2007, **129**, 2871.
91. K. Debnath, K. Mandal and N. R. Jana, *Langmuir*, 2016, **32**, 2798.
92. X. Wu, H. Liu, J. Liu, K. N. Haley, J. A. Treadway, J. P. Larson, N. Ge, F. Peale and M. P. Bruchez, *Nat. Biotechnol.*, 2003, **21**, 41.
93. D. Larson, W. R. Zipfel, R. M. Williams, S. W. Clark, M. P. Bruchez, F. W. Wise and W. W. Webb, *Science*, 2003, **300**, 1434.
94. L. C. Mattheakis, J. M. Dias, Y.-J. Choi, J. Gong, M. P. Brichez, J. Liu and E. Wang, *Anal. Biochem.*, 2004, **327**, 200.
95. C. Luccardini, C. Tribet, F. Vial, V. Marchi-Artzner and M. Dahan, *Langmuir*, 2006, **22**, 2304.
96. R. E. Anderson and W. C. Chan, *ACS Nano*, 2008, **2**, 1341.
97. T. Pellegrino, L. Manna, S. Kudera, T. Liedl, D. Koktysh, A. L. Rogach, S. Keller, J. Rädler, G. Natile and W. J. Parak, *Nano Lett.*, 2004, **4**, 703.

98. M. T. Fernández-Argüelles, A. Yakovlev, R. A. Sperling, C. Luccardini, S. Gaillard, A. S. Medel, J.-M. Mallet, J.-C. Brochon, A. Feltz, M. Ohein and W. J. Parak, *Nano Lett.*, 2007, **7**, 2613.
99. M. T. Fernández-Argüelles, J. M. Costa-Fernández, R. Pereiro and A. Sanz-Medel, *Analyst*, 2008, **133**, 444.
100. E. E. Lees, T.-L. Nguyen, A. H. A. Clayton, B. W. Muir and P. Mulvaney, *ACS Nano*, 2009, **3**, 1121.
101. H. Duan, M. Kuang and Y. A. Wang, *Chem. Mater.*, 2010, **22**, 4372.
102. C. Zhou, H. Shen, Y. Guo, L. Xu, J. Niu, Z. Zhang, Z. Du, J. Chen and L. S. Li, *J. Colloid Interface Sci.*, 2010, **344**, 279.
103. S. A. Díaz, G. O. Menéndez, M. H. Etchehon, L. Giordano, T. M. Jovin and E. Q. Jares-Erijman, *ACS Nano*, 2011, **5**, 2795.
104. S. B. Rizvi, S. Y. Yang, M. Green, M. Keshtgar and A. M. Seifalian, *Bioconjugate Chem.*, 2015, **26**, 2384.
105. J. Chen, B. Yang, C. Li, K. Zheng, K. Žídek and T. Pullerits, *ACS Omega*, 2017, **2**, 1922.
106. I. Potapova, R. Mruk, S. Prehl, R. Zentel, T. Basché and A. Mews, *J. Am. Chem. Soc.*, 2003, **125**, 320.
107. J. Li, B. Liu and J. Li, *Langmuir*, 2006, **22**, 528.
108. H. Zhang, C. Wang, M. Li, J. Zhang, G. Lu and B. Yang, *Adv. Mater.*, 2005, **17**, 853.
109. H. Mattoussi, J. M. Mauro, E. R. Goldman, T. M. Green, G. P. Anderson, V. C. Sundar and M. G. Bawendi, *Phys. Status Solidi B*, 2001, **224**, 277.
110. W. B. Tan and Y. Zhang, *Adv. Mater.*, 2005, **17**, 2375.
111. U. Hasegawa, S. M. Nomura, S. C. Kaul, T. Hirano and K. Akiyoshi, *Biochem. Biophys. Res. Commun.*, 2005, **331**, 917.
112. E. V. Lengert, S. I. Koltsov, J. Li, A. V. Ermakov, B. V. Parakhonskiy, E. V. Skorb and A. G. Skirtach, *Coatings*, 2020, **10**, 1131.
113. A. L. Rogach, N. A. Kotov, D. S. Koktysh, A. S. Susha and F. Caruso, *Colloids Surf., A*, 2002, **202**, 135.
114. M. Adamczak, H. J. Hoel, G. Gaudernack, J. Barbasz, K. Szczepanowicz and P. Warszyński, *Colloids Surf., B*, 2012, **90**, 211.
115. D. Zimnitsky, C. Jiang, J. Xu, Z. Lin, L. Zhang and V. V. Tsukruk, *Langmuir*, 2007, **23**, 10176.
116. A. T. Nagaraja, A. Sooresh, K. E. Meissner and M. J. McShane, *ACS Nano*, 2013, **7**, 6194.
117. S. Jaffar, K. T. Nam, A. Khademhosseini, J. Xing, R. S. Langer and A. M. Belcher, *Nano Lett.*, 2004, **4**, 1421.
118. G. Nifontova, A. Efimov, O. Agapova, I. Agapov, I. Nabiev and A. Sukhanova, *Nanoscale Res. Lett.*, 2019, **14**, 29.
119. G. Nifontova, F. Ramos-Gomes, M. Baryshnikova, F. Alves, I. Nabiev and A. Sukhanova, *Front. Chem.*, 2019, **7**, 34.
120. W. K. Bae, J. Kwak, J. Lim, D. Lee, M. K. Nam, K. Char, C. Lee and S. Lee, *Nano Lett.*, 2010, **10**, 2368.
121. D. Wang, A. Rogach and F. Caruso, *Nano Lett.*, 2002, **2**, 857.
122. Y. Chen, T. Ji and Z. Rosenweig, *Nano Lett.*, 2003, **3**, 581.

123. C. A. Constantine, K. M. Gattás-Asfura, S. V. Mello, G. Crespo, V. Rastogi, T.-C. Cheng, J. J. DeFrank and R. M. Leblanc, *Langmuir*, 2003, **19**, 9863.
124. B. I. Lemon and R. M. Crooks, *J. Am. Chem. Soc.*, 2000, **122**, 12886.
125. L. Zhou, C. Gao, X. Hu and W. Xu, *Chem. Mater.*, 2011, **23**, 1461.
126. J. Zhang, N. Coombs and E. Kumacheva, *J. Am. Chem. Soc.*, 2002, **124**, 14512.
127. S. Xu, J. Zhang and E. Kumacheva, *Compos. Interfaces*, 2003, **10**, 405.
128. S. Xu, J. Zhang, C. Paquet, Y. Lin and E. Kumacheva, *Adv. Funct. Mater.*, 2003, **13**, 468.
129. J. Zhang, S. Xu and E. Kumacheva, *J. Am. Chem. Soc.*, 2004, **126**, 7908.
130. C. C. Wang, A.-L. Chen and I.-H. Chen, *J. Inorg. Organomet. Polym. Mater.*, 2006, **16**, 31.
131. C. C. Wang, A.-L. Chen and I.-H. Chen, *Polym. Adv. Technol.*, 2006, **17**, 598.
132. Y.-C. Chu, C.-C. Wang, Y.-H. Huang and C.-Y. Chen, *Nanotechnology*, 2005, **16**, 376.
133. J. V. Antony, P. Kurian, N. P. N. Vadakkedathu and G. E. Kochimoolayil, *Ind. Eng. Chem. Res.*, 2014, **53**, 2261.
134. Y. Cang, R. Zhang, G. Shi, J. Zhang, L. Lui, X. Hou, Z. Yu, D. Fang and X. Guo, *J. Mater. Chem. C*, 2015, **3**, 3745.
135. Y. Zhang, *High Perform. Polym.*, 2015, **28**, 198.
136. Y. Zhang, X. Hu and D. Jiang, *Plast., Rubber Compos.*, 2017, **46**, 381.
137. Q. Wang, A. Tang, Y. Lui, Z. Fang and S. Fu, *Nanomaterials*, 2016, **6**, 164.
138. S. J. Rosenthal, J. C. Chang, O. Kovtun, J. R. McBride and I. D. Tomlinson, *Chem. Biol.*, 2011, **18**, 10.
139. C. T. Matea, T. Mocan, F. Tabaran, T. Pop, O. Mosteanu, C. Pula, C. Iancu and L. Mocan, *Int. J. Nanomed.*, 2017, **12**, 5421.
140. Y. Shi, M. Liu, F. Deng, G. Zenf, Q. Wan, X. Zhang and Y. Wei, *J. Mater. Chem. B*, 2017, **5**, 194.
141. M. Chu, in *Semiconductors Quantum Dots and Rods for In Vivo Imaging and Cancer Phototherapy*, 2017, ch. 6, pp. 111–139, DOI: 10.1142/9789812142893_0006.
142. E. A. Hussein, M. M. Zagho, G. K. Nasrallah and A. A. Elzatahry, *Int. J. Nanomed.*, 2018, **13**, 2897.
143. A. H. Doughty, A. R. Hoover, E. Layton, C. Murray, E. W. Howard and W. R. Chen, *Materials*, 2019, **12**, 779.
144. Z. Yang, Z. Sun, Y. Ren, X. Chen, W. Zhang, X. Zhu, Z. Mao, J. Shen and S. Nie, *Mol. Med. Rep.*, 2019, **20**, 5.
145. X. Wu, G. Y. Chen, G. Owens, D. Chu and H. Xu, *Mater. Today Energy*, 2019, **12**, 277.
146. L. Gellci and M. Mehrmohammdai, in *Encyclopedia of Cancer*, ed. M. Schwab, Springer, Berlin, Heidelberg, 2015, DOI: 10.1007/978-3-642-27841-9_7097-1.
147. J. A. Webb and R. Bardhan, *Nanoscale*, 2014, **6**, 2502.

148. G. Z. Jia, W. K. Lou, F. Cheng, X. L. Wang, J. H. Yao, N. Dai, H. Q. Lin and K. Chang, *Nano Res.*, 2015, **8**, 1443.
149. M. Chu, X. Pan, D. Zhang, Q. Wu, J. Peng and W. Hai, *Biomaterials*, 2012, **33**, 7071.
150. A. L. Volsi, C. Fiorica, M. D'Amico, C. Scialabba, F. S. Palumno, G. Giammona and M. Licciarda, *Eur. Polym. J.*, 2018, **105**, 38.
151. G. Song, C. Liang, H. Gong, M. Li, X. Zheng, L. Cheng, K. Yang, X. Jiang and Z. Liu, *Adv. Mater.*, 2015, **27**, 6110.
152. C. Zhang, Y. Yong, L. Song, X. Dong, X. Zhang, X. Liu, Z. Gu, Y. Zhao and Z. Hu, *Adv. Healthcare Mater.*, 2016, **5**, 2776.
153. D.-H. Zhao, X.-Q. Yang, X.-L. Hou, Y. Xuan, X.-L. Song, Y.-D. Zhao, W. Chen, Q. Wang and B. Liu, *J. Mater. Chem. B*, 2019, **7**, 2484.

CHAPTER 8

Near-infrared Upconversion Nanomaterial-mediated Photothermal Conversion for Various Applications

ZHAOYOU CHU,[a,b] BENJIN CHEN,[a] WANNI WANG,[a] HAO CHEN[a,b] AND HAISHENG QIAN*[a,b]

[a] School of Biomedical Engineering, Anhui Medical University, Hefei 230032, Anhui, China; [b] School of Basic Medical Sciences, Anhui Medical University, Hefei 230032, Anhui, China
*Email: shqian@ahmu.edu.cn

8.1 Introduction

Rare earth ion-doped upconversion fluorescent materials usually consist of a host and dopant ions. Although the matrix has no luminescent characteristics, it provides a crystal field for the activator, which determines the ion spacing, relative spatial position, coordination number, and types of surrounding anions of the dopant ions, which greatly affect the upconversion fluorescence performance.[1] At present, host materials are mostly fluorides with stable structures and low phonon energy, such as $NaYF_4$, $NaGdF_4$, $NaLuF_4$, KYF_4, LaF_3, CaF_2, $KMnF_3$, YF_3, $KGdF_4$, and BaF_2, especially the composite fluoride $NaYF_4$, which can effectively reduce multiphonon relaxation of the luminous center and weaken non-irradiative transitions for higher fluorescence efficiency.[2–11] In view of the low efficiency of

Nanoscience & Nanotechnology Series No. 54
Photothermal Nanomaterials
Edited by Enyi Ye and Zibiao Li

Published by the Royal Society of Chemistry, www.rsc.org

upconversion nanoparticles (UCNPs) doped with a single rare earth ion, sensitizing ions and activating ions are usually co-doped. It is possible to transfer the absorbed energy from the excitation light to the activator (such as Er^{3+}, Tm^{3+}, Tb^{3+}, Pr^{3+}, and other rare earth ions with up-conversion luminescence properties) through resonance transfer, which is called sensitized luminescence. At present, β-$NaYF_4$:Yb,Tm and β-$NaYF_4$:Yb,Er are the materials with the highest up-conversion efficiency among similar fluorescent materials. UCNPs have the advantages of large Stokes shift, low toxicity, low light bleaching and good stability due to their adjustable emission spectrum from ultraviolet light to visible and near infrared light.[12–19] UCNPs have high potential for applications as integrated probes with diagnostic and therapeutic effects. The combination of UCNPs and other functional materials can give them a high degree of functionality, such as the integration of diagnosis and treatment for image-guided tumor therapy.[19–40] Among them, photothermal therapy (PTT) as a phototherapy method employs photo-absorbing agents to generate heat from NIR, leading to thermal ablation of cancer cells and subsequent cell death. It is also a non-invasive therapy that can convert NIR into heat energy for anticancer treatment. Therefore, UCNPs show more and more application potential in photothermal therapy. In general, we mainly focus on the synthesis of

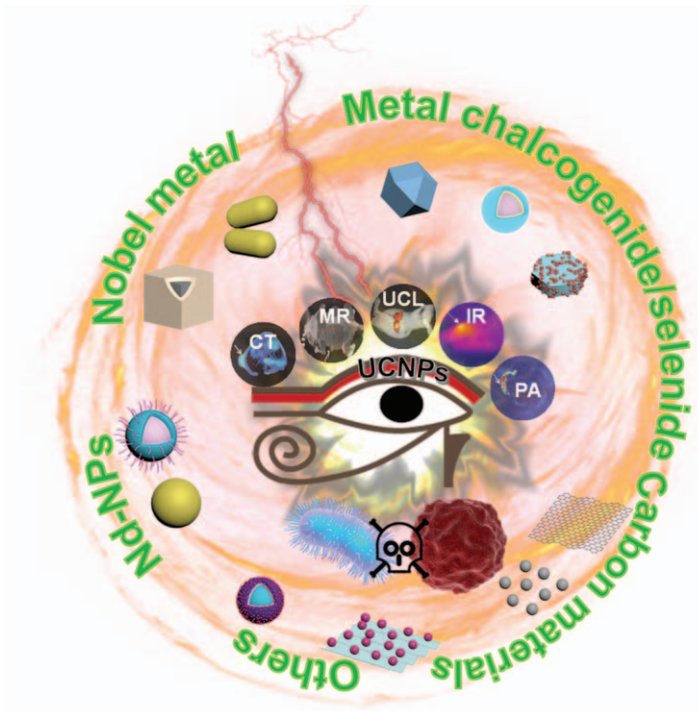

Figure 8.1 Schematic of UCNPs combined with photothermal agent multifunctional nanoplatforms for diagnosis and treatment.

UCNPs and the multifunctional material platform formed by UCNPs themselves or other photothermal components. A schematic of UCNPs combined with photothermal agent multifunctional nanoplatforms for diagnosis and treatment is given in Figure 8.1.

8.2 Chemical Synthesis of Upconversion Nanostructures

8.2.1 UCNPs

UCNPs are essential for different applications such as antimicrobial and anti-tumor applications. Up to now, to tune the properties including size, shape, morphology, and luminescence efficiency of the rare-earth doped UCNPs, many methods to synthesize UCNPs have been implemented such as thermal decomposition,[41–48] hydro(solvo)thermal,[49–54] and chemical co-precipitation.[55]

8.2.1.1 Thermal Decomposition

The thermal decomposition method is a method of dissolving a rare earth ion-doped metal organic precursor in a high-temperature organic solvent and then decomposing and re-synthesizing it under the action of high temperature. Therefore, in the process of thermal decomposition synthesis, some of the reactants are directly synthesized by one-step heating, and others are synthesized in steps, that is, a part of the high-temperature synthesis process is added and another part is further reacted at a high temperature. Rare earth trifluoroacetate, rare earth acetate, and rare earth oleate are common reaction precursors in thermal decomposition. The thermal decomposition method generally requires high temperature reaction conditions, usually around 300 °C, corresponding to high temperature resistant organic solvents, such as oleic acid, octadecene, oleylamine, and octadecene. To provide a high-temperature synthesis environment, oleic acid and oleylamine are generally used as coordination solvents and surfactants to participate in the reaction. Therefore, most of the particles synthesized by this method have oily ligands on the surface, and surface modification treatment is required for biological experiments. For the synthesis of particles with different morphologies, the synthesis of uniform particles with different morphologies can also be achieved by controlling the ratio of reaction solvent and coordination solvent. Na *et al.* achieved this by adjusting the ratio of OA and ODE. Although the particle morphology changes, the synthesized particles are uniform in size in each case[45] (see Figure 8.2).

8.2.1.2 Hydro(Solvo)thermal Synthesis

Hydro(Solvo)thermal synthesis is a synthetic method based on an aqueous solution. A rare earth ion-doped metal inorganic salt aqueous solution and

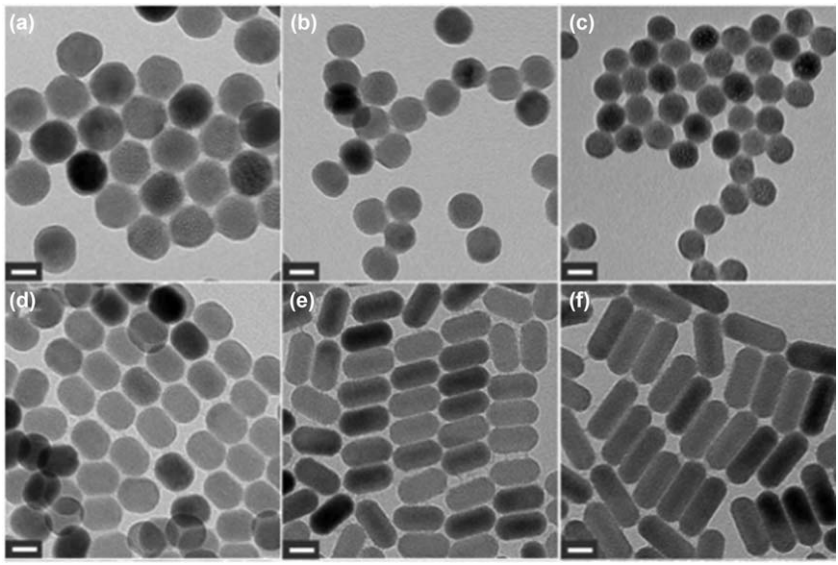

Figure 8.2 TEM images of β-NaYF4:Yb/Er UCNPs synthesized at various ratios of OA to ODE.
Reproduced from ref. 45 with permission from the Royal Society of Chemistry.

some organic solvents are mixed together to carry out the reaction in a high-temperature and high-pressure sealed reactor. In a typical water (solvent) thermal synthesis process, rare earth chloride, rare earth acetate, and rare earth nitrate are usually used as the source of rare earth elements, and HF, NH_4F, NaF, $NaBF_4$, *etc*. are used as fluoride precursors. The morphology of the synthesized particles can be adjusted by controlling the ratio of rare earth elements and fluorine elements, and the synthesis of particles can also be controlled by adjusting the pH,[49,50] OH-ion,[51] citric acid,[52] EDTA,[49,53] CTAB,[54] *etc*. Li *et al*. found that during hydrothermal synthesis, the addition of different amounts of NaOH will affect the morphology of nanocrystals and finally synthesize nanocrystals with different morphologies (see Figure 8.3).[51]

8.2.1.3 Chemical Co-precipitation

In the chemical co-precipitation method there are two or more metal cations in a homogeneous solution. After adding a precipitating agent, different metal ions are simultaneously precipitated out to obtain a uniform precipitate of various components. Martin *et al*. used chemical co-precipitation to synthesize $NaYF_4$:Yb/Pr nanoparticles at a temperature of 80 °C for the first time (see Figure 8.4).[56] Although nanoparticles can be synthesized under low temperature conditions, the particles synthesized by this method often have poor luminescence properties.

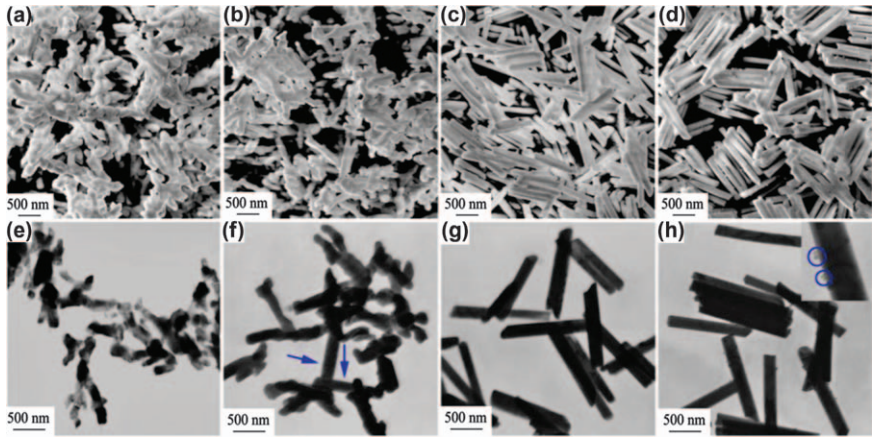

Figure 8.3 SEM and TEM images of β-NaYF4:Yb^{3+}/Er^{3+} nanocrystals synthesized with different amounts of NaOH.
Reproduced from ref. 51 with permission from the Royal Society of Chemistry.

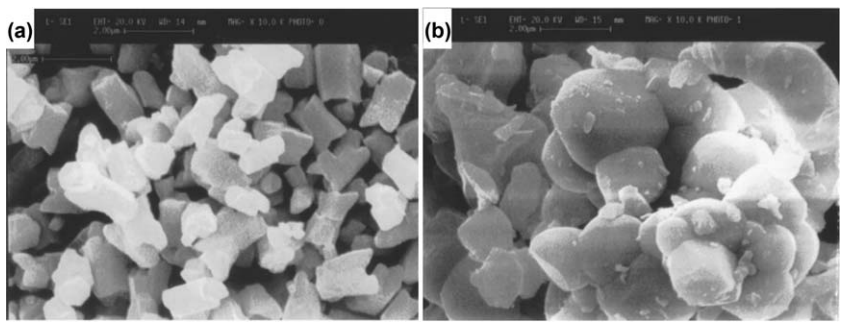

Figure 8.4 SEM micrographs showing the microstructure of $NaYF_4$ fluorides.
Reproduced from ref. 56 with permission from the Royal Society of Chemistry.

8.2.2 Upconversion Core–Shell Nanostructures

Although a nanometer-sized upconversion fluorescent material has a large specific surface area, some of the light-emitting ions doped in the crystal are exposed on the particle surface. The smaller the particle size, the more the light-emitting ions exposed on the outer surface, and the particle surface or external quenching centers such as organic groups and solvents can easily cause non-radiative transitions of rare earth ions, resulting in the fluorescence quenching of particles or a decrease in the fluorescence efficiency.[57] Therefore, researchers have prepared up-converted fluorescent nanomaterials with a core–shell structure to reduce quenching centers and improve the up-converted fluorescence efficiency. A core–shell structure nanomaterial is mainly composed of an internal core–inert shell layer, and

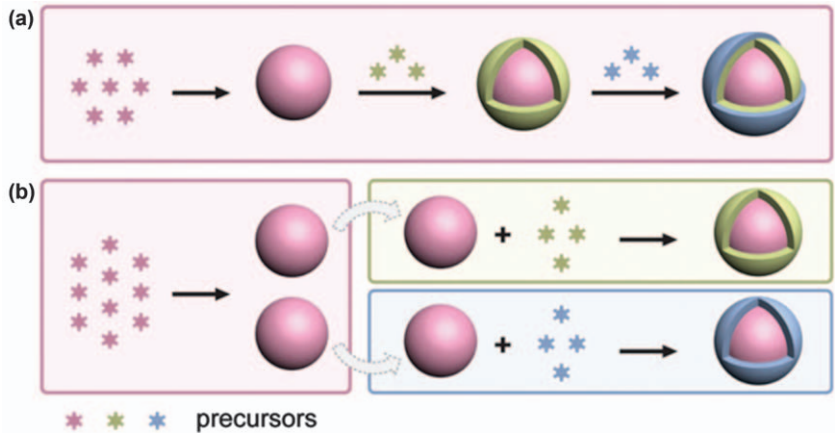

Figure 8.5 (a) Rapid synthesis of multi-shelled nanoparticles through serial hot-injections of diverse shell precursors. (b) Facile tuning of the shell composition through a parallel heating-up of pre-synthesized core nanoparticles with varying shell precursors.
Reproduced from ref. 58 with permission from the Royal Society of Chemistry.

the shell layer is mainly composed of an undoped main crystal to minimize non-radiation. In order to reduce the lattice strain as much as possible, it is generally required that the inert shell material introduced has the same or similar lattice constants as the core structure. The early synthesized core–shell structure nanocomposite is usually a layer of shell material with the same lattice on the surface of the core layer material, but no sensitizing ions or activating ions were doped. Owing to the lack of sensitizing ions or activating ions in the inert shell layer, the shell layer prevents the energy transfer path of the activated or sensitized ions to the surface quenching center, thereby reducing non-irradiative transitions and improving the up-conversion fluorescence efficiency. The doped rare earth ions generally do not easily cause changes in the lattice constant of the main crystal ascribed to the similar properties and ionic radii. So far, seed-mediated epitaxial growth and continuous growth methods have been developed to fabricate up-conversion fluorescent nanomaterials with core–shell structures and tunable fluorescence emissions (see Figure 8.5).[58]

8.2.2.1 Seed-mediated Epitaxial Growth

The seed-mediated epitaxial growth method is a very common method for synthesizing high-quality homogeneous core–shell nanoparticles. This process is mainly divided into two steps. First, the core-layer nanoparticles are prepared, and after a series of treatments, they are added as seeds. In the shell reaction system, the shell component is induced to grow another layer of crystals on the seed surface to form a core–shell nanomaterial. In order to

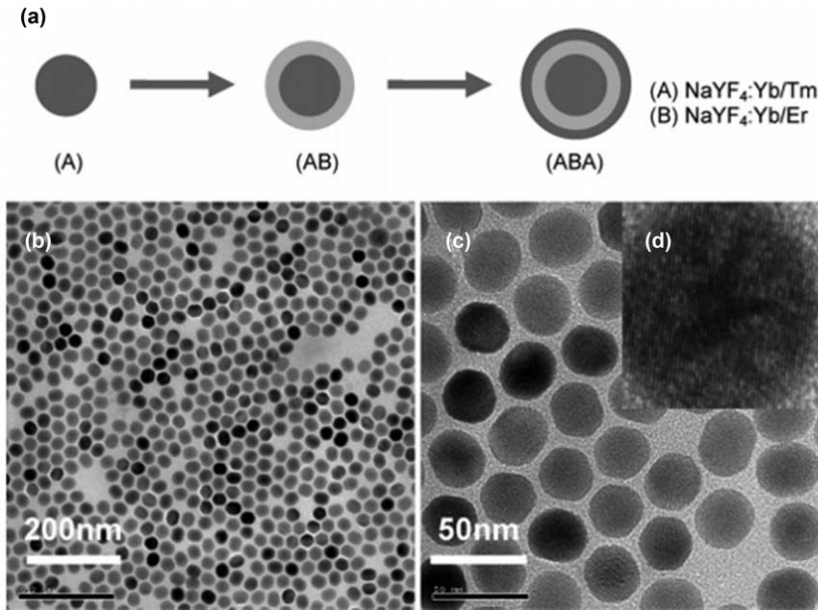

Figure 8.6 Schematic illustration of the formation of core–shell $NaYF_4$:Yb,Tm@-$NaYF_4$:Yb,Er (AB) and $NaYF_4$:Yb,Tm@$NaYF_4$:Yb,Er@$NaYF_4$:Yb,Tm (ABA) nanocrystals.
Reproduced from ref. 59 with permission from American Chemical Society, Copyright 2008.

prevent the seed crystal particles from growing up after maturity, the shell layer is usually grown at a lower temperature than the preparation of the nanocrystalline core. The shell layer can easily nucleate itself under an excessively large concentration of the shell precursor, so the concentration of the component added to the second material must be relatively low to effectively avoid self-nucleation. The method can change the reaction temperature, particle concentration, reaction time, and other related factors to achieve the controlled synthesis of the converted fluorescent nanoparticles on the core–shell structure. Qian *et al.* prepared β-$NaYF_4$:Yb/Tm@β-$NaYF_4$:Yb/Er (AB type) and β-$NaYF_4$:Yb/Tm@β-$NaYF_4$:Yb/Er@β-$NaYF_4$:Yb/Tm (ABA type) nanocrystalline structures. Compared with single-layer β-$NaYF_4$:Yb/Tm, β-$NaYF_4$:Yb/Er or β-$NaYF_4$:Yb/Tm/Er, not only is its corresponding fluorescence intensity greatly enhanced, but multi-color fluorescence was also obtained at wavelengths of 450, 475, 409, 520, 541, and 653 nm attributed to the combination of the emission peaks of Tm and Er (see Figure 8.6).[59]

8.2.2.2 Sequential Growth

Johnson *et al.* firstly proposed the Ostwald ripening mechanism.[60] Ostwald ripening is a process of growing larger particles by sacrificing smaller

particles. The specific process is that all smaller particles shrink, while larger particles grow to form a core/shell structure. They first prepared smaller α-$NaYF_4$ sacrificial nanocrystals (SNCs) as precursors. At high temperature, the precursors were injected into the core layer nanoparticle reaction solution, resulting in the rapid decomposition of SCN and recrystallization. The β-$NaYF_4$ shell layer grows on the surface of the larger core layer β-$NaYF_4$: Yb/Er particles, thereby forming particles with a core–shell structure. This process requires the SCN to be smaller than the core particles, and the shell precursor must be slowly added to minimize the simultaneous existence of anions and cations in the shell structure in the reaction system, thereby effectively preventing the shell nanocrystals from nucleating themselves. Qian *et al*. prepared high quality sub-10 nm $NaYF_4$:Yb/Er@$NaGdF_4$ core–shell nanocrystals successfully *via* a sequential growth process using an amorphous shell component-crystallization strategy (see Figure 8.7a).[61] By observing the changes in UCNPs at different times, a large number of

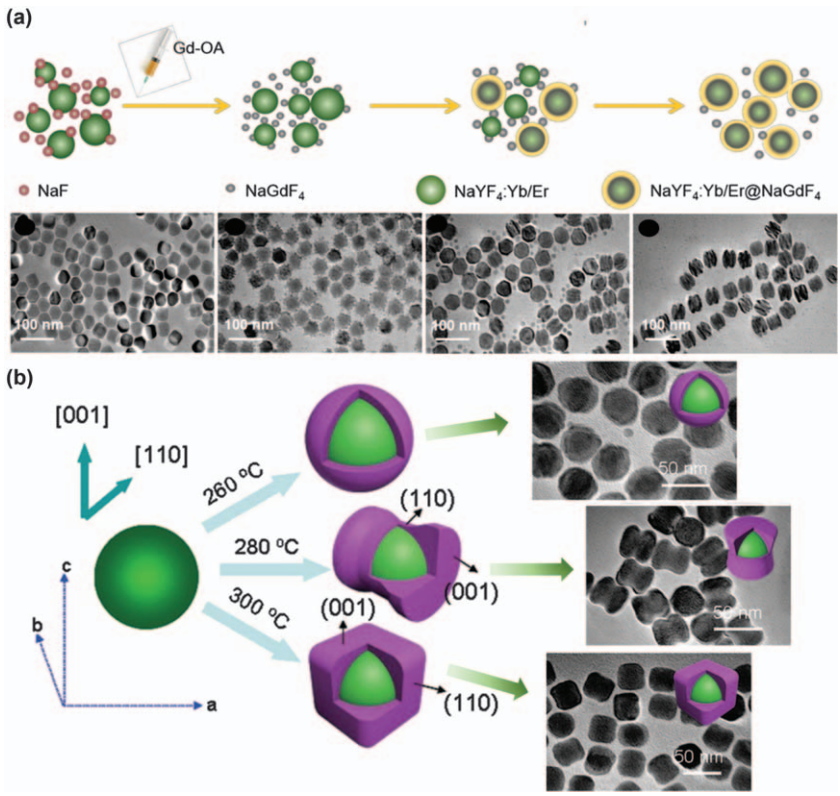

Figure 8.7 UCNP shell growth mechanism when grown at different times and temperatures.
Reproduced from ref. 61 with permission from American Chemical Society, Copyright 2019. Reproduced from ref. 62 with permission from John Wiley and Sons, © 2015 WILEY-VCH Verlag GmbH & Co. KGaA, Weinheim.

small crystals decrease differently while large crystals continue to grow to form their own crystal shape. In this method, the thickness of the shell crystal can be controlled by adjusting the ratio of the shell precursor α-$NaYF_4$ to the core β-$NaYF_4$:Yb/Er particles. Qian *et al*. also conducted research on this issue (see Figure 8.7b).[62] The RE ions oleate precursor solution was injected into a solution previously containing pre-synthesized core nanocrystals, and epitaxial growth was performed, and a thin layer of $NaREF_4$ forms core–shell nanocrystals. Through this strategy, a series of UCNPs were synthesized at different temperatures, with different generated crystal structures. This work may provide new devices for the production of new UCNP core–shell nanoparticles with different characteristics, which is of great significance for their applications. Zeng *et al*. prepared a precursor of a mixture of rare earth ions, oleic acid, octadecene, ammonium fluoride, and sodium hydroxide.[63] After the formation of core nanoparticles, the shell precursor reaction solution was injected to obtain the up-conversion of the core–shell structure fluorescent nanoparticles. In addition, they further studied the growth characteristics of the shell precursor in the reaction system at different temperatures, and the experimental results show that only when the reaction temperature reaches 260 °C can a core with uniform morphology and uniform size be obtained. The shell structure up-converts fluorescent nanoparticles.

8.3 UCNP-based Photothermal Materials for Various Applications

Photothermal therapy is a phototherapy method that uses light-induced heat to thermally ablate cancer cells and bacterial cells. It is a non-invasive treatment that converts NIR light into thermal energy for anti-cancer treatment. Tumor cells are more sensitive to heat than normal cells, by contrast, normal cells are more resistant to heat or when combined with radiation, and normal cells usually recover faster from injury than cancer cells. Therefore, tumor cells are more easily killed compared with normal cells in the same high temperature conditions, above 42 °C.[64] Under specific NIR laser irradiation, photothermal agents can effectively convert NIR light into intense localized heat, thereby inducing cell death in malignant tissue subjected to high temperature, which in turn leads to tumor shrinkage. In recent years, researchers have found that PTT can change the effect of hyperthermia by adjusting the accurate positioning of external laser power, and such an operational method has the advantage of being non-selective for tumor cells. Although there are many advantages for PTT, its prognosis is still unsatisfactory, because of poor and inhomogeneous heat delivery to tumor regions. Combination therapy has emerged to meet the fast-growing demands of a variety of malignancies.[65–67] For example, PTT combined with chemotherapy induces a synergistic effect which increases its therapeutic effectiveness compared with PTT or chemotherapy alone and leads to a

reduction in the number of times required that might reduce the chance of the emergence of drug-resistance.[68–70]

8.3.1 UCNP Photothermal Materials

The rare earth element neodymium (Nd) has a good 808 nm light absorption capacity, and Nd^{3+} doped nanoparticles (NdNPs) have been proven to be inorganic photothermal agents,[71] because the photothermal effect of NdNPs is mainly mediated by the cross-relaxation (CR) between Nd^{3+} ions, which the CR effect increases with the doping ratio of Nd^{3+} content. In a previous report, Nd^{3+} doped LaF_3 nanoparticles (Nd:LaF_3 NPs) were successfully fabricated using a wet-chemistry method, and Jaque's *et al*. were successful in the selective ablation of tumor cells using heat and accurate monitoring of real temperature (see Figure 8.8a).[72] The intratumoral tissue reaches high temperatures after only a very short time, and it can be monitored by the characteristic fluorescence performance of a high concentration of Nd^{3+}. On this basis, Jaque *et al*. also synthesized 100% constituent Nd^{3+} ion-doped ultrasmall $NdVO_4$ UCNPs, which achieved a distinctive light-to-heat conversion efficiency and particular spectroscopic properties simultaneously.[73] The photothermal conversion efficiency of $NdVO_4$ NPs at 808 nm low-power (0.6 $W\,cm^{-2}$) exposure was found to be in the order of 72.1%, which manifested as rapid heating in the tumor tissue. The excellent photothermal effect of $NdVO_4$ is caused by the CR pathways between the ladder-like energy levels of Nd^{3+} ions, which show a low quantum yield and short fluorescence lifetime. In addition to the CR pathways between Nd^{3+} and Nd^{3+}, Tan *et al*. designed a new cross-relaxation effect between the ladder-like energy levels of Nd^{3+} ions and continuous energy band of Prussian blue (PB) by coating PB on $NaNdF_4$ nanoparticles to fabricate core–shell nanocomplexes, and the photothermal conversion efficiency was improved exceptionally (see Figure 8.8b).[74] When Nd^{3+} ions are exposed to 808 nm irradiation, the photon can be excited to the $^4F_{5/2}$ state, and then relaxes down to the $^4F_{3/2}$ atomic state (see Figure 8.8c). The photon can be attenuated to a lower energy state through a radiative process, thereby through emission at 900, 1058, and 1332 nm (see Figure 8.8d). The fluorescence lifetime of the composite materials at 1058 nm (see Figure 8.8e) was clearly reduced, which indicates that the photon has gone through other pathways (Table 8.1).

8.3.2 UCNP Hybrid Photothermal Materials

Generally, core–shell nanoparticles or hybrid nanostructures exhibit enhanced physical and chemical properties. The energy conversion process can be adjusted by construction of the UCNPs with noble metals, semiconductors, polymers, *etc*. Thus, better UCNP-based photothermal nanostructures have been achieved so far.

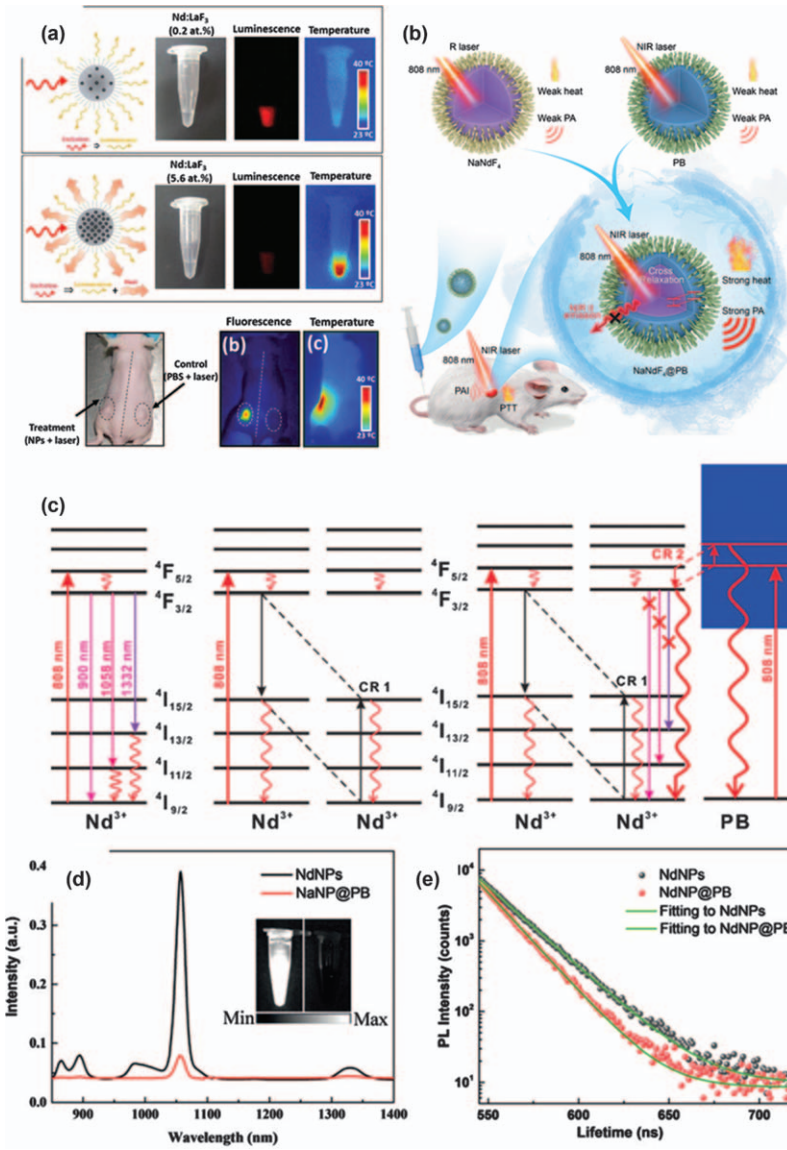

Figure 8.8 (a) Schematic illustration of changes in the fluorescence intensity and temperature at different concentrations of Nd^{3+}. Reproduced from ref. 72 with permission from John Wiley and Sons, Copyright © 2014 WILEY-VCH Verlag GmbH & Co. KGaA, Weinheim. (b) Schematic illustration of the enhancement of photoacoustic imaging signals and photothermal therapy efficacy by generating new cross-relaxation pathways between $NaNdF_4$ and PB. (c) Simplified diagrams of the radiative and non-radiative processes in single Nd^{3+} ions, cross-relaxation between Nd^{3+} ions, generation of new cross-relaxation pathways between Nd^{3+} ions and PB. (d and e) NIR emission and lifetime decay curves of NdNPs and NdNPs@PB. Reproduced from ref. 74 with permission from John Wiley and Sons, Copyright © 2019 Wiley-VCH Verlag GmbH & Co. KGaA, Weinheim.

Table 8.1 Summary of the presented UCNPs photothermal material multifunctional nanoplatforms.

UCNPs	Photothermal agents	Composite structures	NIR light (nm)	Features	References
LaF_3	**Nd:LaF_3**	**Nd:LaF_3**	808	1. Intratumoral thermal reading 2. PTT	72
$NdVO_4$	**$NdVO_4$**	**$NdVO_4$**	808	1. Near-infrared fluorescence imaging 2. PTT	73
$NaNdF_4$	**$NaNdF_4$@PB**	**$NaNdF_4$@PB**	808	1. PA 2. PTT	74

8.3.2.1 UCNP-noble Metals

The noble metals used include Au, Pd, Ru, Pt, and Ag, and among these noble metals, Au and Ag have strong surface plasmon resonance (SPR) absorption and are often used in hyperthermia therapy under NIR light.[75–78] Gold nanoparticles (AuNPs), as a kind of plasma material, have been used to construct UCNP hybrid photothermal materials with high photothermal effects. Like other nanoscale materials, UCNP–AuNPs are able to passively accumulate and preferentially be retained at the tumor site *via* an enhanced permeability and retention (EPR) effect arising from leaky vasculature and ineffective lymphatic drainage of the tumor tissue.[79] In addition, AuNPs can be easily functionalized with active targeting of proteins, peptides, monoclonal antibodies, and small molecules to avoid non-specific uptake and achieve tumor-specific targeting.[80–83]

The combination of UCNPs and AuNPs is a major challenge, and different approaches are currently being pursued. Sun *et al*. constructed a gold plasmon particle (NR) dimer–UCNP–chlorin e6 (Ce6), which is used for multimodal imaging guided combined phototherapy (see Figure 8.9a).[84] It establishes a nuclear-satellite structure through a DNA backbone, in which gold NR dimers (nucleus) and Ce6-linked UCNPs ($NaGdF_4$) (satellite) are assembled in layers through complementary base pairing and designed a multifunctional nanostructure. In this way, Ce6 linked by DNA overcomes the shortcomings of easy aggregation and also maintains the optimal dose and high PDT treatment effect, which provides broad prospects for clinical cancer photodynamic therapy. In addition to the method of DNA connection, a hybrid core/shell nanocomposite with multifunctional properties was developed by Huang *et al.*, which uses a multistep strategy consisting of a gold nanorod (GNR) core with an upconverting $NaYF_4$:Yb/Er shell (GNR@$NaYF_4$:Yb/Er) (see Figure 8.9b).[85] The GNR@$NaYF_4$:Yb/Er nanocomposites were also loaded with the chemotherapy drug doxorubicin (DOX), and the drug release characteristics were evaluated. The results showed that the release of doxorubicin increased significantly under low pH and high temperature induced by the photothermal effect.

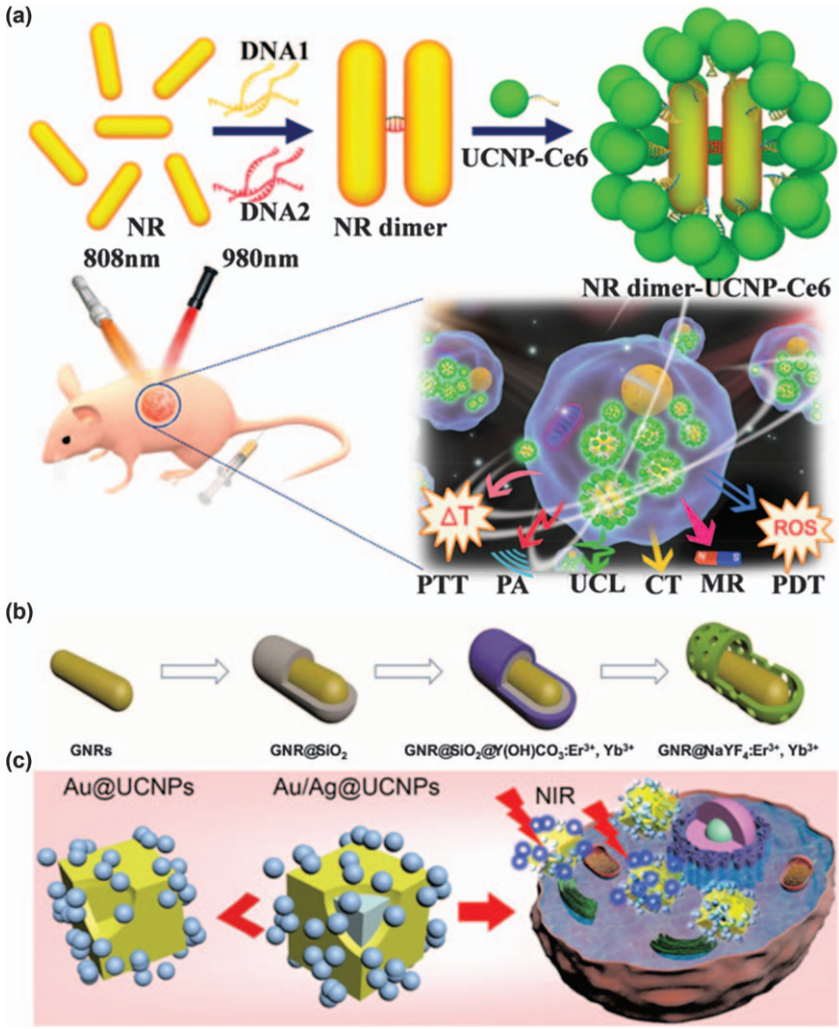

Figure 8.9 (a) Schematic illustration of multifunctional phototherapy of NR dimer–UCNPs–Ce6. Reproduced from ref. 84 with permission from John Wiley and Sons, Copyright © 2015 WILEY-VCH Verlag GmbH & Co. KGaA, Weinheim. (b) Schematic illustration of the synthetic procedure for the GNR@$NaYF_4$:Er^{3+}, Yb^{3+} nanocomposite. Reproduced from ref. 85 with permission from the Royal Society of Chemistry. (c) Schematic illustration of Au/Ag@UCNPs for UCL guided combination PDT and PTT. Reproduced from ref. 86 with permission from American Chemical Society, Copyright 2019.

The characteristics of local heating and drug release mean the multifunctional nanocomposites have great potential in cancer treatment. Liu *et al.* designed the integration of Au/Ag nanocages with UCNPs for higher imaging guided PDT and PTT performance with 808 nm irradiation (see Figure 8.9c).[86]

In addition to the above connection methods, AuNRs can be connected to UCNPs by adsorbing on the hole of SiO_2. A new core/shell structured nanotheranostic was designed by coupling photosensitive $Au_{25}(SR)_{18}$ (SR refers to thiolate) clusters, pH/temperature-responsive polymer P(NIPAm–MAA), and anti-cancer drug (DOX) onto the surface of mesoporous silica coated core–shell UCNPs (see Figure 8.10a).[87] Moreover, the anti-cancer drug DOX can be loaded into the pores of $mSiO_2$. Thanks to Au_{25}, PDT and PTT can be triggered

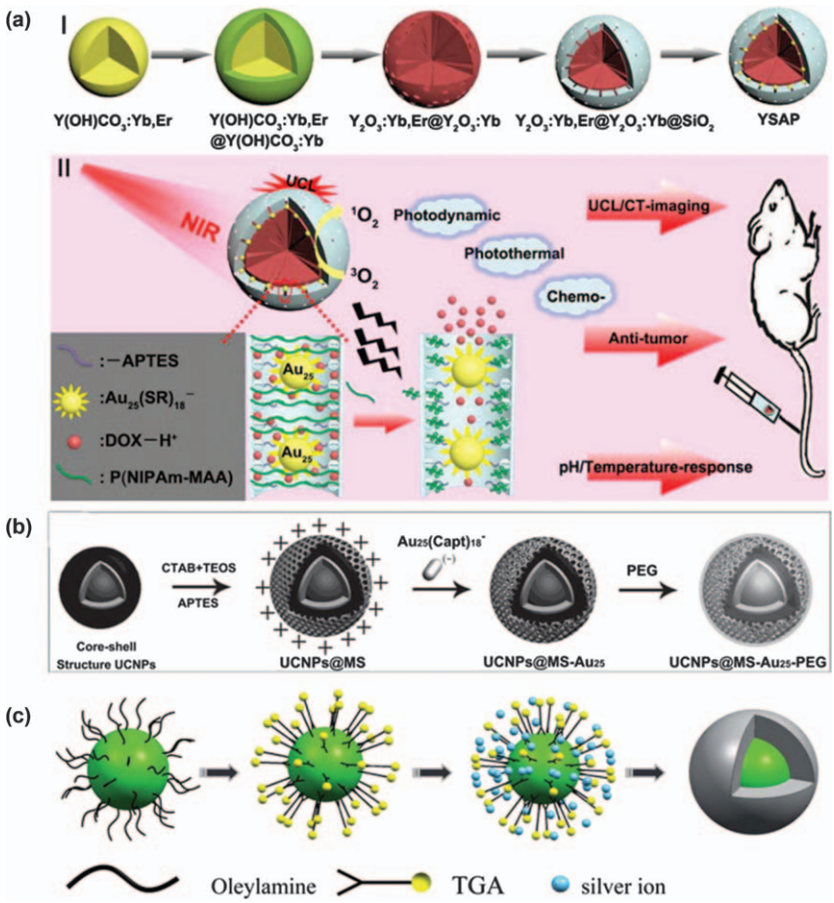

Figure 8.10 (a) Schematic illustration of the synthetic procedure and the multimodal imaging guided combination anticancer therapy for the UCNPs@$mSiO_2$–Au_{25}–P(NIPAm–MAA) nanocomposite. Reproduced from ref. 87 with permission from Elsevier, Copyright 2015. (b) Schematic illustration of the synthetic procedure for the UCNPs@MS–Au_{25}–PEG nanocomposite. Reproduced from ref. 88 with permission from John Wiley and Sons, Copyright © 2015 WILEY-VCH Verlag GmbH & Co. KGaA, Weinheim. (c) Schematic illustration of the synthetic procedure for the Ag-coated UCNP nanocomposite. Reproduced from ref. 91 with permission from the Royal Society of Chemistry.

synchronously using single 980 nm light. In addition, the thermal effect can also stimulate the pH/temperature-sensitive polymer at the cancer sites to achieve targeted and controllable DOX release. Therefore, PDT and PTT combined with pH/temperature responsive chemotherapy can significantly improve the efficacy. To reduce the overheating effects associated with the use of 980 nm lasers, 808 nm NIR is considered an ideal candidate. He *et al*. designed captopril stabilized-Au nanoclusters $Au_{25}(Capt)_{18}$–(Au_{25}) assembled into the mesoporous silica shell coating outside of Nd^{3+}-sensitized UCNPs (see Figure 8.10b).[88] The newly formed Au_{25} shell shows great photothermal effect, which produces photothermal imaging and photoacoustic imaging characteristics combined with upconversion luminescence imaging. Lin's group has done a lot of work on Au clusters.[89,90] Silver nanoparticles also have Au-like properties. Here, Dong *et al*. introduced the synthesis of $NaYF_4$:Yb,Er@Ag nanoparticles with a hexagonal nucleus shell structure and unique biological functional properties (see Figure 8.10c and Table 8.2).[91]

8.3.2.2 UCNP-metal Chalcogenide/Selenide Heterostructures

In some recent reports, metal chalcogenide and metal selenide have been regarded as potential photothermal agents with significant photothermal conversion efficiency, low-cost synthesis, and acceptable toxicity, including CuS,[92–97] MoS_2,[98,99] VS_2,[100] Ag_2S,[101] AgSe,[102] and BiSe.[103] In particular, CuS exhibits a quantum size confinement phenomenon, resulting in strong and tunable NIR localized surface plasmon resonance.[104–106] Lattice mismatch between CuS and UCNPs is the biggest challenge in preparing UCNP–CuS nanocomposites. It is a reasonable method to connect negatively-charged CuS nanoparticles to silicon dioxide (SiO_2) or carbon-shell-coated UCNP surfaces through an electrostatic interaction strategy. Since the inner and outer surfaces of SiO_2 can be easily modified, using SiO_2 or $mSiO_2$ as the intermediate layer is an effective way to provide reaction sites for connecting different functional nanoparticles. Herein, Liu *et al*. developed a novel anticancer nanoplatform by coating a uniform shell of poly(acrylic acid) (PAA) on the surface of CuS-decorated UCNPs (see Figure 8.11a).[92] Xiao *et al*. coated ultrafine CuS nanoparticles on silicon-coated rare earth ions and transformed nanoparticle surfaces to engineer a new multifunctional core/satellite nano adsorbent (CSNT) (see Figure 8.11b).[93] These CSNTs could cause significantly enhanced radiation damage *in vivo* and *in vitro*, by converting near-infrared light into heat for effective thermal ablation and inducing an increase in the highly localized radiation dose. Under the synergistic effect of PTA and enhanced RT, the tumor disappeared gradually at 120 days without recurrence. For the first time, Xu *et al*. integrated CuS nanoparticles and black phosphorus (BP) nanosheets *via* mesoporous silica-coated upconversion UCNPs (see Figure 8.11c).[94] Synergistic treatment of photothermal, photodynamic, and chemotherapy can be achieved after loading DOX. In a similar way, in addition to SiO_2 as the intermediate layer, Lin *et al*. employed a positively-charged layer of carbon to attach CuS, which synthesized

Table 8.2 Summary of the presented UCNPs-noble metal multifunctional nanoplatforms.

UCNPs	Photothermal agents	Composite structures	NIR light (nm)	Features	References
$NaGdF_4$:Yb/Er-	**Au nanorod dimers**	**NR**–UCNPs–Ce6	980 808	1. UCL/MRI/PA/CT 2. PDT/PTT	84
$NaYF_4$:Er/Yb	**Au nanorod**	**Au**@UCNPs	980	1. Drug release DOX 2. PTT	85
$NaYF_4$:Yb/Tm@$NaYF_4$:Yb/Nd	**Au/Ag nanocages**	**Au/Ag**@UCNPs	808	1. UCL 2. PDT/PTT	86
Y_2O_3:Yb/Er@Y_2O_3:Yb	**Au clusters**	UCNPs@$mSiO_2$–**Au_{25}**–P(NIPAm–MAA)	980	1. UCL/CT 2. PDT/PTT/Chemotherapy	87
β-$NaGdF_4$:Yb/Er@β-$NaGdF_4$:Yb@β-$NaNdF_4$:Yb	**Au clusters**	UCNPs@MS–**Au_{25}**–PEG	808	1. CT/PA/PTI 2. PTT/PDT	88
$NaGdF_4$:Yb/Er@$NaGdF_4$:Yb@$NaNdF_4$:Yb	**Au clusters**	UCNPs@$mSiO_2$–**Au**–PEG	808	1. UCL/MR/CT/PA/PTI 2. PDT/PTT	89
$NaGdF_4$:Nd@$NaGdF_4$@$NaGdF_4$:Yb/Er@$NaGdF_4$:Yb@$NaNdF_4$:Yb	**Au clusters**	UCNPs–**Au**–PEG	980 808	1. FI/PTI/PA 2. PDT/PTT	90
$NaYF_4$:Yb,Er	**Ag nanoparticles**	UCNPs@**Ag**	980	1. UCL 2. PTT	91

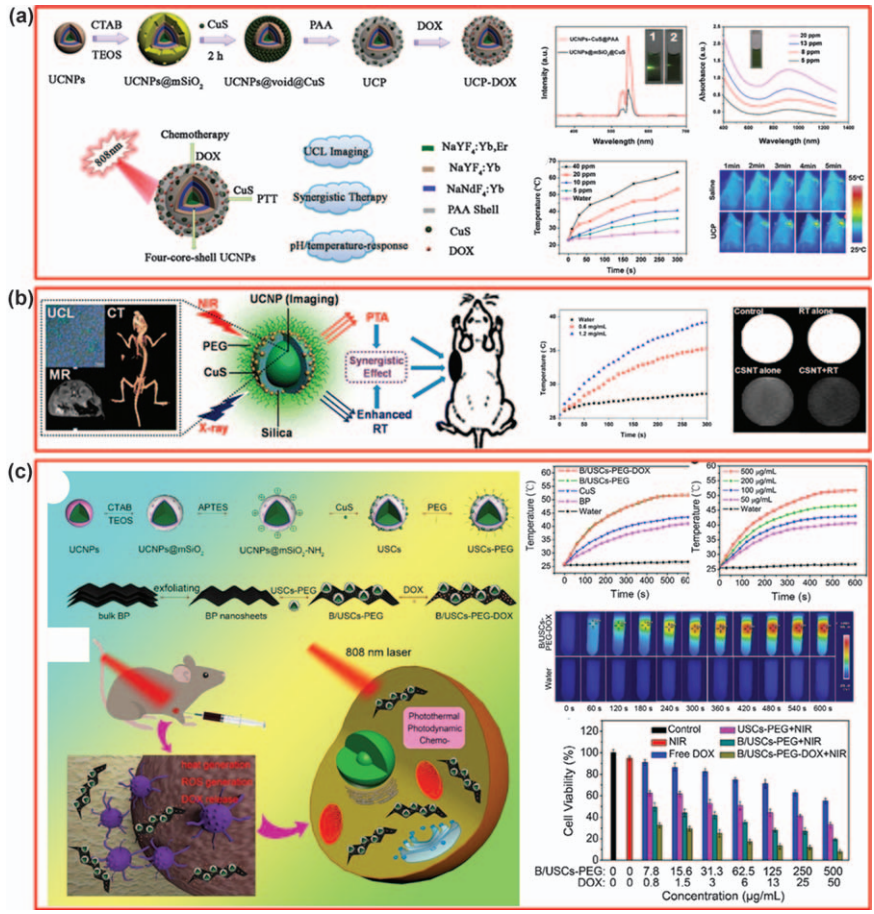

Figure 8.11 (a) Schematic illustration of the synthetic procedure and the UCL-guided combination anticancer therapy for the UCNPs–CuS@PAA–DOX nanocomposite. Upconversion fluorescence and thermal effect of UCNPs@m-SiO_2@CuS nanoparticles under 808 nm NIR laser excitation. Reproduced from ref. 92 with permission from the Royal Society of Chemistry. (b) Schematic illustration of the UCNP@SiO_2–CuS nanocomposite for enhanced photothermal ablation and radiotherapy. Reproduced from ref. 93 with permission from American Chemical Society, Copyright 2013. (c) Schematic illustration of the preparation of B/USCs–PEG–DOX and the release of loaded DOX for multimodal imaging-guided combination anticancer therapy. The thermal effect of the nanocomposite under 808 nm laser excitation. And the *in vitro* cell viability of L929 fibroblasts cells at various contents under 808 nm laser irradiation. Reproduced from ref. 94 with permission from Elsevier, Copyright 2020.

Y_2O_3:Yb/Er–CuS hollow nanospheres through co-precipitation and subsequent hydrothermal pathways.[95] Simply, the yolk–shell Y(OH)CO_3:Yb/Er@C nanospheres acted as templates for hollow Y_2O_3:Yb/Er nanospheres *via* the Kirkendall effect. The final product Y_2O_3:Yb/Er–FA–CuS–DOX was

obtained by combination of the targeting molecular FA, chemotherapeutic drug DOX, and photothermal agent hexagonal CuS nanoparticles assembled onto the surface of the Y_2O_3:Yb/Er nanospheres, and the UCL guided combination chemotherapy and PTT resulted in an improved antitumor efficiency effect. Qian *et al*. synthesized yolk–shell nanoparticles UCNPs@CuS by using another intermediate layer AA–$[Zn(OH)_4]^{2-}$.[96] Strictly speaking, the amorphous layer AA–$[Zn(OH)_4]^{2-}$ can be easily coated onto UCNPs and subsequently reacted with ZnS under an H_2S gas atmosphere. Since the difference between the solubility products of ZnS and CuS is too large, the ion exchange reaction was too rapid resulting in the disintegration of the material structure preventing formation of a complete structure. So it was further reacted to the more stable component $Zn_xCd_{1-x}S$, following the obtainment of CuS coated UCNP yolk shell nanoparticles through a one-step ion exchange reaction, which exhibited the synergistic effect of PDT and PTT of cancer cells. Besides the intermediate layer, CuS linked the UCNPs through a cleavable disulfide bond. mUCNPs@DOX/CuS/HA have been constructed by Du *et al*. by exploiting this concept, in which CuS acts as a gatekeeper under the influence of glutathione, and it was further developed for UCL/MRI/PAT guided synergetic chemo-thermotherapy.[97]

In addition to CuS, other sulfides such as MoS_2,[98,99] VS_2[100] and Ag_2S[101] also have good light-to-heat conversion capabilities. Xu *et al*. used two enhancers (dye sensitization and core–shell enhancement) to jointly amplify the upconversion efficiency, thus achieving ultra-bright visible light emission at low 808 nm light excitation (see Figure 8.12a).[98] The significantly amplified red light then triggers the photosensitizer (Ce6) to produce enough ROS for effective PDT. When silica has a positive surface, these PDT nanoparticles can be easily grafted onto the molybdenum disulfide nanosheet. Since the optimal laser wavelength of UCNPs is consistent with that of the MoS_2 nanometer sheet used for PTT, the nanoplatform of the present invention produces a large amount of ROS and local hyperthermia under a single laser irradiation of 808 nm. Kang *et al*. reported layered MoS_2 as a PTT agent to integrate with $NaYF_4$:Yb/Er so as to realize UCL image-guided PTT/PDT combined tumor therapy.[99] Du *et al*. developed functionalized $NaYF_4$:Yb,Er with chitosan ($NaYF_4$:Yb,Er@CS) *via* a facile approach, which not only improved the hydrophilicity of $NaYF_4$:Yb,Er but also formed stable chelates with transition-metal ions (see Figure 8.12b).[101] Then, ultrasmall metal sulfide ($M^{n+}S$, M = Ag, Cu, Cd) quantum dots (QDs) can be conjugated homogeneously on the surface of $NaYF_4$:Yb,Er@CS. Du *et al*. used the same intermediate layer CS, and a novel multifunctional theranostic nanoplatform was fabricated *via* the *in situ* growth of ultrasmall Ag_2Se nanodots on the surface of CS-coated $NaYF_4$:Yb,Er@$NaLuF_4$:Nd,Yb@$NaLuF_4$ UCNPs (see Figure 8.13a).[102] The excellent photothermal properties, good biocompatibility, and negligible toxicity of nanocomposites make it a promising adsorbent for tumor PTT guided by four-mode imaging. Zhao *et al*. developed a novel nanohybrid based on Bi_2Se_3-conjugated UCNPs (see Figure 8.13b).[103] UCNPs can emit bright visible light with the irradiation of an 808 nm near-infrared (NIR) laser, while the

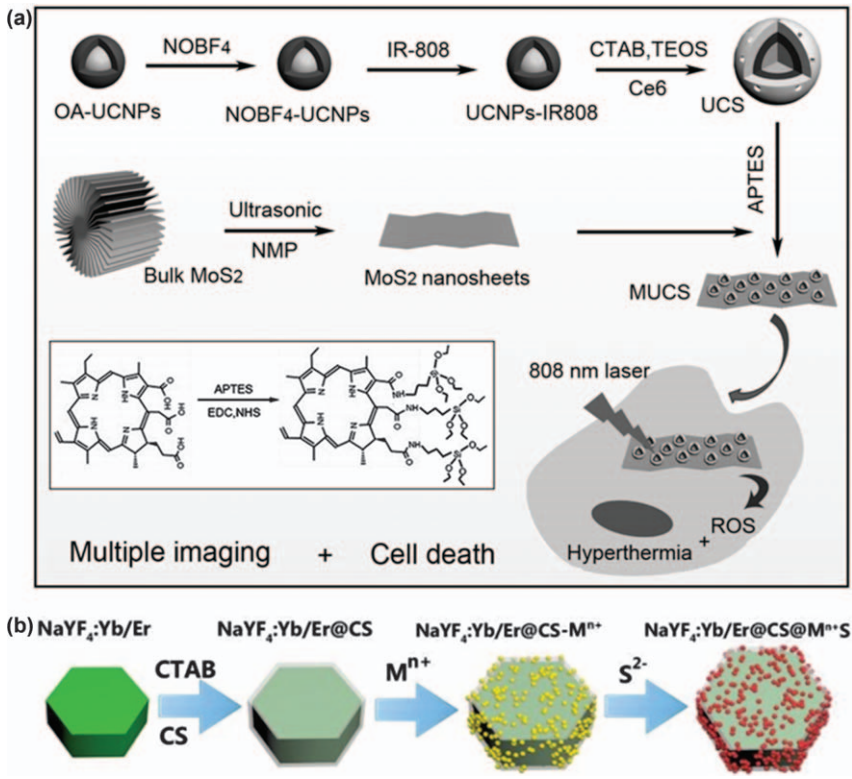

Figure 8.12 (a) Schematic illustration of the synthetic procedure and the multimodal imaging guided combination phototherapy for the Dye–UCNPs–Ce6–MoS_2–FA nanocomposite. Reproduced from ref. 98 with permission from John Wiley and Sons, Copyright © 2017 WILEY-VCH Verlag GmbH & Co. KGaA, Weinheim. (b) Schematic illustration of the synthetic procedure for the UCNPs@CS@ $M^{n+}S$ (Mn = Ag, Cu, Cd) nanocomposite. Reproduced from ref. 101 with permission from the Royal Society of Chemistry.

Bi_2Se_3 nanomaterial showed an efficient photothermal conversion capability. In addition, the UCNPs–Bi_2Se_3 nanohybrid showed high efficiency for cell upconversion luminescence, reasonable CT imaging, and good ablative ability for cancer cells (Table 8.3).

8.3.2.3 UCNP-Carbon Hybrid Materials

Despite the fact that inorganic PTT materials have made considerable achievements in cancer theranostics based on their good photothermal conversion efficiency, their potential non-biodegradability and long-term residence after systemic administration in the body limit their application in biomedicine.[107] Therefore, biocompatible organic photothermal reagents with strong NIR absorption have gradually attracted more attention in recent

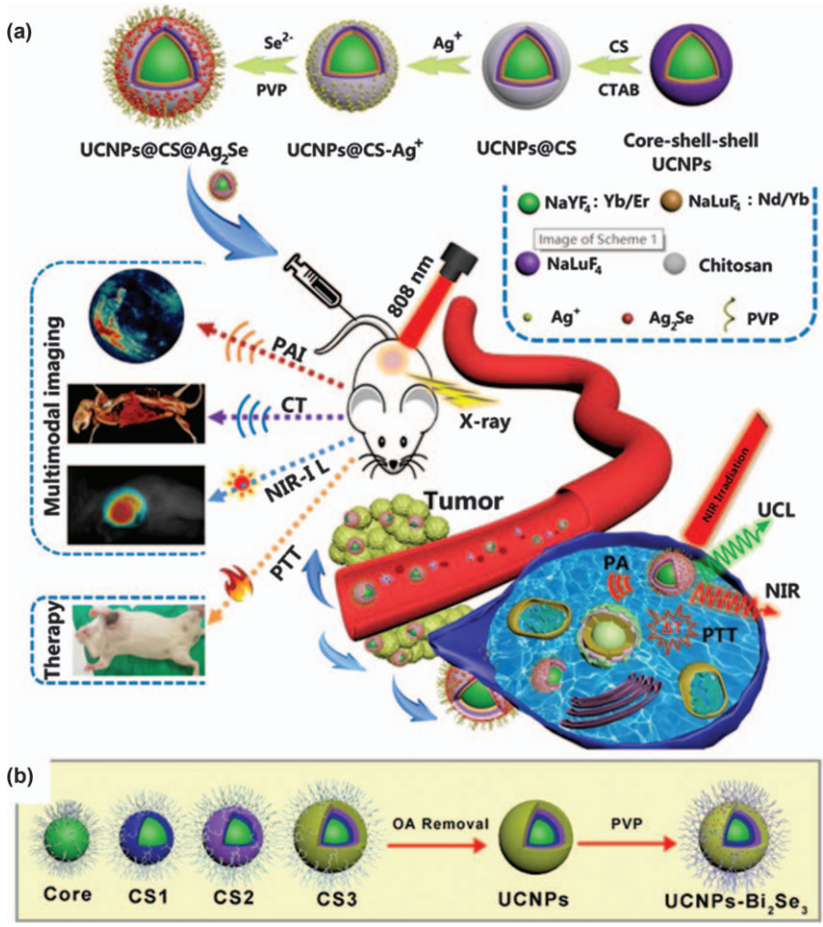

Figure 8.13 (a) Schematic illustration of the synthetic procedure and the multimodal imaging guided combination phototherapy for the UCNPs@Ag_2Se nanocomposite. Reproduced from ref. 102 with permission from Elsevier, Copyright 2020. (b) Schematic illustration of the synthetic procedure for the UCNPs–Bi_2Se_3 nanocomposite. Reproduced from ref. 103 with permission from John Wiley and Sons, Copyright © 2019 Wiley-VCH Verlag GmbH & Co. KGaA, Weinheim.

years. In particular, polypyrrole (PPy),[108,109] polydopamine (PDA),[110,111] polyaniline (PAI),[112] indocyanine green (ICG),[110] carbon,[113] and graphene oxide (GO)[114,115] have drawn extensive attention.

PPy has been shown to have great potential in tumor theranostics based on its good biocompatibility and photothermal performance.[116,117] Cai *et al.* developed a core–shell–shell nanostructure with a UCNPs core coating by a mesoporous silica layer decorated with ZnO nanodots, and an outer layer of PPy that can concurrently generate a thermal effect upon NIR irradiation, resulting in great antitumor efficacy *in vitro* and *in vivo* (see Figure 8.14a).[108]

Table 8.3 Summary of the presented UCNPs–metal chalcogenide/selenide multifunctional nanoplatforms.

UCNPs	Photothermal agents	Composite structures	NIR light (nm)	Features	References
$NaYF_4$:Yb/ Er@$NaYF_4$:Yb@$NaNdF_4$:Yb@$NaYF_4$	**CuS dots**	UCNPs–**CuS**@PAA–DOX	808	1. UCL 2. Chemotherapy/PTT	92
$NaYbF_4$:Gd/ Er	**CuS dots**	UCNP@SiO_2–**CuS**	980	1. PTT 2. Enhanced RT	93
$NaGdF_4$:Yb/Er@$NaGdF_4$:Yb@$NaNdF_4$:Yb	**CuS dots**	BP/UCNPs-**CuS**–PEG–DOX	808	1. CT/PTI 2. PTT/PDT/ Chemotherapy	94
Y_2O_3:Yb/Er	**CuS dots**	UCNPs–**CuS**	980	1. UCL 2. Chemotherapy/PTT	95
$NaYF_4$:Yb/Nd/Er@$NaYF_4$:Nd	**CuS nanosphers**	UCNPs@**CuS**	808	PTT/PDT	96
$NaYF_4$:Yb/Er@$NaGdF_4$	**CuS dots**	mUCNPs@DOX/**CuS**/HA	980	1. UCL/MR/PAT 2. Chemotherapy/PTT	97
$NaGaF_4$:Nd/Yb	**MoS_2 Nanosheets**	Dye–UCNPs–Ce6–**MoS_2**–FA	808	1. UCL, CT, MRI 2. PDT, PTT	98
$NaYF_4$:Yb/Er	**MoS_2 Nanosheets**	**MoS_2**–UCNPs–FA–ZnPc	980/808	1. UCL 2. 808 nm for PTT and 980 nm for PDT	99
$NaYF_4$:Yb/Tm@$NaGdF_4$ and $NaYF_4$:Yb/Er@$NaGdF_4$	**VS_2 nanosheets**	UCNPs@**VS_2**	980/808	1. MR and 980 nm for UCL 2. 808 nm for PTT	100
$NaYF_4$:Yb/Er	**$M^{n+}S$ (Mn = Ag, Cu, Cd) quantum dots**	UCNPs@CS@ **$M^{n+}S$**	980	1. UCL 2. PTT	101
$NaYF_4$:Yb,Er@$NaLuF_4$:Nd,Yb@$NaLuF_4$	**Ag_2Se dots**	UCNPs@**Ag_2Se**	808	1. UCL 2. PTT	102
$NaYF_4$:Yb,Er@$NaLuF_4$:Yb@$NaNdF_4$: Yb@$NaLuF_4$:Yb	**Bi_2Se_3 dots**	UCNPs@**Bi_2Se_3**	808	1. UCL/CT 2. PTT	103

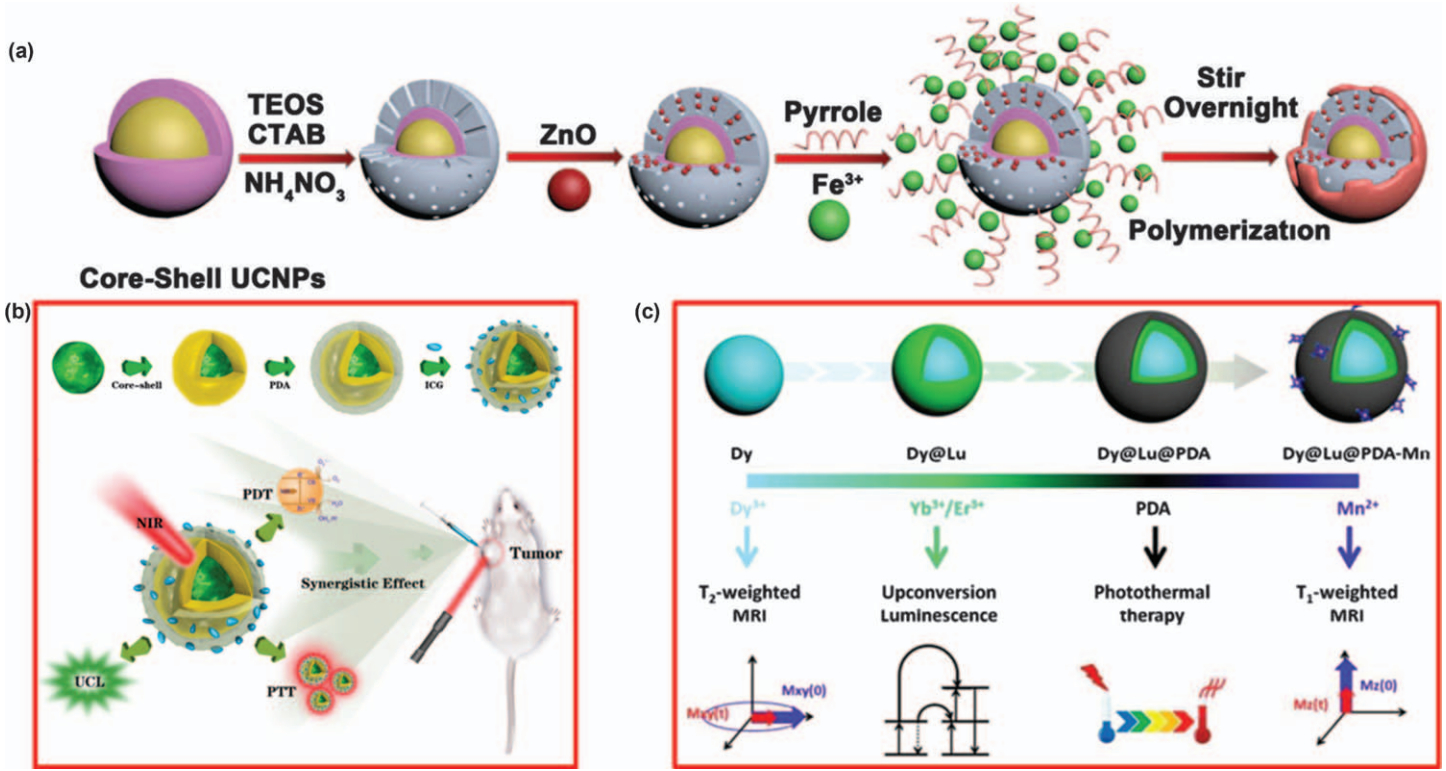

Figure 8.14 (a) Schematic illustration of the synthetic procedure for the UCNPs@mSiO_2@ZnO@Ppy nanocomposite. Reproduced from ref. 108 with permission from the Royal Society of Chemistry. (b) Schematic illustration of the synthetic procedure and the UCL guided combination phototherapy for the UCNPs@PDA–ICG nanocomposite. Reproduced from ref. 110 with permission from the Royal Society of Chemistry. (c) Schematic illustration of the synthetic procedure and the Dy, Mn, and Dy@Lu for T_2-weighted/T_2-weighted/UCL for guided PTT for the UCNPs@PDA–Mn nanocomposite. Reproduced from ref. 111 with permission from the Royal Society of Chemistry.

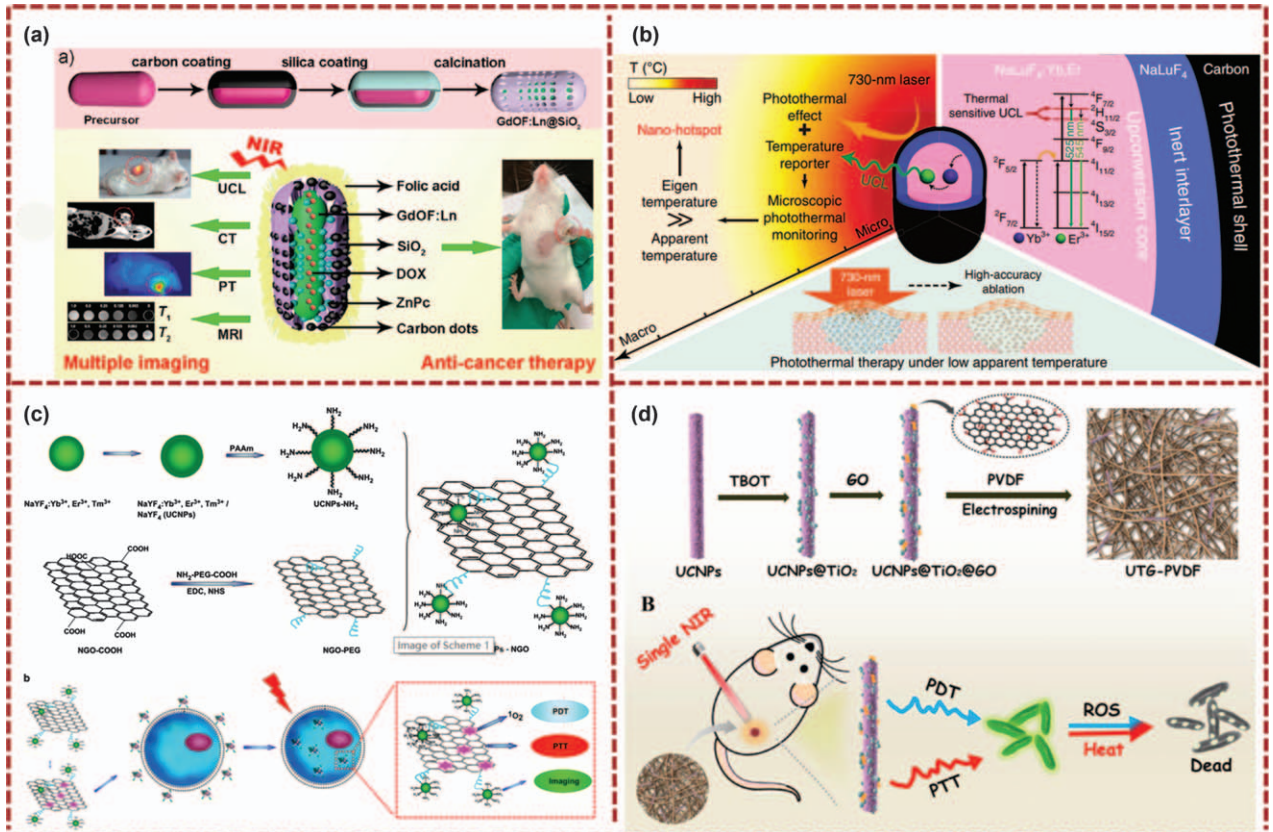
(a)
carbon coating
silica coating
calcination
Precursor
GdOF:Ln@SiO2
NIR
UCL
CT
PT
MRI
T1
T2
Folic acid
GdOF:Ln
SiO2
DOX
ZnPc
Carbon dots
Multiple imaging
Anti-cancer therapy
(b)
T (°C)
Low
High
730-nm laser
Photothermal effect
+
Temperature reporter
Nano-hotspot
Eigen temperature
Apparent temperature
Microscopic photothermal monitoring
UCL
Micro
Macro
Thermal sensitive UCL
Yb3+
Er3+
NaLuF4
Carbon
Inert interlayer
Photothermal shell
High-accuracy ablation
Photothermal therapy under low apparent temperature
(c)
PAAm
UCNPs-NH2
NH2-PEG-COOH
EDC, NHS
NGO-COOH
NGO-PEG
(d)
TBOT
GO
PVDF
Electrospining
UCNPs
UCNPs@TiO2
UCNPs@TiO2@GO
UTG-PVDF
B
Single NIR
PDT
PTT
ROS
Heat
Dead

Hu *et al*. illustrated core–shell nanoplates of UCNPs@PPy which realized both CT and UCL imaging-guided tumor ablation. Apart from PPy, PDA and ICG also played an important role in organic photothermal reagents.[109] Liu *et al*. developed PDA-coated $NaYF_4$:Yb,Er@$NaYF_4$:Yb nanoparticles decorated with ICG molecules *via* p–p stacking, electrostatic adsorption, and hydrophobic interaction (see Figure 8.14b).[110] The designed UCNPs@PDA-ICG realized UCL imaging-mediated PTT/PDT combined antitumor efficacy. Then, Liu *et al*. prepared multifunctional nanocomposites with Mn-complex decorated $NaDyF_4$:Yb@$NaLuF_4$:Yb,Er@PDA (Dy@Lu@PDA–Mn), which resulted in excellent photothermal antitumor efficiency relying on the strong absorbance of PDA in the NIR region (see Figure 8.14c).[111] Based on its conductivity, low cost, non-cytotoxicity, and mechanical flexibility, PAI is one of the oldest and most useful conducting polymers. Fu *et al*. displayed a nanosystem in which PAI nanoparticles were coated on the surface of an UCNP core to form core–shell UCNPs@PAI, realizing that UCL induces PTT under 980 nm and 808 nm dual laser excitation.[118]

In recent years, in addition to the polymers PPy, PDA, and PAI, carbon layers have received increasing attention with regard to PTT. Lin *et al*. developed a strategy to fabricate novel multifunctional GdOF:Ln@SiO_2–DOX–ZnPc@CDs mesoporous capsules to combine PTT with chemotherapy and PDT for enhanced antitumor efficiency using strong UCL and CT reagents of GdOF:Ln as the cores and a mesoporous silica layer modified with PDT agent (ZnPc) and DOX as the shells, followed by a coated carbon dot layer, thus realizing UCL, MRI, and CT imaging guided triple therapies (see Figure 8.15a).[119] Figure 8.15 illustrates a schematic of an UCNP-induced accurate photothermal therapeutic temperature-feedback nanocomposite csUCNPs@C (see Figure 8.15b).[120] The csUCNPs@C served as a temperature-sensitive UCL launcher to monitor the microscopic temperature change of a carbon shell upon 730 nm irradiation. The eigen temperature of csUCNPs@C was much higher than the apparent temperature observed macroscopically, indicating that csUCNPs@C acted as a nano-hotspot at the microscopic level. By utilizing a high eigen temperature during the photothermal process, accurate PTT, avoiding

Figure 8.15 (a) Schematic illustration of the synthetic procedure and the multimodal imaging guided combination anticancer for the GdOF:Ln@SiO_2–DOX–ZnPc@CDs nanocomposite. Reproduced from ref. 119 with permission from American Chemical Society, Copyright 2015. (b) Schematic illustration of the csUCNP@C to real-time monitoring of the microscopic temperature for accurate PTT. Reproduced from ref. 120, https://doi.org/10.1038/ncomms10437, under the terms of the CC BY 4.0 license, https://creativecommons.org/licenses/by/4.0/. (c) Schematic illustration of the synthetic procedure and the UCL guided combination phototherapy for the UCNPs–GO/ZnPc nanocomposite. Reproduced from ref. 114 with permission from Elsevier, Copyright 2013. (d) Schematic illustration of the synthesis of a UTG–PVDF nanocomposite membrane for bactericidal activities upon near-infrared light illumination. Reproduced from ref. 121 with permission from American Chemical Society, Copyright 2019.

damage to normal tissues, can be realized. GO has been widely used in many fields based on good photothermal performance. Wang *et al*. obtained UCL-guided combinatorial PDT/PTT cancer therapy agents, UCNPs–NGO/ZnPc nanocomposites utilizing graphene oxide (GO) loaded with ZnPc as the photothermal agent to combine $NaYF_4$: Yb/Er/Tm@$NaYF_4$ *via* bifunctional polyethylene glycol (PEG) (see Figure 8.15c).[114] GO modified by PEG not only exhibited good compatibility and stability in physiological solutions including serum but also retained a desirable photothermal performance. The temperature of GO–PEG solution increased rapidly from 23 to 58 °C within 3 min when subjected to an 808 nm NIR laser (2 W cm^{-2}), suggesting that GO possesses excellent photothermal performance. Therefore, a greater tumor ablation effect was achieved by the photothermal efficiency of GO (808 nm NIR light) combined with the PDT effect of ZnPc (980 nm NIR light). Zhao *et al*. generated a nanocomposite membrane (UTG-PVDF) *via* electrospinning, which could trigger synergistic antibacterial effects on both Gram-positive and Gram-negative bacteria attributing to the photodynamic therapy and photothermal therapy effects upon the irradiation of 980 nm NIR for 5 min (see Figure 8.15d).[121] The UTG that was conducted by the nanorod UCNPs ($NaYF_4$:Yb/Tm) and TiO_2 nanoparticles decorated with GO dissolved in PVDF and were sprayed to form a membrane which could simultaneously generate ROS and moderate the temperature rise (Table 8.4).

8.3.2.4 Others

Black phosphorus (BP) as a 2D photosensitizer has attracted much interest in recent years due to its various applications in cancer therapy, nanoelectronic multifunctional devices, and hydrogen generation. Due to its high quantum yields (up to 0.91), fascinating photoelectronic properties, ultrahigh surface areas, and negligible cytotoxicity, BP exhibited great potential as a PDT/PTT agent. Sun *et al*. integrated polylysine (PL)-modified black phosphorus nanosheets with magnetic Fe_3O_4@MnO_2-doped $NaYF_4$:Yb/Er/Nd *via* adopting polyacrylic acid (PAA) as a chemical crosslinker to form MUCNPs@BPNs nanocomposites (see Figure 8.16a).[122] Then, Ce6 was decorated onto the MUCNPs@BPNs to synthesize MUCNPs@BPNs–Ce6 nanocomposites. UCNPs with an imaging function played a unique role in monitoring the material movements, showing great potential in cancer theranostics when combined with biocompatible and photothermal BP to activate PTT under an imaging guide. Zhang *et al*. described a tumor microenvironment responsive photothermal agent consisting of a UCL nanoparticle core and a shell layer of Fe(III)/gallic acid complex (see Figure 8.16b).[123] Fe(III) can be released in the slightly acidic pH in a tumor microenvironment ascribed to the unsaturated coordination structure in the shell layer, whilst a gallic acid complex can be used as a photothermal agent. It was found that Bi nanoparticles are an effective CT imaging and photothermal agent. Core–shell nanoparticles of $NaYF_4$:Yb/Er@$NaYF_4$:Yb@$NaGdF_4$@Bi were prepared through growing Bi nanoparticles on the surface of UCNPs (see Figure 8.16c).[124] A series of *in vivo* experiments

Table 8.4 Summary of the presented UCNPs-organic multifunctional nanoplatforms.

UCNPs	Photothermal agents	Composite structures	NIR light (nm)	Features	References
$NaGdF_4$:Yb,Tm@$NaGdF_4$:Yb	**PPy**	UCNPs@mSiO_2@ZnO@**Ppy**	980	1. UCL/UCL/CT 2. PDT/PTT	108
$NaYF_4$:Yb/Er	**PPy**	UCNPs@**Ppy**	980/808	1. UCL/CT 2. PTT	109
$NaYF_4$:Yb,Er@$NaYF_4$:Yb	**PDA–ICG**	UCNPs@**PDA–ICG**	980	1. UCL 2. PDT/PTT	110
$NaDyF_4$:Yb@$NaLuF_4$:Yb/Er	**PDA**	UCNPs@**PDA**–Mn	980/808	1. UCL/MR 2. PTT	111
$NaLuF_4$:Yb/Er	**PAI**	UCNPs–**PAI**	980/808	808 nm for PTT and 980 nm for UCL	118
GdOF: Yb/Er/Mn	**Carbon dots**	GdOF:Ln@SiO_2–DOX–ZnPc@**CDs**	980	1. UCL/CT/PTI/MRI 2. PDT/PTT/Chemo	119
$NaLuF_4$:Yb/Er@$NaLuF_4$	**Carbon shell**	UCNPs@**C**	730/980	1. UCL 2. PTT 3. Real-time monitoring of microscopic temperature	120
$NaYF_4$:Yb/Er/Tm@$NaYF_4$	**GO**	UCNPs–**GO**/ZnPc	980	1. UCL 2. PDT/PTT	114
$NaYF_4$:Yb/Tm	**GO**	UCNPs@TiO_2@**GO**	980	1. PDT/PTT	121

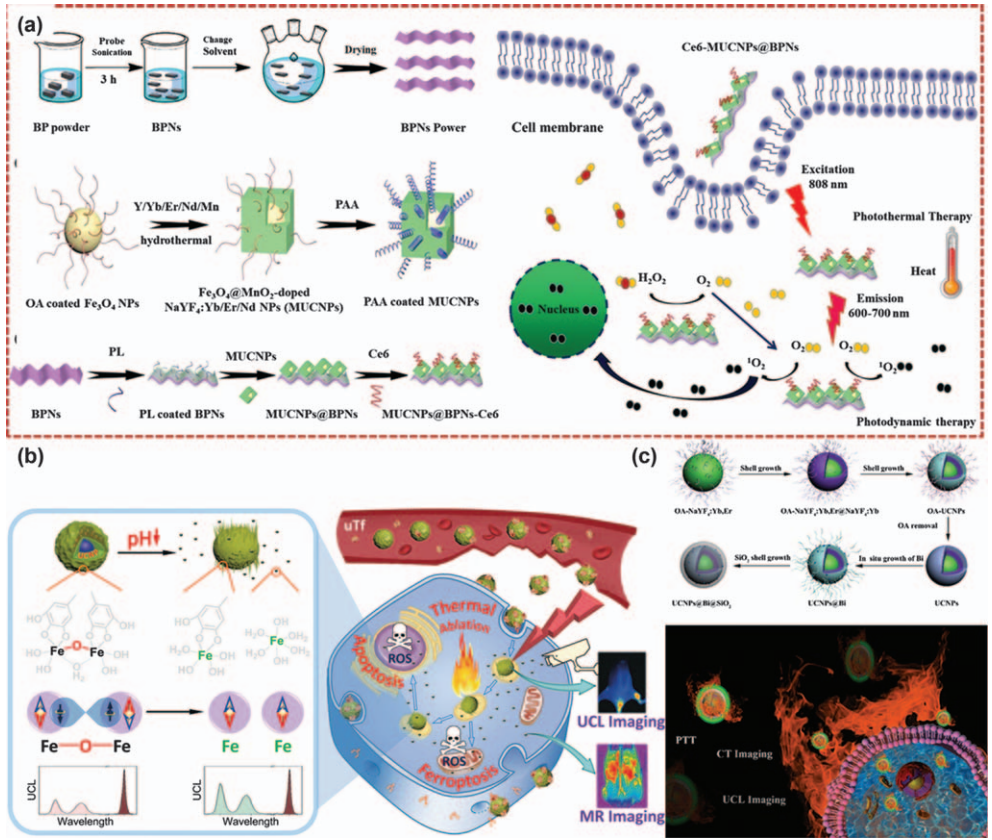

Figure 8.16 (a) Schematic illustration of the synthetic procedure and the multimodal imaging guided combination anticancer for the Fe_3O_4@MnO_2–UCNPs@BPNs–Ce6 nanocomposite. Reproduced from ref. 122 with permission from Elsevier, Copyright 2020. (b) Illustration to demonstrate the activatable function of the UCNP@GA–Fe^{III} probe for MRI and its therapeutic function involving multiple pathways. Reproduced from ref. 123 with permission from John Wiley and Sons, Copyright © 2019 Wiley-VCH Verlag GmbH & Co. KGaA, Weinheim. (c) Schematic illustration of the synthetic procedure and the multimodal imaging guided PTT for the UCNPs@Bi@SiO_2 nanocomposite. Reproduced from ref. 125 with permission from American Chemical Society, Copyright 2015.

Table 8.5 Summary of the presented UCNPs-others multifunctional nanoplatforms.

UCNPs	Photothermal agents	Composite structures	NIR light (nm)	Features	References
$NaYF_4$:Yb/Er/Nd	**BP**	Fe_3O_4@MnO_2–UCNPs@**BP**Ns–Ce6	808	1. MRI 2. PDT/PTT	122
$NaGdF_4$:Yb,Tm@$NaGdF_4$	**GA-Fe**	UCNPs@**GA–Fe**	980	1. UCL/MRI imaging 2. PTT	123
$NaYF_4$:Yb,Er@$NaYF_4$:Yb@$NaGdF_4$	**Bi**	UCNPs@**Bi**@SiO	980	1. UCL/CT 2. PTT	124
YOF:Yb/Tm	**$Y_2Ti_2O_7$@YOF:Yb/Tm**	TiO_2@**$Y_2Ti_2O_7$@YOF:Yb/Tm**	980	1. UCL/CT 2. PDT/PTT	125

were conducted to emphasize the effective UCL/CT imaging-mediated PTT performances of the integrated nanoplatform suggesting great potential in the biomedicine. Additionally, Lin *et al*. designed core/shell/shell structured TiO_2@$Y_2Ti_2O_7$@YOF:Yb/Tm realizing desirable anti-tumor efficiency by combining PDT with PTT upon 980 nm NIR irradiation.[125] Owing to the decrease of band gap energy, the middle-layer $Y_2Ti_2O_7$ photocatalyst generated ROS at a high level when indirectly activated by the blue upconverted emission from YOF:Yb/Tm. Thermal effects could also be obtained through non-radiative processes and the recombination of electron and hole pairs during the process of energy transfer. More importantly, nuclear collapse and cancer cell apoptosis occurred with the generation of ROS and thermal effects. The UCNP-induced strategy can overcome the shortcomings of low tissue penetration and avoid possible damage to the skin caused by UV-triggered TiO_2 (Table 8.5).

8.4 Outlook and Prospects

In summary, we have highlighted the advances in the design of near-infrared light medicated photothermal conversion systems. In particular, many examples have been selected and discussed to demonstrate the energy conversion and synthetic strategies of UCNP-based composite nanostructures for enhanced photothermal conversion performance. It is believed that upconversion nanoparticle-mediated NIR energy conversion would be extended to wide and important applications, such as in energy conversion, catalysis, and solar cells among others.

Abbreviations

UCNPS	Upconversion nanoparticles
PTT	Photothermal therapy
SNC	Sacrificial nanocrystal
NdNPs	Nd^{3+} doped nanoparticles
CR	Cross-relaxation
PB	Prussian blue
SPR	Surface plasmon resonance

AuNPs	Gold nanoparticles
EPR	Enhanced permeability and retention
GNR	Gold nanorod
Ce6	Chlorin e6
DOX	Doxorubicin
SiO_2	Silicon dioxide
PAA	Polyacrylic acid
CSNT	Nuclear/satellite nano-adsorbent
BP	Black phosphorus
QDs	Quantum dots
NIR	Near-infrared
PPy	Polypyrrole
PDA	Polydopamine
PAI	Polyaniline
ICG	Indocyanine green
GO	Graphene oxide
PEG	Polyethylene glycol
PL	Polylysine

References

1. M. Haase and H. Schafer, *Angew. Chem., Int. Ed. Engl.*, 2011, **50**, 5808–5829.
2. L. Wang, R. Yan, Z. Huo, L. Wang, J. Zeng, J. Bao, X. Wang, Q. Peng and Y. Li, *Angew. Chem., Int. Ed. Engl.*, 2005, **44**, 6054–6057.
3. H. Xing, W. Bu, S. Zhang, X. Zheng, M. Li, F. Chen, Q. He, L. Zhou, W. Peng, Y. Hua and J. Shi, *Biomaterials*, 2012, **33**, 1079–1089.
4. Q. Liu, Y. Sun, T. Yang, W. Feng, C. Li and F. Li, *J. Am. Chem. Soc.*, 2011, **133**, 17122–17125.
5. H. Schäfer, P. Ptacek, O. Zerzouf and M. Haase, *Adv. Funct. Mater.*, 2008, **18**, 2913–2918.
6. Y. W. Zhang, X. Sun, R. Si, L. P. You and C. H. Yan, *J. Am. Chem. Soc.*, 2005, **127**, 3260–3261.
7. N. N. Dong, M. Pedroni, F. Piccinelli, G. Conti, A. Sbarbati, J. Enrique Ramirez-Hernandez, L. Martinez Maestro, M. Carmen Iglesias-de la Cruz, F. Sanz-Rodriguez, A. Juarranz, F. Chen, F. Vetrone, J. A. Capobianco, J. Garcia Sole, M. Bettinelli, D. Jaque and A. Speghini, *ACS Nano*, 2011, **5**, 8665–8671.
8. J. Wang, F. Wang, C. Wang, Z. Liu and X. Liu, *Angew. Chem. Int. Ed. Engl.*, 2011, **50**, 10369–10372.
9. A. C. Yanes, A. Santana-Alonso, J. Méndez-Ramos, J. del-Castillo and V. D. Rodríguez, *Adv. Funct. Mater.*, 2011, **21**, 3136–3142.
10. Q. Ju, D. Tu, Y. Liu, R. Li, H. Zhu, J. Chen, Z. Chen, M. Huang and X. Chen, *J. Am. Chem. Soc.*, 2012, **134**, 1323–1330.
11. C. Renero-Lecuna, R. Martín-Rodríguez, R. Valiente, J. González, F. Rodríguez, K. W. Krämer and H. U. Güdel, *Chem. Mater.*, 2011, **23**, 3442–3448.

12. H. Wen, H. Zhu, X. Chen, T. F. Hung, B. Wang, G. Zhu, S. F. Yu and F. Wang, *Angew. Chem., Int. Ed.*, 2013, **52**, 13419–13423.
13. Q. Liu, W. Feng, T. Yang, T. Yi and F. Li, *Nat. Protoc.*, 2013, **8**, 2033–2044.
14. H. M. Kim and B. R. Cho, *Acc. Chem. Res.*, 2009, **42**, 863–872.
15. F. O. Auzel, *Chem. Rev.*, 2004, **104**, 139–173.
16. S. Heer, K. Kömpe, H. U. Güdel and M. Haase, *Adv. Mater.*, 2004, **16**, 2102–2105.
17. H. Q. Wang, M. Batentschuk, A. Osvet, L. Pinna and C. J. Brabec, *Adv. Mater.*, 2011, **23**, 2675–2680.
18. F. Zhang, G. B. Braun, Y. Shi, Y. Zhang, X. Sun, N. O. Reich, D. Zhao and G. Stucky, *J. Am. Chem. Soc.*, 2010, **132**, 2850.
19. Z. Zhang, S. Shikha, J. Liu, J. Zhang, Q. Mei and Y. Zhang, *Anal. Chem.*, 2019, **91**, 548–568.
20. X. Li, F. Zhang and D. Zhao, *Chem. Soc. Rev.*, 2015, **44**, 1346–1378.
21. A. Bagheri, H. Arandiyan, C. Boyer and M. Lim, *Adv. Sci.*, 2016, **3**, 1500437.
22. W. Fan, W. Bu and J. Shi, *Adv. Mater.*, 2016, **28**, 3987–4011.
23. S. Wu and H. J. Butt, *Adv. Mater.*, 2016, **28**, 1208–1226.
24. D. Wang, B. Liu, Z. Quan, C. Li, Z. Hou, B. Xing and J. Lin, *J. Mater. Chem. B*, 2017, **5**, 2209–2230.
25. X. Wang, R. R. Valiev, T. Y. Ohulchanskyy, H. Agren, C. Yang and G. Chen, *Chem. Soc. Rev.*, 2017, **46**, 4150–4167.
26. Y. Yang, J. Aw and B. Xing, *Nanoscale*, 2017, **9**, 3698–3718.
27. P. Das, A. Sedighi and U. J. Krull, *Anal. Chim. Acta*, 2018, **1041**, 1–24.
28. A. Gautam and P. Komal, *Coord. Chem. Rev.*, 2018, **376**, 393–404.
29. B. Gu and Q. Zhang, *Adv. Sci.*, 2018, **5**, 1700609.
30. M. Wang, Z. Hou, A. A. Al Kheraif, B. Xing and J. Lin, *Adv. Healthcare Mater.*, 2018, **7**, e1800351.
31. Y. Fan, L. Liu and F. Zhang, *Nano Today*, 2019, **25**, 68–84.
32. E. Hong, L. Liu, L. Bai, C. Xia, L. Gao, L. Zhang and B. Wang, *Mater. Sci. Eng. C*, 2019, **105**, 110097.
33. M. Jafari and A. Rezvanpour, *Adv. Powder Technol.*, 2019, **30**, 1731–1753.
34. K. Li, E. Hong, B. Wang, Z. Wang, L. Zhang, R. Hu and B. Wang, *Photodiagn. Photodyn. Ther.*, 2019, **25**, 177–192.
35. H. Oliveira, A. Bednarkiewicz, A. Falk, E. Frohlich, D. Lisjak, A. Prina-Mello, S. Resch, C. Schimpel, I. V. Vrcek, E. Wysokinska and H. H. Gorris, *Adv. Healthcare Mater.*, 2019, **8**, e1801233.
36. Q. Tian, W. Yao, W. Wu and C. Jiang, *Nanoscale Horiz.*, 2019, **4**, 10–25.
37. Y. Wang, S. Song, S. Zhang and H. Zhang, *Nano Today*, 2019, **25**, 38–67.
38. W. Chen, Y. Xie, M. Wang and C. Li, *Front. Chem.*, 2020, **8**, 596658.
39. Z. Zhang, Q. Han, J. W. Lau and B. Xing, *ACS Mater. Lett.*, 2020, **2**, 1516–1531.
40. K. Zhao, J. Sun, F. Wang, A. Song, K. Liu and H. Zhang, *ACS Appl. Bio Mater.*, 2020, **3**, 3975–3986.

41. S. Liu, G. De, Y. Xu, X. Wang, Y. Liu, C. Cheng and J. Wang, *J. Rare Earths*, 2018, **36**, 1060–1066.
42. S. Lu, D. Tu, X. Li, R. Li and X. Chen, *Nano Res.*, 2015, **9**, 187–197.
43. Y. Zhu, S. Zhao, B. Zhou, H. Zhu and Y. Wang, *J. Phys. Chem. C*, 2017, **121**, 18909–18916.
44. B. Zhou, B. Xu, H. He, Z. Gu, B. Tang, Y. Ma and T. Zhai, *Nanoscale*, 2018, **10**, 2834–2840.
45. H. Na, K. Woo, K. Lim and H. S. Jang, *Nanoscale*, 2013, **5**, 4242–4251.
46. Z. Li and Y. Zhang, *Nanotechnology*, 2008, **19**, 345606.
47. Z. Li, Y. Zhang and S. Jiang, *Adv. Mater.*, 2008, **20**, 4765–4769.
48. H. S. Qian and Y. Zhang, *Langmuir*, 2008, **24**, 12123–12125.
49. H. Qiu, G. Chen, L. Sun, S. Hao, G. Han and C. Yang, *J. Mater. Chem.*, 2011, **21**, 17202–17208.
50. M. Ding, S. Yin, D. Chen, J. Zhong, Y. Ni, C. Lu, Z. Xu and Z. Ji, *Appl. Surf. Sci.*, 2015, **333**, 23–33.
51. S. Li, S. Ye, X. Chen, T. Liu, Z. Guo and D. Wang, *J. Rare Earths*, 2017, **35**, 753–760.
52. H. Lin, D. Xu, A. Li, D. Teng, S. Yang and Y. Zhang, *Sci. Rep.*, 2016, **6**, 28051.
53. J. Xie, J. Bin, M. Guan, H. Liu, D. Yang, J. Xue, L. Liao and L. Mei, *J. Lumin.*, 2018, **200**, 133–140.
54. P. Qiu, R. Sun, G. Gao, C. Zhang, B. Chen, N. Yan, T. Yin, Y. Liu, J. Zhang, Y. Yang and D. Cui, *Theranostics*, 2015, **5**, 456–468.
55. J. Lai, Y. Zhang, N. Pasquale and K. B. Lee, *Angew. Chem. Int. Ed. Engl.*, 2014, **53**, 14419–14423.
56. N. Martin, P. Boutinaud, R. Mahiou, J. C. Cousseins and M. Bouderbala, *J. Mater. Chem.*, 1999, **9**, 125–128.
57. X. Xie, N. Gao, R. Deng, Q. Sun, Q. H. Xu and X. Liu, *J. Am. Chem. Soc.*, 2013, **135**, 12608–12611.
58. X. Chen, D. Peng, Q. Ju and F. Wang, *Chem. Soc. Rev.*, 2015, **44**, 1318–1330.
59. H. Qian and Y. Zhang, *Langmuir*, 2008, **24**, 12123–12125.
60. N. J. Johnson, A. Korinek, C. Dong and F. C. van Veggel, *J. Am. Chem. Soc.*, 2012, **134**, 11068–11071.
61. M. L. Zhao, L. N. Hao, J. Zhang, C. Y. Zhang, Y. Lu and H. S. Qian, *Langmuir*, 2019, **35**, 489–494.
62. B. B. Ding, H. Y. Peng, H. S. Qian, L. Zheng and S. H. Yu, *Adv. Mater. Interfaces*, 2016, **3**, 1500649.
63. Q. Zeng, B. Xue, Y. Zhang, D. Wang, X. Liu, L. Tu, H. Zhao, X. Kong and H. Zhang, *CrystEngComm*, 2013, **15**, 4765–4772.
64. F. Ding, X. Gao, X. Huang, H. Ge, M. Xie, J. Qian, J. Song, Y. Li, X. Zhu and C. Zhang, *Biomaterials*, 2020, **245**, 119976.
65. E. Y. Lukianova-Hleb, X. Ren, R. R. Sawant, X. Wu, V. P. Torchilin and D. O. Lapotko, *Nat. Med.*, 2014, **20**, 778–784.
66. C. He, J. Lu and W. Lin, *J. Controlled Release*, 2015, **219**, 224–236.
67. G. Tian, X. Zhang, Z. Gu and Y. Zhao, *Adv. Mater.*, 2015, **27**, 7692–7712.

68. O. Dahl, *Thermoradiotherapy and Thermochemotherapy: Biology, Physiology, Physics*, 1995.
69. J. van der Zee, *Ann. Oncol.*, 2002, **13**, 1173–1184.
70. J. van der Zee, *Ann. Oncol.*, 2002, **13**, 1173–1184.
71. U. Rocha, K. Upendra Kumar, C. Jacinto, J. Ramiro, A. J. Caamaño, J. García Solé and D. Jaque, *Appl. Phys. Lett.*, 2014, **104**, 053703.
72. E. Carrasco, B. del Rosal, F. Sanz-Rodríguez, Á. J. de la Fuente, P. H. Gonzalez, U. Rocha, K. U. Kumar, C. Jacinto, J. G. Solé and D. Jaque, *Adv. Funct. Mater.*, 2015, **25**, 615–626.
73. B. del Rosal, A. Pérez-Delgado, E. Carrasco, D. J. Jovanović, M. D. Dramićanin, G. Dražić, Á. J. de la Fuente, F. Sanz-Rodriguez and D. Jaque, *Adv. Opt. Mater.*, 2016, **4**, 782–789.
74. Z. Yu, W. Hu, H. Zhao, X. Miao, Y. Guan, W. Cai, Z. Zeng, Q. Fan and T. T. Y. Tan, *Angew. Chem. Int. Ed. Engl.*, 2019, **58**, 8536–8540.
75. A. M. Alkilany, X. Huang, C. J. Murphy, M. A. El-Sayed and E. C. Dreaden, *Chem. Soc. Rev.*, 2012, **41**, 2740.
76. X. Yang, M. Yang, B. Pang, M. Vara and Y. Xia, *Chem. Rev.*, 2015, **115**, 10410–10488.
77. X. Liu, H. J. Chen, X. Chen, C. Parini and D. Wen, *Nanoscale*, 2012, **4**, 3945–3953.
78. H. Maeda, J. Wu, T. Sawa, Y. Matsumura and K. Hori, *J. Controlled Release*, 2000, **65**, 271–284.
79. J. W. H. Maeda, T. Sawa, Y. Matsumura and K. Hori, *J. Controlled Release*, 2000, **65**, 271.
80. A. Shakeri-Zadeh, M. Ghasemifard and G. A. Mansoori, *Phys. E*, 2010, **42**, 1272–1280.
81. H. Banu, B. Stanley, S. M. Faheem, R. Seenivasan, K. Premkumar and G. Vasanthakumar, *Plasmonics*, 2014, **9**, 1341–1349.
82. T. Sun, Y. S. Zhang, B. Pang, D. C. Hyun, M. Yang and Y. Xia, *Angew. Chem. Int. Ed. Engl.*, 2015, **53**, 12320–12364.
83. H. Samadian, S. Hosseini-Nami, S. K. Kamrava, H. Ghaznavi and A. Shakeri-Zadeh, *J. Cancer Res. Clin. Oncol.*, 2016, **142**, 1–13.
84. M. Sun, L. Xu, W. Ma, X. Wu, H. Kuang, L. Wang and C. Xu, *Adv. Mater.*, 2016, **28**, 898–904.
85. Y. Huang, F. Rosei and F. Vetrone, *Nanoscale*, 2015, **7**, 5178–5185.
86. J. Liu, F. Yang, M. Feng, Y. Wang, X. Peng and R. Lv, *ACS Biomater. Sci. Eng.*, 2019, **5**, 5051–5059.
87. R. Lv, P. Yang, F. He, S. Gai, G. Yang, Y. Dai, Z. Hou and J. Lin, *Biomaterials*, 2015, **63**, 115–127.
88. F. He, G. Yang, P. Yang, Y. Yu, R. Lv, C. Li, Y. Dai, S. Gai and J. Lin, *Adv. Funct. Mater.*, 2015, **25**, 3966–3976.
89. F. Zhang, Y. Zang, D. Huang, C.-a. Di, X. Gao, H. Sirringhaus and D. Zhu, *Adv. Funct. Mater.*, 2015, **25**, 3004–3012.
90. F. He, L. Feng, P. Yang, B. Liu, S. Gai, G. Yang, Y. Dai and J. Lin, *Biomaterials*, 2016, 77–88.

91. B. Dong, S. Xu, J. Sun, S. Bi, D. Li, X. Bai, Y. Wang, L. Wang and H. Song, *J. Mater. Chem.*, 2011, **21**, 6193.
92. B. Liu, C. Li, Z. Xie, Z. Hou, Z. Cheng, D. Jin and J. Lin, *Dalton Trans.*, 2016, **45**, 13061–13069.
93. Q. Xiao, X. Zheng, W. Bu, W. Ge, S. Zhang, F. Chen, H. Xing, Q. Ren, W. Fan, K. Zhao, Y. Hua and J. Shi, *J. Am. Chem. Soc.*, 2013, **135**, 13041–13048.
94. M. Xu, G. Yang, H. Bi, J. Xu, S. Dong, T. Jia, Z. Wang, R. Zhao, Q. Sun, S. Gai, F. He, D. Yang and P. Yang, *Chem. Eng. J.*, 2020, **382**, 122822.
95. R. Lv, P. Yang, F. He, S. Gai, G. Yang and J. Lin, *Chem. Mater.*, 2015, **27**, 483–496.
96. C. X. Huang, H. J. Chen, F. Li, W. N. Wang, D. D. Li, X. Z. Yang, Z. H. Miao, Z. B. Zha, Y. Lu and H. S. Qian, *J. Mater. Chem. B*, 2017, **5**, 9487–9496.
97. X. Su, F. Zhao, Y. Wang, X. Yan, S. Jia and B. Du, *Nanomedicine*, 2017, **13**, 1761–1772.
98. J. Xu, A. Gulzar, Y. Liu, H. Bi, S. Gai, B. Liu, D. Yang, F. He and P. Yang, *Small*, 2017, **13**, 1701841.
99. J. Han, H. Xia, Y. Wu, S. N. Kong, A. Deivasigamani, R. Xu, K. M. Hui and Y. Kang, *Nanoscale*, 2016, **8**, 7861–7865.
100. S. Wang, W. Xi, Z. Wang, H. Zhao, L. Zhao, J. Fang, H. Wang and L. Sun, *J. Mater. Chem. B*, 2020, **8**, 5883–5891.
101. K. Du, P. Lei, M. Zhang, X. Gao, S. Yao, C. Li, J. Feng and H. Zhang, *Nanoscale*, 2020, **12**, 3977–3987.
102. K. Du, P. Lei, L. Dong, M. Zhang, X. Gao, S. Yao, J. Feng and H. Zhang, *Appl. Mater. Today*, 2020, **18**, 100497.
103. S. Zhao, R. Tian, B. Shao, Y. Feng, S. Yuan, L. Dong, L. Zhang, Z. Wang and H. You, *Chemistry*, 2020, **26**, 1127–1135.
104. X. Liu, X. Wang, B. Zhou, W. C. Law, A. N. Cartwright and M. T. Swihart, *Adv. Funct. Mater.*, 2012, **23**, 1256–1264.
105. G. Ku, M. Zhou, S. Song, Q. Huang and C. Li, *ACS Nano*, 2013, **6**, 7489.
106. Z. C. Wu, W. P. Li, C. H. Luo, C. H. Su and C. S. Yeh, *Adv. Funct. Mater.*, 2015, **25**, 6527–6537.
107. Q. Chen, H. Ke, Z. Dai and Z. Liu, *Biomaterials*, 2015, **73**, 214–230.
108. Q. Cai, J. Xu, D. Yang, Y. Dai, G. Yang, C. Zhong, S. Gai, F. He and P. Yang, *J. Mater. Chem. B*, 2018, **6**, 8148–8162.
109. X. Huang, B. Li, C. Peng, G. Song, Y. Peng, Z. Xiao, X. Liu, J. Yang, L. Yu and J. Hu, *Nanoscale*, 2016, **8**, 1040–1048.
110. B. Liu, C. Li, B. Xing, P. Yang and J. Lin, *J. Mater. Chem. B*, 2016, **4**, 4884–4894.
111. T. Liu, S. Li, Y. Liu, Q. Guo, L. Wang, D. Liu and J. Zhou, *J. Mater. Chem. B*, 2016, **4**, 2697–2705.
112. R. Lv, P. Yang, F. He, S. Gai, C. Li, Y. Dai, G. Yang and J. Lin, *ACS Nano*, 2015, **9**, 1630–1647.

113. X. Zhu, W. Feng, J. Chang, Y. W. Tan, J. Li, M. Chen, Y. Sun and F. Li, *Nat. Commun.*, 2016, **7**, 10437.
114. Y. Wang, H. Wang, D. Liu, S. Song, X. Wang and H. Zhang, *Biomaterials*, 2013, **34**, 7715–7724.
115. C. Wang, H. Xu, C. Liang, Y. Liu, Z. Li, G. Yang, L. Cheng, Y. Li and Z. Liu, *ACS Nano*, 2013, **7**, 6782–6795.
116. K. Yang, H. Xu, L. Cheng, C. Sun, J. Wang and Z. Liu, *Adv. Mater.*, 2012, **24**, 5586–5592.
117. Z. Zha, X. Yue, Q. Ren and Z. Dai, *Adv. Mater.*, 2013, **25**, 777–782.
118. Y. Xing, L. Li, X. Ai and L. Fu, *Int. J. Nanomed.*, 2016, **11**, 4327–4338.
119. R. Lv, P. Yang, F. He, S. Gai, C. Li, Y. Dai, G. Yang and J. Lin, *ACS Nano*, 2015, **9**, 1630–1647.
120. X. Zhu, W. Feng, J. Chang, Y. W. Tan, J. Li, M. Chen, Y. Sun and F. Li, *Nat. Commun.*, 2016, **7**, 10437.
121. J. Sun, L. Song, Y. Fan, L. Tian, S. Luan, S. Niu, L. Ren, W. Ming and J. Zhao, *ACS Appl. Mater. Interfaces*, 2019, **11**, 26581–26589.
122. Q. Zhang, W. Wang, M. Zhang, F. Wu, T. Zheng, B. Sheng, Y. Liu, J. Shen, N. Zhou and Y. Sun, *Chem. Eng. J.*, 2020, **391**, 123525.
123. P. Zhang, Y. Hou, J. Zeng, Y. Li, Z. Wang, R. Zhu, T. Ma and M. Gao, *Angew. Chem. Int. Ed. Engl.*, 2019, **58**, 11088–11096.
124. S. Zhao, R. Tian, B. Shao, Y. Feng, S. Yuan, L. Dong, L. Zhang, K. Liu, Z. Wang and H. You, *ACS Appl. Mater. Interfaces*, 2019, **11**, 394–402.
125. R. Lv, C. Zhong, R. Li, P. Yang, F. He, S. Gai, Z. Hou, G. Yang and J. Lin, *Chem. Mater.*, 2015, **27**, 1751–1763.

CHAPTER 9

Covalent Organic Frameworks (COFs) for Photothermal Therapy

XUE-HAO ZHANG,[a,b] YIN-SHENG XU,[a] ZENG-YING QIAO*[a] AND HAO WANG*[a]

[a] CAS Center for Excellence in Nanoscience, CAS Key Laboratory for Biomedical Effects of Nanomaterials and Nanosafety, National Center for Nanoscience and Technology (NCNST), Beijing 100190, China; [b] College of Science, Huazhong Agricultural University, Wuhan 430070, China
*Emails: ygxiang@mail.hzau.edu.cn; qiaozy@nanoctr.cn; wanghao@nanoctr.cn

9.1 Introduction

Cancer, as a highly lethal disease, continues to threaten human life and health.[1] Radiotherapy and chemotherapy, as common cancer treatments, are usually accompanied by extensive collateral damage. Chemotherapy drugs that lack a targeting ability will inevitably cause indirect damage to normal cells while killing cancer cells.[2] Similarly, the high-energy radiation produced in the course of radiotherapy can also damage the healthy tissues around the lesion, and even the sequelae such as radiation dermatitis.[3] Therefore, the development of a non-invasive, or minimally invasive, and effective new therapy is a hot spot in the medical field. As a new method of tumor treatment, photothermal therapy based on nanomaterials has gradually attracted wide attention because of its advantages such as non-invasiveness,

Nanoscience & Nanotechnology Series No. 54
Photothermal Nanomaterials
Edited by Enyi Ye and Zibiao Li

Published by the Royal Society of Chemistry, www.rsc.org

high tumor specificity, less trauma, and fewer complications. Photothermal therapy uses near-infrared light with strong tissue penetration as its energy source to enrich nano-photothermal therapeutic agents in the affected area actively or passively through various targeting technologies, and to increase the local tumor temperature under the irradiation of near-infrared light, so as to realize tumor tissue ablation and tumor treatment.[4,5]

9.1.1 Photothermal Therapy

Photothermal therapy (PTT) has attracted much attention in the treatment of cancer because of its non-invasiveness, high spatial and temporal resolution, and low toxicity.[6] PTT relies on nanomaterials with photothermal effects to convert light into heat. Compared with tumor cells, normal cells have better heat resistance. PTT can effectively avoid damage to normal cells while killing cancer cells at the high temperature of local tumor formation (Figure 9.1).[7] In recent years, many studies have found that new nano photothermal materials have been found and applied in tumor PTT. During PTT, the photothermal agent irradiates light at a certain wavelength to generate local heat, which can cause protein denaturation, DNA damage, and cell membrane destruction, leading to selective ablation of tumor tissue.[8] Since near-infrared light (650–1700 nm) exhibits reduced absorption and scattering and can penetrate more deeply into organisms than visible light and ultraviolet, near-infrared light has been widely used in PTT.[6,9]

9.1.2 Photothermal Agent

An effective photothermal agent should have a high photothermal conversion efficiency, a certain absorption capacity, and certain light stability under a certain laser irradiation time. A variety of inorganic nanomaterials, such as noble metal nanomaterials (such as Au, Ag, Pt), carbon nanomaterials, polymeric nanomaterials, and transition metal sulfide or oxide nanoparticles,[4,6,10–13] have been widely used. As a class of newly discovered porous framework materials, covalent organic frameworks (COFs) have shown unique advantages in the fields of intelligent wearables, catalysis, clean energy, and analytical science. Similarly, as a metal-free multi-void material, COFs can basically be viewed as a nanomedicine candidate for

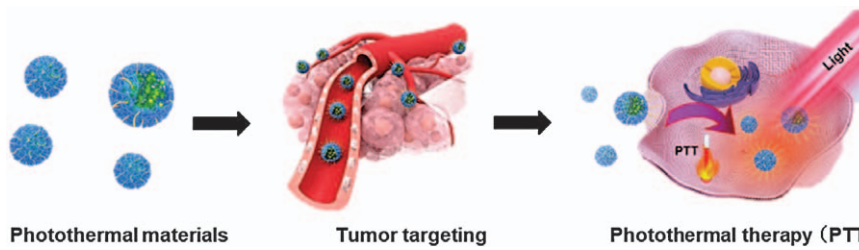

Figure 9.1 PTT mediated by nanomaterials.

cancer therapy. Nanoscale COFs have some unique advantages that make them more suitable for biomedical applications. Based on the above, polymeric organic polymers are a unique class of porous materials constructed by linking building blocks through covalent bonds, and pure organic compositions make them low-toxic and biocompatible. Therefore, it has been identified that extended π-conjugated polymeric materials and COFs can be utilized and are worth investigating.

9.1.3 COFs in PTT

COFs have a long-range ordered structure in which the position of organic components is controlled in two or three dimensions. This structural feature results in regular pores with large diameters and helps to load large photothermal agents such as porphyrin and phthalonitrile. Nano COFs (NCOFs) have some unique advantages that make it more suitable for biomedical applications (Figure 9.2).

i) Modularity: The composition and structure of COFs completely depend on the reactive functional groups and geometry of organic monomers. By logically selecting functional monomers, their chemical composition, topological structure, pore size, and functionality should be predictable and customizable.[14,15]
ii) Porosity: The inherent pores and high specific surface area of COFs can promote the loading of guest medical species to construct a host–guest nanomedicine system.
iii) Stability: COFs are driven by strong covalent bonds. Therefore, most COFs have good thermal and chemical stability. More importantly, COFs are not easily affected by the environment, especially in aqueous biological media.
iv) Versatility: Due to the diversity of organic reactions, the functionalization of COFs is relatively easy. In addition to various functional monomers, COFs driven by covalent bonds can withstand more types of organic transformations. In addition, more types of functional organic molecules can be introduced into the COFs framework through post-synthesis modification (PSM).[16]

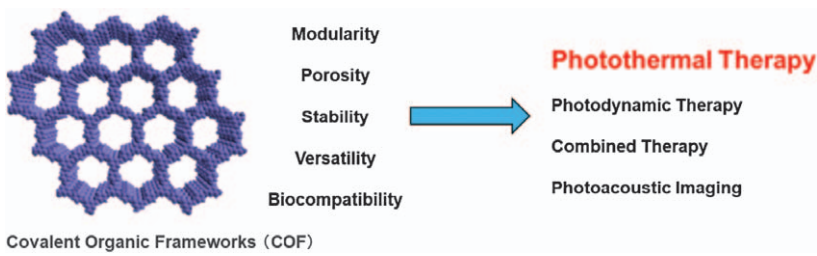

Figure 9.2 Advantages and applications of COFs in cancer therapy.

v) Biocompatibility: COFs do not contain metals, so the potential toxicity related to metals can be completely avoided, especially the potential toxicity related to heavy metals. In addition, their inherent organic properties may make COFs more biocompatible and suitable for biomedical treatments.

9.2 PTT with COFs

The synthesis of nanoscale COFs with absorption in the infrared region is the cornerstone of COFs as a photothermal therapeutic agent. Xie's group reported a size-controllable synthesis of spherical COFs (DPPN).[17] A series of nanoscale DPPN COFs was obtained under mild conditions through a Schiff base reaction (Figure 9.3). After being assembled with 1,2-distearoyl-*sn*-glycero-3-phosphoethanolamine-*N*-[methoxy (polyethylene glycol)] (MPEG2000-DSPE), these synthesized DPPN COFs possess excellent colloidal stability in water, which enables them to be well applied in biological fields. Particularly, these nanoscale COFs show an obvious red-shift of absorbance even to the second near-infrared (NIR-II) region (>1000 nm) based on a donor–acceptor (D–A) strategy. The nanoscale COFs with NIR absorption possess a photothermal conversion ability under 808 nm laser irradiation and exhibit a significant cancer killing effect. The effect of the COF material in PTT is

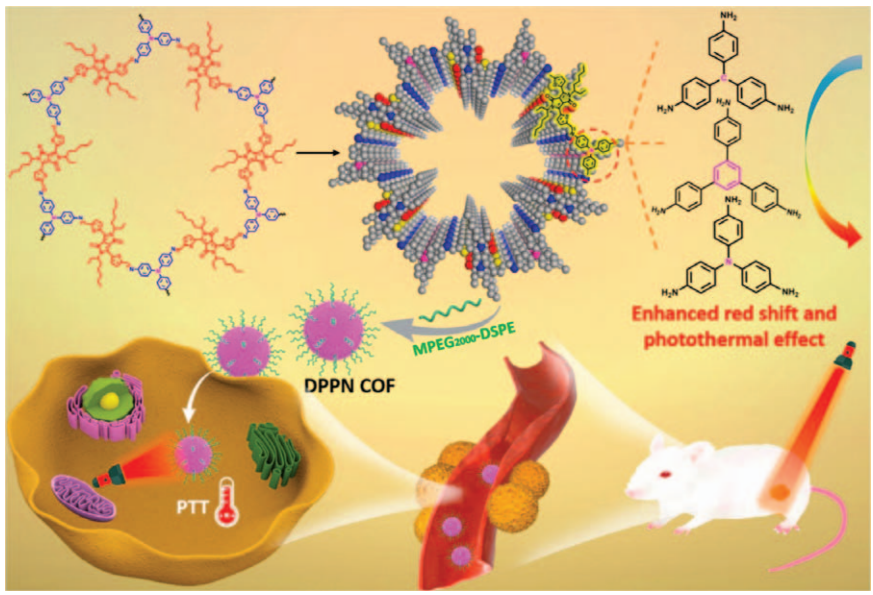

Figure 9.3 Schematic illustration of synthetic COFs based on D–A Structures, and the light triggered photothermal performance of DPPN COFs *in vitro* and *in vivo*.
Reproduced from ref. 17 with permission from American Chemical Society, Copyright 2021.

remarkable. It is to be expected that more COF materials will be developed for PTT and ablation of tumors.

9.2.1 Combined PTT with Photodynamic Therapy (PDT)

Due to the heterogeneity and complexity of tumors, simple PTT has many limitations and it is difficult to completely ablate a tumor tissue. Combination therapy can effectively overcome the shortcomings of single therapy and further improve the therapeutic effect. Dong *et al.* reported a nanoscale COF (NCOF)-based PDT/PTT dual-modal therapeutic agent obtained *via* stepwise BDF and guest encapsulation processes (Figure 9.4). The obtained VONc@-COF–Por with surface-decorated porphyrin (Por) and encapsulated naphthalocyanine (VONc) species exhibited highly efficient singlet oxygen generation and photothermal conversion ability and could significantly inhibit MCF-7 breast cancer cell proliferation and metastasis *in vitro* and *in vivo*.[19]

9.2.2 PTT with Photoacoustic Imaging (PAI)

In general, COFs with photothermal effects can also be used as contrast agents in PAI, which brings a new idea for the integration of diagnosis and treatment of tumors. Guo *et al.* reported a 2,2′-bipyridine-based COF from neutral to positively-charged and ultimately to a cationic radical framework,

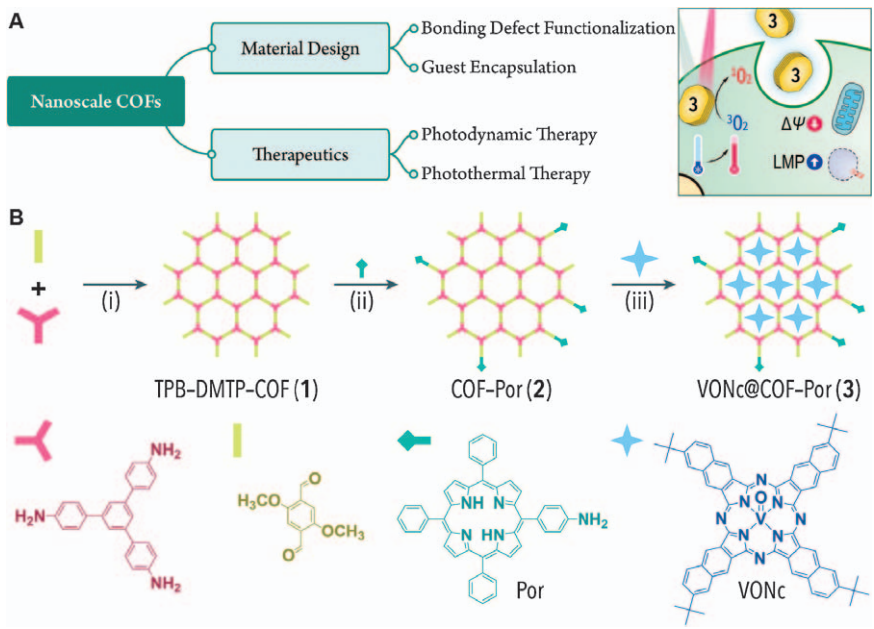

Figure 9.4 VONc@COF–Por design and synthesis.
Reproduced from ref. 19 with permission from American Chemical Society, Copyright 2019.

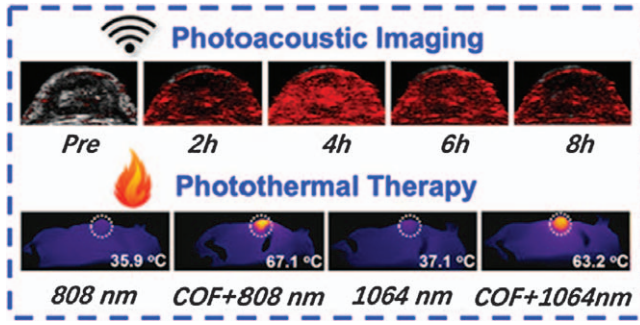

Figure 9.5 PTT with PAI.
Reproduced from ref. 18 with permission from American Chemical Society, Copyright 2019.

which enables the superimposition of redox centers with each other in the framework. The intercharge transfer, occurring through the π-coupling multilayers, contributes to the outstanding photophysical properties, namely, near-infrared (NIR) absorption and photothermal conversion by a non-radiative relaxation process. Furthermore, a structure-to-activity relationship with respect to the photothermal effect has been established to acquire an exceptionally high efficiency of heat generation from NIR photoexcitation (Figure 9.5).[18]

9.2.3 Theranostics with PTT, PDT, and PAI

Chen *et al.* synthesized a porphyrin-based covalent organic framework material (COF-366).[20] It was dispersed into covalent organic framework nanoparticles (COF-366 NPs) with a size of about 100 nm by an ultrasonic homogenizer and the COF-366 NPs could be stably stored in different mediums for a period of time. The prepared COF-366 NPs were used to achieve photoacoustic (PA) imaging-guided combined PDT and PTT therapy *in vivo*. COF-366 NPs as a kind of photoactive agent possessed the following characteristics. (1) Similar to MOF materials, this porphyrin-based COF would increase the distance between molecules due to its regular structure, which could reduce the quenching of porphyrin. (2) Meanwhile, the synthesis process was metal-free and the dynamic reversible bond had the possibility of degradation, and these properties endow COFs with biosafety. (3) The conjugated structure broadened the absorption spectrum of the COF-366 NPs. These COF-366 NPs were expected to act as both the photosensitizer and photothermal agent, to produce ROS and heat under single wavelength light irradiation. (4) The large surface areas of COF-366 NPs would also increase the light-harvesting ability, and the porous structure was beneficial to the storage of oxygen and the diffusion of reactive oxygen species (ROS), which would contribute to phototherapy. (5) COF-366 NPs with a PA imaging capability would achieve precise treatment *in vivo*. This was the first time

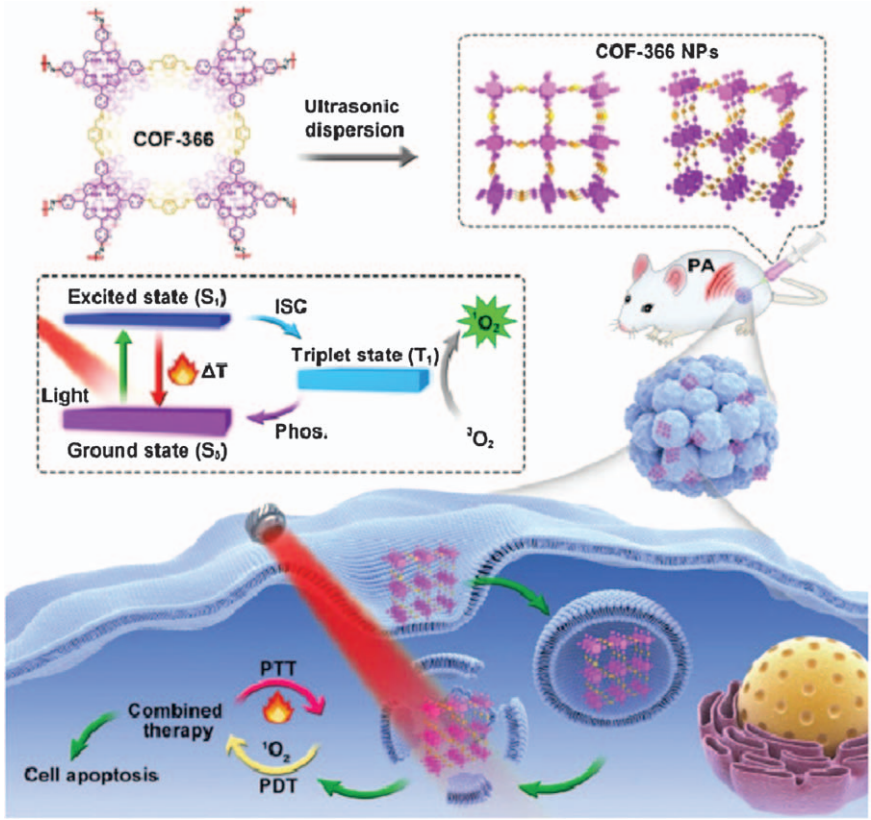

Figure 9.6 Theranostics of COF-366 NPs.
Reproduced from ref. 20 with permission from Elsevier, Copyright 2019.

that COF-366 NPs had been used to achieve combined PDT and PTT therapy *in vivo*. This work not only provided new ideas for the design of photoactive agents with both PDT and PTT effects but also expanded the biomedical applications of COFs (Figure 9.6).

9.3 Inorganic Material-doped COFs

In recent years, the combination of organic porous materials and inorganic nanoparticles to construct a multi-functional theranostic platform has received extensive attention. The large surface area, large pore volume, and various functional groups of organic porous materials provide many reaction sites for inorganic reactions. Nanoparticles are integrated with it, avoiding the aggregation of nanoparticles and effectively reducing the particles to the nanoscale. Meanwhile, the performance of organic porous materials and nanoparticles will be optimized and enhanced synergistically after being combined.[21] Therefore, it is very important to explore a convenient and effective way to combine these two parts.

COFs are porous materials formed by a reversible condensation reaction between various organic structural units.[22] Due to their low density, highly ordered π–π stack structure, adjustable pore size, and large surface area, these materials have been extensively studied in many research fields. However, biomedical applications are still in the early stages.[23–27] In fact, these materials are excellent candidates for photocatalysis or phototherapy applications. In addition, COFs can serve as an ideal support for encapsulating and capturing various functional nanoparticles in a controllable and predictable manner.

9.3.1 Fe_3O_4@COF

Wang *et al.* developed a general method for the precise construction and functionalization of nano COFs by a disorder-to-order dynamic process, which allows for rearrangement of amorphous polyimine networks into crystalline imine-linked COFs without a change of morphology and size. The resulting nano COFs are employed to construct a well-defined core–shell nanostructure while retaining crystallinity and periodic micropores and could be further modulated with a shell of controllable thickness *via* template-mediated polymerization and *in situ* crystallization. An efficient photothermal conversion is found for the Fe_3O_4@COF (TpBD) microspheres, which allows the quick transduction of NIR energy to local heat by strengthening the p-electronic conjugation within the stacking 2D layers (Figure 9.7). This strategy is general and, in principle, can be used to

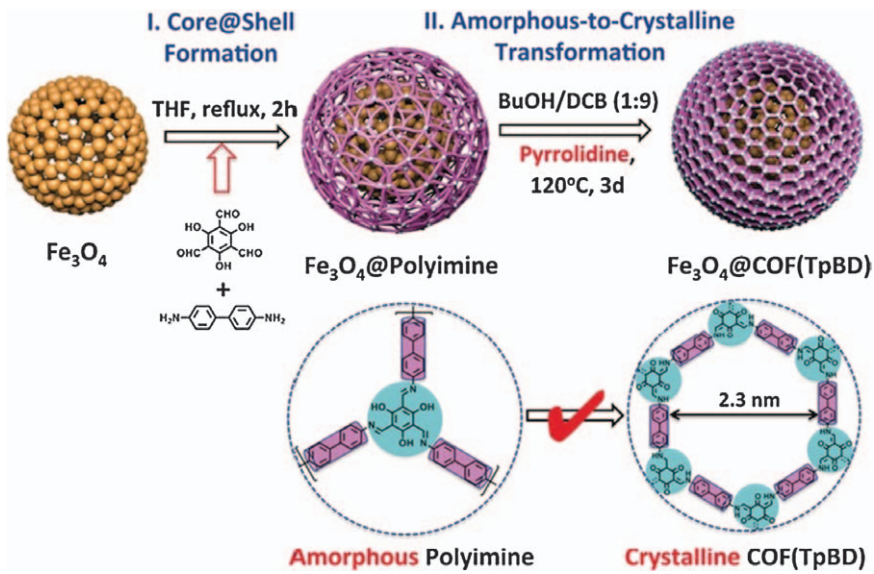

Figure 9.7 Fe_3O_4@COF design and synthesis.
Reproduced from ref. 28 with permission from John Wiley and Sons, Copyright © 2016 Wiley-VCH Verlag GmbH & Co. KGaA, Weinheim.

generate a large pool of COF-based nanomaterials with applicability and functionality that can be deliberately and finely tuned through the design of organic/inorganic components. Looking forward, this work should also facilitate the coating of COFs onto structurally tailorable supports, opening up a promising pathway for realizing porous organic polymers with applications spanning bio-imaging, phototherapy, and drug delivery.[28]

9.3.2 COF Metalation with Fe^{3+}

Pang *et al.* reported the successful fabrication, without using any hard or soft template, of monodispersed hierarchical TpPa–COF [*p*-phenylenediamine (Pa), 1,3,5-triformylphloroglucinol (Tp)] spheres by a template-free solution-phase aging method at room temperature. For the first time, after metalation with Fe^{3+}, a good photothermal effect and an excellent *in vivo* antitumor efficacy (87.8%) were achieved for the resultant Fe–HCOF for treatment of cancer cells under laser irradiation (Figure 9.8). This study illustrated that the relatively slow polymerization and crystal growth process of the aging method permits the formation of product with a well-defined morphology, and this strategy also enriches our understanding toward the preparation and formation mechanisms of COFs. Moreover, the post-synthetic method further demonstrated its feasibility to functionalize COFs to meet the requirements of various applications.[29]

9.3.3 COF–CuSe Nanocomposites

Pang reported highly monodispersed COF–LZU-1 nanoparticles with an average size of 150 nm that were prepared *via* a mild wet solution method at room temperature (Figure 9.9). The nitrogen-related functional groups of COF–LZU-1 were coordinated with CuSe to form COF–CuSe nanocomposites. The COF–LZU-1 nanoparticles could generate $^1O_2$ efficiently under 650 or 808 nm laser irradiation. The photodynamic effect of COFs was enhanced significantly after being coordinated with CuSe nanoparticles. The resultant COF–CuSe nanocomposites also exhibited an excellent photothermal effect under 808 nm laser irradiation with a photothermal conversion efficiency of 26.34%. The *in vitro* and *in vivo* assessment indicated that the COF–CuSe nanoplatform was an ideal photosensitizer for PDT and PTT with enhanced antitumor efficacy. This work demonstrates PDT application of the non-porphyrin functional group containing COFs and the combination with CuSe for PDT/PTT applications *in vivo*. It also provides an efficient approach to fabricate COF-based multifunctional theranostic agents for treatment of tumors and/or other applications by combining COFs with other functional materials.[30]

9.3.4 COF–Ag_2Se Nanocomposites

Pang *et al.* reported COF–Ag_2Se nanoparticles successfully synthesized under mild conditions *via* a cation exchange approach using COFs

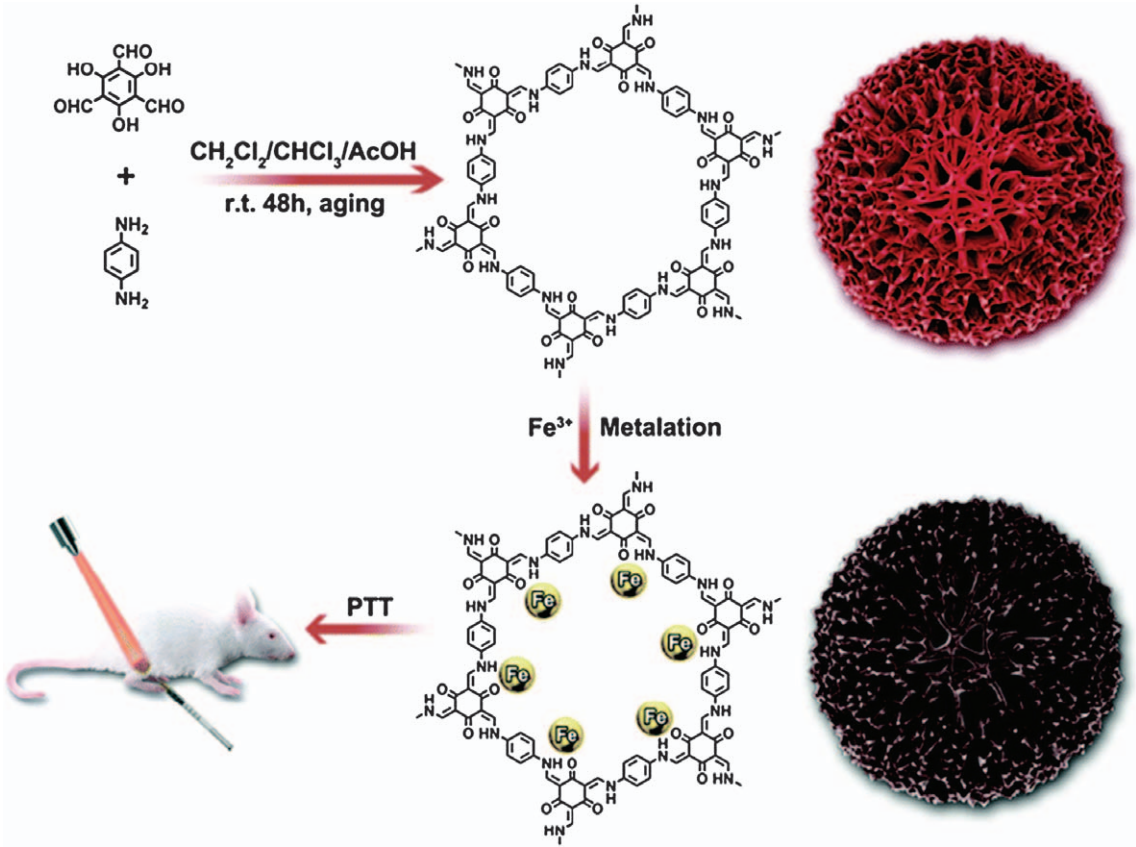

Figure 9.8 Preparation and post-synthetic metalation of HCOF for PTT.
Reproduced from ref. 29 with permission from the Royal Society of Chemistry.

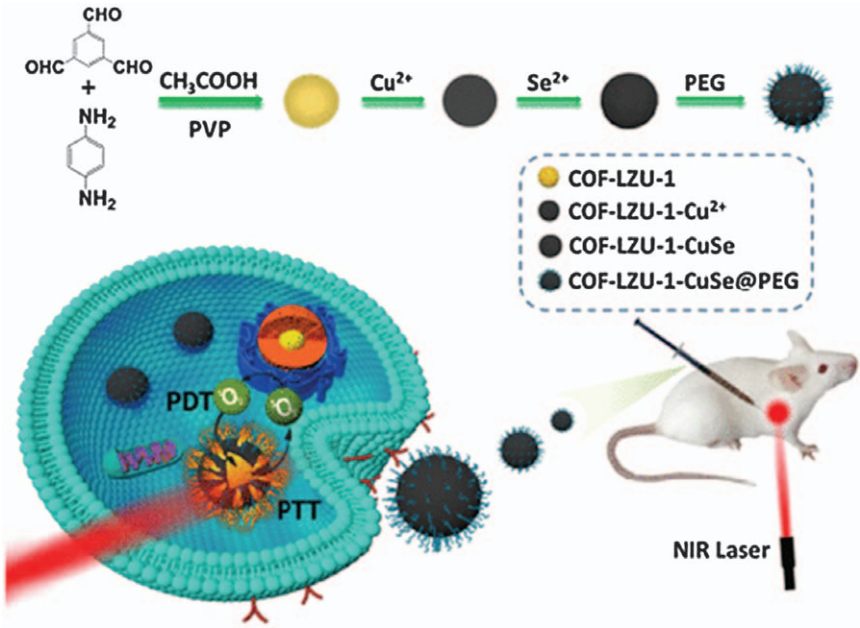

Figure 9.9 COF–LZU-1–CuSe@PEG design and synthesis.
Reproduced from ref. 30 with permission from American Chemical Society, Copyright 2019.

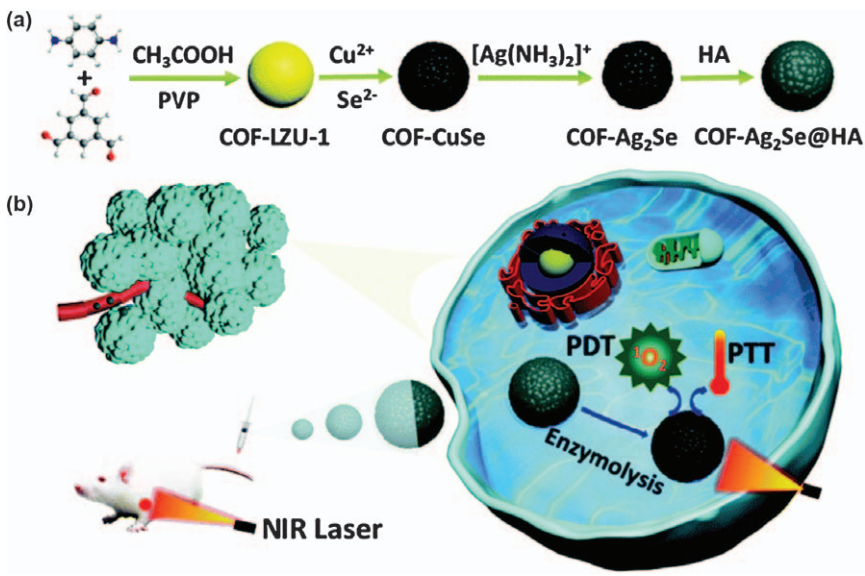

Figure 9.10 COF–Ag_2Se@HA design and synthesis.
Reproduced from ref. 31 with permission from the Royal Society of Chemistry.

and CuSe as templates (Figure 9.10). The non-porphyrin group containing COF–LZU-1 demonstrated its excellent photodynamic effect, which was notably improved after combination with Ag_2Se nanoparticles. The *in vitro* and *in vivo* experiments verified the excellent cancer cell killing effect and antitumor efficacy of COF–Ag_2Se nanoparticles *via* combined PDT and PTT. This study demonstrates the excellent photodynamic effect of COFs on the inhibition of tumor growth and indicates its good template effect on controlling the size of nanoparticles. It also provides a new approach to construct COF-based multifunctional materials for various applications.[31]

9.3.5 MnO_2/Zn COF@Au&BSA Nanosheets

Yuan *et al.* prepared a type of porphyrin fluorescent dye (FD) based nanoplatform (MnO_2/Zn COF@Au&BSA) using MnO_2 nanosheets (NSs) as a template to guide the synthesis of zinc COFs (Zn COF) between zinc-meso-tetra(4-aminophenyl) porphyrin (Zn–TAPP) FDs and glyoxal through a Schiff base reaction. The repeating Zn–TAPP units will efficiently increase the loading amount of FD in the nanoplatform. Bovine serum albumin (BSA), as a reducing and stabilizing agent, was adsorbed on the surface of MnO_2/Zn COF NSs for realizing the *in situ* preparation of Au NPs (Figure 9.11). During blood circulation (pH = 7.4), the interlinked FD in MnO_2/Zn COF@Au&BSA NSs will not show a FL signal due to the ACQ effect by π–π interaction, which will effectively overcome the interference caused by background noise during the imaging process. Together with the pH-triggered disintegration of Zn COF in tumor cells (pH = 5.5), the FL ability of the scattered FD will be activated from ''off'' to ''on'', and simultaneously the FL signal of the scattered FD will be ingeniously amplified by the metal-enhanced fluorescence (MEF) effect of the shedding BSA-coated Au NPs. In addition, the excellent photothermal conversion properties of the MnO_2/Zn COF@Au&BSA NS components will produce a great antitumor effect during the PTT process. Therefore, our strategy has good potential to be applied in the biomedical field for cancer diagnosis and treatment.[32]

9.3.6 Carbon Material-doped COFs

Xie *et al.* reported, for the first time, two CD-based nanoscale COFs (NCOFs) (named CCOF-1 and CCOF-2, respectively), which were generated from aldehyde-decorated CDs and *p*-phenylenediamine/BODIPY, through Schiff base reactions. After modification with poly (ethylene glycol) (PEG), the formed CCOF-1@PEG and CCOF-2@PEG not only maintained a crystalline structure and superior photoluminescence (PL) properties but also possess high stability and good dispersibility. Furthermore, CCOF-2@PEG features highly efficient reactive oxygen species generation upon irradiation and high cancer cell uptake, which can serve as a promising PDT agent for cancer treatment (Figure 9.12).[33]

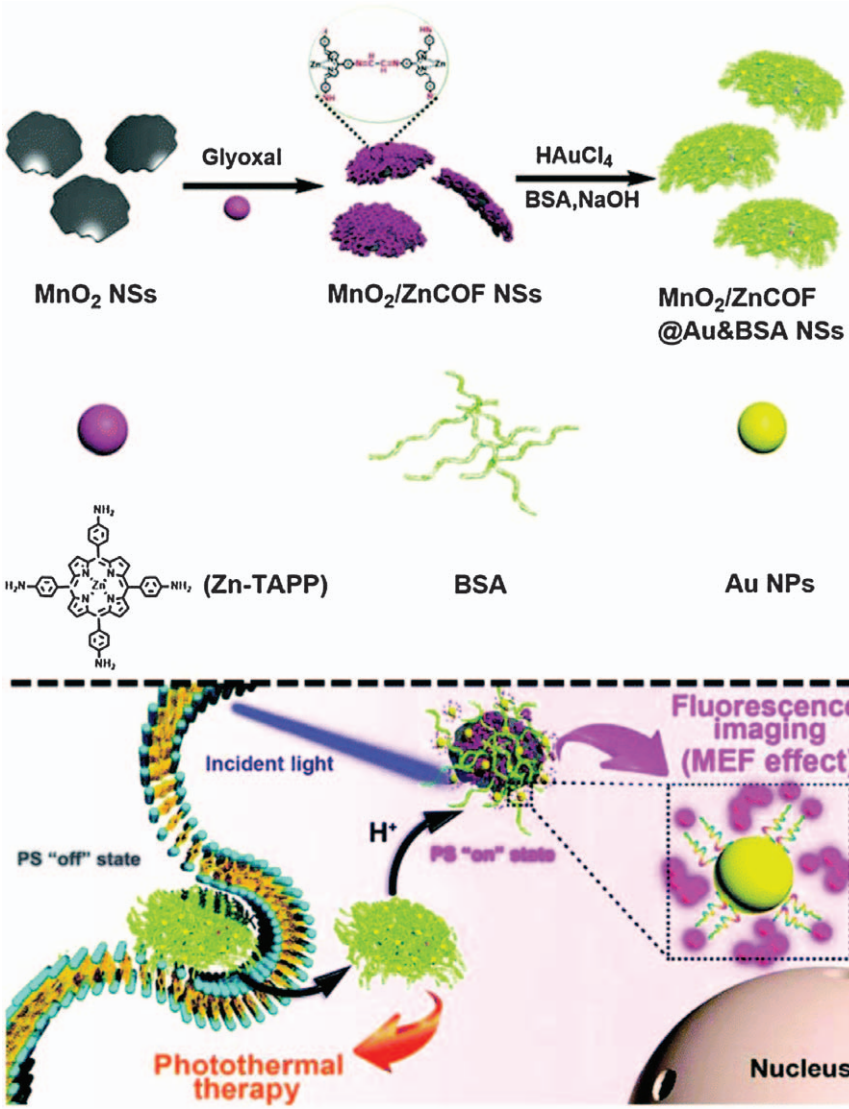

Figure 9.11 MnO_2/Zn COF@Au&BSA nanosheet design and PTT. Reproduced from ref. 32 with permission from the Royal Society of Chemistry.

9.4 Other

Nano-scale microporous carbon nanoparticles (CNPs) can be prepared by pyrolysis of nano-COF precursors. The obtained CNPs show appropriate biocompatibility and physiological stability (Figure 9.13). In addition, they possess extensive absorption in the NIR spectral region and display a

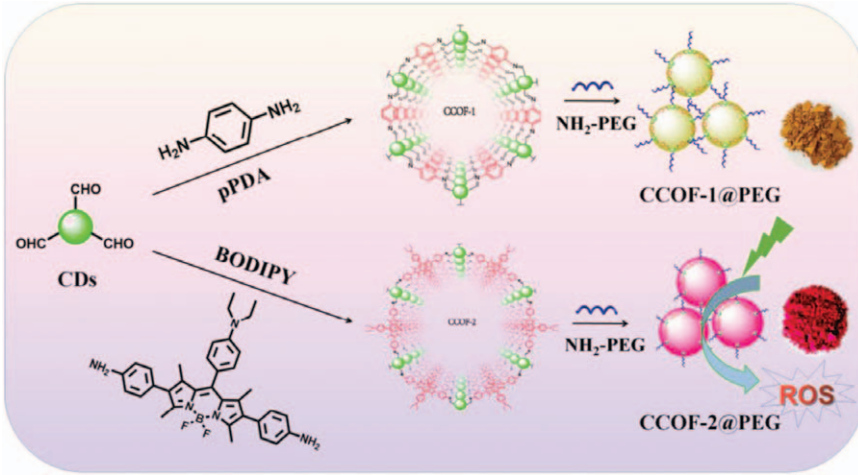

Figure 9.12 CCOF@PEG design and PTT.
Reproduced from ref. 33 with permission from John Wiley and Sons, Copyright © 2020 Wiley-VCH GmbH.

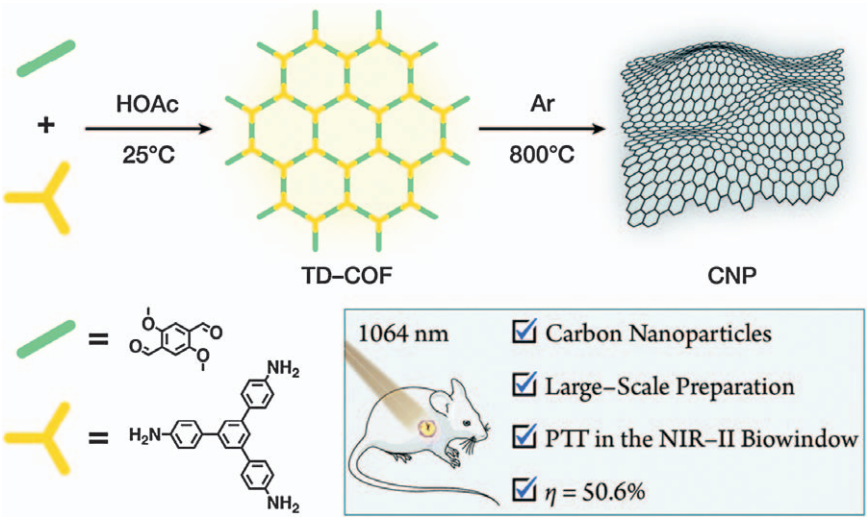

Figure 9.13 Preparation of CNPs by pyrolysis of COF precursors.
Reproduced from ref. 34 with permission from the Royal Society of Chemistry.

high photothermal conversion efficiency of up to 50.6% upon 1064 nm laser irradiation. This nanoscale carbon material fully meets the multiple requirements of antitumor treatment *via* PTT in the NIR-II biowindow. Its impressive tumor ablation capacity is evidenced by *in vitro* and *in vivo*

experiments. They believe that their strategy can be applied as a versatile approach for the fabrication of many more carbon-based nanomaterials for a variety of biomedical applications in the NIR-II biowindow and offers a promising perspective for locoregional tumor therapy.[34]

Recently, an interesting study reported the photothermal phenomenon catalysis of COFs. M@CCOF–CuTPP (M=Au or Pd, TPP = tetra bromo phenolphthalein) are multifunctional catalytic materials and they can highly promote thermally-driven asymmetric catalysis at an elevated temperature by photothermal conversion (Figure 9.14). First, CCOF–CuTPP (1) is a rigid homochiral host-framework, and it can be a powerful chiral temple to steer the organic substrates in the specific spatial orientation within the CCOF confined space even at high temperature, consequently, providing the desired products with high enantiopurity; second, 1 contains a porphyrin moiety which is a widely recognized PTCM that can readily transfer light into thermal energy. Therefore, the obtained porphyrin involved CCOF herein can supply the thermal energy needed for the reaction upon visible light irradiation; and third, 1 is a highly porous and heteroatom-rich COF host which is qualified for M metal nanoparticle (NP) loading and stabilization.[35]

9.5 Summary

In recent years, great progress has been made in the field of photothermal agents based on organic molecules. It has been found that many structures including COFs, cyanine, diketopyrrolopyrrole, theobromine, porphyrin, polymer, *etc.* produce good photothermal effects. Compared with inorganic materials that have been extensively studied for PTT, COFs have good biodegradability. In addition, COF PTT sensitizers have advantages in reproducibility, controllable preparation, and ease of synthesis and modification. Therefore, it is suggested that PTT reagents based on COFs and materials will play a key role in the development of new cancer treatment methods with potential clinical utility.

The field of COF photothermal agents is still relatively young. Although the latest developments have been documented in the literature, many obstacles still need to be overcome to translate current developments into clinical practice. It may be necessary to conduct more detailed mechanical studies and strive to maximize the efficacy of PTT and the sensitivity of cells toward heat. In optimizing the delivery of PTT agents to suitable tissues and the most sensitive subcellular compartments, further progress is needed to advance the development of this field. A combination strategy where PTT is used in combination with other treatments and diagnostics can be developed rapidly without having to overcome many of the limitations associated with current PTT drugs. We hope that many investigative methods will become the subject of in-depth research in the next few years.

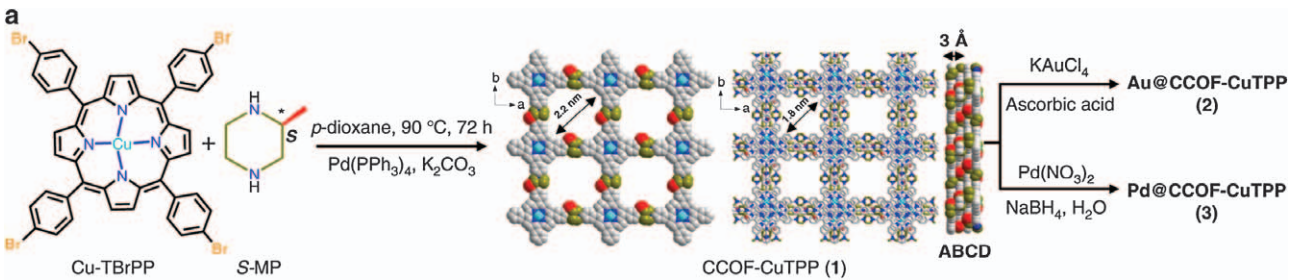

Figure 9.14 M@CCOF–CuTPP design.
Reproduced from ref. 35, https://doi.org/10.1038/s41467-019-11355-x, under the terms of the CC BY 4.0 license, https://creativecommons.org/licenses/by/4.0/.

References

1. J. Suzuka, M. Tsuda, L. Wang, S. Kohsaka, K. Kishida, S. Semba, H. Sugino, S. Aburatani, M. Frauenlob, T. Kurokawa, S. Kojima, T. Ueno, Y. Ohmiya, H. Mano, K. Yasuda, J. P. Gong and S. Tanaka, Rapid reprogramming of tumour cells into cancer stem cells on double-network hydrogels, *Nat. Biomed. Eng.*, 2021, **5**, 914–925.
2. Z. J. Chen, J. Zhao, S. L. Guo and Y. B. Zhao, A PN code acquisition scheme in the presence of data modulation and Doppler shift, in *Proceedings of 2007 International Conference on Machine Learning and Cybernetics*, 2007, vol. 1–7, p. 2653.
3. J. Chen, C. Ning, Z. Zhou, P. Yu, Y. Zhu, G. Tan and C. Mao, Nanomaterials as photothermal therapeutic agents, *Prog. Mater. Sci.*, 2019, **99**, 1–26.
4. X. Li, M. Jiang, S. Zeng and H. Liu, Polydopamine coated multifunctional lanthanide theranostic agent for vascular malformation and tumor vessel imaging beyond 1500 nm and imaging-guided photothermal therapy, *Theranostics*, 2019, **9**, 3866–3878.
5. S. Yang, D. Yao, Y. Wang, W. Yang, B. Zhang and D. Wang, Enzyme-triggered self-assembly of gold nanoparticles for enhanced retention effects and photothermal therapy of prostate cancer, *Chem. Commun.*, 2018, **54**, 9841–9844.
6. H. Sun, Q. Zhang, J. Li, S. Peng, X. Wang and R. Cai, Near-infrared photoactivated nanomedicines for photothermal synergistic cancer therapy, *Nano Today*, 2021, **37**, 101073.
7. D. Xi, M. Xiao, J. Cao, L. Zhao, N. Xu, S. Long, J. Fan, K. Shao, W. Sun, X. Yan and X. Peng, NIR Light-Driving Barrier-Free Group Rotation in Nanoparticles with an 88.3% Photothermal Conversion Efficiency for Photothermal Therapy, *Adv. Mater.*, 2020, **32**, 1907855.
8. D. F. Zhi, T. Yang, J. O'hagan, S. B. Zhang and R. F. Donnelly, Photothermal therapy, *J. Control. Release*, 2020, **325**, 52–71.
9. Y. Sasaki, M. Oshikawa, P. Bharmoria, H. Kouno, A. Hayashi-Takagi, M. Sato, I. Ajioka, N. Yanai and N. Kimizuka, Near-Infrared Optogenetic Genome Engineering Based on Photon-Upconversion Hydrogels, *Angew. Chem., Int. Ed.*, 2019, **58**, 17827–17833.
10. Y. Cai, P. Liang, Q. Tang, X. Yang, W. Si, W. Huang, Q. Zhang and X. Dong, Diketopyrrolopyrrole-Triphenylamine Organic Nanoparticles as Multifunctional Reagents for Photoacoustic Imaging-Guided Photodynamic/Photothermal Synergistic Tumor Therapy, *ACS Nano*, 2017, **11**, 1054–1063.
11. Z. Yu, W. K. Chan, Y. Zhang and T. T. Y. Tan, Near-infrared-II activated inorganic photothermal nanomedicines, *Biomaterials*, 2021, **269**, 120459.
12. C. Zhang, W. Sun, Y. Wang, F. Xu, J. Qu, J. Xia, M. Shen and X. Shi, Gd-/CuS-Loaded Functional Nanogels for MR/PA Imaging-Guided Tumor-Targeted Photothermal Therapy, *ACS Appl. Mater. Interfaces*, 2020, **12**, 9107–9117.

13. H. Cai, T. Shen, A. M. Kirillov, Y. Zhang, C. Shan, X. Li, W. Liu and Y. Tang, Self-Assembled Upconversion Nanoparticle Clusters for NIR-controlled Drug Release and Synergistic Therapy after Conjugation with Gold Nanoparticles, *Inorg. Chem.*, 2017, **56**, 5295–5304.
14. R. R. Liang and X. Zhao, Heteropore covalent organic frameworks: a new class of porous organic polymers with well-ordered hierarchical porosities, *Org. Chem. Front.*, 2018, **5**, 3341–3356.
15. X. Chen, K. Geng, R. Liu, K. T. Tan, Y. Gong, Z. Li, S. Tao, Q. Jiang and D. Jiang, Covalent Organic Frameworks: Chemical Approaches to Designer Structures and Built-In Functions, *Angew. Chem., Int. Ed.*, 2020, **59**, 5050–5091.
16. J. L. Segura, S. Royuela and M. M. Ramos, Post-synthetic modification of covalent organic frameworks, *Chem. Soc. Rev.*, 2019, **48**, 3903–3945.
17. R. Xia, X. Zheng, C. Li, X. Yuan, J. Wang, Z. Xie and X. Jing, Nanoscale Covalent Organic Frameworks with Donor–Acceptor Structure for Enhanced Photothermal Ablation of Tumors, *ACS Nano*, 2021, **15**, 7638–7648.
18. Z. Mi, P. Yang, R. Wang, J. Unruangsri, W. Yang, C. Wang and J. Guo, Stable Radical Cation-Containing Covalent Organic Frameworks Exhibiting Remarkable Structure-Enhanced Photothermal Conversion, *J. Am. Chem. Soc.*, 2019, **141**, 14433–14442.
19. Q. Guan, L.-L. Zhou, Y.-A. Li, W.-Y. Li, S. Wang, C. Song and Y.-B. Dong, Nanoscale Covalent Organic Framework for Combinatorial Antitumor Photodynamic and Photothermal Therapy, *ACS Nano*, 2019, **13**, 13304–13316.
20. D. Wang, Z. Zhang, L. Lin, F. Liu, Y. Wang, Z. Guo, Y. Li, H. Tian and X. Chen, Porphyrin-based covalent organic framework nanoparticles for photoacoustic imaging-guided photodynamic and photothermal combination cancer therapy, *Biomaterials*, 2019, **223**, 119459.
21. J.-Y. Zeng, M.-K. Zhang, M.-Y. Peng, D. Gong and X.-Z. Zhang, Porphyrinic Metal-Organic Frameworks Coated Gold Nanorods as a Versatile Nanoplatform for Combined Photodynamic/Photothermal/Chemotherapy of Tumor, *Adv. Fun. Mater.*, 2018, **28**, 1705451.
22. F. L. Zhao, H. M. Liu, S. D. R. Mathe, A. J. Dong and J. H. Zhang, Covalent Organic Frameworks: From Materials Design to Biomedical Application, *Nanomaterials*, 2018, **8**, 15.
23. Y. Shi, X. Deng, S. Bao, B. Liu, B. Liu, P. Ma, Z. Cheng, M. Pang and J. Lin, Self-Templated Stepwise Synthesis of Monodispersed Nanoscale Metalated Covalent Organic Polymers for In Vivo Bioimaging and Photothermal Therapy, *Chem. – Asian J.*, 2017, **12**, 2183–2188.
24. L. Bai, S. Z. Phua, W. Q. Lim, A. Jana, Z. Luo, H. P. Tham, L. Zhao, Q. Gao and Y. Zhao, Nanoscale covalent organic frameworks as smart carriers for drug delivery, *Chem. Commun.*, 2016, **52**, 4128–4131.
25. Q. Fang, J. Wang, S. Gu, R. B. Kaspar, Z. Zhuang, J. Zheng, H. Guo, S. Qiu and Y. Yan, 3D Porous Crystalline Polyimide Covalent Organic Frameworks for Drug Delivery, *J. Am. Chem. Soc.*, 2015, **137**, 8352–8355.

26. K. Wang, Z. Zhang, L. Lin, J. Chen, K. Hao, H. Tian and X. Chen, Covalent Organic Nanosheets Integrated Heterojunction with Two Strategies To Overcome Hypoxic-Tumor Photodynamic Therapy, *Chem. Mater.*, 2019, **31**, 3313–3323.
27. H. Wang, W. Zhu, L. Feng, Q. Chen, Y. Chao, Z. Dong and Z. Liu, Nanoscale covalent organic polymers as a biodegradable nanomedicine for chemotherapy-enhanced photodynamic therapy of cancer, *Nano Res.*, 2018, **11**, 3244–3257.
28. J. Tan, S. Namuangruk, W. Kong, N. Kungwan, J. Guo and C. Wang, Manipulation of Amorphous-to-Crystalline Transformation: Towards the Construction of Covalent Organic Framework Hybrid Microspheres with NIR Photothermal Conversion Ability, *Angew. Chem., Int. Ed.*, 2016, **55**, 13979–13984.
29. Y. Shi, S. Liu, Z. Zhang, Y. Liu and M. Pang, Template-free synthesis and metalation of hierarchical covalent organic framework spheres for photothermal therapy, *Chem. Commun.*, 2019, **55**, 14315–14318.
30. C. Hu, Z. Zhang, S. Liu, X. Liu and M. Pang, Monodispersed CuSe Sensitized Covalent Organic Framework Photosensitizer with an Enhanced Photodynamic and Photothermal Effect for Cancer Therapy, *ACS Appl. Mater. Interfaces*, 2019, **11**, 23072–23082.
31. C. Hu, L. Cai, S. Liu and M. Pang, Integration of a highly monodisperse covalent organic framework photosensitizer with cation exchange synthesized Ag2Se nanoparticles for enhanced phototherapy, *Chem. Commun.*, 2019, **55**, 9164–9167.
32. Y. Liu, Y. Zhang, X. Li, X. Gao, X. Niu, W. Wang, Q. Wu and Z. Yuan, Fluorescence-enhanced covalent organic framework nanosystem for tumor imaging and photothermal therapy, *Nanoscale*, 2019, **11**, 10429–10438.
33. S. Chen, T. Sun, M. Zheng and Z. Xie, Carbon Dots Based Nanoscale Covalent Organic Frameworks for Photodynamic Therapy, *Adv. Fun. Mater.*, 2020, **30**, 2004680.
34. Q. Guan, L. L. Zhou, L. N. Zhou, M. Li, G. X. Qin, W. Y. Li, Y. A. Li and Y. B. Dong, A carbon nanomaterial derived from a nanoscale covalent organic framework for photothermal therapy in the NIR-II biowindow, *Chem. Commun.*, 2020, **56**, 7793–7796.
35. H. C. Ma, C. C. Zhao, G. J. Chen and Y. B. Dong, Photothermal conversion triggered thermal asymmetric catalysis within metal nanoparticles loaded homochiral covalent organic framework, *Nat. Commun.*, 2019, **10**, 3368.

CHAPTER 10

Carbon-based Nanomaterials

HONG CHI,*[a] YAOGUANG WANG,[a] ZIBIAO LI[b,c] AND ENYI YE[b]

[a] Shandong Provincial Key Laboratory of Molecular Engineering, School of Chemistry and Chemical Engineering, Qilu University of Technology (Shandong Academy of Sciences), Jinan, 250353 China; [b] Institute of Materials Research and Engineering, Agency for Science, Technology and Research (A*STAR), 2 Fusionopolis Way, 138634 Singapore, Singapore; [c] Department of Materials Science and Engineering, National University of Singapore, 9 Engineering Drive 1, Singapore 117576, Singapore
*Email: chihong@qlu.edu.cn

10.1 Introduction

Photothermal conversion refers to the process of gathering solar radiation energy through absorption, reflection, or other methods and converting it into heat to effectively meet different load requirements. Photothermal conversion materials are special materials synthesized with this as the goal. The material science community has continuously made new progress in the research of photothermal materials, but the limited photothermal conversion efficiency of single-component materials is far from meeting practical needs.

The principle of photothermal conversion produced by photothermal materials is different, mainly related to the electronic structure or energy band structure of the material itself. The physical mechanism of the photothermal conversion process is the absorption of photons by matter. The above is the absorption and energy conversion of light energy. Generally, the mechanism by which photothermal materials convert light energy into heat energy mainly includes: surface plasmon resonance (SPR) effect and local

Nanoscience & Nanotechnology Series No. 54
Photothermal Nanomaterials
Edited by Enyi Ye and Zibiao Li

Published by the Royal Society of Chemistry, www.rsc.org

surface plasmon resonance (LSPR) effect, interference absorption, photothermal electronic excitation, conjugation effect and hyper-conjugation effect, *etc.* The SPR effect is the main reason why metal-based materials have photothermal conversion capabilities.[1] The conjugation effect, that is, the hyper-conjugation effect, is in essence the interaction between bonded or non-bonded electronic orbitals and anti-bonded electronic orbitals in the molecule. In a conjugated system, adjacent π electrons overlap or the interaction between π bonds and p electrons makes the electron cloud density on each bond in the system equal, so the difference between adjacent single bonds and multiple bonds disappears partially or completely, producing a conjugation effect (delocalization effect). In addition to the conjugation effect of the π–π system, p–π system, and p–p system with greater conjugation, there is also co-existence between σ and π, σ and p, and σ and σ interactions.

As an immerging new photothermal conversion material, carbon-based photothermal materials are also very rich. Different forms of carbon nanomaterials, such as carbon nanotubes (CNTs), graphene derivatives, carbon nanospheres, *etc.*, have been successfully developed as solar thermal materials. Band transition and a π structure make CNTs have UV–vis and near-infrared region absorption based on their conjugated degree. The unique structure and properties of CNTs make it more suitable for solar energy absorption and efficient photothermal conversion and are regarded as efficient photon traps and molecular heaters.[2,3] The conjugation effect provides opportunity for electrons to flow and absorb energy through the electron transitions in-between molecular orbitals. This type of carbon material converts the absorbed light energy into heat energy, showing a photothermal effect. Such photothermal materials have large conjugated π bonding orbitals, and π anti-bonding molecular orbitals have a hyper-conjugation effect and a small orbital energy gap. After absorbing the energy of light, the π electron on the bonding molecular orbital would transit to the π anti-bonding molecular orbital. When the excited electrons fall back to the ground state, part of the energy is released in the form of heat, resulting in a photothermal effect, using the ability of conjugated molecules to conduct electrons and holes quickly, and carbon materials as well.

The single-layer structure of the surface layer is more conducive to the separation and migration of carriers; the conjugation effect provides a good channel for the transfer of photogenerated carriers and improves its visible light absorption capacity. In addition, some organic polymer photothermal materials also have a π-electron delocalized conjugate structure and a narrow band gap, which can transfer energy through changes in electrical conductivity or photothermal conversion under near-infrared light irradiation.

10.1.1 Photo-thermal Catalytic Conversion

Volatile organic compounds (VOCs) are an important part of atmospheric environmental pollutants. In the control and treatment of VOCs, catalytic

combustion treatment technology is the most extensively used, but the high energy consumption of fossil fuels used in catalytic combustion has caused an energy crisis and environmental pollution problems as well. Solar photocatalytic degradation is a new and green treatment method that has emerged in recent years. High energy consumption is an important factor restricting the development of traditional catalytic combustion technology. Using solar energy to convert and store heat energy to drive the catalytic reaction is expected to replace traditional thermal catalytic technology, thereby realizing low-energy industrial applications. However, the traditional solar photocatalytic degradation of VOCs is limited by the band gap energy of semiconductor materials. Only ultraviolet and part of visible light are used. For example, for the most widely studied TiO_2 semiconductor photo catalyst, its light absorption is limited to only ultraviolet ray (which accounts for only 3% of sunlight), and a lack of highly active sites and high-charge carrier recombination on the catalyst surface make its photochemical conversion efficiency low.[4] In order to improve the utilization of sunlight, various strategies have been adopted,[5,6] such as doping with metals and/or non-metals, using organic sensitizers or compounding with other developed semiconductors to enhance the catalytic efficiency of TiO_2.

Most of the infrared light, which accounts for 48% of solar energy, is lost in the form of thermal radiation. Therefore, the key point lies in the research and development of high-efficiency photothermal conversion materials, so as to achieve a wider capture of solar energy, reduce the loss of solar energy quality, and convert it into heat to be introduced into the catalytic reaction.

To achieve high photothermal conversion efficiency, the materials must absorb a large amount of infrared light, couple the collected photons, convert them to thermal energy and active the catalysis sites. In order to maximally use infrared light, many infrared light-induced photo catalysts have been developed. Among them, due to low photon energy and inappropriate band structure, narrow energy gap semiconductor materials are considered to lack photocatalytic activity.[7] Up-conversion rare earth materials can trigger a photocatalytic reaction by converting near-infrared (NIR) light to UV or visible light emission,[8,9] but the efficiency of the up-conversion process is subject to very narrow light absorption and rapid depletion of energy limits.[10] In addition, carbon quantum dots (CQD) have been developed as an upconversion material as well,[11,12] and the light absorption wavelength is relatively wide.

Graphene has the advantages of broad-spectrum absorption properties and excellent light-to-heat conversion performance. Graphene is an infinitely expanding two-dimensional nanomaterial with six-membered ring benzene units formed by sp^2 hybrid carbon atoms. In addition to the large specific surface area and porosity, there is strong π–π interaction between graphene and toluene reactant molecules. Thus, a large amount of toluene can be adsorbed and enriched on the surface of graphene through a π–π function, increasing the retaining time of reactant molecules on the catalyst, thereby improving catalytic activity. Combined with the traditional thermal

catalyst Pt–TiO_2, a new type of graphene assembly Pt–rGO–TiO_2 was designed through optical, thermal, and catalytic reaction sites to achieve 14.1% light-to-heat conversion efficiency by Hongpeng Jia and co-workers (see Figure 10.1).[13] Efficient conversion of VOCs was achieved under the following conditions: infrared light intensity 116 mW cm^{-2}, light heating temperature 150 °C. Toluene was found to be converted to harmless CO_2 at a rate of 95%, and yield of 72%, see Figure 10.1A and B). Compared with graphene-supported platinum–titanium dioxide (Pt–rGO–TiO_2), toluene penetration experiments and temperature-programmed desorption experiments confirmed that the graphene adsorption layer-supported platinum catalyst (Pt–rGO) was still at infrared light temperature and shows a higher saturated adsorption capacity (see Figure 10.1C). The innovative construction of Pt on the rGO adsorption layer achieves 17.6% light-to-heat conversion efficiency and complete harmless conversion of toluene under non-condensing conditions (infrared light intensity 146 mW cm^{-2}, light-heating temperature 180 °C, toluene conversion rate 98%). It is concluded from the O_2 temperature-programmed desorption (O_2-TPD) result that the oxidation of a given VOC is determined by the activated oxygen, namely lattice oxygen and/or adsorbed oxygen. Under anaerobic conditions, the surface lattice oxygen of 1% Pt–rGO–TiO_2 reacts with adsorbed toluene through the Mars–van Krevelen mechanism. Carboxylate intermediates will be generated before the final product CO_2 comes out. Under infrared radiation, the 1% composite material shows broad absorption and heat utilization. The heat generated by rGO is increased by phonon–phonon coupling to increase the local temperature of the system, leading to the oxidation of toluene with the assistance of Pt.

Since Akira Fujishima and others achieved photocatalytic water splitting in 1970, semiconductor photocatalysis as a clean and pollution-free technology has been widely studied by the academic community. The research field of semiconductor photocatalysis mainly involves the energy, environment, and many other fields. However, thermodynamic analysis shows that some complex chemical reactions have high Gibbs free energy and can only be excited *via* ultraviolet light, which greatly limits the use of the solar spectrum. In order to broaden the use of the solar spectrum as much as possible, there are two main considerations. One is to expand the absorption edge of semiconductor catalysts and develop visible light catalysis. But even under the premise of making full use of visible light, the utilization rate of the full spectrum of the sun does not exceed 50%. The energy in the infrared region is mainly dissipated in the form of heat dissipation and is wasted. How to efficiently make use of the energy in the infrared region has become a problem that must be considered.

It can be roughly divided into three categories. One is photocatalysis and thermocatalysis in series mode; the second is a light-driven thermocatalytic reaction, in which light only serves as a heat source. In terms of the reaction mechanism, the essence of the reaction is a thermocatalytic process. The third is the thermally assisted photocatalytic reaction. Light plays a

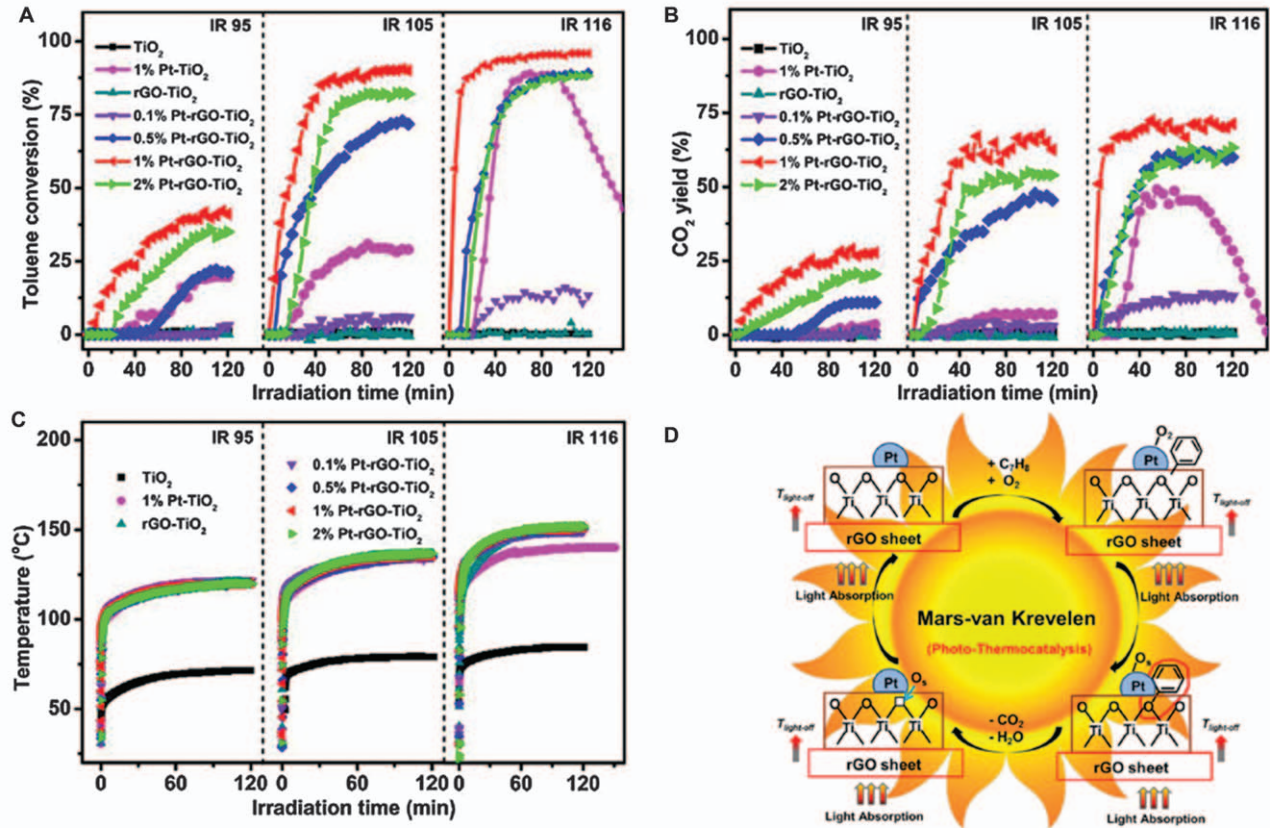

Figure 10.1 (A) Conversion of toluene and (B) CO_2 yield that was photocatalyzed by x% Pt–rGO–TiO_2 ($x = 0$, 0.1, 0.5, 1 and 2), 1% Pt–TiO_2, and TiO_2 under different IR irradiation (95, 106 and 116 mW cm^{-2}). (C) The temperature increases with the IR irradiation. (D) Schematic illustration of the proposed Pt-assisted mechanism of photo-thermal catalysis.
Reproduced from ref. 13 with permission from Elsevier, Copyright 2018.

decisive role in the reaction, and heating can promote an increase in the reaction rate.

The plasmon carrier generated by the oscillation of free charge on the surface of certain metals can drive the catalytic action of the photocatalyst surface. However, traditional noble metal-based plasma photocatalysts are high in cost. Although copper (Cu) is a non-noble metal, it has catalytic properties similar to noble metals and excellent optical properties except for the disadvantage of being easily oxidized. Piyong Zhang *et al.*[14] prepared a non-noble metal CuCo bimetal-based photocatalyst. After alloying Co, the oxidation of Cu can be suppressed and the photocatalytic activity would thus be improved. At the same time, the introduction of carbon dots (CD) into the photocatalyst can improve the separation of photoinduced electron–hole pairs, thereby enhancing the photocatalytic activity. Scanning electron microscopy (SEM) suggested a dendrite-like morphology of the bimetal (see Figure 10.2A). Composites with different contents of CD have similar absorption spectra (see Figure 10.2B) because of the low CD content and weak absorption. $CuCo_{7:3}$ bimetal and $CuCo_{7:3}$/CD show the characteristic SPR absorption band of Cu at 600 nm. The absorption and utilization of sunlight

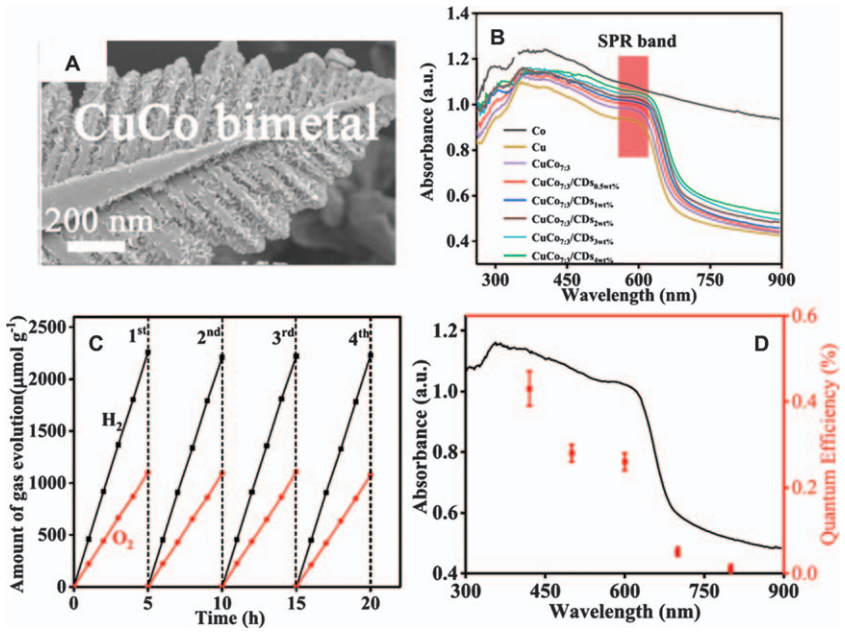

Figure 10.2 (A) $CuCo_{7:3}$ bimetals, where 7 : 3 indicates the molar proportion of Cu and Co. (B) UV–visible absorbance of the pure metal and composites. $CuCo_{7:3}$/CDs zwt% indicates that the content of CDs is zwt% in the composite. (C) Photocatalytic activity of $CuCo_{7:3}$/CDs 2wt% in 20 hours. (D) Quantum efficiency (QE) of $CuCo_{7:3}$/CDs 2wt% for H_2 evolution as a function of the incident wavelength.
Reproduced from ref. 14 with permission from American Chemical Society, Copyright 2020.

are greatly improved due to the full spectrum absorption of Co in ultraviolet, visible, and near infrared light. The prepared CuCo/CDs composite material has an excellent and stable photocatalytic water decomposition ability, the highest gas escape rate of H_2 is 459.3 $\mu mol\, g^{-1}\, h^{-1}$, and the highest gas escape rate of O_2 is 221.6 $\mu mol\, g^{-1}\, h^{-1}$ (see Figure 10.2C). The trend of QEs is in good agreement with the absorption spectrum, indicating that the photocatalyst undergoes a photocatalytic reaction through light absorption (see Figure 10.2D).

10.1.2 Photothermal Seawater Desalination

Converting solar energy into heat energy for water evaporation is considered to be an efficient and energy-saving method of salt water desalination and clean water production. However, the efficiency of water evaporation under natural sunlight is very low. The direct solar distillation method can only reach a total conversion efficiency of 30–40%. Only by increasing the local temperature of the water–gas interface and promoting the evaporation of water can we achieve efficient salt water desalination. The efficiency of photothermal desalination is closely related to the performance of photothermal conversion materials. Under light conditions, the precondition for the photothermal conversion material to convert light irradiation into heat energy through the photothermal conversion principle is the radiation of sunlight.

The solar radiation energy occupied by infrared light is almost the same, it can directly produce a photothermal effect, and almost 90% of the energy is concentrated in the near infrared light region. Therefore, at present, the absorption of infrared light, especially near-infrared light, by light-to-heat conversion materials is particularly important to improve its light-to-heat conversion performance. The main impact factor relies on the surface of the material to absorb solar radiation and transfer the accumulated heat directly or through an intermediate heat transfer fluid to the water body.

The radiation energy is efficiently absorbed. A good photothermal conversion material should have a broad-spectrum absorption capacity from ultraviolet light to the near-infrared range ($250 \sim 2500$ nm), not limited to the visible light range. In order to alleviate the shortage of fresh water resources, seawater desalination has always been the focus of attention of scientists. On the other hand, due to the environmental pollution caused by the use of fossil fuels, the development of new forms of energy is urgently needed. The use of photothermal materials to convert solar energy into high-quality thermal energy with high efficiency can not only be used in seawater desalination but also can further convert thermal energy into electrical energy through the thermoelectric power generation effect, providing auxiliary energy for small and medium-sized all-weather intelligent power supply systems. At present, scientific researchers have made significant progress in the study of photothermal materials, but single-component materials cannot meet the actual needs due to their limited photothermal conversion

efficiency. Therefore, through further design and control, the preparation of composite materials with higher light-to-heat conversion efficiency is the focus of current research. A nanocomposite material composed of noble metals, semiconductors, and carbon dots was prepared by chemical methods.[15] Because of the synergistic effect of the three components and good charge transfer channel, the composite material realized an improvement in the photothermal conversion efficiency.

Wan Yanfen and Yang Peng *et al.* designed and prepared a nano-solar energy absorption composite material with a bionic coral structure. The composite material Au@Bi_2MoO_6–CDs includes three components of Au nanocones, Bi_2MoO_6 semiconductors, and biomass carbon dots (CDs), which were used to realize the packaging of Au nanocones inside the 3D Bi_2MoO_6 and the adsorption of a large number of carbon dots on the outside of a Bi_2MoO_6 coral-like structure (see Figure 10.3A). Compared with pure Au nanocones, Bi_2MoO_6 and CDs, the ternary composite material achieves effective charge transfer, facilitates the separation of photogenerated electron–hole pairs, and improves the photothermal conversion efficiency of the material (under solar radiation) (see Figure 10.3B). The light-to-heat conversion efficiency is 97.1%, and the water evaporation rate is 1.69 $kg\,m^{-2}\,h^{-1}$. At the same time, the whole structure on the surface of the material provides many points for the collection of sunlight, and the light absorption rate of 70% is achieved through the multi-level reflection of light by the holes. In addition, the composite material was deposited on a commercial thermoelectric power generation sheet to make a solar thermoelectric power generation device (see Figure 10.3C). The results show that the device has enhanced thermoelectric power generation performance, and its output power is as high as 97.4 $\mu W\,cm^{-2}$ (see Figure 10.3D). This research provides an important experimental basis for the research of efficient light-to-heat conversion materials, and at the same time brings new ideas for the research and development of seawater desalination and new energy devices and systems.

10.1.3 Photothermal Therapy

Cancer is a major threat to human life. Currently, surgery, radiotherapy, and chemotherapy are widely employed in cancer treatment. However, the above-mentioned treatment methods can destroy normal tissues and the immune system while killing cancer cells, or cause cancer cells to become more resistant to the treatment, thereby worsening the condition. In recent years, photothermal therapy (PTT), as a new tumor treatment method, has attracted wide attention due to its advantages of small trauma to the body and resistance to cancer cells. Its technical principle is injecting medicinal materials with photothermal conversion function into a human tissue or body, and using targeted recognition technology to gather them near the tumor. Laser irradiation of an external light source (usually near-infrared light) converts light irradiation into heat energy to kill cancer cells.

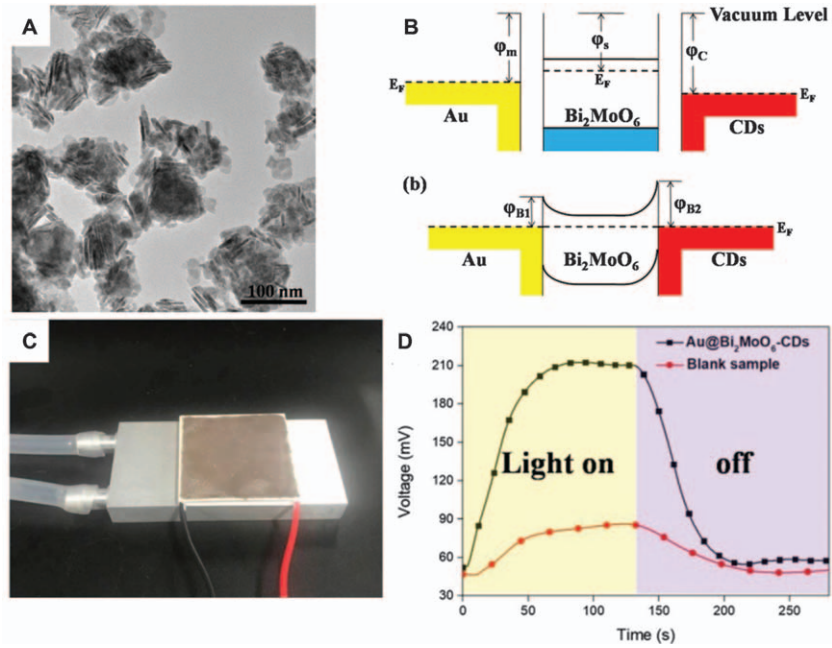

Figure 10.3 (A) Transmission electron microscope (TEM) image of a Au@Bi_2MoO_6–CDs nanocomposite. (B) Energy band scheme of Au@Bi_2MoO_6–CDs with and without contact. (C) Photograph of the fabricated device for thermoelectric measurement. The upper surface was coated with the composite material. The bottom was connected to the water circulation to amplify the temperature difference. (D) Open-circuit voltage (V_{oc}) of the blank sample and Au@Bi_2MoO_6–CDs generator. The temperature gap between the Au@Bi_2MoO_6–CDs thermoelectric devices generated a voltage output of 203 mV compared to a voltage output of 88 mV for the blank device.
Reproduced from ref. 15 with permission from Elsevier, Copyright 2020.

PTT usually uses materials with high light-to-heat conversion efficiency to enrich the tumor area and then generates a high temperature locally to kill cancer cells *via* irradiation with an external near-infrared light source (due to penetration depth). What are the advantages of photothermal materials?

First of all, the most important thing is to have good photothermal conversion efficiency, which is the key to the application of this material.

Secondly, it should be non-toxic or have only low biological toxicity, as this material is to be applied to organisms. If it is more toxic, the consequences would be disastrous.

Third, the material should possess rich functional groups for further modification, and other molecules such as drug molecules and photosensitizers can be modified on its surface.

However, when a laser is irradiated, the photothermal material often emits fluorescence. The more the fluorescence emitted, the less the heat

energy can be converted. To solve this problem, researchers have developed a ''fluorescence quenching'' technology, which ''induces'' the fluorescence between molecules to be extinguished and ''concentrates'' on heating.

To improve the thermal conversion efficiency of the material, recently, Liang Gaolin *et al.* adopted simultaneous intra- and intermolecular fluorescence quenching of Biotin–Cystamine–Cys–Lys(Cypate)–CBT (photothermal agent). They designed and synthesized a new type of organic small molecule material and applied an *in-situ* self-assembly-induced fluorescence quenching technique to the PTA. When this material is internalized by cancer cells, it will be reduced by intracellular glutathione ''intelligently'' first quenching ''intramolecular fluorescence'' and then quenching ''intermolecular fluorescence'' by self-assembly to form nanoparticles.[16] Through theoretical calculations and experiments, they have shown that compared with the commonly used ''induced fluorescence quenching'' technology, the conversion efficiency is more than doubled, and the photothermal treatment effect on living tumors is greatly enhanced.

The core of PTT is the preparation of photothermal reagents (PTAs). Although a variety of organic and inorganic PTAs have been developed, most organic PTAs are unstable under light or have unsatisfactory photothermal conversion rates. Inorganic PTAs usually contain heavy metals, and their long-term accumulation in the body may cause safety problems. Therefore, the development of new PTAs is of great significance in tumor diagnosis and treatment. A variety of carbon materials (such as carbon nanotubes, graphene oxide, some carbon quantum dots, nanodiamonds, *etc.*) have good biocompatibility and absorption in the near infrared region, so they are used as PTAs.

Recently, Wu Fugen *et al.* reported a water-dispersible carbon nano-onion cluster (CNOCs) derived from candle ash and used it for image-mediated photothermal treatment of tumors. The cluster-shaped carbon nano-onions are obtained by ultrasonically treating candle ash which was generated during the burning of candles. Well-dispersed carbon nano-onions were obtained *via* treating in a mixture of sulfuric acid and nitric acid with a volume ratio of 3 : 1 at 50 °C for 4 hours. It can be stably dispersed in phosphate buffered saline (PBS), water, and cell culture media for more than one year without precipitation, which is beneficial for their biomedical applications. In addition, the CNOCs showed an extinction coefficient as high as 15.0 $L\,g^{-1}\,cm^{-1}$, a photothermal conversion rate as high as 57.5%, good light stability and biocompatibility. In order to increase endocytosis, the authors used short-chain polyethyleneimine (PEI, $Mw \approx 600$ Da) and polyethylene glycol (PEG, $Mw \approx 5000$ Da) to modify the surface of CNOCs. The obtained CNOCs–PEI–PEG on the one hand inherited the excellent photothermal properties (photothermal conversion rate of 56.5%) and biocompatibility of CNOCs, on the other hand, it greatly promotes endocytosis.

Observed by confocal microscopy, CNOCs–PEI–PEG will aggregate in the lysosome after being endocytosed by cells. Subsequently, through the dual mediation of photothermal imaging/photoacoustic imaging *in vivo*

experiments, the authors proved that CNOCs–PEI–PEG can passively target tumors through the enhanced permeability and retention (EPR) effect, and heat up the tumor area under near-infrared light irradiation. Then, complete ablation of the transplanted tumor under the skin of the mouse is realized.[17]

10.1.4 Photoacoustic/Fluorescence Imaging

The use of light converted into heat (photothermal therapy, PTT) or acoustic energy (photoacoustic imaging, PAI) to treat and diagnose cancer has been studied in depth. Through nanocarriers, scientists have fully studied imaging and therapeutic functions. Liu Xiaojing and others gave a good overview of the development of inorganic and organic light and heat transfer agents (PTA), including small molecules, semiconducting polymer nanoparticles, and metal and carbon-based nanoparticles.[18] The strategies for improving PTT and the emerging applications in cancer-related research of combining PTT with other therapies in cancer treatment have been discussed as well.

Basically, infrared thermal imaging technology needs to meet two factors, namely infrared and thermal difference, based on the two to finally form an image. It is understood that all objects above absolute zero (−273 °C) emit infrared radiation, and because of the difference in temperature of each part of the object, different energies of infrared rays are radiated out, and then a special electronic device is used to surface the object. The temperature distribution is then converted to the image that is visible to the human eye, and the surface temperature distribution of the object is displayed in different colors.

Photothermal imaging is an optical method to detect the change in refractive index of absorbing nanoparticles caused by photothermal effect in a local environment. Carbon nanotubes (CNTs) are widely used photothermal materials for different applications, including photothermal therapy and imaging. To explore the degradation potential of CNT by photothermal imaging technology, Julie Russier *et al.*[19] produced cationic nanotubes (MWCNT-NH_3^+) through 1,3-dipolar cycloaddition reaction in microglia cells. The cells were kept in culture for different periods of time. Before photothermal imaging, on different days (1, 7 and 14 days), the CNT-loaded cells were fixed before they were embedded in resin and sectioned. On the first day, a large amount of MWCNT-NH_3^+ existed inside the cells. After 14 days, they were more dispersed and more personalized, indicating that they were partially degraded or eliminated in the cell.

Carbon nanotubes were also used in combination with noble metals as multimode photothermal or photoacoustic agents.[20] Xiaojing Wang *et al.* modified DNA functionalized single-walled carbon nanotubes (SWCNT) with precious metals (Ag or Au) to realize surface-enhanced Raman scattering imaging together with photothermal therapy.[21] The SWCNT adsorbed gold seeds before it underwent further seed-growing and was modified by polyethylene glycol (PEG). SWCNT–metal nanocomposites are stable in physiological environments. The surface enhanced Raman scattering (SERS)

effect was found to be dependent on the concentration and excitation source. When a near-infrared (NIR) laser was used as the excitation source, targeted Raman imaging of SWCNT–Au nanocomposite (SWCNT–Au–PEG–FA) cells labeled with folic acid (FA) was achieved. Due to the contribution of the SPR absorption of the gold shell, the effect of photothermal killing of cancer cells is significantly improved.

Carbon dots (CD) with low biological toxicity and high photostability are another good optical bioimaging agent. Since the visible/first near-infrared (NIR-1) emission of most CDs is shorter than 820 nm, the penetration depth during imaging is reduced. Youbin Li *et al.*[22] reported a CD with NIR-II emission prepared from watermelon juice, which can significantly reduce the scattering loss, so that deeper biological tissues in living animals can be observed. Under excitation of an 808 nm laser, the prepared luminescent CD has a high quantum yield (QY-0.4%) and high photothermal efficiency (30.6%) at 900–1200 nm. It is irradiated at a high power density ($1.4\ W\,cm^{-2}$). The temperature of the CD solution increases by 25 °C at 8 minutes, making it an ideal material for imaging and cancer thermal ablation. Within 1 minute of the injection, a strong NIR-II emission signal appeared in the mouse kidney, and 6 hours after the injection, the CDs can be quickly eliminated from the mouse kidney.

10.1.5 Others

10.1.5.1 Photothermal-responsive Oil/Water Separation

Oil-contaminated wastewater, especially when stabilized by surfactants, threatens our environment and health. For nanoemulsions stabilized by surfactants, conventional separation methods become ineffective due to their nanometer-scale droplets and extremely high stability.[23] In the petrochemical, food, and pesticide industries, emulsified nano-oil/water mixtures or nano-emulsions are often encountered in the particle size range of 2–200 nm. Due to its very stable properties, there is usually a trade-off between throughput and selectivity.

According to the Hagen–Poiseuille equation, an ideal membrane with an ultra-thin selective separation layer and a maintained effective pore size is advantageous. $J = \varepsilon r^2 \Delta p / 8\mu L$ (where J is the flux of liquid passing through the membrane, ε is the surface porosity, r is the effective pore radius, Δp is the pressure, μ is the liquid viscosity, and L is the thickness of the membrane).[24] In order to better separate emulsions, Liang Hu *et al.*[25] reported an ultra-thin film with light modulated aperture. The film is composed of gold nanorod (ANR)/poly(*N*-isopropylacrylamide/acrylamide) (pNIPAm-*co*-AAm) hybrid ultra-thin single-walled carbon nanotubes (SWCNT) (see Figure 10.4). Ultra-fast separation of an O/W nanoemulsion can be switched by laser irradiation. pNIPAm-*co*-AAm makes the ultra-thin SWCNT network membrane hydrophilic and has ultra-fast separation and potential antifouling properties. The copolymer of PNIPAm is used to achieve the reversible

Figure 10.4 Preparation of a photothermal responsive gold nanorod (ANR)/poly(*N*-isopropylacrylamide-acrylamide) (pNIPAm-*co*-AAm) hybrid ultra-thin film. SWCNT is used to indicate single-walled carbon nanotubes. Reproduced from ref. 25 with permission from American Chemical Society, Copyright 2015.

transformation of the thermally-induced concept, resulting in an adjustable pore radius. The ANR is anchored in the membrane to achieve uninterrupted and remote-controlled pore size.

In their work, a series of O/W nano-emulsions, including *n*-hexadecane-sodium dodecyl sulfate (SDS) stabilized nano-emulsion (H/W), are used to test the separation performance of the composite membrane. Once the H/W is filtered through the membrane, a transparent liquid with a droplet size of less than 5 nm can be collected in the filtrate. The principle of separation is that when H/W emulsion droplets contact the membrane, *n*-hexadecane is basically repelled due to the oleophobicity under water. The nano-sized pore radius hinders the penetration of H/W micelles into the membrane. When water passes through the membrane, the H/W micelles decompose at the same time due to the imbalance of the oil/water/emulsifier phase, leaving *n*-hexadecane above the membrane. The droplet size in the combined filtrate is consistent with the size of the SDS micelles in the water, indicating that a small amount of emulsifier has penetrated the membrane during this process.

They next moved to study how light beams influence the permeation flux, or *J*, using a smaller vacuum filtration system under 0.015 MPa. With increasing illumination time, relative flux of the membrane increases to 2.22 (0.12). The enhanced J for the cohybrid membrane under light illumination can be mainly due to the change in r.

10.1.5.2 Photothermal Reusable and Recyclable Mask

The new coronavirus (COVID-19) pandemic that broke out at the end of 2019 mainly relies on droplets to spread to the human respiratory tract and cause

infection. However, the current general surgical masks cannot be reused through self-sterilization or simple sterilization, causing major economic and environmental problems to the society. Based on this, Guijun Li and co-workers developed an innovative method for functional modification of disposable medical masks so that ordinary medical masks have both self-cleaning and photothermal properties (see Figure 10.5). The surface of the original mask with polymer fibers is nano-smooth and has no super-hydrophobic properties. Graphene can be produced at low cost by a laser induction method using commercially available precursors (such as polyimide, SPEEK, and Bakelite).[26] Also, the surface hydrophobicity can be modulated by controlling the laser processing environment.[27]

A graphene protective layer is prepared and deposited on the surface of the low melting point non-woven fabric on the outer layer of the ordinary mask. Studies have shown that the static water contact angle of the nanoporous graphene layer prepared by this method is as high as 140°, and water droplets can bounce off the surface of this hydrophobic material, making it difficult to adhere to the outer layer of the mask (see Figure 10.5B). Moreover, due to its excellent light and heat performance, the surface temperature of the mask can quickly rise to above 90 °C, which can be used

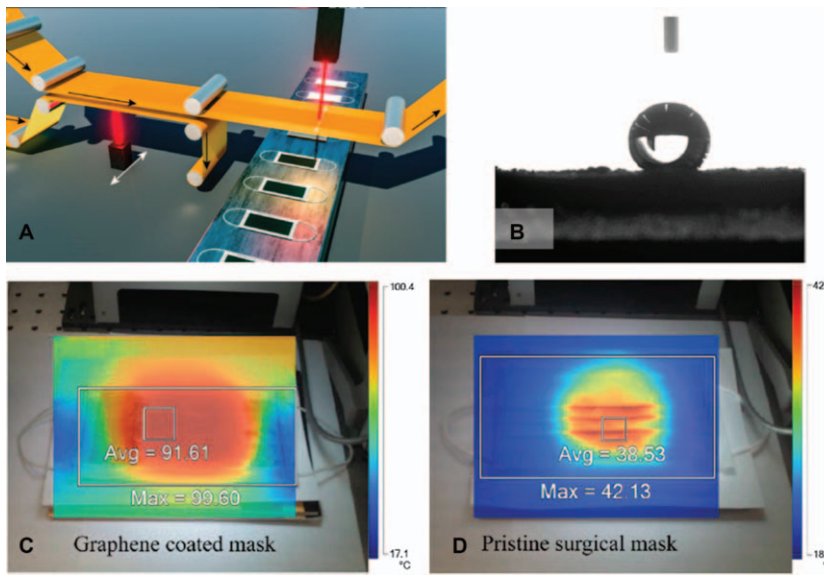

Figure 10.5 (A) Roll-to-roll production of a graphene coated mask. The black arrow indicates the direction of scrolling movement, and the white arrow indicates the direction of laser movement. (B) The contact angle of water droplets on the graphene coated mask after 5 minutes of light exposure. (C) Thermal imaging camera image coated with graphene and (D) original surgical mask.
Reproduced from ref. 28 with permission from American Chemical Society, Copyright 2020.

as a self-sterile coating (see Figure 10.5C), which is much higher than the pristine one (38.5 °C) (see Figure 10.5D) under the sun. This temperature can effectively kill the virus, and the mask after self-disinfection can be worn and used repeatedly. This kind of disposable medical surgical mask functionalized by the dual-mode laser-induced forward transfer method makes up for the three shortcomings of ordinary disposable masks on the market: 1. The hydrophobic surface of the mask will still have residual virus in attached droplets; 2. The melting point of polypropylene non-woven fabric limits the disinfection and reusability of ordinary masks; 3. A large number of discarded masks are difficult to reuse and cause environmental problems.[28]

10.2 Conclusion

In summary, carbon-based materials with excellent light-to-heat conversion ability usually have a rich microporous structure and a large specific surface area. Most of them have the characteristics of broad-spectrum solar absorption, good light absorption stability, high thermal conductivity, biodegradability, and low toxicity, which are beneficial to various summarized applications: photo-thermal catalytic conversion, seawater desalination, photothermal therapy, photoacoustic/fluorescence imaging, *etc.* In addition to converting solar energy into thermal energy, carbon-based materials can also convert solar energy into electrical energy to further assist heating materials; thereby broadening their photothermal conversion performance.

References

1. S.-C. Cai, J.-J. Li, E.-Q. Yu, X. Chen, J. Chen and H.-P. Jia, *ACS Appl. Nano Mater.*, 2018, **1**, 6368–6377.
2. Y. Wang, B. Tang and S. Zhang, *Adv. Funct. Mater.*, 2013, **23**, 4354–4360.
3. Y. Wang, L. Zhang and P. Wang, *ACS Sustainable Chem. Eng.*, 2016, **4**, 1223–1230.
4. X. Zheng and L. Zhang, *Energy Environ. Sci.*, 2016, **9**, 2511–2532.
5. J. Long, H. Chang, Q. Gu, J. Xu, L. Fan, S. Wang, Y. Zhou, W. Wei, L. Huang, X. Wang, P. Liu and W. Huang, *Energy Environ. Sci.*, 2014, **7**, 973–977.
6. Z. Shayegan, C.-S. Lee and F. Haghighat, *Chem. Eng. J.*, 2018, **334**, 2408–2439.
7. Y. Sang, Z. Zhao, M. Zhao, P. Hao, Y. Leng and H. Liu, *Adv. Mater.*, 2015, **27**, 363–369.
8. C. Li, F. Wang, J. Zhu and J. C. Yu, *Appl. Catal., B*, 2010, **100**, 433–439.
9. S. Wu and H.-J. Butt, *Adv. Mater.*, 2016, **28**, 1208–1226.
10. L. Wang, X. Li, Z. Li, W. Chu, R. Li, K. Lin, H. Qian, Y. Wang, C. Wu, J. Li, D. Tu, Q. Zhang, L. Song, J. Jiang, X. Chen, Y. Luo, Y. Xie and Y. Xiong, *Adv. Mater.*, 2015, **27**, 5528–5533.
11. Q. Mei, B. Liu, G. Han, R. Liu, M.-Y. Han and Z. Zhang, *Adv. Sci.*, 2019, **6**, 1900855.

12. C. Wang, X. Wu, X. Li, W. Wang, L. Wang, M. Gu and Q. Li, *J. Mater. Chem.*, 2012, **22**, 15522–15525.
13. J.-J. Li, S.-C. Cai, E.-Q. Yu, B. Weng, X. Chen, J. Chen, H.-P. Jia and Y.-J. Xu, *Appl. Catal., B*, 2018, **233**, 260–271.
14. P. Zhang, H. Liu and X. Li, *ACS Sustainable Chem. Eng.*, 2020, **8**, 17979–17987.
15. Z. Zheng, H. Li, X. Zhang, H. Jiang, X. Geng, S. Li, H. Tu, X. Cheng, P. Yang and Y. Wan, *Nano Energy*, 2020, **68**, 104298.
16. W. Du, Y. Chong, X. Hu, Y. Wang, Y. Zhu, J. Chen, X. Li, Q. Zhang, G. Wang and J. Jiang, *Adv. Funct. Mater.*, 2020, **30**, 1908073.
17. W. Sun, X. Zhang, H.-R. Jia, Y.-X. Zhu, Y. Guo, G. Gao, Y.-H. Li and F.-G. Wu, *Small*, 2019, **15**, 1804575.
18. Y. Liu, P. Bhattarai, Z. Dai and X. Chen, *Chem. Soc. Rev.*, 2019, **48**, 2053–2108.
19. J. Russier, L. Oudjedi, M. Piponnier, C. Bussy, M. Prato, K. Kostarelos, B. Lounis, A. Bianco and L. Cognet, *Nanoscale*, 2017, **9**, 4642–4645.
20. J.-W. Kim, E. I. Galanzha, E. V. Shashkov, H.-M. Moon and V. P. Zharov, *Nat. Nanotechnol.*, 2009, **4**, 688–694.
21. X. Wang, C. Wang, L. Cheng, S.-T. Lee and Z. Liu, *J. Am. Chem. Soc.*, 2012, **134**, 7414–7422.
22. Y. Li, G. Bai, S. Zeng and J. Hao, *ACS Appl. Mater. Interfaces*, 2019, **11**, 4737–4744.
23. H. Chi, S. Wang, T. Li and Z. Li, *Chemosphere*, 2021, **263**, 128380.
24. R. W. Baker, *Membrane Technology and Applications*, John Wiley & Sons, 2012.
25. L. Hu, S. Gao, X. Ding, D. Wang, J. Jiang, J. Jin and L. Jiang, *ACS Nano*, 2015, **9**, 4835–4842.
26. G. Li, *J. Appl. Phys.*, 2020, **127**, 010901.
27. Y. Li, D. X. Luong, J. Zhang, Y. R. Tarkunde, C. Kittrell, F. Sargunaraj, Y. Ji, C. J. Arnusch and J. M. Tour, *Adv. Mater.*, 2017, **29**, 1700496.
28. H. Zhong, Z. Zhu, J. Lin, C. F. Cheung, V. L. Lu, F. Yan, C.-Y. Chan and G. Li, *ACS Nano*, 2020, **14**, 6213–6221.

CHAPTER 11

Photothermal Nanomaterials for Oncological Hyperthermia

MINGLIANG YOU,*[a] HOUJUAN ZHU,[b] ZIBIAO LI[b,c] AND ENYI YE[b]

[a] Hangzhou Cancer Institute, Key Laboratory of Clinical Cancer Pharmacology and Toxicology Research of Zhejiang Province, Affiliated Hangzhou Cancer Hospital, Zhejiang University School of Medicine, Hangzhou 310002, China; [b] Institute of Materials Research and Engineering, Agency for Science, Technology & Research, 2 Fusionopolis Way, Singapore 138634, Singapore; [c] Department of Materials Science and Engineering, National University of Singapore, 9 Engineering Drive 1, Singapore 117576, Singapore
*Email: youml@zjhealth.org

11.1 Introduction

Photothermal nanomaterials have the potential to have a tremendous impact on medical applications. On one hand, heat generated by photothermal nanomaterials is one of the main factors to achieving the therapeutic effects.[1] On the other hand, these nanomaterials can be used for diagnosis by tracking cells that facilitate disease diagnoses and measure therapeutic efficacy.[2] In addition, photothermal nanomaterials are commonly applied as delivery vehicles for targeted delivery of drugs to reduce cytotoxicities.[3] However, there are distinct challenges that must be considered in the development and application of these materials, including careful analysis of the distribution and clearance of nanomaterials, as well as the unpredictable off-target effects.[4] By carefully designing materials early in their concept of

Nanoscience & Nanotechnology Series No. 54
Photothermal Nanomaterials
Edited by Enyi Ye and Zibiao Li

Published by the Royal Society of Chemistry, www.rsc.org

proof phase, scientists may be able to find successful approaches through to the clinic more rapidly, which is indeed the ultimate goal of this research area. There are still many unmet needs using the current diagnoses and treatments, and photothermal nanomaterials have the potential to fill that gap for oncological hyperthermia.[5] To successfully translate these promising technologies to clinical application, researchers from different disciplinaries should collaborate to overcome the challenges. Preclinical and clinical testing is necessary to address all these concerns. Eventually, all this dedication will contribute to new diagnoses and therapies.[6,7]

11.2 Recent Development of Photothermal Nanomaterials for Oncological Hyperthermia

Photothermal nanomaterials have been in use for oncological hyperthermia for decades due to their preferential tumor accumulation, the fact that they are monitorable upon application of external light energy, and their minimal invasiveness with better therapeutic effects.[4] Near-infrared (NIR) light-triggered hyperthermia utilizes nanomaterials such as carbon nanotubes, gold nanorods, and graphene oxide sheets to enhance photothermal therapies and target the effect on the tumor.[8] Photothermal nanomaterial-mediated hyperthermia has revealed promising results in numerous preclinical and pilot clinical studies. Not only material scientists but also oncologists look forward to having this new technique in clinical application. Indocyanine green (ICG), an FDA-approved medical contrast agent with excellent photothermal effect upon NIR, has been applied as an effective NIR-absorbing hyperthermia agent for cancer treatment.[9,10] In 1996, photothermal effects using ICG were investigated to address the efficacy of the photothermal interaction for tumor cell destruction in a controllable method using a mouse breast tumor model.[11] In 2011, ICG was assessed for the feasibility to treat metastatic breast cancer in a preliminary safety and efficacy clinical trial.[12] Local injection of ICG and immunoadjuvant (glycated chitosan) for immunological stimulation, followed by 805 nm laser irradiation at a power density of 1 $W\,cm^{-2}$ were performed in 10 patients with advanced-stage metastatic breast cancer. An objective response rate of 62.5% and a clinical benefit response rate of 75% were achieved, while no significant side effects were observed after treatment.[12]

Gold nanoparticles have been utilized in various biomedicinal applications.[13] Colloidal gold nanoparticles possess localized surface plasmon resonance (LSPR), so can absorb light energy, resulting in photothermal properties, rendering them promising for oncological hyperthermia for cancer treatments.[14] The photothermal properties can be enhanced by adjusting the shape, size, and components of the gold nanoparticles.[15] Naomi Halas and Jennifer West invented a technique using gold–silica nanoshells (GSN) which are composed of a silica core and a gold shell with a diameter of 150 nanometers, called AuroLase Therapy.[16] This photothermal nanomaterial

Table 11.1 List of photothermal nanomaterials for oncological hyperthermia in clinical trials.

Nanoparticle type	Indication	Reference
Indocyanine green for selective thermal effect, and immunoadjuvant (glycated chitosan) for immunological stimulation	Late-stage breast cancer (pilot clinical trial)	12
PEG-coated silica–gold nanoshells for near infrared light facilitated thermal ablation	Thermal ablation of solid primary tumors	16
Heat-sensitive liposome that releases doxorubicin	Breast cancer, liver cancer, and other refractor solid tumors	22
Iron-oxide nanoparticle, external radiation source to enhance cell death at the radiation site	Advanced soft tissue sarcoma	23

was designed to absorb energy from NRI light and convert it to heat, resulting in selective hyperthermic cell death without affecting adjacent non-tumorous tissue. The treatment was previously proved to be safe and effective in cell studies and animal models.[17,18] There are a total of 4 clinical trials using this novel therapeutic approach including metastatic lung cancer, head and neck cancer, as well as prostate cancer. In a recently initiated pivotal study, it was proven to be feasible and safe for use in men with low- or intermediate-risk localized prostate cancer using a custom-built MR US fusion guided platform in collaboration with Philips Healthcare.[16] Gold–silica nanoshell-mediated focal laser ablation was successfully achieved in 94% (15/16) of patients, with no significant difference in The International Prostate Symptoms Score (IPSS) and the Sexual Health Inventory for Men (SHIM) observed after treatment.[16]

Despite the enormous amount of nanomaterial research articles published in the oncological field, there is a despondent disbalance between the large number of preclinical nanomaterial papers and relatively small number of nanomedicine drug products applied in clinical settings.[19] In 2016, it was reviewed that 25 Food and Drug Administration (FDA) or European Medicines Agency (EMA) approved nanomedicines and over 45 other nanoparticle technologies were in the clinical trial phase.[20] Until 2019, only two new intravenously administered nanoparticle technologies had been approved by the FDA and EMA.[21] Among the above updates, there have been very limited clinical trials for photothermal nanomaterials for oncological hyperthermia (see Table 11.1).

11.3 Advantages of Photothermal Nanomaterials for Oncological Hyperthermia

Photothermal nanomaterial-mediated oncological hyperthermia has many advantages to overcome the unmet needs for clinical cancer treatment.

Photothermal nanomaterials have been applied to treat tumor metastasis which is the leading cause of cancer-related deaths.[24] Photothermal effects using Arg–Gly–Asp (RGD) peptide-functionalized gold nanorods upon receiving NIR light can target integrins and deregulate their downstream regulators of oral squamous cell carcinoma cells.[25] Considering the critical role of integrins in controlling cell functions, this targeted oncological hyperthermia approach remarkedly affects cell morphology change and cell migration. This strategy provides a potential application for controlling cancer metastasis.[25] There is increasing evidence implying that cancer stem cells (CSCs) account for cancer metastasis and that targeting CSCs therapy is a potential approach to overcome metastasis.[14,26] Paholak and colleagues demonstrated that oncological hyperthermia mediated by polymer-coated highly crystallized iron oxide nanoparticles (HCIONPs) could effectively eliminate breast cancer stem cells in a mouse model.[27] Polymer-coated HCIONPs selectively target epithelial-like $ALDH^+$ breast cancer stem cells compared to mesenchymal-like $CD44^+/CD24^-$ breast cancer stem cells *in vitro* and dramatically inhibited metastasis to the lung and lymph nodes in an *in vivo* model.[27]

Therapeutic resistance is another clinical challenge for cancer treatment.[28] Enhancing therapeutic efficiency through improved drug delivery using photothermal nanomaterials would facilitate treatment of chemoresistant cancers. Gold nanoparticle-modified polylactic acid (PLA) stereocomplex micelles have been proved to synergize chemotherapy with photothermia[29] (see Figure 11.1).

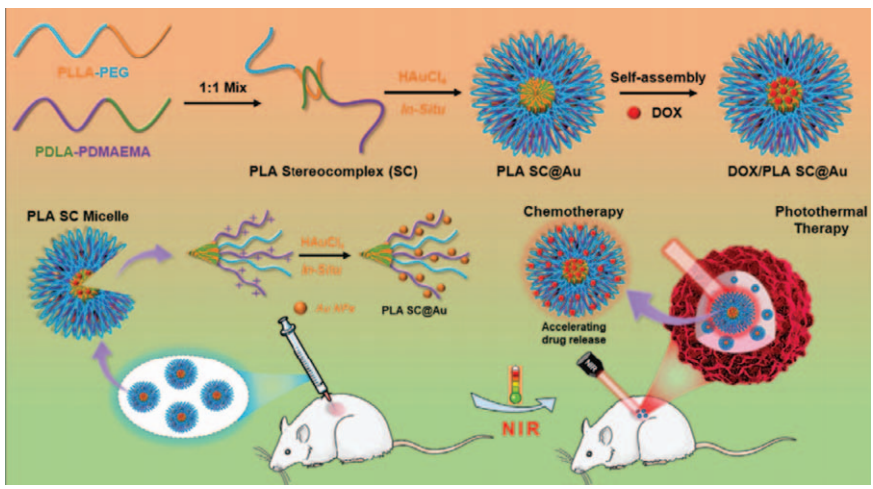

Figure 11.1 Illustration showing the design approach of gold nanoparticle-modified PLA SC micelles (PLA SC@Au) to synergize chemotherapy with photothermia.
Reproduced from ref. 29 with permission from John Wiley and Sons, Copyright © 2021 Wiley-VCH GmbH.

Increasing biological rationale suggests that heat could enhance the effect of radiotherapy in cancer treatment.[30] Li and his colleagues demonstrated a hyperthermia strategy to enhance radiotherapy by decreasing tumor hypoxia and preventing irradiation-induced DNA damage repair which account for radioresistence.[31] In this study, the tumor hyperthermia temperature was well-controlled by an NRI with minimal side effects using PEGylated nanobipyramids (PNBys). PNBys have a narrow longitudinal localized surface plasmon resonance peak in the NIR-II window with a high extinction coefficient (2.0×10^{11} $M^{-1}cm^{-1}$) and an excellent photothermal conversion efficiency (44.2%). PNBys-induced mild hyperthermia (MHt) prior to radiotherapy enables vessel dilation, blood perfusion, and hypoxia relief, resulting in an increased susceptibility of tumor cell response to radiotherapy. On the other hand, MHt after radiotherapy inhibits the repair of DNA damage generated by irradiation. The PNBys exert hierarchically superior antitumor effects by the combination of MHt pre- and post-radiotherapy in a murine mammary tumor model.[31]

The increasing anti-tumor immunotherapies have made dramatic progress in clinical application.[32] However, single immunotherapy is not effective for all anti-tumor treatments, owing to the low objective response rate and the risk of immune-related side effects.[33] Combining photothermal therapy with immunotherapy overcomes the issue that a single photothermal therapy cannot eradicate tumors with metastasis and recurrence.[34] It has been suggested that photothermal therapy improves the therapeutic effect of immunotherapy by promoting the release of tumor-related antigens, triggering an immune response *via* immunogenic cell death (ICD).[35] Novel photothermal nanomaterials possess unique properties to stimulate an immune response to increase the therapeutic effect in cancer treatment.[36] Palladium nanosheets (Pd NSs) have been applied as the carriers of immunoadjuvant cytosine–phosphate–guanine oligodeoxynucleotides (CpG ODNs), which are recognized by Toll-like receptor 9 (TLR9) in the endosomes of antigen-presenting cells (APCs), have potent immunostimulatory activities, and have become a promising immunotherapeutic agent for treating cancer. Pd(5)–CpG(PS) could significantly increase the uptake of CpG by immune cells and enhance the immunostimulatory activity of CpG. This novel bifunctional photothermal nanomaterial inspires scientists to utilize photothermal nanomaterials for a safer and more efficient cancer hyperthermia combined immunotherapy.[36] Another study investigated an appropriate mixture using hexapod-like structured DNA (hexapodna) with CpG sequences and gold nanoparticles, resulting in the formation of composite-type gold nanoparticle–DNA hydrogels.[37] Laser irradiation of the hydrogel resulted in the release of hexapodna, which efficiently stimulated immune cells to release proinflammatory cytokines. Moreover, the treatment significantly retarded the tumor growth and extended the survival of the tumor-bearing mice.[37]

The integration of oncological hyperthermia with imaging guiding in a nanoparticle system is considered to have remarkable potential for cancer therapy. In 2020, ICG-conjugated and radionuclide iodine-125 (^{125}I)-labeled

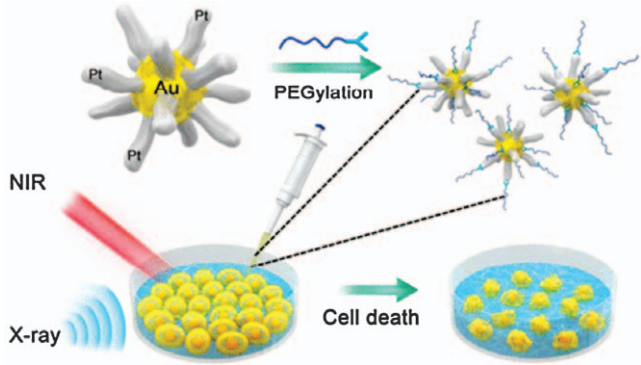

Figure 11.2 Illustration showing the design approach of PEGylated Au@Pt nanodendrites (NDs) to achieve imaging-guided photothermal/radio-therapy. Reproduced from ref. 38 with permission from American Chemical Society, Copyright 2017.

polymeric micelles (PEG-PTyr(^{125}I)-ICG PMs) were investigated as a non-invasive imaging-guided photothermal therapy in tumors.[38] This study demonstrated that PEG-PTyr(^{125}I)-ICG PMs had favorable biocompatibility, excellent stability, high light-heat conversion efficiency, tumor-targeting ability, and a fluorescence imaging property after tail intravenous injection. Upon 808 nm NRI light stimulation, tumor size is significantly shrunk by photothermal therapy with negligible side effects. Liu and colleagues designed PEGylated Au@Pt nanodendrites (NDs) as a unique X-ray computed tomography (CT) and photothermal/radio-therapy enhanced theranostic platform for cancer therapy.[38] The combination of Au@Pt ND-enhanced radiotherapy with photothermal therapy had a synergistic effect to suppress cancer cell growth more efficiently than that in other groups. More importantly, the Au@Pt NDs possess enhanced CT imaging signals that facilitate precision photothermal therapy[38] (see Figure 11.2).

11.4 Challenges in Photothermal Nanomaterials for Oncological Hyperthermia

The majority of nanomaterials possess passive accumulation *via* the enhanced permeability and retention (EPR) effect or active targeting to cellular receptors in solid tumors.[39] Although the EPR effect has been postulated to carry the nanoparticles and spread inside the cancer tissue, only a small percentage of the total administered nanoparticle dose is usually able to reach a solid tumor.[40] Physicochemical properties including its size, charge, pH, and hydrophobicity can dramatically affect its distribution and retention in tumor tissue. Meanwhile, more attention should be paid to investigate how their stability in the blood and tumor, cancer cell uptake, and cytotoxicity contribute to efficacy once the nanoparticle has reached the tumor's interstitial space.[41] A recent study revealed an elaborated nanosystem to

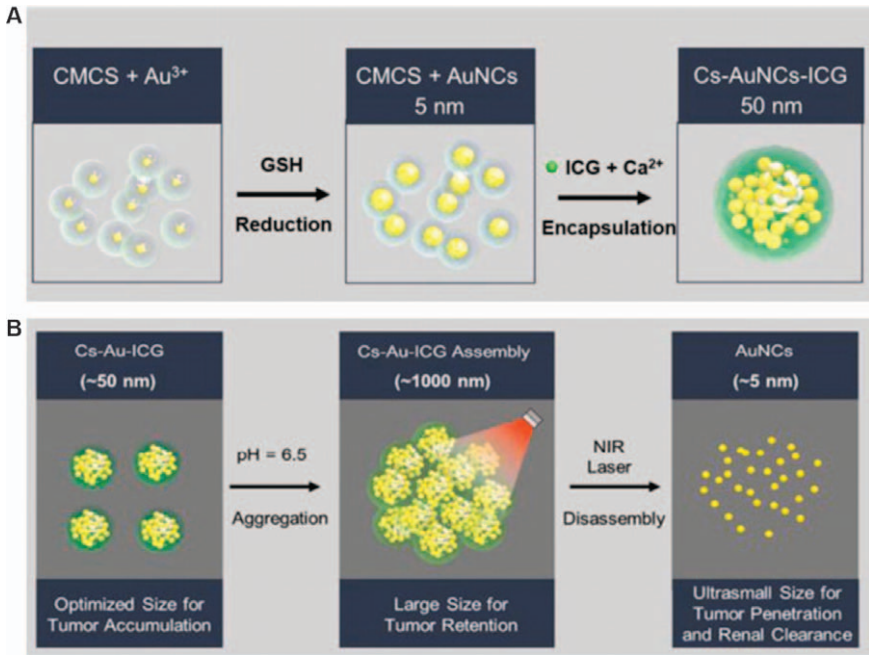

Figure 11.3 Multistage-responsive clustered nanosystem to improve tumor accumulation and penetration. (A) Schematic illustration for the formation of Cs–Au-ICG NPs. (B) Size change of Cs–Au-ICG NPs upon different pH and photothermal conditions.
Reproduced from ref. 42 with permission from Elsevier, Copyright 2021.

adjust particle size upon pH and photothermal effects, which facilitated tumor accumulation, retention, as well as penetration and renal clearance[42] (see Figure 11.3). More specifically, this size-tunable nanosystem contains carboxymethyl chitosan (CS) modified Au nanoparticles which encapculate indocyanine green (ICG) to achieve multi-functionality for applications such as photothermal therapy, radiotherapy, and photoacoustic and fluorescence imaging. Interestingly, such nanoparticles can first aggregate in the tumor around 50 nm taking advantage of the EPR effect to accumulate in the tumor. Then, these pH-responsive nanoparticles undergo acid-triggered aggregation to form large-sized aggregates (around 1000 nm) in the tumor under the acidic microenvironment (pH 5.5) and achieve great tumor retention. Finally, photothermal treatment was performed, and more Cs–Au–ICG NPs could penetrate into the tumor after the photothermal treatment. By combining the PTT and radiotherapy, excellent tumor inhibiting efficacy was found in the breast tumor-bearing mice model, showing excellent potential in clinical tumor therapy applications.

The clearance of nanomaterials by the mononuclear phagocyte system (MPS) from blood leads to high liver and spleen uptake and negatively impacts their therapeutic effect. Thakur and colleagues investigated the

nanomaterial–MPS interactions by evaluating the different shapes of nanomaterials including Au nanorings, Au nanospheres, and Au nanoplates of similar size. They found that Au nanorings achieved the lowest MPS uptake and highest tumor accumulation. Especially, Au nanorings with a size of 50 nm exhibited the highest tumor accumulation. Thus, optimized engineering of the shape, surface area, and size of gold nanostructures is critical in managing nanomaterial–MPS interactions and enhancing nanomaterial accumulation in the tumor.[43]

Laser devices are indispensable components for clinical application of PTT therapies, because they not only execute thermal ablation by heating tumor tissue but also stimulate photothermal nanomaterials to achieve more precise treatment. The US Food and Drug Administration (FDA) approved two devices involving MRI guidance for the stereotactic laser ablation of high-grade glioma using Visualase Thermal Therapy® (150 W, 980 nm laser) and a NeuroBlate® laser ablation system (12 W, 1064 nm laser). These devices may reduce the complexity of PTT therapies. For example, laser treatment has already been used as a safe and effective approach for several solid tumors, such as in the liver and prostate tumors, under magnetic resonance imaging (MRI) guidance.[44] Recently, many novel photothermal nanomaterials with excellent photothermal property upon the second NIR biowindow (NIR-II, 1000–1700 nm) with less absorbance and scattering by skin, and deep tissue penetration, have recently received increasing attention for oncological hyperthermia.[45]

11.5 Safety and Toxicity of Photothermal Nanomaterials

Despite the promising properties and therapeutic potential demonstrated by the approaches based on hyperthermia mediated by nanomaterials, their translation into the clinic has still been poorly investigated. A major concern related to biomedical applications of photothermal nanomaterials is long-term safety and toxicity.[46,47]

To date, a majority of the toxicology studies have focused on the assessment of cell viability or cell death using 2D cell culture. Typically, researchers tend to investigate the efficacy of nanoparticle-based oncological hyperthermia in preclinical studies using *in vitro* 2D cell cultures, but this method cannot completely mimic the complex tumor organization, bioactivity, and physiology that all control the complex penetration depth, biodistribution, and tissue diffusion parameters of nanomaterials *in vivo*.[48] However, animal models are expensive and time-consuming operations for researchers. New *in vitro* and *in vivo* models for safety and toxicity evaluation must be the next research topic for biomedical application of photothermal nanomaterials, such as the *in vitro* organoids model, which is beneficial for evaluating nanomaterial therapies and toxicity prior to *in vivo* study.[49,50] Organoids recapitulate the three-dimensional organization of human

organs, such as the kidney[51] and liver,[52] which is important in detoxifying the organs of human beings. Astashkina and colleagues used a kidney organoids proximal tubule model to measure *in vitro* toxicity of the hydroxylated generation-5 PAMAM dendrimer (G5-OH) compared to *in vivo* rodent nephrotoxicity. PAMAM nanoparticle dendrimers elicit *in vivo*-relevant kidney biomarkers and cell viability in a 3D kidney organoid culture that closely reflects toxicity markers reported *in vivo* in rodent nephrotoxicity models.[51] To fill this knowledge gap, 3D culture systems have been explored for PTT analysis. These models provide more realistic microenvironments that allow spatiotemporal oxygen gradients and cancer cell adaptations to be considered. McCarthy and colleagues applied colorectal tumor organoids to evaluate semiconducting polymer nanoparticles for oncological hyperthermia.[53] Park and his group conducted systemic assessments on the toxicity of silicon dioxide (SiO_2) and titanium dioxide (TiO_2) nanoparticles using human colon organoids and an animal model.[54] Interestingly, they found more than 2000 $mg\,kg^{-1}$ LD50 values for both the SiO_2 and TiO_2 nanoparticles in an *in vivo* acute oral toxicity test, but induced cytotoxicity in 2D cells and 3D colon organoids was found at relatively low concentrations. The data suggest that toxicity results may vary between *in vivo* and *in vitro* tests.

Most toxicity evaluations measure cell viability and cell death for the detection of plasma membrane integrity or mitochondrial function or assessment of cellular morphology. However, increasing evidence implies that various toxic effects of photothermal nanomaterials, including ROS generation, DNA damage, lysosomal damage, mitochondrial dysfunction, and cell apoptosis or necrosis exist. The cytotoxic effects of photothermal nanomaterials can be influenced by specific programmed cell death, such as apoptosis, autophagic cell death and regulated necrosis.[55] Researchers need not only to consider whether cells are dead or alive but also to assess which of the numerous, highly specific pathways of cell death might be involved. Technically, most nanoparticles are absorbed from the blood by the reticuloendothelial system and accumulate predominately in the liver and spleen after intravenous infusion. Increasing attention should also be paid to the potential for unexpected hazardous effects of these nanomaterials considering their translational application in the future.

The nanoscale size of nanomaterials facilitates them to achieve targeted drug delivery and passive tumor accumulation, which increase the therapeutic efficacy and reduce side-effects.[56] However, this nanoscale size may be a double-edged sword. The small size may enable nanoparticles to negotiate various biological barriers in the body which could, in turn, give rise to unexpected toxicities.[57] Compared to larger-sized Pd nanosheets, smaller-sized Pd nanosheets exhibit more advanced photoacoustic imaging and photothermal effects upon ultralow laser irradiation. Moreover, *in vivo* results indicated that 5 nm Pd nanosheets escape from the reticuloendothelial system with a longer blood half-life and can be cleared by renal excretion, while Pd nanosheets with larger sizes mainly accumulate in the liver and spleen. 30 nm Pd nanosheets exhibited the highest tumor accumulation.

Although Pd nanosheets did not cause any appreciable toxicity at the cellular level, we observed slight lipid accumulation in the liver and inflammation in the spleen. Genomic gene expression analysis showed that 80 nm Pd nanosheets interacted with more cellular components and affected more biological processes in the liver, as compared to 5 nm Pd nanosheets. We believe this work will provide valuable information and insights into the clinical application of 2D Pd nanosheets as nanomedicines.[58]

New insights and developments in nanomaterials science continue to push nanomaterial-enhanced PTT forward toward clinical application. However, much work must still be done before this can happen. New comparative studies between the various nanosystems can help to elucidate the optimal treatment regimen, and new biocompatibility studies can help to determine what qualifies as safe and appropriate usage of these materials. In addition, many materials have been developed that have expanded the functional tools available for cancer therapy, yet their biological properties, particularly regarding toxicity and fate after injection, are poorly understood. Until these materials have been proven to clear after treatment with no adverse effects, it is unlikely that they will see clinical application. With future studies, however, it is likely that the capabilities of nanomaterials to enhance cancer therapy will continue to improve. Many of the pre-clinical results of nanomaterial-enhanced PTT have demonstrated strong prospects to present new, low side-effect treatment options for patients in the future.[8]

11.6 Conclusions and Future Prospects

Cancer is still one of the leading causes of death worldwide. Photothermal nanomaterials with unique physicochemical properties have huge potential to address the unmet clinical needs of cancer treatments. Currently, oncological hyperthermia using photothermal nanomaterials is still a beta version, a long way from meeting the requirement of the FDA or other administrations in other countries. Afterall, safety is the top priority for drug and therapy development. However, more attention should be focused on investigating nanomaterial exposure to health hazards. Actually, it is encouraged to evaluate the potential toxic effects and find out the related properties that are responsible for toxicity at the beginning of research and development of any photothermal nanomaterials. The current understanding of nanotoxicity is insufficient relative to the rate of their emission in the environment and the lack of predictive platforms that mimic human physiology. This calls for the development of more physiologically relevant models, which permit the comprehensive and systematic examination of toxic properties of nanoparticles. The most recent organ-on-a-chip models to recapitulate *in vivo*-like microenvironments and responses offer a new avenue for nanotoxicological research. Additionally, it is crucial to clarify the molecular mechanisms of photothermal nanomaterial-induced cytotoxicity.

References

1. J. Chen, C. Ning, Z. Zhou, P. Yu, Y. Zhu, G. Tan and C. Mao, *Prog. Mater. Sci.*, 2019, **99**, 1–26.
2. G. Wang, Z. Li, X. Luo, R. Yue, Y. Shen and N. Ma, *Nanoscale*, 2018, **10**, 16508–16520.
3. L. Zhao, Y. Liu, R. Chang, R. Xing and X. Yan, *Adv. Funct. Mater.*, 2019, **29**, 1806877.
4. D. de Melo-Diogo, C. Pais-Silva, D. R. Dias, A. F. Moreira and I. J. Correia, *Adv. Healthc. Mater.*, 2017, **6**, 1700073.
5. C.-W. Chen, P.-H. Lee, Y.-C. Chan, M. Hsiao, C.-H. Chen, P. C. Wu, P. R. Wu, D. P. Tsai, D. Tu and X. Chen, *J. Mater. Chem. B*, 2015, **3**, 8293–8302.
6. E. Lavik and H. von Recum, *ACS Nano*, 2011, **5**, 3419–3424.
7. J. Pellico, P. J. Gawne and R. T. de Rosales, *Chem. Soc. Rev.*, 2021, **50**, 3355–3423.
8. A. C. Doughty, A. R. Hoover, E. Layton, C. K. Murray, E. W. Howard and W. R. Chen, *Materials*, 2019, **12**, 779.
9. C. Shirata, J. Kaneko, Y. Inagaki, T. Kokudo, M. Sato, S. Kiritani, N. Akamatsu, J. Arita, Y. Sakamoto and K. Hasegawa, *Sci. Rep.*, 2017, **7**, 1–8.
10. Y. Tang and A. J. McGoron, *Int. J. Hyperthermia*, 2013, **29**, 145–155.
11. W. R. Chen, R. L. Adams, A. K. Higgins, K. E. Bartels and R. E. Nordquist, *Cancer Lett.*, 1996, **98**, 169–173.
12. X. Li, G. L. Ferrel, M. C. Guerra, T. Hode, J. A. Lunn, O. Adalsteinsson, R. E. Nordquist, H. Liu and W. R. Chen, *Photochem. Photobiol. Sci.*, 2011, **10**, 817–821.
13. D. A. Giljohann, D. S. Seferos, W. L. Daniel, M. D. Massich, P. C. Patel and C. A. Mirkin, *Angew. Chem., Int. Ed.*, 2010, **49**, 3280–3294.
14. W. Qin, G. Huang, Z. Chen and Y. Zhang, *Front. Pharmacol.*, 2017, **8**, 1.
15. J. B. Vines, J.-H. Yoon, N.-E. Ryu, D.-J. Lim and H. Park, *Front. Chem.*, 2019, **7**, 167.
16. A. R. Rastinehad, H. Anastos, E. Wajswol, J. S. Winoker, J. P. Sfakianos, S. K. Doppalapudi, M. R. Carrick, C. J. Knauer, B. Taouli and S. C. Lewis, *Proc. Natl. Acad. Sci.*, 2019, **116**, 18590–18596.
17. S. C. Gad, K. L. Sharp, C. Montgomery, J. D. Payne and G. P. Goodrich, *Int. J. Toxicol.*, 2012, **31**, 584–594.
18. J. M. Stern, V. V. Kibanov Solomonov, E. Sazykina, J. A. Schwartz, S. C. Gad and G. P. Goodrich, *Int. J. Toxicol.*, 2016, **35**, 38–46.
19. Y. Shi, R. Van der Meel, X. Chen and T. Lammers, *Theranostics*, 2020, **10**, 7921.
20. A. C. Anselmo and S. Mitragotri, *Bioeng. Transl. Med.*, 2016, **1**, 10–29.
21. A. C. Anselmo and S. Mitragotri, *Bioeng. Transl. Med.*, 2019, **4**, e10143.
22. W. Y. Tak, S.-M. Lin, Y. Wang, J. Zheng, A. Vecchione, S. Y. Park, M. H. Chen, S. Wong, R. Xu and C.-Y. Peng, *Clin. Cancer Res.*, 2018, **24**, 73–83.
23. S. Bonvalot, P. L. Rutkowski, J. Thariat, S. Carrère, A. Ducassou, M.-P. Sunyach, P. Agoston, A. Hong, A. Mervoyer and M. Rastrelli, *Lancet Oncol.*, 2019, **20**, 1148–1159.

24. L. Zou, H. Wang, B. He, L. Zeng, T. Tan, H. Cao, X. He, Z. Zhang, S. Guo and Y. Li, *Theranostics*, 2016, **6**, 762.
25. M. R. Ali, Y. Wu, Y. Tang, H. Xiao, K. Chen, T. Han, N. Fang, R. Wu and M. A. El-Sayed, *Proc. Natl. Acad. Sci.*, 2017, **114**, E5655–E5663.
26. F. Asghari, R. Khademi, F. E. Ranjbar, Z. V. Malekshahi and R. F. Majidi, *Int. J. Stem Cells*, 2019, **12**, 227.
27. H. J. Paholak, N. O. Stevers, H. Chen, J. P. Burnett, M. He, H. Korkaya, S. P. McDermott, Y. Deol, S. G. Clouthier and T. Luther, *Biomaterials*, 2016, **104**, 145–157.
28. C. E. Eyler and J. N. Rich, *J. Clin. Oncol.: Off. J. Am. J. Clin. Oncol.*, 2008, **26**, 2839.
29. X. Fan, Z. Luo, E. Ye, M. You, M. Liu, Y. Yun, X. J. Loh, Y.-L. Wu and Z. Li, *Macromol. Biosci.*, 2021, e2100062.
30. J. C. Peeken, P. Vaupel and S. E. Combs, *Front. Oncol.*, 2017, **7**, 132.
31. Q. Li, L. Hang, W. Jiang, J. Dou, L. Xiao, X. Tang, Y. Yao and Y. Wang, *Biomaterials*, 2020, **257**, 120235.
32. J. D. Martin, H. Cabral, T. Stylianopoulos and R. K. Jain, *Nat. Rev. Clin. Oncol.*, 2020, **17**, 251–266.
33. M. S. Goldberg, *Nat. Rev. Cancer*, 2019, **19**, 587–602.
34. Y. Liu, B. M. Crawford and T. Vo-Dinh, *Immunotherapy*, 2018, **10**, 1175–1188.
35. T. Shang, X. Yu, S. Han and B. Yang, *Biomater. Sci.*, 2020, **8**, 5241–5259.
36. J. Ming, J. Zhang, Y. Shi, W. Yang, J. Li, D. Sun, S. Xiang, X. Chen, L. Chen and N. Zheng, *Nanoscale*, 2020, **12**, 3916–3930.
37. T. Yata, Y. Takahashi, M. Tan, H. Nakatsuji, S. Ohtsuki, T. Murakami, H. Imahori, Y. Umeki, T. Shiomi and Y. Takakura, *Biomaterials*, 2017, **146**, 136–145.
38. X. Liu, X. Zhang, M. Zhu, G. Lin, J. Liu, Z. Zhou, X. Tian and Y. Pan, *ACS Appl. Mater. Interfaces*, 2017, **9**, 279–285.
39. S. Hirsjarvi, C. Passirani and J.-P. Benoit, *Curr. Drug Discovery Technol.*, 2011, **8**, 188–196.
40. H. Maeda, *Adv. Drug Delivery Rev.*, 2015, **91**, 3–6.
41. S. Wilhelm, A. J. Tavares, Q. Dai, S. Ohta, J. Audet, H. F. Dvorak and W. C. Chan, *Nat. Rev. Mater.*, 2016, **1**, 1–12.
42. S. Hua, J. He, F. Zhang, J. Yu, W. Zhang, L. Gao, Y. Li and M. Zhou, *Biomaterials*, 2021, **268**, 120590.
43. Y. Liu, Z. Wang, Y. Liu, G. Zhu, O. Jacobson, X. Fu, R. Bai, X. Lin, N. Lu and X. Yang, *ACS Nano*, 2017, **11**, 10539–10548.
44. T. J. Vogl, R. Straub, K. Eichler, O. Söllner and M. G. Mack, *Radiology*, 2004, **230**, 450–458.
45. L. Dong, K. Li, D. Wen, X. Gao, J. Feng and H. Zhang, *Small*, 2020, **16**, 2003508.
46. J. Wolfram, M. Zhu, Y. Yang, J. Shen, E. Gentile, D. Paolino, M. Fresta, G. Nie, C. Chen and H. Shen, *Curr. Drug Targets*, 2015, **16**, 1671–1681.
47. X. Liu, I. Tang, Z. A. Wainberg and H. Meng, *Small*, 2020, **16**, 2000673.

48. E. Darrigues, Z. A. Nima, R. J. Griffin, J. M. Anderson, A. S. Biris and A. Rodriguez, *Nanoscale Horiz.*, 2020, **5**, 400–430.
49. A. Dominijanni, A. Mazzocchi, E. Shelkey, S. Forsythe, M. Devarsetty and S. Soker, *Curr. Opin. Biomed. Eng.*, 2020, **13**, 168–173.
50. R. X. Z. Lu and M. Radisic, *Bioact. Mater.*, 2021, **6**, 2801–2819.
51. A. I. Astashkina, C. F. Jones, G. Thiagarajan, K. Kurtzeborn, H. Ghandehari, B. D. Brooks and D. W. Grainger, *Biomaterials*, 2014, **35**, 6323–6331.
52. G. Mekky, M. Seeds, A. E. A. Diab, A. M. Shehata, O. A. H. Ahmed-Farid, D. Alzebdeh, C. Bishop and A. Atala, *J. Biochem. Mol. Toxicol.*, 2020, e22676.
53. B. McCarthy, A. Cudykier, R. Singh, N. Levi-Polyachenko and S. Soker, *Sci. Rep.*, 2021, **11**, 1–12.
54. S. B. Park, W. H. Jung, K. Y. Kim and B. Koh, *Molecules*, 2020, **25**, 3594.
55. F. T. Andón and B. Fadeel, *Acc. Chem. Res.*, 2013, **46**, 733–742.
56. G. Oberdörster, *J. Intern. Med.*, 2010, **267**, 89–105.
57. A. M. Nyström and B. Fadeel, *J. Controlled Release*, 2012, **161**, 403–408.
58. M. Chen, S. Chen, C. He, S. Mo, X. Wang, G. Liu and N. Zheng, *Nano Res.*, 2017, **10**, 1234–1248.

Subject Index